SERIES IN OPTICS AND OPTOELECTRONICS

Handbook of Optoelectronic Device Modeling & Simulation

Lasers, Modulators, Photodetectors, Solar Cells, and Numerical Methods

Volume II

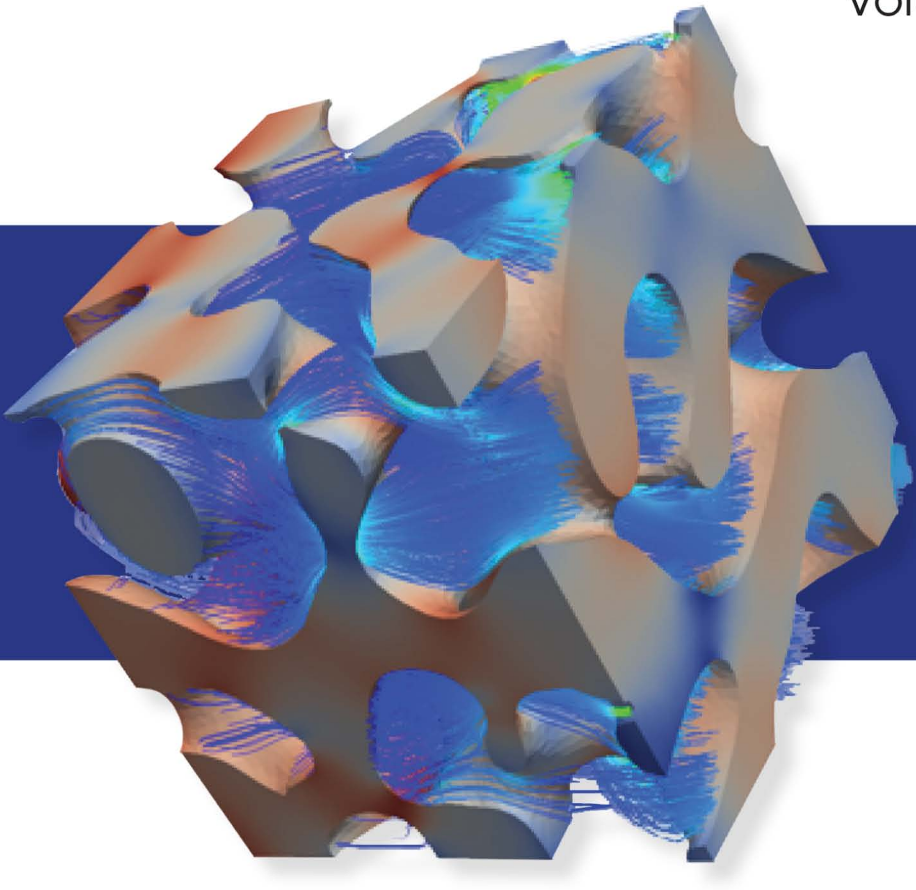

Edited by

Joachim Piprek

CRC Press
Taylor & Francis Group

Handbook of Optoelectronic Device Modeling and Simulation

Series in Optics and Optoelectronics

Series Editors: **Robert G W Brown**
University of California, Irvine, USA

E Roy Pike
Kings College, London, UK

Recent titles in the series

Optical MEMS, Nanophotonics, and Their Applications
Guangya Zhou and Vincent C. Lee (Eds.)

Optical Microring Resonators: Theory, Techniques, and Applications
Vien Van

Thin-Film Optical Filters, Fifth Edition
H. Angus Macleod

Handbook of Optoelectronics, Second Edition: Concepts, Devices, and Techniques – Volume One
John P. Dakin and Robert Brown (Eds.)

Handbook of Optoelectronics, Second Edition: Enabling Technologies – Volume Two
John P. Dakin and Robert Brown (Eds.)

Handbook of Optoelectronics, Second Edition: Applied Optical Electronics – Volume Three
John P. Dakin and Robert Brown (Eds.)

Handbook of GaN Semiconductor Materials and Devices
Wengang (Wayne) Bi, Hao-chung (Henry) Kuo, Pei-Cheng Ku, and Bo Shen (Eds.)

Handbook of Optoelectronic Device Modeling and Simulation: Fundamentals, Materials, Nanostructures, LEDs, and Amplifiers – Volume One
Joachim Piprek (Ed.)

Handbook of Optoelectronic Device Modeling and Simulation: Lasers, Modulators, Photodetectors, Solar Cells, and Numerical Methods – Volume Two
Joachim Piprek (Ed.)

Nanophotonics and Plasmonics: An Integrated View
Dr. Ching Eng (Jason) Png and Dr. Yuriy Akimov

Handbook of Solid-State Lighting and LEDs
Zhe Chuan Feng (Ed.)

Optical Compressive Imaging
Adrian Stern

Singular Optics
Gregory J. Gbur

Handbook of Optoelectronic Device Modeling and Simulation

Lasers, Modulators, Photodetectors, Solar Cells, and Numerical Methods

VOLUME TWO

Edited by

Joachim Piprek

CRC Press
Taylor & Francis Group
Boca Raton London New York

CRC Press is an imprint of the
Taylor & Francis Group, an **informa** business

MATLAB® is a trademark of The MathWorks, Inc. and is used with permission. The MathWorks does not warrant the accuracy of the text or exercises in this book. This book's use or discussion of MATLAB software or related products does not constitute endorsement or sponsorship by The MathWorks of a particular pedagogical approach or particular use of the MATLAB software.

CRC Press
Taylor & Francis Group
6000 Broken Sound Parkway NW, Suite 300
Boca Raton, FL 33487-2742

© 2018 by Taylor & Francis Group, LLC

CRC Press is an imprint of Taylor & Francis Group, an Informa business

No claim to original U.S. Government works

Printed on acid-free paper

International Standard Book Number-13: 978-1-4987-4956-5 (Hardback)

This book contains information obtained from authentic and highly regarded sources. Reasonable efforts have been made to publish reliable data and information, but the author and publisher cannot assume responsibility for the validity of all materials or the consequences of their use. The authors and publishers have attempted to trace the copyright holders of all material reproduced in this publication and apologize to copyright holders if permission to publish in this form has not been obtained. If any copyright material has not been acknowledged please write and let us know so we may rectify in any future reprint.

Except as permitted under U.S. Copyright Law, no part of this book may be reprinted, reproduced, transmitted, or utilized in any form by any electronic, mechanical, or other means, now known or hereafter invented, including photocopying, microfilming, and recording, or in any information storage or retrieval system, without written permission from the publishers.

For permission to photocopy or use material electronically from this work, please access www.copyright.com (http://www.copyright.com/) or contact the Copyright Clearance Center, Inc. (CCC), 222 Rosewood Drive, Danvers, MA 01923, 978-750-8400. CCC is a not-for-profit organization that provides licenses and registration for a variety of users. For organizations that have been granted a photocopy license by the CCC, a separate system of payment has been arranged.

Trademark Notice: Product or corporate names may be trademarks or registered trademarks, and are used only for identification and explanation without intent to infringe.

Library of Congress Cataloging-in-Publication Data

Names: Piprek, Joachim, editor.
Title: Handbook of optoelectronic device modeling and simulation / edited by Joachim Piprek.
Other titles: Series in optics and optoelectronics (CRC Press) ; 27.
Description: Boca Raton, FL : CRC Press, Taylor & Francis Group, [2017] |
Series: Series in optics and optoelectronics ; 27 | Includes bibliographical references and index.
Contents: volume 1. Fundamentals, materials, nanostructures, LEDS, and amplifiers – volume 2.
Lasers, modulators, photodetectors, solar cells, and numerical methods.
Identifiers: LCCN 2016058063 | ISBN 9781498749466 (v. 1; hardback ; alk. paper) |
ISBN 1498749461 (v. 1; hardback ; alk. paper) | ISBN 9781498749565 (v. 2 ; hardback ; alk. paper) |
ISBN 1498749569 (v. 2 ; hardback ; alk. paper)
Subjects: LCSH: Optoelectronic devices–Mathematical models–Handbooks, manuals, etc. |
Optoelectronic devices–Simulation methods–Handbooks, manuals, etc. |
Semiconductors–Handbooks, manuals, etc. | Nanostructures–Handbooks, manuals, etc.
Classification: LCC TK8304 .H343 2017 | DDC 621.381/045011–dc23
LC record available at https://lccn.loc.gov/2016058063

Visit the Taylor & Francis Web site at
http://www.taylorandfrancis.com

and the CRC Press Web site at
http://www.crcpress.com

Contents

PART VI Laser Diodes

PART VII Photodetectors and Modulators

PART VIII Solar Cells

PART IX Novel Applications

PART X Mathematical Methods

Series Preface

This international series covers all aspects of theoretical and applied optics and optoelectronics. Active since 1986, eminent authors have long been choosing to publish with this series, and it is now established as a premier forum for high-impact monographs and textbooks. The editors are proud of the breadth and depth showcased by the published works, with levels ranging from advanced undergraduate and graduate student texts to professional references. Topics addressed are both cutting edge and fundamental, basic science and applications-oriented, on subject matter that includes lasers, photonic devices, nonlinear optics, interferometry, waves, crystals, optical materials, biomedical optics, optical tweezers, optical metrology, solid-state lighting, nanophotonics, and silicon photonics. Readers of the series are students, scientists, and engineers working in optics, optoelectronics, and related fields in the industry.

Proposals for new volumes in the series may be directed to Lu Han, senior publishing editor at CRC Press/Taylor & Francis Group (lu.han@taylorandfrancis.com).

Preface

Optoelectronic devices have become ubiquitous in our daily lives. For example, light-emitting diodes (LEDs) are used in almost all household appliances, in traffic and streetlights, and in full-color displays. Laser diodes, optical modulators, and photodetectors are key components of the Internet. Solar cells are core elements of energy supply systems. Optoelectronic devices are typically based on nanoscale semiconductor structures that utilize the interaction of electrons and photons. The underlying and highly complex physical processes require mathematical models and numerical simulation for device design, analysis, and performance optimization. This handbook gives an introduction to modern optoelectronic devices, models, and simulation methods.

Driven by the expanding diversity of available and envisioned practical applications, mathematical models and numerical simulation software for optoelectronic devices have experienced a rapid development in recent years. In the past, advanced modeling and simulation was the domain of a few specialists using proprietary software in computational research groups. The increasing user-friendliness of commercial software now also opens the door for nontheoreticians and experimentalists to perform sophisticated modeling and simulation tasks. However, the ever-growing variety and complexity of devices, materials, physical mechanisms, theoretical models, and numerical techniques make it often difficult to identify the best approach to a given project or problem. This book presents an up-to-date review of optoelectronic device models and numerical techniques. The handbook format is ideal for beginners but also gives experienced researchers an opportunity to renew and broaden their knowledge in this expanding field.

Semiconductors are the key material of optoelectronic devices, as they enable propagation and interaction of electrons and photons. The handbook starts with an overview of fundamental semiconductor device models, which apply to almost all device types, followed by sections on novel materials and nanostructures. The main part of the handbook is ordered by device type (LED, amplifier, laser diode, photodetector, and solar cell). For each device type, an introductory chapter is followed by chapters on specialized device designs and applications, describing characteristic effects and models. Finally, novel device concepts and applications are reviewed. At the end of the handbook, an overview of numerical techniques is provided, both for electronic and photonic simulations.

I would like to thank the publisher for initiating this important handbook project and for giving me the opportunity to serve as editor. Many years of organizing the annual international conference on *Numerical Simulation of Optoelectronic Devices (NUSOD)* enabled me to attract a large number of experts from all over the world to write handbook chapters on their research area. I sincerely thank all authors for their valuable contributions.

Joachim Piprek
Newark, Delaware, USA

Editor

Joachim Piprek received his diploma and doctoral degrees in physics from the Humboldt University in Berlin, Germany. For more than two decades, he worked in industry and academia on modeling, simulation, and analysis of various semiconductor devices used in optoelectronics. Currently, he serves as president of the NUSOD Institute, Newark, Delaware (see http://www.nusod.org). During his previous career in higher education, Dr. Piprek taught various graduate courses at universities in Germany, Sweden, and the United States. Since 2001, he has been organizing the annual international conference on *Numerical Simulation of Optoelectronic Devices (NUSOD)*. Thus far, Dr. Piprek has published three books, six book chapters, and about 250 research papers, which have received more than 6000 citations. He was an invited guest editor for several journal issues on optoelectronic device simulation and currently serves as an executive/associate editor of two research journals in this field.

Contributors

Urs Aeberhard
IEK-5 Photovoltaik
Forschungszentrum Jülich
Jülich, Germany

Tim Albes
Department of Electrical Engineering
Technical University of Munich
Munich, Germany

Matthias Auf der Maur
Department of Electronic Engineering
University of Rome Tor Vergata
Rome, Italy

Eugene Avrutin
University of York
York, United Kingdom

Prasanta Basu
Institute of Radio Physics and Electronics
University of Calcutta
Kolkata, India

Steve Bull
Department of Electrical and Electronic Engineering
University of Nottingham
Nottingham, United Kingdom

Kwong-Kit Choi
Sensors and Electron Devices Directorate
U.S. Army Research Laboratory
Adelphi, Maryland

Weng W. Chow
Sandia National Laboratories,
Albuquerque, USA

Tomasz Czyszanowski
Institute of Physics
Lodz University of Technology
Lodz, Poland

Robin Daugherty
Arizona State University
Tempe, Arizona

Maciej Dems
Institute of Physics
Lodz University of Technology
Lodz, Poland

Duy Hai Doan
Research Group Partial Differential Equations
Weierstrass Institute
Berlin, Germany

Ignacio Esquivias
Center of Advanced Materials and Devices for ICT Applications
Universidad Politécnica de Madrid
Madrid, Spain

Patricio Farrell
Research Group Numerical Mathematics and Scientific Computing
Weierstrass Institute
Berlin, Germany

Leszek Frasunkiewicz
Institute of Physics
Lodz University of Technology
Lodz, Poland

Jürgen Fuhrmann
Research Group Numerical Mathematics and Scientific Computing
Weierstrass Institute
Berlin, Germany

Alessio Gagliardi
Department of Electrical Engineering
Technical University of Munich
Munich, Germany

Dominic F.G. Gallagher
Photon Design Ltd.
Oxford, United Kingdom

Christopher Gies
Institute for Theoretical Physics
University of Bremen
Bremen, Germany

Stephen M. Goodnick
Arizona State University
Tempe, Arizona

Niels Gregersen
Technical University of Denmark
Lyngby, Denmark

Raghuraj Hathwar
Arizona State University
Tempe, Arizona

Mohamad Anas Helal
Department of Electrical and Electronic Engineering
University of Nottingham
Nottingham, United Kingdom

Ortwin Hess
Imperial College
London, United Kingdom

Karin Hinzer
School of Electrical Engineering and Computer Science
University of Ottawa
Ottawa, Canada

Weida Hu
State Key Laboratory of Infrared Physics
Shanghai Institute of Technical Physics
Shanghai, China

Frank Jahnke
Institute for Theoretical Physics,
University of Bremen
Bremen, Germany

Julien Javaloyes
Universitat de les Illes Balears,
Palma de Mallorca, Spain

Olafur Jonasson
Department of Electrical and Computer Engineering
University of Wisconsin
Madison, Wisconsin

Markus Kantner
Research Group Laser Dynamics
Weierstrass Institute
Berlin, Germany

Simeon N. Kaunga-Nyirenda
Department of Electrical and Electronic Engineering
University of Nottingham
Nottingham, United Kingdom

Irena Knezevic
Department of Electrical and Computer Engineering
University of Wisconsin
Madison, Wisconsin

Mirella Koleva
Department of Physics
University of Oxford
Oxford, United Kingdom

Thomas Koprucki
Research Group Partial Differential Equations
Weierstrass Institute
Berlin, Germany

Dmitry Labukhin
Photon Design Ltd.
Oxford, United Kingdom

Eric Larkins
Department of Electrical and Electronic Engineering
University of Nottingham
Nottingham, United Kingdom

Akash Laturia
Arizona State University
Tempe, Arizona

Kuan-Chen Lee
National Chiao Tung University
Hsinchu, Taiwan

Xun Li
Department of Electrical and Computer Engineering
McMaster University
Hamilton, Canada

Michael Lorke
Institute for Theoretical Physics
University of Bremen
Bremen, Germany

Dara P.S. McCutcheon
Quantum Engineering Technologies Labs
University of Bristol
Bristol, United Kingdom

Song Mei
Department of Electrical and Computer Engineering
University of Wisconsin
Madison, Wisconsin

Jesper Mørk
Technical University of Denmark
Lyngby, Denmark

Matthias Müller
Institute of Applied Physics
Technical University Bergakademie Freiberg
Freiberg, Germany

A. Freddie Page
Imperial College London
London, United Kingdom

Antonio Pérez-Serrano
Center of Advanced Materials and Devices for ICT Applications
Universidad Politécnica de Madrid
Madrid, Spain

Joachim Piprek
NUSOD Institute LLC
Newark, Delaware

Suleman S. Qazi
Arizona State University
Tempe, Arizona

Mindaugas Radziunas
Research Group *Laser Dynamics*
Weierstrass Institute
Berlin, Germany

Katerina Raleva
University Sts. Cyril and Methodius
Skopje, Macedonia

Nella Rotundo
Research Group Partial Differential Equations
Weierstrass Institute
Berlin, Germany

Frank Schmidt
Zuse Institute
Berlin, Germany

Abdul R. Shaik
Arizona State University
Tempe, Arizona

Yanbing Shi
Department of Electrical and Computer Engineering
University of Wisconsin
Madison, Wisconsin

Gabriela Slavcheva
Centre for Photonics and Photonic Materials
Department of Physics
University of Bath
Bath, United Kingdom

José-Manuel G. Tijero
Center of Advanced Materials and Devices for ICT Applications
Universidad Politécnica de Madrid
Madrid, Spain

Dragica Vasileska
Arizona State University
Tempe, Arizona

Hans Wenzel
Ferdinand Braun Institute
Berlin, Germany

Matthew Wilkins
School of Electrical Engineering and Computer Science
University of Ottawa
Ottawa, Canada

Bernd Witzigmann
Department of Electrical Engineering and Computer Science
University of Kassel
Kassel, Germany

Shun-Tung Yen
National Chiao Tung University
Hsinchu, Taiwan

Anissa Zeghuzi
Ferdinand Braun Institute
Berlin, Germany

VI

Laser Diodes

26

Laser Diode Fundamentals

Joachim Piprek

26.1 Introduction

Semiconductor laser diodes are key components in optical fiber communication, data storage, sensing, material processing, and other applications. They are based on sophisticated interactions of electrons and photons in semiconductor nanostructures (see Chapter 3). Advanced theoretical models and simulation tools are required for the development and analysis of future generations of laser diodes. The following chapters describe some of these complex models in detail. This introductory chapter is aimed at readers who are not yet familiar with basic models and parameters of semiconductor lasers. By exploring simple analytical models, this chapter tries to develop an intuitive understanding of internal laser physics that will help to digest the more complicated theory outlined in subsequent chapters. While these analytical models are quite popular, they often have limits beyond which numerical simulations are required, as shown below.

Section 26.2 examines basic formulas for optical gain and optical losses in semiconductor lasers, followed by the introduction of key performance parameters, threshold current, and slope efficiency. As practical applications often suffer from undesired self-heating of the laser, temperature effects are discussed in Section 26.4 and the resulting changes in laser efficiency in Section 26.5. The rate equation model for dynamic lasing processes is introduced in Section 26.6, including formulas for small signal analysis. Section 26.7 briefly reviews basic laser cavity designs.

26.2 Optical Gain and Optical Loss

Traveling through a semiconductor, a single photon with an energy close to the band gap is able to generate an identical second photon by stimulating the recombination of an electron–hole pair. This is the basic physical mechanism of lasing. The second photon exhibits the same wavelength and the same phase as of the first photon, doubling the amplitude of their monochromatic wave. Subsequent repetition of this process leads to strong light amplification. However, the competing process is the absorption of photons by the generation of new electron–hole pairs (see Figure 26.1). Stimulated emission prevails when more electrons are present at the higher energy level (conduction band) than at the lower energy level (valence band).

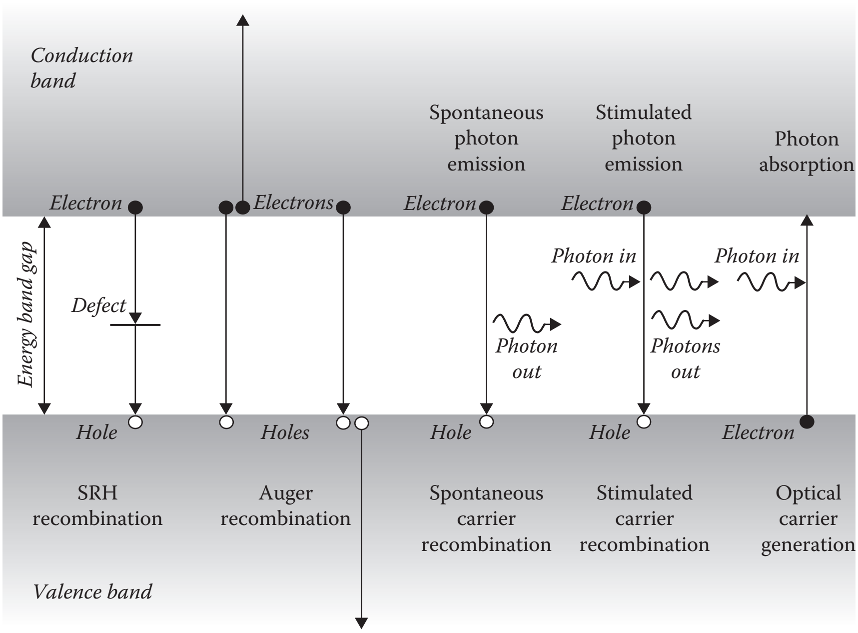

FIGURE 26.1 Electron–hole recombination and generation mechanisms in semiconductors. (SRH, Shockley–Read–Hall.)

This population inversion is one of the key requirements for lasing. Semiconductor lasers typically employ *pin* junctions with a thin active layer of lower band gap (Figure 26.2). At forward bias, electrons and holes are collected in the active layer to achieve inversion. Continuous current injection into the device leads to a continuous stimulated emission of photons, but only if enough photons are constantly present in the device to trigger this process. Thus, only part of all photons can be allowed to leave the laser diode as a lasing beam, the rest must be reflected to remain inside the diode and to generate new photons (Figure 26.3). This optical feedback and confinement of photons in an optical resonator is the second basic requirement of lasing.

The light amplification in the active layer is described by the optical gain $g(n, p, T, \lambda, S)$ as a function of the density of electrons n and holes p inside the active layer, the optical wavelength λ (or photon energy), the photon density S, and the temperature T. This gain function is the heart of laser physics, and a realistic calculation may require sophisticated models (see Chapter 3 for details). We here briefly discuss some popular analytical approximations. The linear gain approximation $g(N) = a(N - N_{tr})$ is often used, employing the transparency density N_{tr} and assuming a fixed differential gain $a = dg/dN$ as well as identical densities of electrons and holes ($N = n = p$). For $N = N_{tr}$, the absorption and gain are the same and the material is transparent. The differential gain dg/dN is a key parameter for laser light modulation (which is discussed Section 26.6). It can only be considered constant for small variations of the carrier density since dg/dN is known to decline with increasing carrier densities (Figure 26.4). This is described by the more general logarithmic function (Coldren and Corzine 1995)

$$g(N, S) = \frac{g_o}{1 + \varepsilon S} \ln\left(\frac{N + N_s}{N_{tr} + N_s}\right) \tag{26.1}$$

The gain compression factor ε describes the gain saturation at high photon densities, e.g., due to carrier depletion (g_o and N_s are fit parameters). All parameters in Equation 26.1 need to be extracted from more fundamental gain models, as measurements are difficult (Shtengel et al. 1998). However, the lack of

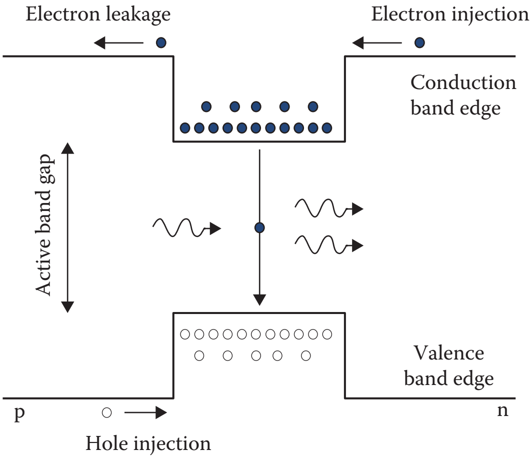

FIGURE 26.2 Electron and hole injection into the light-emitting active layer that is sandwiched between a p-doped and an n-doped material of higher energy bandgap. (Adapted from Piprek, J., In S. S. Sun and L.R. Dalton [eds.], *Introduction to Organic Electronic and Optoelectronic Materials and Devices*, Boca Raton, FL: CRC Press, 2008.)

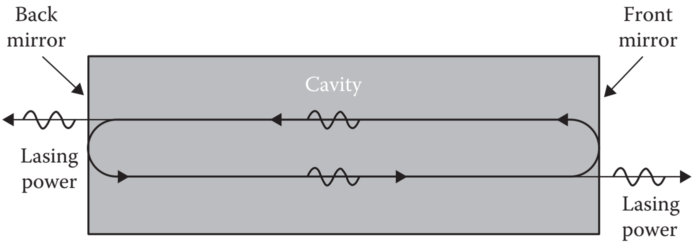

FIGURE 26.3 Optical wave propagation in an Fabry–Pérot (FP) laser cavity (resonator) formed between two reflecting facets. (Adapted from Piprek, J., In S. S. Sun and L. R. Dalton [eds.], *Introduction to Organic Electronic and Optoelectronic Materials and Devices*, Boca Raton, FL: CRC Press, 2008.)

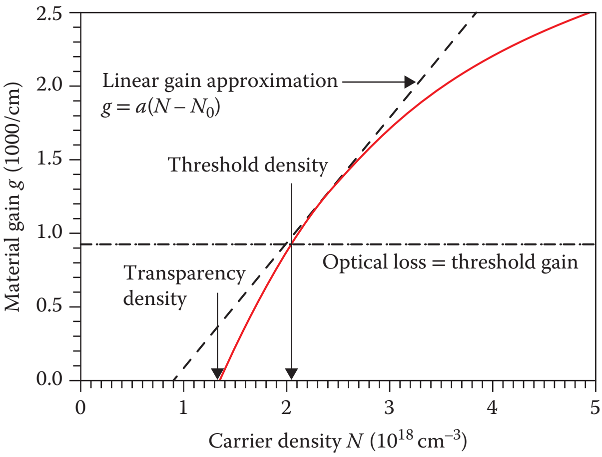

FIGURE 26.4 Optical gain provided by the active layer material as function of the carrier density.

experimental validation of the gain model creates a major uncertainty in any laser simulation. The analysis of laser measurements typically only delivers the relationship $g_m(j) = G_o \ln(j/j_{tr})$ between the modal gain $g_m = \Gamma_a g$ and the current density j, with G_o and the transparency current density j_{tr} as fit parameters (see Chapter 27). The optical confinement factor Γ_a gives the overlap of the active layer and the lasing mode, which is usually extracted from waveguide simulations (see Chapter 4).

Figure 26.4 indicates optical losses that are caused by photon emission from the laser as well as by the internal absorption and photon scattering. For the simple Fabry–Pérot (FP) laser structure shown in Figure 26.3, the optical loss at the two cavity mirrors is given by

$$\alpha_m = \frac{1}{2L} \ln\left(\frac{1}{R_f R_b}\right) \tag{26.2}$$

with the cavity length L and the reflectances R_f and R_b of front and back mirrors, respectively. The internal optical loss α_i can be extracted from laser measurements (see Chapter 27) but the microscopic mechanisms causing this loss are often hard to identify. They are typically approximated as

$$\alpha_i = \alpha_b + \sum_i \Gamma_i \left(k_{n,i} n + k_{p,i} p\right) \tag{26.3}$$

with the background loss α_b (e.g., due to photon scattering) and the sum over all free-carrier-related loss in any individual layer i of the laser structure (where k is a free-carrier absorption parameter). The confinement factor Γ_i is the ratio of the layer volume to the volume of the optical lasing mode. Photon absorption by free carriers depends on the energy band structure of the conduction and valence bands. It is typically stronger for holes due to intervalence band absorption (Piprek et al. 2000).

To reach the lasing threshold, the optical gain must compensate for the internal optical loss (α_i) and for photon emission from the device (α_m). Both loss parameters apply to the whole lasing mode so that the threshold gain g_{th} is defined by

$$\Gamma_a g_{th}\left(N_{th}\right) = \alpha_m + \alpha_i \tag{26.4}$$

with the active layer confinement factor Γ_a and the threshold carrier density N_{th} (see Figure 26.4).

26.3 Threshold Current and Slope Efficiency

The threshold current I_{th} provides the threshold carrier density N_{th} and compensates for various carrier loss mechanisms, some of which are illustrated in Figure 26.1. A spontaneous electron–hole recombination is needed to provide initial photons for stimulated recombination (lasing), but most spontaneously emitted photons are lost. In a common analytical approach, the spontaneous emission rate $R_{spon} = BN^2$ is proportional to the square of the carrier density. Nonradiative recombination mechanisms are either defect-related Shockley–Read–Hall (SRH) recombinations ($R_{SRH} = AN$) or Auger recombinations ($R_{Aug} = CN^3$). The former transfers the recombination energy to lattice vibrations (phonons) and the latter to other free carriers. This simple but very popular ABC recombination model leads to the threshold current

$$I_{th} = \frac{eV_a}{\eta_a} R_{ABC}(N_{th}) = \frac{eV_a}{\eta_a}\left(AN_{th} + BN_{th}^2 + CN_{th}^3\right) = I_{SRH} + I_{spon} + I_{Aug} + I_{leak} \tag{26.5}$$

with the injection efficiency η_a giving the fraction of electrons that recombines within the active layer of volume V_a, thereby accounting for carriers that recombine outside the active layer, e.g., due to electron leakage (see Figure 26.2). Leakage can occur by various mechanisms (Piprek et al. 2000). It is hard to asses

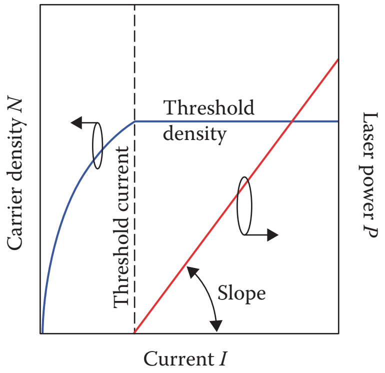

FIGURE 26.5 Illustration of carrier density and lasing power as function of the injected current without self-heating.

with analytical models and typically requires full solutions of the semiconductor transport equations (see Chapter 2). Simpler models often neglect leakage or use a fictitious parameter η_a.

With a stronger current injection $I > I_{th}$, the carrier density remains constant at N_{th} as additional electron–hole pairs are consumed by stimulated recombination (Figure 26.5). The stimulated recombination rate is $R_{stim} = v_g g S$ (where v_g is photon group velocity). Under ideal conditions without self-heating, the laser power rises proportional to $I_{stim} = I - I_{th}$ as

$$P = \eta_d \frac{h\nu}{e}\left(I - I_{th}\right) = \eta_i \frac{\alpha_m}{\alpha_m + \alpha_i} \frac{h\nu}{e}\left(I - I_{th}\right) \tag{26.6}$$

with the photon energy $h\nu$. Note that P gives the total emission from both facets. The differential quantum efficiency η_d is the fraction of carriers injected above threshold that contributes photons to the laser beams. It can be separated into internal differential efficiency η_i and optical efficiency η_{opt}. The latter is equal to $\alpha_m(\alpha_m + \alpha_i)^{-1}$ and gives the fraction of stimulated photons that leaves the laser. The internal differential efficiency η_i is often close to unity above threshold as there are no further recombination losses with constant carrier density N_{th} in the active layer. However, the leakage current may rise above the threshold, especially at higher temperatures (Piprek et al. 2000).

26.4 Temperature Effects

The current flow through the laser diode as well as nonradiative recombination processes generate heat inside the laser and elevate the internal temperature distribution $T(x, y, z)$. This temperature rise more or less affects all material parameters. One of the most fundamental changes occurs with the semiconductor bandgap $E_g(T)$, which is commonly modeled by the Varshni formula

$$E_g(T) = E_g(0) - \frac{AT^2}{B + T} \tag{26.7}$$

using the phenomenological parameters A and B (Piprek 2003). As the band gap shrinks, the lasing wavelength increases (redshifts). In addition, the Fermi distribution of carriers inside the energy bands broadens with higher temperature. Both these effects change the gain spectrum. Figure 26.6 illustrates this change for a fixed carrier density. The gain peak determines the emission wavelength of FP lasers, and it redshifts with higher temperature. But the gain peak also declines, so that more carriers are needed to maintain the lasing threshold (cf. Figure 26.4). Consequently, the threshold current rises with higher temperature, which is often described by the characteristic temperature $T_0 = (T_2 - T_1)/\ln(I_2/I_1)$ that can be extracted

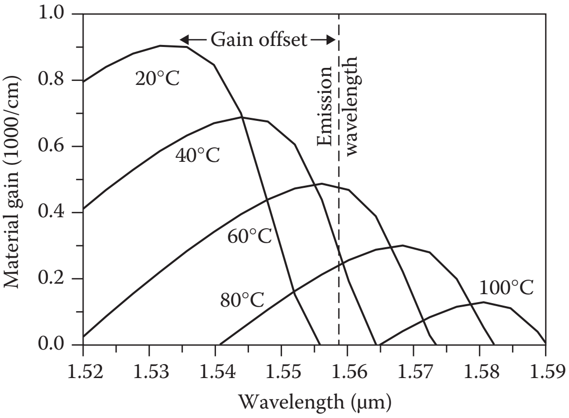

FIGURE 26.6 Optical gain spectrum shift with increasing temperature and constant carrier density.

from measurements of $I_{th}(T)$. The decline of the slope efficiency is calculated in a similar way. These phenomenological parameters are useful in characterizing the temperature sensitivity of a given laser diode (see Chapter 27). However, they don't reveal the physical mechanism behind temperature effects and are not suitable for predictive simulations. For instance, if the lasing wavelength is fixed by the optical cavity design, the impact of the gain shift very much depends on the initial difference between emission wavelength and gain peak wavelength (gain offset). An example is illustrated in Figure 26.6 (Piprek et al. 1998). Here, the rising temperature first increases the gain available at the emission wavelength. The threshold current initially declines and reaches a minimum near 60°C when the gain offset is zero. With further heating, the threshold current rises rapidly. Thus, T_0 depends on the temperature in this case and fails even as a descriptive parameter.

More advanced laser models don't employ fit parameters such as T_0 and describe the underlying physical mechanisms instead, starting with the shift of the gain spectrum (Piprek et al. 2000). An increasing carrier density in the active layer goes hand in hand with increasing carrier losses. For instance, the Auger recombination rate is not affected only by the increasing carrier density, but also by the temperature sensitivity of the Auger process, which depends on its activation energy E_a: $C(T) \propto \exp(-E_a/kT)$. Carrier leakage is also sensitive to temperature changes, and it may raise the threshold current and reduce the slope efficiency. The slope efficiency also depends on the free-carrier absorption, which increases with the carrier density. All these interdependencies require advanced numerical laser models for a more reliable analysis of the temperature sensitivity (see Chapter 27).

26.5 Efficiency Analysis

As an illustrative example for this section, Figure 26.7 shows the simulated power–current and bias–current characteristics of a GaN-based laser diode in continuous-wave (CW) operation (Piprek 2016). Self-heating apparently causes a decline of the slope efficiency, which limits the maximum power achievable. Another key performance parameter is the power conversion efficiency η_{PCE}. It is defined as the ratio of light output power P to electrical input power IV (where V is bias). It can be separated into electrical efficiency $\eta_{ele} = h\nu/eV$ and external quantum efficiency η_{EQE}. The latter is the ratio of emitted photon number to injected number of electron–hole pairs. Equation 26.6 leads to the following power conversion efficiency formula:

$$\eta_{PCE}(I) = \frac{h\nu}{eV}\eta_i \frac{\alpha_m}{\alpha_m + \alpha_i} \frac{I - I_{th}}{I} = \eta_{ele}\eta_{EQE} = \eta_{ele}\eta_s\eta_{th} \tag{26.8}$$

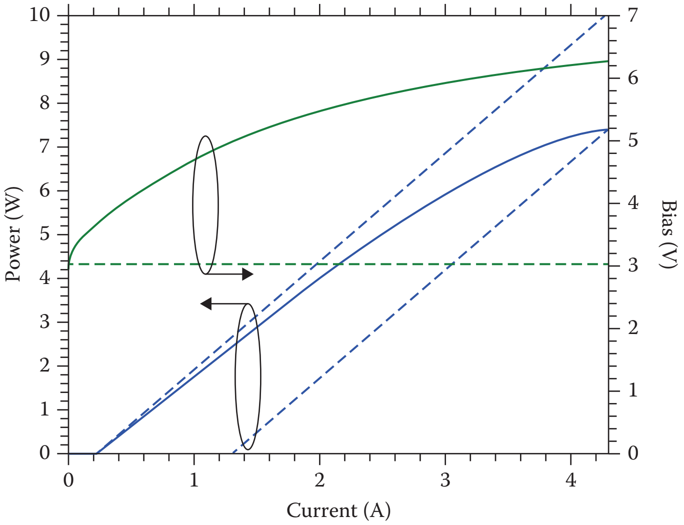

FIGURE 26.7 Lasing power and bias versus current. The dashed bias line indicates the photon energy. The dashed power lines indicate the change in threshold current for constant slope efficiency.

including the unitless slope efficiency η_s and the threshold current efficiency $\eta_{th} = (I - I_{th})/I$. Note that η_s is different from the differential slope efficiency dP/dI and from the averaged slope efficiency $P/(I - I_{th})$, which are both given in W/A and not used here. However, this popular analytical model is somewhat ambiguous when the laser experiences relevant self-heating, which causes a sublinear $P(I)$ characteristic as shown in Figure 26.7. Most parameters in Equation 26.8 change as the internal laser temperature rises with increasing current. The threshold current rises together with the threshold carrier density due to declining material gain. The slope efficiency declines due to increasing carrier leakage and/or rising internal absorption.

Figure 26.8 illustrates these efficiencies as simulated for an InGaN/GaN laser diode (Piprek 2016). At low current, η_{PCE} is mainly limited by the threshold current efficiency (which is zero for $I < I_{th}$). At high current, the strongest efficiency limitation is caused by the decline of the electrical efficiency due to the increasing excess bias above the minimum required bias $h\nu/e$ (dashed bias line shown in Figure 26.7). This excess bias is relatively high in GaN-based lasers, partially due to the low hole conductivity. However, the influence of slope efficiency and threshold efficiency depends on the assumption made in the analysis. The assumption of a constant, temperature-insensitive threshold current leads to the solid curves shown in Figure 26.8, so that temperature effects are mainly reflected by the slope efficiency. This is a convenient and common approach to extract efficiency plots directly from the measured *PI* and *VI* characteristics, without any simulation (Crump et al. 2013). However, with strong self-heating, the dependence on $I_{th}(T)$ needs to be considered, which is hard to extract directly from experimental results. Numerical simulations are indicated by the dashed lines in Figure 26.8, which reveal that the threshold efficiency is more temperature sensitive than the slope efficiency (Piprek 2016). For constant, temperature-insensitive slope efficiency, an approximate method of extracting $I_{th}(I)$ directly from measurements is illustrated by the dashed power lines shown in Figure 26.7. Starting with the measured slope dP/dI at threshold, the dashed line is shifted parallel to the current axis so that each power $P(I)$ is connected to a threshold current $I_{th}(I)$.

26.6 Rate Equation Analysis

Time-dependent effects are often analyzed in terms of rate equations considering all physical processes that change the densities of photons and carriers. We here discuss a set of two rate equations for the

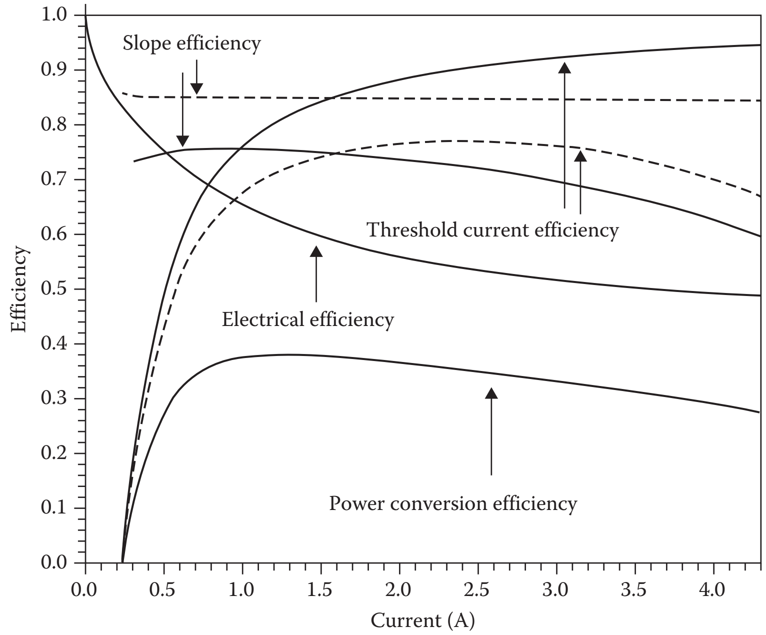

FIGURE 26.8 Changes in efficiency with increasing injection current. The solid lines indicate constant threshold current and the dashed lines indicate constant slope efficiency.

single-mode photon density S averaged over the modal volume V_m and the carrier density N averaged over the active volume V_a:

$$\frac{dN}{dt} = \frac{\eta_a I}{eV_a} - \left[AN + BN^2 + CN^3\right] - v_g g(N,S)S \tag{26.9}$$

$$\frac{dS}{dt} = \Gamma_a v_g g(N,S)S + \beta\Gamma_a BN^2 - v_g\left[\alpha_i + \alpha_m\right]S \tag{26.10}$$

The active layer carrier density $N(t)$ in Equation 26.9 is increased by current injection (first term, including the injection efficiency η_a) and is reduced by all four recombination processes (see Figure 26.1) that limit the carrier lifetime. The photon density $S(t)$ in Equation 26.10 is increased by stimulated emission (first term) and by the small fraction β of spontaneously emitted photons that enters the lasing mode (second term). $S(t)$ is reduced by photon emission and internal photon losses (third term in Equation 26.10), which limit the photon lifetime τ_p defined by $\tau_p^{-1} = v_g(\alpha_i + \alpha_m)$. The dynamic response of both densities can be understood from these rate equations. For instance, when $N(t)$ increases, $S(t)$ increases due to the rising gain $g(N)$. But that decreases the carrier density according to the last term in Equation 26.9. $N(t)$ is also reduced by ABC recombination. Consequently, the photon density $S(t)$ drops again, also due to photon losses. Thus, the dynamic behavior of both densities is strongly influenced by loss mechanisms.

However, this approach neglects the nonuniform distribution of carriers and photons (Carroll et al. 1998). A nonuniform distribution of photons can result in spatial hole burning into the carrier distribution in regions with high photon density, reduce the gain, and increase the refractive index (see Chapter 27). Multiple optical modes would require multiple rate equations for calculating each photon density (Petermann 1988). Lateral diffusion of carriers out of the active layer is partially considered by the injection efficiency η_a and is often minimized by lateral carrier confinement.

Under steady-state conditions ($dS/dt = 0$) with vanishing β, Equation 26.10 gives the relation $\Gamma_a g(N,S) = \alpha_i(N) + \alpha_m$ describing the balance of gain and losses required for lasing (see Figure 26.4).

The first equation $dN/dt = 0$ then yields the steady-state photon density $S_o = \eta_i\tau_p(I - I_{th})(eV_m)^{-1}$. The steady-state optical power emitted through both mirrors is given by $P_o = v_g\alpha_m h\nu V_m S_o$ in agreement with Equation 26.6.

With analog modulation, sinusoidal variations are added to the steady-state input current I_o. In the simple case of just one angular frequency $\omega = 2\pi f$ and constant amplitude ΔI, the injection current in Equation 26.9 becomes $I(t) = I_o + \Delta I \times \sin(\omega t)$. If the period of the modulation is much larger than any time constant, the output power still follows the steady-state solution (Equation 26.6). But in the general dynamic case, analytical solutions of the rate equations cannot be found and numerical methods need to be applied.

Current modulations ΔI well below $(I_o - I_{th})$ lead to variations ΔN, ΔS, and ΔP, which are much smaller than the steady-state values N_{th}, S_o, and P_o, respectively. This small signal case allows the rate equations to be solved analytically (Coldren and Corzine 1995) using the linear gain approximation illustrated in Figure 26.4. Assuming $\beta = 0$, the small signal solution to the rate equations is

$$\Delta P(\omega) = M(\omega) \times \Delta P = \frac{\omega_r^2}{\omega_r^2 - \omega^2 + i\omega\gamma} \times \eta_i \frac{\alpha_m}{\alpha_i + \alpha_m} \frac{h\nu}{e} \Delta I \qquad (26.11)$$

with the angular electron–photon resonance frequency $\omega_r = 2\pi f_r$ given by

$$\omega_r^2 = \frac{a v_g S_o}{\tau_p \left(1 + \varepsilon S_o\right)} \left(1 + \frac{\varepsilon}{v_g a \tau_c}\right) \qquad (26.12)$$

including the photon lifetime τ_p and the gain compression factor ε from Equation 26.1. At low photon densities ($\varepsilon = 0$), Equation 26.12 is reduced to $\omega_r^2 = (\tau_{st}\tau_p)^{-1}$ with the differential stimulated emission time $\tau_{st} = dR_{stim}/dN = (av_g S_o)^{-1}$. The damping constant is given by $\gamma = \tau_{st}^{-1} + \tau_c^{-1}$ including the differential carrier lifetime τ_c, with $\tau_c^{-1} = dR_{ABC}/dN = A + 2BN_{th} + 3CN_{th}^2$.

Figure 26.9 illustrates the normalized modulation response $|M(\omega)|$ as a function of modulation frequency for different gain compression factors ε (Piprek and Bowers 2002). At low frequencies, the photon

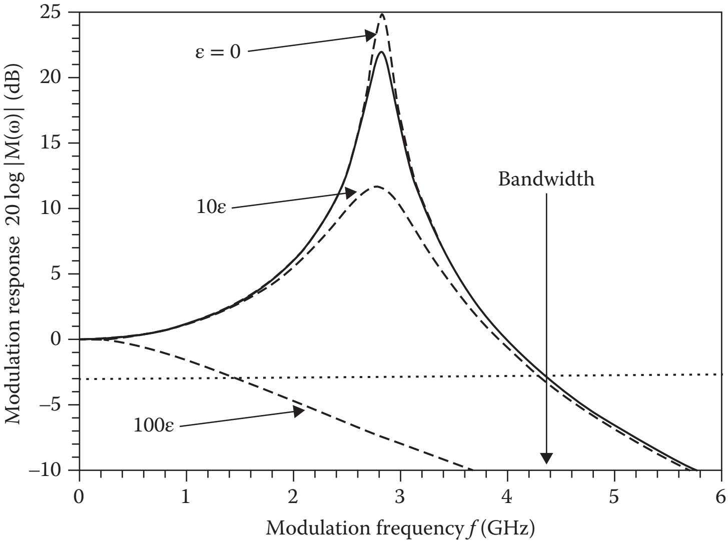

FIGURE 26.9 Modulation response versus modulation frequency. The dashed lines show the effect of changing the gain suppression factor ε.

density can easily follow the current modulation and the response function is quite flat. The response is most intense near the resonance frequency ω_r. The peak frequency is given by $\omega_p^2 = \omega_r^2 - \gamma^2/2$. At even faster current modulation, the photons cannot follow any more and the response function declines. The modulation bandwidth f_b is the frequency at which the response drops to $|M(2\pi f_b)| = 2^{-1/2} = -3dB$ (see Figure 26.9). The bandwidth rises with the steady-state current but saturates at high currents due to increased damping, device heating, gain compression, transport effects, or parasitics (Kjebon et al. 1996).

26.7 Basic Laser Cavity Designs

Chapters 27 through 34 feature specific laser designs and applications in much more detail, we here only give a brief overview of the main types of optical resonators. The most simple cavity design uses the reflection at the two laser facets for optical feedback (FP laser, see Figures 26.3 and 26.10, and Chapter 27). Constructive interference of forward and backward traveling optical waves is restricted to specific wavelengths. Those wavelengths constitute the longitudinal mode spectrum of the laser. The cavity length is typically on the order of several hundred microns, much larger than the lasing wavelength, so that many longitudinal modes may exist. The actual lasing modes are those receiving strong optical gain. Single-mode lasing is hard to achieve in simple FP structures, especially under modulation. Dynamic single-mode operation is required in many applications and is achieved using optical cavities with selective reflection. The distributed feedback (DFB) laser is widely used in single-mode fiber optic applications (Figure 26.10). Typical DFB lasers exhibit a periodic longitudinal variation of the refractive index within one layer of the edge-emitting waveguide structure. This index variation provides continuous (distributed) reflection at a wavelength given by the variation period. Facet reflection is not needed in DFB lasers; however, facet coating may be used to increase the light emission from one end of the cavity. Other laser resonators terminate the optical cavity by two distributed Bragg reflectors (DBRs) with a stepwise alternating index. More details on DFB and DBR lasers are given in Chapters 30 and 31.

A special type of DBR laser is the vertical-cavity surface-emitting laser (VCSEL) which emits light through the bottom and/or top surface of the layered structure (see Figure 26.10 and Chapters 34 and 45). The light travels perpendicular to the active layer and receives optical gain only over a very short travel distance. Thus, many more photon roundtrips and highly reflective VCSEL mirrors with more than 99% reflectivity are needed for lasing.

In transversal directions, the optical wave is typically confined by the refractive index profile, using a ridge (DFB laser) or a pillar (VCSEL) to form the waveguide. Even with restriction to one longitudinal mode, multiple transversal optical modes may occur in all three types of lasers.

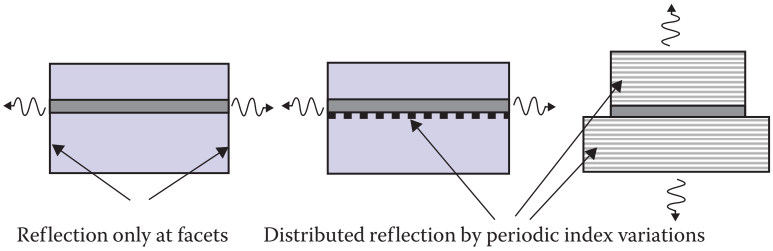

FIGURE 26.10 Illustration of basic laser cavity designs. [DFB, distributed feedback; FP, Fabry–Pérot; VCSEL, vertical-cavity surface-emitting laser. (Adapted from Piprek, J., In S. S. Sun and L. R. Dalton [eds.], *Introduction to Organic Electronic and Optoelectronic Materials and Devices*, Boca Raton, FL: CRC Press, 2008.)]

References

Carroll, J., Whiteaway, J., and Plumb, D. *Distributed Feedback Semiconductor Lasers*. London/Washington: IEE/SPIE Press, 1998.

Coldren, L. A., and Corzine, S. W. *Diode Lasers and Photonic Integrated Circuits*. New York, NY: Wiley, 1995.

Crump, P., Erbert, G., Wenzel, H. et al. Efficient high-power laser diodes. *IEEE Journal of Selected Topics in Quantum Electronics*, vol. 19, p. 1501211, 2013.

Kjebon, O., Schatz, R., Lourdudoss, S., Nilsson, S., and Stalnacke, B. Modulation response measurement and evaluation of MQW InGaAsP lasers of various design. *SPIE Proceedings*, vol. 2687, pp. 138–152, 1996.

Petermann, K. *Laser Diode Modulation and Noise*. Dordrecht, the Netherlands: Kluwer Academic Publishers, 1988.

Piprek, J., Akulova, Y. A., Babic, D. I., Coldren, L. A., and Bowers, J. E. Minimum temperature sensitivity of 1.55-micron vertical-cavity lasers at −30 nm gain offset. *Applied Physics Letters*, vol. 72, no. 15, pp. 1814–1816, 1998.

Piprek, J., Abraham, P., and Bowers, J. E. Self-consistent analysis of high-temperature effects on strained-layer multi-quantum well InGaAsP/InP lasers. *IEEE Journal of Quantum Electronics*, vol. 36, no. 3, pp. 366–374, 2000.

Piprek, J. and Bowers, J. E. Analog modulation of semiconductor lasers, Chapter 3. In *RF Photonic Technology in Optical Fiber Links*. Chang, W., ed. Cambridge, UK: Cambridge University Press, 2002.

Piprek, J. *Semiconductor Optoelectronic Devices: Introduction to Physics and Simulation*. San Diego, CA: Academic Press, 2003.

Piprek, J. Introduction to optoelectronic device principles, Chapter 2. In *Introduction to Organic Electronic and Optoelectronic Materials and Devices*. Sun, S. S. and Dalton, L. R, eds. Boca Raton, FL: CRC Press, 2008, pp. 25–46.

Piprek, J. Analysis of efficiency limitations in high-power InGaN/GaN laser diodes, *Optical Quantum Electron*, vol. 48, p. 471, 2016.

Shtengel, G. E., Kazarinov, R. F., Belenky, G. L., Hybertsen, M. S., and Ackerman, D. A. Advances in measurements of physical parameters of semiconductor lasers. *International Journal of High Speed Electronics and Systems*, vol. 9, pp. 901–940, 1998.

27

High-Power Lasers

Hans Wenzel
and
Anissa Zeghuzi

27.1 Introduction

High-power diode lasers deliver the energy to all high-performance laser systems, either as a pump source or as a source for direct material processing. Comprehensive descriptions of their manufacturing and applications can be found in, for example, References [1–4].

The lasers are constructed like all edge-emitting diode lasers as shown in Figure 27.1. The layer structure grown by metal-organic vapor phase epitaxy (MOVPE) or molecular beam epitaxy (MBE) on a crystalline substrate (e.g., GaAs, InP, GaN) consists basically of n-doped cladding and optical confinement layers, an active region (typically a single quantum well [QW]) and p-doped optical confinement and cladding layers and is completed by a highly p-doped cap (contact) layer. However, there are three peculiarities compared to other lasers: first, the vertical waveguide is weak (large total thickness of confinement layers or small index step between confinement and cladding lasers). Second, the emitting aperture is very broad, ranging from tens to hundreds of micrometers, which results in a nonstationary behavior [5,6]. Third, the cavity between the cleaved facets is very long, reaching values of several millimeters and the two facets are extremely differently coated.

The lateral optical and current confinement can be achieved by several means. In the most simple case, there is no built-in waveguide at all so that the optical field is confined to the region below the contact

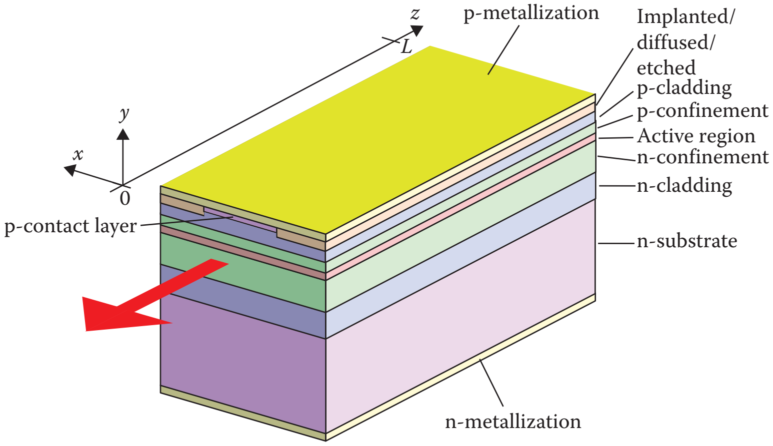

FIGURE 27.1 Schematic view of a high-power broad-area semiconductor laser.

stripe by gain guiding at low power and under pulsed operation, but is strongly influenced by the thermally induced waveguide created under continuous-wave (CW) operation at high power. In order to restrict the current spreading, the electrical conductivity of parts of the p-doped region besides the contact stripe can be reduced by ion implantation, impurity diffusion, or by implementation of a reverse-biased p-n junction. If the semiconductor besides the p-contact is etched away up to a defined depth and subsequently filled with an insulator, the index contrast between the semiconductor below the contact stripe and the insulator results in a lateral built-in index guide, which stabilizes the optical field at low power and under pulsed operation, but increases the far-field divergence.

The cleaved facets located at $z = 0$ and $z = L$ in Figure 27.1 are low reflection coated on the front side ($R_0 \propto 0.01$) and high reflection coated on the rear side ($R_L > 0.9$). If a small optical spectrum and a reduced drift of the wavelength with temperature and injection current are required, Bragg gratings could be implemented into the cavity, resulting in distributed feedback (DFB) or distributed Bragg-reflection (DBR) lasers [7]. However, here we focus on the Fabry–Pérot (FP) type of high-power lasers where the coated facets provide the feedback.

The simulation of broad-area lasers is challenging because of the different temporal and spatial scales involved. The timescales for the variations of the optical field, the carrier densities, and the temperature are ps, ns, and μs, respectively. The spatial scales range from nanometers (active QW) and micrometers (epitaxial layers and lateral waveguides) up to millimeters (cavity). Another difficulty arises from the highly nonlinear behavior because of the coupling of the optical, electronic, and thermal phenomena. Therefore, until now, no simulation tool covering all spatiotemporal scales and physical phenomena has been available. In this chapter, we survey models with different complexity for the simulation of high-power lasers [6].

This chapter is organized as follows. In Section 27.2, we present a model for high-power lasers based on measurable parameters, which can be used to compare different laser structures and to predict the electro-optical characteristics as a function of cavity length and facet reflectivities, for example. In Section 27.3, we investigate the profile of the optical power in the cavity in more detail and derive some of the equations used in Section 27.2. Furthermore, we discuss several effects responsible for the saturation of the output power with increasing injection current. The parabolic paraxial wave equation based on the slowly varying amplitude and rotating wave approximations, taking into account gain dispersion, spontaneous emission, and a third-order nonlinear susceptibility, is derived in Section 27.4. A balance equation for the electromagnetic energy density will be given. In Section 27.5, we present the equations that can be used to calculate the nonlinear lateral optical modes of broad-area lasers and discuss several root causes for the multipeaked and not diffraction-limited lateral field profile of broad-area lasers. Finally, in Section 27.6, we summarize a thermodynamic-based model for the transport of the charged carriers and the temperature flow. Particular attention is paid to a consistent formulation with the model for the optical field presented in Section 27.4.

27.2 Phenomenological Model

In this section, a model for high-power lasers based on measurable parameters is presented. The model can be used to compare different laser structures and to predict the electro-optical characteristics in dependence on cavity length and facet reflectivities, for example.

27.2.1 Summary of the Governing Equations

The total output power P_{out} of a semiconductor laser in dependence on the injection current I is given by

$$P_{\mathrm{out}} = \frac{\hbar\omega}{e}\eta_{\mathrm{ext}}\left(I - I_{\mathrm{thr}}\right) \tag{27.1}$$

where η_{ext} is the external differential efficiency, I_{thr} the threshold current, ω the angular lasing frequency, $\hbar$ the reduced Planck constant, and e the elementary charge. Here and in what follows $I \geq I_{\mathrm{thr}}$ is assumed. The photon energy $\hbar\omega$ can be written as (c vacuum speed of light, h Planck constant)

$$\hbar\omega = \frac{hc}{\lambda} \tag{27.2}$$

where the vacuum lasing wavelength λ is assumed to vary linearly with the temperature T in the cavity as

$$\lambda = \lambda_{\mathrm{ref}} + \frac{\mathrm{d}\lambda}{\mathrm{d}T}\Delta T \qquad \text{with} \qquad \Delta T = T - T_{\mathrm{ref}} \tag{27.3}$$

with T_{ref} being the reference (heat sink or ambient) temperature. The output powers P_0 at the left ($z = 0$) facet and P_L at the right ($z = L$) facet with intensity reflection coefficients R_0 and R_L, respectively, are obtained from the total power as

$$P_0 = \frac{P_{\mathrm{out}}}{1 + (1 - R_L)(1 - R_0)^{-1}\sqrt{R_0 R_L^{-1}}} \quad \text{and} \quad P_L = \frac{P_{\mathrm{out}}}{1 + (1 - R_0)(1 - R_L)^{-1}\sqrt{R_L R_0^{-1}}} \tag{27.4}$$

(cf. Equation 27.40).

To calculate the threshold current, a model for the modal gain is required. First one should be aware that the gain depends on both the wavelength and the current density. For a fixed wavelength λ, the dependence of the modal gain of QW lasers on the current density can be well approximated by a logarithmic relation,

$$g_{\mathrm{m}} = G_0 \ln \frac{j}{j_{\mathrm{tr}}} \tag{27.5}$$

where G_0 is the gain prefactor (proportional to the differential gain) and j_{tr} the transparency current density. At $j = j_{\mathrm{tr}}$ the gain vanishes, i.e., a wave with the wavelength λ propagating along the QW embedded in a nonabsorbing medium is neither absorbed nor amplified (transparency). Due to the fact that FP lasers lase at the maximum of the gain spectrum, we need the dependence of the peak gain on the current density for which the relation Equation 27.5 can be used, too. However, one must keep in mind that the peak gain never becomes negative, but approaches zero for vanishing current. Therefore, $j \gg j_{\mathrm{tr}}$ must be observed and the transparency current density obtained by the analysis of the length dependencies of external differential efficiency and threshold current as described in Section 27.2.2 has no direct physical interpretation. One should mention that of course any other functional dependence $g_{\mathrm{m}}(j)$ that can be solved analytically for j, such as a linear one, could be used. However, then the procedure presented in Section 27.2.2 would yield differing parameters G_0 and j_{tr}.

Assuming the logarithmic dependence of the modal gain on the current density and an exponential dependence of the threshold current on the temperature, the threshold current can thus be written as

$$I_{\text{thr}} = WLj_{\text{tr}}e^{\frac{g_{\text{thr}}}{G_0}}e^{\frac{\Delta T}{T_0}} \tag{27.6}$$

where W is the contact width, L the contact length (assumed equal to the cavity length), and T_0 the characteristic temperature of the threshold current. Similarly, the external differential efficiency can be written as (cf. Equation 27.44)

$$\eta_{\text{ext}} = \frac{\alpha_{\text{out}}}{g_{\text{thr}}}\eta_{\text{i}}e^{-\frac{\Delta T}{T_1}} \tag{27.7}$$

where T_1 is the characteristic temperature of the external differential efficiency. The internal efficiency η_{i} gives the fraction of the total current increment that results in stimulated emission of photons. It describes the effect that not all electron–hole pairs *additionally* injected above threshold are converted into photons by stimulated emission. The threshold gain g_{thr} is

$$g_{\text{thr}} = \alpha_{\text{out}} + \alpha_{\text{i}} \tag{27.8}$$

with the internal losses α_{i} and the outcoupling (mirror) losses

$$\alpha_{\text{out}} = -\frac{1}{2L}\ln(R_0R_L) \tag{27.9}$$

Finally, the temperature rise can be calculated from the dissipated power Q and the thermal resistance r_{th} related to the contact area,

$$\Delta T = \frac{r_{\text{th}}}{WL}Q \tag{27.10}$$

The dissipated power is given by the difference between electrical input power and optical output power,

$$Q = UI - P_{\text{out}} \tag{27.11}$$

with the voltage–current characteristics

$$U = \Delta U + \frac{\hbar\omega}{e} + \frac{r_{\text{s}}}{WL}I \tag{27.12}$$

where ΔU is the so-called defect voltage and r_{s} the series resistance related to the contact area. The main contribution to the defect voltage arises from the spacing of the quasi-Fermi potentials of electrons and holes in the active region (Fermi voltage), which is assumed to be clamped above threshold and is always larger than the photon energy divided by the elementary charge. The last term in Equation 27.12 is due to the Ohmic voltage drop in the bulk semiconductor layers, at the heteroboundaries, and at the semiconductor–metal junctions.

Instead of Equation 27.11 sometimes other expressions are reported. For example, by inserting Equations 27.1 and 27.12 into Equation 27.11 and rearranging the terms,

$$Q = \frac{\hbar\omega}{e}I_{\text{thr}} + \frac{\hbar\omega}{e}(1-\eta_{\text{i}}e^{-\frac{\Delta T}{T_1}})(I-I_{\text{thr}}) + \frac{\hbar\omega}{e}(\eta_{\text{i}}e^{-\frac{\Delta T}{T_1}} - \eta_{\text{ext}})(I-I_{\text{thr}}) + \Delta UI + \frac{r_{\text{s}}}{WL}I^2 \tag{27.13}$$

is obtained. The third term can be also written as

$$\frac{\hbar\omega}{e}(\eta_i e^{-\frac{\Delta T}{T_1}} - \eta_{ext})(I - I_{thr}) = \alpha_i L\bar{P} \tag{27.14}$$

where we have used Equations 27.7, 27.8, and 27.43. The averaged internal power $\bar{P}$ is defined in Equation 27.32. The dissipated power is thus the sum of the heat generated at threshold by nonradiative and spontaneous recombination (first term in Equation 27.13), the heat generated above the threshold due to additional nonstimulated recombination and carrier leakage (second term), the heat generated by absorption (third term), the heat caused by the defect voltage (fourth term), and the Joule heat (last term). It is worth to mention that in Equations 27.11 and 27.13, it is assumed that the spontaneously emitted radiation is completely absorbed in the cavity so that P_{out} contains only the stimulated emission.

All equations have been written in such a manner that the geometrical scaling given by W and L is explicitly separated. Note, however, that the dependence of r_{th} on W cannot be neglected because the thermal resistance $R_{th} = r_{th}/(WL)$ is not inverse proportional to W. For example, for a rectangular-shaped infinitely thin heat source,

$$r_{th,\,2D} \approx \frac{W}{\kappa\pi}\ln\left(\frac{4h}{W}\right) \tag{27.15}$$

holds under the condition $W \ll h < W_s$, where κ is the thermal conductivity of the material with thickness h and width $2W_s$ separating the heat source of width W from the heat sink [8]. Only for a purely one-dimensional heat flow

$$r_{th,\,1D} = \frac{h}{\kappa} \tag{27.16}$$

is independent of W.

For shallow-edged samples with substantial lateral current spreading, the transparency current density obtained by the procedure presented in Section 27.2.2 depends on the p-contact width, too [9]. In order to determine the transparency current density for an infinite p-contact width $j_{tr,W\to\infty}$ without current spreading, the transparency *current* has to be plotted and linearly fitted in dependence on W. From the slope dI_{tr}/dW one obtains $j_{tr,W\to\infty}$ and from the extrapolation $W \to 0$ the spreading current $I_{tr,\,spread}$ according to the relation [9]

$$I_{tr}(W) = j_{tr,W\to\infty}LW + I_{tr,\,spread} \tag{27.17}$$

The basic assumption underlying Equation 27.17 is that $I_{tr,\,spread}$ is independent of W. If different cavity lengths are considered, Equation 27.17 has to be divided by L.

For a numerical calculation of the electro-optical characteristics, Equation 27.10 is best suited because $\Delta T(I)$ is a monotonous function (in contrast to $P(I)$). Knowing ΔT, the threshold current and external efficiency can be determined from Equations 27.6 and 27.7, respectively, and finally the output power from Equation 27.1.

27.2.2 Determination of the Parameters Entering the Model

In what follows we consider an asymmetric super-large optical-cavity structure published in Reference [10]. The parameters η_i, α_i, G_0, and j_{tr} are determined by measuring the power–current characteristics of as-cleaved lasers having different cavity lengths L, operated under pulsed conditions to avoid self-heating ($\Delta T = 0$). Thus pulse lengths below 1 μs and duty cycles below 1% are required. Note that the lasing wavelength could substantially vary with L, which must be taken into account in the calculation of the optical power from the measured photovoltage of the detector by adjusting the calibration factor. The measured *P–I* characteristics have to be linearly fitted to extract the slope efficiencies and threshold currents for the different cavity lengths.

If the inverse external differential efficiency is plotted versus cavity length (cf. Figure 27.2a),

$$\eta_{\mathrm{ext}}^{-1}(L) = \eta_{\mathrm{i}}^{-1}\left(1 - \frac{\alpha_{\mathrm{i}}}{\ln(R)}L\right) \tag{27.18}$$

a linear fit delivers $-\eta_{\mathrm{i}}^{-1}\alpha_{\mathrm{i}}/\ln(R)$ from the slope $\eta_{\mathrm{ext}}^{-1}(L)$ and η_{i}^{-1} from the extrapolation of η_{ext}^{-1} to $L \rightarrow 0$. A linear fit of the logarithm of the threshold current density versus the inverse cavity length

$$\ln(j_{\mathrm{thr}})(L^{-1}) = \ln(j_{\mathrm{tr}}) + G_0^{-1}\left(\alpha_{\mathrm{i}} - \ln(R)L^{-1}\right) \tag{27.19}$$

as shown in Figure 27.2b yields $-G_0^{-1}\ln(R)$ from the slope $\ln(j_{\mathrm{thr}})(L^{-1})$ and the threshold current density for an infinite cavity length $\ln(j_{\mathrm{thr},\infty}) = \ln(j_{\mathrm{tr}}) + G_0^{-1}\alpha_{\mathrm{i}}$ from the extrapolation of $\ln(j_{\mathrm{thr}})$ to $L^{-1} \rightarrow 0$. The results of this procedure are contained in Table 27.1, where facet reflectivities $R_0 = R_L = 0.3$ have been assumed in the evaluation. For other cases they must be correspondingly chosen.

The cavity lengths L have to be carefully chosen to ensure linear dependencies $\eta_{\mathrm{ext}}^{-1}(L)$ and $\ln(j_{\mathrm{thr}})(L^{-1})$. If L is too small (large threshold gain), η_{ext}^{-1} could increase with decreasing L due to an increase of α_{i} (enhanced free-carrier absorption) and a decrease of η_{i} (enhanced carrier leakage). If L is too large (small threshold gain), the threshold gain does not depend logarithmically on the threshold current density because $j_{\mathrm{th}} \rightarrow j_{\mathrm{tr}}$ so that the model fails, too.

The characteristic temperatures should be determined by measuring the power–current characteristics at different chip temperatures under pulsed conditions. The outcoupling losses (determined by cavity length and facet reflectivities) of the laser under investigation should coincide, nearly, with the intended values for CW operation, because T_0 and T_1 decrease with increasing threshold gain. The temperature range must be correspondingly chosen, too, because T_0 and T_1 decrease with increasing temperature. The results of the measurements and the linear fits of the logarithms of the threshold current density and external

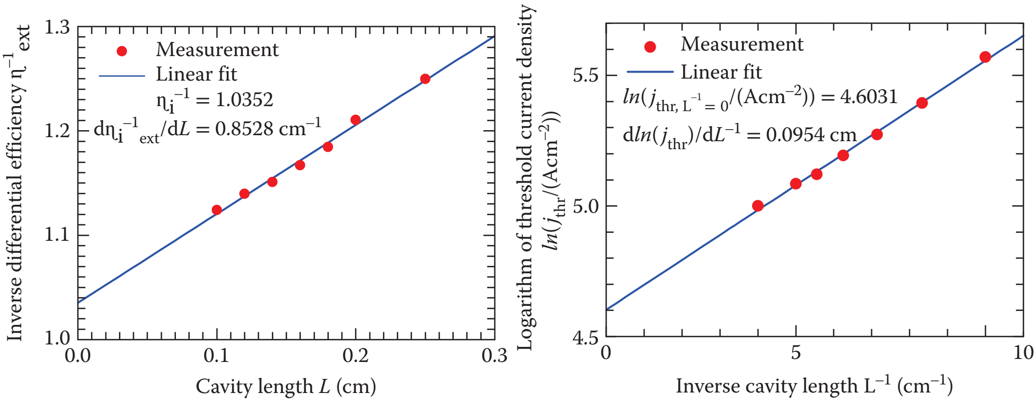

(a)

(b)

FIGURE 27.2 Determination of internal efficiency η_{i}, internal optical losses α_{i}, gain prefactor G_0, and transparency current density j_{tr}. (a) Inverse external differential efficiency versus cavity length. Bullets indicate measurements and solid line indicates linear fit. (b) Logarithm of threshold current density versus inverse cavity length. Bullets indicate measurements and solid line indicate linear fit.

TABLE 27.1 Phenomenological Laser Parameters

Parameter	Symbol	Value	Unit
Front facet reflectivity	R_0	0.012	
Rear facet reflectivity	R_L	0.95	
Width of active region	W	90	μm
Cavity length	L	4000	μm
Internal efficiency	η_i	0.97	
Internal optical losses	α_i	0.99	cm^{-1}
Gain prefactor	G_0	12.6	cm^{-1}
Transparency current density	j_{tr}	92.2	$\mathrm{A/cm}^2$
Characteristic temperature of threshold current	T_0	98	K
Characteristic temperature of external efficiency	T_1	341	K
Reference wavelength	λ_{ref}	899	nm
Change of wavelength with temperature	$d\lambda/dT$	0.331	nm/K
Series resistance	r_s	$0.767 \cdot 10^{-4}$	$\Omega \cdot \mathrm{cm}^2$
Thermal resistance	r_{th}	$0.936 \cdot 10^{-2}$	$\mathrm{K} \cdot \mathrm{cm}^2/\mathrm{W}$
Defect voltage	ΔU	0.033	V
Differential threshold current	j'_{thr}	5	cm^{-2}
Saturation current density	j_{sat}	$5 \cdot 10^{-6}$	cm^2/A
Differential series resistance	r'_s	$-5 \cdot 10^{-3}$	$\Omega \cdot \mathrm{cm}^4/A$

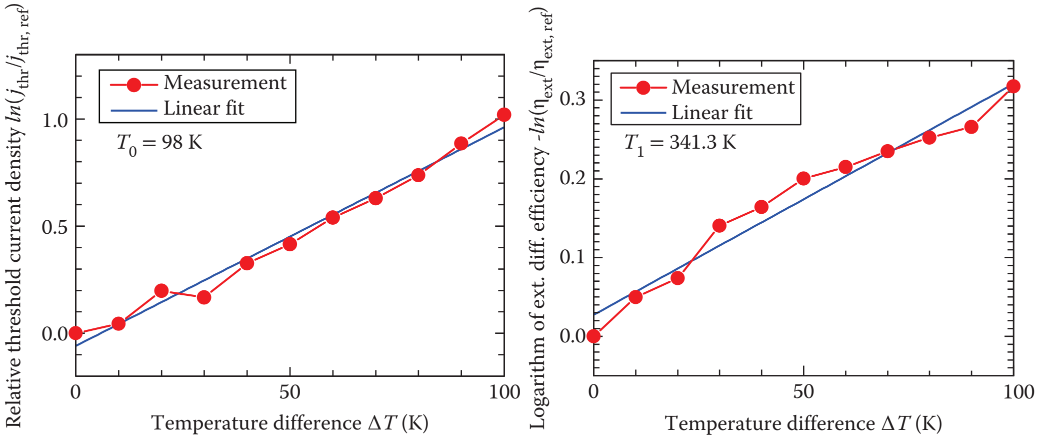

(a)

(b)

FIGURE 27.3 Determination of characteristic temperatures. Cavity length and facet reflectivities are given in Table 27.1. (a) Logarithm of threshold current density versus temperature rise. Bullets indicate measurements and solid line indicate linear fit. (b) Logarithm of external differential efficiency versus temperature rise. Bullets indicate measurements and solid line indicate linear fit.

differential efficiency versus temperature rise,

$$\ln\left(\frac{j_{thr}(T)}{j_{thr}(T_{ref})}\right) = \frac{\Delta T}{T_0} \quad \text{and} \quad -\ln\left(\frac{\eta_{ext}(T)}{\eta_{ext}(T_{ref})}\right) = \frac{\Delta T}{T_1} \tag{27.20}$$

are shown in Figure 27.3a and 27.3b.

The series resistance and defect voltage are obtained from a fit of the linear part of the voltage–current characteristics above threshold:

$$U = U_0 + \frac{r_s}{WL} I \qquad \text{and} \qquad \Delta U = U_0 - \frac{hc}{e\lambda_{\text{ref}}} \tag{27.21}$$

The result is shown in Figure 27.4a. The voltage must be measured with care to ensure that the true series resistance of the chip is obtained. Typically a so-called four-terminal or 4-wire sensing separating the current and voltage electrodes has to be applied. Finally, the thermal resistance can be determined from a linear fit of the lasing wavelength versus the dissipated power,

$$\lambda(Q) = \lambda_{\text{ref}} + \frac{\mathrm{d}\lambda}{\mathrm{d}T} \frac{r_{\text{th}}}{WL} Q, \tag{27.22}$$

where Q is calculated according to Equation 27.11

There are two possibilities to employ Equation 27.22. The first possibility is based on the measurement of the center wavelength λ_{center} of the emission spectrum above threshold versus injection current. This yields a correct result, if a sufficiently large number of modes is lasing and the envelope of the spectrum exhibits a Gaussian-like shape. The shift of λ_{center} is mainly determined by the temperature dependence of the energy gap of the active region, but sometimes also by the temperature dependence of the confinement factor or screening of polarization fields in GaN-based lasers, for example. The method has the advantage, that the requirement on the spectral resolution of the optical spectrometer is modest. A disadvantage is that a unique center wavelength cannot always be determined.

The second possibility is to trace the wavelength of a single longitudinal mode while increasing the current, using a high-resolution optical spectrometer. The shift of the wavelength λ_{mode} of a mode is determined by the temperature dependence of its modal phase index, which results in a much weaker coefficient $\mathrm{d}\lambda_{\text{mode}}/\mathrm{d}T$ than for the center wavelength $\mathrm{d}\lambda_{\text{center}}/\mathrm{d}T$ of the emission spectrum. This method yields more reliable results for the thermal resistance. In any case, $\mathrm{d}\lambda_{\text{center}}/\mathrm{d}T$ or $\mathrm{d}\lambda_{\text{mode}}/\mathrm{d}T$ has to be determined in advance by measuring the functions $\lambda_{\text{center}}(T)$ or $\lambda_{\text{mode}}(T)$, respectively, where T is the chip temperature.

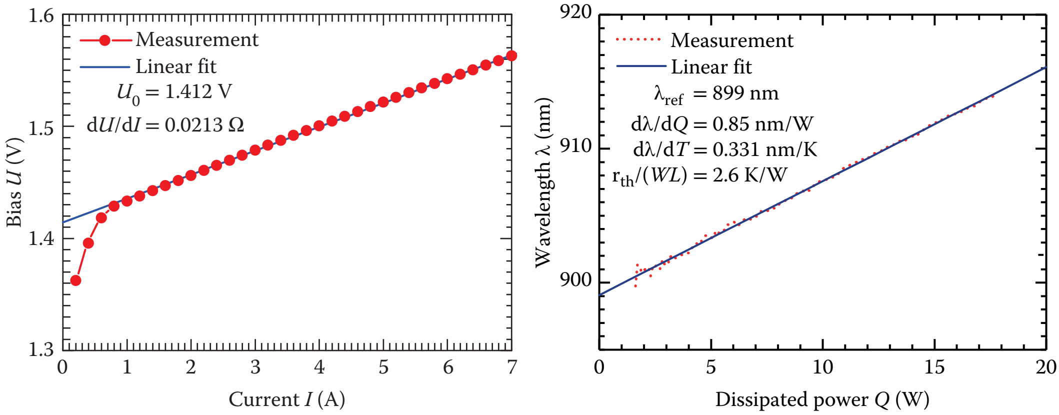

(a) (b)

FIGURE 27.4 Determination of series and thermal resistances. (a) Voltage–current characteristic. Bullets indicate measurements. Solid line indicates linear fit. (b) Center wavelength versus dissipated power. Light grey line indicates measurements. Straight line indicates linear fit. Cavity length and facet reflectivities are given in Table 27.1.

27.2.3 Comparison of Simulated and Measured CW Characteristics

In Figure 27.5 the measured $P-I$, $U-I$ and $\eta_c - I$ characteristics (solid lines) are compared with the results obtained with the phenomenological model (dashed lines) presented above in Section 27.2.1. The conversion efficiency η_c is defined as

$$\eta_c = \frac{P_{out}}{UI} \tag{27.23}$$

The bending of the power–current characteristics at high bias is caused by the temperature-induced increase of the threshold current and decrease of the slope efficiency (determined by the parameters T_0 and T_1 here) due to the power dissipation. It leads to what is commonly referred to as "thermal roll-over." However, the measured bending is stronger than the simulated one.

This discrepancy is caused by the fact that there are nonthermal reasons for the bending of the P–I characteristic at high bias (also referred as "power saturation") which cannot be addressed by the phenomenological laser models based on parameters measured at low bias. For example, bending of the conduction and valence bands and carrier accumulation effects occurring at large bias leading to enhanced nonstimulated recombination and internal absorption [11] result in an increased threshold current and a decreased external differential efficiency. Other effects are longitudinal spatial holeburning (LSH), nonlinear gain compression, and two-photon absorption as discussed in Sections 27.3.2 and 27.3.5, which result in a saturation of the output power.

These effects could be modeled phenomenologically by additional explicit current dependencies $I_{thr}(I)$ and $\eta_{ext}(I)$ with parameters j'_{thr} and j_{sat},

$$I_{thr} = I_{thr,0} + WLj'_{thr}\left(I - I_{thr,0}\right) \tag{27.24}$$

and

$$\eta_{ext} = \frac{\eta_{ext,0}}{1 + \frac{I - I_{thr,0}}{WLj_{sat}}}, \tag{27.25}$$

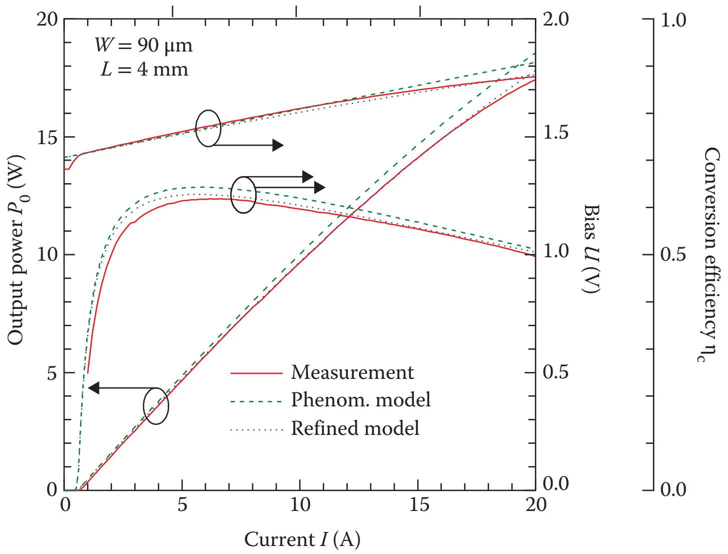

FIGURE 27.5 Output power at $z = 0$ (left axis), applied voltage (right axis), and conversion efficiency (right-most axis) versus injection current. Solid line indicates measurement and dashed line indicates phenomenological laser model. Dotted line indicates refined model.

respectively. The proportionality factor $j'_{\mathrm{thr}} > 0$ models the increase of the threshold current due to nonthermal effects with $I_{\mathrm{thr},0}$ given by Equation 27.6. Similarly, the parameter $j_{\mathrm{sat}} > 0$ causes a reduction of the external differential efficiency where $\eta_{\mathrm{ext},0}$ is given by Equation 27.7.

Furthermore, the series resistance varies also far above threshold, either caused by carrier accumulation (differential resistance $r'_{\mathrm{s}} < 0$) or temperature effects ($r'_{\mathrm{s}} > 0$),

$$r_{\mathrm{s}} = r_{\mathrm{s},0} + \frac{r'_{\mathrm{s}}}{WL}\left(I - I_{\mathrm{thr},0}\right) \tag{27.26}$$

With the refined model (dotted lines), a better match can be achieved as Figure 27.5 reveals. Note that the used parameters j'_{thr}, j_{sat}, and r'_{s} given in Table 27.1 are guess values. An even better agreement between theory and experiment could be achieved by employing a fitting procedure, probably.

27.3 Models for the Optical Power

In this section, we investigate the profile of the optical power in the cavity in more detail and derive some of the equations used in Section 27.2. Furthermore, we discuss the nonthermal effects responsible for the saturation of the output power with increasing injection current.

27.3.1 Basic Relations

The total power P can be always separated into forward and backward propagating parts,

$$P(z,t) = P^{+}(z,t) + P^{-}(z,t) \tag{27.27}$$

In an FP cavity, they fulfil the partial differential equations ($\partial_t = \partial/\partial t$, $\partial_z = \partial/\partial z$)

$$\partial_t P^{\pm} \pm v_{\mathrm{g}} \partial_z P^{\pm} = v_{\mathrm{g}}(g_{\mathrm{m}} - \alpha_{\mathrm{m}})P^{\pm} + \frac{\dot{P}_{\mathrm{sp}}}{2} \tag{27.28}$$

subject to the boundary conditions

$$\begin{aligned} P^{+}(0,t) &= R_0 P^{-}(0,t) \\ P^{-}(L,t) &= R_L P^{+}(L,t) \end{aligned} \tag{27.29}$$

Here $g_{\mathrm{m}} - \alpha_{\mathrm{m}}$ is the modal net gain in the cavity with g_{m} being the modal gain and α_{m} the modal losses, L the cavity length, $v_{\mathrm{g}} = c/n_{\mathrm{g}}$ the group velocity with n_{g} being the modal group index, and $\dot{P}_{\mathrm{sp}}$ the rate of spontaneous emission coupled into the lasing modes. The total output power at the facets is $P_{\mathrm{out}} = P_0 + P_{\mathrm{L}}$ with

$$P_0 = (1 - R_0)P^{-}(0), \quad P_{\mathrm{L}} = (1 - R_{\mathrm{L}})P^{+}(L) \tag{27.30}$$

Integrating Equation 27.28 along z, adding both equations, and taking into account Equation 27.29 we obtain the power balance

$$\frac{1}{v_{\mathrm{g}}}\frac{\mathrm{d}\bar{P}}{\mathrm{d}t} = -\frac{P_{\mathrm{out}}}{L} + \frac{1}{L}\int_0^L (g_{\mathrm{m}} - \alpha_{\mathrm{m}})P\,\mathrm{d}z + \frac{1}{v_{\mathrm{g}}L}\int_0^L \dot{P}_{\mathrm{sp}}\,\mathrm{d}z \tag{27.31}$$

with the average internal power

$$\bar{P} = \frac{1}{L}\int_0^L (P^+ + P^-)\,\mathrm{d}z. \tag{27.32}$$

In what follows, we consider the steady state ($\partial_t = 0$) and two special cases, namely the case around threshold and the case above threshold.

27.3.1.1 Steady State around Threshold

Around threshold both $g_\mathrm{m} - \alpha_\mathrm{m}$ and $\dot{P}_\mathrm{sp}$ can be assumed to be constant (z-independent). Therefore, the solution of Equation 27.28 taking into account Equation 27.29 is

$$P^\pm(z) = \frac{\dot{P}_\mathrm{sp}}{2v_\mathrm{g}} \cdot \frac{C^\pm e^{\pm(g_\mathrm{m}-\alpha_\mathrm{m})z} - 1}{g_\mathrm{m} - \alpha_\mathrm{m}} \tag{27.33}$$

with

$$C^+ = \frac{1 - R_0 + (1 - R_L)R_0 e^{(g_\mathrm{m}-\alpha_\mathrm{m})L}}{1 - R_0 R_L e^{2(g_\mathrm{m}-\alpha_\mathrm{m})L}} \tag{27.34}$$

$$C^- = \frac{1 - R_L + (1 - R_0)R_L e^{(g_\mathrm{m}-\alpha_\mathrm{m})L}}{1 - R_0 R_L e^{2(g_\mathrm{m}-\alpha_\mathrm{m})L}} e^{(g_\mathrm{m}-\alpha_\mathrm{m})L}. \tag{27.35}$$

The ratio between the outcoupled powers at the facets is given by

$$\frac{P_L}{P_0} = \frac{1 - R_L}{1 - R_0} \cdot \frac{1 + R_0 e^{(g_\mathrm{m}-\alpha_\mathrm{m})L}}{1 + R_L e^{(g_\mathrm{m}-\alpha_\mathrm{m})L}} \tag{27.36}$$

If the spontaneous emission approaches zero, $C^\pm$ must go to infinity to obtain a nonzero output power, which yields the so-called threshold condition $g_\mathrm{m} - \alpha_\mathrm{m} = \alpha_\mathrm{out}$.

27.3.1.2 Steady State above Threshold

Above threshold $g_\mathrm{m} - \alpha_\mathrm{m}$ cannot longer be assumed to be constant due to LSH, but the spontaneous emission can be neglected, $\dot{P}_\mathrm{sp} = 0$. Hence, the solution of Equation 27.33 is

$$P^\pm(z) = P^\pm(0) e^{\pm \int_0^z [g_\mathrm{m}(z') - \alpha_\mathrm{m}(z')]\,dz'}. \tag{27.37}$$

In order to obey the boundary conditions Equation 27.29, the threshold condition

$$g_\mathrm{thr} = \frac{1}{L}\int_0^L \alpha_\mathrm{m}\,\mathrm{d}z + \alpha_\mathrm{out} \tag{27.38}$$

must hold, where α_out are the outcoupling losses Equation 27.9 and

$$g_\mathrm{thr} = \frac{1}{L}\int_0^L g_\mathrm{m}\,\mathrm{d}z \tag{27.39}$$

is the threshold gain. The ratio between the outcoupled powers

$$\frac{P_L}{P_0} = \frac{1 - R_L}{1 - R_0}\sqrt{\frac{R_0}{R_L}} \tag{27.40}$$

follows from the boundary conditions Equation 27.29, the general relation

$$\partial_z(P^+P^-) = 0 \tag{27.41}$$

and from the ratio between the internal and external powers given by Equation 27.30.

27.3.1.3 External Differential Efficiency

From the threshold condition Equation 27.38, the modal threshold gain g_{thr} can be calculated and from that, depending on the model used, the threshold carrier density N_{thr}, the threshold voltage U_{thr}, or the threshold current I_{thr}. Finally, the external differential efficiency is the ratio between the energy leaving the cavity and the energy generated by stimulated recombination (cf. Equation 27.47),

$$\eta_{\mathrm{ext}} = \frac{P_{\mathrm{out}}}{\hbar\omega \int R_{\mathrm{st}}\,\mathrm{d}V} = \frac{P_{\mathrm{out}}}{\int g_{\mathrm{m}} P\,\mathrm{d}z}. \tag{27.42}$$

Assuming z-independent $g_{\mathrm{m}} - \alpha_{\mathrm{m}}$, the relation between the total output power and the average internal power follows from Equations 27.31 and 27.38 to

$$P_{\mathrm{out}} = \alpha_{\mathrm{out}} L \bar{P} \tag{27.43}$$

and the external differential efficiency is

$$\eta_{\mathrm{ext}} = \frac{\alpha_{\mathrm{out}}}{g_{\mathrm{thr}}} \tag{27.44}$$

27.3.2 Rigrod Model

In order to determine the variation of the modal gain along z above threshold, a model for the carrier densities is required. The simplest model consists of a rate equation for the excess carrier density N in the active region

$$\frac{\mathrm{d}N}{\mathrm{d}t} = \frac{j}{ed} - R(N, P) \tag{27.45}$$

with a constant injection current density j. The recombination rate [12]

$$R = R_{\text{non-rad}} + R_{\mathrm{sp}} + R_{\mathrm{st}} \tag{27.46}$$

consists of nonradiative (Shockley–Read–Hall, Auger) recombination $R_{\text{non-rad}}$, radiative spontaneous recombination R_{sp}, and radiative stimulated recombination:

$$R_{\mathrm{st}} = \frac{g_{\mathrm{m}} P}{dW\hbar\omega} \tag{27.47}$$

where $P = P^{+} + P^{-}$, g_{m} is the modal gain, $\hbar\omega$ the photon energy, d the thickness of the active region, and W the width of the active region.[†]

Even for the steady-state above threshold, there exists no analytical solution of Equations 27.28 and 27.45. However, if the nonstimulated recombination rate and the gain are linearized,

$$R_{\text{non-rad}} + R_{\mathrm{sp}} = \frac{N}{\tau_N} \tag{27.48}$$

and

$$g_{\mathrm{m}} = g'_{\mathrm{m}}(N - N_{\mathrm{tr}}), \tag{27.49}$$

respectively, and inserted into Equation 27.45, the excess carrier density N can be determined.

Introducing the obtained expression for N again into Equation 27.49 yields

$$g_{\mathrm{m}} = \frac{g_0}{1 + \frac{P}{P_{\mathrm{sat}}}} \tag{27.50}$$

with the unsaturated gain

$$g_0 = \frac{g'_{\mathrm{m}}\tau_N}{ed}(j - j_{\mathrm{tr}}) \tag{27.51}$$

where g'_{m} is the differential gain, τ_N the effective carrier lifetime, $j_{\mathrm{tr}} = edN_{\mathrm{tr}}/\tau_N$ the transparency current density, N_{tr} the transparency carrier density, and

$$P_{\mathrm{sat}} = \frac{dW\hbar\omega}{g'_{\mathrm{m}}\tau_N} \tag{27.52}$$

is the saturation power. For the typical values of $d = 10$ nm, $W = 100$ µm, $g'_{\mathrm{m}} = 10 \cdot 10^{-18}\ \mathrm{cm}^2$, $\tau_N = 1$ ns, and $\hbar\omega = 1.24$ eV, we obtain $P_{\mathrm{sat}} = 0.2$ W, which is much smaller than the internal power of state-of-the-art broad-area lasers operated far above threshold.

The resulting equation for the steady-state

$$\pm\frac{\mathrm{d}P^{\pm}}{\mathrm{d}z} = \left(\frac{g_0}{1 + \frac{P^{+}+P^{-}}{P_{\mathrm{sat}}}} - \alpha_{\mathrm{m}}\right)P^{\pm} + \frac{\dot{P}_{\mathrm{sp}}}{2v_{\mathrm{g}}} \tag{27.53}$$

has been analytically solved by Rigrod [13] neglecting spontaneous emission and modal losses ($\dot{P}_{\mathrm{sp}} = \alpha_{\mathrm{m}} = 0$). For the general case a numerical solution has to be employed.

For $P_{\mathrm{sat}} \ll P$, $P^{+} \ll P^{-}$, $g_{\mathrm{m}} \approx g_0 P_{\mathrm{sat}}/P^{-}$ and the resulting equation

$$-\frac{\mathrm{d}P^{-}}{\mathrm{d}z} = g_0 P_{\mathrm{sat}} - \alpha_{\mathrm{m}}P^{-} + \frac{\dot{P}_{\mathrm{sp}}}{2v_{\mathrm{g}}} \tag{27.54}$$

[†] Equation 27.47 follows from Equation 27.140 by averaging over the active region $1/(\mathrm{d}W)\iint \mathrm{d}x\mathrm{d}y$, taking into account Equation 27.106 and $n_{\mathrm{m}} = \bar{n}$.

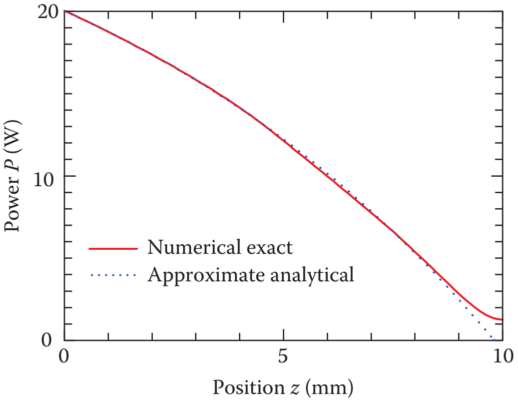

FIGURE 27.6 Longitudinal profiles of the total power for the parameters in Table 27.2 based on the numerical solution of Equation 27.53 (solid) and the analytical solution of Equation 27.55 (dashed).

has an analytical solution, too, namely

$$P(z) \approx P^-(z) = P^-(0)e^{\alpha_m z} + \left(g_0 P_{\text{sat}} + \frac{\dot{P}_{\text{sp}}}{2v_g} \right) \left(\frac{1 - e^{\alpha_m z}}{\alpha_m} \right) \tag{27.55}$$

In Figure 27.6, the exact and approximate solutions are compared. Except near the right facet located at $z = 10$ mm where the condition $P^+ \ll P^-$ is not fulfilled, a good agreement can be noted. Note that according to Equation 27.55 $P(z)$ varies linearly for vanishing modal absorption $\alpha_m = 0$.

27.3.3 Treat-Power-as-a-Parameter Method

The equation for the steady-state longitudinal power profile above threshold

$$\pm \frac{dP^\pm}{dz} = \left[g_m(P) - \alpha_m \right] P^\pm \tag{27.56}$$

subject to the boundary conditions Equation 27.29 can be conveniently solved numerically by the “treat-power-as-a-parameter” (TPP) method as introduced for the simulation of DFB lasers in Reference [14] and applied to high-power Fabry–Pérot lasers in Reference [15]. In a first step, g_m is calculated as a function of an external parameter (such as injection current I or bias U) and the power P, and stored in a look-up table, together with other quantities of interest (e.g., λ and I). In a second step, the boundary value problem (Equation 27.56) is solved by interpolating g_m in the look-up table. For given I or U, one chooses a guess value $P^-(0)$ and integrates Equation 27.56 from $z = 0$ to $z = L$ where typically the boundary condition is not fulfilled. Therefore, the function $P^-(L) - R_L P^+(L)$ has to be nullified by varying $P^-(0)$. It is also possible to give $P^-(0)$ and to vary I or U to fulfil the boundary condition.

The lasing wavelength can be determined approximately by searching the maximum of integral $\int_0^L (g_m - \alpha_m)\, dz$ with respect to λ. LSH is included automatically via the power dependence of g_m in Equation 27.56. If g_m is evaluated at the average power $\bar{P}$ in the cavity, the usual model neglecting LSH is recovered.

27.3.4 LSH and the Impact of Series Resistance and Internal Loss

The assumption of a constant injection current density in Equation 27.45 results in an overestimation of spatial hole burning. At the ohmic contacts, the quasi-Fermi potentials of electrons and holes, φ_n and

φ_p, respectively, are fixed and given by the applied bias, $\varphi_n = 0$ at the n-contact and $\varphi_p = U$ at the p-contact. The injection current density can be set equal to the hole current density and thus proportional to the gradient of the quasi-Fermi potential of the holes at the boundary between the active region and the p-doped region. Assuming isothermal conditions, one-dimensional current flow, and vanishing recombination outside the active region as well as infinitely high electron conductivity ($\sigma_n \to \infty$) in the n-doped region,

$$j(N) = \frac{U - \varphi_F(N)}{r_s} \tag{27.57}$$

can be derived from Equations 27.138 and 27.149 for the region beneath the p-contact, where $\varphi_F(N) = \varphi_p(N) - \varphi_n(N)$ is the Fermi voltage and

$$r_s = \sum_i \frac{d_i}{\sigma_{p,i}} \tag{27.58}$$

is the area-related total series resistance of the p-doped layers with thicknesses d_i and hole conductivities $\sigma_{p,i}$ between the active region and p-contact stripe.

For parabolic bands the relations between quasi-Fermi potentials φ_n and φ_p and the electron and hole densities n and p, respectively, are given by

$$e\varphi_n = -k_B T \mathcal{F}_i^{\text{inv}}\left(\frac{n}{N_c}\right) - E_c + e\varphi \qquad \text{and} \qquad e\varphi_p = k_B T \mathcal{F}_i^{\text{inv}}\left(\frac{p}{N_v}\right) - E_v + e\varphi, \tag{27.59}$$

where E_c, E_v are the (effective) conduction and valence band edges, N_c and N_v the conduction and valence band edge density of states, $\mathcal{F}_i^{\text{inv}}$ the inverse Fermi integrals with $i = 1/2$ for bulk and $i = 0$ for QW active regions and φ the electrostatic potential. Hence, the Fermi voltage is given by

$$\varphi_F = \frac{k_B T}{e}\left[\mathcal{F}_i^{\text{inv}}\left(\frac{p}{N_v}\right) + \mathcal{F}_i^{\text{inv}}\left(\frac{n}{N_c}\right)\right] + \frac{E_g}{e} \tag{27.60}$$

where $E_g = E_c - E_v$ is the energy gap. In Equation 27.57, local charge neutrality $p - n + p_D - n_A = 0$ is assumed so that the electron and hole densities are given by $n = n_0 + N$ and $p = p_0 + N$, respectively, with n_0, p_0 being the equilibrium densities and N the excess carrier density.

For $r_s \to \infty$, the usual model of a constant current density is recovered, whereas for $r_s \to 0$, the carrier density becomes constant. This can be more readily seen by expanding $\varphi_F(N)$ around the average carrier density $\bar{N}$ which yields

$$j(N) = \bar{j} - \frac{\varphi_F'}{r_s}(N - \bar{N}) \tag{27.61}$$

where the transition between both models (constant current density and constant carrier density, respectively) is governed by the parameter φ_F'/r_s.

Equations 27.56 and 27.45 with Equations 27.46, 27.47, and 27.57 assuming linear recombination and gain models, Equations 27.48 and 27.49, respectively, have been solved using the TPP method. The parameters used are given in Table 27.2. In Figure 27.7a, the influence of the series resistance on the power–current characteristics is clearly visible. For $r_s = 10^{-6}\ \Omega \cdot \text{cm}^2$ almost the same characteristics as without LSH is obtained.

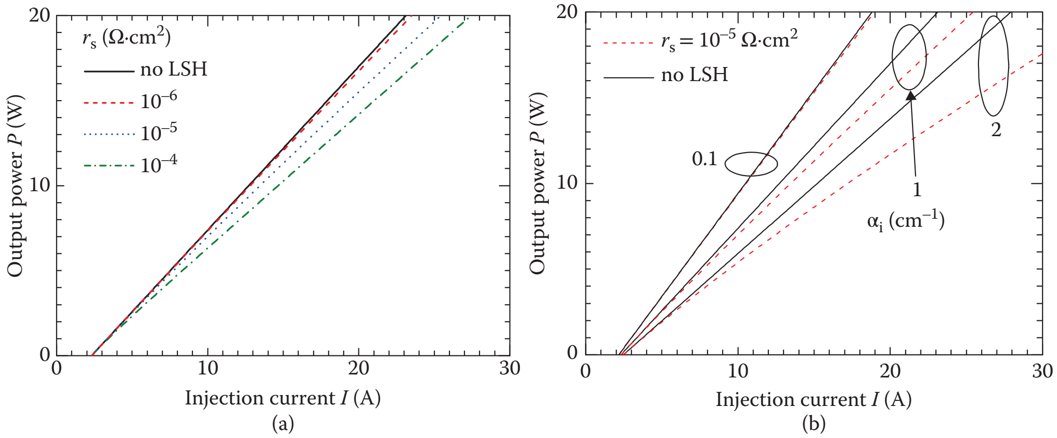

FIGURE 27.7 Power–current characteristics without (black solid) and with longitudinal spatial holeburning for different series resistances r_s and modal losses α_m. (a) Influence of the series resistance for a modal loss of $\alpha_m = 1\ \text{cm}^{-1}$ and (b) Influence of modal losses for a series resistance of $r_s = 10^{-5}\Omega \cdot \text{cm}^2$.

TABLE 27.2 Laser Parameters Used to Investigate Power Saturation Effects

Parameter	Symbol	Value	Unit
Front facet reflectivity	R_0	0.001	
Rear facet reflectivity	R_L	0.95	
Width of active region	W	100	μm
Thickness of active region	d	10	nm
Cavity length	L	1	cm
Modal losses	α_m	1	cm^{-1}
Rate of spontaneous emission	$\dot{P}_{sp}$	0	
Differential modal gain	g'_m	$10 \cdot 10^{-18}$	cm^2
Transparency carrier density	N_{tr}	10^{18}	cm^{-3}
Carrier lifetime	τ_N	1	ns
Wavelength	λ	1000	nm
Series resistance	r_s	10^{-5}	Ω · cm^2
Temperature	T	300	K
Conduction band density of states	N_c	$0.4 \cdot 10^{18}$	cm^{-3}
Valence band density of states	N_v	$13 \cdot 10^{18}$	cm^{-3}

If there are no internal losses, LSH has no impact on the slope efficiency at all, because from Equation 27.31

$$P_{\text{out}} = \int_0^L g_m P \,\mathrm{d}z \tag{27.62}$$

follows and Equation 27.42 gives $\eta_{\text{ext}} = 1$ independent of the spatial profiles of g_m and P. As Figure 27.7b reveals, the difference between the power–current characteristics calculated with and without spatial hole burning increases with increasing modal losses.

The longitudinal profiles of forward, backward, and total power; modal gain; and injected current density are shown in Figure 27.8 for the extreme values of r_s. For a high value of r_s (Figure 27.8a), the injected current density is almost constant, so that the gain varies strongly. In contrast, for a low value of r_s (Figure 27.8b) the injected current density varies strongly so that the gain is almost constant. This results in quite different power profiles. In particular, the averaged internal power differs by almost a factor of 2 ($\bar{P} = 11$ W versus $\bar{P} = 6$ W). Besides by a reduction of the internal losses, the series resistance or the asymmetry in the facet coating ("unfolding the cavity" [16]) LSH could be mitigated by a tapered lateral waveguide design where the contact width W increases from the rear facet toward the front facet [17,18].

27.3.5 Discussion of Further Nonthermal Power Saturation Effects

27.3.5.1 Nonlinear Gain Compression

There are a couple of effects that can be described by an effective decrease of the optical gain with increasing photon density $|u|^2$ or power P, described by the functions

$$g = \frac{g_0}{1 + \epsilon_s |u|^2} \quad \text{or} \quad g = \frac{g_0}{1 + \frac{P}{P_s}} \tag{27.63}$$

similar to Equation 27.50. The relation between the gain compression factor ϵ_s and the saturation power P_s is given by

$$P_s = \frac{dWv_g\hbar\omega}{\Gamma\epsilon_s} \tag{27.64}$$

where Γ is the optical confinement factor of the active region. The gain compression factor is of the order $\epsilon_s \propto 10^{-17}$ cm^3, which results in a saturation power of $P_s \propto 150$ W for typical values $d = 10$ nm, $W = 100$ μm, $\Gamma = 0.01$, $n_g = 4$, $\lambda_0 = 1$ μm. Hence gain compression effects are of minor importance for CW lasers, but might result in power saturation of pulsed lasers where $P = 100$ W from a stripe width of $W = 100$ μm can be achieved [19].

The first effect contributing to nonlinear gain compression is spectral hole burning, which arises due to the interplay of the depletion of the carriers at the lasing wavelength due to stimulated emission and

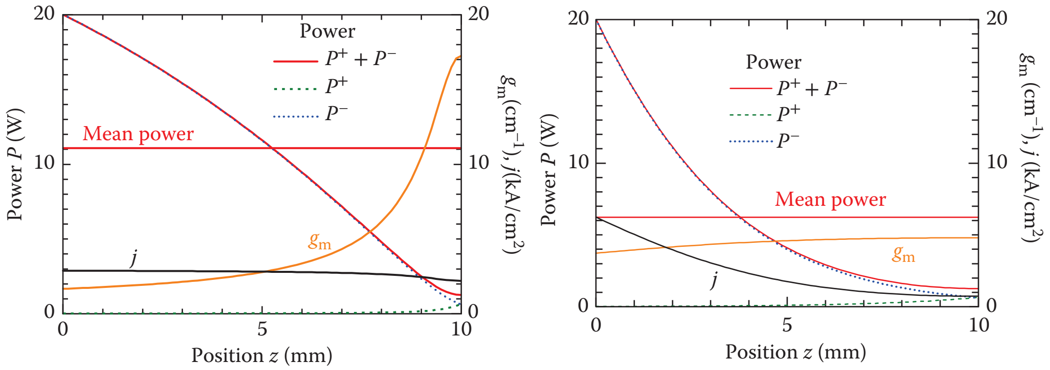

(a) (b)

FIGURE 27.8 Longitudinal profiles of forward (P^+), backward (P^-), and total ($P = P^+ + P^-$), power, modal gain g_m, and injected current density j for two series resistances r_s at an output power of $P_{out} = 20$ W. (a) Series resistance $r_s = 10^{-4}$ cm^2 and (b) series resistance $r_s = 10^{-6}$ cm^2. The horizontal line is the averaged internal (mean) power $\bar{P}$.

the relaxation of injected carriers into the depleted spectral region. At high power densities, the relaxation processes due to intraband carrier–carrier scattering with a time scale of 50–100 fs are not sufficiently fast to fill the spectral hole formed by the optical transitions. This results in a reduction of the optical gain around the lasing wavelength.

A second effect is the increase of the temperatures of the carrier distributions beyond the lattice temperature by the removal of "cold" carriers near the band-edges due to stimulated emission or by the transfer of carriers to high energies within the bands by free-carrier, inter-valence band and two-photon absorption. The temperature increase results in a reduction of the optical gain, too.

Nonlinear gain compression also can be caused by lateral spatial hole burning [20] and the Bragg grating induced by the standing waves in Fabry–Pérot lasers [21]. The impact of both the gain compression and two-photon absorption on the power–current characteristics is discussed in the next section (cf. Figure 27.9).

27.3.5.2 Two-Photon Absorption

The two-photon absorption coefficient β is described in more detail in Section 27.5.2. The resulting modal absorption for a broad-area laser with a lateral top-hat intensity profile is given by (cf. Equation 27.121)

$$\alpha_{2,\mathrm{m}} = \frac{\int n_\mathrm{r}(x,y)\beta(x,y)|\Phi(x,y)|^4\,\mathrm{d}x\mathrm{d}y}{n_\mathrm{m}(\int |\Phi(x,y)|^2\,\mathrm{d}x\mathrm{d}y)^2} P \approx \frac{\int n_\mathrm{r}(y)\beta(y)|\phi(y)|^4\,\mathrm{d}y}{n_\mathrm{m}(\int |\phi(y)|^2\,\mathrm{d}y)^2}\frac{P}{W} = \frac{\bar{\beta}_\mathrm{m}}{A_\mathrm{m}} P, \tag{27.65}$$

where ϕ is the profile of the vertical mode, W the lateral width, n_m the modal index, and A_m the mode area given by

$$A_\mathrm{m} = \frac{W(\int |\phi(y)|^2\,\mathrm{d}y)^2}{\int |\phi(y)|^4\,\mathrm{d}y} \tag{27.66}$$

and

$$\bar{\beta}_\mathrm{m} = \frac{\int n_\mathrm{r}(y)\beta(y)|\phi(y)|^4\,\mathrm{d}y}{n_\mathrm{m}\int |\phi(y)|^4\,\mathrm{d}y} \tag{27.67}$$

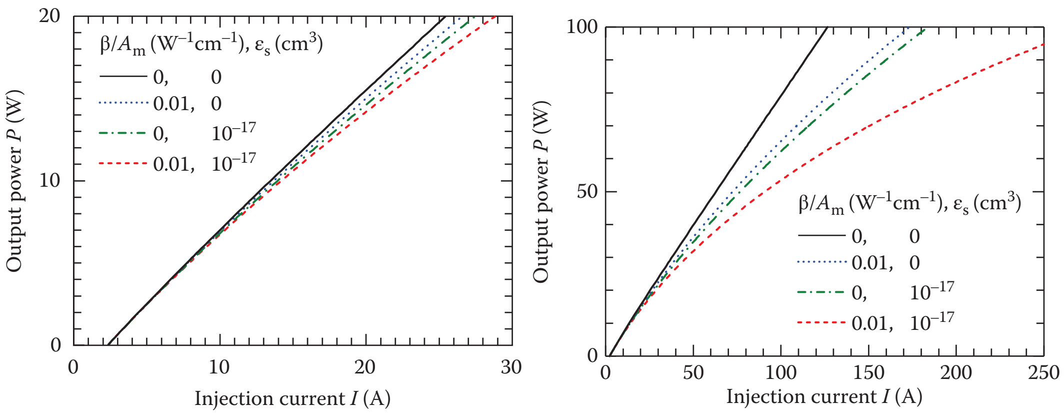

(a)

(b)

FIGURE 27.9 Impact of nonlinear-gain compression ϵ_s and two-photon absorption $\bar{\beta}_\mathrm{m}/A_\mathrm{m}$ on the power–current characteristics. (a) Power range corresponding to CW operation. (b) Power range corresponding to pulsed operation.

Approximating the intensity profile of the vertical mode by a Gaussian with a full width d_{1/e^2} at $1/e^2$ maximum,

$$\phi^2(y) = e^{-8y^2/d_{1/e^2}^2} \tag{27.68}$$

the mode area is $A_\mathrm{m} = \frac{\sqrt{\pi}}{2} d_{1/e^2} W \approx d_{1/e^2} W$. Assuming an averaged two-photon absorption coefficient of $\bar{\beta}_\mathrm{m} = 15\ \mathrm{cm} \cdot \mathrm{GW}^{-1}$ (cf. Figure 27.12a) and $d_{1/e^2} = 1.5\ \mu\mathrm{m}$ as appropriate for a high-power laser we obtain $\bar{\beta}_\mathrm{m}/d_{1/e^2} = 10^{-4}\ \mathrm{W}^{-1}$. For $W = 100\ \mu\mathrm{m}$ and $P = 10$ W this results in a modal absorption coefficient of $\alpha_{2,\mathrm{m}} = 0.1\ \mathrm{cm}^{-1}$. Note that the modal two-photon absorption is maximal at minimum d_{1/e^2}, i.e., for a strong optical confinement. The secondary two-photon loss mechanism due to intraband absorption caused by the free carriers generated by two-photon absorption is strongly dependent on the carrier lifetime and the effective drift-diffusion length. In most cases, the resulting absorption coefficient can be neglected, except in structures where the intensity peak of the vertical mode is not located at the position of the active layer [22].

Figure 27.9 shows the impact of nonlinear gain compression and two-photon absorption on the power–current characteristics using the model presented in Section 27.3.4 with the parameters given in Table 27.2. The following conclusions can be drawn: First, a gain compression factor $\epsilon_\mathrm{s} = 10^{-17}\ \mathrm{cm}^3$ (saturation power $P_\mathrm{s} = 150$ W) or a two-photon absorption coefficient $\bar{\beta}/A_\mathrm{m} = 0.01\ (\mathrm{Wcm})^{-1}$ act very similar. Second, at a current of $I = 15$ A, which is typical for lasers operating in CW mode, the combination of both effects results in a reduction of the optical power by 10% (2 W; cf. Figure 27.9a). However, at a current of $I = 125$ A, which can be reached under pulsed operation [19], the power is reduced from 100 to 60 W, which seems a little bit too large, considering that leakage currents are not accounted for at all. Hence, either the gain compression factor or the two-photon absorption coefficient or both are smaller in reality than assumed here.

27.3.5.3 Leakage Currents

Leakage currents caused by the transport of carriers into regions without stimulated recombination can be divided into vertical and lateral ones. Vertical leakage currents are minority currents caused by the accumulation and subsequent recombination of electrons and holes in the p-doped and n-doped, respectively, optical confinement layers. This effect results in an increased free-carrier absorption, too. An analytical investigation of the carrier accumulation in the confinement layers and its impact on the power–current characteristics can be found in Reference [23] and an exact treatment based on the numerical solution of the drift-diffusion equations has been given in Reference [11,24].

The electron current flowing into the p-doped region can be obtained by integrating the continuity equation for the electron current density (Equation 27.137) over the p-doped region between the upper boundary of the active region $y = y_p$ and the p-metallization for the steady state,

$$\int_{\partial(\text{p-region})} \boldsymbol{j}_n \cdot \boldsymbol{n} dS = e \int_{\text{p-region}} R\, dV \tag{27.69}$$

where ∂ (p-region) denotes the surface of the p-doped region with $\boldsymbol{n}$ being the normal vector. Assuming that the normal components of the electron current density vanish at the outer boundaries including the p-contact, we obtain the electron leakage current

$$I_\mathrm{n,leak} = \iint j_{n,y}|_{y=y_p}\, \mathrm{d}x\mathrm{d}z. \tag{27.70}$$

Hence, the electron leakage current can be calculated either from the electron current density at the boundary between active region and p-doped region or by integrating the recombination rate over the corresponding volume.

Figure 27.10a and b shows the vertical profiles of the current densities and the recombination rate of the asymmetric super-large optical-cavity structure published in [10] at a current of $I = 15$ A. Figure 27.10a reveals that for a properly designed structure the hole current flowing into the n-doped region can be neglected. The leakage current calculated from the electron current density at $y = 1.9$ μm is $I_{n,leak} = 0.44$ A, which is also obtained from the integration of the recombination rate. The relative fraction of the leakage current is $(I - I_{n,leak})/I = 0.97$, which coincides with the internal efficiency $\eta_i = 0.97$, obtained from the length-dependent measurement of the external differential efficiency as described in 27.2.

With increasing bias the leakage current increases due to the bending of the band edges as shown in Reference [11], which contributes to the roll-over of the power–current characteristics. The electron leakage current can be reduced by an increase of the energy gap and doping level or a decrease of the thickness of the p-doped optical confinement layer as it is the case in extreme-asymmetric super large optical cavities. However, one should keep in mind that an increase of the energy gap results in a decrease of the electrical conductivity in the AlGaAs material system, an increase of the doping results in an increase of the free-carrier absorption and an increase of the waveguide asymmetry results in a decrease of the field intensity at the position of the active region.

The lateral leakage current $I_{p,spead}$ caused by current spreading in the p-doped region can be reduced by an insulation of the highly doped p-contact and p-cladding layers beyond the p-metallization by implantation, diffusion of impurities, or etching as indicated in Figure 27.1 or by implementing a reverse-biased p-n junction. The lateral leakage current due to the diffusion of the carriers along the active region is more difficult to mitigate.

An approximate expression for $I_{p,spead}$ has been derived in Reference [25],

$$\frac{I_{p,spead}}{L} \approx -2\frac{\partial \varphi_F}{\partial x}\bigg|_{x=W/2} \sum_i \sigma_{p,i} d_i \tag{27.71}$$

where φ_F is the Fermi voltage given in Equation 27.60, $\sigma_{p,i}$ the hole conductivity of layer i and d_i the corresponding thickness. The derivative has to be taken at the edge of the p-contact stripe, and the summation includes all p-doped continuous semiconductor layers above the active region.

27.3.5.4 Carrier Capture

As it is well known [26–30], the carriers belonging to bound states in the QW(s) of the active region are not necessarily in thermal equilibrium with the carriers resulting from the continuum states located

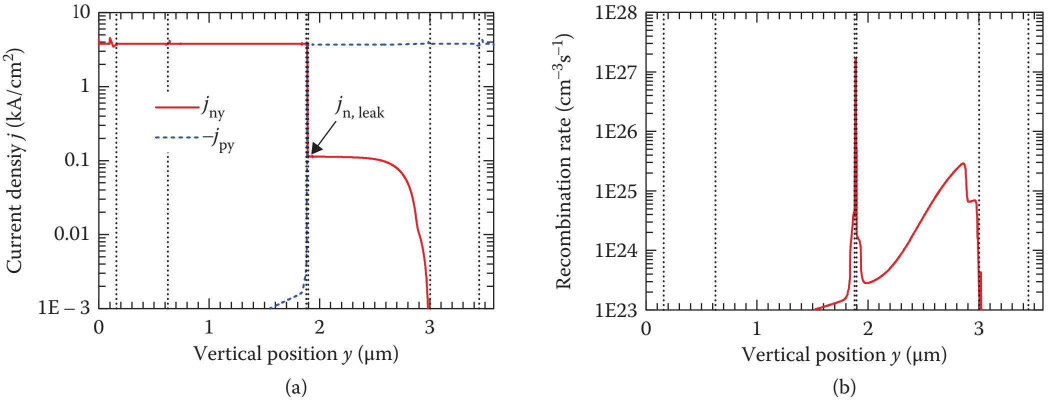

(a)

(b)

FIGURE 27.10 Vertical profiles of (a) current densities and (b) recombination rate for p-contact width $W = 100$ μm, cavity length $L = 4000$ μm, and output power $P = 15$ W. Heteroboundaries are indicated by dotted vertical lines. Note the logarithmic scales of the ordinates.

energetically above the QWs. It can be assumed that both types of carriers coexisting in the QW region are in quasi-equilibrium among themselves described by Fermi–Dirac statistics with independent quasi-Fermi potentials and transferred into each other by capture-escape processes. The transport of both types of carriers in the in-plane directions (x, z) can be described by classical drift diffusion. Most conveniently the bound carriers are described by sheet densities (unit $1/\mathrm{m}^2$) and appear in the rhs of the Poisson equation (27.141) as interface states.

An expression for the capture–escape rate that fulfils universal conditions such as the balance between capture and escape in case of equal quasi-Fermi potentials and no capture but finite escape in case of a fully occupied bound states has been given in [30]. For electrons (similarly for holes) it reads

$$Q_n = \frac{dn_\mathrm{f}}{\tau_\mathrm{c}}\left[1 - \frac{n_\mathrm{b}}{N_\mathrm{b}}\right]\left[1 - e^{\frac{e(\varphi_\mathrm{f}-\varphi_\mathrm{b})}{kT}}\right] \tag{27.72}$$

where n_f and n_b are the free and bound, electron densities, respectively; φ_f and φ_b are the corresponding quasi-Fermi potentials; d is the thickness of the QW(s); τ_c is the capture time; and N_b is the maximum bound electron density ($\varphi_\mathrm{b} \rightarrow -\infty$). Whereas the quasi-Fermi potentials of the free carriers depend directly on the bias applied to the contacts, the quasi-chemical potentials of the bound carriers are determined by the capture-escape rates.

The impact of the nonequilibrium between confined and unconfined carriers in high-power lasers on the power–current characteristics as a function of the hole capture time has been investigated in Reference [28], using, however, a capture-escape rate that differs from the one given in Equation 27.72.

27.4 Model for the Optical Field

We derive the parabolic paraxial wave equation based on the slowly varying amplitude and rotating wave approximations, taking into account gain dispersion, spontaneous emission, and a third-order nonlinear susceptibility. A balance equation for the electromagnetic energy density will be given.

27.4.1 Basic Three-Dimensional Equations

We start with the homogeneous Maxwell equation for the electric field $\boldsymbol{E}$ and the magnetic field $\boldsymbol{H}$:

$$\nabla \cdot \boldsymbol{D} = 0 \tag{27.73}$$

$$\nabla \cdot \boldsymbol{H} = 0 \tag{27.74}$$

$$\nabla \times \boldsymbol{E} + \mu_0 \partial_t \boldsymbol{H} = 0 \tag{27.75}$$

$$\nabla \times \boldsymbol{H} - \partial_t \boldsymbol{D} = 0 \tag{27.76}$$

where $\boldsymbol{D} = \varepsilon_0 \boldsymbol{E} + \boldsymbol{P}$ denotes the electric displacement and $\boldsymbol{P}$ the macroscopic polarization density of the material. The fields $\boldsymbol{E}, \boldsymbol{H}, \boldsymbol{D}$ depend on three spatial variables $\boldsymbol{r} = (x, y, z)$ and the time t. By applying $\nabla\times$ to Equation 27.75, ∂_t to Equation 27.76, and using Equation 27.73 we get the wave equation

$$\frac{1}{\varepsilon_0}\nabla(\nabla \cdot \boldsymbol{P}) + \nabla^2 \boldsymbol{E} = \frac{1}{c^2}\partial_{tt}\boldsymbol{E} + \mu_0 \partial_{tt}\boldsymbol{P} \tag{27.77}$$

The polarization density $\boldsymbol{P}$ contains a linear convolution of the electric field history $\boldsymbol{E}(t - \tau)$, $\tau \geq 0$, with a susceptibility function $\chi(r, \tau)$ and a second-order part which models dispersion ($\boldsymbol{P}_\mathrm{disp}$), nonlinear effects

($\boldsymbol{P}_{\mathrm{NL}}$), and spontaneous emission ($\boldsymbol{P}_{\mathrm{sp}}$):

$$\boldsymbol{P}(\boldsymbol{r},t) = \varepsilon_0 \int\limits_0^{\infty} \chi(r,\tau)\boldsymbol{E}(\boldsymbol{r},t-\tau)\,\mathrm{d}\tau + \boldsymbol{P}_{\mathrm{disp}}(\boldsymbol{r},t) + \boldsymbol{P}_{\mathrm{NL}}(\boldsymbol{r},t) + \boldsymbol{P}_{\mathrm{sp}}(\boldsymbol{r},t) \tag{27.78}$$

The spontaneous emission is modeled by introducing a spontaneous current density,

$$\partial_t \boldsymbol{P}_{\mathrm{sp}}(\boldsymbol{r},t) = \boldsymbol{J}_{\mathrm{sp}}(\boldsymbol{r},t) \tag{27.79}$$

We assume that $\boldsymbol{P}$ either is slowly varying in space, so that $\boldsymbol{\nabla}\cdot\boldsymbol{P} \approx 0$ holds, or has discontinuities at boundaries between different materials. At these boundaries $\boldsymbol{E}$ and $\boldsymbol{H}$ have to fulfill certain continuity rules that can be derived from Maxwell equations. Due to the nearly planar geometry of edge-emitting lasers defined by the epitaxial layer structure, the electromagnetic field is either mainly transverse electric (TE) or transverse magnetic (TM) polarized. By assuming TE polarization and choosing a reference frequency ω_0, we have

$$\begin{aligned}
\boldsymbol{E}(\boldsymbol{r},t) &= \boldsymbol{e}_x \frac{1}{2} E(\boldsymbol{r},t)\mathrm{e}^{i\omega_0 t} + \text{c.c.}\\
\boldsymbol{P}_{\mathrm{disp}}(\boldsymbol{r},t) &= \boldsymbol{e}_x \frac{1}{2} P_{\mathrm{disp}}(\boldsymbol{r},t)\mathrm{e}^{i\omega_0 t} + \text{c.c.}\\
\boldsymbol{P}_{\mathrm{NL}}(\boldsymbol{r},t) &= \boldsymbol{e}_x \frac{1}{2} P_{\mathrm{NL}}(\boldsymbol{r},t)\mathrm{e}^{i\omega_0 t} + \text{c.c.}\\
\boldsymbol{J}_{\mathrm{sp}}(\boldsymbol{r},t) &= \boldsymbol{e}_x \frac{1}{2} j_{\mathrm{sp}}(\boldsymbol{r},t)\mathrm{e}^{i\omega_0 t} + \text{c.c.}
\end{aligned} \tag{27.80}$$

where $\boldsymbol{e}_x$ denotes the unit vector in x direction, c.c. stands for complex conjugation, and $E, P_{\mathrm{disp}}, P_{\mathrm{NL}}, j_{\mathrm{sp}}$ are scalar complex-valued functions. In the slowly varying amplitude approximation the corresponding derivatives are given by

$$\begin{aligned}
\partial_{tt}\boldsymbol{E} &\approx -\boldsymbol{e}_x \frac{1}{2}\left(\omega_0^2 E - 2i\omega_0 \partial_t E\right)\mathrm{e}^{i\omega_0 t} + \text{c.c.}\\
\partial_{tt}\boldsymbol{P}_{\mathrm{disp}} &\approx -\boldsymbol{e}_x \frac{1}{2}\omega_0^2 P_{\mathrm{disp}}\mathrm{e}^{i\omega_0 t} + \text{c.c.}\\
\partial_{tt}\boldsymbol{P}_{\mathrm{NL}} &\approx -\boldsymbol{e}_x \frac{1}{2}\omega_0^2 P_{\mathrm{NL}}\mathrm{e}^{i\omega_0 t} + \text{c.c.}\\
\partial_{tt}\boldsymbol{P}_{\mathrm{sp}} &\approx \boldsymbol{e}_x \frac{1}{2} i\omega_0 j_{\mathrm{sp}}\mathrm{e}^{i\omega_0 t} + \text{c.c.}
\end{aligned} \tag{27.81}$$

Let $\chi(\boldsymbol{r},\omega)$ denote the Fourier transform of $\chi(\boldsymbol{r},t)$ evaluated at frequency ω. First we insert Equation 27.80 into Equation 27.78 and replace $E(\boldsymbol{r},t-\tau)$ by its first-order approximation $E(\boldsymbol{r},t) - \partial_t E(\boldsymbol{r},t)\tau$. Then we insert the result and Equation 27.80 into Equation 27.77 taking into account Equation 27.81. Finally, we multiply by $e^{-i\omega_0 t}$ and neglect the rapidly varying terms containing $e^{-i2\omega_0 t}$ (rotating wave approximation) and get

$$\begin{aligned}
\Delta E = {} & -\frac{\omega_0^2}{c^2}E + \frac{2i\omega_0}{c^2}\partial_t E - \frac{\omega_0^2}{c^2}\chi(\boldsymbol{r},\omega_0)E + \frac{i\omega_0}{c^2}\left(2\chi(\boldsymbol{r},\omega_0) + \omega_0 \partial_\omega \chi(\boldsymbol{r},\omega)_{|\omega=\omega_0}\right)\partial_t E\\
& - \mu_0\omega_0^2\left(P_{\mathrm{disp}} + P_{\mathrm{NL}}\right) + i\mu_0\omega_0 j_{\mathrm{sp}}
\end{aligned} \tag{27.82}$$

Consistent with the neglection of $\partial_{tt}E(\boldsymbol{r},t)$ we approximate in front of $\partial_t E(\boldsymbol{r},t)$:

$$2\chi(\boldsymbol{r},\omega_0)+\omega_0\partial_\omega\chi(\boldsymbol{r},\omega)_{|\omega=\omega_0}\approx 2\bar{\chi}(\omega_0)+\omega_0\partial_\omega\bar{\chi}(\omega)_{|\omega=\omega_0} \tag{27.83}$$

where $\bar{\chi}$ is an averaged real-valued susceptibility of the medium. This means that the spatial variation and the imaginary part of χ is considered to be a first-order correction, which can be neglected in front of the time derivative.

Introducing the complex refractive index $n^2(\boldsymbol{r},\omega)=1+\chi(\boldsymbol{r},\omega)$, the real-valued reference index $\bar{n}^2=1+\bar{\chi}$, the real-valued group index $n_\mathrm{g}=\bar{n}+\omega_0\partial_\omega\bar{n}(\omega)_{|\omega=\omega_0}$ and $k_0=\omega_0/c$, we get

$$\Delta E=2ik_0\frac{\bar{n}n_\mathrm{g}}{c}\partial_t E-k_0^2n^2E-\mu_0\omega_0^2\left(P_\mathrm{disp}+P_\mathrm{NL}\right)+i\mu_0\omega_0 j_\mathrm{sp} \tag{27.84}$$

Next we remove the rapid oscillations along the longitudinal z direction with the Ansatz

$$E(\boldsymbol{r},t)=E^+(\boldsymbol{r},t)\mathrm{e}^{-i\bar{n}k_0z}+E^-(\boldsymbol{r},t)\mathrm{e}^{i\bar{n}k_0z} \tag{27.85}$$

Inserting Equation 27.85 into Equation 27.84, neglecting $\partial_{zz}E^\pm$, multiplying the result with $\mathrm{e}^{\pm i\bar{n}k_0z}$, dropping rapidly varying terms containing $\mathrm{e}^{\pm 2i\bar{n}k_0z}$, and dividing by $2i\bar{n}k_0$, we get

$$\begin{aligned}\frac{1}{v_\mathrm{g}}\partial_t E^\pm(\boldsymbol{r},t)\pm\partial_z E^\pm(\boldsymbol{r},t)&=\frac{1}{2i\bar{n}k_0}\left[(\partial_x)^2+(\partial_y)^2\right]E^\pm(\boldsymbol{r},t)-ik_0\frac{n^2(\boldsymbol{r},\omega_0)-\bar{n}^2}{2\bar{n}}E^\pm(\boldsymbol{r},t)\\&\quad+\frac{\mu_0\omega_0^2}{2i\bar{n}k_0}\left[P_\mathrm{disp}(\boldsymbol{r},t)+P_\mathrm{NL}(\boldsymbol{r},t)\right]\mathrm{e}^{\pm i\bar{n}k_0z}-\frac{\mu_0\omega_0}{2\bar{n}k_0}j_\mathrm{sp}(\boldsymbol{r},t)\mathrm{e}^{\pm i\bar{n}k_0z}\end{aligned} \tag{27.86}$$

where $v_\mathrm{g}=c/n_g$.

Equation 27.86 must be supplemented by appropriate boundary conditions. At the plane facets of the laser located at $z=0$ and $z=L$

$$\begin{aligned}E^+(x,y,0,t)-r_0E^-(x,y,0,t)&=0\\E^-(x,y,L,t)-r_Le^{-i2\bar{n}k_0L}E^+(x,y,L,t)&=0\end{aligned} \tag{27.87}$$

hold. We should mention that in the paraxial approximation, the amplitude reflection coefficients r_0 and r_L are input parameters, which have to be calculated in advance.

At the transverse boundary denoted by Γ one can assume, for example, decaying fields or a perfect electric wall,

$$\lim_{|r_\mathrm{t}|\to\infty}E^\pm=0\quad\text{or}\quad E^\pm|_{r_\mathrm{t}\in\Gamma}=0, \tag{27.88}$$

respectively. If only a part of the cross section of the cavity is simulated, a nonreflecting or transparent boundary condition has to be used, which models the fact that only outgoing waves should be present. A very popular method to implement a boundary condition of this type is the introduction of a so-called perfectly matched layer (PML) [31]. However, in the frequency domain, it results in a large number of spurious modes [32]. Within the slowly varying approximation discontinuities of n can only be treated by employing corresponding transition conditions, except for resonant Bragg waveguide gratings, which can be described by extra terms coupling the forward and backward propagating waves.

27.4.2 Ansatz for Dispersion, Nonlinear Susceptibility, and Spontaneous Emission

27.4.2.1 Dispersion

We use the following Ansatz for $P_{\text{disp}}(\boldsymbol{r}, t)$:

$$P_{\text{disp}}(\boldsymbol{r}, t) = -i\frac{n_{\text{r}}(\boldsymbol{r}, t)g_{\text{r}}(\boldsymbol{r}, t)k_0}{\omega_0^2\mu_0}\left[\mathcal{P}(\boldsymbol{r}, t) - E(\boldsymbol{r}, t)\right] \tag{27.89}$$

where the electric field E is subtracted to ensure that the contribution to the dispersion vanishes at the gain peak. We model dispersion via the following response function in the frequency domain [33–35]

$$\mathcal{P}(\boldsymbol{r}, \omega) = \mathfrak{L}(\boldsymbol{r}, \omega)E(\boldsymbol{r}, \omega) \tag{27.90}$$

with

$$\mathfrak{L}(\boldsymbol{r}, \omega) = \frac{\gamma(\boldsymbol{r})}{i[\omega - \omega_0 - (\omega_{\text{p}}(\boldsymbol{r}) - \omega_0)] + \gamma(\boldsymbol{r})} \tag{27.91}$$

The Lorentzian $\mathfrak{L}(\boldsymbol{r}, \omega)$ achieves its maximum value 1 at the frequency ω_{p}. The imaginary part Im $\mathfrak{L}(r, \omega)$ has a half width γ at half of the maximum. The approximation is valid only within a small frequency region around ω_0 corresponding to the frequency range of optical transitions in the active material. By multiplying Equation 27.90 with the denominator and taking the inverse Fourier transform with respect to $\omega - \omega_0$ we get the ordinary differential equation

$$\partial_t\mathcal{P}(\boldsymbol{r}, t) = \left[i(\omega_{\text{p}}(\boldsymbol{r}) - \omega_0) - \gamma(\boldsymbol{r})\right]\mathcal{P}(\boldsymbol{r}, t) + \gamma(\boldsymbol{r})E(\boldsymbol{r}, t) \tag{27.92}$$

We use similar decompositions for the polarization $\mathcal{P}(\boldsymbol{r}, t)$ as for the electric field $E(\boldsymbol{r}, t)$,

$$\mathcal{P}(\boldsymbol{r}, t) = \mathcal{P}^+(\boldsymbol{r}, t)\mathrm{e}^{-i\bar{n}k_0z} + \mathcal{P}^-(\boldsymbol{r}, t)\mathrm{e}^{i\bar{n}k_0z} \tag{27.93}$$

Inserting Equations 27.93 and 27.85 into Equation 27.92, multiplying with $\mathrm{e}^{\pm i\bar{n}k_0z}$, and again neglecting $\mathrm{e}^{\pm 2i\bar{n}k_0z}$ we get

$$\partial_t\mathcal{P}^\pm(\boldsymbol{r}, t) = i(\omega_{\text{p}}(\boldsymbol{r}) - \omega_0)\mathcal{P}^\pm(\boldsymbol{r}, t) + \gamma(\boldsymbol{r})\left[E^\pm(\boldsymbol{r}, t) - \mathcal{P}^\pm(\boldsymbol{r}, t)\right] \tag{27.94}$$

Dispersion can also be taken into account with higher order time derivatives [36], on a microscopic level [37–39], by means of a digital filter [40], or by a convolution integral [41].

27.4.2.2 Nonlinear Susceptibility

Considering a third-order nonlinearity and assuming an isotropic medium the nonlinear polarization density reads [42–44]

$$P_{\text{NL}}(\boldsymbol{r}, t) = \varepsilon_0\frac{3}{4}\chi^{(3)}_{xxxx}(\boldsymbol{r}, t)|E(\boldsymbol{r}, t)|^2E(\boldsymbol{r}, t) \tag{27.95}$$

with the third-order susceptibility $\chi^{(3)}_{xxxx}(\omega_0; -\omega_0, -\omega_0, \omega_0)$. The optical Kerr coefficient $\tilde{n}_2$ and the two-photon absorption coefficient $\tilde{\beta}$ are defined as

$$\tilde{n}_2 - i\frac{\tilde{\beta}}{2k_0} = \frac{3}{8n_\mathrm{r}}\chi^{(3)}_{xxxx} \equiv \Delta\tilde{n}. \tag{27.96}$$

The connection with the commonly used coefficients n_2 and β related to the time-averaged intensity $I = \varepsilon_0 \bar{n} c |E|^2/2$ and discussed in Section 27.5.2 is given by

$$n_2 - i\frac{\beta}{2k_0} = \frac{2\Delta\tilde{n}_2}{\varepsilon_0 \bar{n} c} \equiv \Delta n_2 \tag{27.97}$$

where n_2 has the unit m^2/W and β the unit m/W.

27.4.2.3 Spontaneous Emission

The stochastic forces

$$F^{\pm}_{\mathrm{sp}}(\boldsymbol{r}, t) = -\frac{\mu_0\omega_0}{2\bar{n}k_0} j_{\mathrm{sp}}(\boldsymbol{r}, t)\mathrm{e}^{\pm i\bar{n}k_0 z} \tag{27.98}$$

in Equation 27.86 have the properties

$$\langle F^{+}_{\mathrm{sp}}(\boldsymbol{r}, t)\rangle = \langle F^{-}_{\mathrm{sp}}(\boldsymbol{r}, t)\rangle = 0 \tag{27.99}$$

$$\langle F^{+}_{\mathrm{sp}}(\boldsymbol{r}, t)F^{+*}_{\mathrm{sp}}(\boldsymbol{r}, t')\rangle = \langle F^{-}_{\mathrm{sp}}(\boldsymbol{r}, t)F^{-*}_{\mathrm{sp}}(\boldsymbol{r}', t')\rangle = \frac{2\hbar\omega_0 n_\mathrm{r}(\boldsymbol{r}, t) g(\boldsymbol{r}, t) n_{\mathrm{sp}}(\boldsymbol{r}, t)}{\bar{n}^2\varepsilon_0 c}\delta(\boldsymbol{r} - \boldsymbol{r}')\delta(t - t') \tag{27.100}$$

where $\langle\rangle$ denotes ensemble average and $\delta(x)$ is the Dirac delta function. Equation 27.100 is not suited for a numerical evaluation, because in dependence on the carrier densities the inversion (or spontaneous emission) factor n_{sp} has a singularity when the gain g changes its sign (transparency) so that the product $g \cdot n_{\mathrm{sp}}$ is undefined. One possibility to circumvent this is to take the second moment (Equation 27.100) proportional to $\beta_{\mathrm{sp}}R_{\mathrm{sp}}$ where R_{sp} given in Equation 27.139 is the rate of spontaneous emission into all modes and the dimensionless factor β_{sp} is chosen such that at threshold the correct values of the second moments are obtained [8].

27.4.3 Final Field Equation and Balance of Radiative Energy

Summarizing the results of the previous subchapter, the paraxial wave equation can be written as

$$\begin{aligned}\frac{1}{v_\mathrm{g}}\partial_t E^{\pm}(\boldsymbol{r}, t) \pm \partial_z E^{\pm}(\boldsymbol{r}, t) = &-\frac{i}{2\bar{n}k_0}\left(\partial_{xx} + \partial_{yy}\right)E^{\pm}(\boldsymbol{r}, t)\\ &-\frac{ik_0}{2\bar{n}}\Delta n^2(\boldsymbol{r}, t)E^{\pm}(\boldsymbol{r}, t) - \frac{n_\mathrm{r}(\boldsymbol{r}, t)g_\mathrm{r}(\boldsymbol{r}, t)}{2\bar{n}}\left[E^{\pm}(\boldsymbol{r}, t) - \mathcal{P}^{\pm}(\boldsymbol{r}, t)\right]\\ &-\frac{ik_0 n_\mathrm{r}(\boldsymbol{r}, t)}{\bar{n}}\Delta\tilde{n}_2(\boldsymbol{r}, t)\left[|E^{+}|^2 + |E^{-}|^2\right]E^{\pm}(\boldsymbol{r}, t) + F^{\pm}_{\mathrm{sp}}(\boldsymbol{r}, t)\end{aligned} \tag{27.101}$$

where

$$\Delta n^2(\boldsymbol{r},t) \equiv n^2(\boldsymbol{r},t,\omega_0) - \bar{n}^2 = \Delta n_{\mathrm{r}}^2 + i\frac{n_{\mathrm{r}}\,(g-\alpha)}{k_0} \tag{27.102}$$

Here Δn_{r}^2 is the real part of Δn^2, n_{r} the real part of n, g the coefficient of optical gain originating from the emission or absorption of photons due to transitions between the conduction and valence bands, and α the coefficient of absorption of photons due to transitions within the conduction and valence bands (such as free-carrier absorption and intervalence band absorption). Optical losses due to scattering on waveguide imperfections could be included in α, too.

Multiplying Equation 27.101 with the complex conjugate $E^{\pm *}$, multiplying the complex conjugate of Equation 27.101 with $E^{\pm}$ and adding all equations results in

$$\begin{aligned}\frac{1}{v_{\mathrm{g}}}\frac{d\|E\|^2}{dt} =& \frac{1}{\bar{n}k_0}\mathrm{Im}\left[\partial_x(E^{+*}\partial_x E^+ + E^{-*}\partial_x E^-) + \partial_y(E^{+*}\partial_y E^+ + E^{-*}\partial_y E^-)\right]\\ &+ \partial_z\left[|E^-|^2 - |E^+|^2\right]\\ &+ \frac{n_{\mathrm{r}}(g-\alpha)}{\bar{n}}\|E\|^2 + \frac{n_{\mathrm{r}}g_{\mathrm{r}}}{\bar{n}}\left[\mathrm{Re}(E^{+*}\mathcal{P}^+ + E^{-*}\mathcal{P}^-) - \|E\|^2\right]\\ &- \frac{n_{\mathrm{r}}\tilde{\beta}}{\bar{n}}\|E\|^4 + 2\mathrm{Re}(E^{+*}F_{\mathrm{sp}}^+ + E^{-*}F_{\mathrm{sp}}^-)\end{aligned} \tag{27.103}$$

with $\|E\|^2 = |E^+|^2 + |E^-|^2$. This equation can be interpreted as a balance equation for the radiative energy density

$$u_{\mathrm{rad}}(\boldsymbol{r},t) = \frac{\varepsilon_0\bar{n}n_{\mathrm{g}}}{2}\|E(\boldsymbol{r},t)\|^2 \tag{27.104}$$

Integrating Equation 27.103 over the device volume V and using the boundary conditions Equations 27.88 and 27.87 leads to

$$\begin{aligned}\frac{\mathrm{d}\int_V u_{\mathrm{rad}}\,\mathrm{d}V}{\mathrm{d}t} =& -P_{\mathrm{out}} + \frac{\varepsilon_0 c}{2}\int_V n_{\mathrm{r}}(g-g_{\mathrm{r}}-\alpha)\|E\|^2\,\mathrm{d}V\\ &+ \frac{\varepsilon_0 c}{2}\int_V n_{\mathrm{r}}g_{\mathrm{r}}\left[\mathrm{Re}(E^{+*}\mathcal{P}^+ + E^{-*}\mathcal{P}^-)\right]\,\mathrm{d}V - \frac{\varepsilon_0 c}{2}\int_V n_{\mathrm{r}}\tilde{\beta}\|E\|^4\,\mathrm{d}V\\ &+ \frac{\varepsilon_0 c}{\bar{n}}\int_V \mathrm{Re}(E^{+*}F_{\mathrm{sp}}^+ + E^{-*}F_{\mathrm{sp}}^-)\,\mathrm{d}V\end{aligned} \tag{27.105}$$

which is a generalization of Equation 27.31. The output power $P_{\mathrm{out}} = P_0 + P_L$ is given in Equation 27.30 where $R_0 = |r_0|^2$ and $R_L = |r_L|^2$. The optical power is

$$P^{\pm}(z) = \frac{\varepsilon_0\bar{n}c}{2}\iint |E^{\pm}(x,y,z)|^2\,\mathrm{d}x\mathrm{d}y. \tag{27.106}$$

Thus the first term in Equation 27.103 is the divergence of the transverse energy flux density, which is assumed to vansish on the transverse surface of the device. The second term gives the radiation leaving the cavity. The third and fourth terms describe the increase or decrease of the energy due to stimulated emission or absorption, respectively, and the last two terms due to two-photon absorption and spontaneous emission.

27.4.4 Cavity Modes, Beam Propagation Method, and Roundtrip Operator

The cavity modes are time-periodic solutions of the form $E_{\mathrm{m}}^{\pm}\exp(i\Omega_{\mathrm{m}}t)$, $\mathcal{P}^{\pm}\exp(i\Omega_{\mathrm{m}}t)$ and obey the linear equations

$$\pm i\partial_z E_{\mathrm{m}}^{\pm}(\boldsymbol{r}) = \left[\frac{\Omega_{\mathrm{m}}}{v_{\mathrm{g}}} + \mathbf{H}(\boldsymbol{r},z)\right] E_{\mathrm{m}}^{\pm}(\boldsymbol{r}) \tag{27.107}$$

subject to the boundary conditions (Equations 27.87 and 27.88). The operator **H** is given by

$$\mathbf{H}(\boldsymbol{r},z) = \frac{1}{2\bar{n}k_0}\left(\partial_{xx} + \partial_{yy}\right) + \frac{k_0}{2\bar{n}}\Delta n^2(\boldsymbol{r}) + i\frac{n_{\mathrm{r}}(\boldsymbol{r})g_{\mathrm{r}}(\boldsymbol{r})}{2\bar{n}}\left[\frac{\gamma(\boldsymbol{r})}{i\Omega_{\mathrm{m}} - i(\omega_{\mathrm{p}}(\boldsymbol{r}) - \omega_0) + \gamma(\boldsymbol{r})} - 1\right] \tag{27.108}$$

The nontrivial solutions of (Equation 27.107) may depend on time via the dependence of the complex-valued refractive index on temporally varying carrier densities and temperature. The complex-valued relative mode frequencies Ω_{m} are the eigenvalues and the mode profiles $E_{\mathrm{m}}^{\pm}$ are the eigenfunctions of Equation 27.107. The real parts of Ω_{m} give the wavelengths relative to the reference wavelength λ_0,

$$\Delta\lambda_m = \left.\frac{\mathrm{d}\lambda}{\mathrm{d}\omega}\right|_{\lambda_0} \mathrm{Re}(\Omega_{\mathrm{m}}) \tag{27.109}$$

and the imaginary parts describe the damping of the modes. For a passive cavity, $\mathrm{Im}(\Omega_{\mathrm{m}}) > 0$ must hold. Lasing modes of an active cavity are distinguished by vanishing damping, $\mathrm{Im}(\Omega_{\mathrm{m}}) = 0$, due to the balance of the outcoupling and internal losses and the gain.

It can be shown that the cavity modes fulfil an orthogonality relation which does not define a scalar product because of the non-Hermitian character of Equation 27.107. Due to the dispersion term in Equation 27.107 the orthogonality relation differs from that given in [6], but can be derived in the same manner.

If the operator **H** depends only on the transverse coordinates $\boldsymbol{r}_{\mathrm{t}}$, the solution of Equation 27.107 can be formally written as

$$E_{\mathrm{m}}^{\pm}(\boldsymbol{r}_{\mathrm{t}}, z') = \mathrm{e}^{\mp i(\frac{\Omega_{\mathrm{m}}}{v_{\mathrm{g}}} + \mathbf{H})(z'-z)} E_{\mathrm{m}}^{\pm}(\boldsymbol{r}_{\mathrm{t}}, z) \tag{27.110}$$

The numerical evaluation of Equation 27.110 is the basis of what is known as the beam propagation method (BPM) [45–47]. For the case of a spatially and temporally constant index, $n = \text{const.}$, Equation 27.110 can be evaluated exactly to yield

$$E_{\mathrm{m}}^{\pm}(\boldsymbol{r}'_{\mathrm{t}}, z') = \mathrm{e}^{\mp i(\frac{\Omega_{\mathrm{m}}}{v_{\mathrm{g}}} + \frac{k_0}{2\bar{n}}\Delta n^2)(z'-z)} \int G^{\pm}(\boldsymbol{r}'_{\mathrm{t}} - \boldsymbol{r}_{\mathrm{t}}, z' - z) E_{\mathrm{m}}^{\pm}(\boldsymbol{r}_{\mathrm{t}}, z)\,\mathrm{d}x\mathrm{d}y \tag{27.111}$$

with

$$G^{\pm}(\boldsymbol{r}'_{\mathrm{t}} - \boldsymbol{r}_{\mathrm{t}}, z' - z) = \Theta\big(\pm(z' - z)\big)\left[\sqrt{\pm\frac{i\bar{n}k_0}{2\pi(z' - z)}}\right]^2 \mathrm{e}^{\mp\frac{i\bar{n}k_0|\boldsymbol{r}'_{\mathrm{t}} - \boldsymbol{r}_{\mathrm{t}}|^2}{2(z'-z)}} \tag{27.112}$$

where Θ denotes the Heaviside step function. The integral equation (Equation 27.111) together with the propagator Equation 27.112 is known as Huygen's integral in the Fresnel approximation.

Based on Equation 27.110 and the boundary conditions (Equation 27.87), it is possible to construct roundtrip operators $\mathbf{M}^{\pm}$. One starts at some position $z = z_0$ within the cavity and performs a full roundtrip. Depending on whether we start into forward (+) or backward (−) directions, the eigenvalue problems

$$\mathbf{M}^{\pm}(\Omega_{\mathrm{m}})E_{\mathrm{m}}^{\pm}(\boldsymbol{r}_{\mathrm{t}}, z_0) = \mathrm{e}^{i\frac{2\Omega_{\mathrm{m}}}{v_{\mathrm{g}}}L}E_{\mathrm{m}}^{\pm}(\boldsymbol{r}_{\mathrm{t}}, z_0) \tag{27.113}$$

are obtained. Note that the roundtrip operators $\mathbf{M}^{\pm}$ depend on the eigenvalues Ω_{m} if dispersion is taken into account. The eigenfunctions of $\mathbf{M}^{\pm}$ are the mode distributions $E_{\mathrm{m}}^{\pm}(\boldsymbol{r}_{\mathrm{t}}, z_0)$ at the position z_0. A very popular method for solving Equation 27.113 is based on the Fox–Li approach, cf. [48] and the references therein. The idea is to choose a normalized, more or less arbitrary start distribution $E_{\mathrm{m}}^{\pm}(\boldsymbol{r}_{\mathrm{t}}, z_0)$ and to apply the roundtrip operator $\boldsymbol{M}^{\pm}$ recurrently until one arrives (hopefully) at a steady state. It is known that the algorithm fails if there are cavity modes having identical or nearly identical damping $\mathrm{Im}(\Omega_{\mathrm{m}})$, as it is the case in broad-area lasers. The association of the nonconvergence of the Fox–Li iteration with an dynamically unstable laser behavior should be done with care. Instead, for multimode high-power lasers, a time-dependent approach based on Equation 27.101 should be preferred, although it is numerically more challenging.

27.5 Models for Nonlinear Modes and Filamentation

The multipeaked and not diffraction-limited lateral field profile of wide-aperture semiconductor lasers has been a long-standing problem and has been investigated in the past by numerous authors [49–55]. Although the broadening of the far field of CW operating lasers with increasing power (also called far-field blooming) can be at least partially attributed to the thermal lensing effect [56–58], a complete picture of the origin and mechanism has not revealed yet.

One mechanism is believed to be due to carrier-induced antiguiding, i.e., the reduction of the refractive index with increasing carrier density. This leads to a self-focusing mechanism because the index increases in regions of high intensity due to a depletion of the injected carrier density and can result in the formation of what is sometimes called lasing filaments.

Another mechanism that could explain the multipeaked structure and the broadening of the farfield is the simultaneous lasing of a large number of waveguide modes, originating from a built-in or thermally induced waveguide. Indeed, recent experiments reveal, that even at currents several times above threshold the lateral modes can be clearly identified by spectrally resolved near- and far-field measurements [58,59]. However, with increasing current, a broadening of the individual modes and the appearance of new modes with broad near and far fields can be observed [60].

Here, we derive the equation for the description of the lateral field profile and discuss two basic nonlinearities due to the virtual transitions and due to lateral spatial hole burning.

27.5.1 Longitudinal–Lateral Approximate Projected Equations

First we project the basic equations onto the dominant vertical mode using the Ansatz

$$E^{\pm}(\boldsymbol{r}, t) = \sqrt{\frac{2d\hbar\omega_0}{\varepsilon_0\bar{n}n_{\mathrm{g}}}}\phi(y, x, z)u^{\pm}(x, z, t) \tag{27.114}$$

where the mode profile $\phi(y, x, z)$ is normalized according to $\int |\phi|^2\, dy = 1$. The scaling in Equation 27.114 is chosen such that $|u^\pm|^2$ is a photon density (unit m^{-3}). The power is given by

$$P^\pm = \hbar\omega_0 v_g d \int |u^\pm|^2\, dx \tag{27.115}$$

where d is the thickness of the active region.

For each (x, z), $\phi(y, x, z)$ is a solution of a vertical waveguide equation with a real-valued index profile n_0 not dependent on carrier densities and temperature,

$$\partial_{yy}\phi(x, y, z) + k_0^2 n_0^2(x, y, z)\phi(x, z, y) = k_0^2 n_{\mathrm{eff},0}^2(x, z)\phi(x, y, z) \tag{27.116}$$

where the real-valued effective index $n_{\mathrm{eff},0}$ is the eigenvalue of Equation 27.116. Inserting Equation 27.114 into Equation 27.101, multiplying with ϕ, and integrating along y yields the equations

$$\begin{aligned}\frac{1}{v_g}\partial_t u^\pm(x, z, t) = &-\frac{i}{2\bar{n}k_0}\partial_{xx}u^\pm(x, z, t) \mp \partial_z u^\pm(x, z, t) - \frac{ik_0}{2\bar{n}}\left[n_{\mathrm{eff}}^2(x, z, t) - \bar{n}^2\right] u^\pm(x, z, t)\\ &- ik_0\Delta n_{2,\mathrm{eff}}(x, z, t)\hbar\omega_0 v_g d\|u(x, z, t)\|^2 u^\pm(x, z, t)\end{aligned} \tag{27.117}$$

where we omitted the dispersion and spontaneous emission terms for simplicity and

$$n_{\mathrm{eff}}^2 = n_{\mathrm{eff,r}}^2 + i\frac{\bar{n}\left(g_{\mathrm{eff}} - \alpha_{\mathrm{eff}}\right)}{k_0}, \tag{27.118}$$

$$n_{\mathrm{eff,r}}^2 = n_{\mathrm{eff},0}^2 + \int (n_{\mathrm{r}}^2 - n_0^2)|\phi|^2\, \mathrm{d}y, \tag{27.119}$$

$$g_{\mathrm{eff}} - \alpha_{\mathrm{eff}} = \frac{\int n_{\mathrm{r}}(g - \alpha)|\phi|^2\, \mathrm{d}y}{\bar{n}} \tag{27.120}$$

and

$$\Delta n_{2,\mathrm{eff}} = \frac{\int n_{\mathrm{r}}\Delta n_2|\phi|^4\, dy}{\bar{n}} \approx \frac{\Delta\bar{n}_2}{d_{1/e^2}} \tag{27.121}$$

The second term in Equation 27.119 treats effects, which are not included in n_0 and thus $n_{\mathrm{eff},0}$, for example, the dependence of the real and imaginary parts of n_{r} on the carrier densities or the temperature. The vertical mode size d_{1/e^2} has been introduced in Equation 27.68. The approach sketched is called the "effective index method" in the semiconductor laser community. Inserting Equation 27.114 into the rate of stimulated recombination Equation 27.140 and averaging over the active region $1/d \int_0^d\, dy$ yields

$$R_{\mathrm{st}} = v_g\, g_{\mathrm{eff}}\|u\|^2 \tag{27.122}$$

with $\|u\|^2 = |u^+|^2 + |u^-|^2$.

Equation 27.117 together with correspondingly projected equations for the polarization (Equation 27.94) and a lateral diffusion equation for the excess carriers have been successfully applied to the simulation of a large variety of high-power laser structures [61–66]. A discussion on numerical issues can be found in [67].

27.5.2 Nonlinearities due to Virtual Transitions

The energy gaps of the confinement and cladding layers of a laser structure are larger than the energy of the photons generated by stimulated emission. In this situation, the photon energy is too small to allow absorption of single-photons due to transitions of electrons between the valence and conduction bands, as intended. However, virtual transitions involving two photons are still possible, which result in a third-order susceptibility defined in Equation 27.96. An approximate expression for the dispersion of the two-photon absorption coefficient β for direct transitions has been given in [68]:

$$\beta(\omega) = K\frac{\sqrt{E_\mathrm{p}}}{n_\mathrm{r}^2 E_\mathrm{g}^3} F_2\left(\frac{\hbar\omega}{E_\mathrm{g}}\right) \tag{27.123}$$

where E_p is the energy equivalent of the momentum matrix element for direct transitions between the valence and conduction bands, E_g is the (direct) energy gap and

$$F_2(x) = \frac{(2x-1)^{1.5}}{(2x)^5} \quad \text{for} \quad 2x > 1 \tag{27.124}$$

The factor K can be considered to be a free parameter. The two-photon absorption coefficient $\beta = 260$ m/TW experimentally determined for GaAs at a wavelength of $\lambda = 1064$ nm [44] is obtained with $K = 41{,}200\ \mathrm{m/TW} \times \mathrm{eV}^3/\sqrt{\mathrm{eV}}$, using $E_\mathrm{g} = 1.42$ eV, $E_\mathrm{p} = 26.1$ eV, and $n_\mathrm{r} = 3.48$. Note the E_g^{-3} dependence of β.

Two-photon absorption as well as Raman and Stark effects result also in an intensity-dependent contribution to the real part of the refractive index expressed as the optical Kerr coefficient n_2,

$$n_2(\omega) = \tilde{K}\frac{\hbar c\sqrt{E_\mathrm{p}}}{2n_\mathrm{r}^2 E_\mathrm{g}^4} G_2\left(\frac{\hbar\omega}{E_\mathrm{g}}\right) \tag{27.125}$$

where the function $G_2(\hbar\omega/E_\mathrm{g})$ given in [68] is shown in Figure 27.11 together with the function $F_2(\hbar\omega/E_\mathrm{g})$. It can be seen, that G_2 is maximal around $\hbar\omega = 0.5E_\mathrm{g}$ and changes its sign at $\hbar\omega = 0.7E_\mathrm{g}$, where F_2 is

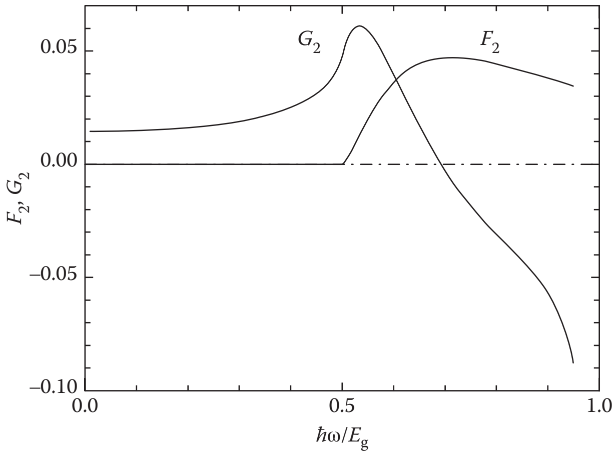

FIGURE 27.11 Functions F_2 and G_2 used in Equations 27.123 and 27.125.

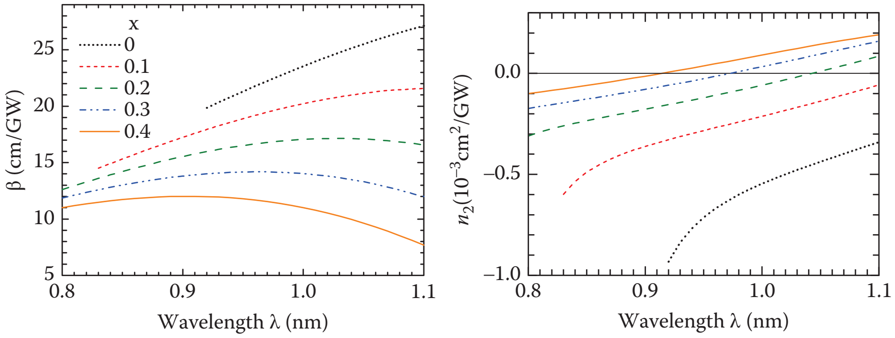

(a) (b)

FIGURE 27.12 Nonlinear coefficients calculated by Equations 27.123 and 27.125 versus wavelength for different Al compositions x in $\text{Al}_x\text{Ga}_{1-x}\text{As}$. (a) Two-photon absorption coefficient and (b) Optical Kerr coefficient.

maximal[†]. The factor $\tilde{K}$ can again be considered as a free parameter. The optical Kerr coefficient $n_2 = -4.1 \cdot 10^{-17}$ m/W experimentally determined for GaAs at a wavelength of $\lambda = 1064$ nm [44] is obtained with $\tilde{K} = 7.212 \cdot 10^{11}$ m/W × 1/(Ws m) × $\text{eV}^4/\sqrt{\text{eV}}$.

The dependencies of β and n_2 of $\text{Al}_x\text{Ga}_{1-x}\text{As}$ on λ are shown in Figure 27.12a and 27.12b, respectively. The two-photon absorption increases from $\beta \propto 10$ cm/GW to $\beta \propto 25$ cm/GW if the Al composition is decreased from $x = 0.4$ to $x = 0$ due to the decrease of E_g. It shows a nonmonotonous dependence on the wavelength given by $F_2(\lambda)$. The optical Kerr coefficient decreases with increasing x and changes its sign in dependence on λ at higher Al compositions within the wavelength range investigated. For smaller Al compositions and wavelengths n_2 is negative, but for larger Al compositions and wavelengths n_2 is positive. For $\lambda = 980$ nm and relevant compositions $|n_2| < 2 \cdot 10^{-4}\ \text{cm}^2/\text{GW}$. Under CW operation, the maximum power density of broad-area lasers, which are state of the art during the writing of the book is of the order $10^{-2}\ \text{GW/cm}^2$. Hence the resulting index change $|\Delta n| < 4 \cdot 10^{-6}$ should not have a big impact on the optical field.

It should be noted that in nonisotropic media the relation between the nonlinear polarization and the electric field is more complicated than given in Equation 27.95. Hence the two-photon absorption and the optical Kerr effect depend on the crystallographic orientation and on the polarization direction of the optical field.

27.5.3 Nonlinearity Induced by Lateral Spatial Hole Burning

We now derive equations for the right and left traveling fields alone, eliminating the carrier density. This is only possible for a (hypothetical) steady state. To this end, the real and imaginary parts of Δn_{eff}^2 are linearized around a reference carrier density N_{ref}, which is typically set to the transparency carrier density N_{tr} were $g_{\text{eff}}(N_{\text{tr}}) = 0$. Other possible choices could be the carrier density for waveguide transparency (solution of $g_{\text{eff}}(N_{\text{ref}}) = \alpha_{\text{eff}}$) or the threshold carrier density of a laterally infinite laser (solution of $g_{\text{eff}}(N_{\text{thr}}) = \alpha_{\text{eff}} + \alpha_{\text{out}}$).

For the steady state, linearizing the recombination rate as in Section 27.3.2, neglecting drift-diffusion, and assuming a constant injection current density the rate equation can be solved for the excess

---

[†] The functions F_2 and G_2 due to indirect transitions behave differently [69]: The maximum of F_2 occurs slightly above the indirect bandgap, and G_2 is positive throughout the transparent wavelength range and crosses zero only above the indirect gap. The two-photon absorption coefficient is dominated by direct transitions for $\hbar\omega > E_{\text{g,direct}}/2$ if $E_{\text{g,indirect}} > E_{\text{g,direct}}/2$.

carrier density,

$$N - N_{\mathrm{tr}} = \frac{\frac{j\tau_N}{ed} - N_{\mathrm{tr}}}{1 + v_{\mathrm{g}} g'_{\mathrm{eff}} \tau_N \|u_{\mathrm{s}}\|^2}. \tag{27.126}$$

From Equation 27.126 it can be seen that $N \rightarrow N_{\mathrm{tr}}$ for $\|u_{\mathrm{s}}\|^2 \rightarrow \infty$, i.e., the carrier density cannot be depleted below the transparency carrier density. Inserting Equation 27.126 into $\Delta n^2_{\mathrm{eff,r}}(N)$, $g_{\mathrm{eff}}(N)$, and $\alpha_{\mathrm{eff}}(N)$ yields

$$g_{\mathrm{eff}}(j) = \frac{g'_{\mathrm{eff}} \tau_N (j - j_{\mathrm{tr}})}{ed(1 + \epsilon_{\mathrm{sat}} \|u_{\mathrm{s}}\|^2)}, \tag{27.127}$$

$$\alpha_{\mathrm{eff}}(j) = \alpha_{\mathrm{eff}}(N_{\mathrm{tr}}) + \frac{\alpha'_{\mathrm{eff}} \tau_N (j - j_{\mathrm{tr}})}{ed(1 + \epsilon_{\mathrm{sat}} \|u_{\mathrm{s}}\|^2)}, \tag{27.128}$$

$$n^2_{\mathrm{eff,r}}(j) = n^2_{\mathrm{eff,r}}(N_{\mathrm{tr}}) + \frac{\alpha_{\mathrm{H}} \bar{n} g'_{\mathrm{eff}} \tau_N (j - j_{\mathrm{tr}})}{edk_0(1 + \epsilon_{\mathrm{sat}} \|u_{\mathrm{s}}\|^2)} \tag{27.129}$$

with the saturation parameter

$$\epsilon_{\mathrm{sat}} = v_{\mathrm{g}} g'_{\mathrm{eff}} \tau_N \tag{27.130}$$

and Henry's α-factor

$$\alpha_{\mathrm{H}} = 2k_0 n'_{\mathrm{eff}} / g'_{\mathrm{eff}}. \tag{27.131}$$

For typical values $n_{\mathrm{g}} = 4$, $g'_{\mathrm{eff}} = 10 \cdot 10^{-18}$ cm^2, and $\tau_N = 1$ ns we obtain $\varepsilon_{\mathrm{sat}} = 7.5 \cdot 10^{-17}$ cm^3. In general, $g'_{\mathrm{eff}} > 0$ and $n'_{\mathrm{eff}} < 0$ and hence $\alpha_{\mathrm{H}} < 0$ for frequencies around the gain peak. Typical values of α_{H} range from -1 to -10.

The stationary states correspond to time-harmonic solutions

$$u^{\pm}(x, z, t) = u^{\pm}_{\mathrm{s}}(x, z) e^{i\Omega t} \tag{27.132}$$

of Equation 27.117 with $\mathrm{Im}(\Omega) = 0$. Inserting Equations 27.132, 27.127, and 27.129 into Equation 27.117, we obtain

$$\begin{aligned} \pm i\partial_z u^{\pm}_{\mathrm{s}} = {} & \frac{1}{2\bar{n}k_0} \partial_{xx} u^{\pm}_{\mathrm{s}}(x, z, t) + \frac{\Omega}{v_{\mathrm{g}}} u^{\pm}_{\mathrm{s}} + \frac{k_0}{2\bar{n}} \left[n^2_{\mathrm{eff,r}}(N_{\mathrm{tr}}) - \bar{n}^2 \right] u^{\pm}_{\mathrm{s}} - \frac{i}{2} \alpha_{\mathrm{eff}}(N_{\mathrm{tr}}) u^{\pm}_{\mathrm{s}} \\ & + \frac{\tau_N \left[(i + \alpha_{\mathrm{H}}) g'_{\mathrm{eff}} - i\alpha'_{\mathrm{eff}} \right] (j - j_{\mathrm{tr}})}{2ed(1 + \epsilon_{\mathrm{sat}} \|u_{\mathrm{s}}\|^2)} u^{\pm}_{\mathrm{s}} + k_0 \Delta n_{2,\mathrm{eff}} \hbar\omega_0 v_{\mathrm{g}} d \|u_{\mathrm{s}}\|^2 u^{\pm}_{\mathrm{s}} \end{aligned} \tag{27.133}$$

For $\varepsilon_{\mathrm{sat}} \|u\|^2 \ll 1$ we can expand

$$(1 + \epsilon_{\mathrm{sat}} \|u_{\mathrm{s}}\|^2)^{-1} \approx 1 - \epsilon_{\mathrm{sat}} \|u_{\mathrm{s}}\|^2 \tag{27.134}$$

so that the second-last term in Equation 27.133 resembles the last term with

$$\Delta n_{2,\mathrm{SHB}} = -\frac{\tau_N \left[(\alpha_{\mathrm{H}} + i) g'_{\mathrm{eff}} - i\alpha'_{\mathrm{eff}} \right] (j - j_{\mathrm{tr}}) \, \epsilon_{\mathrm{sat}}}{2ek_0 \hbar\omega_0 v_{\mathrm{g}} d^2} \tag{27.135}$$

For typical values $\alpha_H = -2$, $g'_{\mathrm{eff}} = 10 \cdot 10^{-18}$ cm^2, $j = 10$ kA/cm^2, $d = 10$ nm, $\tau_N = 1$ ns, $j_{\mathrm{tr}} = 0.16$ kA/cm^2 (corresponding to $N_{\mathrm{tr}} = 10^{18}$ cm^{-3}), $\lambda_0 = 1$ µm, $n_{\mathrm{g}} = 4$, $\varepsilon_{\mathrm{sat}} = 75 \cdot 10^{-18}$ cm^3 we obtain $\mathrm{Real}(\Delta n_{2,\mathrm{SHB}}) = 5 \cdot 10^{-4}$ cm/W, which is several orders of magnitudes larger than the absolute value of the effective optical Kerr coefficient due to non-resonant virtual transitions $\mathrm{Real}(\Delta n_{2,\mathrm{eff}}) \approx -7 \cdot 10^{-10}$ cm/W for $\bar{n}_2 = -10^{-13}$ cm^2/W (cf. Figure 27.12b) and $d_{1/e^2} = 1.5$ µm (cf. Equation 27.121).

Due to the fact that $\mathrm{Real}(\Delta n_{2,\mathrm{SHB}})$ is positive, two basic instabilities sometimes termed "filamentation" arise [44]. First, a local intensity maximum induces a variation of the real part of the effective index with a larger value at the position of the intensity peak than outside. Thus a local index waveguide is created (self-focusing) [49]. However, at the position of the intensity peak the effective gain is decreased which results in an reduced amplification in the local-waveguide core and an enhanced amplification outside (self-defocusing).

The other instability, first described by Bespalov and Talanov [70], is the breakup of a laser beam with a homogeneous intensity distribution into a beam with a random intensity distribution as a consequence of the growth of irregularities initially present on the laser wavefront. For a mathematical description of the effect, the forward and backward propagating waves have to be expressed as a sum of three plane-wave components each [44,71].

In [51,72] the mean-field approximation, $\bar{u}_{\mathrm{s}}^{\pm} = 1/L \int_0^L u_{\mathrm{s}}^{\pm}\,\mathrm{d}z$ has been applied to Equation 27.133 and the resulting nonlinear second-order ordinary differential equation has been solved numerically. In both references, the case of a purely gain-guided laser is considered, i.e., any impact of a built-in or thermally induced index guide has not been investigated. In [72], a zoo of solutions of different types, including asymmetric ones, has been found. The basic stationary states are the linear modes with the wavelengths

$$\Delta\lambda_{\nu k} = -\frac{\lambda_0}{Lk_0 n_{\mathrm{g}}}\left[\frac{\varphi_0 + \varphi_L}{2} + \pi k - Lk_0\bar{n} - \frac{Lk_0}{2\bar{n}}\mathrm{Re}(n_\nu^2 - \bar{n}^2)\right] \tag{27.136}$$

where k denotes the longitudinal mode, n_ν is the modal index of the νth lateral mode, φ_0 and φ_L are the phases of the reflectivities. The other types of modes exist only due to the nonlinearity in the complex effective index and arise above the thresholds of the linear-guided modes.

There are a number of shortcomings of the theory presented so far. The assumption of a constant injection current density, i.e., an infinite series resistance as in Section 27.3.2 discussed, and the neglect of drift-diffusion result in an overestimation of spatial hole burning. A local variation of the complex effective index is not only caused by its dependence on the carrier density but also on the temperature ($\partial n/\partial T > 0$). Furthermore, in all analytical investigations, we are aware of no built-in or thermally induced index waveguides have been taken into account. These waveguides stabilize the linear guided modes, which are thus observable even far above threshold [60].

Based on an expansion of the optical field on the linear-guided modes and a numerical solution of the drift-diffusion equations in the mean-field approximation the far-field blooming of an index-guided broad-area laser has been investigated in [73]. The simulations revealed that a substantial part of the far-field blooming is not caused by self-heating but by increasing gain nonuniformity due to lateral spatial holeburning and laterally varying hole injection into the QWs. A discussion of filamentation effects based on a numerical solution of Equation 27.117 can be found in [53–55].

27.6 Thermodynamic-Based Energy-Transport Model

In high-power lasers operated in CW mode the transport of the charged carriers (electrons and holes) and the photons must be consistently formulated with the temperature flow in order to describe self-heating effects such as thermal roll-over and thermal lensing properly. A derivation of such a self-consistent energy-transport model by applying fundamental thermodynamic principles has been given in [74] using Boltzmann statistics. The model fulfils the first and second laws of thermodynamics as well as Onsager's reciprocity relations for the current densities. We note, that in this model electron, hole, and lattice temperatures are assumed to be equal, opposed to other energy-transport models [29,75]. A more general energy-transport model for semiconductor devices has been derived in [76] taking into account Fermi statistics and different temperatures for the charged carriers and the lattice, but disregarding optical fields. Previous formulations have been also given in [77,78], for example. In what follows we will summarize the energy-transport model paying particular attention to a consistent formulation with the model for the optical field presented in Section 27.4.

27.6.1 Basic Equations

The particle current flow is governed by the continuity equations for electrons and holes,

$$\nabla \boldsymbol{j}_n = +e\left(R + \partial_t n\right) \tag{27.137}$$

$$\nabla \boldsymbol{j}_p = -e\left(R + \partial_t p\right) \tag{27.138}$$

were $\boldsymbol{j}_n$ and $\boldsymbol{j}_p$ are the current densities for electrons and holes, respectively. The recombination rate R given in Equation 27.46 consists of nonradiative recombination $R_{\text{non-rad}}$, radiative spontaneous recombination R_{sp}, and radiative stimulated recombination R_{st}. The rate of radiative spontaneous recombination is often written as

$$R_{\text{sp}} = B(np - n_0 p_0) \tag{27.139}$$

with the equilibrium electron and hole densities n_0 and p_0, respectively. In the case of Boltzmann statistics, the coefficient B is constant whereas in the general case of Fermi statistics B decreases with increasing carrier densities.

The rate of stimulated recombination is the rate by which the energy density of the optical field changes by stimulated emission or absorption of a photon due to transitions between the conduction and valence bands, divided by the energy of the emitted or absorbed photon and follows from Equations 27.104 and 27.103 to

$$R_{\text{st}} = \frac{\varepsilon_0 c n_{\text{r}}}{2\hbar\omega_0}\left[g\|E\|^2 + g_{\text{r}} \sum_{\nu=+,-} \text{Re}\left(E^{\nu *}\mathcal{P}^{\nu} - E^{\nu *}E^{\nu}\right)\right] \tag{27.140}$$

The electrostatic field itself is affected by the charge distribution of mobile (n and p) and fixed (n_{A} and p_{D}) carrier densities. The corresponding electrostatic potential φ solves the Poisson equation

$$-\nabla(\varepsilon_0 \varepsilon_{\text{s}} \nabla\varphi) = e(p - n + p_{\text{D}} - n_{\text{A}}) \tag{27.141}$$

with the relative static dielectric constant ε_{s}. For parabolic bands the relations between quasi-Fermi potentials φ_n and φ_p, electrostatic potential φ and carrier densities n and p are given by Equation 27.59.

In what follows we introduce the entropies per particle[†]

$$s_n = k_B\left[1 + R_n - \frac{\partial_T E_c}{k_B} + \frac{e\varphi_n + E_c - e\varphi}{k_B T}\right] \tag{27.142}$$

$$s_p = k_B\left[1 + R_p + \frac{\partial_T E_v}{k_B} - \frac{e\varphi_p + E_v - e\varphi}{k_B T}\right] \tag{27.143}$$

and the energies per particle

$$u_n = k_B T R_n - T\partial_T E_c + E_c = T(s_n - k_B) + e(\varphi - \varphi_n) \tag{27.144}$$

$$u_p = k_B T R_p + T\partial_T E_v - E_v = T(s_p - k_B) + e(\varphi_p - \varphi) \tag{27.145}$$

The functions R_n and R_p are given by the temperature derivatives of the inverse Fermi integrals,

$$R_n = -k_B T \partial_T \mathcal{F}_i^{\mathrm{inv}}\left(\frac{n}{N_c}\right) \tag{27.146}$$

$$R_p = -k_B T \partial_T \mathcal{F}_i^{\mathrm{inv}}\left(\frac{p}{N_v}\right) \tag{27.147}$$

For the bulk case ($i = 1/2$), Boltzmann statistics, parabolic bands, and temperature-independent electron and holes masses R_n and R_p are equal to 3/2.

The electron and hole current densites are given by

$$\boldsymbol{j}_n = -\,\sigma_n(\nabla\varphi_n - P_n\nabla T) \tag{27.148}$$

$$\boldsymbol{j}_p = -\,\sigma_p(\nabla\varphi_p + P_p\nabla T) \tag{27.149}$$

where σ_n and σ_p are the electrical conductivities and P_n and P_p are the Seebeck coefficients or thermoelectric powers being the entropies per particle divided by the elementary charge e,

$$P_n = \frac{s_n}{e} \quad \text{and} \quad P_p = \frac{s_p}{e} \tag{27.150}$$

If the coefficients in front of the temperature derivatives in Equations 27.148 and 27.149 are derived from the Boltzmann equation in relaxation time approximation, then the factorization $\sigma_n \cdot P_n$ and $\sigma_p \cdot P_p$ is only possible for parabolic bands and Boltzmann statistics. The same holds for the factorization of the electrical conductivities into products of carrier-density independent mobilities and carrier densities, $\sigma_n = e\mu_n \cdot n$ and $\sigma_p = e\mu_p \cdot p$. Furthermore, the magnitudes of P_n, P_p similarly as μ_n, μ_p depend on the scattering processes involved [79]. For example, if the dependence of the relaxation time on the energy is given by $\tau_0[E/(k_B T)]^r$ where r ranges typically between $-3/2$ and $+3/2$, then $R_n = R_p = 3/2+r$ in Equations 27.142 and 27.143. Thus $R_n = R_p = 3/2$ holds only for an energy-independent relaxation time. The temperature derivatives $\partial_T E_c$ and $\partial_T E_v$ of the conduction and valence band edges are often not included in the definition of the Seebeck coefficients.

According to Reference [74] the heat flow equation reads

$$c_h \partial_t T - \nabla\kappa_L\nabla T = h \tag{27.151}$$

[†] The entropies can be also written as $s_n = e\partial_T(\varphi_n)_{(n,p)} + k_B$, $s_p = -e\partial_T(\varphi_p)_{(n,p)} + k_B$, where n, p are kept constant in the differentiation.

with the thermal conductivity of the crystal lattice κ_L, the heat capacity

$$c_\mathrm{h} = c_\mathrm{L} + n\partial_T u_n + p\partial_T u_\mathrm{p} \tag{27.152}$$

with c_L being the heat capacity of the lattice and the heat source density

$$\begin{aligned} h = {} & \frac{k_\mathrm{B}T}{e}\boldsymbol{\nabla}(\boldsymbol{j}_n - \boldsymbol{j}_p) + T(\boldsymbol{j}_n\boldsymbol{\nabla}P_n - \boldsymbol{j}_p\boldsymbol{\nabla}P_p) \\ & + \frac{1}{\sigma_n}\boldsymbol{j}_n^2 + \frac{1}{\sigma_p}\boldsymbol{j}_p^2 + (u_n + u_p)R - \partial_t u_\mathrm{rad} - \gamma_\mathrm{rad} \end{aligned} \tag{27.153}$$

The first term in Equation 27.153 is related to thermodiffusion and can be written as

$$\frac{k_\mathrm{B}T}{e}\boldsymbol{\nabla}\cdot(\boldsymbol{j}_n - \boldsymbol{j}_p) = 2k_\mathrm{B}TR + k_\mathrm{B}T(\partial_t n + \partial_t p) \tag{27.154}$$

taking into account Equations 27.137 and 27.138. The second term describes Thomson–Peltier heat,

$$h_\mathrm{TP} = T(\boldsymbol{j}_n\boldsymbol{\nabla}P_n - \boldsymbol{j}_p\boldsymbol{\nabla}P_p) = h_\mathrm{Thomson} + h_\mathrm{Peltier} \tag{27.155}$$

which is generated by a current flow along the gradients of the Seebeck coefficients ∇P_n and ∇P_p. By applying the chain rule to the gradients, the contributions due to Thompson heat and Peltier heat can be separated,

$$h_\mathrm{Thomson} = T\boldsymbol{\nabla}T\left(\boldsymbol{j}_n\partial_T P_n|_{(n,p)} - \boldsymbol{j}_p\partial_T P_p|_{(n,p)}\right) \tag{27.156}$$

$$h_\mathrm{Peltier} = T\left(\boldsymbol{j}_n\partial_n P_n|_T\boldsymbol{\nabla}n - \boldsymbol{j}_p\partial_p P_p|_T\boldsymbol{\nabla}p\right) \tag{27.157}$$

The third and forth terms correspond to Joule heat:

$$h_\mathrm{J} = \frac{1}{\sigma_n}\boldsymbol{j}_n^2 + \frac{1}{\sigma_p}\boldsymbol{j}_p^2 \tag{27.158}$$

generated by scattering of the carriers on phonons resulting in a energy loss to the lattice. The last term is due to contributions of the recombination of electron–hole pairs which sets free the energy $u_n + u_p$ that is either transferred to the lattice as heat or transferred to the radiative field. The latter part is described by the term $\partial_t u_\mathrm{rad}$, which has to be subtracted from the source term, like the term γ_rad, which denotes the energy loss from the cavity. Inserting Equations 27.154, 27.155, and 27.158 into Equation 27.153 gives

$$h = k_\mathrm{B}T(\partial_t n + \partial_t p) + h_\mathrm{TP} + h_\mathrm{J} + h_\mathrm{rec+abs} \tag{27.159}$$

with the recombination and absorption heat

$$h_\mathrm{rec+abs} = e(TP_n + TP_p + \varphi_p - \varphi_n)R - \partial_t u_\mathrm{rad} - \gamma_\mathrm{rad} \tag{27.160}$$

where $R = R_\mathrm{non\text{-}rad} + R_\mathrm{sp} + R_\mathrm{st}$. Likewise the rate of radiative recombination, the radiative energy density u_rad and the radiative energy loss γ_rad have contributions from spontaneous and stimulated emission, $u_\mathrm{rad} = u_\mathrm{sp} + u_\mathrm{st}$ and $\gamma_\mathrm{rad} = \gamma_\mathrm{sp} + \gamma_\mathrm{st}$. Here, u_sp is the energy density and γ_sp the corresponding cavity loss of the radiation generated by spontaneous emission into all modes (i.e., spatial directions, polarization directions of the field and frequencies) not included in $E^\pm$ given by Equation 27.101.

The balance equation for the energy density of the radiation generated by stimulated emission is given by Equations 27.103 and 27.104. As it has been stated before the first term on the rhs of Equation 27.103 gives the divergence of the transverse energy flux density and the second term the radiation leaving the cavity in propagation direction. Both terms combined give the total stimulated-energy loss from the cavity $-\gamma_{\mathrm{st}}$,

$$\begin{aligned} -\gamma_{\mathrm{st}} = {} & \frac{\varepsilon_0 c}{2k_0}\mathrm{Im}\left[\partial_x(E^{+*}\partial_x E^{+} + E^{-*}\partial_x E^{-}) + \partial_y(E^{+*}\partial_y E^{+} + E^{-*}\partial_y E^{-})\right] \\ & + \frac{\varepsilon_0 \bar{n} c}{2}\partial_z\left[|E^{-}(r,t)|^2 - |E^{+}(r,t)|^2\right] \end{aligned} \tag{27.161}$$

and hence

$$\partial_t u_{\mathrm{st}} = \frac{\varepsilon_0 c n_{\mathrm{r}}}{2}\left((g - g_r - \alpha)\|E\|^2 + g_r \mathrm{Re}(E^{+*}\mathcal{P}^{+} + E^{-*}\mathcal{P}^{-})\right) - \frac{\varepsilon_0 c n_{\mathrm{r}}\tilde{\beta}}{2}\|E\|^4 - \gamma_{\mathrm{st}}. \tag{27.162}$$

Inserting Equations 27.162 and 27.140 into Equation 27.160 gives

$$\begin{aligned} h_{\mathrm{rec+abs}} = {} & e(\mathrm{TP}_n + \mathrm{TP}_p + \varphi_p - \varphi_n)R_{\mathrm{non\text{-}rad}} + \frac{\varepsilon_0 c n_{\mathrm{r}}\alpha}{2}\|E\|^2 + \frac{\varepsilon_0 c n_{\mathrm{r}}\tilde{\beta}}{2}\|E\|^4 \\ & + \left[e(\mathrm{TP}_n + \mathrm{TP}_p + \varphi_p - \varphi_n) - \hbar\omega_0\right] R_{\mathrm{st}} \\ & + e(\mathrm{TP}_n + \mathrm{TP}_p + \varphi_p - \varphi_n)R_{\mathrm{sp}} - \partial_t u_{\mathrm{sp}} - \gamma_{\mathrm{sp}} \end{aligned} \tag{27.163}$$

with the rate of stimulated recombination Equation 27.140. Equation 27.163 is the net heat source caused by recombination and absorption. The first term is the heat generated by nonradiative recombination. The second and third terms describe the heat due to absorption of the stimulated radiation. The fourth term is caused by a possible incomplete energy transfer from the carrier ensemble to the radiation field during stimulated emission, also referred to as quantum defect energy. The last terms describe the heat due to the absorption of the spontaneous radiation, which could be treated similarly as the stimulated radiation but approximations have to be employed because the field generated by spontaneous emission is more challenging to calculate.

27.6.2 Spatial Distributions of the Heat Sources

The profiles of the heat sources of an asymmetric super-large optical-cavity structure similar to that published in [10] are shown in Figure 27.13a through 27.13d for the steady state for an output power of $P_{\mathrm{out}} = 18$ W and an averaged internal power of $\bar{P} = 8$ W. Some of the parameters are given in Table 27.1. The one-dimensional simulation (along y) has been performed with the simulator WIAS-TeSCA [80]. The absorption heat

$$h_{\mathrm{abs}} = (f_{\mathrm{c},n} n + f_{\mathrm{c},p} p)\bar{P}\frac{|\phi|^2}{W} \tag{27.164}$$

with $\phi(y)$ being the vertical normalized mode profile is shown in Figure 27.13. The cross sections for free-carrier absorption are $f_{\mathrm{c},n} = 4 \cdot 10^{-18}$ cm^2 and $f_{\mathrm{c},p} = 12 \cdot 10^{-18}$ cm^2. The main contributions arise in the active layer located at $y \approx 1.9$ μm due to the high nonequilibrium electron and hole densities and in the adjacent p- and n-doped confinement layers where the optical mode resides. The recombination heat

$$h_{\mathrm{rec}} = (5k_{\mathrm{B}}T + E_{\mathrm{g}})\left(R_{\mathrm{non\text{-}rad}} + R_{\mathrm{sp}}\right) \tag{27.165}$$

in Boltzmann approximation is maximal in the active layer as expected. Note that the temperature dependencies of E_c and E_v were not taken into account. The recombination of leaky electrons and holes in the p-confinement layer (cf. Figure 27.10b) generates heat, too. The quantum defect heat

$$h_{\text{defect}} = (5k_B T + E_g - \hbar\omega_0)\frac{g\bar{P}|\phi|^2}{\hbar\omega_0 W} \tag{27.166}$$

in a Boltzmann approximation, not shown here, is nonvanishing only in the active region and has the same order of magnitude like the recombination heat there ($h_{\text{defect}} \approx 8 \cdot 10^{14}$ W/m^3). The Joule heat (Equation 27.158) shown in Figure 27.13c is mainly generated in the p-confinement layer due to its low doping and the small mobility of the holes. Finally, Thomson heat

$$h_{\text{Thompson}} = \frac{3}{2}\frac{k_B}{e}\frac{dT}{dy}\left(j_{n,y} - j_{p,y}\right) \tag{27.167}$$

and Peltier heat

$$h_{\text{Peltier}} = -\frac{k_B T}{e}\left[\frac{d\ln(n)}{dy}j_{n,y} - \frac{d\ln(p)}{dy}j_{p,y}\right] \tag{27.168}$$

in Boltzmann approximations are shown in Figure 27.13d. The Thompson heat is negative due to the temperature gradient. The Peltier heat is positive or negative corresponding to the signs of the gradients of the carrier densities. Except in the p-cladding layer ($y > 3$ μm) it dominates over the Peltier heat. Note that the Peltier heat results in a cooling of the p-confinement layer. The integrated heat powers are $Q_{\text{Joule}} = 10.2$ W, $Q_{\text{abs}} = 2.7$ W, $Q_{\text{rec}} = 1.3$ W, and $Q_{\text{defect}} = 1.9$ W. Hence Joule heat amounts to more than 50% of the total heat.

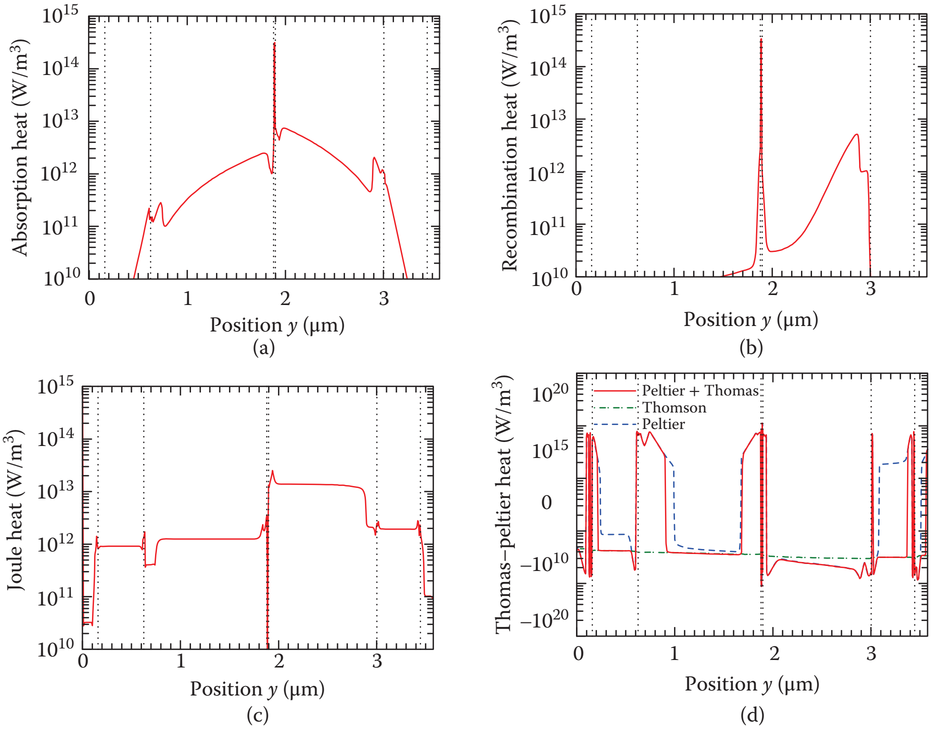

FIGURE 27.13 Vertical profiles of the heat sources of a high-power laser. (a) Absorption heat, (b) recombination heat, (c) Joule heat, and (d) Thomson–Peltier heat. Heteroboundaries are indicated by dotted vertical lines.

27.6.3 Energy Conservation

Inserting Equations 27.149 and 27.148 into the heat sources (Equations 27.155, 27.158 through 27.160) and integrating over the device volume V leads to

$$\begin{aligned}\int_V c_{\mathrm{h}}\partial_t T\,dV - \int_V \boldsymbol{\nabla}\kappa_{\mathrm{L}}\boldsymbol{\nabla}T\,dV = k_{\mathrm{B}}\int_V T(\partial_t n+\partial_t p)\,\mathrm{d}V \\ +\int_V \boldsymbol{j}_n\boldsymbol{\nabla}(TP_n-\varphi_n)\,dV - \int_V \boldsymbol{j}_p\boldsymbol{\nabla}(TP_p+\varphi_p)\,\mathrm{d}V + \int_V eR(TP_n-\varphi_n)\,\mathrm{d}V \\ +\int_V eR(TP_p+\varphi_p)\mathrm{d}V - \partial_t\int_V u_{\mathrm{rad}}\,\mathrm{d}V - \int_V \gamma_{\mathrm{rad}}\,\mathrm{d}V \qquad (27.169)\end{aligned}$$

Using a Green's identity we can convert

$$\int_V \boldsymbol{j}_n\boldsymbol{\nabla}(\mathrm{TP}_n-\varphi_n)\,\mathrm{d}V = \int_{\partial V}(\mathrm{TP}_n-\varphi_n)\boldsymbol{j}_n\cdot\boldsymbol{n}dS - \int_V(\mathrm{TP}_n-\varphi_n)\underbrace{\boldsymbol{\nabla j}_n}_{e(R+\partial_t n)}\,\mathrm{d}V \qquad (27.170)$$

and

$$-\int_V \boldsymbol{j}_p\boldsymbol{\nabla}(\mathrm{TP}_p+\varphi_p)\,\mathrm{d}V = -\int_{\partial V}(\mathrm{TP}_p+\varphi_p)\boldsymbol{j}_p\cdot\boldsymbol{n}\mathrm{d}S + \int_V(\mathrm{TP}_p+\varphi_p)\underbrace{\boldsymbol{\nabla j}_p}_{-e(R+\partial_t p)}\,\mathrm{d}V \qquad (27.171)$$

where ∂V denotes the surface of the device with $\boldsymbol{n}$ being the normal vector. Hence the terms containing the recombination rate cancel, and after rearranging we obtain

$$\begin{aligned}&\int_V c_{\mathrm{h}}\partial_t T\,\mathrm{d}V - \int_{\partial V}\kappa_{\mathrm{L}}\boldsymbol{\nabla}T\cdot\boldsymbol{n}dS \\ &= \int_V\underbrace{(Tk_{\mathrm{B}}-e\mathrm{TP}_n+e\varphi_n)}_{-u_n+e\varphi}\partial_t n\,\mathrm{d}V + \int_V\underbrace{(Tk_{\mathrm{B}}-e\mathrm{T}P_p-e\varphi_p)}_{-u_p-e\varphi}\partial_t p\,\mathrm{d}V \\ &+\int_{\partial V}(\mathrm{TP}_n-\varphi_n)\boldsymbol{j}_n\cdot\boldsymbol{n}\mathrm{d}S - \int_{\partial V}(\mathrm{T}P_p+\varphi_p)\boldsymbol{j}_p\cdot\boldsymbol{n}\mathrm{d}S \\ &-\partial_t\int_V u_{\mathrm{rad}}\,dV - \int_V\gamma_{\mathrm{rad}}\,\mathrm{d}V \qquad (27.172)\end{aligned}$$

From the Poisson equation (Equation 27.141) we can derive the relation

$$e\int_V\varphi(\partial_t n-\partial_t p)\,\mathrm{d}V = \varepsilon_0\int_{\partial V}\varphi\varepsilon_{\mathrm{s}}\partial_t\boldsymbol{\nabla}\varphi\cdot\boldsymbol{n}\mathrm{d}S - \frac{\varepsilon_0}{2}\int_V\varepsilon_{\mathrm{s}}\partial_t|\boldsymbol{\nabla}\varphi|^2\,\mathrm{d}V \qquad (27.173)$$

where we applied again a Green's identity. Using this relation and the expression for the heat capacity Equation 27.152 we obtain the energy balance equation

$$\frac{d\int_V u\,\mathrm{d}V}{\mathrm{d}t} = -\int_{\partial V}\boldsymbol{j}_u\cdot\boldsymbol{n}dS - \int_V\gamma_{\mathrm{rad}}\,\mathrm{d}V \qquad (27.174)$$

where u is the total energy density (sum of electro-static, internal, and radiative energy)

$$u = \frac{\varepsilon_0 \varepsilon_s}{2} |\nabla\varphi|^2 + c_L T + u_n n + u_p p + u_{\text{rad}}, \tag{27.175}$$

and $\boldsymbol{j}_u$ is the energy current density,

$$\boldsymbol{j}_u = -\varepsilon_0 \varepsilon_s \varphi \partial_t \nabla\varphi - \kappa_L \nabla T - (TP_n - \varphi_n)\boldsymbol{j}_n + (TP_p + \varphi_p)\boldsymbol{j}_p \tag{27.176}$$

both already introduced in [74]. The first term in Equation 27.176 is related to the displacement current density. The other terms can be reduced to the entropy current density multiplied by T and the particle flux multiplied by the respective quasi-Fermi potentials.

In what follows, we consider the steady state ($d/dt = \partial_t = 0$) and evaluate the surface integral in Equation 27.174. We assume no flow of electrical current through the surface, except at the n-contact located at $y = 0$ and the p-contact at $y = H$:

$$\left.\begin{aligned} \boldsymbol{j}_n \cdot \boldsymbol{n} = 0 \\ \boldsymbol{j}_p \cdot \boldsymbol{n} = 0 \end{aligned}\right\} \quad \text{for} \quad y \neq 0 \quad \text{and} \quad y \neq H \tag{27.177}$$

Between the contacts a forward bias U is applied, so that

$$\varphi_n|_{y=H} = \varphi_p|_{y=H} = U \qquad \text{and} \qquad \varphi_n|_{y=0} = \varphi_p|_{y=0} = 0 \tag{27.178}$$

hold. The normal components of the electron current density at the p-contact $y = H$ and the hole current density at the n-contact $y = 0$ are assumed to vanish,

$$j_{n,y}|_{y=H} = j_{p,y}|_{y=0} = 0 \tag{27.179}$$

Similarly, we assume no heat flow through the surface, except at the surface, located at $y = H$, attached to the heatsink where

$$\kappa_L \partial_y T|_{y=H} = \frac{T_{\text{ref}} - T|_{y=H}}{r_{\text{th}}} \tag{27.180}$$

with r_{th} being the thermal transmission resistance (unit Km^2/W). By inserting the boundary conditions into Equation 27.174 we get for the steady state

$$\iint \frac{T|_{y=H} - T_{\text{ref}}}{r_{\text{th}}} \, dxdz = UI - \int_V \gamma_{\text{rad}} \, dV + \iint [(TP_p)|_{y=H} - (TP_n)|_{y=0}] j \, dxdz \tag{27.181}$$

with $j = j_{n,y}|_{y=0} = -j_{p,y}|_{y=H}$ and $I = \iint j \, dxdz$. The lhs of Equation 27.181 is the heat flow to the heatsink. The first term on the rhs is the electric input power UI and the second term is the optical power that leaves the cavity. The last term can be considered as Peltier power, which is generated between the electric contacts in the presence of a current flow and results into heating or cooling. Assuming that the spontaneous emission is absorbed in the cavity so that $\gamma_{\text{rad}} = \gamma_{\text{st}}$, using Equation 27.161 and the boundary conditions Equations 27.88 and 27.87, the second term can be shown to be (cf. Equation 27.105)

$$\int_V \gamma_{\text{rad}} \, dV = P_{\text{out}} \tag{27.182}$$

Thus in the steady state the total heat generated in the cavity is given by the electrical input power *UI* minus the optical output power, which coincides with Equation 27.11, minus or plus the Peltier heat.

Acknowledgment

The authors are indebted to K. H. Hasler, M. Lichtner, M. Platz, R. Staske, and H. J. Wünsche for their contributions to the chapter.

References

1. D. F. Welch. A brief history of high-power semiconductor lasers. *IEEE J. Sel. Topics Quantum Electron.*, 6(6):1470–1477, 2000.
2. R. Diehl. *High-power Diode Lasers: Fundamentals, Technology, Applications*, volume 78. Berlin, Heidelberg, New York, NY: Springer, 2000.
3. M. Behringer. High-power diode laser technology and characteristics. In F. Bachmann, P. Loosen, and R. Poprawe, editors, *High Power Diode Lasers*, volume 128 of *Springer Series in Optical Sciences*, pp. 5–74. New York, NY: Springer, 2007.
4. X. Liu, W. Zhao, L. Xiong, and H. Liu. *Packaging of High Power Semiconductor Lasers*. Berlin, Heidelberg, New York, NY: Springer, 2014.
5. I. Fischer, O. Hess, W. Elsäßer, and E. Göebel. Complex spatio-temporal dynamics in the near-field of a broad-area semiconductor laser. *Europhys Lett.*, 35(8):579–584, 1996.
6. H. Wenzel. Basic aspects of high-power semiconductor laser simulation. *IEEE J. Sel. Topics Quantum Electron.*, 19(5):1–13, 2013.
7. P. Crump, O. Brox, F. Bugge, J. Fricke, C. Schultz, M. Spreemann, B. Sumpf, H. Wenzel, and G. Erbert. High-power, high-efficiency monolithic edge-emitting GaAs based lasers with narrow spectral widths. In J. J. Colemann, A. C. Bryce, and C. Jagadish, editors, *Advances in Semiconductor Lasers*, volume 86 of *Semiconductor and Semimetals*, chapter 2. Amsterdam: Elsevier, 2012.
8. L. A. Coldren, S. W. Corzine, and M. L. Mashanovitch. *Diode Lasers and Photonic Integrated Circuits*. Hoboken, NJ: John Wiley & Sons, 2012.
9. H. Wenzel, G. Erbert, A. Knauer, A. Oster, K. Vogel, and G. Tränkle. Influence of current spreading on the transparency current density of quantum-well lasers. *Semicond. Sci. Technol.*, 15(6):557, 2000.
10. K. H. Hasler, H. Wenzel, P. Crump, S. Knigge, A. Maaßdorf, R. Platz, R. Staske, and G. Erbert. Comparative theoretical and experimental studies of two designs of high-power diode lasers. *Semicond. Sci. Technol.*, 29(4):045010, 2014.
11. H. Wenzel, P. Crump, A. Pietrzak, X. Wang, G. Erbert, and G. Tränkle. Theoretical and experimental investigations of the limits to the maximum output power of laser diodes. *New J. Phys.*, 12(8):085007, 2010.
12. J. Piprek. *Semiconductor Optoelectronic Devices: Introduction to Physics and Simulation*. London, Oxford, Boston, New York and San Diego: Academic Press, 2003.
13. W. W. Rigrod. Saturation effects in high-gain lasers. *J. Appl. Phys.*, 36(8):2487–2490, 1965.
14. H.-J. Wünsche, U. Bandelow, and H. Wenzel. Calculation of combined lateral and longitudinal spatial hole burning in $\lambda/4$ shifted DFB lasers. *IEEE J. Quantum Electron.*, 17:1751–1760, 1993.
15. H. Wenzel and G. Erbert. Simulation of single-mode high-power semiconductor lasers. *Proc. SPIE.*, 2693:418–429, 1996.
16. A. Demir, M. Peters, R. Duesterberg, V. Rossin, and E. Zucker. Semiconductor laser power enhancement by control of gain and power profiles. *IEEE Photon Techn. Lett.*, 27(20):2178–2181, 2015.
17. A. Guermache, V. Voiriot, D. Locatelli, F. Legrand, R.-M. Capella, P. Gallion, and J. Jacquet. Experimental demonstration of spatial hole burning reduction leading to 1480-nm pump lasers output power improvement. *IEEE Photon. Techn. Lett.*, 17(10):2023, 2005.

18. Z. Chen, L. Bao, J. Bai, M. Grimshaw, R. Martinsen, M. DeVito, J. Haden, and P. Leisher. Performance limitation and mitigation of longitudinal spatial hole burning in high-power diode lasers. In *Proceedings SPIE*, pp. 82771J–82771J, 2012.
19. X. Wang, P. Crump, H. Wenzel, A. Liero, T. Hoffmann, A. Pietrzak, C. M. Schultz, A. Klehr, A. Ginolas, S. Einfeldt, et al. Root-cause analysis of peak power saturation in pulse-pumped 1100 nm broad area single emitter diode lasers. *IEEE J. Quantum Electron.*, 46(5):658–665, 2010.
20. S. F. Yu, R. G. S. Plumb, L. M. Zhang, M. C. Nowell, and J. E. Carroll. Large-signal dynamic behavior of distributed-feedback lasers including lateral effects. *IEEE J. Quantum Electron.*, 30(8):1740–1750, 1994.
21. H. E. Lassen, H. Olesen, and B. Tromborg. Gain compression and asymmetric gain due to the Bragg grating induced by the standing waves in Fabry-Perot lasers. *IEEE Photon Technol. Lett.*, 1(9):261–263, 1989.
22. E. A. Avrutin and B. S. Ryvkin. Theory of direct and indirect effect of two photon absorption on nonlinear optical losses in high power semiconductor laser. *Semicond. Sci. Technol.*, 32(1): 015004, 2016.
23. E. A. Avrutin and B. S. Ryvkin. Theory and modelling of the power conversion efficiency of large optical cavity laser diodes. In *2015 IEEE High Power Diode Lasers and Systems Conference (HPD)*, pp. 9–10, 2015.
24. H. Wenzel, P. Crump, A. Pietrzak, C. Roder, X. Wang, and G. Erbert. The analysis of factors limiting the maximum output power of broad-area laser diodes. *Opt. Quantum Electron.*, 41(9):645–652, 2009.
25. W. B. Joyce. Current-crowded carrier confinement in double-hetero-structure lasers. *J. Appl. Phys.*, 51(5):2394–2401, 1980.
26. M. Grupen and K. Hess. Simulation of carrier transport and nonlinearities in quantum-well laser diodes. *IEEE J. Quantum Electron.*, 34(1):120–140, 1998.
27. B. Witzigmann, A. Witzig, and W. Fichtner. A multidimensional laser simulator for edge-emitters including quantum carrier capture. *IEEE Trans. Electron Devices.*, 47(10):1926–1934, 2000.
28. L. Borruel, J. Arias, B. Romero, and I. Esquivias. Incorporation of carrier capture and escape processes into a self-consistent cw model for quantum well lasers. *Microelectron J.*, 34(5):675–677, 2003.
29. Y. Liu, W. C. Ng, K. D. Choquette, and K. Hess. Numerical investigation of self-heating effects of oxide-confined vertical-cavity surface-emitting lasers. *IEEE J. Quantum Electron.*, 41(1):15–25, 2005.
30. S. Steiger, R. G. Veprek, and B. Witzigmann. Unified simulation of transport and luminescence in optoelectronic nanostructures. *J. Comp. Electron.*, 7(4):509–520, 2008.
31. A. F. Oskooi, L. Zhang, Y. Avniel, and S. G. Johnson. The failure of perfectly matched layers, and towards their redemption by adiabatic absorbers. *Optics Express.*, 16(15):11376–11392, 2008.
32. T. Tischler. *Die Perfectly-Matched-Layer-Randbedingung in der Finite-Differenzen-Methode im Frequenzbereich: Implementierung und Einsatzbereiche*. Innovationen mit Mikrowellen und Licht. Goettingen: Cuvillier, 2004.
33. C. Z. Ning, R. A. Indik, and J. V. Moloney. Effective Bloch equations for semiconductor lasers and amplifiers. *IEEE J. Quantum Electron.*, 33(9):1543–1550, Sep 1997.
34. U. Bandelow, M. Radziunas, J. Sieber, and M. Wolfrum. Impact of gain dispersion on the spatio-temporal dynamics of multisection lasers. *IEEE J. Quantum Electron.*, 37(2):183–188, 2001.
35. M. Lichtner, M. Radziunas, U. Bandelow, M. Spreemann, and H. Wenzel. Dynamic simulation of high brightness semiconductor lasers. *Proc NUSOD '08*, pp. 65–66, 2008.
36. S. Balsamo, F. Sartori, and I. Montrosset. Dynamic beam propagation method for flared semiconductor power amplifiers. *IEEE J. Quantum Electron.*, 2(2):378–384, Jun 1996.
37. C. Z. Ning, R. A. Indik, J. V. Moloney, W. W. Chow, A. Girndt, S. W. Koch, and R. H. Binder. Incorporating many-body effects into modeling of semiconductor lasers and amplifiers. *Proc. SPIE*, 2994:666–677, 1997.

38. E. Gehrig and O. Hess. Spatio-temporal dynamics of light amplification and amplified spontaneous emission in high-power tapered semiconductor laser amplifiers. *IEEE J. Quantum Electron.*, 37(10):1345–1355, Oct 2001.
39. W. W. Chow and H. Amano. Analysis of lateral-mode behavior in broad-area InGaN quantum-well lasers. *IEEE J. Quantum Electron.*, 37(2):265–273, 2001.
40. M. Kolesik and J. V. Moloney. A spatial digital filter method for broad-band simulation of semiconductor lasers. *IEEE J. Quantum Electron.*, 37(7):936–944, Jul 2001.
41. J. Javaloyes and S. Balle. Quasiequilibrium time-domain susceptibility of semiconductor quantum wells. *Phys. Rev. A*, 81(6):062505, 2010.
42. P. N. Butcher and D. Cotter. *The Elements of Nonlinear Optics*, volume 9. Melbourne, Australia: Cambridge University Press, 1991.
43. G. P. Agrawal. *Nonlinear Fiber Optics*. London, Oxford, Boston, New York and San Diego: Academic Press, 2007.
44. R. W. Boyd. *Nonlinear Optics*. London, Oxford, Boston, New York and San Diego: Academic Press, 2008.
45. R. März. *Integrated Optics: Design and Modeling*. Norwood, MA: Artech House, 1995.
46. R. Scarmozzino, A. Gopinath, R. Pregla, and S. Helfert. Numerical techniques for modeling guided-wave photonic devices. *IEEE J. Sel. Topics Quantum Electron.*, 6(1):150–162, Jan–Feb 2000.
47. T. M. Benson, B. B. Hu, A. Vukovic, and P. Sewell. What is the future for beam propagation methods? *Proc. SPIE.*, 5579:351–358, 2004.
48. A. E. Siegman. Laser beams and resonators: The 1960s. *IEEE J. Sel. Topics Quantum Electron.*, 6(6):1380–1388, Nov–Dec 2000.
49. G. H. B. Thompson. A theory for filamentation in semiconductor lasers including the dependence of dielectric constant on injected carrier density. *Opto-electronics.*, 4:257–310, 1972.
50. D. Mehuys, R. Lang, M. Mittelstein, J. Salzman, and A. Yariv. Self-stabilized nonlinear lateral modes of broad area lasers. *IEEE J. Quantum Electron.*, 23(11):1909–1920, 1987.
51. R. J. Lang, A. G. Larsson, and J. G. Cody. Lateral modes of broad area semiconductor lasers: Theory and experiment. *IEEE J. Quantum Electron.*, 27(3):312–320, 1991.
52. J. R. Marciante and G. P. Agrawal. Nonlinear mechanisms of filamentation in broad-area semiconductor lasers. *IEEE J. Quantum Electron.*, 32(4):590–596, 1996.
53. J. V. Moloney. Semiconductor laser device modeling. In B. Krauskopf and D. Lenstra, editors, *Fundamental Issues of Nonlinear Laser Dynamics*, pp. 149–172. College Park, MD: American Institute of Physics, 2000.
54. E. Gehrig and O. Hess. *Spatio-Temporal Dynamics and Quantum Fluctuations in Semiconductor Lasers*, volume 189. Springer Science & Business Media, 2003.
55. K. Böhringer. *Microscopic Spatio-Temporal Dynamics of Semiconductor Quantum Well Lasers and Amplifiers*. PhD thesis, Institut fuer Technische Physik, Deutsches Zentrum fuer Luft- und Raumfahrt, 2007.
56. J. V. Moloney, M. Kolesik, J. Hader, and S. W. Koch. Modeling high-power semiconductor lasers: From microscopic physics to device applications. *Proc. SPIE.*, 3889:120–127, 2000.
57. H. Wenzel, P. Crump, H. Ekhterei, C. Schultz, J. Pomplun, S. Burger, L. Zschiedrich, F. Schmidt, and G. Erbert. Theoretical and experimental analysis of the lateral modes of high-power broad-area lasers. *Proc NUSOD '11*, pp. 143–144, 2011.
58. P. Crump, S. Böldicke, C. M. Schultz, H. Ekhteraei, H. Wenzel, and G. Erbert. Experimental and theoretical analysis of the dominant lateral waveguiding mechanism in 975 nm high power broad area diode lasers. *Semicond. Sci. Technol.*, 27(4):045001, 2012.
59. N. Stelmakh and M. Flowers. Measurement of spatial modes of broad-area diode lasers with 1-GHz resolution grating spectrometer. *IEEE Photon Technol. Lett.*, 18(15):1618–1620, 2006.

60. P. Crump, M. Ekteraei, C. M. Schultz, G. Erbert, and G. Tränkle. Studies of limitations to lateral brightness in high power diode lasers using spectrally-resolved mode profiles. In *2014 IEEE International Semiconductor Laser Conference (ISLC)*, pp. 23–24, 2014.
61. M. Spreemann, M. Lichtner, M. Radziunas, U. Bandelow, and H. Wenzel. Measurement and simulation of distributed-feedback tapered master-oscillator power amplifiers. *IEEE J. Quantum Electron.*, 45(6):609–616, 2009.
62. C. Fiebig, V. Z. Tronciu, M. Lichtner, K. Paschke, and H. Wenzel. Experimental and numerical study of distributed-Bragg-reector tapered lasers. *Appl. Phys. B.*, 99(1):209–214, 2010.
63. M. Spreemann, H. Wenzel, B. Eppich, M. Lichtner, and G. Erbert. Novel approach to finite-aperture tapered unstable resonator lasers. *IEEE J. Quantum Electron.*, 47(1):117–125, Jan 2011.
64. S. Tronciu, V. Z Schwertfeger, M. Radziunas, A. Klehr, U. Bandelow, and H. Wenzel. Numerical simulation of the amplification of picosecond laser pulses in tapered semiconductor amplifiers and comparison with experimental results. *Optics Communications.*, 285(12):2897–2904, 2012.
65. M. Lichtner, V. Z. Tronciu, and A. G. Vladimirov. Theoretical investigation of striped and non-striped broad area lasers with off-axis feedback. *IEEE J. Quantum Electron.*, 48(3):353–360, 2012.
66. M. Radziunas, R. Herrero, M. Botey, and K. Staliunas. Far-field narrowing in spatially modulated broad-area edge-emitting semiconductor amplifiers. *J. Opt. Soc. Am. B.*, 32(5):993–1000, 2015.
67. M. Radziunas and R. Ciegis. Effective numerical algorithm for simulations of beam stabilization in broad area semiconductor lasers and amplifiers. *Math. Model. Anal.*, 19(5):627–646, 2014.
68. M. Sheik-Bahae and E. W. Van Stryland. Optical nonlinearities in the transparency region of bulk semiconductors. In R. K. Willardson, E. R. Weber, E. Garmire, and A. Kost, editors, *Nonlinear Optics in Semiconductors I*, volume 58 of *Semiconductor and Semimetals*, pp. 257–318. Amsterdam: Elsevier, 1998.
69. M. Dinu. Dispersion of phonon-assisted nonresonant third-order nonlinearities. *IEEE J. Quantum Electron.*, 39(11):1498–1503, 2003.
70. V. I. Bespalov and V. I. Talanov. Filamentary structure of light beams in nonlinear liquids. *ZhETF Pisma Redaktsiiu.*, 3:471, 1966.
71. A. P. Bogatov. Lateral field instability and six-wave mixing in a diode laser with broad active area. *J. Russian Laser Res.*, 15(5):417–453, 1994.
72. S. Blaaberg, P. M. Petersen, and B. Tromborg. Structure, stability, and spectra of lateral modes of a broad-area semiconductor laser. *IEEE J. Quantum Electron.*, 43(11):959–973, 2007.
73. J. Piprek and Z. M. S. Li. On the importance of non-thermal far-field blooming in broad-area high-power laser diodes. *Appl. Phys. Lett.*, 102(22):221110, 2013.
74. U. Bandelow, H. Gajewski, and R. Hünlich. Fabry-Perot lasers: Thermodynamics based modeling. In J. Piprek, editor, *Optoelectronic Devices—Advanced Simulation and Analysis*, pp. 63–85. New York, NY: Springer, 2005.
75. T. Grasser, T.-W. Tang, H. Kosina, and S. Selberherr. A review of hydrodynamic and energy-transport models for semiconductor device simulation. *Proc. IEEE.*, 91(2):251–274, 2003.
76. G. Albinus, H. Gajewski, and R. Hünlich. Thermodynamic design of energy models of semiconductor devices. *Nonlinearity.*, 15(2):367, 2002.
77. G. K. Wachutka. Rigorous thermodynamic treatment of heat generation and conduction in semiconductor device modeling. *IEEE Trans Comput-Aided Design Integr. Circuits Syst.*, 9(11):1141–1149, 1990.
78. J. E. Parrott. Thermodynamic theory of transport processes in semiconductors. *IEEE Trans. Electron Devices.*, 43(5):809–826, 1996.
79. K. Seeger. *Semiconductor Physics*. Berlin and Heidelberg: Springer Science & Business Media, 2013.
80. H. Gajewski, B. Heinemann, H. Langmach, R. Nürnberg, G. Telschow, K. Zacharias, H.-Chr. Kaiser, and U. Bandelow. WIAS-TeSCA Two-Dimensional Semi-Conductor Analysis Package, 2012.

28

High-Brightness Tapered Lasers

Ignacio Esquivias

Antonio
Pérez-Serrano

and

José-Manuel
G. Tijero

28.1 Introduction

The brightness of an optical source is commonly defined as the emitted power per unit of emitting area and per unit of the solid angle into which the power is emitted (Walpole 1996). Therefore, a high-brightness source requires not only a high value of the emitted power but also a high "beam quality" in terms of a low product of the beam size and the beam divergence. The product of the beam radius at waist and the beam divergence half angle is called "beam parameter product" and based on it, the most widely used figure of merit for beam quality, the beam propagation ratio M^2, is defined as the ratio of the beam parameter product of the beam of interest to the beam parameter product of a diffraction-limited, perfect Gaussian beam (TEM_{00}) of the same wavelength λ (ISO 2005; Siegman et al. 1998). Therefore, a value $M^2 = 1$ represents an ideal diffraction-limited source, while values higher than unity indicate a degradation of the beam quality.

Semiconductor lasers are optical sources with very well-known advantages over other types of optical sources: small size, high conversion efficiency, and low cost. There are many applications of semiconductor lasers demanding high brightness: material processing, optical pumping of solid state and fiber lasers, medical treatments, optical wireless communications, and in general all applications requiring high power launched into an optical fiber. However, the brightness of a semiconductor laser is usually limited due to two counteracting requirements: a large emitting area is required to produce high power with reduced bulk and surface heating, while reduced dimensions are required to maintain a single spatial mode and thus a high-quality beam. High-power semiconductor lasers are based on broad-area (BA) devices, with a poor beam quality along the lateral axis, while devices with reduced lateral dimensions and good beam quality, such as ridge waveguide (RW) lasers, suffer from a limited maximum output power.

As a consequence, an important research effort has been devoted to improve the brightness of semiconductor lasers during the last years and various new approaches have been proposed, including lasers with a tapered gain region (Walpole 1996; Wenzel et al. 2003; Sumpf et al. 2009), the master-oscillator power amplifier configuration (O'Brien et al. 1993; Spreemann et al. 2009), and the angled grating distributed feedback laser (Lang et al. 1998; Paschke et al. 2003). Tapered lasers, also called flared unstable cavity lasers, are possibly the best choice to achieve high brightness at moderate cost, due to the technological simplicity of their fabrication process.

The schematic of a typical tapered laser is shown in Figure 28.1a. It is similar to the tapered semiconductor optical amplifier (SOA) described in Chapter 22 of this book (Tijero et al. 2017). In brief, it is composed of a straight and narrow index-guided (IG) section, usually an RW structure, and a gain or IG tapered section where the beam is amplified. Ideally, the optical beam of a taper laser is a single lateral mode that diffracts at the exit of the RW section and is amplified in the tapered section while preserving its shape. The main difference with the tapered SOA is that the reflectivities of the facets are modified to provide laser oscillation at a reasonable value of the injection current. The output facet is usually antireflection (AR) coated while the back facet is coated to provide a high reflectance (HR) in order to decrease the threshold current and to maximize the output power. In many cases, the designs include beam spoiler elements in the form of trenches located in the neighborhood of the border between the RW and the tapered section (Figure 28.1a) (Kintzer et al. 1993). The main role of these elements is to filter the backward propagating field out of the RW. Most of the tapered lasers are based on a standard Fabry–Pérot cavity and therefore they present multiple longitudinal mode spectra. Some designs include a distributed Bragg reflector (DBR) at the end of the RW in order to provide narrow and stable emission spectra (Hasler et al. 2008).

In comparison with other semiconductor lasers, the specific design of tapered lasers leads to an optical beam with strong astigmatism. The virtual source for the vertical (y) axis (sometimes referred to as fast axis) is located at the output facet of the laser from where the beam diffracts in air. However, in the lateral (x) axis (sometimes referred to as slow axis), the beam diffracts from the exit of the RW section in the semiconductor medium and therefore, at low power, the separation between the two virtual sources (astigmatism) is approximately given by the taper section length L_{TAP} divided by the effective index n_{eff}. This is illustrated in Figure 28.1b. In the vertical axis, the beam can be considered as diffraction limited no matter the power. However, in the lateral axis the beam often degrades losing its diffraction-limited character when the power increases. As mentioned earlier, this degradation is usually characterized by the beam propagation ratio M^2. Referring to Figure 28.1c, the beam parameter product, bpp, and M^2 in the lateral axis are, respectively, given by

$$\text{bpp} = W_{0x}\theta_x \text{ and } M^2 = \frac{\pi}{\lambda}\text{bpp} \tag{28.1}$$

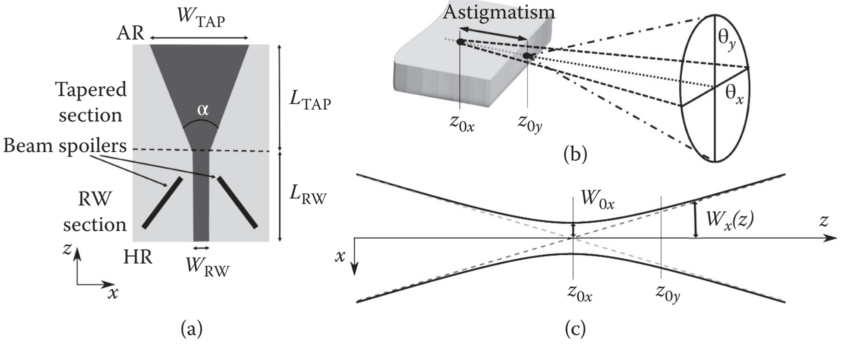

(a) (c)

FIGURE 28.1 (a) Schematics of a gain-guided tapered laser. The shaded area is the contact region. Grooves acting as beam spoilers are also depicted. (b) Schematics showing the far field distribution of a tapered laser as a consequence of astigmatism. (c) Evolution of the beam size in the lateral direction along the propagation axis z.

(λ/π being the bpp of a Gaussian beam of wavelength λ). In Equation 28.1, W_{0x} is the beam half width at the virtual source position (beam waist half width), and θ_x is the beam divergence half angle (far-field half width) given by

$$\theta_x = \lim_{z\to\infty} \frac{W_x(z)}{(z - z_{0x})} \tag{28.2}$$

where $W_x(z)$ is the beam half width at the z position and z_{0x} the virtual source location. It is important to point out here that the beam sizes in Equations 28.1 and 28.2 (and therefore the beam divergence) are defined in terms of the second-order moment (variance) of the power density distribution by $W_x(z) = 2\sigma_x(z)$ where

$$\sigma_x^2(z) = \frac{\int\limits_{-\infty}^{\infty}\int\limits_{-\infty}^{\infty} P(x,y,z)(x-\bar{x})^2 \mathrm{d}x\,\mathrm{d}y}{\int\limits_{-\infty}^{\infty}\int\limits_{-\infty}^{\infty} P(x,y,z)\mathrm{d}x\,\mathrm{d}y} \tag{28.3}$$

and $\bar{x}$ is the first order moment of the power density distribution (x coordinate of the centroid) (ISO 2005). When $W_x(z)$ is defined in this way, and only in this case, the evolution of the beam lateral size along the propagation axis z for any simple astigmatic beam can be described by the hyperbola depicted in Figure 28.1c and given by

$$W_x(z) = W_{0x}\sqrt{1 + \left(\frac{M^2\lambda(z - z_{0x})}{\pi(W_{0x})^2}\right)^2} \tag{28.4}$$

The fitting of the measured $W_x(z)$ to this expression is a method for the experimental determination of M^2, W_{0x}, and z_{0x} (ISO 2005).

Nevertheless, it is a common practice in the research groups having developed tapered lasers in the last years to characterize the beam quality by the parameter $M^2(1/e^2)$ (Krakowski et al. 2002; Sumpf et al. 2002), using the expression

$$M^2(1/e^2) = \frac{\pi}{\lambda}\theta_x(1/e^2)W_{0x}(1/e^2) \tag{28.5}$$

where $\theta_x(1/e^2)$ and $W_{0x}(1/e^2)$ are the half widths of the divergence and virtual source at $1/e^2$, respectively. For Gaussian beams $M^2(1/e^2) = M^2 = 1$ and in general $M^2(1/e^2)$ is a useful parameter to compare different lasers and to estimate the efficiency of the source to couple power into a reduced area device, such as a single mode fiber. However, $M^2(1/e^2)$ for non-Gaussian beams is usually much lower than M^2 and it is not actually a beam propagation ratio in the sense that it is not an invariant of the beam when it propagates in air or across passive, nonaberrating optical elements as required by a real beam propagation ratio. Therefore, the reader should be aware of this when interpreting the real relevance of this parameter. An example of the severe discrepancies between M^2 and $M^2(1/e^2)$ for a non-Gaussian beam will be commented in Section 28.3.5.

Two clearly different types of tapered lasers have been reported to date: gain-guided (GG) and IG lasers. The GG tapered lasers feature a relatively large full taper angle, α_{tap}, electrically defined in the p-contact layer. In these lasers, α_{tap} is designed to match the free diffraction angle (typically 4°–8°, depending on wavelength), as we will describe later. In the IG tapered lasers a small taper angle ($\alpha_{\text{tap}} < 1°$) is defined both, electrically in the p-contact layer and optically by an effective index step created by removing a fraction of the upper epitaxial layers. The beam properties of the two kind of tapered lasers are significantly different (Borruel et al. 2004a). GG tapered lasers with a taper angle close to the free diffraction angle have been fabricated at many different wavelengths from red (Blume et al. 2012) to around 2µm (Pfahler et al. 2006). A review of previous work on these devices can be found in Wenzel et al. (2003) and Sumpf et al. (2009). GG tapered lasers have demonstrated good beam quality and continuous wave (cw) output powers higher than 10 W at 980 nm (Fiebig et al. 2009), 1060 nm (Sumpf et al. 2009), and 1030 nm (Müller et al. 2016). Narrow IG tapered lasers have achieved more than 1 W at 980 nm (Krakowski et al. 2003) and 915 nm (Michel et al. 2005). Narrow IG lasers are usually combined in parallel arrays in high-power laser bars (Auzanneau et al. 2003; Wilson et al. 1999).

It is well known that the interaction between the optical field and the semiconductor gain media promotes a complex spatial-spectral dynamics in semiconductor lasers. In the case of tapered lasers, nonlinear effects, such as spatial hole burning (SHB) and thermal lensing add complexity to the physical phenomena involved and make the high power behavior to significantly deviate from the ideal low-power performance. Efficient and accurate modeling approaches are thus necessary to analyze and predict the beam properties of tapered lasers in order to design new geometries with improved performance. During last 20 years, different approaches have been applied to the modeling and simulation of tapered lasers and amplifiers. For a review see (Tijero et al. 2017) in this book.

Our group at the Universidad Politécnica of Madrid, in collaboration with the University of Nottingham, developed CONAN (Borruel et al. 2002, 2004a; Sujecki et al. 2003), a sophisticated simulator for tapered lasers that solves the electrical, optical, and thermal equations for these devices. Despite the assumptions needed to reduce the model complexity (steady state, single frequency, two-dimensional [2D] propagation of the optical mode), the simulations showed good qualitative and quantitative agreement with experimental results in tapered lasers with different geometries and based on different materials (Sujecki et al. 2003; Borruel et al. 2004a; Odriozola et al. 2009; Esquivias et al. 2010). Furthermore, the simulator demonstrated to be a useful tool to predict the behavior of novel designs prior to their fabrication (Borruel et al. 2005; Michel et al. 2009). Other models in literature (Williams et al. 1999; Mariojouls et al. 2000), based on similar approaches, have also reproduced the main trends observed experimentally.

In this chapter, we present a didactic overview of how the main beam characteristics of high-brightness tapered lasers can be accounted by simulation approaches with specific detail devoted to our simulation tool, and provide illustrative examples representative of some of the most typical behaviors of these devices. After this introduction, Section 28.2 presents a brief description of our simulation model and our procedure to calibrate the model in comparison with experimental results; in Section 28.3, we apply the model to three devices representative of some of the most common geometries and guiding mechanisms and analyze how geometry and guiding determine the beam characteristics. The chapter ends with a summary in Section 28.4.

28.2 Simulation Model

28.2.1 Model Overview

Our quasi-3D (three-dimensional) model (Borruel et al. 2002, 2004a; Sujecki et al. 2003) solves self-consistently the complete steady-state electrical, thermal, and optical equations for the tapered laser, assuming single-frequency operation. The laser simulator includes a 3D electrical solver of the Poisson and continuity equations coupled to a 3D thermal solver of the heat-flow equation with the local heat sources provided by the electrical solution. The optical fields in the tapered laser are solved using a 2D wide-angle finite-difference beam propagation method (WA-FDBPM) making use of the effective index approximation (Hadley 1992). Further details of the model can be found in Chapter 22 of this book, which is devoted to tapered SOAs (Tijero et al. 2017). Here, we briefly describe the model for completeness, in order to emphasize the differences when applying it to tapered lasers instead of tapered amplifiers. In fact, the main difference is that in the simulator for tapered amplifiers the WA-FDBPM is applied for the propagation of the optical solution only in the forward direction, while in the case of tapered lasers, the optical solution has to be propagated in both, the forward and then in the backward direction taking into account the corresponding reflectivities of the front and rear facets as corresponds to an optical resonator (Fox and Li 1961). Table 28.1 summarizes the main physical effects included in the model and how their dependence on temperature, wavelength, or carrier densities has been considered.

The simulator flow is shown in Figure 28.2. The solution procedure is initialized by a one-dimensional (1D) laser simulator (Harold, 3.0) which provides for each bias current the lasing wavelength, the bias voltage, and the average photon density in the laser cavity. The tapered laser is divided into 2D slices perpendicular to the z-axis at positions z_i where $i = 1, \dots, N$. The 1D average photon density is used to define an initial guess optical field at the first slice, at the rear facet of the device. The photon density of this field is used as input for the electrothermal solver to calculate the lateral gain and refractive index perturbation profiles in the first slice. With these inputs, a 2D WA-FDBPM making use of the effective index approximation propagates the optical field through the first slice and provides the electrothermal solver with the photon density profile corresponding to the next slice. This procedure is repeated until arriving to the front facet of the device, $i = N$. After applying the electrothermal solver to the last slice, the output power P_{out} and the excess power P_{exc} are calculated (Tijero et al. 2017) and used as inputs for a 3D thermal solver that is applied to the entire cavity and provides a new temperature profile. The whole process is repeated backward, i.e., propagating the solution from the front to the rear facet. After a number of round trips or iterations, the steady state for all the electrical, thermal, and optical variables is found.

TABLE 28.1 Main Physical Effects Included in the Model

Physical Effect or Parameter	Included	Comments
Temperature dependence of energy gap	YES	Empirical Varshni form
Band-gap renormalization	NOT	
Contribution to current density from thermal gradients	YES	Defined by the electron and hole thermoelectric powers
Carrier capture/escape processes in the quantum well (QW)	YES	Defined by electron and hole capture times
Thermionic emission in heterojunctions	NOT	
Fermi–Dirac statistics in bulk materials	NOT	
Dependence of electron and hole mobilities on dopant concentration	YES	Electric field and temperature dependencies not included
Auger recombination	YES	Temperature-dependent Auger parameters
Shockley–Read–Hall (SRH) nonradiative recombination	YES	Complete SRH formula, dependent on both electron and hole carrier concentrations, and on trap properties (density, energy, and degeneration factor of the trap, considering a temperature-dependent capture cross section)
Wavelength dependence of refractive index	YES	Temperature dependence not included
Free-carrier absorption	YES	Linear with local carrier concentration, defined by electron and hole free-carrier absorption coefficients
Nonconstant linewidth enhancement factor	YES	Calculated in QW region from a carrier-dependent differential refractive index, and carrier and wavelength-dependent differential gain
Gain broadening	YES	Lorentzian function
Coulomb enhancement of the gain	NOT	
Spontaneous emission noise	NOT	
Detailed calculation of local heat sources	YES	Local heat sources: Joule effect, nonradiative recombination, free-carrier absorption
Temperature dependence of thermal conductivities	YES	Included in semiconductor layers

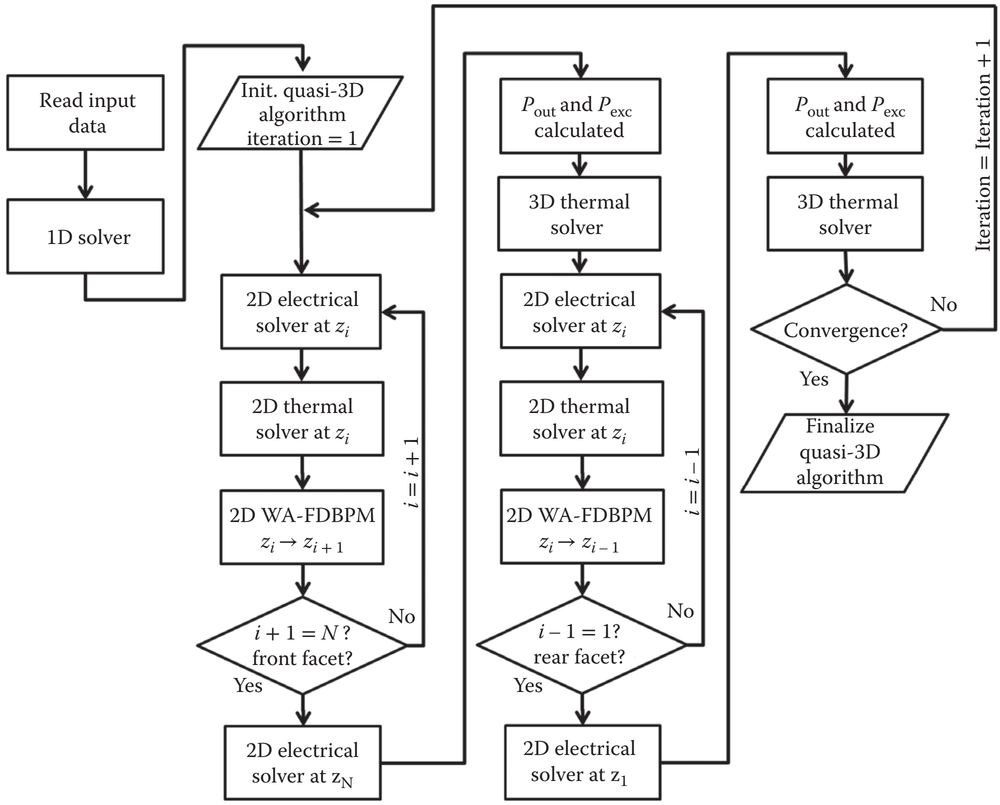

FIGURE 28.2 Main flow of the quasi-3D simulator for tapered lasers CONAN.

The convergence criterion is based on the stability of the optical field at the rear facet after consecutive iterations, both in shape and power. It can be expressed in terms of a parameter ε as

$$\varepsilon = \frac{\left\langle \left|E_n(x) - E_{n-1}(x)\right|, \left|E_n(x) - E_{n-1}(x)\right| \right\rangle}{\left\langle \left|E_n(x) + E_{n-1}(x)\right|, \left|E_n(x) + E_{n-1}(x)\right| \right\rangle} \tag{28.6}$$

where $E_n(x)$ is the optical field at the rear facet after n iterations and $\langle,\rangle$ denotes the scalar product. The iterative process finishes when ε is lower than a threshold value supplied by the user, typically 5×10^{-5}.

As commented previously, in order to filter the front facet back-reflected optical field reaching the ridge section, some tapered devices include beam spoilers (Walpole 1996). The beam spoilers are modeled by setting the optical field to zero at the beam spoiler locations (Mariojouls et al. 2000).

It should be noticed that our algorithm uses a fixed lasing wavelength provided by the 1D simulator. In a more rigorous approach, the lasing wavelength should be recalculated during the quasi-3D algorithm in order to take into account the spatial effects on it. Nevertheless, the comparison with experimental results has proven the approximate validity of our approach.

In some cases, the tapered lasers are fabricated with separate contacts for each section (Paschke et al. 2005; Odriozola et al. 2009; Michel et al. 2009). The model takes into account this possibility and allows the different sections to have different bias voltages. This is implemented as follows: after the initialization, the 1D simulator provides the laser wavelength, the initial photon density, and a bias voltage V_0. Then, for each section i, the applied bias voltage is recalculated as $V_i = V_0 + \Delta V_i$, where ΔV_i can be positive or negative. With these voltage inputs, the simulator proceeds normally and finally, the current at each section is calculated by integration of the current density.

The model can also be applied to the simulation of tapered lasers under patterned injection current (Borruel et al. 2004b). This is an interesting strategy aimed at counteracting the detrimental effects of the SHB. For this, a predefined function that laterally scales the epilayer material conductivities is introduced in the simulator. In this way, the local resistance is modified and therefore the current density profile is also modified according to the conductivity profile.

28.2.2 Model Options Regarding Symmetry

Our simulation procedure is based on launching a trial optical field and solving the forward and backward propagation until convergence (Fox and Li 1961). Depending on the symmetry of the initial trial optical field, the model has three versions:

- Half-cavity (HC) model: This is the basic version of the model. In this version, as in similar models (Williams et al. 1999; Mariojouls et al. 2000), the trial optical field is the fundamental mode of the passive RW section (an even function), although we have checked that the final optical field is independent of the shape of the initial field, provided it is an even function. Since the beam propagation method (BPM) preserves the parity of the field and the device is symmetric, only half of the cavity needs to be explicitly solved, thus reducing the computational effort. However, this version cannot take into consideration the effect of the odd components of the field and fails in reproducing some experimental features of the beam properties of IG tapered lasers, such as the excitation of secondary lateral modes. Therefore, the model was upgraded and two versions including optical fields with both odd and even components were created (Esquivias et al. 2010).
- Full cavity coherent coupling (FCCC) model: In this version, the equations are solved in the full cavity and the initial trial field is an asymmetric field $E_a(x)$, containing odd and even components, i.e., $E_a(x) = E_e(x) + E_o(x)$. The photon density is taken as proportional to $|E_a(x)|^2$ with $E_a(x)$ being the optical field after the propagation by the BPM through the previous slice. This photon density is in general asymmetric, although it can result in a final symmetric solution, depending on the particular device under study. This version often produces a snake-like intensity profile in the plane of the active layer. The corresponding near-field (NF) and far-field (FF) profiles are asymmetric and the intensity profile is not stable after subsequent roundtrips. This kind of behavior has been experimentally observed and attributed to the coherent coupling of frequency-locked lateral modes (Guthre et al. 1994).
- Full cavity incoherent coupling (FCIC) model: As in the FCCC version, the equations are solved in the full cavity and the initial trial field is an asymmetric field $E_a(x)$, but in this case, the photon density is calculated as proportional to $|E_s(x)|^2$, the addition of the field intensities of the even and odd components of $E_a(x)$: $|E_s(x)|^2 = |E_e(x)|^2 + |E_o(x)|^2$. In this way, the photon density is symmetric, and consequently also the carrier and temperature profiles. This approach is equivalent to the simultaneous propagation of an even and an odd field with slightly different frequencies and therefore only coupled through its interaction with the gain medium, i.e., incoherently coupled. This version is more appropriate than the HC model for IG lasers supporting higher order lateral modes besides the fundamental mode.

28.2.3 Model Calibration and Comparison with Experiments

A critical point in all sophisticated laser models is the high number of relatively unknown material parameters. Some of them (energy band parameters, refractive index, etc.) are specific of the different semiconductor materials used in the device. These are usually well known only for the most common binary materials (GaAs, InP), relatively well known for some ternary alloys and relatively unknown for many other alloys. Even for the best known materials, the temperature or wavelength dependence of some parameters has not been reported. In addition, other important parameters (scattering losses, trap characteristics, etc.) depend on the particular fabrication process, and can be different for nominally identical materials. As a consequence, it is always necessary to calibrate the model parameters with experimental results in order to reproduce the experiments and to predict the trends of the device performance when modifying the material composition or the device geometry.

The main idea is to find, if possible, a set of simulation parameters such that the model reproduces the main trends of relevant experimental results, such as power–voltage–current characteristics, FF and NF patterns, and evolution of M^2 and FF and NF patterns with current. If these simulation parameters conveniently account for the main physical effects causing the observed beam properties, then the model will predict qualitatively, and even quantitatively, the performance of new devices based on the same materials but with different design. In other words, it is not so important to use a complete set of correct material parameters, but rather to find out those parameters relevant for the model and related to the main internal process limiting the maximum power or degrading the beam quality.

Our calibration process includes three steps, the first one at theoretical level, the second one by comparing with experimental results in BA lasers, and the third one by comparing with results in tapered lasers. Prior to the calibration, it is important to consider the entire epilayer structure and find out in the literature as many material parameters as possible, especially in the most standard references (Adachi 1992; Vurgaftman et al. 2001). Unfortunately, as stated above, many important parameters, such as refractive index, Auger, and free-carrier absorption coefficients, have never been measured for new materials or alloy compositions, in which case we use judicious guess values based on the parameter values in other alloys with similar gap or composition.

The first step of the calibration procedure is the fitting of the parameters used to calculate the material gain spectra $g_{\mathrm{mat}}(\lambda)$ and the spontaneous recombination rate R_{sp}, as a function of the electron and hole quasi-Fermi energies. As it is described in Tijero et al. (2017), the simulation tool operates with a parabolic band model for the calculation of these functions but takes into account band mixing effects by the following fitting procedure: first, we use a valence band (VB) mixing model (Coldren and Corzine 1995), to calculate the quantum well (QW) energy levels and the maximum gain and the spontaneous recombination rate versus carrier concentration, $g_{\max}(n)$, and $R_{\mathrm{sp}}(n)$. Then, these calculations are fitted by the results provided by the simulation tool using same formulation but considering parabolic valence subbands. The fitting parameters are the QW energy levels, the effective mass of each level, and two scaling parameters (multiplying factors) for $g_{\mathrm{mat}}(\lambda)$ and for R_{sp}. Finally, the tool is fed with the parameters that best fit $g_{\max}(n)$ and $R_{\mathrm{sp}}(n)$ obtained by the VB mixing model. Very good agreement was achieved for a wide range of carrier densities.

The second step in the calibration procedure is to compare 1D simulations with experimental results in BA lasers fabricated with the same epitaxial material than the tapered lasers. It is important to include power–current (P–I) characteristics for lasers with different cavity lengths measured at different temperatures, as well as the FF patterns along the vertical axis. The goal of this step is to determine those simulation parameters related to the material quality (scattering losses and Shockley–Reed–Hall recombination parameters), and also to modify those relevant parameters, which are not well known, such as the Auger coefficient and its temperature dependence. The comparison is made between measured and simulated results in terms of the threshold current density (J_{th}) dependence on the cavity length L, internal quantum efficiency, internal losses, and characteristic temperature T_0. The comparison between measured and calculated FF patterns provides a method to modify the refractive indices, especially that of the QW, which is very important for the calculation of the optical confinement factor in the simulations. The comparison between experimental and simulated current–voltage characteristics provides information on the total resistance of the device, which is relevant for a correct estimation of the Joule heating in the simulations.

The final stage of our calibration procedure includes two parameters: one to account for the carrier-induced refractive index change, and the other one to account for the heat transfer efficiency. For the first one, we focus on its effect on the beam divergence and fit the experimental value of the beam divergence at a fixed output power to the simulated value. This can be achieved by using as fitting parameter the coefficient n_1 that relates the index change and the carrier density assuming a square root dependence (Borruel et al. 2004a). Regarding heat transfer, in order to avoid extending the thermal simulation region, we artificially consider a heat-sink area equal to the device area and use the heat-sink thickness as fitting parameter. We use it to fit the experimental average temperature increase when increasing the current to the simulated temperature increase (on average). The experimental average temperature increase is estimated from the shift of the lasing wavelength when increasing the current, assuming a standard dependence. We have checked that by changing the heat sink thickness, the average value of the temperature changes without important modifications in the lateral and longitudinal temperature profiles.

This procedure was applied to 975 nm (IG and GG with beam-spoilers) and to 735 nm (GG without beam spoilers) tapered lasers in Borruel et al. (2004a). We found a good agreement in the P–I characteristics, shape of the NF and FF patterns, and especially in the evolution of beam properties (M^2, astigmatism, widths of NF at waist and FF patterns) with the injection level. Furthermore, we also found a good agreement between the maximum measured power in the 975 nm GG devices and the maximum power with numerical convergence in the simulations, indicating that the physical mechanism limiting the power was correctly reproduced. This good agreement provided the basis for a new geometrical design, the clarinet laser (Borruel et al. 2005), which showed beam properties similar to those predicted by the simulations. Our model was also applied to simulate the 915-nm IG lasers described in Michel et al. (2005), but in this case the experiments showed a double peak in the NF and FF which was not reproduced by the simulations and gave rise to the upgraded FCIC version of the model previously described. Additional comparisons between experiments and simulations can be found in Odriozola et al. (2009), Michel et al. (2009), and Esquivias et al. (2010).

28.3 Simulation Examples

In order to illustrate the capabilities of the simulation tools for accounting for the behavior of typical tapered laser geometries and guiding mechanisms, we have selected three representative geometries and guiding mechanisms sharing the same epitaxial structure. In this section, we analyze with our simulation tool CONAN the effect of these design parameters on the device performance. We devote specific attention to the comparative analysis of the effects on the beam properties of the device geometry and injection conditions. Since this analysis is presented here mainly for illustrative purposes, some interesting effects will be just overviewed without a detailed study. The half-cavity version of the simulator was used in the three examples. The simulations were performed under isothermal conditions to concentrate the focus in carrier-related effects, since thermal effects are strongly dependent on the value of some relatively unknown material parameters. A detailed discussion on the role of thermal effects in tapered lasers can be found in Esquivias et al. (2010).

28.3.1 Device Geometries and Simulation Parameters

The epitaxial structure of the simulated devices corresponds to that of the 1060 nm GG tapered lasers reported in Ruiz et al. (2009). In brief, it consists of a strained InGaAs QW embedded in a large InGaAsP symmetric optical cavity with AlGaAs cladding regions. We will compare the beam properties of three devices: (1) a GG tapered laser with beam spoilers (GG-BS), (2) a GG tapered laser without beam spoilers (GG-NBS), and (3) a narrow IG laser without beam spoilers (IG).

The geometrical and material parameters used in the simulations are identical for the three devices except for the taper angle and guiding mechanism in the tapered section. The total cavity length is 3 mm and the taper angles are 6° and 1° for the GG and IG devices, respectively. Table 28.2 shows these parameters as well as a brief summary of the most influential material and device parameters used in the

TABLE 28.2 Geometrical Parameters of the Tapered Lasers and Summary of the Most Relevant Material and Device Parameters Used in the Simulation

Symbol	Parameter	Value	Units
L_{RW}	Length of the RW section	1	mm
W_{RW}	Width of the RW section	2.5	μm
L_{TAP}	Length of the taper section	2	mm
R_f	Front facet reflectivity	0.025	
R_b	Back facet reflectivity	0.95	
	Full aperture of beam spoilers	17	μm
	Distance from beam spoilers to back facet	1	mm
α_{tap}	Full taper angle	6 (GG); 1 (IG)	°
Δn_{eff}	Effective index step of the RW section	4.7×10^{-3}	
T_{HS}	Heat sink temperature	20	°C
Γ	Confinement factor	0.0084	
α_{scat}	Scattering losses coefficient	0.5	cm^{-1}
$C_n(C_p)$	Electron (hole) Auger recombination coefficient	$2(2) \times 10^{-30}$	cm^6s^{-1}
k_e, (k_h)	Electron (hole) free-carrier absorption coefficient	$3(7) \times 10^{-18}$	cm^2
n_I	Differential refractive index coefficient	4.5×10^{-11}	$cm^{3/2}$

simulation. These parameters were extracted from standard references or fitted after applying the calibration procedure described in Section 2.3 to the GG-BS device (Esquivias et al. 2010). The taper angle of the GG devices was selected so as to fit the calculated free diffraction angle assuming an index step $\Delta n_{eff} = 4.7 \times 10^{-3}$.

28.3.2 GG Tapered Laser with Beam Spoilers

The GG-BS device presented here is representative of GG tapered lasers with beam spoilers. At low power, these devices show single-lobed NF and FF patterns and low values of M^2. Figure 28.3a and b illustrates the evolution of the profile of the forward and backward optical field intensities along the cavity at low power (slightly above threshold). A more detailed view of the beam profiles at different longitudinal positions is provided in Figure 28.4a and b. The shape of the fundamental lateral mode of the RW section entering the gain section (see curve A in Figure 28.4a) can be approximated by a Gaussian function. In this example, the calculated full width of the mode at $1/e^2$ (W_{mode}) is 4 μm.

When entering the tapered section, the mode is subjected to two different effects: (1) amplification by the gain medium and (2) free diffraction if the full taper angle is larger than the free diffraction full angle θ_D (at $1/e^2$). The free diffraction angle of an ideal Gaussian beam is given by

$$tg\left(\theta_D/_2\right) = \frac{2 \cdot \lambda}{\pi \cdot n_{eff} \cdot w_{mode}} \tag{28.7}$$

where n_{eff} is the effective index of the vertical waveguide. In the case of the GG-BS device under analysis, the full taper angle (6°) has been chosen to match the value of θ_D. Figure 28.4a shows the lateral intensity profile of the forward traveling light at cross sections taken at several positions along the cavity (curve A at $z = 1$ mm, curve B at $z = 2$ mm, and curve C at $z = 3$ mm, $z = 0$ and $z = 3$ mm being the back and the output facet, respectively). The beam expands smoothly as it propagates along the tapered section and reaches the output facet keeping its Gaussian-like profile (curve C), although the wave front has a convex shape, and therefore the phase at the facet is far from being uniform. The reflected (or backward) field continues diffracting in its way back but now the freely diffracting beam does not overlap any more with the gain region and therefore the beam becomes narrower as it propagates backward. This evolution is

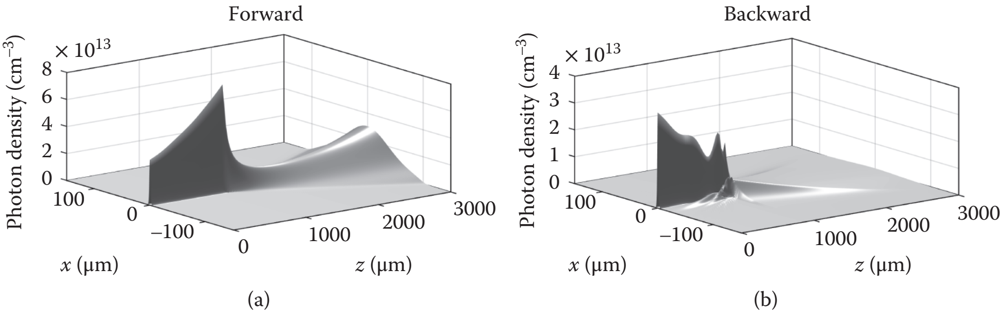

(a) (b)

FIGURE 28.3 (a) Forward and (b) backward optical field intensity inside the cavity for the GG-BS tapered laser, when operated at low power ($P_{\text{out}} = 38$ mW).

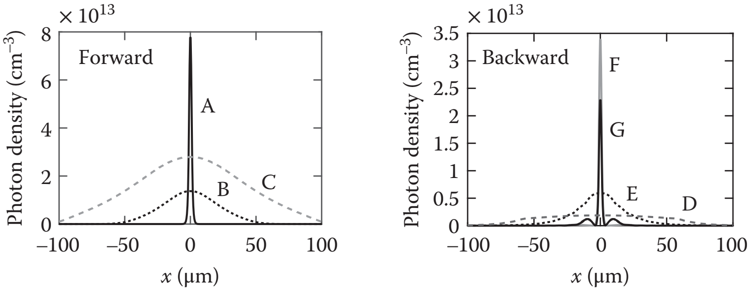

(a) (b)

FIGURE 28.4 (a) Forward and (b) backward optical field intensities at different positions inside the cavity for the GG-BS device, when operated at low power ($P_{\text{out}} = 38$ mW). In panel (a): A at $z = 1$ mm, B at $z = 2$ mm, and C at $z = 3$ mm (output facet). In panel (b): D at $z = 2$ mm, E at $z = 1$ mm, F at $z = 0.5$ mm, and G at $z = 0$ mm (back facet).

illustrated in Figure 28.4b, where curves D and E show the intensity profiles at an intermediate position in the tapered region ($z = 2$ mm) and at the entrance of the RW section, respectively. As the beam entering the RW section is wider than the fundamental mode of this section (70 versus 4 μm at $1/e^2$), a substantial part of the power is not coupled producing the so-called coupling losses (Walpole 1996) or taper losses. The beam propagating along the RW section is filtered by the single-mode waveguide, with the help of the beam spoilers. Curves F and G are the profiles at the middle of the RW section and at the back facet of the device, respectively. The side lobes of curve F reveal that the filtering effect is still imperfect at the middle of the RW section (see also Figure 28.5b). However, at the back facet, the lobes have virtually disappeared and the beam is as narrow as the fundamental mode of the waveguide revealing that in this case the filtering effect is fully accomplished at the back facet. In other cases, the filtering could be still accomplished in the subsequent forward propagation along the RW and the second pass through the beam spoilers after the reflection at the back facet.

Even more insight into the evolution of the beam inside the cavity can be gained by the gray-scale plots in Figure 28.5. In these plots, the forward (Figure 28.5a) and backward (Figure 28.5b) photon densities in each slice perpendicular to the longitudinal axis have been normalized to their maximum value in the slice and white lines have been drawn at the border of the injected region and at the position of the beam spoilers. In comparison with the smooth and homogeneous expansion of the photon density profile of the forward field in the tapered section, the width of the backward field photon density profile increases from $z = 3$ mm to about $z = 2.5$ mm and decreases afterward due to the gain guiding in the narrower part of the tapered region. Nevertheless, at the entrance of the RW section, the photon density profile of the

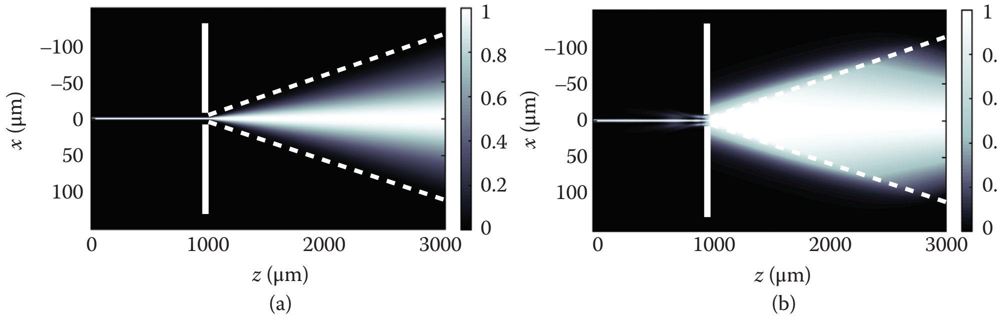

(a)

(b)

FIGURE 28.5 Normalized (a) forward and (b) backward optical field intensity inside the cavity at each z slice for the GG-BS device, when operated at low power (P_{out} = 38 mW). The white dashed lines indicate the pumped tapered region, while the white solid lines indicate the position of the beam spoilers.

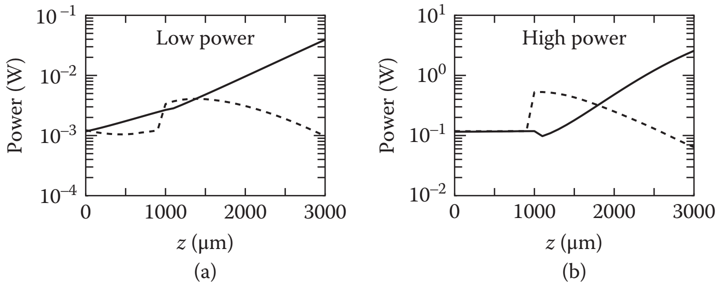

(a)

(b)

FIGURE 28.6 Optical power of the forward (solid) and backward (dashed) traveling optical fields along the cavity for the GG-BS laser, when operated at (a) low power (P_{out} = 38 mW) and (b) high power (P_{out} = 2.5 W).

backward field still expands far beyond the limits of the injected area. At this point, the filtering role of the beam spoilers is crucial and only tiny diffraction lobes survive after entering the RW section.

To complete the picture, the evolution along the cavity of the total powers carried by the forward and backward beams is shown in Figure 28.6. These powers were obtained by integration of the forward and backward photon densities in the lateral direction at each longitudinal position. In the logarithmic scale of Figure 28.6, an exponential growth of the power is represented by a straight line in which slope is proportional to the effective modal gain, defined as the difference between the modal gain and all the losses occurring in the beam propagation. At low power (Figure 28.6a), the forward field effective gain is constant in both sections. In this case, it is slightly lower in the RW section due to a lower material gain and a slightly worse overlapping with the optical mode in the RW section (not shown). The backward beam power shows initially an exponential growth up to about z = 2.5 mm due to the good overlapping with the gain region. The progressively worse overlapping makes the beam amplification to decreases down to negative values at the entrance of the RW section. At this point, the power drops down due to the filtering effect of the beam spoilers. The subsequent evolution of the backward propagating power is the result of the competing mechanisms of filtering and gain in the RW section, the balance being slightly positive at the back facet. The evolution of the forward and backward propagating powers at high power is illustrated in Figure 28.6b and is mentioned later in this section.

The nearly ideal behavior of the GG-BS device observed at low power changes dramatically when increasing the output power. The main reason for this is the mutual interaction in the semiconductor material between photons and carriers in a feedback loop leading eventually to power saturation and self-focusing at high output powers. Let us start with the optical mode profile. At high injection the mode narrows, thus concentrating a high photon density in the cavity axis. This high photon density depletes the carrier density along the cavity axis due to the higher stimulated recombination in this region, the so-called SHB effect. Figure 28.7a shows the simulated carrier density for the GG-BS device at the output facet for increasing output powers. The initially flat profile of the carrier density evolves when the injection increases to a "batman-ears" like profile, with maxima at the sides and minimum at the center. This profile has been experimentally observed through spontaneous emission measurements (Pagano et al. 2011). The carrier density minimum is limited by the transparency carrier density, 1.2×10^{18} cm^{-3} in our example. The initial simplified approach by Walpole (1996) suggested that the local gain saturation in the cavity axis caused by the SHB would induce an increase of the photon density in the side regions, leading to a top hat shape. But in semiconductor materials, a change of the carrier density produces simultaneously changes in the gain and in the refractive index, which are related by the linewidth enhancement factor. Figure 28.7b and c shows the corresponding gain and index profiles at the power levels of Figure 28.7a. The gain decreases at the cavity axis and the refractive index increases. The shape of the index profile produces a parasitic waveguide for the beam, with more important consequences on the beam shape than the gain profile. The carrier-induced waveguide produces a convergent lens effect during the beam propagation along the tapered region, which concentrates the power density at the center of the beam, thus closing the feedback loop (see Figure 28.4d).

At high power density, the strong feedback induces self-focusing of the beam, leading to saturation of the output power. This effect can be visualized with the help of Figure 28.8, where (as in Figure 28.5) we have plotted the forward (Figure 28.8a) and backward (Figure 28.8b) normalized photon densities at a high power level. In comparison with Figure 28.5a, the forward beam is much narrower, showing clearly the self-focusing. More difficult is the interpretation of the backward beam shape in the tapered section (Figure 28.8b). The expansion of the backward beam beyond the limits of the injected region adds to the gain guiding and the induced index guiding a new degree of complexity making the beam shape extremely difficult to interpret in simple terms. Again, the filtering role of the beam spoilers is apparent in the RW

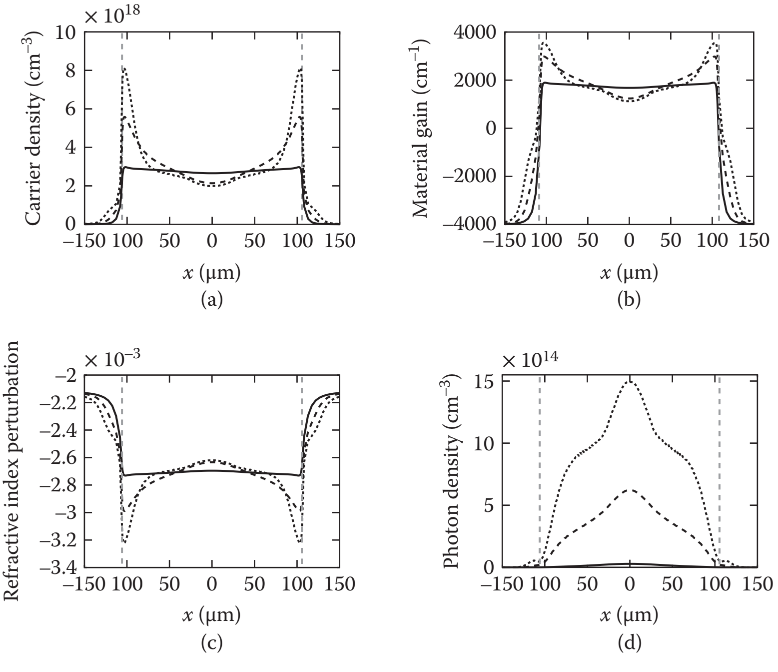

FIGURE 28.7 (a) Carrier density, (b) material gain, (c) refractive index perturbation, and (d) photon density profiles at the output facet for the GG-BS laser at different output powers: $P_{\text{out}} = 38$ mW (solid), $P_{\text{out}} = 955$ mW (dashed), and $P_{\text{out}} = 2.5$ W (dotted). Vertical dashed gray lines indicate the pumped region limits.

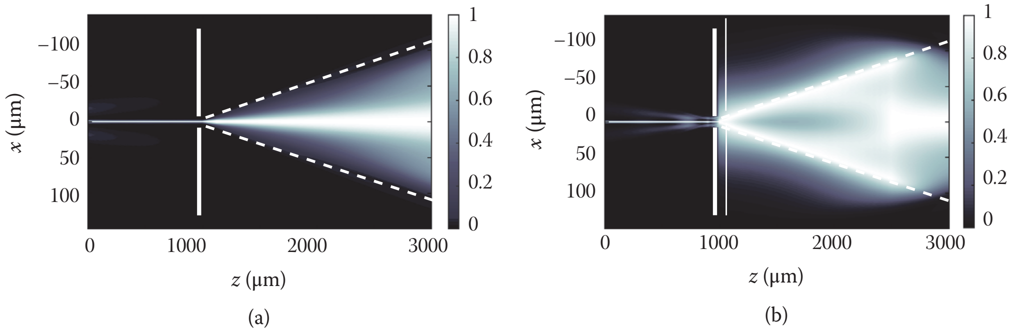

FIGURE 28.8 Normalized (a) forward and (b) backward optical field intensity inside the cavity at each z slice for the GG-BS device, when operated at high power (P_{out} = 2.5 W). The white dashed lines indicate the pumped tapered region, while the white solid lines indicate the position of the beam spoilers.

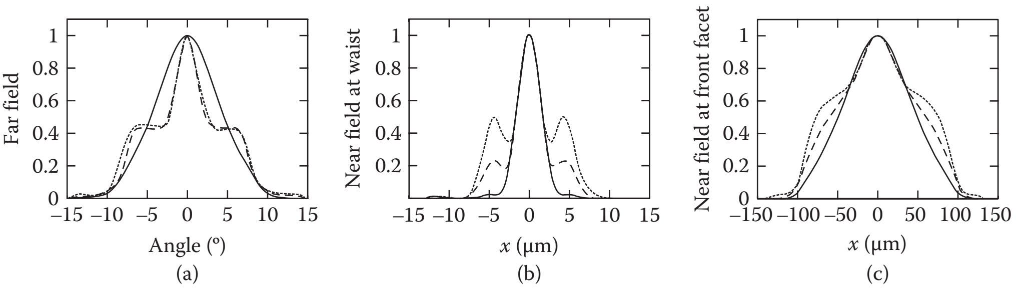

FIGURE 28.9 (a) Far field, (b) near field at waist, and (c) near field at the front facet for the GG-BS device at three power levels, P_{out} = 38 mW (solid), P_{out} = 955 mW (dashed), and P_{out} = 2.5 W (dotted).

section. The small diffraction lobes surviving at low power are now more noticeable and can even reach the back facet from where they are reflected as can be (hardly) seen in Figure 28.8a.

The evolution of the integrated forward propagating power at high injection (Figure 28.6b) shows also clear differences with respect to the low injection behavior. The nearly homogeneous effective gain for the forward field at low power (Figure 28.6a) becomes clearly different in the RW and tapered sections at high power. In the RW section, the effective gain vanishes revealing a strong gain saturation confirmed by a carrier density in this section slightly higher than the transparency value (not shown). As the total round-trip gain should be constant, the absence of gain in the RW section is compensated with the high values of the effective gain at the beginning of the tapered section. Further in the tapered section, the forward effective gain decreases slowly due once more to gain saturation. In contrast, the evolution of the backward propagating power at high injection is not significantly different from the low-injection behavior. In the RW section, after the sudden drop of the power due to the beam spoilers, the modal gain remains constant at a value close to zero as for the forward beam.

The SHB and self-focusing of the beam at high injection not only limit the maximum power, but also degrade the beam quality. Figure 28.9 shows the FF pattern and the NF patterns at waist and at the facet, at three power levels. Under simplifying ideal assumptions, the expected value of the FF width can be estimated by applying Snell's law to the beam at the output facet. In this case, this yields a full beam divergence angle θ_{out} (at $1/e^2$) $\sim n_{eff} \cdot \theta_D = 20°$ ($n_{eff} = 3.34$). The simulated value at low power is $\theta_{out} = 16.5°$, not far from the previous estimation. It is clear how the shape of the beam is modified by the carrier-induced convergent lens when increasing the power: the NF patterns at waist and at the front facet develop shoulders and the FF patterns evolve into a narrower central lobe together with the apparition of side lobes. These effects produce also an increase of the astigmatism and the value of M^2 is shown in Section 3.5.

28.3.3 GG Tapered Laser without Beam Spoilers

The GG-NBS device presented here is representative of GG tapered lasers without beam spoilers. In spite of the advantages of the use of beam spoilers, they have also drawbacks due to the additional processing steps and also to the possible introduction of defects close to the active region. In fact, very high power levels have been reported for tapered lasers without beam spoilers (Sumpf et al. 2009; Müller et al. 2016). In this case, the filtering properties of the RW section had been improved by increasing its length, after a careful balance to optimize this design parameter (Wenzel et al. 2003). The main characteristic of the beam experimentally observed in tapered lasers without beam spoilers is a multilobed FF pattern, with an increasing number of lobes together with an increase of the peak to valley ratio when increasing the output power (Borruel et al. 2004a; Fiebig et al. 2009; Sumpf et al. 2009; Müller et al. 2016).

Figure 28.10 shows the simulated evolution of the FF and NF profiles of the GG-NBS device as a function of the output power. The relatively smooth profiles of the FF and NF at low power evolve when the injection increases to a more structured profile with an increasing number of more and more distinguishable lobes. The FF width at $1/e^2$ decreases slightly when the power increases, while the $1/e^2$ NF width at waist remains almost invariant, in agreement with what has been experimentally observed (Fiebig et al. 2009). These behaviors yield an almost invariant low value of $M^2(1/e^2)$. However, the value of M^2 (second moment) significantly increases with the power, mainly due to the tiny side lobes below the $1/e^2$ level in the NF at waist (see inset in Figure 28.10b). These differences will be commented later in Section 3.5. The agreement between the appearance and the evolution of the FF and NF lobes in simulation and experiments provides support for the use of the simulation tool to provide a physical understanding of the origin of these lobes in devices without beam spoilers.

Aiming at this, for an output power level of 0.26 W, Figure 28.11 shows gray-scale plots of the forward (Figure 28.11a) and backward (Figure 28.11b) propagating photon densities, normalized to their maximum value at each cavity position. The side lobes that are already apparent at the beginning of the tapered section, propagate toward the front facet, and finally result in the multilobed NF pattern shown in Figure 28.10c. During the backward propagation (Figure 28.11b), the highest intensity side lobes run away the tapered region where they extinguish without reaching the RW section. However, the backward field entering the RW section is not perfectly filtered and a fraction of it is diffracted by the RW section aperture producing side lobes in the field that reaches the back facet. This residual field at the sides of the RW section is reflected by the back facet and interferes in the tapered section with the forward field arising directly from the RW section, thus producing the multiple peaks observed in the beam characteristics.

The lack of a complete filtering in the RW section is more important at high power, as the intensity of the backward field increases and optically pumps the sides regions around the RW, thus reducing the absorption. This effect is further illustrated in Figure 28.12, where we have plotted the forward and backward photon densities (Figure 28.12a) and the carrier density (Figure 28.12b) at the interface between the

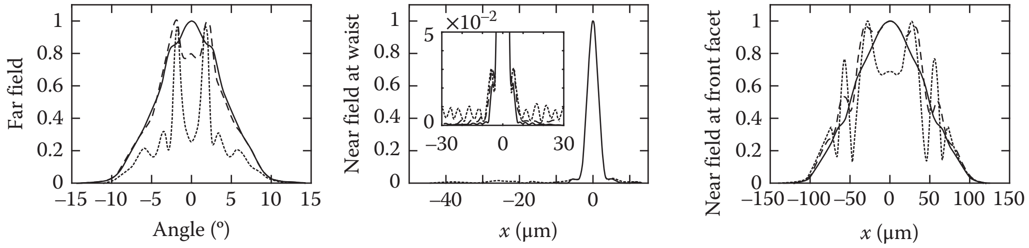

(a) (b) (c)

FIGURE 28.10 (a) Far field, (b) near field at waist, and (c) near field at the front facet for the GG-NBS device at three power levels, $P_{out} = 40$ mW (solid), $P_{out} = 260$ mW (dashed), and $P_{out} = 393$ mW (dotted). The inset in (b) is a magnification emphasizing the side lobes far from the axis appearing at $P_{out} = 260$ and 393 mW.

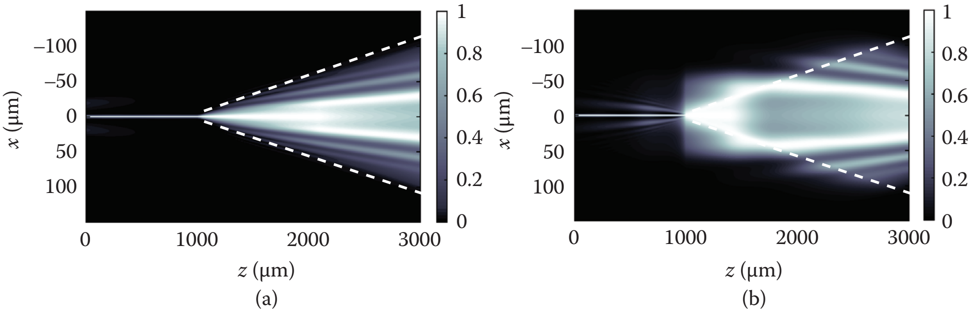

FIGURE 28.11 Normalized (a) forward and (b) backward optical field intensity inside the cavity at each z slice for the GG-NBS device, when operated at high power (P_{out} = 260 mW). The white dashed lines indicate the pumped tapered region.

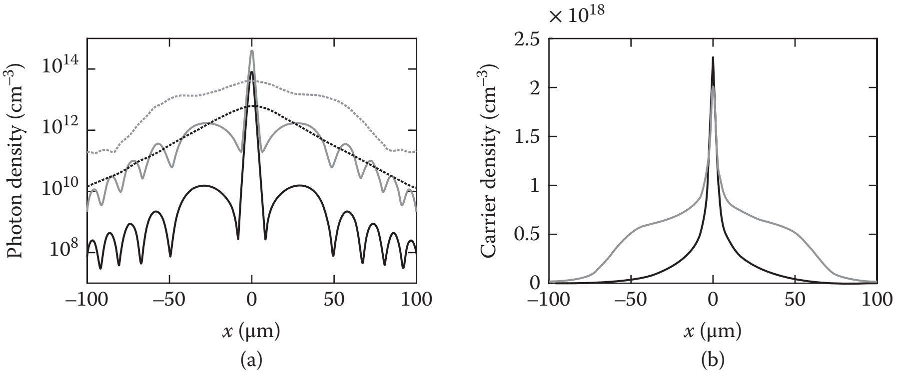

FIGURE 28.12 (a) Forward (solid) and backward (dotted) photon densities and (b) carrier density profiles at the interface between the RW (2.5μm wide) and tapered sections for the GG-NBS device at two output powers P_{out} = 40 mW (black), P_{out} = 260 mW (gray).

RW and tapered sections at two power levels. At low power, the side lobes of the forward field are around 40 dB below the main lobe in the RW (Figure 28.12a) and therefore, this results in a single-lobed NF at the facet (see Figure 28.10c). The backward field at the sides of the RW is low and therefore the induced carrier density (Figure 28.12b) is far below transparency; in consequence, this region is highly absorbent. However, at medium and high injection levels, the backward field intensity is high enough for pumping the sides of the RW to a carrier concentration close to transparency (Figure 28.12b), thus decreasing their absorption. As a result, the forward field intensity at the side lobes becomes only around 20 dB lower than the maximum (Figure 28.12a) giving rise to the multilobed profile obtained at medium and high power level.

Our previous simulations of GG tapered lasers without beam spoilers have shown the same trends as the experimental results (Borruel et al. 2004a; Odriozola et al. 2009), but the quantitative agreement is not as good as we have found in tapered laser with beam spoilers. Furthermore, the maximum output power with numerical convergence in the simulations is usually lower than the measured maximum power. We attribute these discrepancies to the limitations of our steady-state single-frequency model. We think that in the real device, there is a complex dynamics of the different lateral modes giving rise to rapidly varying NF and FF patterns. As the measured NF and FF patterns are temporal averages, it is expected that the narrow and pronounced lobes would average resulting in smoother profiles. In fact, the lack of convergence in the simulations is due to different shapes and positions of the lobes after subsequent round-trips, yielding a stable output power but a different field profile after each iteration. This is illustrated in Figure 28.13, where we have plotted the NF at the facet after two consecutive round-trips for simulation conditions in which a stable solution is not found. The averaging of the field intensity after different roundtrips would produce less pronounced lobes as they appear in the experimental results.

28.3.4 Narrow Index-Guided Tapered Laser

The IG device analyzed in this section is representative of narrow IG tapered lasers. Significant differences with respect to the behavior of large angle GG devices arise from the fact that the single lateral optical mode launched by the RW section does not just expand by free diffraction into an injected tapered region designed to match the free diffraction angle. Instead, the beam is guided in a narrow tapered section defined by the refractive index step, where injection takes place.

The gray-scale plots of Figure 28.14 are illustrative of the forward and backward beam propagation in the IG device at low power (notice the different lateral dimension with respect to the corresponding plots for GG devices). The forward beam expands preserving its shape, with most of the power (99.8% at $z = 2$ mm) inside the guiding region (Figure 28.14a). The propagation of the backward field is determined by a combination of competitive phenomena: diffraction, gain and index guiding, and reflections at the waveguide interface, resulting in a multilobed profile (Figure 28.14b). The index guiding, as well as the relatively small taper angle, produces a beam entering the RW which is narrower than that of the GG devices, hence reducing the taper losses. The RW section acts again as a spatial filter, and the beam recovers its original single-mode shape after a complete round trip.

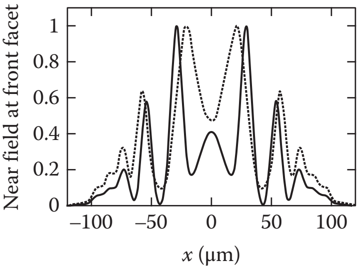

FIGURE 28.13 Example of the simulated NF profiles at the facet for two consecutive iterations of a simulation of the GG-NBS device under conditions in which a stable solution is not found.

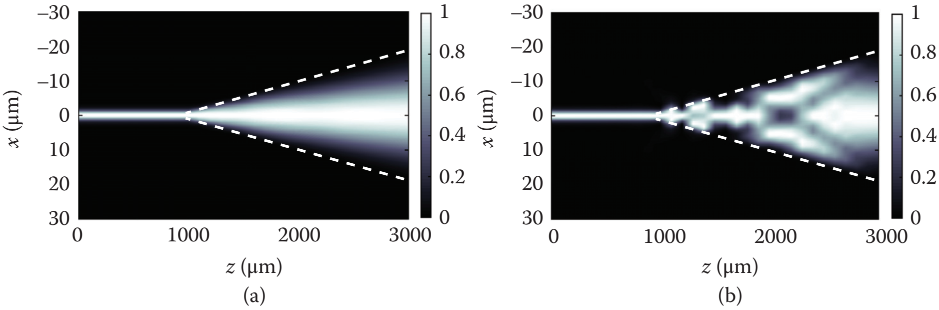

FIGURE 28.14 Normalized (a) forward and (b) backward optical field intensity inside the cavity at each z slice for the IG device, when operated at very low power ($P_{\text{out}} = 40$ mW). The white dashed lines indicate the pumped tapered region and the index step.

The main effect degrading the beam quality of IG tapered lasers is carrier-induced lensing and self-focusing, similar to the effect analyzed in Section 28.3.2 for GG devices, but with important differences. Figure 28.15 shows the simulated evolution of the FF and NF profiles of the IG device as a function of the output power. Both the profiles as well as the evolution with power are completely different than those of the GG devices shown in Figures 28.9 and 28.10. At very low power (40 mW), since the beam expands in the tapered section covering almost all the guiding region, the simulated FF width at $1/e^2$ is $\theta_{\mathrm{out}} = 3.28°$, close to 3.34°, the value resulting from applying Snell's law to the taper angle. In consequence, the beam is clearly astigmatic (204 μm). But the picture changes dramatically when increasing the power: the carrier lensing reduces the width of the beam at the output facet down to sizes for which diffraction effects become relevant, and consequently, the angular width of the FF patterns increases with the output power while the NF at waist and the NF at the facet narrow. In addition, the carrier lensing also produces an almost collimated beam inside the cavity (see Figure 28.16). Therefore, the virtual source position shifts toward the output facet and even beyond, giving rise to a fast decrease of the astigmatism to zero or even to negative values. The evolution of the beam inside the tapered region, as a consequence of the carrier-induced graded index profile (Figure 28.16), resembles that of a graded-index lens or an optical fiber. The strong SHB at high power produces a self-focusing of the beam leading to saturation of the output power, as will be shown in the next section.

28.3.5 Comparison between Devices

In this section, the main performance parameters of the three simulated devices are comparatively analyzed. Figure 28.17a shows the P–I characteristics, and Table 28.3 summarizes the main parameters

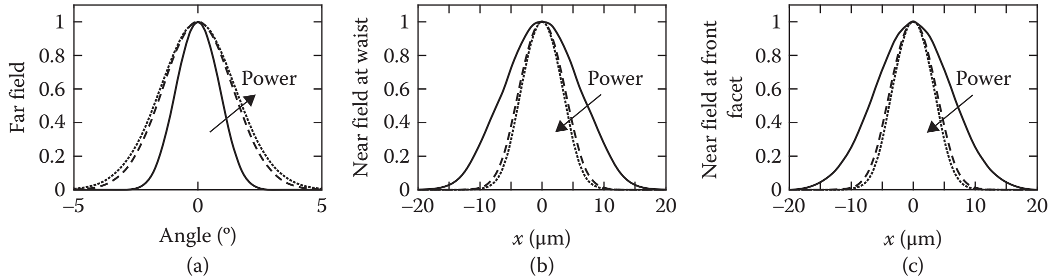

FIGURE 28.15 (a) Far field, (b) near field at waist, and (c) near field at the front facet for the IG device at three power levels, $P_{\mathrm{out}} = 40$ mW (solid), $P_{\mathrm{out}} = 623$ mW (dashed), and $P_{\mathrm{out}} = 912$ mW (dotted).

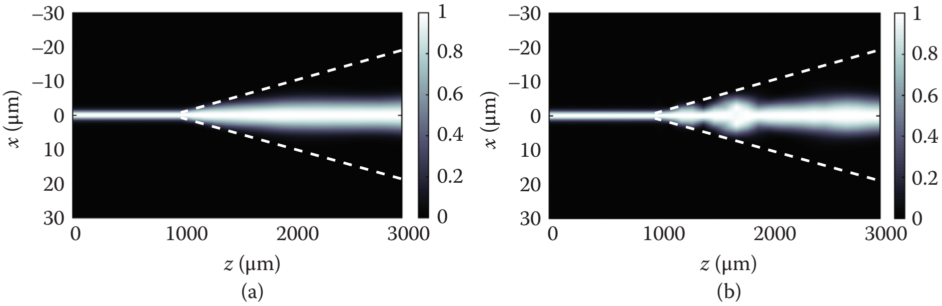

FIGURE 28.16 Normalized (a) forward and (b) backward optical field intensity inside the cavity at each z slice for the IG device, when operated at high power ($P_{\mathrm{out}} = 912$ mW). The white dashed lines indicate the pumped tapered region and the index step.

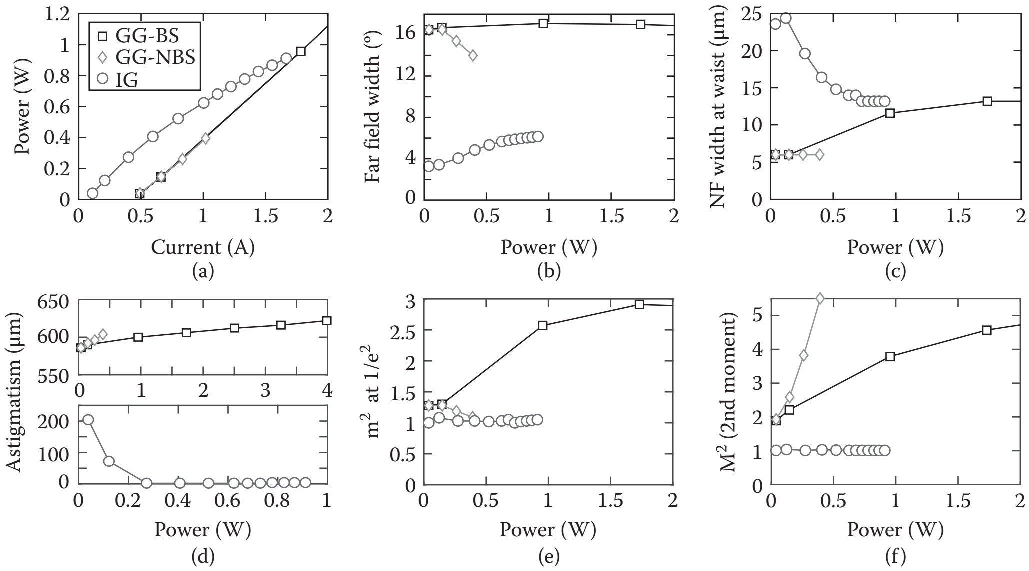

FIGURE 28.17 Comparison of the figures of merit for the different devices: GG-BS (squares), GG-NBS (diamonds), and IG (circles). (a) Power versus current characteristics, (b) far-field width versus power, taken at FWHM (open) and $1/e^2$ (closed), (c) near field at waist width versus power, taken at FWHM (open) and $1/e^2$ (closed), (d) astigmatism versus power, (e) M^2 ($1/e^2$) versus power, and (f) M^2 (FWHM) versus power.

TABLE 28.3 Parameters Extracted from the Simulated P–I Characteristics of the Three Devices

	GG-BS	GG-NBS	IG
Threshold current (A)	0.43	0.43	0.066
Threshold current density (A/cm^2)	198	197	156
Slope efficiency at threshold (W/A)	0.625	0.625	0.85
Taper losses (cm^{-1})	8.6	8.6	5.4

extracted from these results: the threshold current and threshold current density, the slope efficiency, and the taper losses. The threshold currents of the GG-BS and GG-NBS devices are similar and much higher than that of the IG device, as expected from the comparison of the device area; however, the threshold current density of the IG device is lower, due to the lower taper losses. The taper losses at threshold can be estimated from the simulation results by considering the threshold current density and the modal gain versus current density characteristic, and taking into account the mirror and the internal losses. Values of 8.6 and 5.4 cm^{-1} are obtained for the GG and IG devices, respectively, the lower value for the IG device due to the better matching of the backward field. This difference in the taper losses is also the reason for the higher slope efficiency of the IG device. However, the strong narrowing of the beam in this device due to carrier lensing makes the slope efficiency to decrease when the injection increases (see Figure 28.17a).

Figure 28.17b and c shows the evolution of the widths of the FF and of the NF at waist (at $1/e^2$), respectively, for the three simulated devices. At low power, the FF widths of the GG and IG devices are 16.5° and 3.3°, respectively, not far from the expected value for a Gaussian beam applying Snell's law, as previously discussed. On the contrary, the NF at waist is much wider in the case of the IG device, as expected from its lower divergence. The astigmatism at low power (Figure 28.17d) is also quite different, with the virtual source (or beam waist) located at a distance behind the front facet $z_{vs} = 590$ μm and $z_{vs} = 204$ μm for the GG and IG devices, respectively. The former value is close to $L_{tap}/n_{eff} = 599$ μm, the expected value for the free diffraction of a beam at the output of the RW; the latter is lower, even at very low power, due to the index-guiding mechanism.

As previously mentioned, the devices show clear differences in the evolution of their beam characteristics when power increases. In summary: in the GG-BS device, the FF width at $1/e^2$ is approximately constant and the waist increases, in the GG-NBS the waist is constant and the FF width decreases, and in the IG device the FF broadens and the waist remains constant. These differences are also reflected in the behavior of the astigmatism (Figure 28.17d), which increases with the power for the GG devices while decreases for the IG laser. Finally, the evolution of $M^2(1/e^2)$ and M^2 (second moment) for the three devices is compared in Figure 28.17e and f, respectively. The best beam quality is obtained for the IG device with a M^2 (second moment) close to the unity, indicating a diffraction-limited beam. When power increases, the increase of the value of M^2 (second moment) is much faster for the GG-NBS device than for the GG-BS laser due to the fact that the multiple lobes in both the FF and the NF at waist of the first one strongly affect the second moment widths. On the contrary, the value of $M^2(1/e^2)$ is very low, close to the unity, for the GG-NBS device, even at the highest power in the simulations. Similar discrepancies between M^2 (second moment) and $M^2(1/e^2)$ have been reported experimentally for GG devices without beam spoilers (Fiebig et al. 2009).

28.4 Summary

We have presented an overview of the current state of the art in the modeling of high-power tapered lasers, with a detailed description of our steady-state single frequency quasi-3D simulation tool. We have explained the calibration procedure required for making meaningful comparisons with experiments and using the simulator as a predictive tool. The capabilities of the model have been illustrated by comparing the beam properties of three different types of tapered lasers emitting at 1060 nm: GG with beam spoilers, GG without beam spoilers, and narrow IG. The simulations reproduce the different behaviors experimentally observed in the three types of device and can be used for a better understanding of the interaction between carriers and photons that determines the operation of tapered lasers.

Acknowledgments

This work was supported by Ministerio de Economía y Competitividad of Spain under projects RANGER (TEC2012-38864-C03-02) and COMBINA (TEC2015-65212-C3-2-P); and by the Comunidad de Madrid under program SINFOTON-CM (S2013/MIT-2790). A. Pérez-Serrano acknowledges support from Ayudas a la Formación Posdoctoral 2013 program (FPDI-2013-15740). The authors acknowledge the contribution of L. Borruel, H. Odriozola, S. Sujecki, and E. C. Larkins to the development of the model and code for the simulation of tapered lasers.

References

Adachi, S. 1992. *Physical Properties of III-V Semiconductor Compounds: InP, InAs, GaAs, GaP, InGaAs, and InGaAsP*, New York: Wiley-Interscience.

Auzanneau, S., Krakowski, M., Berlie, F., et al. 2003. High-power and high-brightness laser diode structures at 980 nm using an Al-free active region. *Proc SPIE.* 4995:184–195.

Blume, G., Kaspari, C., Feise, D., et al. 2012. Tapered diode lasers and laser modules near 635 nm with efficient fiber coupling for flying-spot display applications. *Opt Rev.* 19(6):395–399.

Borruel, L., Esquivias, I., Moreno, P., et al. 2005. Clarinet laser: Semiconductor laser design for high-brightness applications. *Appl Phys Lett.* 87:101104.

Borruel, L., Sujecki, S., Esquivias, I., et al. 2002. A self-consistent electrical, thermal and optical model of high brightness tapered lasers. *Proc SPIE.* 4646:355–366.

Borruel, L., Sujecki, S., Moreno, P., et al. 2004a. Quasi-3-D simulation of high-brightness tapered lasers. *IEEE J Quantum Electron.* 40:463–472.

Borruel, L., Sujecki, S., Moreno, P., et al. 2004b. Modeling of patterned contacts in tapered lasers. *IEEE J Quantum Electron.* 40:1384–1388.

Coldren, L. A. and Corzine, S. W. 1995. *Diode Lasers and Photonic Integrated Circuits*. New York, NY: John Wiley & Sons.

Esquivias, I., Odriozola, H., Tijero, J. M. G., et al. 2010. Simulation of high brightness tapered lasers. *Proc SPIE.* 7616:76161E.

Fiebig, C., Blume, G., Uebernickel, M., et al. 2009. High-power DBR-tapered laser at 980 nm for single-path second harmonic generation. *IEEE J Sel Top Quantum Electron.* 15(3):978–983.

Fox, A. G. and Li, T. 1961. Resonant modes in a maser interferometer. *Bell Syst Tech J.* 40(2):453–488.

Guthre, J., Tan, G. L., Ohkubo, M., et al. 1994. Beam instability in 980 nm power laser: Experiment and analysis. *IEEE Photon Technol Lett.* 6(12):409–1411.

Hadley, G. R. 1992. Wide-angle beam propagation using Padé approximant operators. *Opt Lett.* 17(20):1426–1428.

Harold^{TM} 3.0 Reference Manual. 2001. Photon Design, Oxford (UK).

Hasler, K.-H., Sumpf, B., Adamiec, P., et al. 2008. 5-W DBR tapered lasers emitting at 1060 nm with a narrow spectral linewidth and a nearly diffraction-limited beam quality. *IEEE Photon Technol Lett.* 20:1648–1650.

ISO 11146. 2005. Lasers and laser-related equipment—Test methods for laser beam widths, divergence angles and beam propagation ratios.

Kintzer, E. S., Walpole, J. N., Chinn, S. R., et al. 1993. High-power, strained-layer amplifiers and lasers with tapered gain regions. *IEEE Photon Technol Lett.* 5:605–607.

Krakowski, M., Auzanneau, S. C., Berlie, F., et al. 2003. 1 W high brightness index guided tapered laser at 980 nm using Al-free active region materials. *Electronics Lett.* 39(15):1122–1123.

Krakowski, M., Auzanneau, S. C., Calligaro, M., et al. 2002. High power and high brightness laser diode structures at 980 nm using Al-free materials. *Proc SPIE.* 4651:80–91.

Lang, R. J., Dzurko, K., Hardy, A. A., et al. 1998. Theory of grating-confined broad-area lasers. *IEEE J Quantum Electron.* 34:2196–2210.

Mariojouls, S., Margott, S., Schmitt, A., et al. 2000. Modeling of the performance of high-brightness tapered lasers. *Proc SPIE.* 3944:395–406.

Michel, N., Hassiaoui, I., Calligaro, M., et al. 2005. High-power diode lasers with an Al-free active region at 915 nm. *Proc SPIE.* 5989:598909.

Michel, N., Odriozola, H., Kwok, C. H., et al. 2009. High modulation efficiency and high power 1060 nm tapered lasers with separate contacts. *Electron Lett.* 45(2):103–104.

Müller, A., Fricke, J., Bugge, F., et al. 2016. DBR tapered diode laser with 12.7 W output power and nearly diffraction-limited, narrowband emission at 1030 nm. *Appl Phys B.* 122:87.

O'Brien, S., Welch, D. F., Parke, R. A., et al. 1993. Operating characteristics of a high-power monolithically integrated flared amplifier master-oscillator power-amplifier. *IEEE J Quantum Electron.* 29:2052–2057.

Odriozola, H., Tijero, J. M. G., Borruel, L., et al. 2009. Beam properties of 980 nm tapered lasers with separate contacts: Experiments and simulations. *IEEE J Quantum Electron.* 45(1):42–50.

Pagano, R., Ziegler, M., Tomm, J. W., et al. 2011. Two-dimensional carrier density distribution inside a high power tapered laser diode. *Appl Phys Lett.* 98(22):221110.

Paschke, K., Bogatov, A., Drakin, A., et al. 2003. Modeling and measurements of the radiative characteristics of high-power α-DFB lasers. *IEEE J Select Topics Quantum Electron.* 9:835–843.

Paschke, K., Sumpf, B., Dittmar, F., et al. 2005. Nearly diffraction limited 980-nm tapered diode lasers with an output power of 7.7W. *IEEE J Select Topics Quantum Electron.* 11(5):1223–1227.

Pfahler, C., Eichhorn, M., Kelemen, M. T., et al. 2006. Gain saturation and high-power pulsed operation of GaSb-based tapered diode lasers with separately contacted ridge and tapered section. *Appl Phys Lett.* 89:021107.

Ruiz, M., Odriozola, H., Kwok, C. H., et al. 2009. High-brightness tapered lasers with an Al-free active region at 1060 nm. *Proc SPIE.* 7230:72301D.

Siegman, A., Nemes, G., and Serna, J. 1998. How to (maybe) measure laser beam quality. *OSA TOPS.* 17(2):184–199.

Spreemann, M., Lichtner, M., Radziunas, M., et al. 2009. Measurement and simulation of distributed-feedback tapered master-oscillator power-amplifiers. *IEEE J Quantum Electron.* 45:609–616.

Sujecki, S., Borruel, L., Wykes, J., et al. 2003. Nonlinear properties of tapered laser cavities. *IEEE J Sel Top Quantum Electron.* 9:823–834.

Sumpf, B., Hasler, K.-H., Adamiec, P., et al. 2009. High-brightness quantum well tapered lasers. *IEEE J Sel Top Quantum Electron.* 15(3):1009–1020.

Sumpf, B., Hülsewede, R., Erbert, G., et al. 2002. High-brightness 735 nm tapered diode lasers. *Electron Lett.* 38(4):183–184.

Tijero, J. M. G., Pérez-Serrano, A., del Pozo, G., and Esquivias, I. 2017. Tapered semiconductor optical amplifiers. In *Handbook of Optoelectronic Device Modeling and Simulation*. vol 1, (Piprek, J., ed.) pp.695–712. Boca Raton, FL: Taylor & Francis.

Vurgaftman, I., Meyer, J. R., and Ram-Mohan, L. R. 2001. Band parameters for III–V compound semiconductors and their alloys. *J Appl Phys.* 89(11):5815–5875.

Walpole, J. N. 1996. Semiconductor amplifiers and lasers with tapered gain regions. *Opt Quantum Electron.* 28:623–645.

Wenzel, H., Sumpf, B., and Erbert, G. 2003. High-brightness diode lasers. *C R Physique.* 4:649–661.

Wilson, F. J., Lewandowski, J. J., Nayar, B. K., et al. 1999. 9.5W cw output power from high brightness 980 nm InGaAs/AlGaAs tapered laser arrays. *Electron Lett.* 35:43–45.

Williams, K. A., Penty, R. V., White, I. H., et al. 1999. Design of high-brightness tapered laser arrays. *IEEE J Select Topics Quantum Electron.* 5:822–831.

29

High-Brightness Laser Diodes with External Feedback

Mohamad Anas Helal

Simeon N. Kaunga-Nyirenda

Steve Bull

and

Eric Larkins

High-power laser diodes first gained interest as pump sources for solid-state lasers, with cost/watt and reliability as the primary market drivers. In recent years, new markets have been opened by increases in the brightness of the laser diode sources and by advances in the optical systems for beam shaping and combining. The work in this chapter is motivated by the development of high-brightness laser diodes for direct-diode laser systems targeting industrial applications and a desire to illustrate the important role of laser simulation tools at both the device and system level. Traditionally, welding and sheet metal cutting are the most lucrative industrial laser markets, but they are also the most demanding in terms of brightness. Laser additive manufacturing processes, such as selective laser melting, are also quickly becoming a reality and allow the fabrication of structures that cannot be made by traditional means. Their automated nature is opening the door to new manufacturing paradigms.

Direct-diode laser systems for industrial applications combine the beams from many individual laser diodes (or diode arrays) to couple them into an optical fiber for delivery to the target. The role of the optical system is to combine the individual beams without losing their brightness. High-power direct-diode lasers rely on multiple beam-combining methods, including incoherent or "side-by-side" beam combining, polarization multiplexing, and spectral beam combining. The first commercial kW-class direct-diode laser system used an external cavity to stabilize the wavelengths of, and spectrally combine, the beams of a large number of broad-area (BA) lasers to couple a 1 kW beam into a 200 μm fiber (Huang et al., 2011). The brightness of the final system is ultimately limited by the brightness of the individual sources.

All beam-combining techniques couple light back into the laser diodes—deliberately, as in external wavelength stabilization and spectral beam combining, or accidentally due to reflections off the optics. This optical feedback is known to affect both the beam quality and the degradation of the laser diodes (Hempel et al., 2013), but little has been published on how this feedback affects the operation of the laser. As the power and performance requirements increase, the role of external optical feedback is becoming increasingly interesting.

This chapter focuses on the impact of external optical feedback on high-brightness laser diodes. We start by introducing the common beam quality metrics used for lasers and briefly review the diode laser technologies most commonly considered for high-brightness direct-diode laser systems, before focusing on the tapered laser and showing why they are strong contenders for future high-power direct-diode laser systems. We then describe the coupling of our continuous wave (CW) simulation tool, *Speclase*, to commercial optical design tools to self-consistently simulate high-brightness diode lasers with external optical feedback. We conclude with a case study exploring the impact of unintentional feedback on the excitation of higher order vertical modes and lateral beam quality in a large optical cavity (LOC) tapered laser.

29.1 Power Scaling and the Role of Beam Quality

The purpose of the beam-combining optics in a direct-diode laser is usually to couple the highest amount of power from the individual laser diode sources into the end of an optical fiber. The brightness of the combined beam (units = W cm^{-2} sr^{-1}) limits the power that can be coupled into the delivery fiber and depends on the brightness of the individual diode sources.

Metrics such as the beam parameter product (BPP) Q or beam propagation factor M^2 are common metrics used by manufacturers and industries to specify the beam quality of both the individual laser diode and direct-diode laser systems. The BPP is the product of beam radius (measured at the beam waist) and the half-angle beam divergence:

$$Q = \omega_0 \times \theta_{\mathrm{div}}, \tag{29.1}$$

where ω_0 is the beam radius measured in millimeter and θ_{div} measured in milliradian and Q is the BPP measured in mm·mrad. The BPP allows optical designers to determine the number of individual beams that can be imaged onto the end of a fiber with a fixed diameter (physical aperture) and maximum acceptance angle (numerical aperture). The power coupled into the fiber also depends on the power of the combined beam (and hence of the individual emitters). The brightness (units: W cm^{-2} sr^{-1}) is defined as

$$B = \frac{P}{\pi^2 Q^2} = \frac{P}{\lambda^2 M^2} = \frac{P}{\lambda^2 M_x^2 M_y^2}, \tag{29.2}$$

where P is the laser output power, Q is the BPP, λ is the wavelength and M^2 is the beam propagation factor. M^2 is another measure of beam quality as defined by ISO 11146. The beam quality metrics, M^2 and Q are related by Equation 29.2, as shown in Table 29.1 for $\lambda = 975$ nm. (A detailed discussion of beam quality metrics is in Chapter 28.)

Figure 29.1 shows the power and beam quality needed for different industrial laser applications. The dashed lines show the improvement in laser diodes (and direct-diode laser systems based on them) between 2000 and 2014. A laser with a power of 20 W and $M^2 \sim 20$–30 (e.g., a good BA laser diode [Thestrup et al., 2003]) is suitable for printing and material processing, but not for additive manufacturing, welding, or cutting. Conversely, a laser with a power of 10 W and $M^2 < 1.5$ (e.g., a good tapered laser diode [Fiebig et al., 2008]) is suitable for sheet metal drilling, marking, additive manufacturing, welding, and cutting of metal.

TABLE 29.1 Correspondent Values of M^2 and Q

M^2	Q mm·mrad
1.0	0.31
1.5	0.47
2.0	0.62
3.0	0.93
5.0	1.6
10.0	3.1
20.0	6.2
30.0	9.3

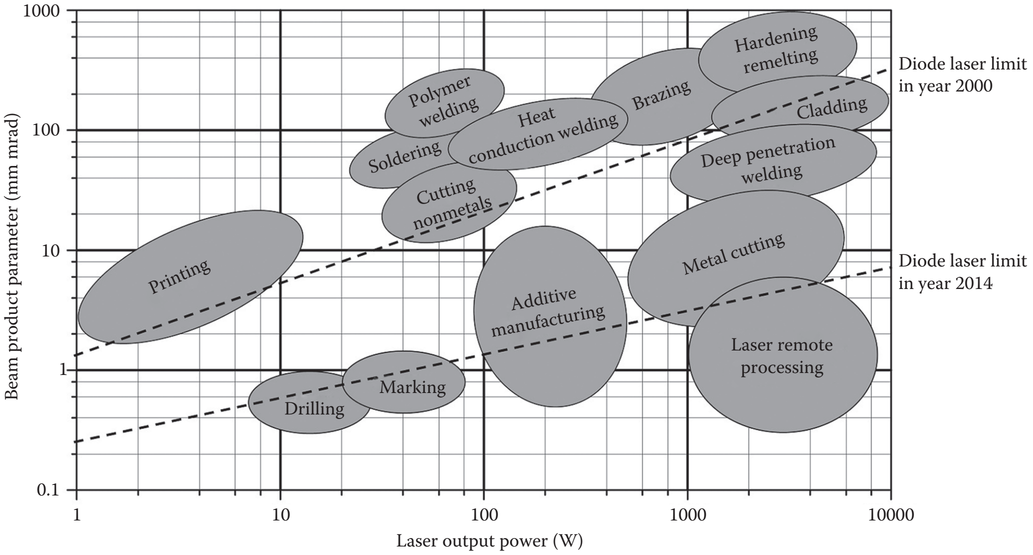

FIGURE 29.1 Beam parameter product versus laser power for different applications.

29.2 High-Brightness Laser Diode Sources

Laser diodes for the most demanding industrial applications should have high brightness (e.g., $P \geq 10$ W, $Q < 1$ mm·mrad, or $M^2 < 3$) and high-power conversion efficiency (PCE) (e.g., $PCE \geq 55\%$). The sources (and their performance) should be reliable and insensitive to reflections.

29.2.1 Vertical Cavity Design

The vertical cavity design of a laser diode for efficient, high-power operation in an external cavity is more complicated than that of an isolated high-power laser diode. First, a wide vertical mode profile (vertical near-field pattern) is needed for efficient external cavity coupling and reduced alignment tolerance. This also increases the tolerance to “smile” (a bend in the horizontal axis of a laser bar, which introduces pointing errors in the slow axis) across a laser array and allows the use of simpler, less costly optics. Second, the excitation and lasing of higher order vertical cavity modes by external optical feedback must be suppressed; photons coupled from external cavity will lead to stimulated emission. Third, a narrow vertical far-field divergence is needed to minimize the impact of optical aberrations, thereby improving the cost and performance of the optical system. Finally, the need for high-PCE means that Joule heating and free-carrier absorption (FCA) play critical roles in the vertical cavity design (Larkins et al., 2014).

High-brightness laser diodes typically use LOC waveguides to produce a wide vertical near-field pattern and narrow far-field divergence pattern. The LOC cavity reduces the power density at the facet (increasing the mirror damage threshold) and reduces the vertical confinement factor (reducing carrier-induced lensing). The confinement factor is the ratio of modal power contained in the active area to that contained in the structure. Below is the definition of the vertical confinement factor:

$$\Gamma(y) = \frac{\int_{-d/2}^{+d/2} E(y)^2 \mathrm{d}y}{\int_{-\infty}^{+\infty} E(y)^2 \mathrm{d}y}. \tag{29.3}$$

The LOC waveguide also facilitates external cavity feedback (e.g., for wavelength stabilization and/or lateral mode filtering), but also makes the device more sensitive to parasitic reflections.

As the LOC waveguide thickness increases beyond a certain point, the influence of the cladding layer diminishes and the waveguide is formed by the index contrast of the active region and the waveguide. Further increases in waveguide thickness raise the Joule heating and FCA losses, but do not significantly increase the near-field width or reduce the far-field divergence. Wider near-field patterns can be achieved (with thinner, more efficient waveguides) using other methods, including low-index quantum barriers to reduce the index contrast between the active region and the waveguide (Wang et al., 2013); or high-index optical traps to draw the field profile out into the waveguide (Buda et al., 1999).

LOC waveguides support multiple vertical modes, but, in the absence of external feedback, lasing is limited to the mode that reaches threshold first. When operated in a system with external feedback, however, back coupling to higher order modes can cause them to lase. Even if the higher order modes do not lase, the additional stimulated emission and FCA can reduce the laser's efficiency and increase self-heating. External feedback also affects the reliability of high-power laser diodes (Tomm et al., 2011). Thus, feedback is becoming important as diode laser systems grow in power and complexity.

The suppression of higher order vertical modes becomes more challenging when the laser is operated in an external cavity, where the optical feedback also excites the higher order vertical modes. First, as little power as possible must couple into the higher order vertical modes. Second, the higher order vertical modes must be prevented from reaching threshold. This can be achieved by engineering the laser cavity to make the confinement factors of higher order modes much lower than that of the fundamental mode, so that their modal gain is lower. Accordingly, we define a new figure of merit for modal discrimination (MD):

$$\mathrm{MD} = \Gamma(1)/\Gamma(n), \tag{29.4}$$

where Γ is the optical confinement factor and n refers to the higher order mode with the largest confinement factor. MD_n can also be used to describe the MD of a particular mode n. (*Note:* Propagation loss is neglected in MD, as it depends on the doping profile and operating bias—which are usually optimized *after* the initial cavity design.)

Power from the external cavity can be coupled into the higher order modes, even if they do not reach threshold. The modal gain of the higher order modes can also be reduced by increasing their propagation loss—either by FCA or by substrate leakage. Damping of the higher order vertical modes also reduces the total amplified spontaneous emission (ASE) from these parasitic modes. ASE and gain of light coupled into these modes do not contribute to the fundamental mode. Instead, they act as current leakage paths, contributing to self-heating and reducing the PCE.

LOC laser structures based on both the low-index quantum barrier and the high-index optical trap approaches were optimized (optically and electrically) for operation with external optical feedback (Larkins

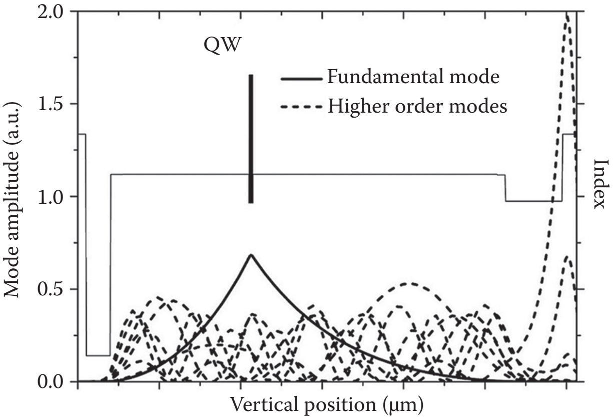

FIGURE 29.2 Vertical mode profiles in the ELoD2 LOC laser structure.

TABLE 29.2 Confinement Factor and MD Values for All Vertical Modes in ELoD2 Structure

Mode Number	Confinement Factor (Γ)	Modal Discrimination (MD)
1	0.0163	1
2	0.00376	4.33
3	0.000282	57.72
4	0.00856	1.90
5	0.00390	4.17
6	1.090E-05	1491.39
7	0.00130	12.58
8	0.00424	1.92

et al., 2014). The tapered lasers in this chapter are based on the ELoD2 vertical cavity with low-index quantum barriers (Crump et al., 2013c). This structure supports eight vertical modes, as shown in Figure 29.2. Their confinement factors and MD are given in Table 29.2.

29.2.2 Lateral Cavity Design

State-of-the-art high-power lasers need a large output power, high PCE, and excellent beam quality. Ridge waveguide (RW) lasers can produce a diffraction limited beam (single lateral mode), but have only achieved output powers of 1.6 W (Yang et al., 2004). Flared RW lasers have achieved a maximum power of 3 W and kink-free power of 2.2 W (Sverdlov et al., 2013). To achieve higher output powers, the laser diode needs a larger gain volume (energy reservoir). This can be most easily achieved by increasing the emitter width, which has the added benefit of lowering the power density at the facet—thereby increasing the catastrophic optical mirror damage (COMD) threshold.

Slab-coupled optical waveguide laser (SCOWL) diodes (Donnelly et al., 2003) use a shallower RW etch to allow the beam profile to expand laterally in the "slab" below. They have been used as high-brightness sources for power scaling by spectral beam combining (Huang et al., 2009). SCOWLs have good beam quality and low astigmatism, but their limitations are similar to those of the flared RW laser and comparatively low power (2.8 W) (Huang et al., 2007) limits their single-emitter brightness.

BA diodes have achieved powers of 29 W, reliable operation at 20 W, and record PCE (76%) at 0°C. BA lasers have simultaneously achieved high power *and* high PCE at 300 K (14.5 W, PCE >60%)

(Crump et al., 2009, 2013a). Their main limitation is their poor slow-axis beam quality ($M^2 \sim 20$–30) (Knigge et al., 2005).

Lim et al. used simulations to investigate the dependence of the beam quality of BA lasers on cavity length and width as a function of power (Lim et al., 2005). Lim's work showed that the brightness of gain-guided BA lasers improved with reduced cavity width and increased cavity length—establishing a new basis for the development of narrow broad-area (NBA) laser diodes. Since then, NBA laser diodes have received increasing attention (Crump et al., 2013b; Decker et al., 2014; Skidmore et al., 2016), with powers of 7.5 W with $Q_{\text{slow axis}} = 1.8$ mm·mrad and high efficiency (PCE = 57%) (Crump et al., 2013b). Despite the impressive performance of NBA laser diodes, they still fall short of the desired performance for the most demanding applications.

The beam quality of BA lasers can also be improved using asymmetric feedback to reduce the threshold of a particular higher order lateral mode (Pillai and Garmire, 1996; Thestrup et al., 2003; Wolff et al., 2003; Lang et al., 2008), exploiting a concept previously demonstrated for phase-locked laser arrays (). However, the usefulness of asymmetric feedback stabilization for high-brightness operation still needs to be demonstrated—in particular, whether they can maintain their high beam quality and PCE at high power

Tapered laser diodes have received great interest, since they combine the lateral mode confinement/filtering of the RW laser and the large gain volume of the BA laser. Thus, tapered lasers are able to produce a high output power (12 W) with high beam quality ($M^2 < 1.2$) and exceptional brightness ($B = 1.1$ GW·cm^{-2} sr^{-1}) (Walpole et al., 1992; Kelemen et al., 2005; Sumpf et al., 2010). This comes at the expense of lower PCE (43%–55%) and power-dependent "wandering" astigmatism (Dittmar et al., 2006; Fiebig et al., 2008). Thus, the tapered laser is promising for high-brightness direct-diode laser systems. The main challenges are to control their beam quality degradation at high power and to understand the role of optical feedback.

29.2.3 Evolution of Lateral Beam Quality of High-Brightness Tapered Laser Diode

The tapered laser diode comprises RW and tapered amplifier (TA) sections. The RW supports a single lateral mode, to inject a diffraction-limited beam into the amplifier. It also filters out higher order lateral modes from the backward traveling fields it receives from the tapered section. The TA provides a large gain volume with a large output aperture. The taper angle is chosen to match the diffraction angle from the RW (Pearson et al., 1969; Walpole et al., 1992), allowing the field to expand in the taper to produce a smooth output field profile, as illustrated in Figure 29.3.

A nearly diffraction-limited lateral beam is obtained from conventional tapered lasers at low to moderate power, but the beam quality degrades rapidly at high power. This beam quality degradation reveals degradation of the RW filter performance due to gain saturation inside the RW and absorption bleaching by the backward traveling fields outside of it (Sujecki et al., 2003; Kaunga-nyirenda et al., 2014; Larkins et al., 2014, 2016). The absorption bleaching (due to band filling by the generated carriers) renders the material transparent and allows the backward traveling fields outside the RW to reach the rear facet, where they are reflected and reenter the TA, as shown in Figure 29.4

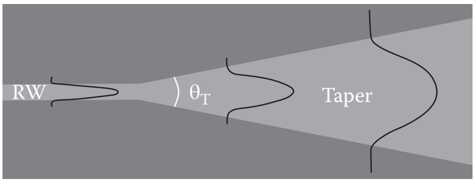

FIGURE 29.3 Schematic diagram of a tapered laser, showing the adiabatic expansion of the beam in the taper.

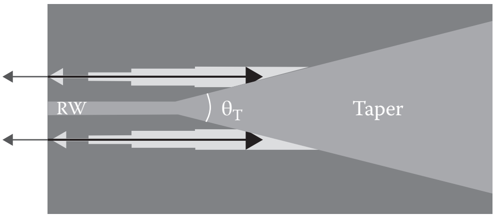

FIGURE 29.4 The beam outside the ridge waveguide (RW) bleaches the absorption in these regions, allowing the reflected beam from the back fact to travel back and couple into the tapered amplifier (TA)

These unfiltered fields create high-spatial-frequency features in the near-field pattern. These high-frequency features or filaments are caused by the propagation and diffraction of the backward-traveling fields in the absorption bleached regions outside the RW (Lim et al., 2012; Larkins et al., 2014). This diffraction is primarily due to the diffraction of the backward propagating fields that are *not* coupled into the RW. Figure 29.5a shows the back propagating field in a 975 nm-tapered laser at $I = 15$A. The backward propagating fields are amplified in the taper and gain guided at the edges of the taper to form a high-intensity spot where the RW joins the TA. The fields diffracting from this spot are clearly visible alongside of the RW. Figure 29.5b shows the backward propagating fields from this high-intensity spot in the absence of index and gain-guiding effects. The field pattern agrees with the corresponding region in Figure 29.5a (inside the white box)—except that the central lobe widens due to the absence of index guiding by the RW. In Figure 29.5c, only the central field lobe (the lobe that couples into the RW) was back propagated, while in Figure 29.5d only the outer lobes of the spot were propagated. Figure 29.5c and d shows that only the fields *not* coupled into the RW give rise to the diffraction pattern—and thus, for the absorption bleaching and beam quality degradation.

Finally, spatial hole burning at the center of the taper and electrical over-pumping at the edges creates high carrier densities and gain at the edges of the taper, as seen in quantitative intracavity spontaneous emission imaging measurements (Bull et al., 2004, 2006). Amplification and carrier-induced waveguiding in these regions cause the "batman" ears in the near-field pattern and amplify/guide the backward fields that degrade the RW filter performance (Williams et al., 1999; Sujecki et al., 2003) Different techniques have been suggested to overcome the degradation of beam quality, such as reducing the front facet reflectivity, using beam spoilers or using a longer RW section. Figure 29.6 shows the impact of reducing front facet reflectivity on the total photon density distribution (i.e. the sum of densities of both the forward and backward traveling waves). These techniques all reduce the backward traveling field and associated absorption bleaching. At the emitter powers sought for high-brightness direct-diode lasers (>10 W), however, these techniques are insufficient. (Beam quality degradation in tapered lasers is also discussed in Chapter 28.)

An integrated distributed Bragg reflector (DBR) mirror at the end of the RW provides a solution with better high-power performance. The rear facet of the laser must be antireflection (AR) coated for the DBR to work properly. The DBR (and AR-coated facet) act a spatial filter, allowing the backward traveling fields in the regions outside the RW to exit the rear facet, as illustrated in Figure 29.7. In order to study the spatial filtering performance of the RW section, and understand how the DBR RW section improves the spatial filtering performance of the conventional tapered laser, we define the RW filter response as the ratio of the forward and backward propagating field distributions at the interface between RW and TA sections:

$$H_{\mathrm{RW}} = \log_{10}\left[\frac{P_{\mathrm{forward}}}{P_{\mathrm{backward}}}\right]. \tag{29.5}$$

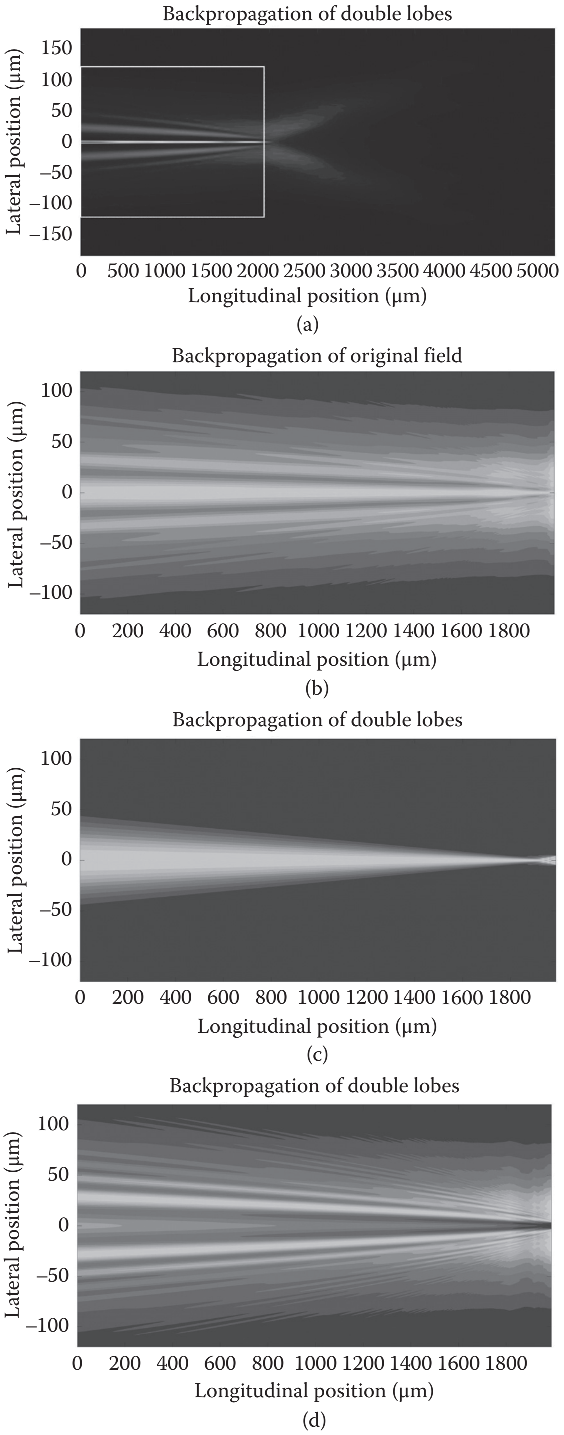

(a)

(b)

(c)

(d)

FIGURE 29.5 (a) Backward propagating field in 975 nm tapered laser ($I = 15$ A) for converged simulation. Backward-propagated photon distribution in the RW section for transparent, uniform index material for: (b) the total field; (c) the central lobe coupled into the RW; and (d) the fields *not* coupled into the RW.

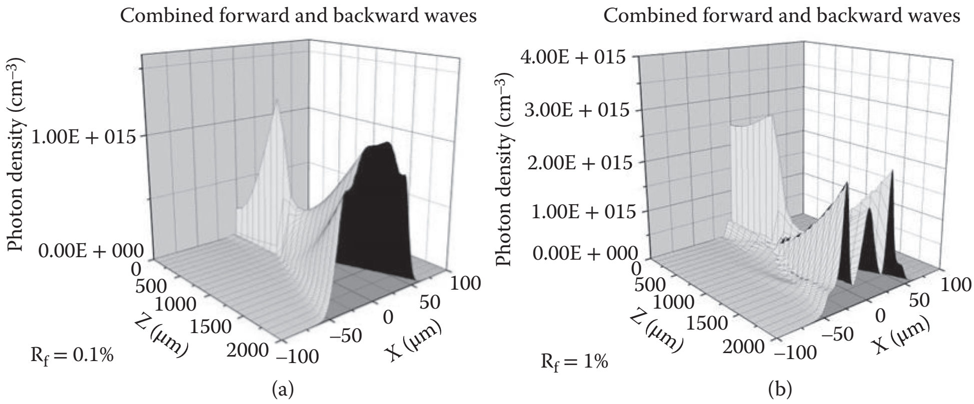

FIGURE 29.6 Impact of front facet reflectivity on the shape of forward and backward traveling waves. Both figures (a and b) show the total photon density distribution (forward + backward).

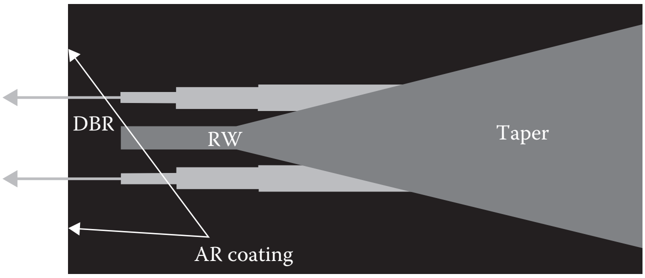

FIGURE 29.7 Schematic diagram of the DBR-tapered laser, showing how the back-propagating beams outside of the RW are allowed to leave the structure, instead of coupling back into the TA.

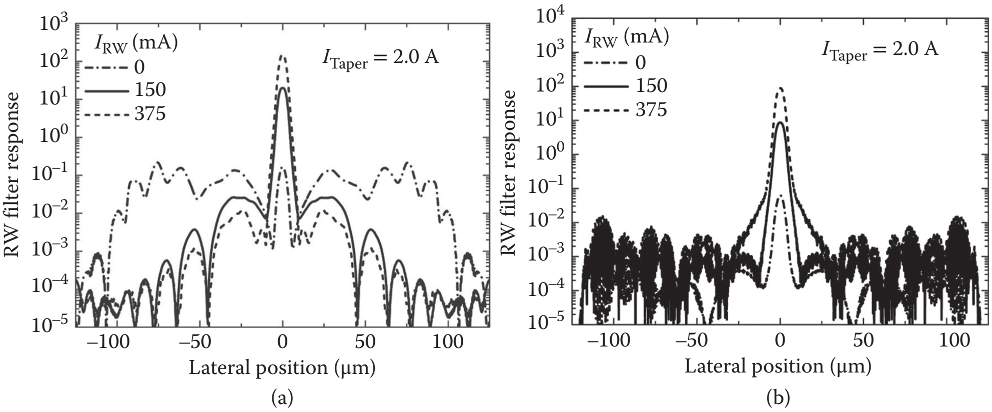

FIGURE 29.8 RW filter performance comparison of conventional (a) and DBR (b) tapered lasers.

Figure 29.8 compares the RW filter responses of DBR and conventional tapered lasers with dual contacts for a constant taper current as a function of RW current. In the conventional tapered laser, the fields in the RW are not amplified at the lowest RW current, but those outside the RW propagate and are reflected—reducing the performance of the RW filter. In the DBRtapered laser, these fields are not reflected and exit

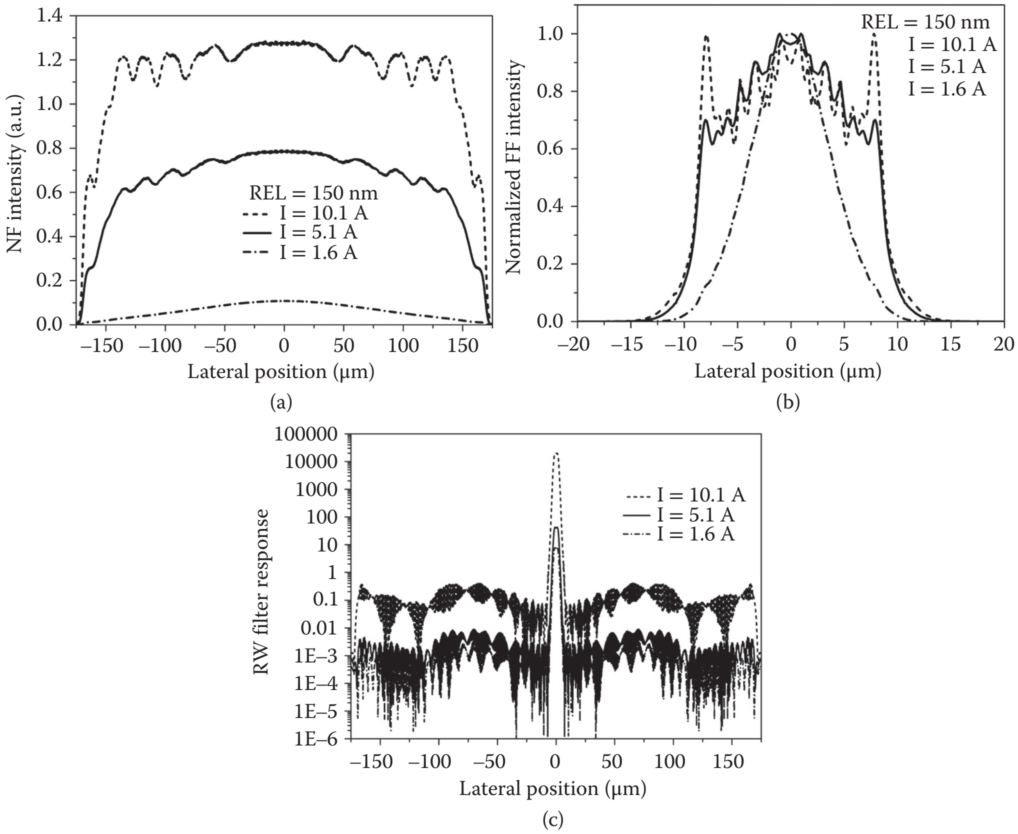

FIGURE 29.9 Evolution of near-field (a), far-field (b) and RW filter response (c) with current.

through the AR-coated rear facet. Thus, the filter performance of the DBRtapered laser remains good up to higher powers.

Despite the large performance improvement of the DBR-tapered laser at high powers, $M^2_{\text{2nd moment}}$ still increases with power. To understand this, we studied the evolution of the near- and far-field patterns and the RW response with current, as shown in Figure 29.9.

As the current increases, high spatial frequency features appear in the near-field pattern and grow in strength, causing degradation of the far-field pattern. The appearance of these features correlates with a sudden reduction in the RW filter performance. Furthermore, the RW width and etch depth have little impact on beam quality as seen in Figure 29.10. (Figure 29.10 also shows that $M^2_{e^{-2}}$ [beam radius w_0 in Equation 29.1 is measured at $1/e^2$] is independent of current, while $M^2_{\text{2nd moment}}$ [beam radius w_0 in Equation 29.1 is measured using second moment of area definition, as defined in Chapter 29] provides a more sensitive measure of the changes in the near and far-field patterns.)

Figure 29.11 shows the forward propagating field at the junction of the RW and TA sections. Although the fields outside the RW are small, they will be strongly amplified.

The fields outside the RW section explain the degradation of the filter function (and the changes in the near- and far-field patterns), but there is a problem: *If the backward propagating fields outside the RW all escape through the AR-coated rear facet, then where do these forward propagating fields come from?* The answer lies in the forward propagating photon distribution in Figure 29.12, which reveals a single aperture diffraction pattern—as confirmed by the positions of the nodes in the pattern. Although these simulations assume a simple patterned rear facet reflectivity, the DBR will also produce aperture diffraction.

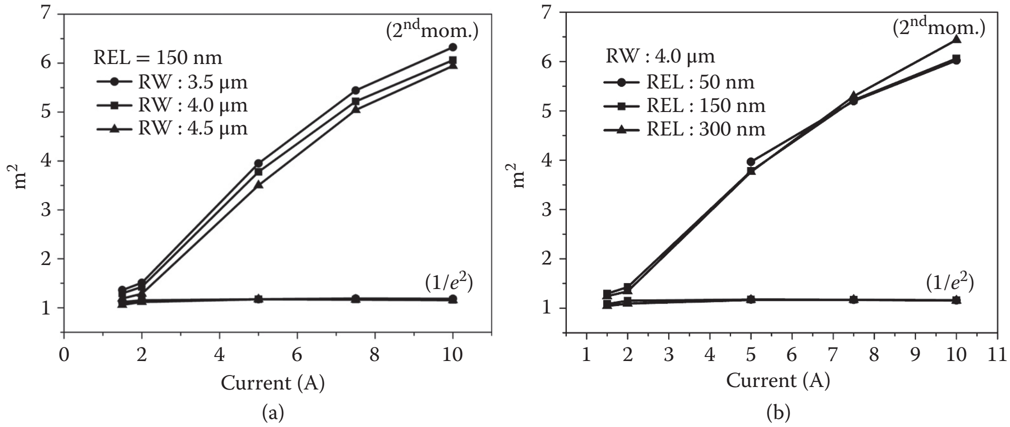

FIGURE 29.10 Impact of RW width (a) and RW etch depth (b) on beam quality.

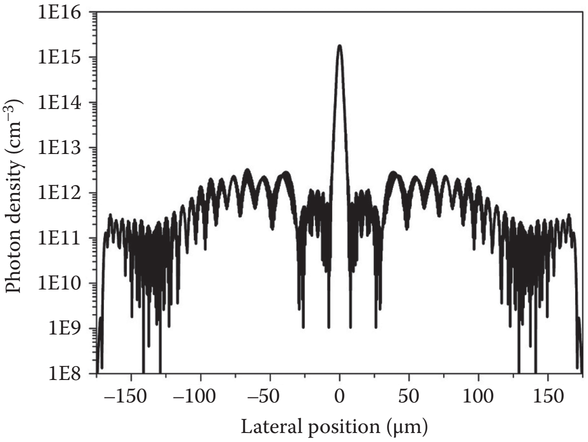

FIGURE 29.11 Forward propagating photon distribution at the RW/TA interface of a DBRtapered laser.

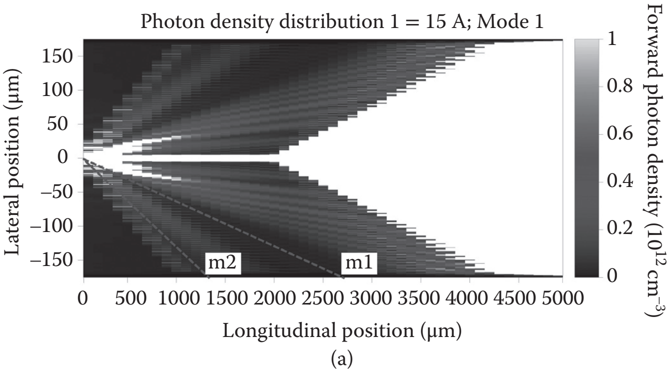

(a)

FIGURE 29.12 2D forward propagating photon density with a perfect AR-coating on the rear facet (a) and with an AR-coating with a power reflectivity of 0.1% (b). (*Continued*)

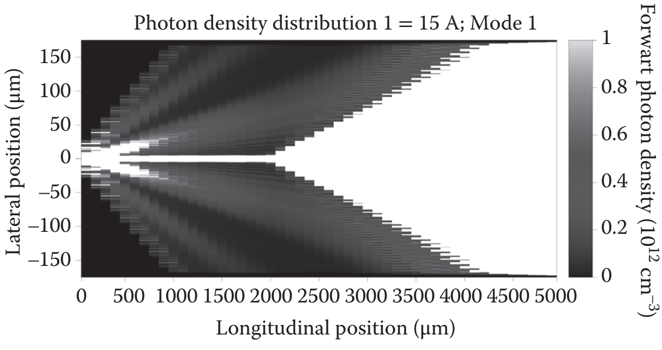

(b)

FIGURE 29.12 (Continued) 2D forward propagating photon density with a perfect AR-coating on the rear facet (a) and with an AR-coating with a power reflectivity of 0.1% (b).

29.3 External Cavity Laser Simulation

New simulation tools are needed to address the problems posed by high-brightness diode lasers operating in a system context with external optical feedback. The laser diode and the external cavity pose different modeling challenges and require the use of different modeling approaches and software tools. These approaches and tools must be brought together to model the laser diode and the external optical system self-consistently.

29.3.1 Laser Diode Simulation Tool "*Speclase*"

The simulation of high-brightness laser diodes is a challenging task, which requires self-consistent modeling of the electrical, optical, and thermal processes throughout the device (Williams et al., 1999; Lim, 2003; Sujecki et al., 2003; Lim et al., 2009). LOC devices with external feedback bring the additional challenge of simulating fields with different vertical mode profiles and their competition for the available gain.

The simulation of the laser diode is performed with an in-house laser simulation tool, *Speclase* (Lim et al., 2009), for the self-consistent quasi-3D optical, electrical, and thermal simulation of high-brightness laser diodes. *Speclase* uses the two-dimensional (2D) wide-angle finite-difference beam-propagation method (WA FD-BPM) for the optical field propagation in the longitudinal and lateral directions (x–z plane). Bipolar electrical simulations are performed in a series of planes orthogonal to the optical axis (x–y planes), neglecting heat and carrier flow in the z-direction. The electrothermal and optical solvers are coupled through the stimulated emission/absorption and ASE processes and refractive index perturbations (calculated from perturbations of the gain/absorption spectra using the Kramers–Kronig relations).

The optical solver models the spectral behavior of the device by propagating multiple wavelengths and their competition through the spectral-spatial gain distribution. Figure 29.13 shows the flow diagram of *Speclase*. The electrothermal and optical models are solved self-consistently, using an accelerated Fox–Li iterative approach (Agrawal, 1984).

In order to model the excitation and competition of fields with different vertical mode profiles, *Speclase* calculates each of the vertical field distributions and their vertical confinement factors. This allows *Speclase* to calculate the effective index and FCA distributions needed for the 2D propagation of the fields with each of the allowed vertical mode profiles. Figure 29.14 describes the flow diagram of *Speclase* for the simulation of a high-brightness LOC laser diode coupled to an external cavity.

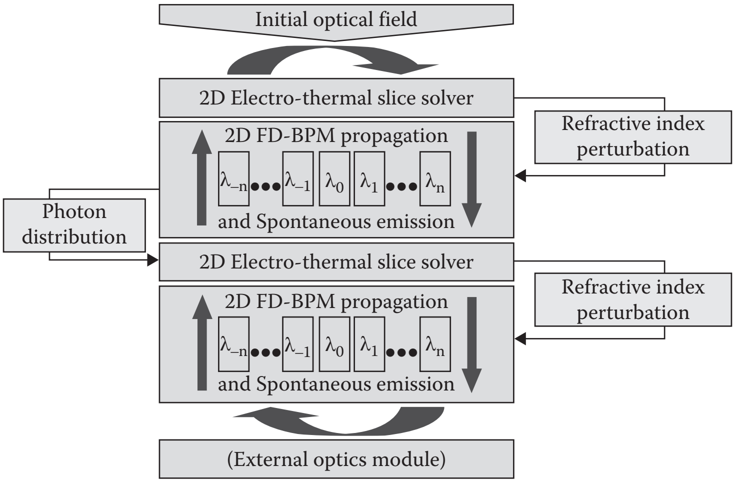

FIGURE 29.13 Flow diagram of stand-alone (SA) *Speclase* with multiple wavelengths.

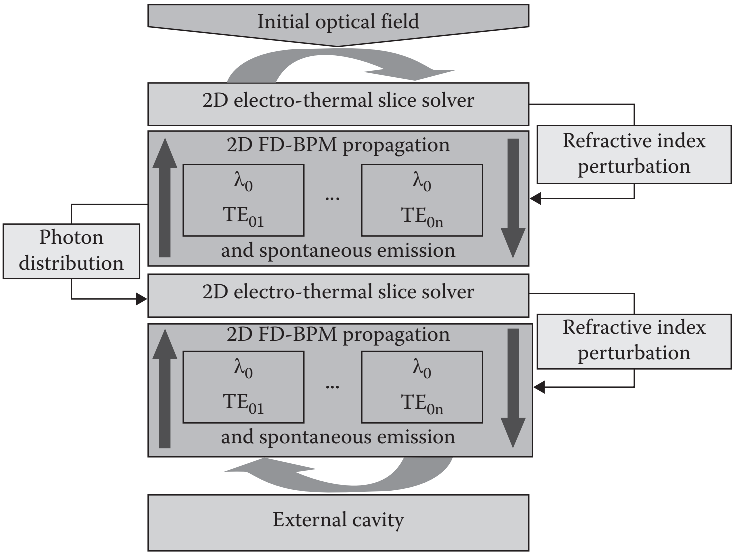

FIGURE 29.14 Flow diagram of *Speclase* with multiple vertical modes with external cavity feedback.

29.3.2 External Cavity Simulation Tool

The modeling of the external cavity requires modeling of free-space optical propagation, including the transmission, reflection, and scattering effects. The optical models used inside the laser diode are not well suited to free-space optical propagation, where Fourier optics (FO) and coherent ray tracing methods are more appropriate. FO models preserve the wave nature of the optical propagation, but the underlying paraxial approximation is best suited to low-divergence beams. Coherent ray tracing is better suited for external cavity laser diodes with large beam divergence. Coherent ray tracing methods are also fast and flexible, making them attractive for modeling complex optical systems. We describe an external cavity modeling tool (*OpticStudio*) based on coherent ray tracing. FO models are also used in this chapter, but do not need wave-ray transformation and are not discussed here.

29.3.3 Coupling of the Laser Diode Simulation Tool and Coherent Ray Tracing Tools

The coupling of the laser simulator and the coherent ray tracing tool for the external cavity is not straight forward, since the light is treated as a wave inside the laser diode, but as rays in the external cavity. Careful analysis of the output beam of the laser diode is needed to produce the input rays for the external cavity model, while maintaining all of the properties of the beam emitted from the laser diode (e.g., near- and far-field patterns, astigmatism). Bidirectional coupling is even more challenging, requiring conversion of the rays back into an optical field distribution, which contains both intensity and phase information.

First, the field data produced by *Speclase* (near-field, far-field and wavelength) must be converted into rays, which represent the laser source in *OpticStudio*. These rays each have a set of attributes: launching coordinates, direction cosines and intensity.

Speclase simulates the lateral field distribution at the facet using 2D WA FD-BPM, so the lateral near-field pattern is multiplied by the associated vertical field profile. The horizontal and vertical far-field patterns are calculated by Fourier transformation:

$$\psi\left(\theta_H\right) = \left(\cos\theta_H\right)^2 \left| \int_{-\infty}^{+\infty} \mathrm{E}(x) e^{j(\sin\theta_H k_0 x)} \mathrm{d}x \right|^2 \tag{29.6}$$

$$\psi(\theta_V) = (\cos\theta_V)^2 \left| \int_{-\infty}^{+\infty} \mathrm{E}(y) e^{j(\sin\theta_V k_0 y)} \mathrm{d}y \right|^2, \tag{29.7}$$

where ψ is far-field profile, θ is the divergence angle, E is the electric field, and k_0 is the wavenumber. Due to the astigmatic nature of the laser beam, the output rays appear to originate from two virtual line sources (nonastigmatic sources have a virtual point source). The output rays must intersect both of these line sources—one for the vertical beam divergence and the other for the horizontal beam divergence. The longitudinal positions of these line sources are obtained by FO back propagation (horizontal line source) and by back tracing the rays (vertical line source). Their transverse positions are the first moments of the near-field patterns

The second challenge is to convert the rays returning to the laser facet back into complex field distributions, taking the ray phases into account. A fraction of the optical energy returned to the laser facet at each lateral position (x) is coupled into the laser for each of the vertical modes supported by the LOC structure, as determined by the overlap integral:

$$\eta_n = \frac{\left| \int_{-\infty}^{+\infty} \left\{ E_{\mathrm{ext}} TE_n^{\,*} \right\} \mathrm{d}y \right|^2}{\int_{-\infty}^{+\infty} \left| E_{\mathrm{ext}} \right|^2 \mathrm{d}y \int_{-\infty}^{+\infty} \left| TE_n \right|^2 \mathrm{d}y}, \tag{29.8}$$

where E_{ext} is the distribution of the external field incident on the facet at this lateral position, TE_n is the nth vertical field profile, and η_n is the percentage of the reflected power coupled into cavity mode n. The phase of the coupled field at each position can be calculated by

$$\varphi = \tan^{-1}\left[\frac{Im\left\{ \int_{-\infty}^{+\infty} \left\{ E_{\mathrm{ext}} TE_n^{\,*} \right\} \mathrm{d}y \right\}}{Re\left\{ \int_{-\infty}^{+\infty} \left\{ E_{\mathrm{ext}} TE_n^{\,*} \right\} \mathrm{d}y \right\}} \right]. \tag{29.9}$$

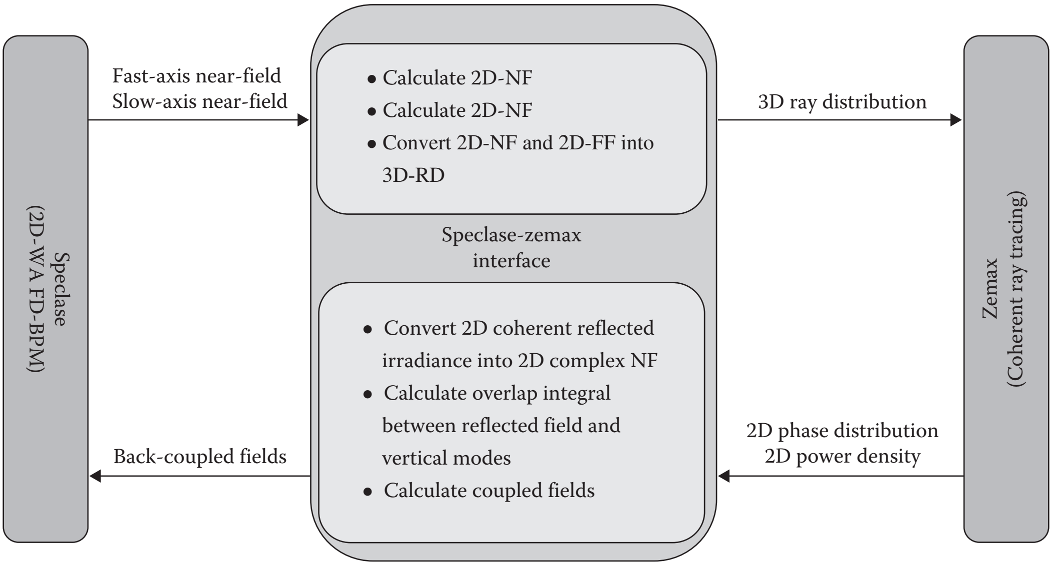

FIGURE 29.15 Schematic of coupling *Speclase* to *OpticStudio*.

This process is repeated for the vertical field distributions at each lateral position along the facet. The resulting one-dimensional (1D) field distributions are coherently added to the internally reflected fields and propagated backward within the laser diode using 2D WA FD-BPM. The entire external cavity simulation is repeated using Fox–Li iterations until it converges. Figure 29.15 shows a schematic diagram of the coupling of *Speclase* and *OpticStudio*

29.4 Case Study: The Impact of Unintentional Reflections on a DBR-Tapered Laser

High-brightness tapered lasers are usually characterized and simulated in isolation, without back reflections to degrade the slow-axis beam quality or couple into higher order vertical modes. In this section, we simulate the simple scenario of an LOC tapered laser with fast- and slow-axis beam collimation lenses with the light incident on the end of an uncoated optical fiber ($R = 5\%$), as illustrated in Figure 29.16. The purpose of this study is to:

1. Observe how the feedback affects the power, PCE, and beam quality
2. Observe the impact of the feedback on the excitation of other vertical modes
3. Reveal the impact of self-heating from the excitation of other vertical modes
4. Investigate approaches for suppressing the impact of higher order vertical modes

The laser diode in this study is a 975-nm LOC DBR-tapered laser based on the ELoD2 structure (Crump et al., 2013c), with a 2-mm RW and a 3-mm gain-guided amplifier with a 6° taper. The DBR is represented by a patterned reflectivity ($R = 31\%$ inside the RW, $R = 0.1\%$ adjacent to it). The front facet reflectivity is 1%. Stray external cavity reflections are included using ray splitting and scattering. Figure 29.17 shows the simulated and experimental power and PCE versus current behavior of an ELoD2 BA laser.

High-power laser diodes are often fabricated as linear bar arrays or laser "bars." Laser bars often bend slightly when they are soldered to a heatsink, so that the emitter near-field patterns deviate from a straight line—an effect referred to as "smile." Figure 29.18 shows how "smile" of packaged laser bars displaces the emitters (±0.5 μm) from the axis This displacement causes the beam to propagate through the external

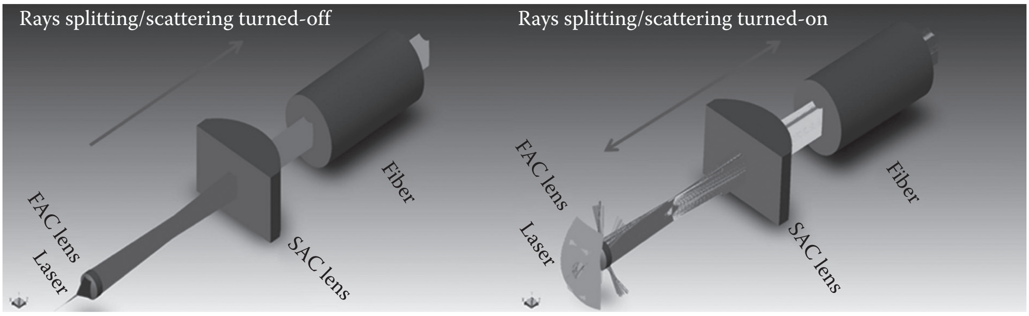

FIGURE 29.16 External cavity setup used in the simulation consists of a fast-axis collimation (FAC) lens, a slow-axis collimation (SAC) lens, and a fiber. Rays splitting and scattering turned off (left). Rays splitting and scattering turned on (right).

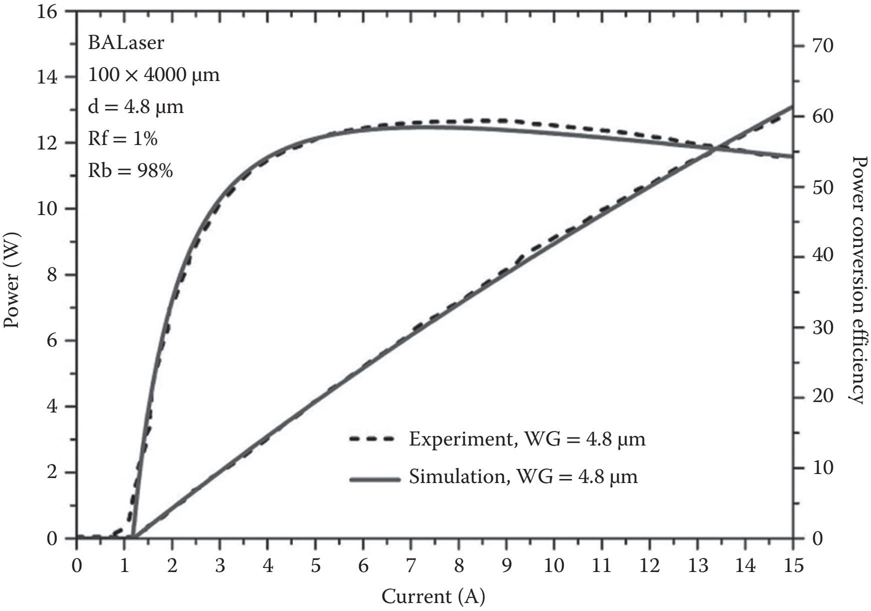

FIGURE 29.17 Simulation versus experiment for ELoD2 structure.

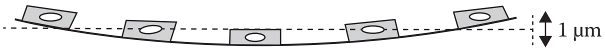

FIGURE 29.18 "Smile" of a linear laser array or bar, which is caused by bending as the bar is soldered to a heatsink.

optics at an angle to the optical axis, a phenomenon known as "pointing error" To emulate the impact of "smile" and "pointing error," the emitter position is shifted vertically with respect to the external optical system.

Two external cavity simulations were performed (on- and off-axis) and compared to a stand-alone (SA) simulation (no external feedback). The overlap integrals of the reflected field of the fundamental mode (from the SA simulation) and the cavity modes were calculated to estimate the coupling coefficients versus displacement, as shown in Figure 29.19. These curves show how displacement affects the feedback coupling to the vertical modes. The off-axis simulation was performed for a displacement of +0.5 μm,

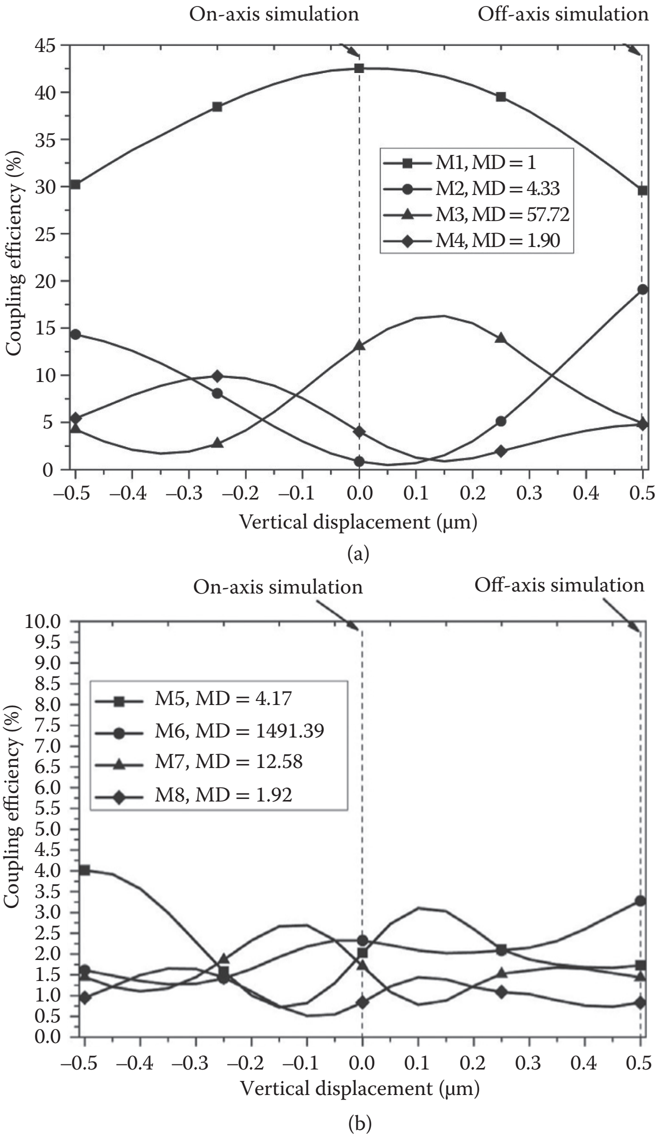

FIGURE 29.19 Impact of smile on external cavity coupling coefficients. Modes 1–4 (a) have coupling >10%, while modes 5–8 (b) have coupling <5%. An off-axis point of interest is displacement = +0.5μm.

where the fundamental mode coupling coefficient (29.5%) approaches that of a higher order mode (19%, mode 2).

29.4.1 Parasitic Reflections with On-Axis Alignment

Simulations were performed for two different external feedback conditions: no feedback; and feedback to the fields for all of the vertical mode profiles. Simulations were performed at bias currents of 2.5, 5.0, 10, 15, and 20 A. Figure 29.20 shows the power versus current and PCE versus current characteristics to compare the performance of the laser for these two feedback conditions. Our discussion will focus on the performance at a bias current of 15 A, since this produces an output power in the range of interest (10–12 W) for the targeted application.

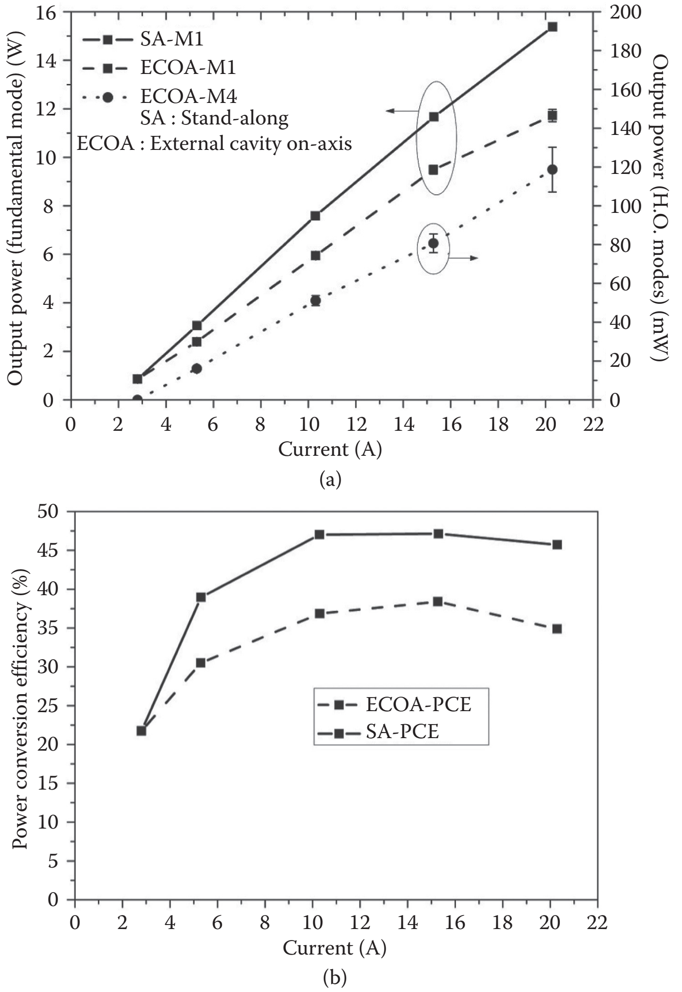

FIGURE 29.20 Simulated power (a) and power conversion efficiency (b) of the tapered laser with and without on-axis feedback.

Figure 29.20 shows that the optical feedback reduces the output power and the PCE. At $I = 15$ A, the on-axis feedback caused the fundamental mode power (mode 1) to drop from 11.67 to 9.49 W, while the PCE fell from 47.1% to 38.4%.

Figure 29.21 compares the near-field patterns (left) and far-field patterns (right) of the on-axis laser for the two feedback conditions. The feedback reduces the output power and increases the modulation depth of the high spatial frequency components in the near-field pattern, as observed experimentally (Hempel et al., 2013; Leonhäuser et al., 2014). The feedback may also lead to excitation and lasing of higher order modes—in this case mode 4.

Figure 29.22 shows the current dependence of the beam propagation parameter M^2 (both the e^{-2} and second moment definitions) for the on-axis external cavity feedback conditions. At $I = 15$ A, the feedback had little effect on $M^2_{e^{-2}}$, but $M^2_{\text{2nd moment}}$ increased from 6.32 to 12.03. This shows that aperture diffraction from the DBR dominates the beam quality degradation.

The total photon distributions (forward and backward propagating) with on-axis feedback are shown in Figure 29.23 for the first four vertical modes. Only modes 1 and 4 are lasing, but light is also coupled into the other modes. Although they do not lase or produce an output beam (and are difficult to characterize and

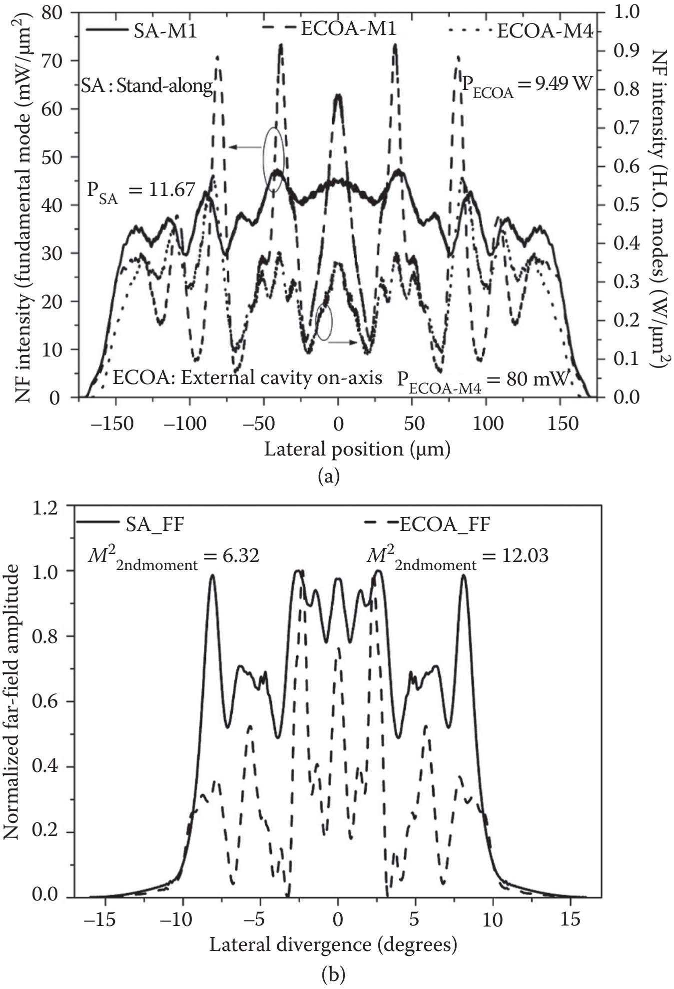

(a)

(b)

FIGURE 29.21 Lateral nearfield profiles of all lasing vertical modes (a) and lateral far-field profiles of the fundamental vertical mode (b) for different on-axis external cavity feedback conditions.

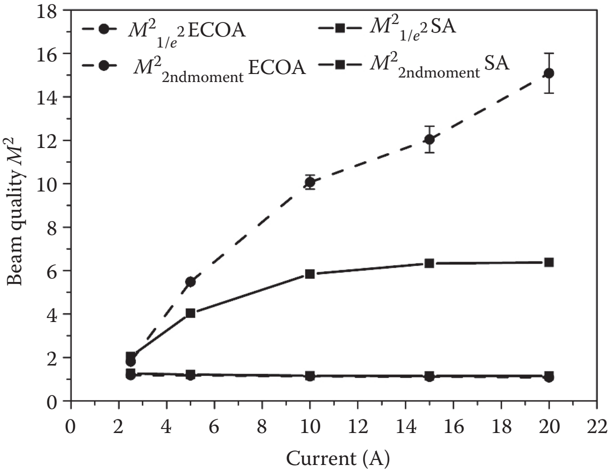

FIGURE 29.22 Dependence of M^2 on bias current for SA and external cavity on-axis simulations.

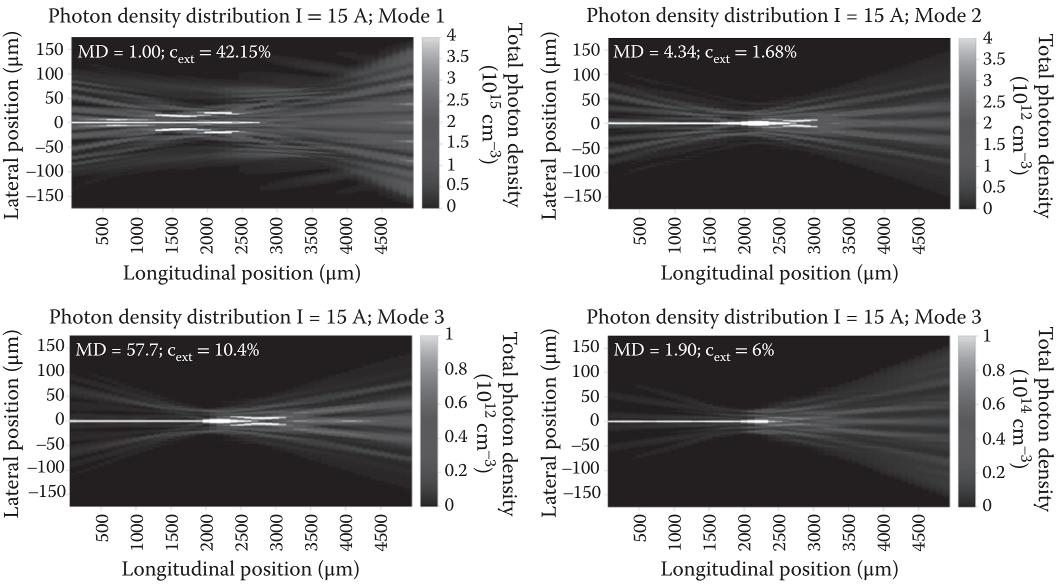

FIGURE 29.23 Total photon density. Mode 1 (top left). Mode 2 (top right). Mode 3 (bottom left). Mode 4 (bottom right). Modal discrimination (MD) and coupling coefficient (C_{ext}) are quoted for each mode.

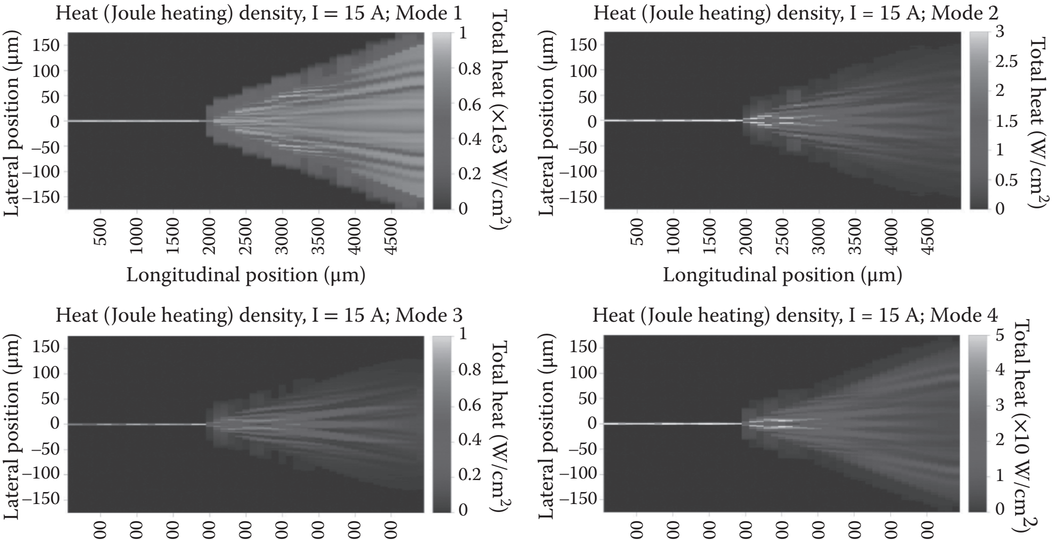

FIGURE 29.24 Self-heating due to Joule heating by each vertical mode at $I = 15$ A.

easy to overlook), they affect the laser through optical pumping (absorption bleaching), parasitic current leakage, and heat generation.

Figure 29.24 shows the Joule heating distributions caused by the currents supporting stimulated emission of the different modes at $I = 15$ A—as well as how the different vertical modes share/compete for the available gain. These distributions show where the stimulated emission occurs within the device for each of the vertical modes. For the higher order modes, this occurs solely because of the power fed back into

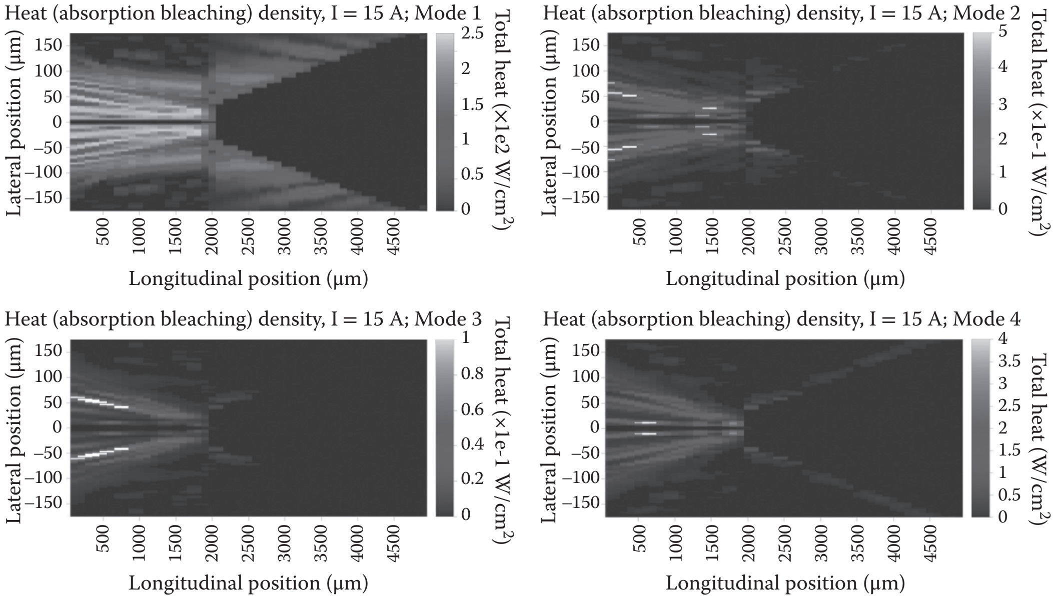

FIGURE 29.25 Self-heating due to optical pumping by each vertical mode at $I = 15$ A.

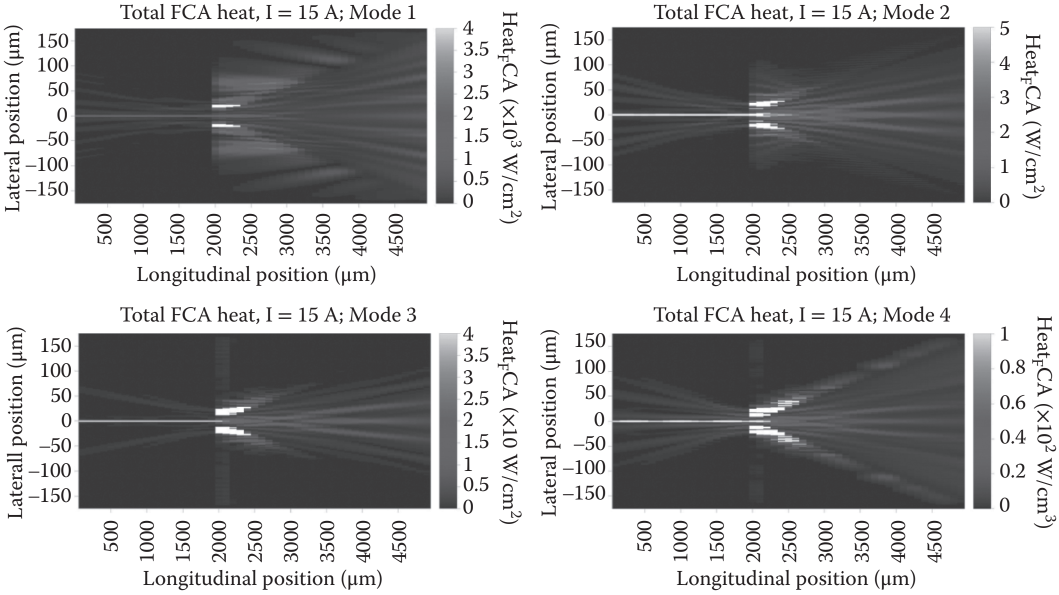

FIGURE 29.26 Self-heating due to free-carrier absorption by each vertical mode at $I = 15$ A.

them from the external cavity. Figure 29.25 shows the self-heating distributions due to optical pumping (absorption) at $I = 15$ A. This pumping causes the absorption bleaching, which plays a critical part in the degradation of the RW spatial filter performance. These distributions show the spatial distribution and relative contributions of the vertical modes to the absorption bleaching. The fundamental mode clearly plays a dominant role in the optical pumping, but the other modes also contribute. Figure 29.26 shows the spatial distributions of self-heating due to FCA. The drop in FCA to the left of the RW–TA interface is due to the RW etch. The higher order modes lose much more power due to FCA than to optical pumping.

TABLE 29.3 Impact of External Cavity Feedback on the Laser Performance (Power, Efficiency, and Beam Quality) for Coupling to All Modes and for Coupling Just to the Fundamental Mode

Simulation	Output Power (W)	PCE (%)	$M^2_{\text{2nd moment}}$
Stand-alone	11.67	47.13	6.32
External cavity (all modes)	9.49	38.39	12.04
External cavity (mode 1 only)	9.46	38.13	12.3

The excited higher order modes clearly play a role in the operation of the device, but their overall power is small compared to that of the fundamental mode (which also has the greatest feedback power). The question is, whether the degradation in PCE and beam quality is primarily controlled by feedback to the higher order vertical modes or to the fundamental mode. Table 29.3 compares the output power, PCE, and $M^2_{\text{2nd moment}}$ for the laser in isolation (SA), with on-axis feedback to all vertical modes and with on-axis feedback to just the fundamental mode. It is clear that the feedback to the fundamental mode has the greatest effect on both PCE and beam quality, while feedback to higher order vertical modes plays a smaller role. This can be understood in the context of an increased output facet reflectivity, which reduces the output power and PCE. At the same time, the optical feedback into the fundamental mode increases the absorption bleaching adjacent to the RW and also the power incident on the DBR reflector inside the RW, as discussed in Section 29.2.2. Both of these effects contribute to the beam quality degradation—the first by reducing the absorption filtering of the diffracted light outside the RW and the second by increasing the power in the side lobes of the diffraction from the DBR reflector.

29.4.2 Parasitic Reflections with Off-Axis Alignment

External feedback couples to the vertical modes differently, when its alignment to the waveguide changes. Here, we explore the impact of a vertical emitter shift of +0.5 μm due to "smile." Table 29.2 shows that modes 2 and 4 have moderate ($\text{MD}_2 = 4.33$) and low ($\text{MD}_4 = 1.90$) values of MD. Figure 29.19 shows they now have large (19%) and moderate (4.8%) coupling coefficients. The performances of these two modes should reveal the relative importance of the MD and the coupling coefficient. The coupling to fundamental mode also decreases from 42.15% (on-axis) to 29.5% (off-axis).

Figure 29.27 shows the power versus current and PCE versus current characteristics of the LOC tapered laser. With the off-axis feedback, the output power and PCE at $I = 15$ A dropped from 11.67 to 9.22 W, while the PCE fell from 47.1% to 37.3%. The coupling into mode 2 increased by a factor of ~11, allowing both modes 2 and 4 to lase.

Figure 29.28 shows the current dependence of the beam propagation parameter M^2 (both the e^{-2} and second moment definitions) for the off-axis external cavity feedback condition. At $I = 15$ A, the off-axis feedback did not change $M^2_{e^{-2}}$, but $M^2_{\text{2nd moment}}$ increased from 6.32 to 11.72.

29.4.3 Analysis and Discussion

In this section, we analyze and discuss what happens to the power fed back into the higher order modes and how it affects the performance of the laser. We are particularly interested in how the feedback effects depend on parameters that can be influenced during the design of the laser: MD, coupling coefficient, and FCA. We are also interested in how the external cavity optics can be designed to minimize feedback effects.

Tables 29.4 and 29.5 summarize a range of power-related performance metrics for each of the vertical modes at a bias current of 15 A. This bias was selected, as it produces an output power of 11.7 W in the absence of external feedback and is within our desired range of 10–12 W. Table 29.4 is for the on-axis simulation. Table 29.5 is for the off-axis simulation when the emitter is vertically displaced by 0.5μm. Modes in boldface font are lasing. H_{stm} is the Joule heating power of the current needed to support the stimulated

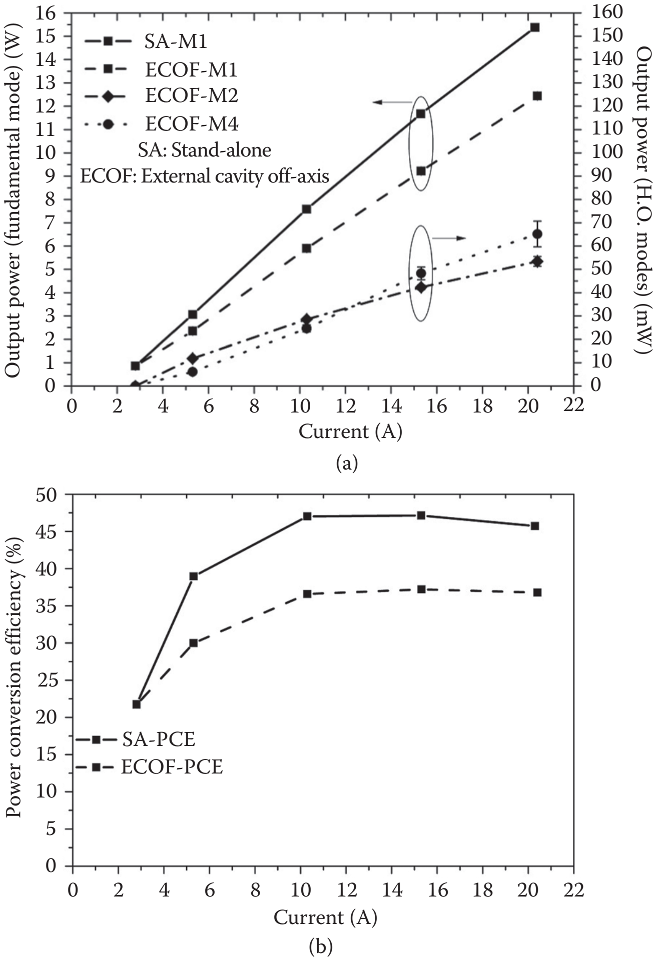

FIGURE 29.27 L–I curves of all lasing modes for tapered lasers in the SA and off-axis external cavity feedback (ECOF) configurations.

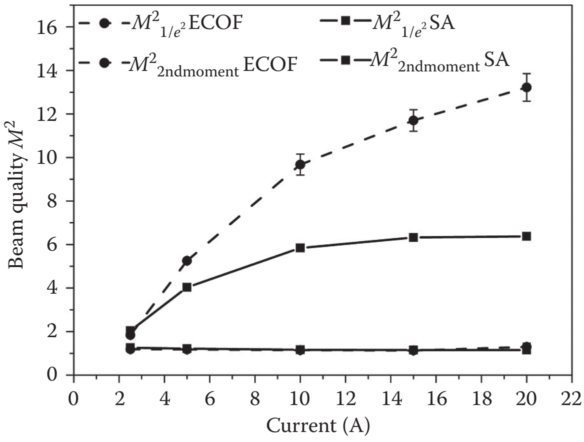

FIGURE 29.28 Dependence of M^2 on bias current for both SA and external cavity off-axis simulations.

TABLE 29.4 Summary of Impact of MD on Optical Metrics of All Modes for On-Axis Simulation for a Current of 15 A.

Mode	MD	Coupling Coefficient (%)	Coupled External Power (mW)	Output Power (W)	H_{stm} (W)	H_{abs} (W)	H_{FCA} (W)	I_{stm} (A)
1	**1.00**	**42.15**	**155.3**	**9.5**	**3.86**	**0.95**	**3.2**	**11.2**
2	4.34	1.68	6.2	3.1e-3	2.4e-3	3.14e-4	4.2e-3	7.1e-3
3	57.7	10.4	38.6	2.6e-3	5.8e-4	4.43e-5	27.7e-3	1.7e-3
4	**1.90**	**6**	**22.2**	**80.1e-3**	**47.7e-3**	**1.7e-3**	**124.6e-3**	**138.1e-3**
5	4.17	1.2	4.6	1e-3	1.5e-3	9.48e-5	10.9e-3	4.5e-3
6	1491.	2.2	8.4	4e-6	3.6e-6	4.83e-8	8e-3	7.6e-6
7	12.58	2.2	8.3	1.6e-4	4.6e-4	3.94e-6	11e-3	1.3e-3
8	1.92	0.65	2.4	5.9e-3	4.6e-3	2.43e-5	22.2e-3	13.4e-3
Total for higher order modes			90.7	92.9e-3	57.2e-3	3e-3	208.6e-3	166.1
Total for all modes			246.0	9.59	3.92	0.953	3.41	11.37

Note: Values in boldface font signify that the mode is lasing

TABLE 29.5 Summary of Impact of MD on Optical Metrics of All Modes for Off-Axis Simulation for a Current of 15 A.

Mode	MD	Coupling Coefficient (%)	Coupled External Power (mW)	Output Power (W)	H_{stm} (W)	H_{abs} (W)	H_{FCA} (W)	I_{stm} (A)
1	**1.00**	**29.5**	**142.6**	**9.22**	**3.71**	**0.96**	**3.03**	**10.96**
2	**4.34**	**19**	**92**	**42.3e-3**	**26.5e-3**	**2.7e-3**	**38.5e-3**	**76.6e-3**
3	57.7	5.23	25.28	1.5e-3	4.13e-4	3.81e-5	13.3e-3	1.2e-3
4	**1.90**	**4.8**	**23.2**	**48.2e-3**	**38.4e-3**	**4.7e-3**	**81.4e-3**	**111.2e-3**
5	4.17	1.73	8.4	1.4e-4	2.5e-3	2.62e-4	17.1e-3	7.1e-3
6	1491.	3.28	15.88	1.94e-6	4.12e-6	1.08e-7	13.3e-3	1.2e-5
7	12.58	1.44	6.97	5e-5	4.58e-4	1.08e-5	8.8e-3	1.3e-3
8	1.92	0.83	4	1.8e-3	4.6e-3	4.35e-4	31.8e-3	13.4e-3
Total for higher order modes			175.7	94.0e-3	72.9e-3	13e-3	204.2e-3	210.8
Total for all modes			318.3	9.31	3.78	0.973	3.23	11.17

Note: Values in boldface font signify that the mode is lasing

emission of the mode, I_{stm}. H_{abs} is the total heat power due to band-to-band absorption outside the gain regions and is responsible for absorption bleaching. H_{FCA} is the total heat power due to FCA. For the case of on-axis feedback, 91 mW of light is coupled into the higher order modes, which consume 166 mA of current and produce 93 mW of light and 269 mW of heat. For the case of off-axis feedback, 176 mW of light is coupled into the higher order modes, which consume 211 mA of current and produce 94 mW of light and 290 mW of heat.

The previous section showed that external feedback can cause higher order vertical modes to lase. For the laser diode and external cavity simulated here, only the fundamental mode lases without feedback, while mode 4 also lases in the case with on-axis feedback. For the case of off-axis feedback, two higher order vertical modes also lase (modes 2 and 4). The feedback reduces the power and PCE of the fundamental mode, which can be attributed partly to higher order mode lasing and partly to an increase in the effective facet reflectivity by feedback to the fundamental mode. For the device and cavity investigated here, Tables 29.4 and 29.5 suggest that modes with MD of MD < 2 are able to start lasing with comparatively small external cavity coupling coefficients of $<5\%$, while modes with MD ~ 4 require larger coupling coefficients (e.g., 10%–20%). Additional simulations showed that the feedback required for higher order mode lasing also depends on the coupling of the reflected beam into the RW (i.e., into the RW aperture at the RW–TA interface). This is also apparent from the photon distributions in Figure 29.23.

As higher order modes began to lase more strongly, they began to compete with the fundamental mode for the spatial gain distribution and modal power oscillations were observed in the simulations. Although these are not true dynamic simulations, the oscillations have some relation to mode beating and mode partition noise. Despite that the higher order mode powers were small, they appear to affect spatial filamentation and contribute to the near- and far-field patterns of the fundamental mode—consistent with experimental observations (Hempel et al., 2013; Leonhäuser et al., 2014). For stable operation, $M^2_{e^{-2}}$ remains below 1.5 and is insensitive to feedback, while $M^2_{\text{2nd moment}} \sim 6$ for SA operation and nearly doubles with feedback (As discussed in Section 29.4.1, increased feedback to the fundamental mode has the greatest impact on beam quality, but excitation of higher order modes also affects $M^2_{\text{2nd moment}}$). For astable operation (modal power oscillations), there is significant degradation in both $M^2_{e^{-2}}$ and $M^2_{\text{2nd moment}}$.

The optical power back-coupled into the higher order vertical modes also creates heat. This occurs even if the modes are not lasing, but increases dramatically if they are. The heat power of the higher order modes is dominated FCA, followed by Joule heating associated with the current supporting stimulated emission into these modes. The heat generated per feedback photon decreases with MD. This shows the importance of both MD and FCA for suppressing feedback amplification and thus, heating by the higher order modes. At this bias level (15 A), the total heat generation in the higher order modes is 0.269–0.290 W (depending on the alignment of the laser diode), corresponding to a 3.2%–3.6% increase in heat power. The heat generation by the higher order modes alone is responsible for a ~2.3%–2.4% drop in PCE, which increases to ~2.5% if their optical output power is also considered. (This is ~20%–25% of the total drop in PCE.) The heat generated by the excitation of these higher order vertical modes is distributed along the entire cavity—irrespective of the MD. Thus, although the excitation of higher order modes affects the beam quality, it is probably not responsible for observed increases in device degradation. Instead, as shown by Kissel et al. (2016), the observed increase in degradation is probably due to feedback that is *not* coupled into the waveguide (i.e., into the substrate)—particularly when the substrate is strongly absorbing (i.e., $E_{\text{g\_substrate}} < E_{\text{photon}}$).

We have shown that external feedback can cause lasing of higher order vertical modes, resulting in self-heating, mode partition instabilities, and beam quality degradation. The question is *How can we design the laser diode and optical system to reduce the impact of optical feedback?* For the design of the laser diode, MD and FCA are key parameters for suppressing the impact of higher order modes. The external cavity coupling coefficients play a smaller role, but are still important. The stray light from aperture diffraction by the DBR at the back of the RW must be suppressed. For the design of the external cavity, the reflected power must be minimized—for example, by using good AR coatings and, perhaps, tilted facets to eliminate specular reflections. For high powers, however, other approaches may also be required, such as off-axis optical alignment to prevent reflected beams from coupling into the RW filter. Finally, care must also be taken to minimize the power coupled into the substrate—particularly if the substrate is absorbing.

29.5 Conclusions

This chapter discussed how, for many applications that employ high-brightness diode lasers, it is necessary to scale the output power through beam combination techniques, while maintaining an excellent beam quality. All beam combination techniques cause light to be fed back into the laser cavity. In some instances, this feedback can be exploited, such as in the wavelength stabilization of diode lasers and arrays. However, any laser placed in an external system will also suffer from unintentional feedback (parasitic reflections). This chapter describes a detailed method of modeling external cavity lasers with both intentional and unintentional feedback. This model, developed at the University of Nottingham, consists of an advanced laser simulation tool coupled to commercial optical design software.

In large vertical cavity lasers, as required to reach the highest output powers, the vertical cavity must be carefully considered. The structure must be designed to minimize the coupling of parasitic feedback to higher order modes. The effects of parasitic feedback on the performance (output power, PCE, and beam quality) of a tapered laser in a simple optical system are studied. The excitation and propagation of higher order modes increases the FCA causing self-heating, eventually causing degradation of the output power and efficiency. Moreover, the parasitic feedback causes more absorption bleaching, leading also to degradation of the lateral beam quality. Therefore, the inclusion of external parasitic feedback in the design process is highly significant. Coupling coefficients and MD values can be used to engineer a laser structure that is less affected by feedback. This can be accomplished by ensuring that modes with low-to-moderate MD values have the lowest coupling coefficients, thereby minimizing the light coupled into them.

The lateral cavity design also has a significant impact on brightness and the tapered laser is a strong contender for high-brightness laser systems. Tapered lasers offer, to a certain extent, the beam quality advantages of an RW laser and the high power advantages of a BA laser. However, despite this and even without external parasitic feedback, tapered lasers still suffer from beam quality degradation at higher powers. Investigations into the cause of this beam quality degradation reveal that diffraction of light at the back aperture leads to regions adjacent to the RW section becoming bleached from carriers—thereby, degrading the beam quality.

Acknowledgments

The authors thank J. Decker and P. Crump at the Ferdinand Braun Institute and N. Michel and M. Krakowski at Alcatel-Thales III–V Lab for experimental results and helpful discussions, and U. Witte and M. Traub at Fraunhofer Institute for Laser Technology for helpful discussions on optical systems for direct-diode lasers. We also thank G. Schimmel, G. Lucas-Leclin, and P. Georges at CNRS Institute d'Optique; and V. Vilokkinen and P. Uusimaa at Modulight Ltd. for helpful discussions. The authors acknowledge L. Borruel and I. Esquivias for their contributions to early collaborations on the simulation of tapered laser diodes during the EC ULTRABRIGHT project. The authors gratefully acknowledge funding from the European Commission projects: BRIDLE (IST–314719, 2012–15), WWW.BRIGHTer.EU (IST–2005–035266, 2006–10), FAST ACCESS (IST-004772, 2004–7 WWW.BRIGHT.EU (IST-511722; 2004–6), POWERPACK (IST-2000-29447, 2001–3), ULTRABRIGHT (IST-1999-10356, 2000–3).

References

Agrawal GP (1984) Fast-Fourier-transform based beam-propagation model for stripe-geometry semiconductor lasers: Inclusion of axial effects. *Journal of Applied Physics* 56:3100–3109.

Buda M, van der Vleuten WC, Iordache G, Acket GA, van de Roer TG, van Es CM, van Roy BH, Smalbrugge E (1999) Low-loss low-confinement GaAs-AlGaAs DQW laser diode with optical trap layer for high-power operation. *IEEE Photonics Technology Letters* 11:161–163.

Bull S, Andrianov A, Wykes JG, Lim JJ, Sujecki S, Auzanneau SC, Calligaro M, Lecomte M, Parillaud O, Krakowski M, Larkins EC (2006) Quantitative imaging of intracavity spontaneous emission distributions using tapered lasers fabricated with windowed n-contacts. *IEEE Proceedings—Optoelectronics* 153:2–7.

Bull S, Wykes JG, Andrianov AV, Lim JJ, Borruel L, Sujecki S, Auzanneau SC, Calligaro M, Krakowski M, Esquivias I, Larkins EC (2004) Imaging of spontaneous emission from 980 nm tapered lasers with windowed N-contacts. *European Physical Journal Applied Physics* 27:455–459.

Crump P, Blume G, Paschke K, Staske R, Pietrzak A, Zeimer U, Einfeldt S, Ginolas A, Bugge F, Häusler K, Ressel P, Wenzel H, Erbert G (2009) 20 W continuous wave reliable operation of 980 nm broad-area single emitter diode lasers with an aperture of 96 μm. *Proceedings of SPIE* 7198:719814–719819.

Crump P, Erbert G, Wenzel H, Frevert C, Schultz CM, Hasler KH, Staske R, Sumpf B, Maaβdorf A, Bugge F, Knigge S, Tränkle G (2013a) Efficient high-power laser diodes. *IEEE Journal of Selected Topics in Quantum Electronics* 19:1501211.

Crump P, Hasler KH, Wenzel H, Knigge S, Bugge F, Erbert G (2013b) High efficiency, 8 W narrow-stripe broad-area lasers with in-plane beam-parameter-product below 2 mm mrad. In: *2013 Conference on Lasers & Electro-Optics Europe & International Quantum Electronics Conference CLEO EUROPE/IQEC*, Munich, 2013, p. 1.

Crump P, Knigge S, Maaßdorf A, Bugge F, Hengesbach S, Witte U, Hoffmann H-D, Köhler B, Hubrich R, Kissel H, Biesenbach J, Erbert G, Traenkle G (2013c) Low-loss smile-insensitive external frequency-stabilization of high power diode lasers enabled by vertical designs with extremely low divergence angle and high efficiency. *Proceedings of SPIE* 8605:86050T–86013.

Decker J, Crump P, Fricke J, Maaβdorf A, Erbert G, Tränkle G (2014) Narrow stripe broad area lasers with high order distributed feedback surface gratings. *IEEE Photonics Technology Letters* 26:829–832.

Dittmar F, Sumpf B, Fricke J, Erbert G, Trankle G (2006) High-power 808-nm tapered diode lasers with nearly diffraction-limited beam quality of M/sup 2/=1.9 at P = 4.4 W. *IEEE Photonics Technology Letters* 18:601–603.

Donnelly JP, Huang RK, Walpole JN, Missaggia LJ, Harris CT, Plant JJ, Bailey RJ, Mull DE, Goodhue WD, Turner GW (2003) AlGaAs-InGaAs slab-coupled optical waveguide lasers. *IEEE Journal of Quantum Electronics* 39:289–298.

Fiebig C, Blume G, Kaspari C, Feise D, Fricke J, Matalla M, John W, Wenzel H, Paschke K, Erbert G (2008) 12 W high-brightness single-frequency DBR tapered diode laser. *Electronics Letters* 44:1253–1255.

Hempel M, Chi M, Petersen PM, Zeimer U, Tomm JW (2013) How does external feedback cause AlGaAs-based diode lasers to degrade? *Applied Physics Letters* 102:023502–023504.

Huang RK, Chann B, Glenn JD (2011) Extremely high-brightness kW-class fiber coupled diode lasers with wavelength stabilization. *Proceedings of SPIE* 8039:80390N–80310.

Huang RK, Chann B, Missaggia LJ, Augst SJ, Connors MK, Turner GW, Sanchez-Rubio A, Donnelly JP, Hostetler JL, Miester C, Dorsch F (2009) Coherent combination of slab-coupled optical waveguide lasers. *Proceedings of SPIE—the International Society for Optical Engineering* 7230:72301G–72312.

Huang RK, Donnelly JP, Missaggia LJ, Harris CT, Chann B, Goyal AK, Sanchez-Rubio A, Fan TY, Turner GW (2007) High-brightness slab-coupled optical waveguide lasers. *Proceedings of SPIE* 6485:64850F–64859.

Kaunga-nyirenda SN, Bull S, Lim JJ, Hasler KH, Fricke J, Larkins EC (2014) Factors influencing brightness and beam quality of conventional and distributed Bragg reflector tapered laser diodes in absence of self-heating. *IET Optoelectronics* 8:99–107.

Kelemen MT, Weber J, Kaufel G, Bihlmann G, Moritz R, Mikulla M, Weimann G (2005) Tapered diode lasers at 976 nm with 8 W nearly diffraction limited output power. *Electronics Letters* 41:1011–1013.

Kissel H, Leonhäuser B, Tomm JW, Hempel M, Biesenbach J (2016) Investigation of accelerated and catastrophic degradation of laser diodes caused by external optical feedback operation. European Semiconductor Laser Workshop, Darmstadt, Germany.

Knigge A, Erbert G, Jonsson J, Pittroff W, Staske R, Sumpf B, Weyers M, Trankle G (2005) Passively cooled 940 nm laser bars with 73% wall-plug efficiency at 70 W and 25/spl deg/C. *Electronics Letters* 41:250–251.

Lang L, Lim JJ, Sujecki S, Larkins EC (2008) Improvement of the beam quality of a broad-area diode laser using asymmetric feedback from an external cavity. *Optical Quantum Electronics* 40:1097–1102.

Larkins EC, Bull S, Kaunga-Nyirenda S, Helal MA, Vilokkinen V, Uusimaa P, Crump P, Erbert G (2014) Design optimisation of high-brightness laser diodes for external cavity operation in the BRIDLE Project. In: *2014 International Semiconductor Laser Conference*, Palma de Mallorca, 2014, pp. 21–22.

Larkins EC, Helal MA, Kaunga-Nyirenda SN, Bull S, Moss D (2016) Design and simulation of high-brightness diode lasers for operation in the presence of external feedback. In: Conference on Novel In-Plane Semiconductor Lasers XV, 2016. (Photonics West, San Francisco, USA) 9767

Leonhäuser B, Kissel H, Unger A, Köhler B, Biesenbach J (2014) Feedback-induced catastrophic optical mirror damage (COMD) on 976 nm broad area single emitters with different AR reflectivity. *Proceedings of SPIE* 8965:896506–896510.

Lim JJ (2003) Investigation of factors influencing the brightness of high-power laser diodes. PhD dissertation, University of Nottingham.

Lim JJ, Benson TM, Larkins EC (2005) Design of wide-emitter single-mode laser diodes. *IEEE Journal of Quantum Electronics* 41:506–516.

Lim JJ, Bull S, Kaunga-Nyirenda S, Sujecki S, Larkins EC, Hasler KH, Fricke J (2012) Factors influencing the brightness and beam quality of tapered laser diodes and bars. IEEE Summer Topical Meeting on High Power Semiconductor Lasers TuA4.1.

Lim JJ, Sujecki S, Lei L, Zhichao Z, Paboeuf D, Pauliat G, Lucas-Leclin G, Georges P, MacKenzie R, Bream P, Bull S, Hasler KH, Sumpf B, Wenzel H, Erbert G, Thestrup B, Petersen PM, Michel N, Krakowski M, Larkins EC (2009) Design and simulation of next-generation high-power, high-brightness laser diodes. *IEEE Journal of Selected Topics in Quantum Electronics* 15:993–1008.

Pearson JE, McGill TC, Kurtin S, Yariv A (1969) Diffraction of gaussian laser beams by a semi-infinite plane. *Journal of the Optical Society of America* 59:1440–1445.

Pillai RMR, Garmire EM (1996) Paraxial-misalignment insensitive external-cavity semiconductor-laser array emitting near-diffraction limited single-lobed beam. *IEEE Journal of Quantum Electronics* 32:996–1008.

Skidmore J, Peters M, Rossin V, Guo J, Xiao Y, Cheng J, Shieh A, Srinivasan R, Singh J, Wei C, Duesterberg R, Morehead JJ, Zucker E (2016) Advances in high-power 9XXnm laser diodes for pumping fiber lasers. *Proceedings of SPIE* 9733:97330B–97337.

Sujecki S, Borruel L, Wykes J, Moreno P, Sumpf B, Sewell P, Wenzel H, Benson TM, Erbert G, Esquivias I, Larkins EC (2003) Nonlinear properties of tapered laser cavities. *IEEE Journal of Selected Topics in Quantum Electronics* 9:823–834.

Sumpf B, Adamiec P, Fricke J, Ressel P, Wenzel H, Erbert G, Tränkle G (2010) Comparison of 650 nm tapered lasers with different lateral geometries at output powers up to 1 W. *Proceedings of SPIE* 7616:76161–76168.

Sverdlov B, Pfeiffer HU, Zibik E, Mohrdiek S, Pliska T, Agresti M, Lichtenstein N (2013) Optimization of fiber coupling in ultra-high power pump modules at $\lambda = 980$ nm. *Proceedings of SPIE* 8605:860508–860510.

Thestrup B, Chi M, Sass B, Petersen PM (2003) High brightness laser source based on polarization coupling of two diode lasers with asymmetric feedback. *Applied Physics Letters* 82:680–682.

Tomm JW, Ziegler M, Hempel M, Elsaesser T (2011) Mechanisms and fast kinetics of the catastrophic optical damage (COD) in GaAs-based diode lasers. *Laser & Photonics Reviews* 5:422–441.

Walpole JN, Kintzer ES, Chinn SR, Wang CA, Missaggia LJ (1992) High-power strained-layer InGaAs/AlGaAs tapered traveling wave amplifier. *Applied Physics Letters* 61:740–742.

Wang X, Erbert G, Wenzel H, Crump P, Eppich B, Knigge S, Ressel P, Ginolas A, Maaßdorf A, Tränkle G (2013) High power, high beam quality laser source with narrow, stable spectra based on truncated-tapered semiconductor amplifier. *Proceedings of SPIE* 8605:86050G–86011.

Williams KA, Penty RV, White IH, Robbins DJ, Wilson FJ, Lewandowski JJ, Nayar BK (1999) Design of high-brightness tapered laser arrays. *IEEE Journal of Selected Topics in Quantum Electronics* 5:822–831.

Wolff S, Rodionov A, Sherstobitov VE, Fouckhardt H (2003) Fourier-optical transverse mode selection in external-cavity broad-area lasers: Experimental and numerical results. *IEEE Journal of Quantum Electronics* 39:448–458.

Yaeli J, Streifer W, Scifres DR, Cross PS, Thornton RL, Burnham RD (1985) Array mode selection utilizing an external cavity configuration. *Applied Physics Letters* 47:89–91.

Yang G, Smith GM, Davis MK, Loeber DAS, Hu M, Chung-en Z, Bhat R (2004) Highly reliable high-power 980-nm pump laser. *IEEE Photonics Technology Letters* 16:2403–2405.

30

Single Longitudinal Mode Laser Diodes

Xun Li

30.1 Introduction

30.1.1 What Is a Single Longitudinal Mode Laser?

Laser is a light source that emits photons described by a "near coherent" optical field. By "coherent optical field," one means the monochromatic electromagnetic field at optical frequency (ω_0) with constant amplitude (A) and phase (θ). Therefore, a coherent optical field can be expressed as $A\cos(\omega_0 t + \theta)$, with phase θ determined by a reference starting time. Any laser built as an oscillator must take spontaneously emitted photons as its initial driven seed, since a laser doesn't have any coherent light as its input. Knowing the fact that the spontaneous emission is a random process, one therefore cannot expect that the laser will give an ideal coherent optical field output. Rather, the laser emits photons described by the ideal coherent optical field, driven by spontaneously emitted photons, for a certain amount of time τ_0 until the emerging of another group of spontaneously emitted photons. Consequently, its output field will experience a sudden change on its amplitude and phase at time τ_0 and this sequence keeps repeating indefinitely. As such, one can express the laser output as a "quasi-monochromatic" electromagnetic field at optical frequency ω_0 as $[A + \delta_a(t)]\cos[\omega_0 t + \theta(t)]$, with $\delta_a(t)$ as a random process with zero mean and $\theta(t)$ also a random process with uniform distribution between 0 and 2π. Once a laser is operated under a bias beyond its threshold, $A >> |\delta_a(t)|$ is satisfied. Hence the only nonideality of a laser output from a coherent optical field lies in its random phase. The difference becomes more apparent if one observes the output optical spectrum of a laser. Actually, as the Fourier transform of an ideal coherent optical field, its frequency-domain spectrum is a delta function that appears at ω_0 with an amplitude of $|A|$. The quasi-monochromatic field, however, has its averaged spectrum in the shape of a "broadened" delta function still peaked at ω_0, but with an amplitude in $\sqrt{1/2\pi}|A|\tau_0$ and a width of $\Delta\omega = 2\pi/\tau_0$. This is because the averaged duration between two consecutive abrupt phase changes is τ_0, which means the quasi-monochromatic field can be described as a series of truncated ideal coherent fields known as a wave train, with τ_0 as the truncation window or the averaged length of the wave train. The Fourier transform of a single truncated coherent field piece corresponds to the convolution between a delta function and a sampling function in the form of $\sin(\omega\tau_0/2)/(\omega\tau_0/2)$ as the Fourier transforms of the ideal coherent field and the flat window function (i.e., 1 for t inside τ_0 and 0 elsewhere), respectively, which gives the result as the aforementioned broadened delta function. Since distinct truncated coherent field pieces in the wave train differ by a time shift only, their Fourier transforms differ just by a phase. Hence, the frequency-domain amplitude spectra of the quasi-monochromatic field as a wave train composed of all these pieces are overlapped as a single peak as shown in Figure 30.1.

It is worth mentioning that the above description is in a "phenomenological" sense, as an accurate treatment of spontaneously emitted photons with a classical electromagnetic field theory is not possible. A physics-based description can be given by exploiting the full quantum mechanics theory, but it will have to involve the quantization of the electromagnetic field and is beyond the scope of this chapter.

The optical frequency ω_0 of the quasi-monochromatic field as the laser output is called the "lasing" frequency. Consequently, the aforementioned spectral peak is called the "lasing" mode or the "longitudinal" mode in order to make a distinction from the "transverse" mode that refers to a spatial field distribution. The term longitudinal comes from the fact that the lasing frequency is determined by the laser resonant cavity. In edge-emitting semiconductor laser diodes, the cavity is set along the longitudinal direction with its geometrical dimension significantly larger than any size in the cross-sectional area. The light is confined inside the cross-sectional area by a waveguide and is only allowed to propagate along the longitudinal direction, or along the cavity. Upon resonance, the lasting longitudinal optical field distribution gives the surviving pattern and determines the lasing frequency. Hence, we have the term longitudinal mode, as opposed to the transverse mode, indicating the confined optical field by the waveguide in the cross-sectional area. Because of the one-to-one correspondence between the optical spectral peak and the lasting longitudinal optical field distribution, conventionally the term longitudinal mode can be referred to either as the spectral peak (or simply as the lasing frequency) or as the spatial field pattern in the cavity

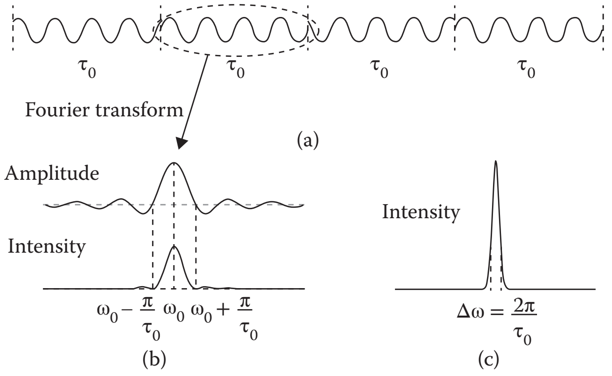

FIGURE 30.1 (a) The quasi-monochromatic field as a wave train in the time domain and a single piece of the truncated coherent field, (b) the frequency-domain amplitude and intensity spectra as the Fourier transform of the wave train (with different pieces all overlapped), and (c) the intensity spectrum with the peak indicating a single (spectral) longitudinal mode.

(longitudinal) direction, whereas the term transverse mode can only be referred to as the spatial field pattern in the cross-sectional area, without any spectral meaning.

Generally, a cavity can support multiple resonant patterns and consequently bear with multiple resonant frequencies. Without exception, a laser can also have multiple longitudinal modes, with multiple peaks shown in its output optical spectrum and multiple lasting optical field patterns inside its cavity. With special designs, however, one is able to leave only one surviving longitudinal mode by eliminating all other resonances inside a cavity. A laser with such a cavity is therefore called a single longitudinal mode (SLM) laser.

30.1.2 Why SLM Laser?

When used as the light source in fiber-optic communication systems, a semiconductor laser operated with multiple longitudinal modes suffers the mode partition noise (MPN) [1,2], which stands as the dominant limiting factor to the transmission span of the optical signal in fiber, as the MPN jeopardizes the signal by introducing the intersymbol interference (ISI) among the pulses in the stream—an effect that cannot be simply suppressed through increasing the laser output power. If a multiple longitudinal mode laser is directly modulated, the power allocated to each of its mode fluctuates in a random manner due to the mixed homogeneous and inhomogeneous gain broadening nature of direct bandgapped semiconductors, with the randomness originated from the spontaneous emission noise. Since the signal components carried by different longitudinal modes propagate at different speed due to fiber dispersion, these components won't arrive at the destination at the same time, which results in the pulse spreading over and spilling out of its allocated time slot, and consequently causes ISI. Such ISI bears a random nature due to the random power fluctuation of the multiple longitudinal modes as the signal carriers. Hence, it cannot be eliminated through linear equalization or phase delay compensation. Also, because the random fluctuation is in proportion to the total power, increasing the laser output power won't solve the problem, if doesn't make it worse. Normally, the power penalty soars even starting from a moderate MPN level. For example, at ~1550 nm (the center of the C-band), the maximum transmission capacity–distance product is only 5 Gbps-km, which means by using a typical multiple longitudinal mode Fabry–Pérot (FP) laser, the 2.5 and 10 Gbps optical signal can only be transmitted for 2 km and 500 m, respectively.

The only viable solution to this problem, therefore, lies in the replacement of the light source with the SLM laser where the MPN naturally disappears.

30.1.3 Current Application Status

Over the past three decades, many SLM laser structures have been proposed and demonstrated; a few dominant structures survived and became popular products on today's market. The super star of the SLM laser is no doubt the distributed feedback (DFB) laser as it takes over 99% shares of the SLM laser market—the throughput of DFB lasers have reached 10 million per year in the recent few years just by one supplier (Wuhan Telecommunication Device Co., Wuhan, China) among the few largest semiconductor laser manufactures.

30.1.4 Why Simple FP Laser Won't Work

It is well known that a piece of straight and smooth optical waveguide with its two mirror-like ends forms a simplest resonant cavity, and semiconductor laser diodes exploiting such a cavity are the FP lasers. A semiconductor optical waveguide, like the typical dielectric waveguide, has the high-pass filter characteristic that cuts off the guiding wave with wavelength longer than some critical value but imposes no constraint on the guiding waves with shorter wavelengths. Although such waveguide does only support discrete space distribution patterns in its cross section and each individual space distribution pattern is also called a transverse mode, one shouldn't mess up it (the transverse mode) with the concept of the longitudinal mode that corresponds a specific field distribution along the cavity and bears a discrete wavelength. Namely, a (dielectric) waveguide picks up the guided transverse mode, but doesn't select a single wavelength from a continuous spectrum of wavelengths that all takes the same transverse mode, except for cutting off the wavelengths below a lower bound. One can also understand it as a given waveguide structure only defines a continuous dispersion relation between the wave propagation constant (β) and the wavelength (λ), which means that, staying with a transverse mode represented by a continuous β–λ curve, one will always manage to find a β indicating a guiding (propagating along the waveguide) wave for a given wavelength λ. Nevertheless, an optical waveguide that only supports a single transverse mode stands as a necessary condition for achieving the SLM operation. As otherwise, each of the multiple nondegenerated transverse modes having its own nonidentical longitudinal mode will have to bear a different wavelength, which makes the SLM operation impossible. We are not going to dig out the waveguide concept further as the focus of this chapter is on the SLM laser. The interested readers can refer to, e.g., References [3,4].

With mirrors on the waveguide ends, the otherwise not interfered forward and backward propagating waves are coupled through the partial reflection. The waves retained inside the waveguide (i.e., the cavity) forms a standing wave pattern that corresponds to a possible longitudinal mode, as the standing wave pattern (other than a homogenous coefficient) doesn't change with time by satisfying the boundary condition at the waveguide ends and consequently bears with a static wavelength. However, in the case where the cavity length (L) is much longer than the wavelength (λ), the boundary condition can be satisfied simultaneously by multiple longitudinal modes. This is because the boundary condition of a simple FP cavity can be equivalent to a round-trip phase condition on aggregate, which reads as follows [5]:

$$2\beta L = 2\pi m \tag{30.1}$$

with m as any integer, $\beta = 2\pi n_{\text{eff}}/\lambda$ denoting the wave propagation constant and n_{eff} the effective index of the waveguide. In Equation 30.1, the facet (end mirror) phase delay has been set to zero as usually the cavity has an effective index higher than that of the surrounding medium, so that the wave experiences the internal (from high refractive index to low refractive index medium) rather than the external (from low refractive index to high refractive index medium) reflection in which the phase delay is indeed zero on reflection. From Equation 30.1, it is apparent that the number of allowed longitudinal modes in an FP cavity is directly proportional to the cavity length scaled by the wavelength, i.e., L/λ. To build an edge-emitting laser with acceptable coherence required by many applications, as well as for obtaining sufficient optical gain for achieving superior laser performance, one has to leave $L \gg \lambda$, hence multiple longitudinal modes exist in such FP cavities.

Other than the aforementioned phase condition, the amplitude condition still needs to be satisfied by the longitudinal mode that survived the phase condition to make it lase. One can therefore consider using the latter mechanism to eliminate the extra longitudinal modes. Unfortunately, the optical gain spectrum of the semiconductor material is much broader (~60 nm) than the FP longitudinal mode spacing that can readily be derived from Equation 30.1 as follows [5]:

$$\Delta\lambda = \frac{\lambda_0^2}{2n_g L} \tag{30.2}$$

with λ_0 as the center wavelength and $n_g = n_{\text{eff}} + (dn_{\text{eff}}/d\lambda)\lambda_0$ denoting the group index. For example, for typical InGaAsP/InP or AlGaInAs/InP semiconductor laser diodes, $n_g \sim 3.4$, their mode spacing vary from 0.6 to 1.2 nm in the O-band ($\lambda_0 \sim 1300$ nm), and from 0.9 to 1.8 nm in the C-band ($\lambda_0 \sim 1550$ nm), respectively, when the cavity length changes from 400 to 200 μm. As such, multiple longitudinal modes with their wavelengths closely packed adjacent to the material gain peak will share almost the same gain. Since the partially inhomogeneous gain in a semiconductor material cannot be fully clamped, small gain differences among these longitudinal modes won't be sufficient to effectively suppress the side modes, which eventually excites multiple longitudinal lasing modes. This is the main reason that the material gain dispersion in general cannot be used for longitudinal mode selection, not to mention that in the case of direct modulation, any dynamic gain change will disrupt the gain profile and consequently jeopardize any attempt of using the gain to discriminate longitudinal modes.

One therefore understands why conventional semiconductor FP laser diodes operate in multiple longitudinal modes. Above analysis also shed some light on the direction one needs to follow in the effort of developing SLM lasers, i.e., the simple FP cavity needs to be replaced by more complicated ones or modified with added structures with further built-in wavelength selectivity.

30.1.5 Classification of SLM Lasers

Canonically, there are three main approaches for semiconductor laser diodes to achieve SLM operation, all by introducing wavelength-selective cavities. These three categories of SLM lasers can be classified as the grating-assisted lasers that exploit the grating in their cavities, the coupled-cavity lasers that have extra optical (band-pass) filters in their cavities, and the external cavity lasers that use either one of the above-mentioned configurations, or the injection locking mechanism to purify the lasing spectrum but by placing the extra components outside of the main FP cavity through hybrid packaging. Theoretically, lasers in the latter category makes no difference from their counterparts in the first two categories, other than some quantitative difference on the coupling strength between the main FP cavity and the added wavelength selection components. Since they never become the mainstream product except in a few specific applications where the cost is not a concern, SLM lasers in this category are not discussed. The interested readers can refer to, e.g., References [6–8].

30.1.6 Organization of this Chapter

Sections 30.2 and 30.3 will be dedicated to discuss the grating-assisted lasers and the coupled-cavity lasers, respectively, covering their structures and working mechanisms, governing equations describing the device physics processes, and numerical simulation results on device performance.

The following section briefly describes the recent development on this topic, by showing a few advanced structures for emerging demands, their operating principles, the measured prototype device performance, in contrast to numerical simulation results.

30.2 Grating-Assisted SLM Laser Diodes

30.2.1 Grating Analysis

Noticing that a normal facet mirror formed by a dielectric (semiconductor)—dielectric (air) interface doesn't have wavelength dependence, which makes the FP cavity formed by a straight and smooth waveguide with such facet mirrors on both ends lacking the ability to select a single lasing wavelength, one would naturally think of exploiting a wavelength-selective reflector to replace the end facet mirror, which directly leads to the birth of distributed Bragg reflector (DBR) laser. This idea can logically be extended to turn the entire or part of the original straight and smooth waveguide inside the cavity into a corrugated waveguide (i.e., the waveguide grating) for lasing wavelength selection, which leads to the innovation of a whole family of DFB lasers, although the original idea of the DFB laser was independently proposed [9]. In all such grating-assisted SLM lasers, the grating obviously plays a center role. We therefore start this section by analyzing the grating itself.

A uniform (passive) grating with period Λ in any shape can be viewed as a linear superposition of many sinusoidal gratings with harmonic periods Λ/m, $m = 1, 2, 3, \ldots$, according to the Fourier expansion, simply because the refractive index change along the grating follows a periodic function. A phase-matching condition can therefore be found as follows [10]:

$$k_i \cos\theta_i = \pm\frac{2\pi}{(\Lambda/m)} + k_{om}\cos\theta_{om} \tag{30.3}$$

with k_i and k_{om} indicating the incident and *m*th order diffracted (by the *m*th order sinusoidal grating) wave numbers, respectively, θ_i and θ_{om} the incident and *m*th order diffracted wave angles as shown in Figure 30.2, respectively.

In this application, the incident light is propagating along the laser waveguide, $\theta_i = 0$ and $k_i = \beta = 2\pi n_{\text{eff}}/\lambda$. What one wants is to have the incident wave turn around by 180°, propagating along the waveguide in the opposite direction, which requires $\theta_{om} = \pi$ and $k_{om} = \beta = 2\pi n_{\text{eff}}/\lambda$, hence one has, from Equation 30.3,

$$2\beta = \frac{4\pi n_{\text{eff}}}{\lambda} = \frac{2\pi m}{\Lambda}, \text{ or } \Lambda = \frac{m\lambda}{2n_{\text{eff}}} \tag{30.4}$$

as the rule to select the grating period for coupling the forward and backward propagating waves in the waveguide at a given wavelength (λ), with n_{eff} still indicating the effective index of the waveguide. The wavelength that satisfies condition (Equation 30.4) is conventionally called Bragg wavelength. It is self-evident that for a given grating with fixed Λ, any wavelength deviated from λ wouldn't satisfy the phase-matching condition (Equation 30.4), consequently at such wavelength there won't be any coupling between the forward and backward propagating waves. As such, an ideal grating (with infinite length) would indeed select a single wavelength to reflect, which makes a perfect mirror as required by an SLM laser cavity. In reality, the grating cannot be made infinitely long. One would therefore expect some residue reflection at deviated wavelengths. Nevertheless, by making the grating sufficiently long, one can always expect a mirror with sufficient wavelength selection required by the SLM operation.

Yet another design consideration is how to choose the grating order. By choosing a sinusoidal grating component with order $m = M$ to be satisfied by Equation 30.4, one understands that those sinusoidal grating components with orders beyond M won't take any effect, simply because if $\lambda = 2n_{\text{eff}}\Lambda/M$, for any grating orders in $M + n$, $n = 1, 2, 3, \ldots$, their diffraction angles according to Equation 30.4,

$$\theta_{o(M+n)} = \arccos\left(1 + \frac{2n}{M}\right) \tag{30.5}$$

offer no real solution at all. Physically, the distance between the two consecutive reflections of the grating in order $M + n$ is $\Lambda/(M + n)$ shorter than half of the equivalent wavelength in waveguide $\lambda/(2n_{\text{eff}}) = \Lambda/M$, therefore, constructive addition of the waves on its reflection is impossible because there is no phase-matching condition (i.e., two identical phases) that can possibly be found within 2π. This can be seen more clearly if we show the round-trip phase delay between the two consecutive reflections explicitly by

$$2\frac{2\pi n_{\text{eff}}[\Lambda/(M+n)]}{\lambda} = 2\frac{2\pi n_{\text{eff}}[\Lambda/(M+n)]}{2n_{\text{eff}}\Lambda/M} = 2\pi\frac{M}{M+n} < 2\pi.$$

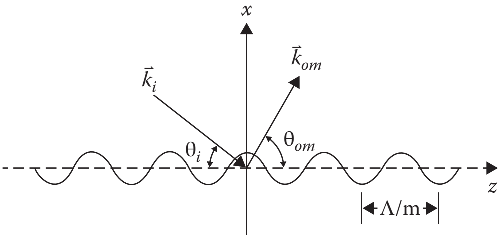

FIGURE 30.2 An illustrative diagram showing the light diffraction by a grating, with Λ/m indicating the *m*th order harmonic period, θ_i and θ_{om} the incident and *m*th order diffracted wave angles in respect to the grating plane, respectively, $\vec{k}_i$ and $\vec{k}_{om}$ the incident and *m*th order diffracted wave vectors, respectively; they must be in the same plane as required by the matching tangential field condition at the grating boundary.

Therefore, those sinusoidal grating components with orders higher than M virtually take no effect, because all the reflected waves by these higher order grating components cannot be added in a constructive way, rather, they all tend to be cancelled out.

For sinusoidal grating components with orders $n = 1, 2, \ldots, M - 1$, they will make the incident wave diffract into different directions, with their angles specified, according to Equation 30.4:

$$\theta_{on} = \arccos\left(1 - \frac{2n}{M}\right) \tag{30.6}$$

For example, if one chose the Bragg wavelength to match the second-order sinusoidal grating component $M = 2$ and $\lambda = n_{\text{eff}}\Lambda$. The second-order sinusoidal grating component therefore couples the forward going wave in the waveguide into the backward going wave, which offers the effect one needs, whereas the first-order sinusoidal grating component couples the forward going wave in the waveguide into a wave going along the vertical direction ($\theta_{o1} = 90°$). The latter appears to be a vertically radiating wave that leaves away from the waveguide. The rest sinusoidal components with their orders higher than 2 all take negligible effect.

In this specific application, one usually doesn't want to create any accompanying radiation that will likely bring in unwanted loss, hence one should align the Bragg wavelength with the first-order sinusoidal grating component $M = 1$ and $\lambda = 2n_{\text{eff}}\Lambda$. As such, the forward and backward waves are coupled at the lowest grating order and consequently it leaves no lower order grating components for the guided waves to be coupled to the radiating wave. Again, those higher order grating components ($M > 1$) virtually bring in no effect.

From the above qualitative analysis, one also knows that it is the period, rather than the shape, that dominates the grating characteristics. And the above analysis is valid under the assumption that the grating is sufficiently long. The required grating length to achieve certain performance, however, can only be evaluated in connection with the grating coupling strength in unit length through numerical approach. Also known as the grating coupling coefficient (κ), the unit length grating coupling strength is determined by the grating shape and the refractive index contrast, or the effective index contrast (Δn_{eff}) on aggregate. In the most general case, one needs to use the mode-matching method (MMM) [11,12] to calculate the reflection, transmission, and loss spectra of a given waveguide grating. A good approximation is to chop the waveguide grating into many short pieces along the guiding direction. By solving the mode in each piece as an eigenvalue problem defined in the local waveguide cross section, one will be able to extract the effective index in each piece as the eigenvalue solution. One can therefore use the one-dimensional (along the guiding direction) transfer matrix method (TMM) [13,14] to solve for the aforementioned grating spectra.

While numerical approaches would offer us an accurate result, one sees little physics and it is also hard to link the grating design parameters to its characteristics. For this reason, one usually uses the full numerical solver as a simulation tool only to validate or confirm a design. One therefore still needs an analytical or semi-analytical tool for the grating design purpose. For this reason, we will show following the expressions [15]. Actually, the refractive index distribution of a waveguide grating can be written in the Fourier series:

$$n^2(x, y, z) = n_0^2(x, y) + \sum_{m \neq 0} \Delta n_m^2(x, y) e^{jm\frac{2\pi z}{\Lambda}} \tag{30.7}$$

due to its periodicity along z (the guiding direction), where n_0^2 and Δn_m^2 indicate the DC and mth order coefficient of the square refractive index in the expansion, respectively, and can readily be found by taking the overlap integral (along z within one period Λ) between the square refractive index (n^2) and the respective sinusoidal grating order (in its complex form $e^{jm2\pi z/\Lambda}$, $m = 0, \pm 1, \pm 2, \ldots$) normalized by the period Λ. The cross-sectional (x, y) dependence of the refractive index reflects the waveguide structure. Consequently, the coupling coefficient of the m^{th} order sinusoidal grating component can be found by

$$\kappa_m = \frac{\pi}{\lambda n_{\text{eff}}} \frac{\iint\limits_{\Sigma} \Delta n_m^2(x, y)|\varphi(x, y)|^2 dxdy}{\iint\limits_{\Sigma} |\varphi(x, y)|^2 dxdy} \tag{30.8}$$

where n_{eff} and $\varphi(x, y)$ denote the effective index and optical field distribution of the waveguide defined by the background refractive index distribution (i.e., the DC component in the Fourier expansion) $n_0^2(x, y)$, respectively, and can be found by solving the following eigenvalue problem (with n_{eff} and φ taken as the eigenvalue and eigenfunction, respectively):

$$\left(\frac{\partial^2}{\partial x^2} + \frac{\partial^2}{\partial y^2}\right)\varphi(x, y) + \left(\frac{2\pi}{\lambda}\right)^2 [n_0^2(x, y) - n_{\text{eff}}^2]\varphi(x, y) = 0 \tag{30.9}$$

In Equation 30.8, the integration area Σ extends to where φ can reach. In following discussions, we will stay with the first-order Bragg grating unless otherwise specified. Hence we will use $\kappa_\pm$ to indicate $\kappa_M = \kappa_{\pm 1}$. One also needs to note that Equation 30.7 is only valid for an infinitely long grating, consequently the grating coupling coefficient $(\kappa_\pm)$ given in Equation 30.8 is subject to the same assumption. Practically for $n_{\text{eff}}L/\lambda > 500$, such extracted $\kappa_\pm$ in conjunction with the analytical spectrum expression (shown below) provides no appreciable difference from the accurate result obtained by the full numerical approaches (e.g., MMM or TMM).

For a fully confined guided mode (hence φ is real), both the grating symmetry and the nature of the complex material refractive index change dictate the coupling complexity. For a purely refractive index-coupled grating with real $n^2 - n_0^2$, one may easily find from Equation 30.7 that $\Delta n_{-1}^2 = (\Delta n_{+1}^2)^*$, hence $\kappa_- = \kappa_+^*$ according to Equation 30.8. One may conclude that, if the grating has a center symmetry, n^2 is an even function of z and $\Delta n_{\pm 1}^2$ are real, $\kappa_\pm$ are real and $\kappa_- = \kappa_+$, whereas if the grating has a center antisymmetry, n^2 is an odd function of z and $\Delta n_{\pm 1}^2$ are imaginary, $\kappa_\pm$ are imaginary and $\kappa_- = -\kappa_+$. For a purely gain- or loss-coupled grating with imaginary $n^2 - n_0^2$, one finds, however, $\Delta n_{-1}^2 = -(\Delta n_{+1}^2)^*$ from Equation 30.7, hence $\kappa_- = -\kappa_+^*$ following Equation 30.8. One therefore knows that, if the grating has a center symmetry, n^2 is an even function of z and $\Delta n_{\pm 1}^2$ are imaginary, $\kappa_\pm$ are imaginary and $\kappa_- = \kappa_+$, whereas if the grating has a center antisymmetry, n^2 is an odd function of z and $\Delta n_{\pm 1}^2$ are real, $\kappa_\pm$ are real and $\kappa_- = -\kappa_+$. Generally, for a complex-coupled grating with complex $n^2 - n_0^2$, or for a grating structure that is neither symmetric nor antisymmetric, $\Delta n_{\pm 1}^2$ are complex so are $\kappa_\pm$.

For a waveguide grating with a length of L without any extra end facet reflection [which can practically be realized by, e.g., antireflection (AR) coating on the end facet], one finds the amplitude reflection spectrum (defined as the ratio of the backward and forward going guided wave at the input port) and the amplitude transmission spectrum (defined as the ratio of the forward going guided wave at the output and input port) as [16]:

$$R_{DBR}^{\pm}(\lambda) = \frac{j\kappa_\mp \sinh(\gamma L)}{\gamma \cosh(\gamma L) - (\alpha + j\delta)\sinh(\gamma L)} \tag{30.10}$$

$$T_{DBR}^{\pm}(\lambda) = \frac{\gamma}{\gamma \cosh(\gamma L) - (\alpha + j\delta)\sinh(\gamma L)} \tag{30.11}$$

where $\gamma^2 = (\alpha + j\delta)^2 + \kappa_+\kappa_-$ and $\delta = 2\pi[n_{\text{eff}}/\lambda - 1/(2\Lambda)]$, with λ now indicating the wavelength variable and α the amplitude modal loss (< 0) or gain (> 0) variable of the waveguide grating. Figure 30.3

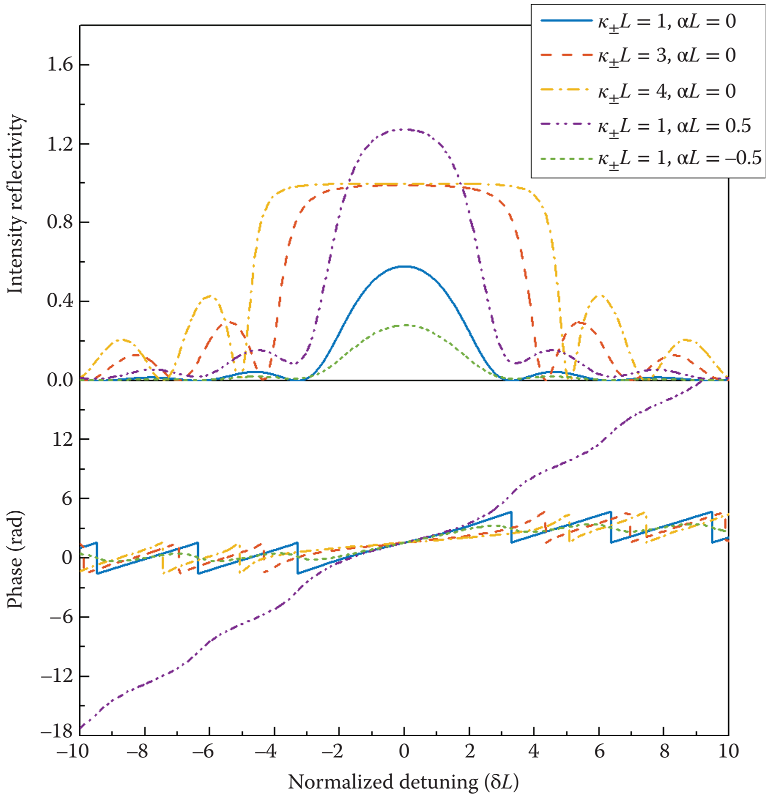

FIGURE 30.3 Reflection spectra of the Bragg grating under different normalized coupling coefficients $\kappa_{\pm}L = 1, 3, 4$ without gain or loss $\alpha L = 0$, and under $\kappa_{\pm}L = 1$ with gain $\alpha L = 0.5$ and loss $\alpha L = -0.5$.

shows respectively the amplitude and phase of the reflection spectrum of a purely refractive index-coupled grating, under different normalized (real) grating coupling coefficient ($\kappa_{\pm}L$) and normalized modal loss/gain (αL).

As can be seen from the spectrum, the maximum reflection happens at the Bragg wavelength. A Bragg stop-band can be identified by the main lobe with its width defined as the difference between the two zero-reflection wavelengths. Zero-reflection happens to the wave at the wavelength with its reflections from two adjacent grating teeth completely canceled out due to a phase delay of π, which makes the further cancel out of all reflections through the entire grating due to the equal tooth distance (i.e., the grating period Λ). Obviously, the wave at the zero-reflection wavelength will pass through the grating with 100% transmissivity as if the waveguide grating offers nothing more than a phase delay unit. For a purely passive, refractive index-coupled grating ($\kappa_+\kappa_- = \kappa_+\kappa_+^*$, hence $\kappa_+\kappa_-$ is real and can be written as $|\kappa|^2$) without any modal gain or loss ($\alpha = 0$), zero-reflections (maximum transmission) happen at $\gamma L = jk\pi$, $k = \pm1, \pm2, \pm3, \ldots$, or $\delta L = \pm\sqrt{(|\kappa_+|L)^2 + (k\pi)^2}$. The Bragg stop-band width is therefore given by [16]

$$2\delta L = 2\sqrt{(|\kappa|L)^2 + \pi^2} \text{ or } \Delta\lambda_B = \frac{\lambda_B^2}{n_{\mathrm{eff}}L}\sqrt{(|\kappa|L/\pi)^2 + 1} \qquad (30.12)$$

with $\lambda_B = 2n_{\mathrm{eff}}\Lambda$ indicating the Bragg wavelength (center of the Bragg stop-band) given by the phase-matching condition (Equation 30.4) for the first-order Bragg grating. It is apparent that the Bragg stop-band width ($\Delta\lambda_B$) increases with the normalized coupling coefficient almost linearly if $|\kappa|L >> \pi$, or quadratically if $|\kappa|L << \pi$. It is worth mentioning that the measured stop-band width of the lasing spectrum in the DFB lasers is always smaller than the Bragg stop-band width, and the former approaches $\Delta\lambda_B$ as $|\kappa|L$ increases. We explain the underlying physics later in discussion of DFB lasers.

In the near infrared fiber-optic communication wavelength range, the first-order Bragg grating has its period in the submicrometer range (e.g., ~200 nm in the O-band centralized at 1300 nm and ~240 nm in the C-band centralized at 1550 nm). It is impossible to fabricate the waveguide surface-relief grating by the standard photolithography technique. Rather, one has to exploit more complicated technologies such as the holographic lithography [17] or the electron-beam lithography (EBL) [18]. While the former doesn't need expensive facility and fits the mass production mode, it can hardly create any nonuniform grating pattern. The latter, conversely, can create arbitrary user-defined grating pattern but needs expensive machine and doesn't fit the production mode for the long hours it needs to scan-write the whole wafer. A newly emerged technique, nano-imprinting [19], seems to be very promising as the ultimate solution to the fabrication of the waveguide grating. With the imprinting mask written by EBL with complicated patterns, one can use the mask repeatedly to transfer its pattern onto wafers by a pressing-and-developing process through the spin-coated pressure-sensitive deforming-resister on the wafer surface. As such, the expensive EBL writing just needs to be done once on the mask, the later pattern transfer process from the mask to wafers (imprinting) is fast and reliable, with an even better quality compared to the widely used holographic lithography technique [20]. It is also worth mentioning that the invention of the "floating" grating idea [21] solves the problem in the precise control of the grating coupling strength and guarantees its repeatability in the mass production mode, as the depth of the grating teeth is now determined by the grating layer thickness which can be made accurate (to sub-10 nm range) in material growth, as opposed to be given by the etching depth which is not only hard to control down to 10~20 nm but also hardly repeatable. This invention sets a milestone on the mass production as well as the cost reduction of DFB lasers.

30.2.2 Distributed Bragg Reflector Laser

A typical DBR laser has a structure shown in Figure 30.4. With the first-order Bragg grating placed on one or both ends of an FP laser as the reflector, the coupling between the forward and backward going waves inside the cavity becomes wavelength dependent.

Similar to the lasing condition derived for the FP laser [5], one can readily find the resonance condition for the DBR laser by following an approach of matching the traveling wave with itself after a

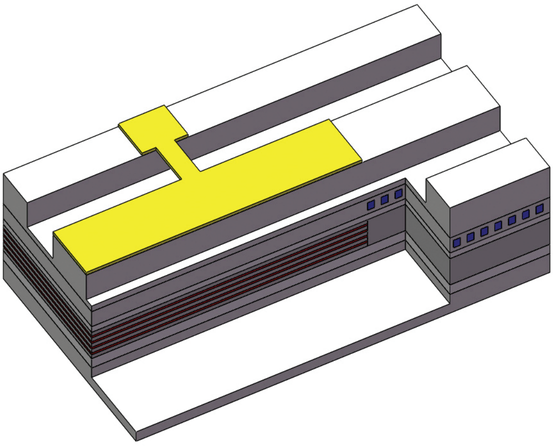

FIGURE 30.4 The DBR laser structure.

round trip inside the cavity:

$$R_l(\lambda)R_r(\lambda)e^{2[g-\alpha_i+j\frac{2\pi n_{\text{eff}}}{\lambda}]L_{ar}} = 1 \tag{30.13}$$

with R_l and R_r denoting the wavelength-dependent amplitude reflectivity of the Bragg grating reflector on the left and right end of the active region, respectively, given in the form of (Equation 30.10), g the modal gain, α_{i} the modal internal loss, and L_{ar} the active region length. One can further split the lasing condition (Equation 30.13) into the amplitude and phase condition as

$$g = g_{th} \equiv \alpha_{\text{i}} + \alpha_{\text{c}} \equiv \alpha_i + \frac{1}{2L_{\text{ar}}} \ln \frac{1}{|R_l(\lambda)||R_r(\lambda)|} \tag{30.14}$$

and

$$\frac{4\pi n_{\text{eff}} L_{ar}}{\lambda} + \phi_l(\lambda) + \phi_r(\lambda) = 2\pi m, \ \ m = 1, 2, 3, \ldots \tag{30.15}$$

where ϕ_{l} and ϕ_{r} indicate the phase of the amplitude reflectivity of the Bragg grating on the left and right end, respectively. It is clear that, following Equation 30.14, only the wave at the Bragg wavelength sees the highest reflection and consequently has the smallest cavity loss defined by $\alpha_{\text{c}} \equiv -(0.5/L_{\text{ar}})\ln(|R_{\text{l}}||R_{\text{r}}|)$, since at least one of the end reflectors will offer the highest reflection (i.e., either R_{l}, or R_{r}, or both will take the largest value) at the Bragg wavelength following the grating reflection spectrum shown in Figure 30.3. It then requires the smallest modal gain to reach the threshold in the neighborhood of the Bragg wavelength. It is not as clear though, following Equation 30.15, that one can find a solution to λ in the neighborhood of the Bragg wavelength, not going beyond $\lambda_B^2/(2n_{\text{eff}}L_{\text{ar}})$, with λ_B indicating the Bragg wavelength ($2n_{\text{eff}}\Lambda$). Actually, if one takes $\lambda = \lambda_{\text{B}} + \Delta\lambda$ ($\Delta\lambda \sim \lambda_{\text{B}}^2/(2n_{\text{eff}}L_{\text{ar}}) << \lambda_{\text{B}}$) in Equation 30.15 to obtain

$$2\pi\Delta\lambda\left(\frac{2n_{\text{eff}}L_{\text{ar}}}{\lambda_{\text{B}}^2}\right) = \frac{4\pi n_{\text{eff}}L_{\text{ar}}}{\lambda_{\text{B}}} + \phi_l(\lambda) + \phi_r(\lambda) - 2\pi m \tag{30.16}$$

and also to notice that the total phase on the right hand side of Equation 30.16 is a slow-varying function of λ in the neighborhood of λ_{B} following Figure 30.3, one immediately finds that as $\Delta\lambda$ changes from 0 to $\lambda_{\text{B}}^2/(2n_{\text{eff}}L_{\text{ar}})$, the total phase on the left-hand side of Equation 30.16 sweeps over an entire range of 2π, which means that the phase on the two sides of Equation 30.16 will have a matching point within the interval between λ_B and $\lambda_B \pm \lambda_B^2/(2n_{\text{eff}}L_{ar})$, given the fact that the phase takes 2π as its modulo. One therefore reaches the conclusion that the phase condition (Equation 30.15) always has a solution in a close neighborhood of the Bragg wavelength bound by $\lambda_{\text{B}}^2/(2n_{\text{eff}}L_{\text{ar}})$. Consequently, one knows that the amplitude condition (Equation 30.14) and the phase condition (Equation 30.15) jointly select a single lasing wavelength near the Bragg stop-band center of the end grating reflector. This explains why the DBR laser operates under the SLM.

The main advantage of the DBR laser lies in the separation of its gain and wavelength selection (i.e., the passive Bragg grating) region. Since the grating region is not biased, the wavelength selection mechanism suffers little change with the injection current in the gain region. One then expects a stable SLM operation with high side-mode-suppression-ratio (SMSR) and small wavelength chirp, which is evidenced by many publications [22,23]. It is also quite convenient to introduce a lasing wavelength tuning in DBR laser, as one can readily bias the grating region by a separate electrode from the gain region. As such, the current injection in the grating region introduces an effective index change, since the carrier-induced gain/loss change will have an accompany refractive index change following the Kramers–Kronig relation. Therefore, the peak reflection wavelength (the Bragg wavelength) given by Equation 30.4 will change with the current injected in the grating region, which causes the lasing wavelength change accordingly. Usually, a phase adjustment section needs to be inserted between the gain and the grating region to separately tune the phase for matching the lasing condition, as otherwise the DBR laser may cease lasing or experience a lasing mode hopping due to the mismatch of the phase condition. However, since the grating region has to be made transparent to the lasing wavelength, as otherwise the light will be absorbed by the unbiased passive grating region if it has the same band-gap with the active region, the fabrication of DBR lasers inevitably involves the monolithic integration technique that still stands as an unsolved problem up to today, for its low yield. With the birth of silicon photonics in the recent decade, it is quite promising to make the Si photonics DBR laser by bonding a direct band-gaped III-V compound semiconductor gain block on top of the silicon-on-insulator (SOI) waveguide, with the Bragg grating engraved on SOI. There is a hope that the DBR laser will be reborn with the booming Si photonics.

30.2.3 Distributed Feedback Lasers

A typical pure refractive index-coupled uniform-grating DFB laser has a structure shown in Figure 30.5. Unlike the DBR laser with a gain region made of smooth waveguide separated from the passive grating region, the DFB laser has these two regions merged into one, which makes the laser cavity substantially different from the aforementioned FP or DBR structures in the sense that the forward and backward going waves are constantly coupled in a distributive manner inside the cavity rather than in a lumped sum manner at the two ends of the cavity only. A wavelength discrimination mechanism is therefore brought in by such distributed coupling, since only the waves at the phase matched wavelength(s) will possibly add constructively to establish a standing wave pattern (i.e., a longitudinal mode) inside the cavity, which imposes a stringent condition that may likely purifies the lasing spectrum by cutting off most of the cavity modes otherwise allowed in the FP cavity.

An immediate finding is that this structure won't have its lasing wavelength at the Bragg wavelength anymore. This is because the wave near the Bragg wavelength sees the highest reflection. It therefore cannot travel far along the waveguide grating that also provides the gain. Consequently, it cannot obtain sufficient gain as required for the lasing to happen. On the contrary, at the Bragg stop band edge where the grating offers zero-reflection as shown in Figure 30.3, a maximum transmission through the grating region is obtained. Although the wave at this particular wavelength experiences the highest single-pass gain as it sees the entire length of the grating (with gain), it cannot be the lasing mode either since no reflection happens to it so that no resonance can be established. In this sense, the lasing should happen somewhere in between, i.e., the traveling waves at the lasing wavelength should be partially reflected by the grating to

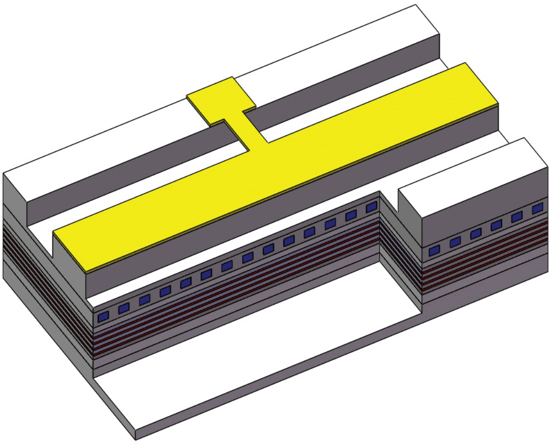

FIGURE 30.5 The DFB laser structure.

establish the resonance. It should be partially transmitted in order to experience the gain in the grating region as well. As such, the phase matching and amplitude sustenance (gain) conditions must be mixed.

Following the same thought, i.e., searching for the consistent condition between the wave and itself after a round trip inside the cavity, one can still obtain the resonance condition for the DFB cavity [24], which will stand as the lasing condition of the DFB laser. In the general case, however, one cannot expect to have analytical expressions for such lasing condition, so that we will cover the general case by the full numerical model introduced later. To gain an insight into the DFB laser, we will analyze a simple case with both of the end facet reflections and longitudinal spatial horn burning (LSHB) effect neglected. Actually, the lasing condition of such a simple DFB laser can be found by setting the denominator of Equation 30.10 and/or Equation 30.11 equal to zero. The associated infinite reflection and transmission indicate that the device can offer output without input—a feature must be carried by an oscillator. Hence one has

$$\gamma \coth(\gamma L) = \alpha + j\delta, \;\; \gamma^2 = (\alpha + j\delta)^2 + \kappa_+\kappa_- \tag{30.17}$$

Usually, for a given $\kappa_\pm L$ as the grating design parameter, one solves for γL from

$$(\gamma L)^2 \coth^2(\gamma L) = (\gamma L)^2 - \kappa_+\kappa_- L^2 \tag{30.18}$$

which has the same solution set as Equation 30.17. Hence the normalized gain (αL) and detuning (δL) can be found by

$$\alpha L + j\delta L = \pm\sqrt{(\gamma L)^2 - \kappa_+\kappa_- L^2} \tag{30.19}$$

from which one will be able to obtain the lasing modal threshold gain (from $g_{\text{th}} \equiv \alpha_\text{i} + \alpha$, α_i the modal internal loss) and the lasing wavelength (by solving $\delta = 2\pi[n_{\text{eff}}/\lambda - 1/(2\Lambda)]$ for λ). The normalized gain (αL) and detuning (δL) for different normalized grating coupling coefficient ($\kappa_\pm L$) are plotted in Figure 30.6, as the solution to Equations 30.18 and 30.19 obtained by a numerical root searching program built on Muller's algorithm [25].

The threshold gain solution indicates that, in a similar role as $\alpha_c = -(0.5/L)\ln(|R_\text{l}||R_\text{r}|)$ to the FP or DBR cavity, α, as the cavity loss to the DFB cavity, is in proportion to $1/(\kappa L)$. For a DFB grating design

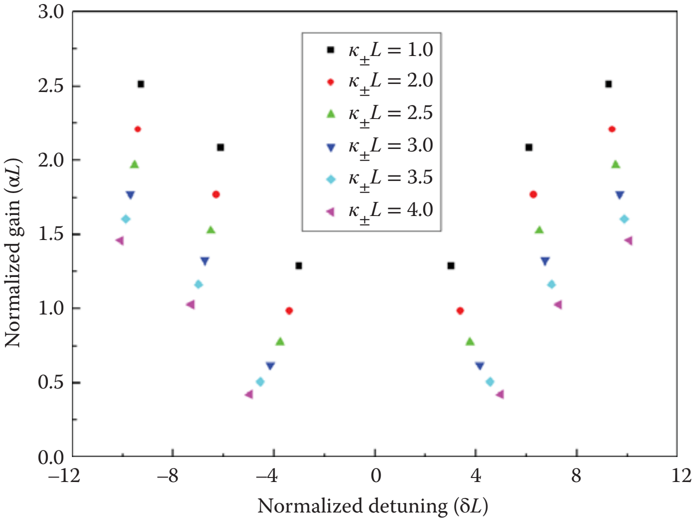

FIGURE 30.6 $\alpha L \sim \delta L$ for different $\kappa_\pm L$ as solutions to Equations 30.18 and 30.19.

with a higher $\kappa_{\pm}$, the cavity is more closed as an FP or DBR cavity with a higher end reflection R, and with the cavity length scaled in the same way. This conclusion, together with the above discussion on its lasing wavelength position, stands as the most basic design guidance for the DFB laser. Also for the DFB laser with high $\kappa_{\pm}L$ design, its cavity loss reduces so as the required modal gain to reach the lasing threshold, the lasing wavelength will therefore approach more closely to the zero-reflection wavelengths, as the wave may have sufficient gain to reach its threshold through fewer passes, and consequently less reflection is necessary. Namely, as the threshold gain approaches to zero, the lasing will happen near the Bragg stop-band edge. Hence one finds that the lasing wavelength of the DFB laser with higher $\kappa_{\pm}L$ should be closer to the zero-reflection wavelength of the unbiased grating, i.e., the Bragg stop-band edge.

A serious issue with the purely refractive index-coupled uniform-grating DFB laser is, however, its dual-mode operation nature originated from the double degeneracy caused by the center mirror-symmetry (or antisymmetry) of the cavity. It is quite obvious that, from Equation 30.18, for any real $\kappa_{+}\kappa_{-}$, once γ is a solution, $-\gamma$ and $\pm\gamma^{*}$ are all solutions. Hence for any solution set (α, δ), $(\pm\alpha, \pm\delta)$ are all possible solutions according to Equation 30.19, which means that for any modal gain required to reach the lasing threshold, also known as the DFB laser cavity loss (α as a solution to the lasing condition), there is a double degeneracy of the lasing wavelength corresponding to $\pm\delta$, respectively. These two lasing wavelengths sit on each side of the Bragg wavelength, and approach to the Bragg stop-band edges as $\kappa_{\pm}L$ increases, in consistency with previous analysis. Physically, this effect can be explained by the two equally possible standing wave patterns shown in Figure 30.7a. In a DFB laser cavity with the center mirror-symmetry ($L/\Lambda = n + 1/2$, n is an integer) or center mirror-antisymmetry ($L/\Lambda = n$ is an integer) and with zero end facet reflections (the latter condition can actually be further relaxed to identical end facet reflections), there exist two possible standing wave patterns as a result of the constructive addition of the distributively coupled forward and backward going waves. They share the same gain inside the cavity and have the identical cavity loss. The only difference between the two patterns is that one of them has its intensity peak aligned with the high refractive index region in every period, whereas the other one has its intensity peak aligned with the low refractive index region in every period. As such, the former and latter pattern will see the cavity mainly in high and low refractive index, respectively. Consequently, the former and latter will take the longer (red) and shorter (blue) lasing wavelength, respectively, on each side of the center Bragg wavelength. The double degenerated longitudinal mode with different standing wave pattern at different lasing wavelength but with

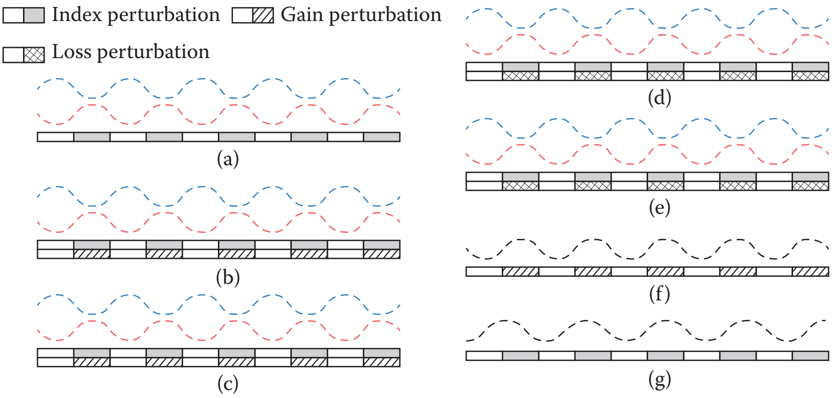

FIGURE 30.7 Schematic diagrams for (a) purely refractive index-coupled uniform-grating DFB, (b) partially gain-coupled in-phase DFB, (c) partially gain-coupled antiphase DFB, (d) partially loss-coupled in-phase DFB, (e) partially loss-coupled antiphase-grating DFB, (f) purely gain-coupled DFB, (g) quarter-wavelength phase-shifted (QWPS) DFB; the blue and red dashed lines in (a)–(e) show the intensity standing wave patterns of the longitudinal modes bearing the short and long wavelength (on the blue and red side of the Bragg wavelength), respectively; the black dashed line in (f) and (g) shows the intensity standing wave pattern of the longitudinal mode bearing the Bragg wavelength.

the same threshold gain breaches the SLM operation condition, which makes the purely refractive index-coupled uniform-grating DFB with a perfect center mirror-symmetric (or antisymmetric) cavity not a SLM laser.

This conclusion can also be generalized to any cavity with the perfect center mirror-symmetry or center mirror-anti-symmetry, once its reflection (or transmission) spectrum is symmetric, a necessary condition to reach the SLM operation is to have its lasing wavelength right in the center of the spectrum. Otherwise, dual-mode operation is inevitable. By recalling the lasing condition for the DBR laser, one may conclude that, in order to ensure its SLM operation with high SMSR, one has to either somehow break the symmetry (or anti-symmetry) of the cavity by, e.g., introducing two slightly different end reflection gratings (usually with slightly misaligned Bragg wavelengths) or use the grating reflector on one end only, or to ensure that the solution to the phase condition (Equation 30.15) is at the Bragg wavelength so that the lasing will happen exactly in the reflection spectrum center.

Since it is impossible to make the purely refractive index-coupled uniform-grating DFB lase at the Bragg wavelength, a conclusion not only drawn from the analysis at the beginning of the discussion on DFB lasers, but also known by the lasing condition (Equation 30.18). This is because for real $\kappa_+\kappa_-L^2$, real γL cannot be a solution as otherwise, the right-hand side is smaller than γL whereas the left-hand side is bigger than γL, hence γL must be complex, which leaves $\delta \neq 0$. The only viable way to reach the SLM operation for such DFB laser is then to break the cavity symmetry (or antisymmetry) by introducing asymmetric facet coatings on the two ends, usually a combination of the AR coating for the front facet and the high-reflection (HR) coating for the rear facet, respectively. However, the SLM yield with high SMSR for such DFB laser is still low since the grating phase at the two ends is usually random, given the condition that the grating period is in 1/5~1/4 of a micrometer whereas the uncertainty of the facet cleaving position is in a range of $\pm(2 \sim 3)\mu m$. Particularly for those DFB lasers with high $\kappa_\pm L$ designs, they usually suffer from very poor SLM yield (only ~15% for $SMSR > 30$ dB with $\kappa_\pm L > 3$) [26]. This is because the DFB laser with high $\kappa_\pm L$ tends to have the envelope of the standing wave pattern piled up in the middle, rather than at the two ends, of the cavity, due to the strong coupling, which makes the cavity less affected by the end facet condition as the waves inside the cavity simply don't "feel" much about the existence of the cavity ends. As a result, the end facet asymmetry applied on a strongly coupled DFB cavity is not sufficient to break the degenerated threshold gain between the two modes. Hence one finds that high $\kappa_\pm L$ often triggers dual mode lasing in DFB lasers. Figure 30.8 shows the standing wave envelope distributions inside the DFB cavity under different coupling strengths, from which one finds that the field stays at the two ends, or piles up in the middle of the cavity, corresponding to the weak (with $\kappa_\pm L < \pi/2$), or strong (with $\kappa_\pm L > \pi/2$) coupling condition, respectively. And the field takes almost an even distribution along the cavity under the critical condition $\kappa_\pm L = \pi/2$, as it has to be.

To thoroughly solve the dual-mode operation problem associated with the purely refractive index-coupled uniform-grating DFB laser, one can have different approaches along with the thought of breaking the cavity symmetry, or forcing the lase at the Bragg wavelength. While the former led to the invention of various complex-coupled DFB lasers [27–30], the latter resulted in the popular product of the QWPS DFB laser [31].

Figure 30.7b shows the working principle of the in-phase partially gain-coupled DFB laser. As an extra gain is introduced periodically inside the high refractive index region, the longitudinal mode with its intensity peak in its standing wave pattern located in the high refractive index region in each period obtains more gain than the other mode, hence the degeneracy between the two longitudinal modes breaks and only the mode with the longer wavelength (on the right/red side of the Bragg wavelength) will lase, which makes such DFB laser operate under SLM. Figure 30.7c shows the working principle by taking the other option to boost the longitudinal mode bearing the shorter wavelength (on the left/blue side of the Bragg wavelength). Known as the antiphase partially gain-coupled DFB laser, the structure has an extra gain introduced periodically inside the low refractive index region, which again breaks the degeneracy between the two longitudinal modes since the longitudinal mode with its intensity peak in its standing wave pattern located in the low refractive index region in each period has more gain than the other

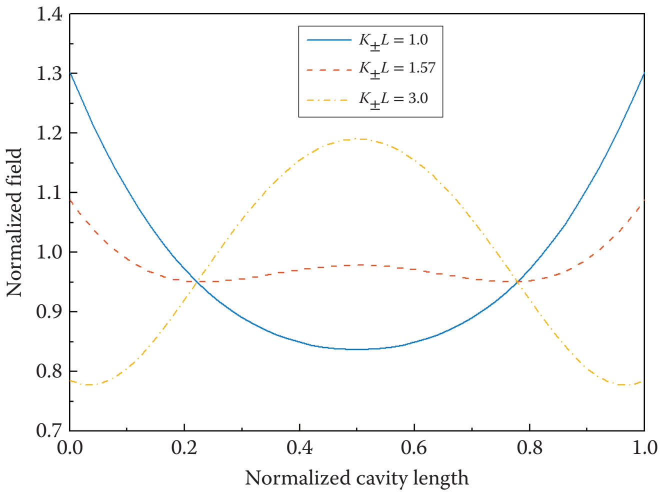

FIGURE 30.8 Field envelope distributions inside the DFB cavity for $\kappa_{\pm}L = 1.0(< 1.57)$, $\kappa_{\pm}L \sim 1.57$, and $\kappa_{\pm}L = 3.0(> 1.57)$.

mode. As a result, only the shorter wavelength mode will lase, which again makes such DFB laser operate under SLM.

Figure 30.7d and e shows the working mechanisms of the partially loss-coupled in-phase and antiphase DFB lasers, respectively. If an extra loss is introduced periodically inside the high (or low) refractive index region, the longitudinal mode with its intensity peak in its standing wave pattern located in the high (or low) refractive index region in each period suffers from more loss than the other mode, hence the degeneracy between the two longitudinal modes breaks and only the mode with the shorter (or longer) wavelength on the left/blue (or right/red) side of the Bragg wavelength will lase, due to the suppression of its counterpart on the other side of the Bragg wavelength, which makes such DFB laser operate under SLM.

One can also understand why the degeneracy breaks in such partially gain- or loss-coupled DFB lasers by the lasing condition (Equation 30.18). For complex-coupled DFBs, $\kappa_+\kappa_-L^2$ is also complex or $\kappa_+\kappa_-L^2 \neq (\kappa_+\kappa_-L^2)^*$. As such, if γ is a solution, γ^* is not necessarily a solution. Following Equation 30.19, one then finds that $\pm\delta$ cannot share the same α as the solutions.

Figure 30.7f shows the working principle of the purely gain-coupled DFB laser. Since the purely gain-coupled laser has a purely negative $\kappa_+\kappa_-$ ($\kappa_- = -\kappa_+^*, \kappa_+\kappa_- = -\kappa_+\kappa_+^* \equiv -|\kappa|^2$), which makes the lasing condition (Equation 30.18) turn into

$$(\gamma L)^2 \coth^2(\gamma L) = (\gamma L)^2 + (|\kappa|L)^2 \tag{30.20}$$

a real solution of γ is then possible which forces the lasing happen at the Bragg wavelength according to Equation 30.19, or

$$\alpha L + j\delta L = \sqrt{(\gamma L)^2 + (|\kappa|L)^2} \tag{30.21}$$

from which one readily achieve $\delta = 0$ for the right-hand side is real. The dual mode lasing in purely gain-coupled DFB laser is not possible as one cannot find two different standing wave patterns inside the cavity that share the same gain. It is obvious that only a single standing wave pattern is allowed inside the cavity with itself completely aligned with the gain grating. Any standing wave pattern in different shape with the gain grating will naturally be suppressed. Therefore, one knows that Equation 30.20 cannot have a complex

γ as its solution associated with the longitudinal mode with the lowest cavity loss (α). As otherwise, γ^* will be an allowed solution as well, according to Equation 30.21, one will then be able to have a pair of lasing wavelengths corresponding to the doubly degenerated solutions $(\alpha, \pm\delta)$, which is in conflict against our previous physics-based analysis on the purely gain-coupled DFB laser cavity. Namely, solution $(\alpha, 0)$ must take the smallest cavity loss $\alpha = \alpha_{\text{min}}$, while any other possible doubly degenerated solutions in the form of $(\alpha, \pm\delta)$ with $\delta \neq 0$ must have a higher cavity loss $\alpha > \alpha_{\text{min}}$ hence cannot be the lasing modes. This conclusion has been evidenced by a numerical searching for all possible solutions of Equation 30.20 [32]. Finally, one may conclude that the purely gain-coupled DFB laser will lase at the Bragg wavelength and naturally stands as the SLM laser.

Figure 30.7g shows the working mechanism of the QWPS DFB laser. The only difference from the uniform-grating purely refractive index-coupled DFB is that there is an extra half period of the grating inserted right at the cavity center. An extra half period of the grating is equivalent to a quarter-wavelength phase shift in the first-order grating following the relationship between the grating period and the Bragg wavelength $\Lambda = \lambda_B/(2n_{\text{eff}})$, which therefore introduces a π phase shift to the reflected wave or a π phase shift to the round trip wave. As such, the wave will have to make two round trips to recover its status, which leads to its resonance. This feature suggests us to fold back the cavity from the center to equivalent the original structure to a uniform-grating DFB with half of its original length and with a perfect facet with 100% reflectivity at one end (the original cavity center). In such a half cavity equivalent structure, if the standing wave pattern has its intensity peak originally aligned with the high refractive index region in every period, upon the 100% reflection at one end, the peak will have to be aligned with the low refractive index region in every period, and vice versa. As such, none of the two original standing wave patterns inside the uniform-grating DFB can exist inside the modified cavity with a quarter-wavelength phase shift introduced at the cavity center. Rather, only a standing wave pattern with its peak aligned at the edge of the grating tooth (i.e., the interface of the high and low refractive index region) in every period can stay. This standing wave pattern is unique inside the cavity and corresponds to the longitudinal mode at the Bragg wavelength, for it sees an averaged refractive index between the high and low index region in every period, which happens to be the effective index of the unperturbed waveguide by the grating. Also physically, a longitudinal mode with its envelope piled up in the middle of the cavity will see the highest reflection from both sides if it bears the Bragg wavelength. Hence this mode will be most tightly confined inside the cavity and sees the most gain. Consequently, it should have the lowest cavity loss and becomes the lasing mode. The numerically calculated longitudinal mode distribution along the cavity of such structure confirms this conclusion [33] as one finds that, with its lasing mode always at the Bragg wavelength, the QWPS DFB laser has a sharp longitudinal mode distribution peak at the center of the cavity. In a uniform-grating DFB without a phase-shifted center inside the cavity, this scenario can never happen, as the maximum reflection at the Bragg wavelength can only be possibly seen by the wave from one side rather than from both sides. Hence the wave at the Bragg wavelength cannot stay long inside the cavity to obtain sufficient gain for lasing, a same conclusion drawn earlier for the uniform-grating purely refractive index-coupled DFB laser. It is worth mentioning that a more detailed analysis would have to have a new lasing condition involved as Equation 30.17 is no longer valid for either a nonuniform grating (the grating with a phase shift) or a uniform grating with nonzero end facet reflection (the equivalently folded cavity with a uniform grating plus 100% reflection at one end). From the newly derived lasing condition for this structure, one will be able to find that $\delta = 0$ is indeed an allowed solution that has the minimum cavity loss ($\alpha = \alpha_{\text{min}}$) [34]. Therefore, the QWPS DFB laser always operates under the SLM and has its lasing mode at the Bragg wavelength.

30.2.4 Governing Equations for Design, Modeling, and Simulation

The following one-dimensional (along the propagation direction, z) traveling wave model is often used as the optical governing equation for the edge-emitting semiconductor lasers with various waveguide-grating structures [16]:

$$\begin{aligned}
\left(\frac{1}{v_g}\frac{\partial}{\partial t}+\frac{\partial}{\partial z}\right)e^f(z,t) &= [j\left(\frac{2\pi n_{\text{eff}}}{\lambda_0}-\frac{\pi}{\Lambda}\right)+j\frac{2\pi}{\lambda_0}\Gamma\Delta n(z,t,\omega_0)\\
&\quad+\frac{1}{2}\Gamma g(z,t,\omega_0)-\frac{1}{2}\alpha_L]e^f(z,t)+j\kappa_+e^b(z,t)+s^f(z,t)\\
\left(\frac{1}{v_g}\frac{\partial}{\partial t}-\frac{\partial}{\partial z}\right)e^b(z,t) &= [j\left(\frac{2\pi n_{\text{eff}}}{\lambda_0}-\frac{\pi}{\Lambda}\right)+j\frac{2\pi}{\lambda_0}\Gamma\Delta n(z,t,\omega_0)\\
&\quad+\frac{1}{2}\Gamma g(z,t,\omega_0)-\frac{1}{2}\alpha_L]e^b(z,t)+j\kappa_-e^f(z,t)+s^b(z,t)
\end{aligned}\tag{30.22}$$

where $e^{f,b}$ denote the slow-varying envelopes of the forward and backward going traveling wave field, respectively, g and Δn the material gain and refractive index change, respectively, α_L the non-interband optical modal loss, ω_0 the reference optical frequency, $\lambda_0 = 2\pi c/\omega_0$ the reference optical wavelength (i.e., the vacuum wavelength of the reference optical frequency), $v_g = c/n_g$ the group velocity, n_{eff} and Γ the effective index (of the waveguide) and confinement factor (of the active region), respectively, Λ and $\kappa_\pm$ the period, the backward-to-forward (+), and the forward-to-backward (−) coupling coefficient of the first-order waveguide Bragg grating, respectively, $s^f = s^b \equiv \tilde{s}$ the spontaneous emission contributions.

The associated optical field can be expressed as

$$\vec{E}(x,y,z,t)=\frac{1}{2}\vec{s}\varphi(x,y)[e^f(z,t)e^{j\frac{\pi}{\Lambda}z}+e^b(z,t)e^{-j\frac{\pi}{\Lambda}z}]e^{-j\omega_0 t}+c.c. \tag{30.23}$$

with $\vec{s}$ indicating the unit vector of along the (linear) field polarization direction, φ the field distribution of the waveguide mode as the solution of Equation 30.9. For a given waveguide-grating structure, one needs to solve Equation 30.9 first to find the effective index (n_{eff}) and the guided mode field distribution (φ). The coupling coefficients ($\kappa_\pm = \kappa_{\pm 1}$) can then be obtained from Equation 30.8 and the confinement factor is given as

$$\Gamma=\int_{A.R.}|\varphi(x,y)|^2dxdy\Big/\int_{\Sigma}|\varphi(x,y)|^2dxdy \tag{30.24}$$

with the integration areas $A.R.$ and Σ indicating the active region (quantum wells) only and the whole area where the optical field extends.

Equation 30.22 is obtained from the optical wave equation under the slow-varying envelope approximation with the second-order derivatives of the envelope ($\partial^2 e^{f,b}/\partial z^2$ and $\partial^2 e^{f,b}/\partial t^2$) all ignored, whereas the optical wave equation is directly obtained from the Maxwell equations with the coupling among the field polarization components $\nabla(\nabla\cdot\vec{E})$ ignored. The former is true for the edge-emitting device with its cavity length L much longer than the operating wavelength λ (usually L is in a few hundreds to a thousand of λ/n_{eff}), in which the optical wave is propagating along the cavity with its traveling wave factors $\phi_\pm = e^{j(\pm\pi z/\Lambda-\omega_0 t)}$ varying much faster as z and t, hence:

$$\begin{aligned}
|\partial^2 e^{f,b}/\partial z^2/e^{f,b}| &<< |\partial^2\phi_\pm/\partial z^2/\phi_\pm| = (\pi/\Lambda)^2\\
|\partial^2 e^{f,b}/\partial t^2/e^{f,b}| &<< |\partial^2\phi_\pm/\partial t^2/\phi_\pm| = \omega_0^2
\end{aligned}\tag{30.25}$$

The latter assumption holds for the weakly confined waveguide, which is generally true of most of the III–V compound semiconductor laser diodes with either ridge waveguide or buried heterojunction structures.

In the field expansion (Equation 30.23), the single-guided-mode assumption has been invoked as a necessary condition for the SLM operation. As different guided modes have different effective indices, for the same grating period Λ, different wavelengths will be chosen to satisfy the phase-matching condition (Equation 30.4). As a result, multiple longitudinal modes in different lasing wavelengths, with each of them corresponding to a guided mode in a different effective index, will be excited, which breaches the SLM condition. A single polarization component is assumed for the same reason, but this is not necessary as the difference between the two effective indices corresponding to the two orthogonally polarized components in a guided mode is usually very small in weakly confined waveguides. As a result, the difference between their corresponding lasing wavelengths can hardly be appreciable. Actually, for most of the III–V compound semiconductor laser diodes, the active region is made of the compressively strained multiple quantum wells (CS-MQW). The compressively strained quantum well can only provide the optical gain in the (100) plane [35], which means only the TE mode with its optical E-field polarized in parallel to the slab waveguide interfaces, i.e., the interfaces of the layer stack grown in the usual <100>direction, can see the gain whereas the other polarization component, i.e., the TM mode with its E-field polarized in the perpendicular direction, will be completely suppressed. Therefore, it is usually sufficient to study the TE mode with its E-field horizontally polarized in parallel with the device top and bottom surfaces.

The material gain of semiconductors can generally be calculated by the physics-based first-principles model [16]. For performance simulation of the SLM laser, however, the following model that phenomenologically links the gain to the (minority) carrier density inside the active region is sufficient:

$$g(z,t,\omega_0) = a(\omega_0)\ln\frac{N(z,t)}{N_{\mathrm{tr}}(\omega_0)}/[1+\varepsilon(|e^f(z,t)|^2+|e^b(z,t)|^2)] \tag{30.26}$$

with $a(\omega_0)$ and $N_{\mathrm{tr}}(\omega_0)$ indicating the gain coefficient and the transparent (minority) carrier density for the active region comprising (strained-layer) multiple quantum wells, ε the nonlinear gain saturation factor. These parameters are usually extracted in the neighborhood of the reference optical frequency (ω_0) from the physics-based material gain model or measured experimentally.

The refractive index change and the material gain, corresponding to the real and imaginary part of the material susceptibility, are connected by the Kramers–Kronig relation. Actually, if one views the susceptibility as the frequency-domain transfer function of the material system in responding to the optical E-field as the input signal, the polarization excited by the optical E-field then becomes the output signal. Following the linear system theory, the time-domain polarization is given as the convolution of the time-domain optical E-field and the inverse Fourier transform of the susceptibility. Since a real physical system must be causal, which means the polarization at any time instant t can only be dependent on the optical E-field given before t, it imposes a strong constraint between the real and imaginary part of the susceptibility and is mathematically given in the form of the Kramers–Kronig transform. By noticing that the SLM laser is a typical narrow-band device with its lasing frequency in the neighborhood of the reference optical frequency (ω_0) and the Kramers–Kronig relation is linear, one can readily express the refractive index change as a linear function of the material gain:

$$\Delta n(z,t,\omega_0) = \alpha_{\mathrm{LEF}}g(z,t,\omega_0) \tag{30.27}$$

with α_{LEF} denoting the linewidth enhancement factor.

Finally, the carrier density inside the active region can be described by the following rate equation [16,36]:

$$\begin{aligned}\frac{\partial N(z,t)}{\partial t} &= \frac{I(z,t)}{qV} - [AN(z,t)+BN^2(z,t)+CN^3(z,t)] \\ &\quad - \frac{n_{\mathrm{eff}}}{2\hbar\omega_0}\sqrt{\frac{\varepsilon_0}{\mu_0}}\frac{L\Gamma}{V}g(z,t,\omega_0)[|e^f(z,t)|^2+|e^b(z,t)|^2]\end{aligned} \tag{30.28}$$

where I represents the bias current; q the unit electron charge; V the active region volume; A, B, and C the minority carrier Shockley–Read–Hall (SRH); bimolecular and spontaneous emission, and Auger recombination coefficients, respectively; $\hbar$ Plank constant; $\sqrt{\varepsilon_0/\mu_0} \approx 1/377[\mathrm{S}]$ the vacuum admittance; and L the active region length (along the cavity direction). Given the fact that the active region of the laser diode has a low (unintentional) doping concentration and the potential drop across it is usually negligible, a quasi-neutrality condition holds and consequently the electrons and holes have the same density inside the active region—we therefore don't have to distinguish the electron and hole density and simply use the term "carrier density" to indicate both.

As the seed of the lasing process, the spontaneous emission contribution cannot be ignored at the beginning as otherwise Equation 30.22 becomes homogenous and only the trivial zero solution exists. Once the lasing starts, i.e., for the device operated under a bias beyond the threshold, however, the contribution from the spontaneous emission becomes negligible, which is reflected as a fact that the self-consistent solution of the above set of equations always converges to the same value regardless of the excitation method of the spontaneous emission, as long as the spontaneously emitted noise power is self-consistently described. The spontaneous emission contribution is usually assigned as a Gaussian distributed zero-mean random variable with its autocorrelation function normalized by the spontaneously emitted noise power [16]:

$$< |\tilde{s}(z,t)||\tilde{s}(z',t')| > = \frac{2\hbar\omega_0}{n_{\text{eff}}}\sqrt{\frac{\mu_0}{\varepsilon_0}}\gamma\Gamma n_{sp} g(z,t,\omega_0)\delta(z-z')\delta(t-t') \tag{30.29}$$

where γ denotes the dimensionless coefficient of the coupling from the spontaneous emission to the entire spatial sphere and over the whole frequency spectrum to the waveguide mode at the reference optical frequency, n_{sp} the dimensionless ratio of the spontaneous emission to stimulated emission gain, and δ the Dirac function.

Equations 30.22, and 30.26 through 30.29 form a closed loop for one to find a set of self-consistent solution on the (minority) carrier density inside the active region (N), the material gain (g), and the slow-varying envelopes of the forward and backward going traveling wave field ($e^{f,b}$), for any given bias (I), with Equations 30.9, 30.8 and 30.24 presolved for a given SLM laser structure. Consequently, the optical field inside the laser can be found through Equation 30.23 and other physics quantities for characterizing the laser, such as the output optical power and the lasing wavelength, can readily be found [16,37]. An efficient solution technique for solving Equation 30.22 is to use the time-domain split-step method [38], with Equation 30.28 solved by the well-known Runge–Kutta method [39].

To describe the thermal effect, one still needs to add on the thermal diffusion equation [40] and to modify the empirical formulas for the material gain and refractive index change by considering their temperature dependence [16]. However, we will exclude the thermal description in this model to focus our study on the SLM operation aspect of semiconductor laser diodes.

30.2.5 Examples of SLM Laser Characteristics

By exploiting the aforementioned model, one can calculate the device performance for SLM DFB lasers with a few different types of grating structures as discussed in Section 30.2.3, shown in Figures 30.5 and 30.7. Figures 30.9 through 30.14 show the numerical simulation results of the output optical power and lasing wavelength as functions of the bias, the optical spectra at a fixed bias, the normalized optical field intensity and (minority) carrier density distributions along the cavity, and the small-signal intensity modulation responses for the purely refractive index-coupled uniform-grating DFB, partially gain/loss-coupled in/antiphase DFB, purely gain-coupled DFB, and QWPS DFB, respectively, with those device parameters involved in the model summarized in Table 30.1.

From Figure 30.9, one finds that while all DFB lasers have similar threshold current, the loss-coupled and QWPS DFB lasers have lower slope efficiency. This is expected for loss-coupled DFB lasers as their loss-coupling coefficient introduces an extra contribution equivalent to the non-interband optical modal

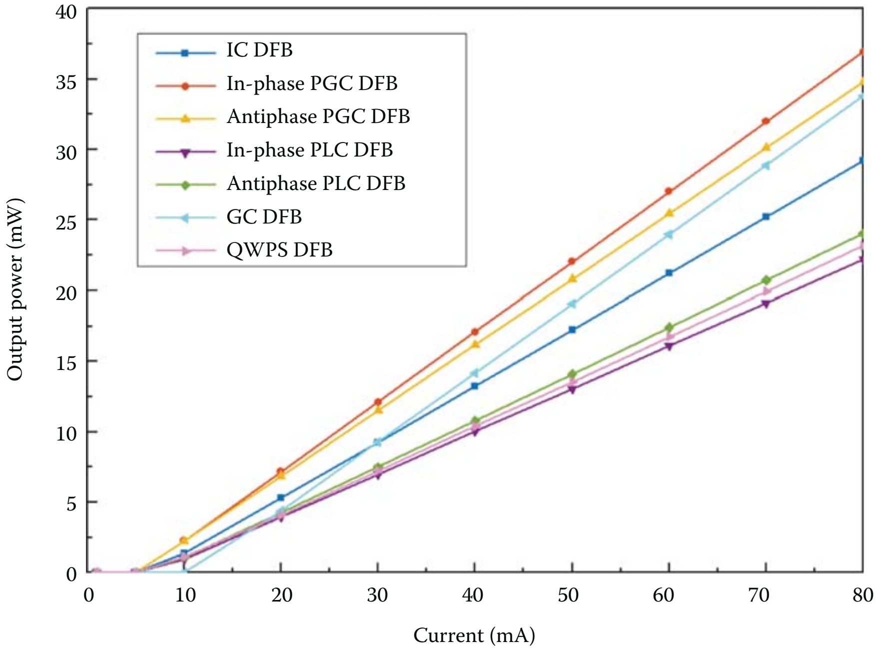

FIGURE 30.9 Output power–bias current curves for different DFB lasers. IC = (purely refractive) index-coupled (uniform grating), PGC = partially gain-coupled, PLC = partially loss-coupled, GC = (purely) gain-coupled, QWPS = quarter-wavelength phase-shifted.

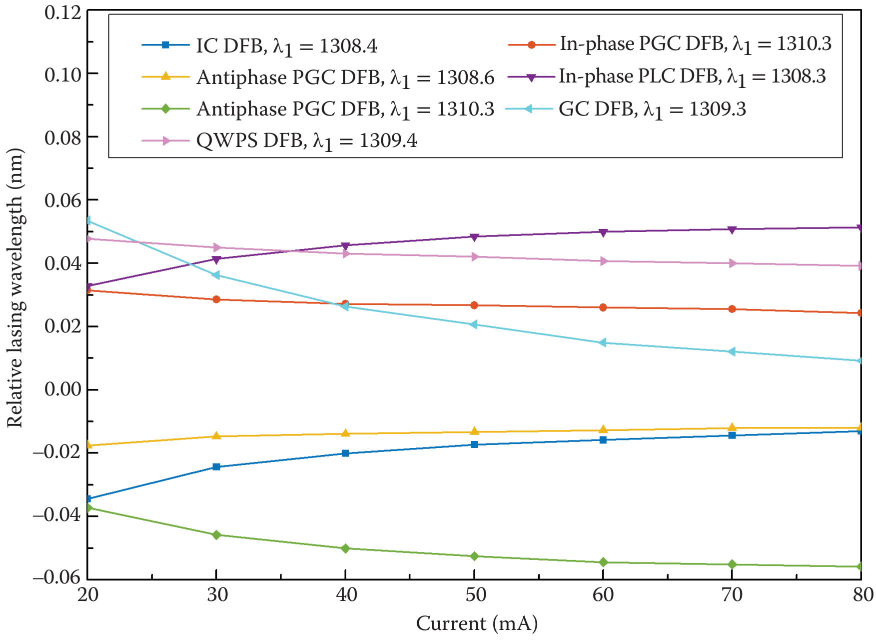

FIGURE 30.10 Relative lasing wavelength shift–bias current curves for different DFB lasers. IC = (purely refractive) index-coupled (uniform grating), PGC = partially gain-coupled, PLC = partially loss-coupled, GC = (purely) gain-coupled, QWPS = quarter-wavelength phase-shifted; the relative lasing wavelength shift is defined as λ-λ_l, with λ indicating the lasing wavelength at any bias current > 20 mA and λ_l the lasing wavelength at bias current = 20 mA for different DFB lasers under comparison.

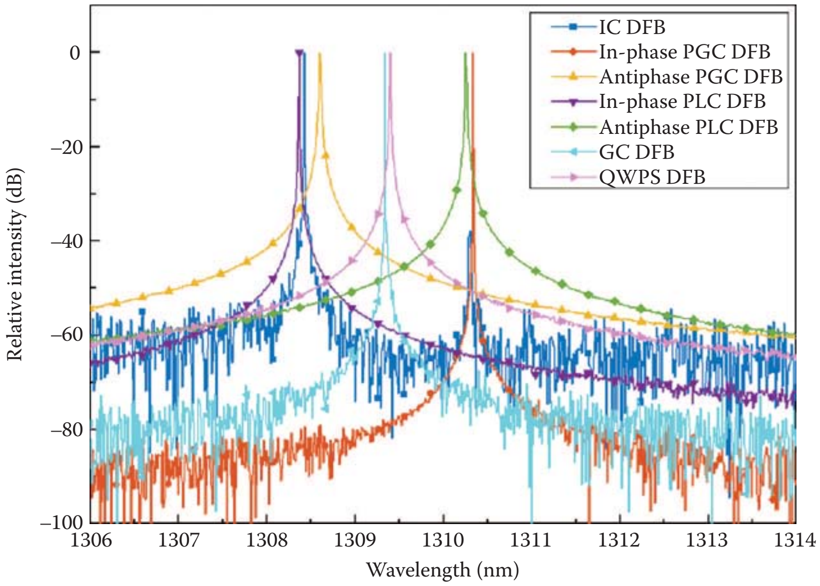

FIGURE 30.11 Lasing spectra for different DFB lasers. IC = (purely refractive) index-coupled (uniform grating), PGC = partially gain-coupled, PLC = partially loss-coupled, GC = (purely) gain-coupled, QWPS = quarter-wavelength phase-shifted.

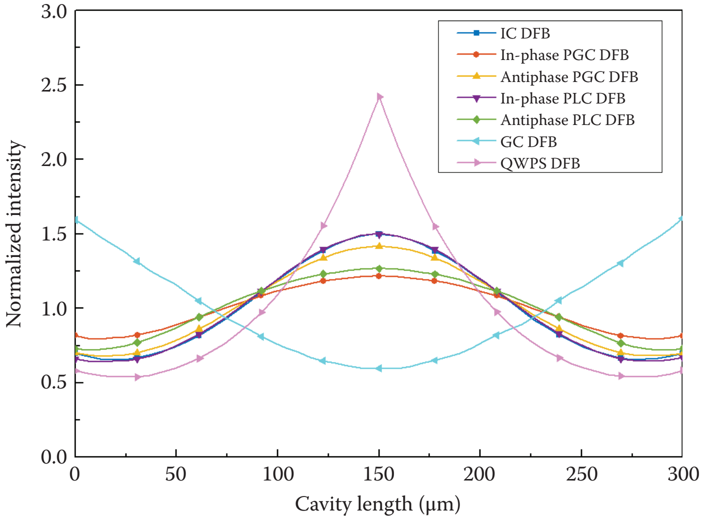

FIGURE 30.12 Normalized optical field intensity distributions for different DFB lasers. IC = (purely refractive) index-coupled (uniform grating), PGC = partially gain-coupled, PLC = partially loss-coupled, GC = (purely) gain-coupled, QWPS = quarter-wavelength phase-shifted.

loss (α_L). As shown in Table 30.1, the assumed non-interband optical modal loss is 10/cm, the normalized loss-coupling coefficient 0.5 would give an extra optical loss around 0.5/L = 0.5/(0.03 cm) ~17/cm. The total optical loss 27/cm indicates a significant increase as compared the original value in 10/cm. Since the slope efficiency is inversely proportional to the optical modal loss, higher loss would certainly cause a lower efficiency. The low slope efficiency of the QWPS DFB laser, however, is not caused by the high

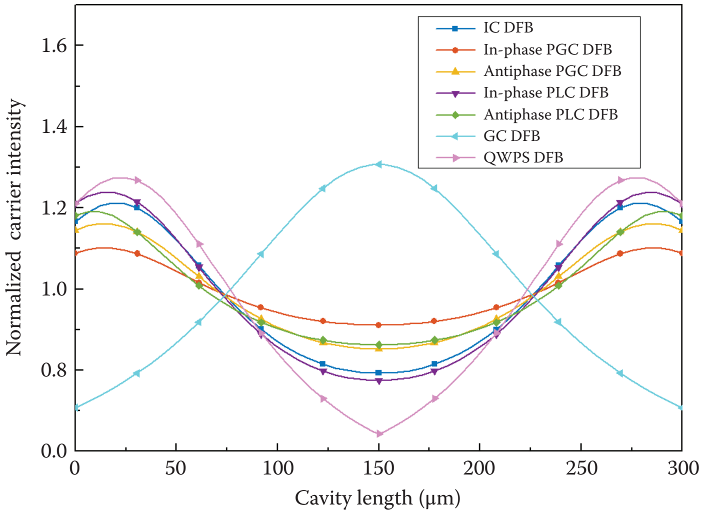

FIGURE 30.13 Normalized (minority) carrier density distributions for different DFB lasers. IC = (purely refractive) index-coupled (uniform grating), PGC = partially gain-coupled, PLC = partially loss-coupled, GC = (purely) gain-coupled, QWPS = quarter-wavelength phase-shifted.

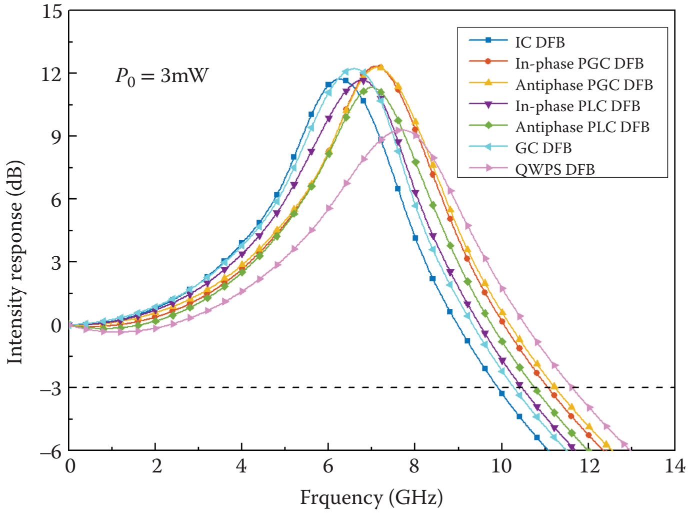

FIGURE 30.14 Small-signal intensity modulation responses for different DFB lasers. IC = (purely refractive) index-coupled (uniform grating), PGC = partially gain-coupled, PLC = partially loss-coupled, GC = (purely) gain-coupled, QWPS = quarter-wavelength phase-shifted.

optical modal loss, but by the low cavity loss. Since this structure has its field intensity mostly concentrated in the middle of the cavity, such a field pattern tends to retain more photons inside the cavity and consequently leads to a low output power by the low field distribution at both facets. This is consistent with our understanding on QWPS DFB as a high Q (quality)-factor laser with low cavity loss. Still because the slope efficiency is determined by the cavity loss over the summation of the cavity loss and the optical modal loss, apparently a low cavity loss will lead to a low slope efficiency once the optical modal loss is a nonvanishing positive value.

TABLE 30.1 Model Parameters

Model Parameter	Value
Cavity length L (μm)	300
Thickness of the quantum well (nm)	5
Number of quantum wells	6
Reflectivity of both laser facets	0, 0
Group index n_g	3.6
Effective index n_{eff}	3.2
Confinement factor Γ	0.06
Ridge width (μm)	2
Normalized index coupling coefficient	2.5
Normalized gain coupling coefficient	0.5
Normalized loss coupling coefficient	0.5
Grating period Λ (nm)	204.7
Gain coefficient a (cm^{-1})	1800
Transparent carrier density N_{tr} (10^{18} cm^{-3})	0.8
Linewidth enhancement factor α_{LEF}	−3
Nonlinear gain saturation factor ε (10^{-2} V^{-2})	9
SRH recombination coefficient A (10^{9} s^{-1})	1
Bimolecular and spontaneous emission recombination coefficient B (10^{-10} cm^{-3}s^{-1})	2
Auger recombination coefficient C (10^{-29} cm^{-6} s^{-1})	4
Non-interband modal loss α_L (cm^{-1})	10
Spontaneous emission coupling coefficient γ	10^{-4}
Spontaneous emission over stimulated emission ration_{sp}	1.7
Reference wavelength λ_0 (μm)	1.310

As ideal laser characteristics, the carrier density as well as the averaged gain should be clamped after lasing, but this is true only when the carrier density and optical field intensity both have uniform distributions along the cavity. In DFB lasers, however, the carrier density and optical field intensity have nonuniform distributions in "opposite" shapes as shown in Figure 30.12. Also, following the Schwartz nonequality, one knows the fact that the overlap integration between two functions with different shapes must be smaller than that between two functions in a similar shape. Under higher bias current, stronger LSHB makes the carrier density and optical field intensity distribution shapes more unlike. As a quantity directly in proportion to the overlap integration of the carrier density and optical field intensity distributions along the cavity, the averaged gain will be smaller. To maintain the lasing status, i.e., to balance the cavity loss plus the optical non-interband modal loss, the carrier density will have to increase with the bias current in order to compensate the "lost" averaged gain due to the enhanced LSHB. The increased carrier density will therefore cause a refractive index reduction of the active region following the Kramers–Kronig relation, which is simplified as Equation 30.27 with the negative linewidth enhancement factor (α_{LEF}). The reduction of the active region refractive index brings down the effective index of the waveguide and consequently makes the Bragg wavelength as well as the whole Bragg stop-band shift toward the shorter wavelength side, according to Equation 30.4 ($\lambda_B = 2n_{\text{eff}}\Lambda$). This effect is indeed reflected in Figure 30.10 by the blueshift with the increased bias current of the lasing wavelengths of the QWPS DFB and GC DFB lasers, located right in the center of the Bragg stop-band (or at the Bragg wavelength).

Figure 30.10 also shows that, without the thermal effect considered in simulation, the lasing wavelengths of the DFB lasers on the left (blue) side the Bragg stop-band (i.e., the IC DFB, the antiphase PGC DFB, and the in-phase PLC DFB; see Figure 30.11) have redshift toward the longer wavelength side with increased bias current, whereas the lasing wavelengths of the DFB lasers on the right (red) side (i.e., the in-phase PGC DFB and the antiphase PLC DFB; see Figure 30.11) take blueshift toward the shorter wavelength side. This is brought in by the shrinkage of the Bragg stop-band width due to the enhanced LSHB with the increased bias current, which further suggests an effective normalized coupling coefficient reduction or a more opened (lower Q-factor) cavity in accompanying with the stronger LSHB under higher injection level.

Figure 30.11 clearly shows that the QWPS and purely gain-coupled DFB lasers lase at the Bragg wavelength, whereas the in-phase and antiphase partially gain-coupled DFB lasers have their lasing wavelengths at the right (red) and left (blue) side of the Bragg stop-band, respectively. The in-phase and antiphase partially loss-coupled DFB lasers have their lasing wavelengths located the other way around, at the left (blue) and right (red) side of the Bragg stop-band, respectively. Finally, the purely refractive index-coupled DFB laser picks the left (blue) side wavelength rather randomly, with a relatively poor SMSR as expected. All these findings are consistent with previous analysis on these DFB lasers with different grating designs.

From Figure 30.12, one finds that the QWPS DFB laser has its field intensity mostly gathered in the middle of the cavity, as opposed to the purely gain-coupled DFB laser with its field intensity largely concentrated at both edges. The former cavity obviously bears the highest Q-factor or smallest cavity loss, whereas the latter one must correspond to the lowest Q-factor or highest cavity loss. Since the threshold current is proportional to the cavity loss, and the slope efficiency also increases with the cavity loss, the high Q-factor QWPS DFB laser bearing a low cavity loss has a low threshold current and a low slope efficiency. On the contrary, the low Q-factor purely gain-coupled DFB laser bearing a high cavity loss has a high threshold current as well as a high slope efficiency. This result has been confirmed by Figure 30.9 exactly. Other DFB lasers have their field intensities more evenly distributed and have their cavity losses in between. Consequently, they have their threshold current and slope efficiency values in between as shown in Figure 30.9. It is also worth mentioning that the sharp field turning in the middle of the QWPS DFB laser cavity is brought in by the half grating period shift exactly at the same location.

All carrier density distributions take the opposite shape as compared to their optical field intensity distributions. This result is expected as the carriers inside the cavity are consumed to generate photons, indicating a low carrier density wherever the optical field intensity is high, and vice versa.

Simulation result shows that there is no significant difference in terms of the 3 dB small-signal intensity modulation bandwidth among different DFB lasers once they are set to output the same optical power. This is quite different from the result obtained in References [41,42], in which the antiphase partially gain-coupled DFB laser shows a significantly broader 3 dB small-signal intensity modulation bandwidth in comparison with its in-phase counterpart. The inconsistency might come from the different selection on device parameters and further investigation is still needed before a final conclusion can be achieved.

30.3 Coupled-Cavity Single Longitudinal Mode Laser Diodes

30.3.1 A General Optical (Band-Pass) Filtering Model

The conventional FP cavity supports many closely packed longitudinal cavity modes with their spacing given in the form of Equation 30.2. For the edge-emitting laser with its cavity length (L) much longer than the center wavelength (λ_0), the mode spacing is much smaller than the full width at half maximum (FWHM) of the material gain peak. As such, multiple longitudinal modes can lase simultaneously, which makes a typical edge-emitting FP laser operate under the multiple longitudinal mode lasing scheme. Other than the aforementioned grating-assisted methods by introducing the wavelength-selective end reflectors (DBR), or by exploiting various DFB cavities, to achieve the SLM operation, one can still take an alternative approach by inserting an optical (band-pass) filter into the FP cavity to eliminate all other longitudinal cavity modes but leave only one for lasing. This approach is generally known as the coupled-cavity laser that forms the other category of SLM lasers, if we don't count in various external cavity SLM laser configurations.

For a coupled-cavity laser generally presented in the form of an FP cavity with an inserted OBPF shown in Figure 30.15, we have [43]:

$$\begin{bmatrix} A_{\text{out}} \\ B_{\text{out}} \end{bmatrix} = \frac{1}{T^2}\begin{bmatrix} 1 & -R \\ -R & 1 \end{bmatrix}\begin{bmatrix} e^{j\varphi_2} & 0 \\ 0 & e^{-j\varphi_2} \end{bmatrix}\frac{1}{t_{21}}\begin{bmatrix} t_{12}t_{21} - r_{12}r_{21} & r_{21} \\ -r_{12} & 1 \end{bmatrix}\begin{bmatrix} e^{j\varphi_1} & 0 \\ 0 & e^{-j\varphi_1} \end{bmatrix}\begin{bmatrix} 1 & R \\ R & 1 \end{bmatrix}\begin{bmatrix} A_{\text{in}} \\ B_{\text{in}} \end{bmatrix} \tag{30.30}$$

with $A_{\text{in,out}}$ and $B_{\text{in,out}}$ denoting the optical field amplitude of the forward and backward propagating waves, with their subscript "in" and "out" indicating the assumed input and output port on the left- and right-hand sides, respectively. One should note that the optical field is polarized in the cross-sectional plane perpendicular to the cavity direction. The arrows associated with them in Figure 30.15 indicate their propagation direction, not their polarization direction. Also in Equation 30.30, R and T indicate the amplitude reflectivity and transmissivity of the end facets when looking from inside of the FP cavity, $r_{12,21}$ the amplitude reflectivities when looking from the FP cavity to the OBPF on the left- and right-hand sides, $t_{12,21}$ the amplitude transmissivities from left to right and from right to left when staying inside the FP cavity, respectively. Finally, $\varphi_{1,2}$ are the phase delays of the wave traveling through the two sections ($L_{1,2}$) of the FP cavity separated by the OBPF.

Equation 30.30 can readily be simplified to

$$\begin{aligned} \begin{bmatrix} A_{\text{out}} \\ B_{\text{out}} \end{bmatrix} &= \frac{1}{t_{21}T^2}\begin{bmatrix} e^{j\varphi_2} & -Re^{-j\varphi_2} \\ -Re^{j\varphi_2} & e^{-j\varphi_2} \end{bmatrix}\begin{bmatrix} \delta & r_{21} \\ -r_{12} & 1 \end{bmatrix}\begin{bmatrix} e^{j\varphi_1} & Re^{j\varphi_1} \\ Re^{-j\varphi_1} & e^{-j\varphi_1} \end{bmatrix}\begin{bmatrix} A_{\text{in}} \\ B_{\text{in}} \end{bmatrix} \\ &\equiv \frac{1}{t_{21}T^2}\begin{bmatrix} A_{11} & A_{12} \\ A_{21} & A_{22} \end{bmatrix}\begin{bmatrix} A_{\text{in}} \\ B_{\text{in}} \end{bmatrix} \end{aligned}, \tag{30.31}$$

where

$$\delta \equiv t_{12}t_{21} - r_{12}r_{21} \text{ and } A_{22} \equiv e^{-j(\varphi_2+\varphi_1)} - r_{12}Re^{-j(\varphi_2-\varphi_1)} - r_{21}Re^{j(\varphi_2-\varphi_1)} - \delta R^2 e^{j(\varphi_2+\varphi_1)} \tag{30.32}$$

The lasing condition is therefore obtained as $A_{\text{in}} = B_{\text{out}} = 0$, but A_{out} and B_{in} are not zero, which requires $A_{22} = 0$, or:

$$[r_{12}e^{-j(\varphi_2-\varphi_1)} + r_{21}e^{j(\varphi_2-\varphi_1)}]Re^{j(\varphi_2+\varphi_1)} + \delta R^2 e^{2j(\varphi_2+\varphi_1)} = 1 \tag{30.33}$$

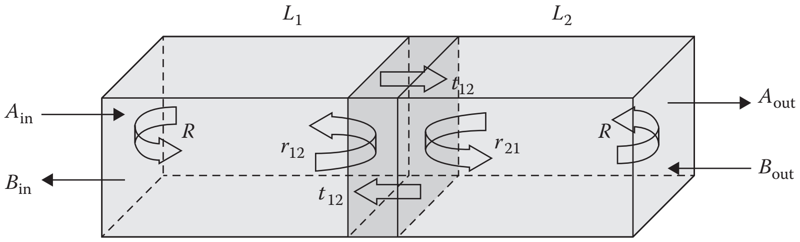

FIGURE 30.15 An illustrative diagram showing the FP cavity with an inserted optical band-pass filter (OBPF), with A_{in} and B_{in}, A_{out} and B_{out} indicating the optical field amplitudes of the forward and backward propagating waves at the input and output port, respectively; r_{12} and t_{12} the amplitude reflectivity and transmissivity from the left section to the inserted OBPF; r_{21} and t_{21} the amplitude reflectivity and transmissivity from the right section to the inserted OBPF; $L_{1,2}$ the lengths of the left and right section, respectively; R the end facet amplitude reflectivity of the FP cavity.

1. FP cavity
   It is obvious that once we remove the OBPF by letting $r_{12} = r_{21} = 0$ and $\delta = 1$, Equation 30.33 reduces to the well-known lasing condition of the FP laser:

$$R^2 e^{2j(\varphi_2+\varphi_1)} = 1 \tag{30.34}$$

2. Bidirectional symmetric filter
   Once the OBPF has the bidirectional symmetry, by letting

$$r_{12} = r_{21} = jre^{j\theta} \tag{30.35}$$

and

$$t_{12} = t_{21} = te^{j\theta} \tag{30.36}$$

we have

$$\delta = (t^2 + r^2)e^{2j\theta} \equiv (1 - l)e^{2j\theta} \tag{30.37}$$

where θ and l stand for the single pass phase and loss of the filter, respectively. Hence we find from Equation 30.33:

$$2jrR\cos(\varphi_2 - \varphi_1)e^{j(\varphi_2+\varphi_1+\theta)} + (1 - l)R^2 e^{2j(\varphi_2+\varphi_1+\theta)} = 1 \tag{30.38}$$

It is apparent that Equation 30.38 can be rewritten as

$$\bar{R}^2 e^{2j(\varphi_2+\varphi_1+\theta)} = 1, \text{ with } \bar{R} \equiv \sqrt{\frac{1 - l}{1 - 2rR\cos(\varphi_2 - \varphi_1)e^{j(\varphi_2+\varphi_1+\theta+\pi/2)}}}\,R \tag{30.39}$$

Unlike in Equation 30.34 where the amplitude reflectivity of the end facets R is a constant for a conventional FP laser, a coupled-cavity laser comprising an FP cavity with an inserted bidirectional symmetric filter has a wavelength-dependent effective amplitude reflectivity in its lasing condition, which, conceptually similar to the lasing condition of the DBR laser given as Equation 30.13, provides an extra wavelength selection mechanism to make a conventional FP laser single-moded. For example, if the inserted filter is lossless ($l = 0$), Equation 30.39 shows that the modification on the lasing condition from the original FP cavity is determined by the reflection (r) and length (θ) of the filter and its position inserted inside the FP cavity (φ_1 and φ_2). It is possible that, within the wavelength range set by the gain spectrum bandwidth, there is a single wavelength that makes $1 - 2rR\cos(\varphi_2 - \varphi_1)e^{j(\varphi_2+\varphi_1+\theta+\pi/2)} = 1 - 2|r|R$, and $2(\varphi_1 + \varphi_2 + \theta) = 2m\pi$, with m as an integer. Hence $\bar{R}$ will be the maximum with the round trip phase-matching condition satisfied at this wavelength. As a result, the lasing will only happen at this wavelength and such a general coupled-cavity structure supports SLM operation.

In the fabrication of real-world coupled-cavity lasers, the OBPF is usually formed by an equivalent FP etalon. The filter reflectivity and transmissivity in Equations 30.35 and 30.36 can then be derived from Equation 30.30 itself with the inserted filter removed from the FP cavity in Figure 30.15. By doing so, we find that Equation 30.30 reduces to

$$\begin{aligned}
\begin{bmatrix} A'_{\text{out}} \\ B'_{\text{out}} \end{bmatrix} &= \frac{1}{T'^2}\begin{bmatrix} 1 & -R' \\ -R' & 1 \end{bmatrix}\begin{bmatrix} e^{j\varphi'} & 0 \\ 0 & e^{-j\varphi'} \end{bmatrix}\begin{bmatrix} 1 & R' \\ R' & 1 \end{bmatrix}\begin{bmatrix} A'_{\text{in}} \\ B'_{\text{in}} \end{bmatrix} \\
&= \frac{1}{T'^2}\begin{bmatrix} e^{j\varphi'}(1 - R'^2 e^{-2j\varphi'}) & 2jR'\sin\varphi' \\ -2jR'\sin\varphi' & e^{-j\varphi'}(1 - R'^2 e^{2j\varphi'}) \end{bmatrix}\begin{bmatrix} A'_{\text{in}} \\ B'_{\text{in}} \end{bmatrix}
\end{aligned}$$

with the prime symbols added to the variables and parameters to differentiate them from those being used in Equation 30.30 for the most outside FP cavity in Figure 30.15. In the absence of the incident light coming from the left-hand side, $B'_{\text{out}} = 0$, we have

$$R_f \equiv \frac{B'_{\text{in}}}{A'_{\text{in}}} = j\frac{2R' \sin\varphi' e^{j\varphi'}}{1 - R'^2 e^{2j\varphi'}}, \text{ and } T_f \equiv \frac{A'_{\text{out}}}{A'_{\text{in}}} = \frac{T'^2 e^{j\varphi'}}{1 - R'^2 e^{2j\varphi'}}$$

Since the common factor $1/(1 - R'^2 e^{2j\varphi'})$ in abovementioned expressions can be expanded in a form of

$$1 + R'^2 e^{2j\varphi'} + (R'^2 e^{2j\varphi'})^2 + \ldots$$

which means that $j2R' \sin\varphi' e^{j\varphi'}$ and $T'^2 e^{j\varphi'}$ are the single pass reflectivity and transmissivity, respectively, Equations 30.35 and 30.36 are valid once we take

$$r = 2R' \sin\varphi' \tag{30.40}$$

$$t = T'^2 \tag{30.41}$$

and

$$\theta = \varphi' \tag{30.42}$$

Equations 30.35 through 30.37 and Equations 30.40 through 30.42 therefore link the model parameters to the design parameters of the physical structure.

30.3.2 Cleaved-Coupled-Cavity (C^3) Laser

A typical cleaved-coupled-cavity (C^3) laser has a structure shown in Figure 30.16.

Following the general coupled-cavity laser model derived in Section 30.3.1, we have

$$R' = (n_{\text{eff}} - 1)/(n_{\text{eff}} + 1) \tag{30.43}$$

$$T'^2 = 4n_{\text{eff}}/(n_{\text{eff}} + 1)^2 \tag{30.44}$$

$$\varphi' = 2\pi d/\lambda \tag{30.45}$$

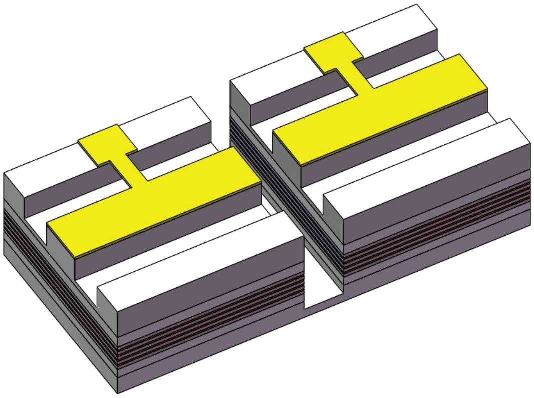

FIGURE 30.16 The C^3 laser structure.

with n_{eff} denoted as the laser waveguide effective index and d the air gap spacing between the pair of coupled cavities. By noting

$$\varphi_{1,2} = [2\pi n_{\text{eff}}/\lambda - j(g - \alpha_i)]L_{1,2} \tag{30.46}$$

and using Equations 30.40 through 30.42, one can express the lasing condition (Equation 30.39) in terms of the C^3 laser design parameters ($n_{\text{eff}}, d, g, \alpha_i, L_{1,2}$). The SLM lasing condition can therefore be found by a proper combination of the two cavity lengths ($L_{1,2}$) and the air gap spacing (d).

A major issue in the fabrication of the C^3 laser is the optical alignment between the two cavities, if the air gap will be formed by cleaving. One can certainly think of using the etching technology to form the air gap, the quality of the facet; however, cannot be guaranteed unless the chemically assisted ion beam etching (CAIBE) is exploited [44]. With CAIBE, the precise control of the air gap spacing becomes difficult, especially when the required spacing is no more than a few micrometers. An elegant approach to form the C^3 laser with a narrow air gap is the microcleaving technique [45]. In this technique, after the air gap section is defined, a selective wet (chemical) etching step is applied first to remove the material (InP) surrounding the active region (InGaAsP or AlGaInAs) inside the air gap, which leaves the latter as a thin bridge hanging over in the middle. The wafer or bar is then soaked inside some liquid and placed inside an ultrasonic cleaning bath for breaking down the active region bridge inside the air gap. The facet formed by this approach has a quality equivalent to the one obtained by the conventional cleaving technique. Since the etching of the air gap won't go very deep after passing though the active region, there is no optical alignment problem as the pair of coupled cavities still sits on top of the same substrate.

Despite its readiness in fabrication [46], the C^3 structure never becomes a popular SLM laser product for its low single-mode yield and the reliability concern. The low yield comes from the sensitive phase-matching condition, which requires precise control on cavity geometrical dimensions, including both cavity lengths and the air gap spacing, as well as the effective index of the waveguide. Since the latter depends not only on the material composition and cross-sectional geometrical dimension design, but also on operating conditions such as the ambient temperature and injection current, it naturally has a very low probability to hit the stable SLM operation condition with a high SMSR over an entire bias range. The reliability concern comes from the extra pair of facets appeared in the C^3 structure, especially when it is difficult to get them protected with dielectric coating layers, for the coating is not only difficult to be applied to the narrow air gap, but also changes the lasing condition.

Figure 30.17 shows the simulated optical spectrum of a typical SLM C^3 laser, with its structural parameter given in Table 30.2, and other parameters the same as those given in Table 30.1.

30.3.3 Etched Slotted Laser

An alternative version of the coupled-cavity structure is the etched slotted SLM laser [47–50] with its typical structure shown in Figure 30.18. The main difference lies in that the coupled cavities in such structure are formed by one or multiple etched slots across the waveguide without passing through the active region. As such, there is no optical alignment issue as the coupled-cavity device still stays as a whole piece. There is no reliability concern either as no extra active region cross section is exposed other than the usual end facets. The major drawback of this structure as compared to the C^3 laser is its much reduced reflectivity (r) of the equivalent OBPF as appeared in Equation 30.39 as the general lasing condition for coupled-cavity lasers. For an individual slot, its reflectivity is given by

$$R' = (n_{\text{eff}} - n'_{\text{eff}})/(n_{\text{eff}} + n'_{\text{eff}}) \tag{30.47}$$

with n_{eff} and n'_{eff} as the effective indices of the normal section and the waveguide inside the etched slot, respectively. As compared to the normal section, the etched slot only has its waveguide cladding layer

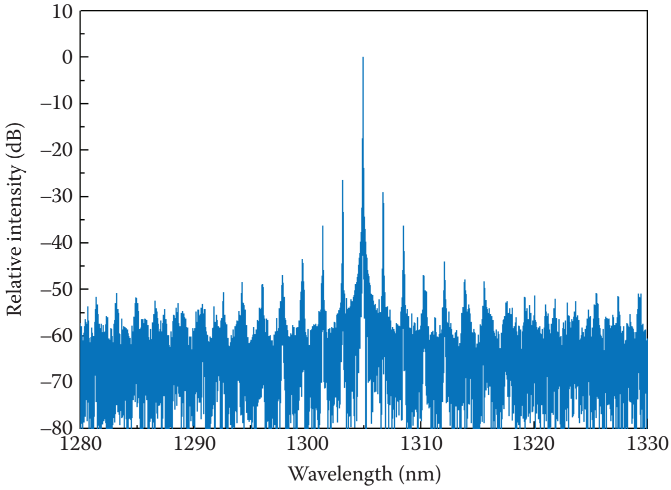

FIGURE 30.17 The simulated lasing spectrum of a typical SLM C^3 laser, with its parameters given in Table 30.2 and Table 30.1, respectively.

TABLE 30.2 C^3 Laser Parameters

Parameter	Value
Cavity lengths L_1, L_2 (μm)	136, 121 [46]
Gap between cavities d (μm)	5
Cleaved facet reflectivity r	0.565

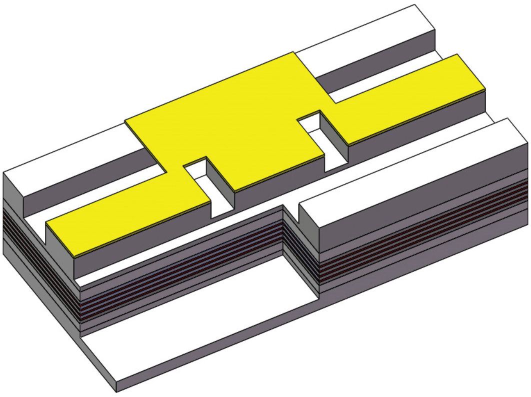

FIGURE 30.18 A typical etched slotted laser structure.

thinned to some extent, one then cannot expect a significant difference between n_{eff} and n'_{eff}. Therefore, R' given by Equation 30.47 is usually much smaller than the corresponding reflectivity in the C^3 laser given by Equation 30.43. From Equations 30.39 and 30.40, one knows that the contrast of the effective reflectivity $\bar{R}$ of the coupled-cavity laser at different wavelength will be reduce with a decreasing reflectivity R', Consequently, its ability on selecting the SLM drops significantly for the etched slotted laser.

To solve the poor mode selection problem, multiple etched slots have been introduced. A cascade of the structure in Figure 30.15 can be exploited to model such coupled-cavity laser with multiple etched slots.

A modified lasing condition similar to Equation 30.39 can also be derived with its effective reflectivity shown as a multiplication of multiple wavelength-dependent factors, with each of the factor corresponding to a single slot. As such, the wavelength spectral contrast of its effective reflectivity will be raised and its mode-selection ability will be improved. However, the multiple slotted coupled-cavity laser usually suffers an even lower single-mode yield, for the associated phase-matching condition becomes more complicated due to the introduction of multiple slots and the chance for it to be satisfied becomes rare.

30.3.4 Discrete Mode Laser

As shown in Figure 30.19, the discrete mode laser [51,52] can be viewed as a specific type of multiple slotted coupled-cavity laser with its slot's spacing properly designed to satisfy the phase-matching condition. As such, its single-mode yield can be significantly improved. With its general design rule given in Reference [52], the discrete mode laser is actually an SLM device between the grating-assisted laser and the coupled-cavity laser. It is apparent that, starting from a pair of coupled FP sections (i.e., the C^3 laser), as one increases the number of coupled FP sections with reduced reflectivities from section to section, and arranges the length of each FP section to satisfy certain phase-matching condition, one readily obtains various of grating-assisted lasers. As a special case, for a design with a uniform unit length from one FP section to another (Λ) selected to match the round trip phase-matching condition $4\pi n_{\mathrm{eff}}\Lambda/\lambda = 2\pi$, one obtains a DFB laser with the first-order Bragg grating, as the uniform unit length design forms a periodic structure (i.e., a grating) with its periodicity (Λ) specified exactly the same as Equation 30.4, the phase-matching condition for the first-order Bragg grating. Therefore, the concept of the discrete mode laser actually bridges the grating-assisted lasers and the coupled-cavity lasers as the two main categories of SLM lasers.

30.3.5 New Aspects in Governing Equations and the Solution Technique

In general, the governing Equations 30.22 through 30.29 can still be used in modeling the coupled-cavity lasers. Since there is no grating involved, π/Λ should be replaced by $2\pi n_{\mathrm{eff}}/\lambda$ with the grating coupling coefficients ($\kappa_{+,-}$) set to zero.

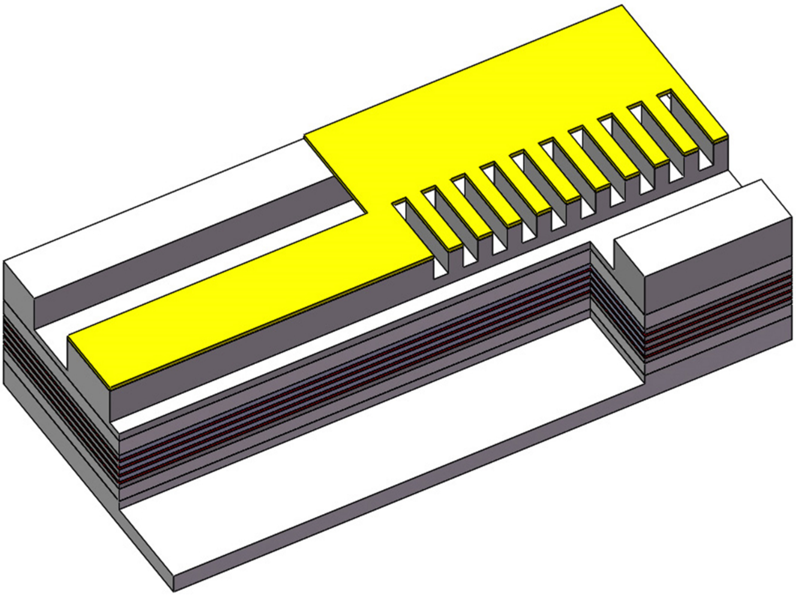

FIGURE 30.19 A typical discrete mode laser structure.

To treat the uniform sections in the coupled-cavity structure, the gain spectral dispersiveness must be considered to make sure that the lasing will happen in the neighborhood of the gain peak, as otherwise there will be no specific wavelength can be referred but the lasing cannot possibly happen at an arbitrary wavelength. Actually, the first term on the right-hand side of Equation 30.22 should be a time-domain convolution between the material gain and the field envelope, rather than be a product of them [53]. This term in its current form in Equation 30.22 is obtained under the assumption that the gain spectral bandwidth is much broader than the field envelope bandwidth, so that the time-domain gain performs as a Dirac δ-function in the convolution, which takes away the integration. For an SLM laser, the latter is usually determined by its linewidth or the modulation signal base bandwidth, whichever is broader, if the laser is under direct modulation. As the gain spectral bandwidth is usually in the range of 60 nm, whereas the field envelope bandwidth of an SLM laser usually is no more than 1 nm, the aforementioned assumption is indeed valid. To restore the gain dispersiveness in the coupled-cavity laser, however, this assumption has to be removed and a special solution technique will have to be introduced in dealing with the time-domain convolution between the material gain and the field envelope. An efficient way to treat the convolution in an initial value problem specified by a set of time-domain differential equations (or more accurately, a mixed initial-boundary value problem specified by a set of time-space domain partial differential equations) is the digital filtering method [16,54]. In this method, the material gain spectral profile is first calculated by the physics-based model within a limited wavelength range [16]. Its shape is then duplicated in the entire wavelength domain to form a periodic function, with nothing changed in its original wavelength range. The time-domain material gain can therefore found by taking the inverse Fourier transform of its spectral function. Since the latter function is turned into a periodic one, the time-domain gain therefore becomes a summation of a set of Dirac δ-functions, weighted by factors obtained as the corresponding coefficients in its Fourier expansion. Consequently, the convolution is reduced to a summation of a set of field envelopes, shifted in time domain and weighted by the said factors. For a given laser structure, these factors just need to be calculated once after the material gain spectral profile is obtained. The digital filtering method is, therefore, very efficient in handling the convolution in conjunction with the time-domain solution techniques, such as the split-step method, for solving Equation 30.22 [38,55].

Yet another problem often appearing in modeling the coupled-cavity laser is the involvement of the passive sections without injection. It is obvious that the material gain, the refractive index change, and the noise contribution in Equation 30.22 all need to be taken away for the passive sections. By noticing that Equation 30.22 become completely decoupled with the rest governing equations, one can solve these in frequency domain only for once to extract the reflectivity and transmissivity of the field envelope for these sections. In the rest (active) sections, the set of governing equations will be solved in time domain as described previously. Upon the propagating waves reach the boundary at the passive section, however, the reflected and transmitted field can be computed by taking the time-domain convolution between the incident field and the inverse Fourier transform of the reflectivity and transmissivity, respectively, as the reflectivity and transmissivity are both defined in frequency domain. Once again, the digital filtering approach can be employed in dealing with the time-domain convolution [56]. Since the reflectivity and transmissivity only need to be calculated once for a given structure, the convolution handled in such a way is very efficient. Generally, the mixed domain method, i.e., treating Equation 30.22 in time domain for active sections and in frequency domain for passive sections, is much more efficient compared with the full time-domain method, especially for passive units with long section lengths, because the frequency-domain treatment links the input and output fields of the passive section directly through transfer functions (i.e., the reflectivity and transmissivity, respectively) in a single step, without any step-by-step marching along the wave propagating direction as required by time-domain approaches.

30.3.6 Performance Comparisons among Coupled-Cavity SLM Lasers

The simulated performance of a few different types coupled-cavity SLM lasers is summarized in Table 30.3. A general tendency is that as the SMSR increases with the number of slots (i.e., the number of coupled

TABLE 30.3 Performance Comparison among Different Coupled-Cavity SLM Lasers

Laser Structure	SMSR (dB)	SLM Yield (SMSR> 15 dB)	SLM Yield (SMSR> 25 dB)
C^3 laser	12–32	60%	20%
Etched slotted laser (2 slots)	6–19	27%	0%
Discrete mode laser (5 slots)	11–29	73%	13%
Discrete mode laser (9 slots)	9–36	60%	40%
Discrete mode laser (19 slots)	7–49 (42, measured value in [52])	47%	33%

Note: The experimentally measured SMSR for a discrete mode laser with 19 slots is given in the brackets.

cavities), the SLM yield decreases. This result agrees with our conclusion drawn by the general OBPF model for the coupled-cavity structures, since the increased slot number enhances the wavelength spectral contrast of the effective reflectivity, thereby enhances the structure's mode selection ability, whereas it simultaneously introduces a more complicated phase-matching condition that is increasingly difficult to be satisfied.

30.4 Recent Development on Single Longitudinal Mode Laser Diode

30.4.1 Open Problems in SLM Lasers

Current SLM lasers are not yet ideal. Grating-assisted lasers generally suffer problems like high fabrication cost and highly sensitive to external feedback. The DBR laser needs the technology to monolithically integrate the active region with the passive grating section in different material compositions. The uniform-grating purely refractive index-coupled DFB laser has a relatively low single-mode yield, whereas the QWPS DFB laser has even poorer immunity to external feedback and wastes half of its output power, and complex-coupled DFB lasers usually have reliability issues. A variety of the grating-assisted laser structures have been proposed, but all as compromised approaches with none of them seeming to be able to solve all the aforementioned problems. Coupled-cavity lasers usually have low fabrication cost and less sensitive to external feedback. However, they all have low single-mode yield and suffer relatively low SMSR. Therefore, it still remains as an open problem on how to obtain reliable SLM lasers with high single-mode yield, high SMSR, high immunity to external feedback, and low fabrication cost.

In the past decade, some progress has been made toward the final solving of the remaining problems in SLM lasers, although most of the recent efforts on laser development have their targets on new applications found in data communication systems and telecommunication access networks with emphases on multiple wavelength accessibility and tunability, and high-speed direct modulation. Effort has also been put on developing SLM lasers with narrow linewidth to meet the strong demand in high-speed long-haul coherent telecommunication systems in advanced modulation-detection schemes with higher spectral efficiency. A thorough description on all these new developments is beyond the scope of this chapter, so that we will only give a brief introduction on the new structures that are closely relevant to SLM lasers.

30.4.2 Bragg Waveguide SLM Laser

A schematic structure of the Bragg waveguide SLM laser [57,58] is shown in Figure 30.20. Unlike the conventional SLM lasers that all utilize their cavity structure to select the single lasing mode, this structure exploits the waveguide itself to eliminate the unwanted modes in an FP cavity.

The working principle of the Bragg waveguide can be understood by a simplified model described in Figure 30.21. By exploiting the effective index method, one reduces the wave vector of an arbitrary plane traveling wave into a two-dimensional plane as shown in Figure 30.21. It can then be decomposed into a pair of orthogonal components, with the one along the waveguide direction (β) as the required wave

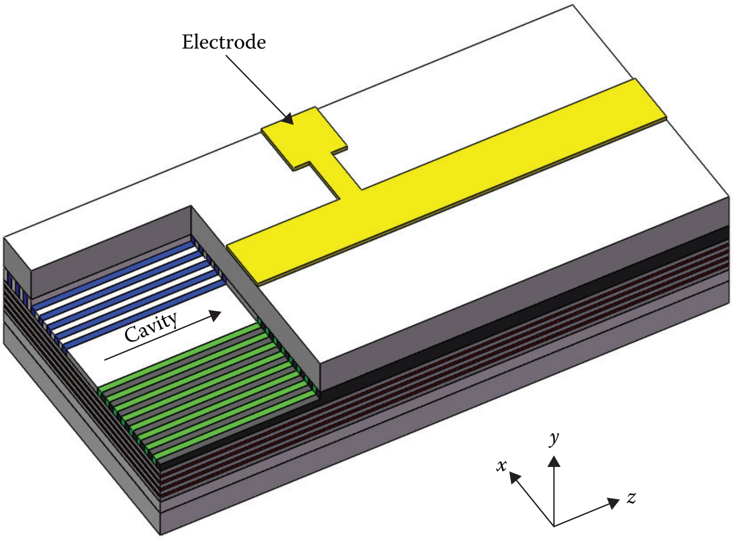

FIGURE 30.20 The Bragg waveguide SLM laser structure.

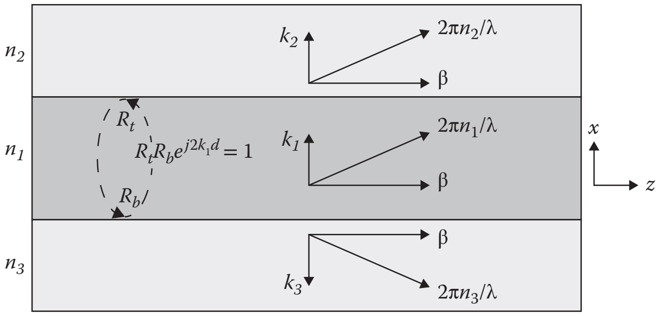

FIGURE 30.21 An illustrative diagram showing the concept of the dielectric waveguide, with $2\pi n_{1,2,3}/\lambda$ indicating the conceptual free-propagating plane wave numbers inside the core, the top cladding, and the bottom cladding layer, respectively, β their corresponding wave vectors' projection along the propagation (z) direction, $k_{1,2,3}$ their corresponding wave vectors' projections along the cross (x) direction in the core, the top cladding, and the bottom cladding layer, respectively, $R_{t,b}$ the amplitude reflectivities between the core and the top cladding layer, and between the core and the bottom cladding layer, respectively; $R_tR_be^{j2k_1d} = 1$ gives the resonance condition along the cross direction with d as the core layer thickness, which stands as the necessary and sufficient condition for guided waves in general waveguides.

propagation constant, the other along the cross direction (k_1) as the wave vector needs to be confined. For the wave component that propagates in the cross direction, a round trip travel would make the initial field E_0 become $E_0R_tR_be^{j2k_1d}$, with $R_{t,b}$ denoting the amplitude reflectivity between the core and the top cladding layer, and the core and the bottom cladding layer, respectively, and d the core layer thickness. Therefore, once the resonance happens in the cross direction, i.e.,

$$R_tR_be^{j2k_1d} = 1 \tag{30.48}$$

the field distribution along the cross direction remains the same at any cut along the waveguide direction, which means the wave is guided and propagates with β along the waveguide. This is actually a necessary and sufficient condition for a general waveguide, i.e., if and only if the wave resonates in the cross section, it will be guided by the waveguide. Consequently, the guided wave will form a standing wave pattern inside the core area of the waveguide, and will be either zero (for metallic waveguide) or evanescent (for dielectric waveguide) outside of the core. The guided wave's cross-sectional distribution doesn't change as the wave propagates along the waveguide. The only change on the wave as it propagates is its phase, scaled by $\beta z - \omega t$, with z and t indicating the space coordinate along the waveguide (i.e., in the wave propagation direction) and the time variable, respectively.

For the conventional dielectric waveguide that utilizes the total internal reflection effect, one finds that

$$k_{1,2,3} = \sqrt{n_{1,2,3}^2(2\pi/\lambda)^2 - \beta^2} \tag{30.49}$$

for the wave vector components along the cross direction in the core (with subscript 1), the top cladding (with subscript 2), and the bottom cladding (with subscript 3) layer, respectively, with $n_{1,2,3}$ denoting the refractive indices of these three layers. The propagation constant β, i.e., the wave vector component along the propagation direction (z), must be the same for the same guided wave distributed in different layers, as otherwise the guided wave would be split apart along with its propagating in z. Under the total internal reflection scheme, the refractive indices are chosen in such a way to make k_1 real ($2\pi n_1/\lambda > \beta$) but $k_{2,3}$ imaginary ($2\pi n_{2,3}/\lambda < \beta$). By noticing that $R_{t,b} = (k_1 - k_{2,3})/(k_1 + k_{2,3})$ for the TE wave with its electric field polarized in parallel with, and $R_{t,b} = (1/k_1 - 1/k_{2,3})/(1/k_1 + 1/k_{2,3})$ for the TM wave with its electric field polarized perpendicularly to, the boundary between different layers, respectively, one has $|R_{t,b}| = 1$ as the reflectivity at the boundary always takes the form of $(a - jb)/(a + jb)$. Consequently, the resonant condition (Equation 30.48) in the cross direction is reduced to

$$\varphi_t + \varphi_b + 2k_1 d = 2m\pi \tag{30.50}$$

with $\varphi_{t,b}$ indicating the phase of $R_{t,b}$, i.e.,

$$\varphi_{t,b} = -2\arctan(|k_{2,3}|/k_1) \tag{30.51}$$

for the TE wave and

$$\varphi_{t,b} = -2\arctan(k_1/|k_{2,3}|) \tag{30.52}$$

for the TM wave, respectively. Equations 30.49 through 30.51 or Equation 30.52 defines the dispersion relation of the guided wave, which tells that, for a given waveguide structure and operating wavelength λ below a maximum value known as the cutoff wavelength, one always manage to find at least one real β within the range between $2\pi \max(n_2, n_3)/\lambda$ and $2\pi n_1/\lambda$ as the solution. Therefore, the conventional dielectric waveguide has no wavelength selection ability as the dispersion relation of its guided wave shows a high-pass filter feature that supports the wave propagation with any wavelength shorter than the cutoff value, which also echoes the same statement we made at the beginning of this chapter. It is not surprising for one to reach this conclusion, once one notices that as the total internal reflection condition is satisfied, $|R_t R_b|$ is always 1 regardless of the associated wavelength. The cross-directional resonant condition, as the indication of the wave being guided, is therefore reduced to a phase-matching condition (i.e., the dispersion relation) that is too loose to select a discrete set of wavelengths, not to mention a single wavelength.

If, however, a grating-based reflection is utilized to substitute the total internal reflection, as shown in the structure given by Figure 30.20, it will be possible to make $R_t R_b$ wavelength dependent. Once not only the phase-matching condition in the form of Equation 30.50, but also a wavelength-dependent amplitude condition in the form of $|R_t(\lambda)R_b(\lambda)| = 1$, will jointly be derived from the general resonant condition

(Equation 30.48), it is possible that only a single wavelength can be found for the guided wave to satisfy both constraints imposed on the phase and amplitude.

The Bragg waveguide laser is such a device that exploits the grating reflection, rather than the total internal reflection, in its waveguide in conjunction with the FP cavity to reach the SLM operation. With a structure similar to the DBR laser arranged in the cross direction perpendicular to the waveguide for wave confinement, even a simple FP cavity makes an SLM laser [58]. A unique feature of the Bragg waveguide lies in that it allows its core layer to have a lower refractive index than that of its cladding. As such, the selection on the gain medium to build the active region for the Bragg waveguide laser will be more flexible.

30.4.3 Double-Trench Resonant Tunneling SLM Laser

As concluded by Section 30.3, the concept of the coupled cavity can generally be understood as the insertion of an OBPF into a conventional FP cavity, for purifying the lasing spectrum by eliminating all unwanted FP cavity modes. An accompanying issue is that both the transmitted light passed through the OBPF and the reflected light experienced the complementary optical band-reject filter (OBRF) stay inside the FP cavity, which add up to give no appreciable mode selection mechanism once their gains are the same, since the added spectrum of the complementary OBPF and OBRF turns out to be flat. Although the additionally introduced phase condition by the equivalent filter and any possible gain discrimination between the transmitted and reflected waves will help to eliminate the unwanted FP cavity modes, the single-mode yield and SMSR for such structures are usually low. And the SLM lasing is usually not very stable in the entire laser operating range. For example, the lasing mode often hops or the SMSR deteriorates as the bias current or ambient temperature changes. This can be attributed to the phase-sensitive lasing condition shown as Equation 30.33 or Equation 30.39, since the phase not only varies with any geometrical dimension deviation of the structure in the fabrication process, but also changes with the laser operating condition.

To ensure the SLM operation with an intensified SMSR with high yield, one needs to effectively eliminate the reflected light from the aforementioned OBPF inside the FP cavity. As shown in Figure 30.22, a double-trench structure has been proposed [59] to introduce dual reflections that cancel out the reflected light at a specific wavelength determined by the gap between the two trenches, an effect known as the resonant tunneling. As such, the transmission spectrum of the double trenches resembles that of an OBPF, which selects one of the many cavity modes in a conventional FP laser for single-mode operation. The most important design in this structure, which significantly improves the SLM laser performance, is to make the double trenches slanted so that the reflected waves with unselected wavelengths by the OBPF will escape

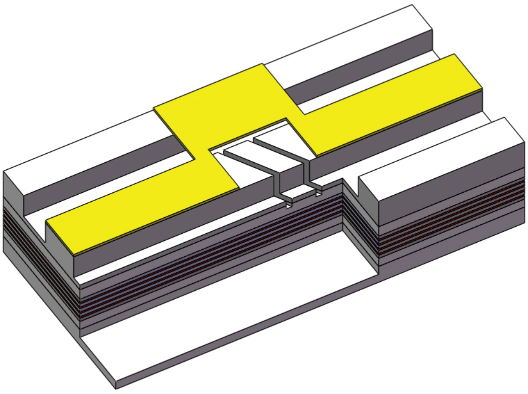

FIGURE 30.22 The double-trench resonant tunneling SLM laser structure.

from the cavity, in order to avoid jeopardizing the single-mode lasing condition, as otherwise the reflected and transmitted light in different wavelengths will compete to each other inside the cavity.

By eliminating the reflection brought in by the OBPF made of the double trenches, i.e., by letting $r_{12}, r_{21} \sim 0$, $\delta = t_{12}t_{21}$, the lasing condition (Equation 30.33) derived for general coupled-cavity lasers reduces to

$$t_{12}t_{21}R^2e^{2j(\varphi_2+\varphi_1)} = 1 \tag{30.53}$$

which indicates that the lasing will be determined by the transmission spectrum of the inserted OBPF. More specifically, the lasing will happen at the wavelength in the neighborhood of the transmission spectrum ($|t_{12}t_{21}|$) peak. Actually, once the transmission spectrum of the filter resembles that of an OBPF, the lasing condition shown in Equation 30.53 is the same as that of the DBR laser (Equation 30.13).

The simulated and measured lasing spectrum and SLM yield of a typical double-trench resonant tunneling SLM laser are given in Figures 30.23 and 30.24, respectively. The simulation result also shows, and experimental data verifies that, with varying positions of the double trenches inside the FP cavity, the slanted trench pair can always select and lock in one and only one of the many FP modes in the full laser operating range [59]. This can be attributed to the fact that, with the reflection from the double trenches effectively eliminated and consequently with the lasing condition determined by Equation 30.53 rather than Equation 30.33 or Equation 30.39 for the device, its mode selection mechanism is no longer phase sensitive. Hence the precise control of the geometrical dimension in the structure is not required in the fabrication process for such a device, which greatly enhances the single-mode yield, the SMSR, and the single-mode stability in operation, as compared to other existing coupled-cavity lasers.

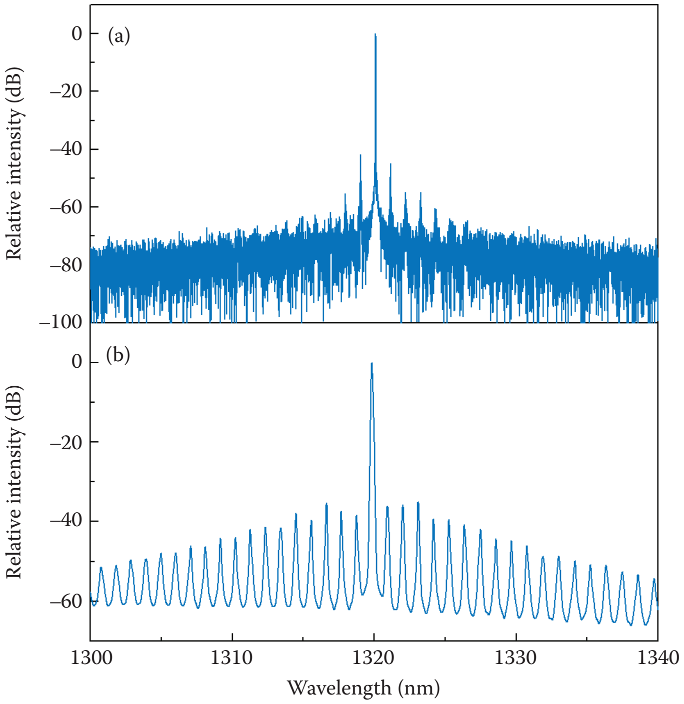

FIGURE 30.23 The (a) simulated and (b) measured lasing spectra of a typical double-trench resonant tunneling SLM laser, with its design parameters given in Reference [59].

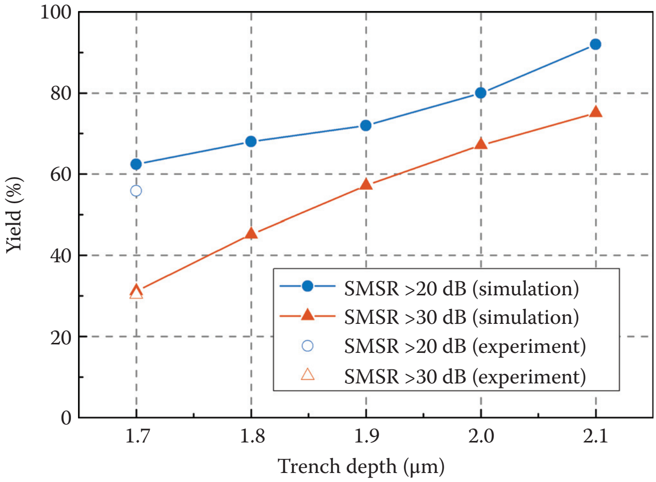

FIGURE 30.24 The SLM yield as a function of the trench depth, with device design parameters given in Reference [59].

30.4.4 Horn Ridge Waveguide (HRW) DFB Laser

With its structure shown in Figure 30.25, the horn ridge waveguide (HRW) DFB laser [60] improves the single-mode yield by breaking the inherent dual-mode degeneracy in the uniform-grating purely refractive index-coupled structure.

In a straight-waveguide purely refractive index-coupled DFB laser with uniform grating, the two longitudinal modes with their respective wavelengths located at each side of the Bragg stopband have the same reflection everywhere along the cavity due to the symmetry in the reflection spectrum, so that they have the degenerated field distribution. The longitudinal modes at the two wavelengths with the degenerated field distribution will then have the same modal gain, which causes either dual-mode operation or SLM lasing with poor SMSR if the degeneracy is somehow removed by the uncontrollable LSHB effect. In the HRW DFB laser, however, an effective chirp to the uniform grating is introduced. As such, the field of the longitudinal mode with the wavelength on the blue side will concentrate in the right section with the wider ridge width, as a consequence of the strong reflection it sees from the left section with the narrow ridge width, where the local Bragg wavelength takes a relative shift toward the shorter wavelength side due to the reduction on the local effective index. On the contrary, the field of the longitudinal mode with the wavelength on the red side will concentrate in the left section with the narrower ridge width, as a consequence of the strong reflection it sees from the right section with the wider ridge width, where the local Bragg wavelength shifts relatively toward the longer wavelength side due to the enhancement on the local effective index. Therefore, the major effect of the effectively chirped grating is to remove the degeneracy of field distributions of the two symmetrical modes on each sides of the Bragg stopband. With the help of such effectively chirped grating, the two longitudinal modes at the Bragg stop-band will take different distributions and have their associated field intensities spatially localized in different sections along the cavity. With the further help of the nonuniform modal gain simultaneously generated by the horn waveguide, the field distribution having a larger overlap with the modal gain turns out to be the only dominant lasing mode. In this particular structure, the modal gain is higher on the wide ridge side due to the larger confinement factor associated. Hence the wavelength at the blue side of the Bragg stop-band, i.e., the shorter wavelength, will be selected to lase, whereas the wavelength at the red side, i.e., the longer wavelength, will be effectively suppressed.

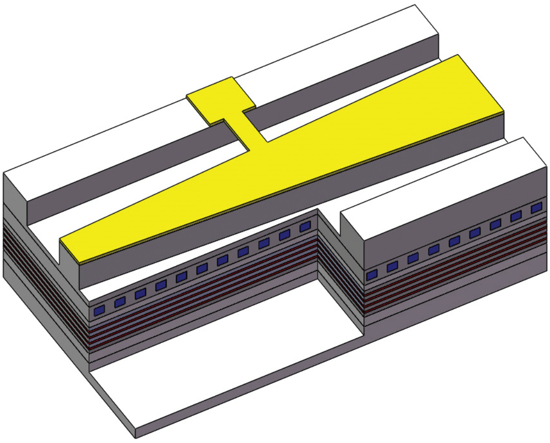

FIGURE 30.25 The horn ridge waveguide (HRW) DFB laser structure.

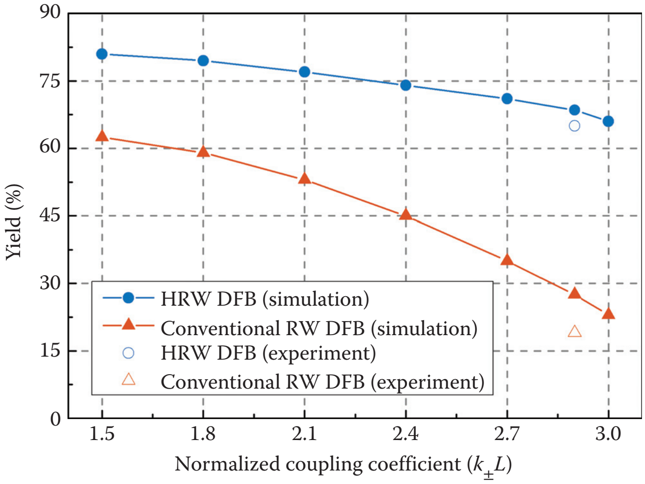

FIGURE 30.26 Comparison on the SLM yield (SMSR >30 dB) between the HRW DFB and the conventional ridge waveguide (RW) DFB with different $\kappa \pm L$; other device design parameters are given in Reference [60].

Simulation result shows, and experimental result demonstrates, that the SLM yield can be drastically raised (by more than threefolds) with an optimized HRW design, especially for the uniform-grating purely refractive index-coupled DFB laser with high normalized coupling coefficient (κL) [60]. This is further evidenced by the comparison result in Figure 30.26. Finally, measured lasing spectra of a typical HRW DFB laser under different bias current are shown in Figure 30.27.

Acknowledgment

The author would like to express his sincere thankfulness to Cheng Ke for his great help on performing most of the numerical calculations and on drawing all the figures.

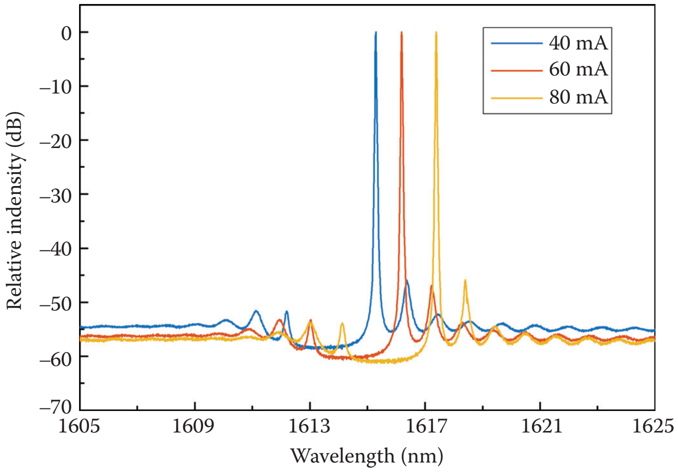

FIGURE 30.27 Measured lasing spectra of a typical HRW DFB laser under different bias current, with its design parameters given in Reference [60].

References

1. K. Ogawa, Analysis of mode partition noise in laser transmission systems, *IEEE Journal of Quantum Electronics*, vol. 18, no. 5, pp. 849–855, May 1982.
2. M. Ahmed and M. Yamada, Theoretical analysis of mode-competition noise in modulated laser diodes and its influence on the noise performance of fibre links, *Journal of Physics D Applied Physics*, vol. 45, no. 40, pp. 4172–4181, Sept. 2012.
3. M. L. Calvo and V. Lakshminarayanan, *Optical Waveguides: From Theory to Applied Technologies*, Boca Raton, FL: CRC Press, Taylor & Francis, ISBN 978-1-57444-698-2, Jan. 2007.
4. D. Marcuse, *Theory of Dielectric Optical Waveguides*, New York, NY: Academic Press, ISBN 0-12-470950-8, 1974.
5. K. Petermann, *Laser Diode Modulation and Noise*, Netherlands: Kluwer Academic Publishers, ISBN 978-0-7923-1204-8, Apr. 1988.
6. B. Mroziewicz, External cavity wavelength tunable semiconductor lasers—a review, *Opto-Electronics Review*, vol. 16, no. 4, pp. 347–366, Sept. 2008.
7. K. Vahala, K. Kyuma, A. Yariv, S. K. Kwong, M. C. Golomb, and K. Y. Lau, Narrow linewidth, single frequency semiconductor laser with a phase conjugate external cavity mirror, *Applied Physics Letters*, vol. 49, no. 23, pp. 1563–1565, Oct. 1986.
8. M. W. Fleming and A. Mooradian, Spectral characteristics of external-cavity controlled semiconductor lasers, *IEEE Journal of Quantum Electronics*, vol. 17, no. 1, pp. 44–59, Jan. 1981.
9. H. Kogelnik and C. V. Shank, Stimulated emission in a periodic structure, *Applied Physics Letters*, vol. 18, no. 4, pp. 152–154, Nov. 1971.
10. S. Wang, Principles of distributed feedback and distributed Bragg-reflector lasers, *IEEE Journal of Quantum Electronics*, vol. 10, no. 4, pp. 413–427, Apr. 1974.
11. J.-W. Mu and W.-P. Huang, Simulation of three-dimensional waveguide discontinuities by a full-vector mode-matching method based on finite-difference schemes, *Optics Express*, vol. 16, no. 22, pp. 18152–18163, Oct. 2008.
12. K. Jiang and W.-P. Huang, Finite-difference-based mode-matching method for 3-D waveguide structures under semivectorial approximation, *Journal of Lightwave Technology*, vol. 23, no. 12, pp. 4239–4248, Dec. 2005.

13. M. Yamada and K. Sakuda, Analysis of almost-periodic distributed feedback slab waveguides via a fundamental matrix approach, *Applied Optics*, vol. 26, no. 16, pp. 3474–3478, Aug. 1987.
14. T. Makino, Transfer-matrix analysis of the intensity and phase noise of multisection DFB semiconductor lasers, *IEEE Journal of Quantum Electronics*, vol. 27, no. 11, pp. 2404–2414, Nov. 1991.
15. G. P. Agrawal and N. K. Dutta, *Semiconductor Lasers*, 2nd ed. New York, NY: Van Nostrand Reinhold, ISBN 0-442-01102-4, 1993.
16. X. Li, *Optoelectronic Devices: Design, Modeling, and Simulation*, Cambridge: Cambridge University Press, ISBN 978-0-521-87510-3, Aug. 2009.
17. W. W. Ng, C. Hong, and A. Yariv, Holographic interference lithography for integrated optics, *IEEE Transactions on Electron Devices*, vol. 25, no. 10, pp. 1193–1200, Oct. 1978.
18. C. J. Armistead, B. R. Butler, S. J. Clements, A. J. Collar, D. J. Moule, S. A. Wheeler, M. J. Fice, and H. Ahmed, DFB ridge waveguide lasers at $\lambda = 1.5$ μm with first-order gratings fabricated using electron beam lithography, *Electronics Letters*, vol. 23, no. 11, pp. 592–593, May 1987.
19. S. Y. Chou, P. R. Krauss, and P. J. Renstrom, Imprint of sub-25 nm vias and trenches in polymers, *Applied Physics Letters*, vol. 67, no. 67, pp. 3114–3116, Sept. 1995.
20. L.-A. Wang, C.-H. Lin, and J.-H. Chen, Fabrication of sub-quarter-micron grating patterns by employing DUV holographic lithography, *Microelectronic Engineering*, vol. 46, no. 1–4, pp. 173–177, Aug. 1999.
21. A. Takemoto, Y. Ohkura, Y. Kawama, Y. Nakajima, T. Kimura, N. Yoshida, S. Kakimoto, and W. Susaki, 1.3-μm distributed feedback laser diode with a grating accurately controlled by a new fabrication technique, *Journal of Lightwave Technology*, vol. 7, no. 12, pp. 2072–2077, Dec. 1989.
22. Y. Abe, K. Kishino, Y. Suematsu, and S. Arai, GaInAsP/InP integrated laser with butt-jointed built-in distributed-Bragg-reflection waveguide, *Electronics Letters*, vol. 17, no. 25, pp. 945–947, Dec. 1981.
23. S. Murata, I. Mito, and K. Kobayashi, Spectral characteristics for 1.5 μm DBR laser with frequency-tuning region, *IEEE Journal of Quantum Electronics*, vol. 23, no. 6, pp. 835–838, June 1987.
24. J. E. Carroll, J. Whiteaway, and D. Plumb, *Distributed Feedback Semiconductor Lasers*, London: Institution of Electrical Engineers, ISBN 0-85296-917-1, Apr. 1998.
25. D. E. Muller, A method for solving algebraic equations using an automatic computer, *Mathematical Tables and Other Aids to Computation*, vol. 10, no. 56, pp. 208–215, Oct. 1956.
26. K. David, G. Morthier, P. Vankwikelberge, R. G. Baets, T. Wolf, and B. Borchert, Gain-coupled DFB lasers versus index-coupled and phase shifted DFB lasers: A comparison based on spatial hole burning corrected yield, *IEEE Journal of Quantum Electronics*, vol. 27, no. 6, pp. 1714–1723, June 1991.
27. H. Su, L. Zhang, A. L. Gray, R. Wang, T. C. Newell, K. J. Malloy, and L. F. Lester, High external feedback resistance of laterally loss-coupled distributed feedback quantum dot semiconductor lasers, *IEEE Photonics Technology Letters*, vol. 15, no. 11, pp. 1504–1506, Nov. 2003.
28. G.-P. Li, T. Makino, R. Moore, N. Puetz, K. Leong, and H. Lu, Partly gain-coupled 1.55 μm strained-layer multiquantum-well DFB lasers, *IEEE Journal of Quantum Electronics*, vol. 29, no. 6, pp. 1736–1742, Jun. 1993.
29. Y. Luo, Y. Nakano, K. Tada, T. Inoue, H. Hosomatsu, and H. Iwaoka, Purely gain-coupled distributed feedback semiconductor lasers, *Applied Physics Letters*, vol. 56, no. 17, pp. 1620–1622, Feb. 1990.
30. Y. Nakano, Y. Luo, and K. Tada, Facet reflection independent, single longitudinal mode oscillation in a GaAlAs/GaAs distributed feedback laser equipped with a gain-coupling mechanism, *Applied Physics Letters*, vol. 55, no. 16, pp. 1606–1608, Aug. 1989.
31. H. A. Haus and C. V. Shank, Antisymmetric taper of distributed feedback lasers, *IEEE Journal of Quantum Electronics*, vol. 12, no. 9, pp. 532–539, Sept. 1976.
32. E. Kapon, A. Hardy, and A. Katzir, The effect of complex coupling coefficients on distributed feedback lasers, *IEEE Journal of Quantum Electronics*, vol. 18, no. 1, pp. 66–71, Jan. 1982.
33. K. Utaka, S. Akiba, K. Sakai, and Y. Matsushima, $\lambda/4$-shifted InGaAsP/InP DFB lasers, *IEEE Journal of Quantum Electronics*, vol. 22, no. 7, pp. 1042–1051, July 1986.

34. S. Akiba, M. Usami, and K. Utaka, 1.5-μmλ/4-shifted InGaAsP/InP DFB lasers, *Journal of Lightwave Technology*, vol. 5, no. 11, pp. 1564–1573, Nov. 1987.
35. S.-L. Chuang, *Physics of Photonic Devices*, 2nd ed. New York, NY: Wiley, ISBN 9781118585658, 2012.
36. A. D. Sadovnikov, X. Li, and W.-P. Huang, A two-dimensional DFB laser model accounting for carrier transport effects, *IEEE Journal of Quantum Electronics*, vol. 31, no. 10, pp. 1856–1862, Oct. 1995.
37. X. Li, A. D. Sadovnikov, W.-P. Huang, and T. Makino, A physics-based three-dimensional model for distributed feedback laser diodes, *IEEE Journal of Quantum Electronics*, vol. 34, no. 9, pp. 1545–1553, Sept. 1998.
38. B. Kim, Y. Chung, and J. Lee, An efficient split-step time-domain dynamic modeling of DFB/DBR laser diodes, *IEEE Journal of Quantum Electronics*, vol. 36, no. 7, pp. 787–794, July 2000.
39. W. H. Press, S. A. Teukolsky, W. T. Vetterling, and B. P. Flannery, *Numerical Recipes: The Art of Scientific Computing*, 3rd ed. Cambridge: Cambridge University Press, ISBN 978-0-511-33555-6, Sept. 2007.
40. X. Li and W.-P. Huang, Simulation of DFB semiconductor lasers incorporating thermal effects, *IEEE Journal of Quantum Electronics*, vol. 31, no. 10, pp. 1848–1855, Oct. 1995.
41. A. J. Lowery and D. Novak, Enhanced maximum intrinsic modulation bandwidth of complex-coupled DFB semiconductor lasers, *Electronics Letters*, vol. 29, no. 5, pp. 461–463, Mar. 1993.
42. L.-M. Zhang and J. E. Carroll, Enhanced AM and FM modulation response of complex coupled DFB lasers, *IEEE Photonics Technology Letters*, vol. 5, no. 5, pp. 506–508, Aug. 1993.
43. S. Hansmann, Transfer matrix analysis of the spectral properties of complex distributed feedback laser structures, *IEEE Journal of Quantum Electronics*, vol. 28, no. 11, pp. 2589–2595, Nov. 1992.
44. C. Youtsey, R. Grundbacher, R. Panepucci, I. Adesida, and C. Caneau, Characterization of chemically assisted ion beam etching of InP, *Journal of Vacuum Science & Technology B*, vol. 12, no. 6, pp. 3317–3321, Dec. 1994.
45. H. Blauvelt, N. Bar Chaim, D. Fekete, S. Margalit, and A. Yariv, AlGaAs lasers with micro-cleaved mirrors suitable for monolithic integration, *Applied Physics Letters*, vol. 40, no. 4, pp. 289–290, Feb. 1982.
46. W. T. Tsang, N. A. Olsson, and R. A. Logan, High-speed direct single-frequency modulation with large tuning rate and frequency excursion in cleaved-coupled-cavity semiconductor lasers, *Applied Physics Letters*, vol. 42, no. 8, pp. 650–652, Feb. 1983.
47. Q.-Y. Lu, W.-H. Guo, D. Byrne, and J. F. Donegan, Design of slotted single-mode lasers suitable for photonic integration, *IEEE Photonics Technology Letters*, vol. 22, no. 11, pp. 787–789, Mar. 2010.
48. Y. Wang, Y.-G. Yang, S. Zhang, L. Wang, and J.-J. He, Narrow linewidth single-mode slotted Fabry–Pérot laser using deep etched trenches, *IEEE Photonics Technology Letters*, vol. 24, no. 14, pp. 1233–1235, May 2012.
49. T.-T. Yu, L. Zou, L. Wang, and J.-J. He, Single-mode and wavelength tunable lasers based on deep-submicron slots fabricated by standard UV-lithography, *Optics Express*, pp. 16291–16299, July 2012.
50. J.-L. Zhao, K. Shi, Y.-L. Yu, and L. P. Barry, Theoretical analysis of tunable three-section slotted Fabry–Perot lasers based on time-domain traveling-wave model, *IEEE Journal of Selected Topics in Quantum Electronics*, vol. 19, no. 5, pp. 1–8, Mar. 2013.
51. S. O'Brien and E. P. O'Reilly, Theory of improved spectral purity in index patterned Fabry–Pérot lasers, *Applied Physics Letters*, vol. 86, no. 20, pp. 201101, May 2005.
52. S. O'Brien, A. Amann, R. Fehse, S. Osborne, E. P. O'Reilly, and J. M. Rondinelli, Spectral manipulation in Fabry–Perot lasers: Perturbative inverse scattering approach, *Journal of the Optical Society of America B*, vol. 23, no. 6, pp. 1046–1056, Jan. 2006.
53. X. Li and J. Park, Time-domain simulation of channel crosstalk and inter-modulation distortion in gain-clamped semiconductor optical amplifiers, *Optics Communications*, vol. 263, no. 2, pp. 219–228, Feb. 2006.

54. W. Li, W.-P. Huang, and X. Li, Digital filter approach for simulation of a complex integrated laser diode based on the traveling-wave model, *IEEE Journal of Quantum Electronics*, vol. 40, no. 5, pp. 473–480, May 2004.
55. Y.-P. Xi, W.-P. Huang, and X. Li, High-order split-step schemes for time-dependent coupled-wave equations, *IEEE Journal of Quantum Electronics*, vol. 43, no. 5, pp. 419–425, May 2007.
56. L. Dong, R.-K. Zhang, D.-L. Wang, S.-Z. Zhao, S. Jiang, Y.-L. Yu, and S.-H. Liu, Modeling widely tunable sampled-grating DBR lasers using traveling-wave model with digital filter approach, *Journal of Lightwave Technology*, vol. 27, no. 15, pp. 3181–3188, Apr. 2009.
57. L. Zhu, A. Scherer, and A. Yariv, Modal gain analysis of transverse Bragg resonance waveguide lasers with and without transverse defects, *IEEE Journal of Quantum Electronics*, vol. 43, no. 10, pp. 934–940, Oct. 2007.
58. Y. Li, Y.-P. Xi, X. Li, and W.-P. Huang, A single-mode laser based on asymmetric Bragg reflection waveguides, *Optics Express*, vol. 17, no. 13, pp. 11179–11186, June 2009.
59. X. Li, Z.-S. Zhu, Y.-P. Xi, L. Han, C. Ke, Y. Pan, and W.-P. Huang, Single-mode Fabry–Perot laser with deeply etched slanted double trenches, *Applied Physics Letters*, vol. 107, no. 9, pp. 091108, Sept. 2015.
60. C. Ke, X. Li, and Y.-P. Xi, A horn ridge waveguide DFB laser for high single longitudinal mode yield, *Journal of Lightwave Technology*, vol. 33, no. 24, pp. 5032–5037, Nov. 2015.

31

Traveling Wave Modeling of Nonlinear Dynamics in Multisection Laser Diodes

Mindaugas Radziunas

31.1 Introduction

Semiconductor lasers, and a narrow waveguide edge-emitting semiconductor lasers, in particular, are attractive devices for different applications. Among others, these are high-speed all-optical signal processing, optical data storage, thermal and xerographic printing, scanning, directional lighting, secure communications, random number generation, frequency conversion, or various interferometric, spectroscopic, instrumentation, and other quantum-optical experiments.

A typical solitary narrow waveguide (single transversal mode) semiconductor laser exhibits a single-wavelength emission required in different applications. In many cases, however, small fluctuations of the operation conditions impose a significant phase noise which, in turn, causes an unwanted broadening of the emission linewidth. Moreover, the stable performance of the laser can be easily violated by optically reinjected light, and there is a huge number of studies devoted to the analysis of the nonlinear dynamics in lasers with a delayed optical feedback.

A properly designed optical feedback, however, can also play a constructive role when seeking to improve an operation of the solitary laser, or create a new dynamical regime. For example, an external cavity with a diffractive grating can be used for emission linewidth reduction or tuning of the lasing wavelength

[1]. Or, on the contrary, specially designed external cavities allow realizing a chaotic emission usable for cryptography [2] or random number generation [3].

Multisection semiconductor lasers (MSLs) in linear or ring configurations and coupled laser devices provide even more possibilities to tailor laser dynamics for certain applications. For example, a variety of important functionalities of the optical data communications [4], such as pulse generation, clock recovery, and fast switching can be realized by specially designed and differently interconnected MSLs. Several examples of theoretically investigated and experimentally verified dynamic performance of MSLs considered in our previous works are excitability [5], high-frequency mode-beating pulsations [6], and modulation band enhancement [7] in distributed feedback (DFB) lasers with an integrated passive phase tuning section (passive feedback lasers); passive [8] or hybrid [9] harmonic and sub-harmonic mode-locking in lasers with saturable absorber, and pulse broadening in quantum dot (QD) mode-locked lasers [10]; tunable high-frequency pulsations in the detuned grating DFB lasers with an integrated phase tuning section (phase controlled mode-beating lasers) [11,12]; stationary, pulsating, and irregular regimes and their bifurcations in DFB lasers with integrated phase tuning and amplifying sections (active feedback laser) [6,13]; Joule heating–induced transitions between steady states in distributed Bragg reflector (DBR) lasers [14] or external cavity diode lasers (ECDLs) [15].

All these examples confirm the practical importance of modeling, simulations, and analysis of MSLs for designing new devices with a particular dynamical behavior. The most precise models usually are given by 2+1 or 3+1 dimensional systems of partial differential equations (PDEs) [16,17]. The numerical simulations in this case, however, are time consuming, whereas application of analytic methods for the analysis of the nonlinear dynamics is very limited. Unfortunately, numerical simulations of such models are time consuming, whereas an application of analytic methods for the model analysis is very limited. For this reason, we prefer to use simpler approaches which, may be, fail to reproduce a quantitative-, but still allow to get a qualitative agreement between theory and experiments.

For some MSLs, already simple ordinary differential equation (ODE) or delay differential equation (DDE) systems (rate equations) admit a reasonable description of the laser dynamics. An advantage of these models is their simplicity allowing fast numerical simulations and application of advanced analytic methods, such as asymptotic analysis, stability analysis, or numerical continuation and bifurcation analysis. These models, however, usually are based on mean-field approximations, i.e., neglect inhomogeneity of laser parameters and dynamical variables along the laser cavity, take into account only a few fundamental characteristics of the considered lasers, or are suited to describe particular MSL configurations [18–20].

The 1+1-dimensional traveling wave (TW) model considered in this chapter is a compromise between simplicity and precision. It is a first-order PDE system having a single spatial dimension corresponding to the longitudinal (z-) direction along the laser cavity and describing dynamics of the slowly varying optical field amplitudes, polarization functions, and carrier density [21–23]. Comparing to ODE and DDE models mentioned earlier, the TW model is computationally more demanding but still enables an advanced analysis, which is hardly possible in the case of the multidimensional PDE models.

By taking into account or neglecting different physical effects, one can derive a whole hierarchy of TW models of different complexities. The standard part of all such models is a pair of TW equations governing the evolution of the complex forward- and back- propagating field amplitudes, $E^+(z,t)$ and $E^-(z,t)$. These equations originate from the decomposition of the dominant fundamental transverse electric (TE) component of the electromagnetic wave,

$$E(\mathbf{r},t) = \Phi(x,y)\left[E^+(z,t)e^{-ik_0z} + E^-(z,t)e^{ik_0z}\right]e^{i\omega_0 t}.$$

Here, ω_0 is the central reference frequency and k_0 the corresponding wave vector. Whereas the transversal waveguide mode profile, $\Phi(x,y)$, is an eigensolution of the waveguide equation, the related complex eigenvalue of the same problem defines the propagation factor β [24], which determines the evolution of the field amplitudes $E^{\pm}$. In general, the propagation factor depends on the complex interaction of carriers and photons. In our modeling approach, we apply a phenomenological dependence of this factor on the real carrier

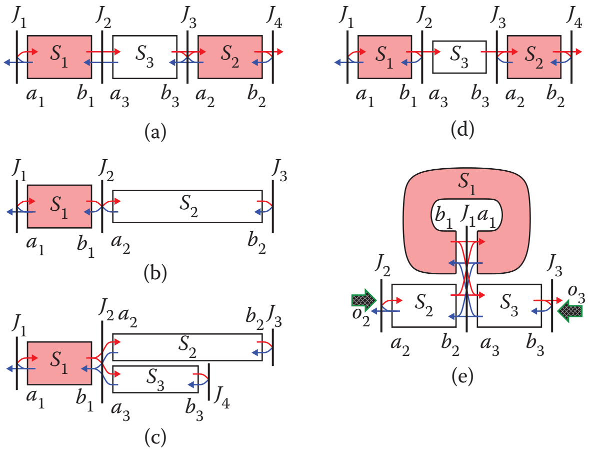

FIGURE 31.1 Schematic representation of five semiconductor laser devices, which can be considered by our modeling approach: (a) three-section laser, (b) laser with a trivial external cavity, (c) laser with a dual external cavity, (d) master–slave laser system, (e) optically injected ring laser with an outcoupling waveguide. Shaded and white frames represent active and passive *sections* (S_*) of the MSL. Thick black segments and thick hatched arrows indicate *junctions* (interfaces of these sections, J_*) and *optical injections* (o_*), respectively. Thin arrows show optical field transmissions and reflections at the interfaces of the laser sections.

density function N, which can represent dynamics of the spatially distributed carrier density, $N(z, t)$, or the section-wise averaged density, $N(t)$. The evolution of N itself is governed by a single or several rate equations.

One can use the TW modeling approach for consideration of various differently interconnected linear and curved, active and passive semiconductor waveguiding parts, taking into account optical injections, field reflections, and transmissions at the interfaces of different laser parts, as well as delayed feedback of the optical fields from the external cavities. For simulation and analysis of the MSLs, we apply our software LDSL-tool [25], which is suited to investigate the longitudinal dynamics of multisection semiconductor lasers. This software allows considering a large variety of MSL devices or coupled laser systems which can be represented by a set of mutually interconnected *sections* and *junctions*, see the schematic representations of several laser devices in Figure 31.1. Besides of numerical integration, LDSL-tool can find longitudinal optical modes and analyze their dynamics [23,26]. In some cases, it locates stable and unstable stationary states of the system [15,27], constructs the reduced ODE models based on a finite number of the optical modes [28], and, together with the software package AUTO [29], performs numerical continuation and bifurcation analysis of these reduced models [7].

In following, we shall introduce a basic TW model for the solitary laser, and present several model extensions allowing to take into account initially neglected physical effects. Next, we shall discuss a possibility to join several laser sections into a single multisection laser or a coupled laser device. For an illustration of the available device complexity, we shall present simulations of a ring laser with four branches of filtered feedback. At the last part of this chapter, we shall briefly introduce the concept of the instantaneous optical modes, discuss the mode analysis, the location and semi analytic continuation of the stationary states, the model reduction, and the numerical bifurcation analysis.

31.2 Basic TW Model in the Solitary Laser

In this section, we formulate the simplest TW model suitable for simulations of a solitary semiconductor laser. Let us consider an edge-emitting narrow-waveguide semiconductor laser (see Figure 31.2a). According to our notations, the "interior" part of this laser is referred as *section* S_1. The longitudinal coordinates

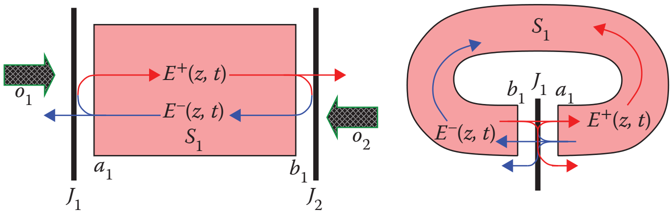

(a) (b)

FIGURE 31.2 Schematic representation of the single section lasers in (a) linear and (b) ring configurations. Thin arrows indicate directions of the counter-propagating fields and their reflections/transmissions at the laser facets [J_1 and J_2, panel (a)] or point outcoupling interface [J_1, panel (b)]. Thick hatched arrows represent optically injected fields.

of the section edges and the length of this section are $z = a_1$, $z = b_1$, and $|S_1| = b_1 - a_1$, respectively. The front and the rear laser facets (*junctions* J_1 and J_2), in this case, correspond to the left and the right edges a_1 and b_1 of S_1.

The backbone of the TW model of this laser is the linear system of partial differential (TW) equations describing an evolution of the slowly varying complex amplitudes $E^+(z, t)$ and $E^-(z, t)$ of the counter-propagating optical fields:

$$\begin{cases} \frac{n_g}{c_0}\partial_t E^+ + \partial_z E^+ = -i\beta E^+ - i\kappa E^- + F_{sp}^+ \\ \frac{n_g}{c_0}\partial_t E^- - \partial_z E^- = -i\beta E^- - i\kappa E^+ + F_{sp}^- \end{cases}, \quad z \in S_1. \tag{31.1}$$

Here, c_0 is the speed of light in vacuum, $F_{sp}^{\pm}$ are the Langevin noise source contributions to the optical fields, and n_g is the group velocity index. The real and the imaginary parts of the complex coefficient κ represent the distributed index and gain/loss coupling of the counter-propagating fields, respectively. κ is nonvanishing in the laser sections containing Bragg grating and is set to zero in the straight sections without the grating. Without an additional scaling of the field functions $E^{\pm}$, $|E(z, t)|^2 = (E, E) = |E^+|^2 + |E^-|^2$ represents the photon density and is proportional to the local field power,

$$\mathcal{P}(z, t) = \frac{\sigma c_0}{n_g}\frac{hc_0}{\lambda_0}|E(z, t)|^2.$$

Here, σ is the cross-section area of the active zone, λ_0 the central wavelength, and h the Planck constant.

Active Sections:

The propagation factor β in the TW equations above can be defined as

$$\beta = \delta_0 + \tilde{n}(N) + \frac{i(g(N) - \alpha)}{2}, \tag{31.2}$$

where the peak gain and refractive index change functions $g(N)$ and $\tilde{n}(N)$ are given by the simple linear relations

$$g(N) = \Gamma g' \left(N - N_{tr}\right), \qquad \tilde{n}(N) = \frac{\alpha_H g(N)}{2}. \tag{31.3}$$

Here, N is the carrier density. The parameters δ_0, α, Γ, g', and α_H are the internal field loss, the initial fixed detuning from the central frequency, the confinement factor, the differential gain, and the linewidth enhancement (Henry) factor evaluated at the transparency carrier density N_{tr}, respectively.

To define the evolution of the spatially averaged carrier density $N(t)$, we use a single rate equation

$$\frac{\mathrm{d}}{\mathrm{dt}}N = \frac{I}{q\sigma|S_1|} - \mathcal{R}(N) - \mathcal{S}(N, E^{\pm}). \tag{31.4}$$

Here, q is the electron charge, I is the injected current into the active zone of the section, whereas $\mathcal{R}$ and $\mathcal{S}$ are spontaneous and stimulated recombination functions, respectively. We use a cubic spontaneous recombination function,

$$\mathcal{R}(N) = AN + BN^2 + CN^3, \tag{31.5}$$

which can be simplified by assuming vanishing recombination parameters B and C and defining $A = \tau_N^{-1}$, where τ_N denotes the carrier lifetime. Function $\mathcal{S}$ in the carrier rate equation 31.4 represents the spatially averaged stimulated recombination:

$$\mathcal{S}(N, E^{\pm}) = \frac{c_0}{n_\mathrm{g}} g(N)\|E\|_1^2. \tag{31.6}$$

Here, $\|E\|_1^2$ is the spatial average of the local photon density along the section S_1,

$$\|E\|_1^2 = \langle (E, E) \rangle_1, \qquad \langle \eta \rangle_1 = \frac{1}{|S_1|} \int_{S_1} \eta(z) \mathrm{d}z, \qquad (\zeta, \xi) = \zeta^{+*}\xi^{+} + \zeta^{-*}\xi^{-},$$

and * denotes the complex conjugate.

To complete the system, we still need to define the incident forward- and backward-propagating fields at the section edges $z = a_1$ and $z = b_1$, respectively. For the solitary laser, these incident fields can be defined by the following reflection/transmission conditions:

$$E^{+}(a_1, t) = -r_1^{*} E^{-}(a_1, t) + o_1(t), \;\; E^{-}(b_1, t) = r_2 E^{+}(b_1, t) + o_2(t). \tag{31.7}$$

Here, r_1 and r_2 are the complex field amplitude reflectivity coefficients at the laser facets (junctions J_1 and J_2), whereas complex functions $o_{1,2}(t)$ represent optical injections at these junctions.

One can also use Equations 31.1 through 31.6 for simulations of narrow-waveguide semiconductor ring lasers with the field in- and out-coupling concentrated in the single point of this laser. Figure 31.2b shows a schematic representation of such single-section ring laser device. According to this scheme, we assume that both, "left" and "right" edges a_1 and b_1 of the section S_1, are connected at the single junction J_1. The boundary conditions (Equation 31.7), in this case, should be replaced by the following field transmission-reflection conditions at J_1:

$$E^{+}(a_1, t) = t_1 E^{+}(b_1, t) - r_1^{*} E^{-}(a_1, t), \;\; E^{-}(b_1, t) = t_1 E^{-}(a_1, t) + r_1 E^{+}(b_1, t). \tag{31.8}$$

Here, t_1 is the real field amplitude transmission factor back into the ring section S_1 at the outcoupling point J_1, whereas the complex factor r_1 represents the localized field backscattering at J_1.

To perform simulations of the basic TW model determined by Equations 31.1 through 31.6 and 31.7 or 31.8, one still needs to choose some initial conditions $E^{\pm}(z, 0)$ and $N(0)$. For the first run of simulations, one can use any small distribution of the optical fields $E^{\pm}(z, 0)$ and a small positive value of $N(0)$. After some transient, the computed trajectory will be attracted by one of the few regular or irregular attractors of the considered dissipative system. To keep tracing the same attractor during the following parameter continuation calculations, one should better use previously obtained carrier density and field distributions.

Passive Sections:

It is noteworthy that one can also use the TW equations 31.1 for a description of the field propagation in the passive sections, such as gratings, free space between the laser and the external mirror, etc. Here, carriers are absent, do not couple to the emission wavelength (the material gain band of these sections does not support the lasing frequencies), or are just kept at transparency level by an appropriately adjusted bias current. In all such cases, $g(N) = \tilde{n}(N) = 0$, the carrier rate equations 31.4 are decoupled from the field equations 31.1 and, therefore, are irrelevant.

In the case of the passive section S_k containing no grating ($\kappa = 0$), simple analytic relations of the field function values on the both sides of S_k,

$$\begin{aligned}
&E^+(b_k,t) = \eta e^{i\varphi/2}E^+(a_k,t-\tau_k), \quad E^-(a_k,t) = \eta e^{i\varphi/2}E^-(b_k,t-\tau_k), \quad \text{where} \\
&\tau_k = \frac{|S_k|n_g}{c_0}, \quad \eta = e^{-\alpha|S_k|/2}, \quad \varphi' = -2\delta_0|S_k|,
\end{aligned} \tag{31.9}$$

can replace the field equations 31.1.

In the case of the passive grating ($\kappa \neq 0$), the analytic solution of the field equations 31.1 in the frequency domain is given by the 2×2-dimensional transfer matrix M [23,26,28],

$$\widehat{E}(z,\omega) = M(\beta,\kappa,\omega;z,a_k)\widehat{E}(a_k,\omega). \tag{31.10}$$

Here, $\beta = \delta_0 - i\alpha/2$, ω is the relative frequency, $\widehat{E}(z,\omega) = \left(\widehat{E}^+, \widehat{E}^-\right)^T$, T denotes the transpose vector, whereas $\widehat{E}^\pm$ are the frequency domain representations of the fields $E^\pm(z,t)$. Within any interval $[z',z]$ where parameters β and κ are constant, the matrix M is defined by

$$\begin{aligned}
&M(\beta,\kappa,\omega;z,z') = \begin{pmatrix} \cos\eta(z{-}z') - \frac{i\mathcal{B}}{\eta}\sin\eta(z{-}z') & -\frac{i\kappa}{\eta}\sin\eta(z{-}z') \\ \frac{i\kappa}{\eta}\sin\eta(z{-}z') & \cos\eta(z{-}z') + \frac{i\mathcal{B}}{\eta}\sin\eta(z{-}z') \end{pmatrix}, \\
&\mathcal{B}(\omega) = \beta + \frac{\omega n_g}{c_0}, \qquad \eta = \sqrt{\mathcal{B}^2 - \kappa^2}.
\end{aligned} \tag{31.11}$$

Once the parameters β or κ are peacewise constants, i.e., constant within each small subinterval $[z_s, z_{s-1}]$, $z' = z_0 < z_1 < \cdots < z_n = z$, the transfer matrix M is the superposition of the corresponding transfer matrices over these small subintervals:

$$M(\beta,\kappa,\omega;z,z') = M_n \times \cdots \times M_1, \quad M_s = M(\beta(z_{s-1/2}),\kappa(z_{s-1/2}),\omega;z_s,z_{s-1}). \tag{31.12}$$

31.3 Model of Material Gain Dispersion

The relations (Equation 31.3) introduced in Section 31.2 are simple linear approximations of the gain and refractive index functions G and $\tilde{N}$. In general, these functions depend not only on the carrier density N, but also on the optical frequency ω, field intensities $|E^+|^2$ and $|E^-|^2$, and some other physical effects, such as temperature, not considered in our modeling approach. In this section, we introduce the model of the gain dispersion of the semiconductor material, which restricts the gain band in the frequency domain and is the primary optical frequency selection mechanism in Fabry–Pérot (FP) lasers.

Before switching to the modeling of the gain dispersion, let us find out the expression of the laser response $F_l(b_1,\omega)$ to the incident plane wave $e^{i\omega t}$ applied to the right edge of the device (see Figure 31.3a). For this reason, we freeze the propagation factor β and substitute the ansatz $E^\pm(z,t) = \widehat{E}^\pm(z,\omega)e^{i\omega t}$ into

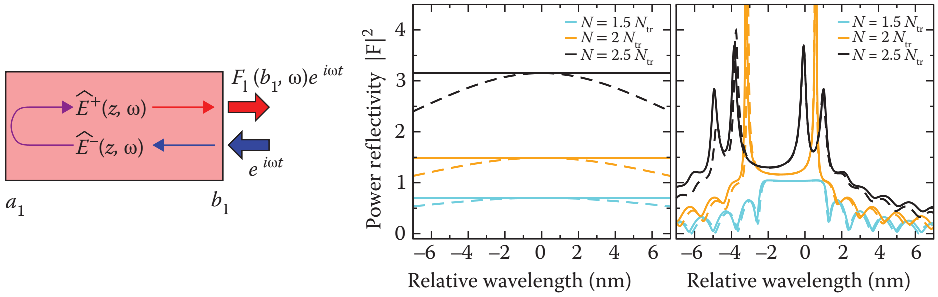

(a) (b) (c)

FIGURE 31.3 Laser response to the incident plane wave $e^{i\omega t}$. (a) Schematic representation: thin and thick arrows show field propagation directions and incident/emitted optical fields. (b) Response intensity of the solitary FP laser: parameters $\lambda_0 = 1.57\,\mu m$, $|S_1| = 0.25\,mm$, $n_g = 3.6$, $\delta_0 = 0$, $\alpha = 20\,cm^{-1}$, $\alpha_H = -4$, $\Gamma = 0.15$, $g' = 4 \cdot 10^{-16}\,cm^2$, $N_{tr} = 10^{18}\,cm^{-3}$, $r_1 = r_2 = \sqrt{0.3}$, $\kappa = 0$. (c) Response intensity of the solitary DFB laser: parameters are the same as in (b), only $\kappa = 130\,cm^{-1}$ and $r_1 = r_2 = 0$. Solid and dashed curves in panels (b) and (c) represent models with ($\bar{g} = 100\,cm^{-1}$, $\bar{\lambda} = 0$, $\bar{\gamma}_\lambda = 40\,nm$) and without ($\bar{g} = 0$) gain dispersion.

the field equations 31.1. The solution of the resulting system of ODEs within S_1 can be represented by Equation 31.10, where the transfer matrix M is defined in Equation 31.11. The ratio of the outgoing and incident waves at $z = b_1$ together with the (noninjective) boundary condition (Equation 31.7) at $z = a_1$ define the function $F_l(b_1, \omega)$, which shows the laser response dependence on the optical frequency of the injected field†. In two simple cases of FP and DFB lasers with vanishing facet reflectivity, the response function is given by

$$F_l(b_1, \omega) = \frac{\widehat{E}^+(b_1,\omega)}{\widehat{E}^-(b_1,\omega)} = \begin{cases} -r_1^* e^{-2i\beta|S_1|} e^{-i2\omega n_g |S_1|/c_0}, & \kappa = 0,\ r_1 \neq 0 \ \text{(FP laser)} \\ \frac{\kappa}{i\eta(\omega)\cot[|S_1|\eta(\omega)] - \mathcal{B}(\omega)}, & \kappa \neq 0,\ r_1 = 0 \ \text{(DFB laser)} \end{cases}. \tag{31.13}$$

Figures 31.3b and c show the intensities of these response functions in FP and DFB lasers calculated for different values of carrier densities N. Note also, that the abscissa axis in these figures represents relative wavelengths λ related to the relative frequencies ω by formula $\lambda \approx -\frac{\lambda_0^2}{2\pi c_0}\omega$.

The flat laser response curves in Figure 31.3b indicate an absence of frequency selection mechanisms for FP lasers in our fundamental TW model. Thus, this simple model is not suitable for simulations of FP lasers. In contrast, the wavelength selection in DFB lasers is mainly determined by the Bragg grating, and numerical integration of the TW model can provide reliable information. One should note, however, that the index-coupled DFB laser (characterized by a real coupling factor κ) can emit at one of two resonance wavelengths located at both sides of the stopband, see a solid dark gray curve in Figure 31.3c, and the parameter tuning implied jumping between these two resonances can be expected in simulations. The gain dispersion, in this case, can be exploited for the suppression of one of the resonances [12,21].

Lorentzian Approximation of the Material Gain Function:

There are several methods for introduction of the frequency-selective gain dispersion into the time-domain TW model. Many of these approaches use an additional digital filtering of the numerically calculated optical field time series [30–34]. In some cases, these digital filters are equivalent to the numerical schemes obtained by discretization of some additional integrodifferential operators or differential equations. For

---

† In the same way, one can also define the response function $F_r(a_1, \omega)$ at the left side of the laser.

the purpose of the analysis of the model equations, it is preferable to introduce the frequency band limiting elements directly into the model equations. For example, the TW model extensions admitting Lorentzian approximation of the material gain dispersion curves can be given by convolution integrals [34] or by an equivalent set of the linear first-order ODEs [21,35]. Another approach to model more sophisticated gain function profiles within the TW modeling frame by including nonlinear polarization equations was used, e.g., in References [22,36,37].

In this chapter, we follow the strategy proposed in References [12,21]. For this reason, we approximate the gain profile in the frequency domain by a Lorentzian with the amplitude $\bar{g}$, the full width at the half maximum $\bar{\gamma} = \frac{2\pi c_0}{\lambda_0^2}\bar{\gamma}_\lambda$, and the detuning of the peak frequency $\bar{\omega} = -\frac{2\pi c_0}{\lambda_0^2}\bar{\lambda}$. Here, $\bar{\gamma}_\lambda$ and $\bar{\lambda}$ are the wavelength representations of the Lorentzian width and its peak position. In the time domain, this approximation is represented by the additional linear operator $\mathcal{D}$ in the TW field equations, and a pair of linear differential equations for polarization functions $P^\pm(z,t)$:

$$\begin{aligned} &\frac{n_\mathrm{g}}{c_0}\partial_t E^\pm = \mp\partial_z E^\pm - i\left(\beta - i\mathcal{D}\right)E^\pm - i\kappa E^\mp + F_\mathrm{sp}^\pm, \quad z \in S_1, \\ &\mathcal{D}E^\pm = \frac{\bar{g}}{2}\left(E^\pm - P^\pm\right), \quad \partial_t P^\pm = \frac{\bar{\gamma}}{2}\left(E^\pm - P^\pm\right) + i\bar{\omega}P^\pm, \quad z \in S_1. \end{aligned} \tag{31.14}$$

The introduction of operator $\mathcal{D}$ also implies the following modification of the stimulated recombination function $\mathcal{S}$ entering the carrier rate equation 31.4:

$$\mathcal{S}(N, E^\pm) = \frac{c_0}{n_\mathrm{g}}\Re\langle\left(E, [g(N) - 2\mathcal{D}]E\right)\rangle_1. \tag{31.15}$$

To understand the impact of the operator $\mathcal{D}$, we consider the laser response function $F_l(b_1,\omega)$ again according to the modified TW equations 31.14. When repeating the procedure described at the beginning of this section, the factor $\mathcal{B}$ entering Equation 31.11 takes the form

$$\mathcal{B}(\omega) = \beta + \frac{\omega n_\mathrm{g}}{c_0} + \chi(\omega), \ \text{ where } \ \chi(\omega) = \frac{\bar{g}}{2}\frac{(\omega-\bar{\omega})}{\bar{\gamma}/2 + i(\omega-\bar{\omega})}, \quad -i\mathcal{D}\hat{E}(z,\omega) = \chi(\omega)\hat{E}(z,\omega). \tag{31.16}$$

Thus, an introduction of the linear dispersion operator $\mathcal{D}$ implies modifications of both, gain and refractive index change functions. The total gain (twice the imaginary part of $\beta - (\delta_0 - i\alpha/2) + \chi(\omega)$) and the refractive index change function (real part of the same factor), in this case, are given by the expressions

$$G(N,\omega) = g(N) - \frac{\bar{g}(\omega-\bar{\omega})^2}{(\bar{\gamma}/2)^2 + (\omega-\bar{\omega})^2}, \quad \tilde{N}(N,\omega) = \tilde{n}(N) + \frac{\bar{g}}{4}\frac{\bar{\gamma}(\omega-\bar{\omega})}{(\bar{\gamma}/2)^2 + (\omega-\bar{\omega})^2}. \tag{31.17}$$

The dashed curves in Figures 31.3b and c illustrate the impact of the introduced gain dispersion. Whereas these corrections in the case of DFB lasers (panel [c]) are small, for the FP lasers they provide an efficient wavelength selection mechanism.

It is noteworthy that vanishing factor κ in the field equations 31.2 and 31.14 implies the following simple expression of the monochromatic field *transmission* through the laser section:

$$\hat{E}^+(b_1,\omega) = e^{-i\mathcal{B}(\omega)|S_1|}\hat{E}^+(a_1,\omega), \quad \hat{E}^-(a_1,\omega) = e^{-i\mathcal{B}(\omega)|S_1|}\hat{E}^-(b_1,\omega),$$

where $\mathcal{B}(\omega)$ is defined in Equation 31.16. Thus, the TW equations 31.2 and 31.14 with vanishing functions $g(N)$ and $\tilde{n}(N)$, large Lorentzian amplitude $\bar{g}$, and small Lorentzian width $\bar{\gamma}$ can be effectively used for modeling of the optical filters, i.e., for extracting field frequency components located close to the relative frequency $\bar{\omega}$.

Further Modifications of the Model for Material Gain Dispersion:

The gain peak $g(N)$ and the simple Lorentzian dependence on the optical frequency determined by three fixed parameters $\bar{g}$, $\bar{\gamma}$, and $\bar{\omega}$ define the material gain profile $G(N, \omega)$ in Equation 31.17. To improve fitting of the gain profiles obtained by calculations of microscopic models for various values of N, one can replace these three factors by appropriately selected carrier-dependent functions $\bar{g}(N)$, $\bar{\gamma}(N)$, and $\bar{\omega}(N)$. In the cases, when the gain spectrum has two and more peaks or the asymmetry of the single peak is important, one can also introduce an additional set or several sets of polarization functions $P^{j\pm}(z, t)$. The gain dispersion operator $\mathcal{D}$ and corresponding total gain and refractive index functions, in this case, read as

$$\mathcal{D}^{(s)}E^{\pm} = \sum_{j=1}^{s} \frac{\bar{g}_j}{2}\left(E^{\pm} - P^{j\pm}\right), \qquad \partial_t P^{j\pm} = \frac{\bar{\gamma}_j}{2}\left(E^{\pm} - P^{j\pm}\right) + i\bar{\omega}_j P^{j\pm}, \quad z \in S_1,$$

$$G(N, \omega) = g(N) + 2\Im\chi^{(s)}(\omega), \;\; \tilde{N}(N, \omega) = \tilde{n}(N) + \Re\chi^{(s)}(\omega), \;\; \chi^{(s)}(\omega) = \sum_{j=1}^{s} \frac{\bar{g}_j}{2} \frac{(\omega - \bar{\omega}_j)}{\bar{\gamma}_j/2 + i(\omega - \bar{\omega}_j)},$$

where s is the number of polarization function sets. Since the maximal value of $2\Im\chi(\omega)$ is, in general, smaller than zero, one should also correct the function $g(N)$.

Concluding the discussion of this section, we note that a proper numerical resolution of the gain and refractive index functions (Equation 31.17) for the broad frequency band when simulating the time-domain TW mode requires a careful selection of the numerical algorithm and temporal discretization steps. The size of the frequency band that can be represented by calculated discrete time series is inversely proportional to the time step, whereas the precision of the numerical simulations when approaching borders of this band are rapidly degrading. Thus, a suitable time discretization step should ensure that all important frequency regions (Bragg resonances, surrounding of a gain peak frequency, a frequency of optically injected beams, if present) are within the central part of the allowed frequency band.

31.4 Thermal Detuning

Let us switch now to the consideration of the thermal effects. An increase of the bias current implies changes of the device temperature and, consequently, changes in the refractive index and the lasing wavelength. To model these thermal tuning effects in our device, we supplement the propagation factor β from Equation 31.2 with an additional thermal detuning term $\tilde{n}_T$ [14,38]:

$$\beta = \delta_0 + \tilde{n}(N) + \tilde{n}_T(I) + \frac{i(g(N) - \alpha)}{2}, \qquad \tilde{n}_T = \frac{2\pi n_g}{\lambda_0^2}\nu_1^1 I. \tag{31.18}$$

The linear thermal detuning function $\tilde{n}_T(I)$ determines the impact of the injection current I to the refractive index change. The factor ν_1^1 in solitary lasers determines an approximate red shift of the lasing wavelength due to increased bias current:

$$\nu_1^1 \approx \frac{\Delta_\lambda}{\Delta_I},$$

Here, Δ_I is the bias current tuning interval, whereas Δ_λ is the (continuous) lasing wavelength change during this current tuning.

Figures 31.4a and c show the simulated wavelength change with the increased bias current in the solitary FP and DFB lasers, respectively. Here, besides the dominant optical modes shown in white, one can see other slightly excited optical modes which are (almost) equidistant in the FP case (a) or indicate the DFB laser resonance located on the other side of the stopband. The estimated wavelength shift $\frac{\Delta_\lambda}{\Delta_I} \approx 3.14$ nm/A obtained for the FP laser and 3.09 nm/A for the DFB laser slightly differs from the factor $\nu_1^1 = 3.2$ nm/A

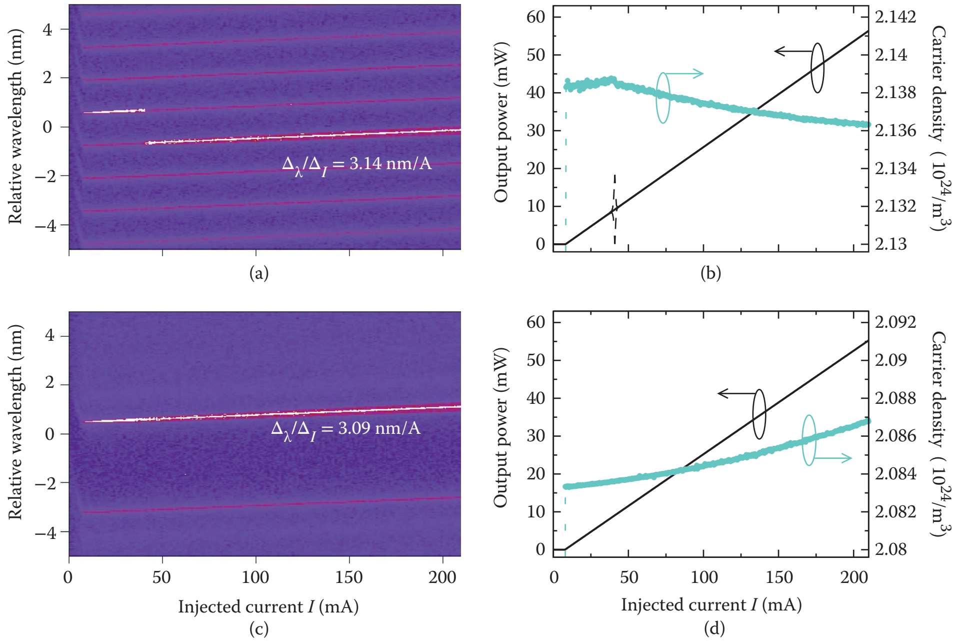

FIGURE 31.4 Mapping of the optical spectra (a), (c), and mean emitted power and carrier density (b), (d) as functions of the increased injected current I in solitary FP (a), (b), and DFB (c), (d) lasers. $\sigma = 2 \cdot 10^{-13}$ m^2, $A = 2 \cdot 10^8$/s, $B = 1 \cdot 10^{-16}$ m^3/s, $C = 1.3 \cdot 10^{-41}$ m^6/s, $\nu_1^1 = 3.2 \cdot 10^{-9}$ m/A, whereas other parameters are the same as in Figures 31.3b and c in the case of nonvanishing gain dispersion. White lines and light shading in (a) and (c) represent main and side peaks of the calculated optical spectra. Solid black and gray curves in (b) and (d) show time-averaged emission intensity and carrier density, respectively. Dashed black lines indicate minima and maxima of the emission intensity.

used in our simulations. We attribute this slight discrepancy to the additional contribution of the full refractive index change function $\tilde{N}(N, \omega)$ defined in Equation 31.17. Namely, the dependence of the carrier density N and the relative lasing wavelength λ on the bias current I (see gray curves in Figures 31.4b and d and wavelength shifts in Figures 31.4a and c, respectively) implies nonvanishing changes of the function $\tilde{N}(N, \omega) = \tilde{N}(N, -\lambda c_0/\lambda_0^2)$ that counteracts the thermal detuning term $\tilde{n}_T(I)$ and slightly reduces the redshift of the lasing wavelength.

It is noteworthy that an introduction of the thermal detuning term $\tilde{n}_T$ in our still simple TW model of the solitary laser implies, in general, only a continuous tuning of the lasing frequency. Once achieving threshold, the carrier density changes only slightly (gray curves in Figures 31.4b and d), whereas the emitted field intensity increases linearly without a visible saturation (black curves in the same panels), which is still not taken into account in our model. This linear growth of the lasing wavelength can be correctly understood when analyzing TW field Equation 31.1 with the propagation factor β defined by Equation 31.18 and neglected gain dispersion. Due to the transfer matrix formalism (Equations 31.10 and 31.11) and the expression of $\mathcal{B}$ in Equation 31.11, the extension of β by the nonvanishing real term $\tilde{n}_T$ is equivalent to the change of the relative frequency ω by $-\tilde{n}_T c_0/n_g$, or, alternatively, the change of λ by $\frac{-\lambda_0^2}{2\pi c_0}\frac{-\tilde{n}_T c_0}{n_g} = \nu_1^1 I$.

The unique, more complicated feature in Figure 31.4 is the transition between two states in the FP laser at $I \approx 40$ mA, see panels (a) and (b). Figure 31.4a shows that in the vicinity of the transition, these two states are determined by two optical modes belonging to the opposite slopes of the wavelength-dependent gain profile with the peak wavelength at $\bar{\lambda} = 0$. Due to the redshift, all optical modes located on the falling (increasing) slope of this gain profile undergo an increase (decrease) of the detuning from the gain peak wavelength and, consequently, a slight rise (fall) in the mode threshold N; see the gray curves in panel (b) for $I < 40$ mA ($I > 40$ mA). A similar increase of the dominant falling-gain-slope mode threshold can also be seen in Figure 31.4d. At the position of the state transition, the wavelengths of two involved modes are symmetric with respect to the gain peak wavelength and, what is more important, their thresholds become equal. Due to a further tuning of the bias current, the previously suppressed mode at the increasing gain profile slope becomes the minimal threshold mode, is amplified and, finally, turns to be the dominant one. See References [14,15,26] for more details on similar and more complex mode transitions.

Modeling of Cross-Talk Heating Effects in Multisection Devices:

In MSLs devices, one can also use a more advanced model for thermal detuning function $\tilde{n}_T$ which takes into account local and nonlocal cross-talk heating effects [38]:

$$\tilde{n}_T|_{z\in S_k} = \tilde{n}_{T,k} = \frac{2\pi n_{g,k}}{\lambda_0^2} \sum_{r=1}^{m} \nu_k^r I_r. \tag{31.19}$$

Here, m is a number of sections in the considered MSL. The coefficients ν_k^r of the linear thermal detuning function $\tilde{n}_T(I)$ determine the impact of the injection currents I_r attributed to the sections S_r on the refractive index change within each laser section S_k.

The effect of the thermal detuning in MSLs is much more complicated than that one of the solitary laser. Besides of the red shift of the lasing wavelength, the MSLs can also exhibit periodically or almost periodically reappearing transitions between different states. The change of mean carrier density in various sections during each such period between state changes can be significant and cannot be explained by simple gain saturation or detuning from the gain peak effects. In some cases, a measured variation of the lasing wavelength with an increase or decrease of the injection current in different laser sections, together with the analysis of the field equations provide good estimates of thermal detuning coefficients including cross-talk effects [14,15,38].

Another well-known effect occurring with the heating of the semiconductor laser is the red shift of the gain peak wavelength [39]. If required, these changes can be accounted by the relation [38]

$$\bar{\lambda}|_{z\in S_k} = \bar{\lambda}_k = \bar{\lambda}_k^0 + \sum_{r=1}^{m} \bar{\nu}_k^r I_r, \tag{31.20}$$

which is quite similar to the thermal detuning relation (Equation 31.19). Here, $\bar{\lambda}_k^0$ denotes an injection-independent part of the gain peak wavelength in the section S_k, and $\bar{\nu}_k^r$ are linear thermal gain peak detuning coefficients. When applying these expressions, one should be aware that a proper numerical time-domain resolution of a significant (tens or even hundreds of nanometers) gain peak shift requires very small time and, consequently, space discretization steps.

31.5 Spatially Inhomogeneous Carrier Density

Another important extension of the basic TW model takes into account sectionally inhomogeneous distributions of carrier density N. Namely, in this case, the sectionally averaged carrier density function $N(t)$ is replaced by the spatially distributed function $N(z, t)$, $z \in S_1$. This model extension can be especially important in the situations admitting localization of the high-intensity fields within the laser cavity, which takes place, e.g., during propagation of ultrashort optical pulses in mode-locked lasers, or DBR lasers with a high coupling factor κ. Due to stimulated recombination, the high-intensity fields at these localized regions can significantly deplete the carrier distribution causing a spatial hole burning (SHB) of the carriers [12,40].

To achieve a quantitative description of SHB, we replace simple carrier rate Equation 31.4 by the following equation for spatially distributed carrier density:

$$\begin{aligned} \partial_t N(z,t) &= \mathcal{J}(I,N) - \mathcal{R}(N) - \mathcal{S}(N,E^{\pm}), \quad z \in S_1, \\ \mathcal{J}(I,N(z,t)) &= \frac{1}{q\sigma|S_1|}\left[I + \frac{U_F'}{r_S}\left(\langle N\rangle_1 - N(z,t)\right)\right]. \end{aligned} \tag{31.21}$$

Here, $\mathcal{J}$ is the inhomogeneous injection current density [12,41,42], N and $\langle N\rangle_1$ are spatially distributed and sectionally averaged carrier densities, U_F' and r_s denote the derivative of the Fermi level separation with respect to N and the series resistivity, whereas $\mathcal{S}$ is the spatially distributed stimulated recombination function,

$$\mathcal{S}(N,E^{\pm}) = \frac{c_0}{n_g}\Re\left(E,[g(N) - 2\mathcal{D}]E\right). \tag{31.22}$$

In the case of the limit $r_s \to 0$, the spatially distributed carrier density, $N(z,t)$, at each position z converges to the sectional average, $N(t) = \langle N\rangle_1$. Since the sectional averaging of the relations 31.21 and 31.22 yields expressions 31.4 and 31.15, the TW models with and without spatial distribution of carriers in this limit case are equivalent.

Figure 31.5 shows some effects occurring due to the SHB of carriers in solitary DFB lasers. The impact of the SHB depends on the injection level. Just above the lasing threshold, the field intensity is small, and the carrier density remains nearly homogeneous, having only a small dip in the center of the laser. With raising injection, this dip increases, but, due to a simultaneous increase of the carrier density at the facets, the mean density remains nearly constant: see only slightly increasing $\langle N\rangle_1$ for $I \leq 90\,\text{mA}$ in panel (b) of the same figure. At these small-to-moderate bias current levels, the carrier density remains symmetric with respect to the laser centrum (dashed curve in panel [d]), and emission at the both facets is the same

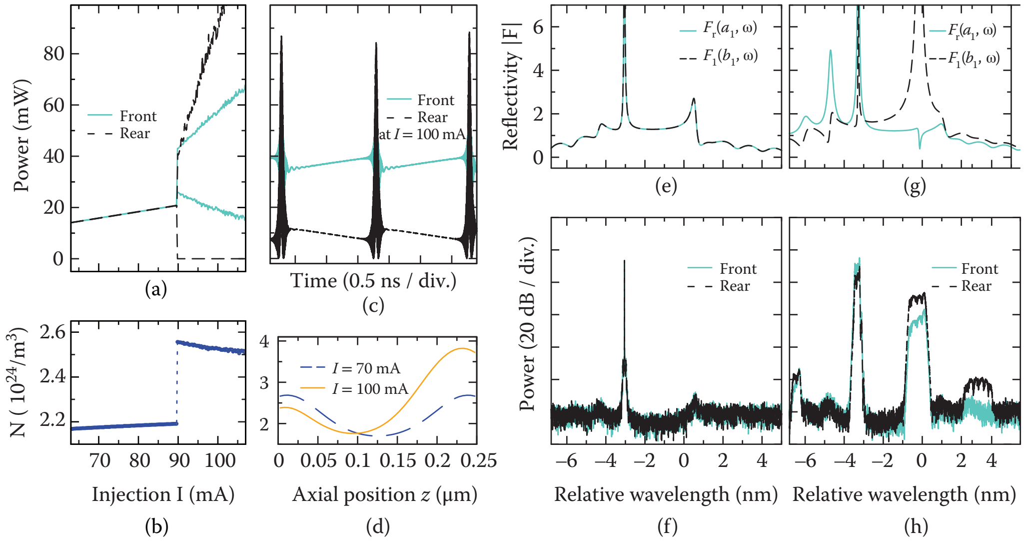

FIGURE 31.5 SHB in solitary DFB laser. (a) Minimal and maximal output power at both facets and (b) sectionally averaged carrier density $\langle N\rangle_1$ as functions of increased bias current. (c) Time trace of the emitted field intensity at both facets for fixed $I = 100\,\text{mA}$. (d) Time-averaged carrier densities for $I = 70\,\text{mA}$ and $I = 100\,\text{mA}$. DFB reflectivity spectra (e), (g), and calculated optical spectra (f), (h) for $I = 70\,\text{mA}$ (e), (f), and $I = 100\,\text{mA}$ (g), (h). Solid gray and black dashed curves in panels (a), (c), (e) through (h) represent optical fields at the front (J_1) and rear (J_2) facets of the laser. $U_F' = 10^{-25}\,\text{Vm}^3$, $r_S = 5\,\Omega$, whereas other parameters are the same as in Figures 31.4c and d except $\nu_1^1 = 0$.

(see coinciding solid gray and black dashed curves in panel (a) for $I \leq 90$ mA and panel (f) at $I = 70$ mA). The inhomogeneous carrier density (dashed curve in Figure 31.5d) causes a corresponding longitudinal variation of the index of refraction. The Bragg resonance of the grating thus has not the identical spectral position along the section but varies over a considerable portion of the stopband [12]. As a consequence, the symmetry of the stopband is lost, and the laser preferably operates on the short wavelength side of its stopband (see Figure 31.5f). The preference of the short-wavelength mode is also shown by the laser response functions $F_l(b_1, \omega)$ and $F_r(a_1, \omega)$ (see Figure 31.5e) calculated for spatially distributed carrier density profile (dashed curve in Figure 31.5d) at $I = 70$ mA according to the formulas 31.10 through 31.12 and the algorithm explained in Section 31.3.

At $I \approx 90$ mA, the symmetric solution loses its stability in symmetry breaking pitchfork bifurcation [43]. According to References [12,43], the supercritical pitchfork bifurcation of the stable symmetric steady state in DFB lasers generates a pair of new stable steady states with asymmetric density profiles (each one the mirror of the other). In our case, the pitchfork bifurcation seems to be of the subcritical type. Instead of finding two asymmetric stable steady states, we immediately jump to the pulsating state with different emission at both laser facets and larger mean carrier density (see panels [a] and (b) for $I > 90$ mA, respectively). The spatial distribution of the carrier density, in this case, is strongly asymmetric, see a solid curve in panel (d). This asymmetry together with noncommuting intermediate transfer matrices M_s from Equation 31.12 implies differences in DFB laser response functions estimated at the front (F_r) and the rear (F_l) sides of the laser, see Figure 31.5g. The optical spectra of the emission at the both sides of the laser (Figure 31.5h) also reveal these differences. Like the response functions of the panel (g), the left (thick gray curves) and the right (thin dashed curves) facet emissions have more pronounced contributions at the shorter and longer wavelength sides of the stopband, respectively.

31.6 Nonlinear Gain Saturation

Until now, our phenomenological models for peak gain and refractive index change (Equation 31.3) were taking into account their dependence on the sectionally averaged or local carrier density N. It is known, however, that the high-intensity optical fields saturate the gain function. To account for such saturation, one can introduce the following modifications of the gain and refractive index functions, which should be used for the definition of the propagation factor β in Equations 31.2 or 31.18 and stimulated recombination function $\mathcal{S}$ in Equations 31.6, 31.15, or 31.22:

$$g(N, E^{\pm}) = g(N)\rho_G(E^{\pm}), \qquad \tilde{n}(N, E^{\pm}) = \tilde{n}(N)\rho_I(E^{\pm}),$$

$$\text{where} \qquad \rho_j = \begin{cases} \left(1 + \varepsilon_j |E|^2\right)^{-1}, & \text{if } N = N(z,t) \\ \left(1 + \varepsilon_j \|E\|^2\right)^{-1}, & \text{if } N = N(t) \end{cases}, \quad j = G, I.$$

Two different parameters, ε_{G} and ε_{I}, separately define the nonlinear gain and refractive index dependence on the local or spatially averaged optical field intensity. A typical assumption $\varepsilon_{\mathrm{G}} = \varepsilon_{\mathrm{I}}$ relates the gain and refractive index functions by the linewidth enhancement factor α_H. Another reasonable assumption $\varepsilon_{\mathrm{I}} = 0$, $\varepsilon_{\mathrm{G}} > 0$ [44] used for modeling of high power amplifiers considers the nonlinear compression of the gain function alone.

The importance of the nonlinear gain compression is best visible in high-power lasers and optical amplifiers showing several Watt emission intensity [44]. Some impact of the gain compression in small-to-moderate ($\leq$100 mW) intensity regimes can also be observed when operating in the vicinity of various bifurcations, where a small change of parameters implies qualitative changes of the operating states. We should note, however, that the gain compression, in this case, implies only small shifts of the bifurcation positions, but has no significant impact on the qualitative description of laser dynamics in a large parameter domain. An analysis of simple TW model Equations 31.1 and 31.4 can explain the little influence of the gain compression in these regimes. A nonvanishing gain compression depletes the gain function $g(N)$ what implies a growth of the carrier density needed to reach threshold gain condition g_{th}. In solitary lasers, this growth is given by factor $g_{\text{th}}\varepsilon_G|E|^2/(g'\Gamma)$, which for typical gain compression coefficients and small-to-moderate field intensities is not exceeding a few percents of threshold carrier density. Consequently, a similar (up to a few percent) decay of the emission intensity can be observed.

A somehow different situation occurs in semiconductor ring lasers [19,22,23,45], where a proper introduction of nonlinear gain compression is crucial when deciding the type of operation states. In this case, one should distinguish the gain compression implied by co- and counter- propagating fields:

$$g^{\pm}(N,E^{\pm}) = g(N)\rho_G^{\pm}(E^{\pm}), \qquad \tilde{n}^{\pm}(N,E^{\pm}) = \tilde{n}(N)\rho_I^{\pm}(E^{\pm}),$$
$$\text{where} \quad \rho_j^{\pm} = \begin{cases} \left(1+\varepsilon_{js}|E^{\pm}|^2+\varepsilon_{jc}|E^{\mp}|^2\right)^{-1}, & \text{if } N = N(z,t) \\ \left(1+\varepsilon_{js}\langle|E^{\pm}|^2\rangle+\varepsilon_{jc}\langle|E^{\mp}|^2\rangle\right)^{-1}, & \text{if } N = N(t) \end{cases}, \quad j \in \{G, I\}, \tag{31.23}$$

whereas parameters ε_{js} and ε_{jc}, $j = G, I$, determine self- and cross-saturation of the gain and refractive index functions. In the ring lasers, usually is assumed that $\varepsilon_{Gc} > \varepsilon_{Gs}$, and $\varepsilon_{Ic} > \varepsilon_{Is}$. A detailed analysis based on the Maxwell–Bloch equations showed that the cross-saturation factor for two resonant modes in the ring cavity is twice larger than the self-saturation one [46].

The generalized functions $g^{\pm}$ and $\tilde{n}^{\pm}$ enter the definition of the propagation factor $\beta = \beta^{\pm}$ and the stimulated recombination function $\mathcal{S}$:

$$\beta^{\pm} = \delta_0 + \tilde{n}^{\pm}(N,E^{\pm}) + \tilde{n}_T(I) + \tfrac{i(g^{\pm}(N,E^{\pm})-\alpha)}{2},$$
$$\mathcal{S}(N,E^{\pm}) = \begin{cases} \frac{c_0}{n_g}\Re\sum_{\nu=\pm} E^{\nu*}[g^{\nu}(N,E^{\pm})-2\mathcal{D}]E^{\nu}, & \text{if } N = N(z,t) \\ \frac{c_0}{n_g}\Re\sum_{\nu=\pm}\langle E^{\nu*}[g^{\nu}(N,E^{\pm})-2\mathcal{D}]E^{\nu}\rangle_1, & \text{if } N = N(t) \end{cases}. \tag{31.24}$$

It is noteworthy that differences in parameters ε_{js} and ε_{jc}, $j = G, I$, imply differences in the propagation factors β^+ and β^- determining the evolution of the fields E^+ and E^-, respectively. These differences are crucial when determining type and stability of operating states in the ring laser, see References [19,23,45] for more details.

To illustrate how an asymmetry of the self- and cross-gain saturation implies different operation states in the ring laser (see Figure 31.2b), we have simulated the TW model equations 31.14, 31.21, 31.8, 31.5, 31.23, 31.24, 31.3 for vanishing ε_{Is} and ε_{Ic}, fixed nonvanishing sum $\varepsilon_{Gc} + \varepsilon_{Gs} = C > 0$ and tuned difference $\varepsilon_{Gc} - \varepsilon_{Gs}$. Figure 31.6 shows the results of these simulations. Solid gray and dashed black curves in all panels of this figure represent clockwise (CW) and counter-clockwise (CCW) propagating field functions $E^-(b_1, t)$ and $E^+(a_1, t)$ at the point scattering source J_1, respectively (see Figure 31.2b). Panel (a) of this figure gives an overview of all obtained states when tuning $\varepsilon_{Gc} - \varepsilon_{Gs}$ from $-C$ (full self-saturation with vanishing ε_{Gc}) up to $+C$ (full cross-saturation with vanishing ε_{Gs}). Panels (b)–(e) of the same figure represent four different observed dynamic regimes. The first three regimes occurring with a consequent increase of the cross-gain saturation are the bidirectional stable stationary state (b), the alternate oscillations (c), and the unidirectional bistable state (d). These three regimes can be observed experimentally and recovered theoretically using a simple two-mode ODE model [19]. An analysis of the TW model performed in Reference [23] has explained the relation between the asymmetry of the gain compression factors, ε_{Gc} and ε_{Gs}, and stability of the bidirectional steady state (regime b) or unidirectional bistable states (regime d). It was also shown, how the difference $\beta^+ - \beta^-$ and localized backscattering r_1 determine the frequency of alternating oscillations (regime c).

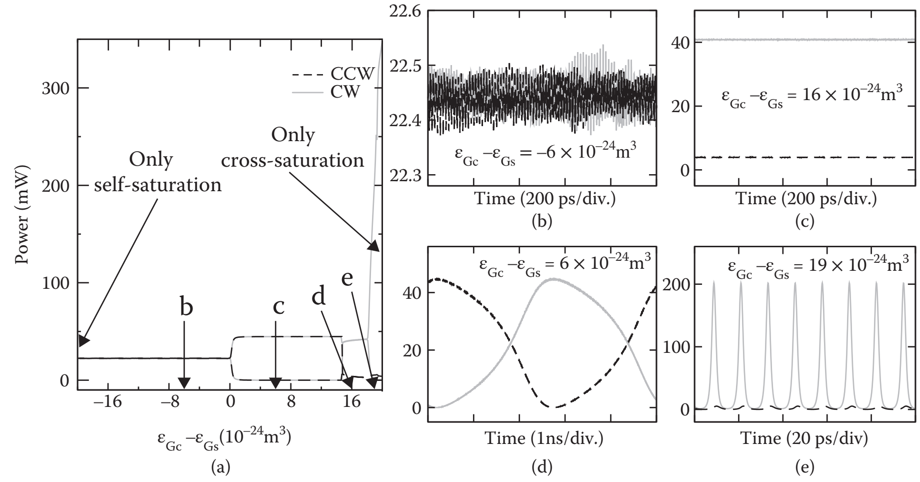

(a) (b) (c) (d) (e)

FIGURE 31.6 Dynamic regimes for different contributions of the cross- and self-gain saturations. (a) Maximal and minimal intensities of the optical fields at J_1 for changing values of $\varepsilon_{Gc} - \varepsilon_{Gs}$ but fixed $\varepsilon_{Gs} + \varepsilon_{Gc} = 20 \cdot 10^{-24}$ m^3. (b)–(e) Typical representatives of the observed regimes. Thick gray and dashed black curves indicate clockwise (CW) and counter-clockwise (CCW) propagating fields. Parameters are similar to those of Figures 31.4a and b, only $|S_1| = 1000\,\mu$m, $\alpha_H = -2$, $\alpha = 2\,\text{cm}^{-1}$, $\nu_1^1 = \varepsilon_{Is} = \varepsilon_{Ic} = 0$, $I = 100$ mA. U_F' and r_S are the same as in Figure 31.5, whereas the field transmission and localized backscattering parameters at J_1 are $t_1 = \sqrt{0.7}$ and $r_1 = 0.007$, respectively.

The last simulated regime (e) was observed for the dominant cross-gain saturation. Like usual mode-locking pulsations, this regime is characterized by large short pulses occurring with the round-trip period. However, in contrast to the mode-locking observed in multisection ring lasers [47], this state is unidirectional and does not require any fast saturable absorption. Similar mode-locked pulsations in a single-section ring laser were found and discussed theoretically in Reference [45].

31.7 Further Modifications of the TW Model

There exist a vast number of further possible modifications of the TW model for MSLs. Each of these modifications, however, requires a few new not very well-known parameters and, therefore, should be used with the great care. On the other hand, some of these modifications being crucial when analyzing a particular group of MSLs can be irrelevant for simulations and analysis of different type MSLs. Later we present several modifications of the TW model used for investigation of specific types of MSLs.

Multiple Carrier Rate Equations in QD Lasers:

When modeling QD lasers, one should take into account carrier exchange processes between a carrier reservoir (CR) and discrete levels in QDs.

One of the simplest ways to account for all these transitions within the TW modeling frame is provided by the rate equations for the normalized carrier density $N^{cr}(z,t)$ (scaled by the factor Θ_N) within the CR, and occupation probabilities $N^{gs}(z,t)$, $N^{es}(z,t)$ of the ground state (GS) and the first excited state (ES) of QDs, respectively [10,48,49].

To keep the structure of the TW field equations 31.14 unchanged, we neglect the inhomogeneous spectral broadening effect due to QD nonuniformity and consider a simple single-Lorentzian gain spectrum profile, which limits the material gain bandwidth. Besides, we assume that the laser operates at the GS transition only. In this case, the propagation factor β depends on the ground state occupation probability

$N^{gs}(z,t)$ only. The expression of $\beta(N^{gs})$ is equivalent to that one given by Equations 31.2 and 31.3 with spatially distributed occupation probability $N^{gs}(z) \in [0,1]$ and factor $1/2$ instead of the carrier density $N(z,t)$ and transparency carrier density N_{tr}, respectively.

To describe carrier exchange processes between the CR, GS, and ES of the QDs in the active section (see Figure 31.7a), we use the following set of rate equations:

$$\begin{aligned}
\frac{\mathrm{d}}{\mathrm{d}t}N^{gs}(z,t) &= -\frac{N^{gs}}{\tau_{gs}} + 2\left(\frac{N^{es}(1-N^{gs})}{\tau_{es\to gs}} - \frac{N^{gs}(1-N^{es})}{2\tau_{gs\to es}}\right) - \frac{1}{\theta_E}\mathcal{S}(N^{gs},E^{\pm}),\\
\frac{\mathrm{d}}{dt}N^{es}(z,t) &= -\frac{N^{es}}{\tau_{es}} - \left(\frac{N^{es}(1-N^{gs})}{\tau_{es\to gs}} - \frac{N^{gs}(1-N^{es})}{2\tau_{gs\to es}}\right) + \left(\frac{N^{cr}(1-N^{es})}{4\tau_{cr\to es}} - \frac{N^{es}}{\tau_{es\to cr}}\right),\\
\frac{\mathrm{d}}{\mathrm{d}t}N^{cr}(z,t) &= \frac{I}{q|S_1|\theta_I} - \frac{N^{cr}}{\tau_{cr}} - 4\left(\frac{N^{cr}(1-N^{es})}{4\tau_{cr\to es}} - \frac{N^{es}}{\tau_{es\to cr}}\right).
\end{aligned} \tag{31.25}$$

Here, $\mathcal{S}(N^{gs},E^{\pm})$ is defined by Equation 31.22, whereas τ_a^{-1} and $\tau_{a\to b}^{-1}$, $a,b \in \{gs,es,cr\}$, denote spontaneous relaxation and transition rates between GS, ES, and CR, respectively. Factors $(1-N^{gs})$ and $(1-N^{es})$ represent the Pauli blocking, factors 2 and 4 account for the spin degeneracy in the QD energy levels. Note that here we neglect direct transitions between CR and GS. θ_I and $\theta_E = \frac{2hc_0\theta_I}{\lambda_0}$ are scaling factors relating the injection current I, the field intensity $|E|^2$, the CR scaling factor θ_N, the differential gain g', and the QD density in the active zone.

In the saturable absorption sections (see Figure 31.7b), there is no pumping, $I = 0$, so that the transitions from CR to ES can be neglected, $\tau_{cr\to es} \to \infty$, and the last of the equations 31.25 can be ignored. The carrier transition from ES to CR can be added to similar spontaneous recombination term: $\bar{\tau}_{es}^{-1} = \tau_{es}^{-1} + \tau_{es\to cr}^{-1}$. Following Reference [48], one can model the carrier transitions in the negatively driven saturable absorber

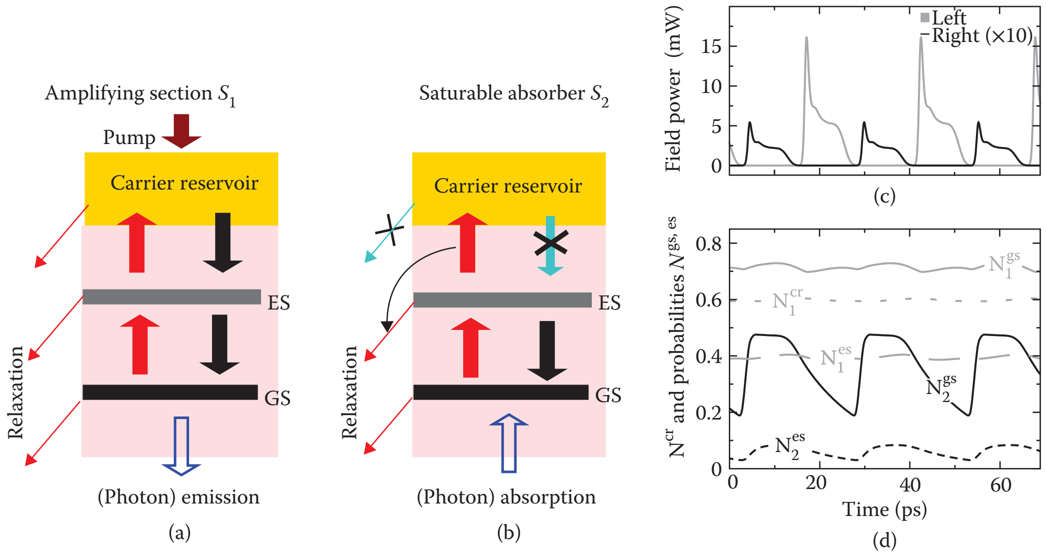

FIGURE 31.7 Schematic representation of carrier transitions in (a) the gain section and (b) the saturable absorption section of the QD MSL. Crossed arrows in panel (b) indicate the transitions which are neglected in the model equations. A sequence of (c) the emitted mode-locking pulses with an enhanced trailing edge plateaux at both sides of the laser and (d) the sectionally averaged carrier functions $N^{gs,es,cr}$ in both laser sections. All parameters and a detail description of the MSL device can be found in References [10,49].

by assuming an exponential decay of $\bar{\tau}_{es}$ with growing negative voltage U, whereas all other relaxation rates remain unchanged.

Figures 31.7c and d presents an example of simulated mode-locked QD laser containing an amplifying and a saturable absorber sections S_1 and S_2. Panel (c) of this figure gives an evidence of strongly asymmetric pulses with a broad trailing edge plateau. Our theoretical analysis has shown that such pulses arise mainly due to noninstant carrier transitions between the CR, ES, and GS of the QD laser shown in panel (d) of the same figure. The presence of these transitions exert a smoothening effect on all spatial/temporal carrier and field intensity distributions and, in turn, imply a broadening of the trailing edge of the pulse. We have also found that an increase of the intradot transition rates leads to a reduction of the filtering effect and, hence, to a growth of the pulse peak intensity and narrowing of the pulse and its trailing edge. More details on our analysis as well as experimental demonstration of such asymmetric pulses can be found in Reference [10,49].

Further modifications of the TW model can be used for more precise simulations of QD lasers. For example, one can improve the model of carrier transitions (Equation 31.25) by separate consideration of electrons and hole densities [50]. To allow a simultaneous radiation on the spectrally well-separated ground and ES, one can introduce another pair of TW equations for optical fields [51]. An inhomogeneous spectral broadening and an accompanying description of the radiation at GS and ES can also be modeled by an introduction of multiple sets of carrier rate and polarization equations representing carrier transitions within the QDs of different size and their impact on the laser emission at different wavelengths [52].

Nonlinear Gain and Refractive Index Functions:

In the earlier discussion, the gain and the refractive index dependence on the carrier density N was modeled by linear functions related to each other by the linewidth enhancement factor α_{H}. This modeling approach is reasonable for small and slow variation of carrier density N, but can fail once N exhibits some significant changes, see, e.g., Figure 31.5d, where a variation of the spatially distributed $N(z, t)$ was of the order of the mean value of the carrier density. In such situations, one should better use nonlinear peak gain functions, $g(N)$, which can better represent measured or precalculated gain spectra profiles. For this reason, the following logarithmic gain peak function dependence on the carrier density is frequently used:

$$g(N) = \Gamma g' N_{\mathrm{tr}} \ln\left(\frac{\max\{N,N^*\}}{N_{\mathrm{tr}}}\right), \qquad \tilde{n}(N) = \frac{\alpha_{\mathrm{H}} g(N)}{2}. \tag{31.26}$$

Here, N^* indicates a cutoff carrier density value, which prevents the convergence $g(N) \to -\infty$ with carriers $N \to 0$. These expressions for the gain and index change functions replace the relations 31.3 used in the TW models discussed earlier.

Another issue is related to the linewidth enhancement factor α_H. Initially, this factor was used to relate gain and refractive index functions at a fixed value of N. Such approach implies a rather simple model for propagation factor, β, and can be quite useful when performing an advanced analysis of model equations. In reality, however, the ratio between the gain and refractive index is not a constant, but a function depending on carrier density, temperature, and several other factors not discussed in this chapter. Thus, an experimental estimation of this factor in the semiconductor laser operating at different conditions or using different methods can lead to rather different values of α_{H}. For this reason, it can be preferable to use separately defined nonlinear peak gain and index change functions $g(N)$ and $\tilde{n}(N)$. These functions depend on the properties of the semiconductor material and the design of the device, and, therefore, should be adjusted individually for each considered laser.

A satisfactory description of these functions for a broad class of semiconductor lasers is given by the logarithmic, and the square-root-like expressions [38]

$$g(N) = \Gamma g' N_{\mathrm{tr}} \ln\left(\frac{\max\{N,N^*\}}{N_{\mathrm{tr}}}\right), \qquad \tilde{n}(N) = \tilde{n} + \alpha_{\mathrm{H}}\, \Gamma g' \sqrt{N \cdot N_{\mathrm{tr}}}. \tag{31.27}$$

Here, $\tilde{n}$ represents the offset of the refractive index change function, $\Gamma g' = \partial_N g(N_{\text{tr}})$, and $\alpha_H = 2\partial_N \tilde{n}(N_{\text{tr}})/\partial_N g(N_{\text{tr}})$ is the linewidth enhancement factor evaluated at the transparency carrier density N_{tr}.

We should admit, however, that linear formulas 31.3 with slightly corrected factors g', α_{H}, N_{tr}, and a proper selection of δ_0 can be used for approximation of nonlinear functions 31.27 not only in the vicinity of N_{tr} but also over a larger range of densities N including the threshold density N_{th}. In many cases, the simplifications of the gain and refractive index functions still imply qualitatively the same results when performing simulations of MSLs with varying parameters [53].

31.8 Multisection Lasers and Coupled Laser Systems

A vast variety of MSLs and coupled laser systems can be represented as a set of differently interconnected laser sections, each characterized by its material and geometry parameters. To distinguish these parameters or functions attributed to different laser sections, we shall use the lower indices. For example, α_k, $g_k(N)$, and a_k denote the field losses, the gain function and the left-edge coordinate of the section S_k. Note also that for unique identification of longitudinal coordinate z within all laser sections, different sections of our device are represented by nonoverlapping intervals (a_k, b_k).

According to our laser device construction, for any edge of all sections S_k, we can attribute a unique junction J_l. On the other hand, each junction has, at least, one section joining it from one or another side, see, e.g., Figure 31.1, where MSLs are represented as sets of laser *sections* mutually interconnected through different *junctions*. To explain the relations between section edges, corresponding junctions, and applied optical injections, we use the following notations in the sequel of this chapter. By l we denote the index of the junction J_l, as well as optical fields and the section edges attributed to this junction. l' (l'') is the vector of length $|l'|$ $(|l''|)$ containing indices of the sections connected to J_l by their left (right) edge $a_{l'_j}$ $(b_{l''_j})$; see Figure 31.8a. $l^e = |l'| + |l''| \geq 1$ is a total number of such section edges connected to J_l. By $o_l(t)$ and $E_l^{\text{out}}(t)$ we denote the applied optical injection and the recorded emission at the same junction, see solid and dashed thick light gray arrows in Figure 31.8a. When the injection or emission at J_l is absent, the corresponding function is simply set to zero.

General field scattering conditions at the arbitrary junction J_l are defined by the $l^e \times l^e$ dimensional complex field scattering matrix $\mathcal{T}_l$, $l^e \times 1$ dimensional injection distribution matrix $\mathcal{T}_l^i$, and $1 \times (l^e + 1)$

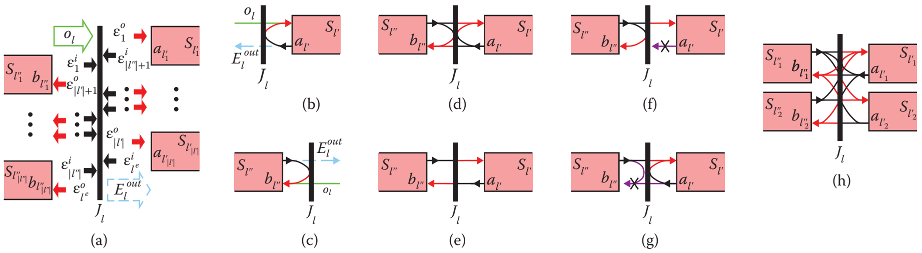

FIGURE 31.8 Schematic representation of different interfaces between the sections at the junction J_l. (a) general configuration, (b) and (c) field reflection and optical injection at laser facets, (d) and (e) reflecting (transmission and reflection) and trivial (transmission only) interface of two section edges, (f) and (g) directionally absorbing interfaces of two section edges for modeling of a master–slave laser system, and (h) transmitting/reflecting interface of four section edges for modeling ring lasers with an outcoupling waveguide. Black segments and gray frames represent junction J_l and all section edges connected to this junction, respectively. Black and dark gray arrows in all diagrams represent all components of the vector fields $\mathcal{E}_l^i$ and $\mathcal{E}_l^o$, respectively. Optical injections o_l and emitted fields E_l^{out} are shown by solid and dashed light gray arrows. Crossed arrows in panels (f) and (g) represent a full absorption of the corresponding fields.

dimensional outcoupling matrix $\mathcal{T}_l^o$:

$$
\begin{aligned}
&\mathcal{E}_l^o = \mathcal{T}_l \mathcal{E}_l^i + \mathcal{T}_l^i o_l, \quad E_l^{\text{out}} = \mathcal{T}_l^o \begin{pmatrix} \mathcal{E}_l^i \\ o_l \end{pmatrix}, \qquad \text{where} \\
&\mathcal{E}_l^o = \left(E^+_{l'_1}(a_{l'_1}, t), \ldots, E^+_{l'_{|l'|}}(a_{l'_{|l'|}}, t), E^-_{l''_1}(b_{l''_1}, t), \ldots, E^-_{l''_{|l''|}}(b_{l''_{|l''|}}, t) \right)^T, \\
&\mathcal{E}_l^i = \left(E^+_{l''_1}(b_{l''_1}, t), \ldots, E^+_{l''_{|l''|}}(b_{l''_{|l''|}}, t), E^-_{l'_1}(a_{l'_1}, t), \ldots, E^-_{l'_{|l'|}}(a_{l'_{|l'|}}, t) \right)^T.
\end{aligned}
\tag{31.28}
$$

The vector functions $\mathcal{E}^i$ and $\mathcal{E}^o$ (see black and dark gray arrows in Figure 31.8a) denote the internal optical fields, which are incident into the junction from all adjacent sections and are scattered from the junction back into these sections, respectively.

In most cases, the interfaces between the sections are much simpler. For example, the scattering matrices at the facets of the solitary laser (Figures 31.8b and c as well as junctions J_1 and J_2 in Figure 31.2a) are determined by the boundary conditions (Equation 31.7), i.e.,

$$
\begin{cases}
\mathcal{T}_l = -r_l^*, \;\; \mathcal{T}_l^i = 1, \;\; \mathcal{T}_l^o = (t_l, 0), & \text{single "left" edge } a_{l'}, \;\; |l'| = 1, \;\; |l''| = 0 \\
\mathcal{T}_l = r_l, \;\; \mathcal{T}_l^i = 1, \;\; \mathcal{T}_l^o = (t_l, 0), & \text{single "right" edge } b_{l''}, \;\; |l''| = 1, \;\; |l'| = 0
\end{cases},
\tag{31.29}
$$

where r_l and t_l are field reflection and transmission coefficients,

$$
|r_l| \leq 1, \qquad t_l \leq \sqrt{1 - |r_l|^2}.
\tag{31.30}
$$

Another frequently used case in MSLs is the interface of two adjacent sections (Figures 31.8d through g). At such interfaces, we have no optical injections and field emission, so that we can set $\mathcal{T}_l^i = (0,0)^T$ and $\mathcal{T}_l^o = (0,0,0)$. The scattering of the field at J_l, in this case, is entirely defined by the 2×2 dimensional matrix

$$
\mathcal{T}_l = \begin{pmatrix} t_l & -r_l^* \\ r_l & t_l \end{pmatrix},
\tag{31.31}
$$

where t_l and r_l satisfy the conditions 31.30 (see Figure 31.8d and, e.g, J_3 in Figure 31.1a). Here, the non-vanishing reflections r_l can appear, e.g., due to different heterostructure of the adjacent sections. In the simplest case of $r_l = 0$ and $t_l = 1$, $\mathcal{T}_l$ is an identity matrix, and the interface admits a full transmission of the optical fields (see Figure 31.8e and J_2 in Figure 31.1a).

When modeling the master–slave laser system (S_1 and S_2 in Figure 31.1d), only one-directional field propagation should be allowed in the air gap between two lasers (section S_3 in the same figure). This effect can be achieved by modification of otherwise standard scattering matrices $\mathcal{T}_l$ (Equation 31.31) at one of the gap section edges. One can model a full absorption of the backward incident beam at the interface of the master laser and the gap section (see Figure 31.8f and J_2 of Figure 31.1d), or prohibit the field backscattering into the air gap at the interface of the slave laser and the gap section (Figure 31.8g and J_3 of Figure 31.1d). Formally, both these situations can be defined by the scattering matrices

$$
\mathcal{T}_j = \begin{pmatrix} t_j & 0 \\ r_j & 0 \end{pmatrix} \text{ (master-gap interface)}, \qquad \mathcal{T}_j = \begin{pmatrix} t_j & -r_j^* \\ 0 & 0 \end{pmatrix} \text{ (gap-slave interface)}.
$$

More complicated situations occur at the junctions connecting more than two section edges of the MSL. For example, Figure 31.8h and J_1 of Figure 31.1e represent an interface connecting two "left" and two "right" section edges. This situation is used for modeling of a localized coupling of the ring laser (section S_1 in Figure 31.1e) and the outcoupling waveguide (S_2 and S_3 in the same figure).

Similarly to the previously discussed case, the optical injection- and field emission-relevant matrices can be defined by $\mathcal{T}_l^i = (0,0,0,0)^T$ and $\mathcal{T}_l^o = (0,0,0,0,0)$. By assuming a nonvanishing field reflection r_l at the ring laser part of this junction (section edges $b_{l''_1}$, $a_{l'_1}$ in Figure 31.8h or b_1, a_1 in Figure 31.1e), we model a *localized* linear backscattering of the fields [23,37]. The 4×4 dimensional scattering matrix $\mathcal{T}_l$, in this case, can be defined as

$$\mathcal{T}_l = \begin{pmatrix} t_l & i\tilde{t}_l & -r_l^* & 0 \\ i\tilde{t}_l & t_l & 0 & 0 \\ r_l & 0 & t_l & i\tilde{t}_l \\ 0 & 0 & i\tilde{t}_l & t_l \end{pmatrix}, \qquad t_l^2 + \tilde{t}_l^2 + |r_l|^2 \leq 1. \tag{31.32}$$

Here, t_l is a real field amplitude transmission factor within the same (ring or outcoupling) waveguide and $i\tilde{t}_l$ is an imaginary coefficient representing part of the field amplitude, which is outcoupled from the ring or transmitted into the ring from the external waveguide. It is noteworthy that a proper estimation of the transmission–reflection–outcoupling matrix $\mathcal{T}_l$ in the ring laser case requires some appropriate measurements or an advanced modeling. Such modeling should take into account the curvature of the ring cavity, the length of the coupling regions, the field diffraction, and the overlapping of the lateral modes in the coupling region [54]. Moreover, the coefficients of the scattering matrix are, in general, frequency dependent. In our TW modeling approach, we use constant coefficients describing field scattering at the central reference frequency.

31.9 Simulations of Nontrivial MSL Device

The concept of differently interconnected *sections* and *junctions* allows modeling rather complicated MSLs. One of such nontrivial configurations is a semiconductor ring laser with four separate branches of the filtered optical feedback, see Figure 31.9a. The multichannel feedback scheme of this laser admits a fast switching between steady states determined by the resonances of the ring laser and the wavelengths of the activated filtering channels [55].

The gray-shaded frames in Figure 31.9a represent device sections of different types. Namely, we distinguish here the amplifying sections $S_{A\cdot}$, where the field and carrier dynamics is governed by the full TW model (Equations 31.5, 31.14, 31.21, 31.23, 31.24, 31.26), and two kinds of passive sections, $S_{P\cdot}$ and $S_{F\cdot}$, where gain and refractive index functions are set to zero, allowing to ignore the carrier rate equations at all. The notations of all sections in the section indexes are made according to the cardinal directions "n," "e," "s," and "w".

Almost all parameters of the TW model in all sections of our MSL are the same as in Figure 31.6. A few exceptions are parameters $\alpha_H = -4$ and $\bar{\gamma}_\lambda = 100\,\mathrm{nm}$. In the passive waveguiding sections, $S_{P\cdot}$ (medium gray), we assume $|S_{Pe}| = |S_{Pw}| = 330\,\mu\mathrm{m}$, $|S_{Pne}| = |S_{Pnw}| = 50\,\mu\mathrm{m}$, $|S_{Pse}| = |S_{Psw}| = 2500\,\mu\mathrm{m}$, and neglect the gain dispersion, $\bar{g} = 0$. In the passive filtering sections, $S_{F\cdot}$ (light gray), we assume $|S_{F\cdot}| = 530\,\mu\mathrm{m}$ and significantly modify the profile of Lorentzian gain dispersion by setting $\bar{g} = 5 \cdot 10^4\,\mathrm{m}^{-1}$ and $\bar{\gamma}_\lambda = 4\,\mathrm{nm}$. The relative peak wavelengths of four filtering branches (sections S_{Fwj} and S_{Fej}, $j = 1, \ldots, 4$) are $\bar{\lambda} = -2, -0.67, 0.67$, and $2\,\mathrm{nm}$, respectively. Finally, in the amplifying sections (dark gray) within the primary ring laser, S_{Ajk}, $j = n, s$ and $k = e, w$, we use $|S_{A\cdot}| = 380\,\mu\mathrm{m}$, $\varepsilon_{Gs} = 6 \cdot 10^{-24}\,\mathrm{m}^3$, $\varepsilon_{Gc} = 2\varepsilon_{Gs}$, and the bias currents $I = 26\,\mathrm{mA}$, which is 1.5 times higher than the lasing threshold in the laser without feedback. In the amplifying sections belonging to the four filtering branches, S_{Asj}, $j = 1, \ldots, 4$, we assume $|S_{A\cdot}| = 190\,\mu\mathrm{m}$ and $\varepsilon_{Gc} = \varepsilon_{Gs} = 9 \cdot 10^{-24}\,\mathrm{m}^3$. Once the bias current in these sections is zero, $I = 0\,\mathrm{mA}$,

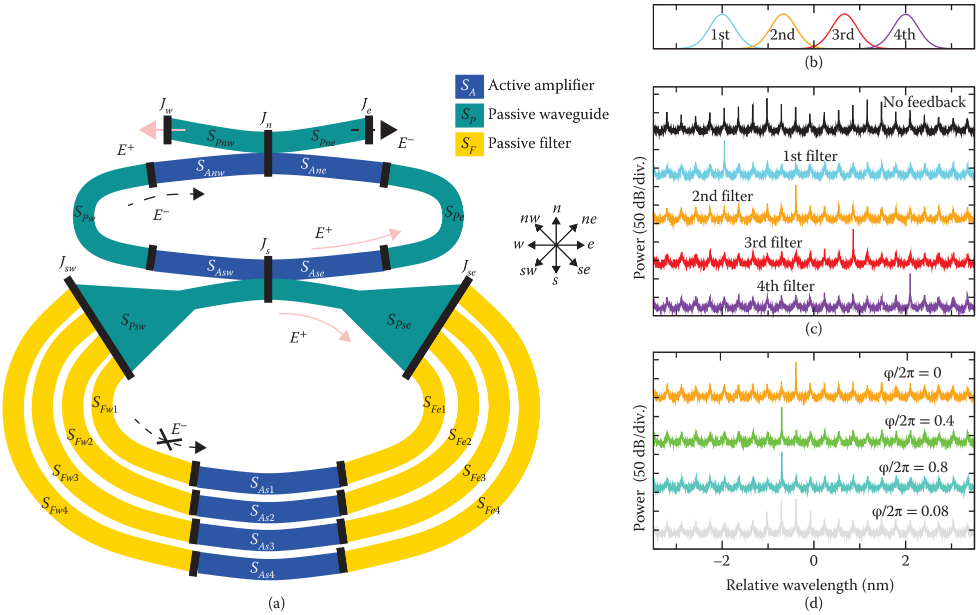

FIGURE 31.9 (a) Scheme of the semiconductor ring laser with four branches of filtered and amplified unidirectional optical feedback. Black segments and gray-shaded frames indicate junctions and different sections of the MSL. Solid light-gray and dashed black arrows show propagation directions and the emission of the fields E^+ and E^-, respectively. (b) Transmission spectra of four filtering branches. Maximal transmission at $I_{Asj} = 10\,\text{mA}, j = 1, \ldots, 4$ is approximately 1.6. (c) Stabilization of the multimode behavior of the ring laser (black) by the single-branch filtered feedback (gray). (d) Dependence of the lasing wavelength on the feedback phase once the second filtering branch is activated.

the feedback branches are efficiently absorbing the optical fields. To activate one of the feedback branches, we set the corresponding injection $I = 10\,\text{mA}$.

The field transmission and reflection conditions at J_n and J_s are given by the conditions 31.32 with $r = 0$, $t = \sqrt{0.8}$, and $\tilde{t} = \sqrt{0.2}$. At J_{se} and J_{sw}, we neglect all possible reflectivity, admit full-field transmission from filtering branches to the passive waveguide sections S_{Psw} or S_{Pse}, equally distribute the intensity of the optical field E^+ propagating from S_{Pse} to the filtering branches, and fully absorb E^- at J_{sw}:

$$E^-(b_{Pse}, t) = \textstyle\sum_{j=1}^{4} E^-(a_{Fej}, t), \qquad E^+(a_{Fej}, t) = \sqrt{\tfrac{1}{4}}\, E^+(b_{Pse}, t), \quad j = 1, \ldots, 4;$$

$$E^+(a_{Psw}, t) = \textstyle\sum_{j=1}^{4} E^+(b_{Fwj}, t), \qquad E^-(b_{Fwj}, t) = 0, \quad j = 1, \ldots, 4.$$

At J_w and J_e, the fields E^+ and E^- are emitted from our MSL. Here, the field reflection–transmission conditions are given by (Equation 31.29) with the reflectivity factors $r_w = r_e = 0.1$. All other junctions of this MSL are trivial, i.e., the optical fields cross the interfaces according to the relations 31.31 with $r_l = 0$ and $t_l = 1$.

A series of simulations represented in the remaining panels of Figure 31.9 are in good agreement with the experimental results reported in Reference [55]. First of all, panel (b) shows the transmission spectra (modulus of the wavelength-dependent complex transmission function) of the optical fields E^+ propagating through each of four optical feedback branches activated by the injected current into the corresponding amplifying section. For 10 mA injections used in these simulations, the peak amplitude transmission is around 1.6.

Panels (c) and (d) of Figure 31.9 show simulated optical spectra of the emitted field at the "west" facet J_w of the MSL for different operation conditions. An upper black curve in panel (c) represents the optical spectrum in the case of deactivated feedback branches. Multiple significant spectral peaks with the mode separation corresponding to the field round-trip time in the ring laser indicate a multimode lasing of the laser. An optical field E^+ propagating along the filtering branches, however, is not entirely absorbed. For higher ring laser injections, we observed the steady states determined by a single ring resonance mode. In these cases, the amplifier within corresponding filtering branch was optically pumped, and the related peak amplitude transmission was around 0.2. The competition between nominally equivalent unpumped filtering branches, however, does not allow predicting the lasing wavelength of such a steady state.

The four lower spectra in Figure 31.9c represent switching between different optical modes by activation of the corresponding filter and deactivation of the remaining ones. A close inspection of these spectra shows, that whereas the first and the fourth filters select the resonance modes which are closest to the filter peak position, the third, and, especially, the second filter prefers modes admitting smaller optical feedback. We have found, that this mode selection is related to the phase of the optical field within the filtering branch. Figure 31.9d demonstrates, how tuning of the feedback phase within the second filtering branch (realized by variation of the detuning factor $\delta_{0,Fw2}$) implies changes between the resonant modes located within the filtering band.

In conclusion, we have simulated the MSL consisting of 22 sections interconnected at 18 junctions. Our theoretical findings were in a good qualitative agreement with experimental observations of similar ring laser device reported in Reference [55].

31.10 Beyond Numerical Simulations of the TW Model

In the previous sections, we have introduced different modifications of 1+1 dimensional TW model suited for simulations of various MSL devices and coupled laser systems. In the remaining part of this chapter, we introduce the concept of instantaneous optical modes and present several applications of these modes for an advanced analysis of MSLs. In all these cases, we consider MSLs without optical injection and neglect a contribution of Langevin noise term $F_{sp}^{\pm}$, which is of minor importance in the lasers operating well above threshold.

Instantaneous Optical Modes:

The concept of optical modes plays a significant role in understanding laser dynamics in general. They represent the natural oscillations of the electromagnetic field and determine the optical frequency and the lifetime of the photons contained in the given laser cavity. The *instantaneous* optical modes correspond to a fixed *instant* distribution of the propagation factor β [26].

In general, compared to a variation of the optical fields, the changes of the carrier density N are slow. The change of N is mainly determined by the carrier relaxation time which, typically, is measured in nanoseconds (or tens of picoseconds when considering saturable absorbers). On the other hand, picosecond or sub-picosecond time windows are sufficient for significant changes of the photon densities. Since the gain compression for small and moderate field intensities is also small, the propagation factor β experiences only minor modifications in the picosecond range. For this reason, in the remaining part of this chapter we analyze the field equations for the frozen distribution of the propagation factor $\beta(\mathrm{z}, \mathrm{t}_0)$ at the time instant t_0.

The instantaneous optical modes of MSLs are pairs $(\Omega(\beta), \Theta(\beta, z))$ of complex frequencies Ω and vector-functions $\Theta = (\Theta_E^+, \Theta_E^-, \Theta_P^+, \Theta_P^-)^T$, where imaginary and real parts of $\Omega(\beta)$ are mainly defining the angular frequency and the damping of the mode, whereas $\Theta(\beta, z)$ determines the spatial distribution of the mode.

Complex frequencies Ω and vector-functions $\Theta(\beta, z)$ solve the linear system of algebro-differential equations

$$\begin{cases} \frac{\mathrm{d}}{\mathrm{d}z}\Theta_E^+ = -i\mathcal{B}(\Omega)\Theta_E^+ - i\kappa\Theta_E^- \\ \frac{\mathrm{d}}{\mathrm{d}z}\Theta_E^- = i\mathcal{B}(\Omega)\Theta_E^- + i\kappa\Theta_E^+ \\ \Theta_P^\pm(\beta, z) = \frac{\bar{\gamma}/2}{\bar{\gamma}/2+i(\Omega-\bar{\omega})}\Theta_E^\pm(\beta, z) \end{cases}, \quad z \in S_k\Big|_{k=1}^{n}, \qquad \theta_l^o(\beta) = \mathcal{T}_l\theta_l^i(\beta)\Big|_{l=1}^{m}, \tag{31.33}$$

obtained by assuming a nonvarying in time propagation factor, $\partial_t\beta = 0$, and substituting the expressions

$$E^\pm(z, t) = \Theta_E^\pm(\beta; z)e^{i\Omega(\beta)}, \qquad P^\pm(z, t) = \Theta_P^\pm(\beta; z)e^{i\Omega(\beta)}$$

into the field equations 31.14 within each of n sections S_k, and boundary conditions 31.28 at each of m junctions J_l. Similarly to the vector functions $\mathcal{E}_l^o$ and $\mathcal{E}_l^i$ in Equation 31.28, complex vectors $\theta_l^i(\beta)$ and $\theta_l^o(\beta)$ in Equation 31.33 represent functions $\Theta_E^\pm(\beta, z)$ at the section edges $z = a_{l_j'}$ or $z = b_{l_j''}$ connected by the junction J_l. The function $\mathcal{B}(\Omega)$ entering Equations 31.33 is defined in 31.16.

Each pair of linear ODEs in Equation 31.33 can be solved by the transfer matrix[†] 31.11 with the coefficients nonlinearly depending on still unknown complex frequency Ω. These matrices define $2n$ homogeneous linear equations relating $4n$ components of the complex vector $\mathcal{S} = (s_1, \ldots, s_{4n})^T$ representing field functions $\Theta_E^\pm(\beta, z)$ at both edges of all sections S_k. Another $2n$ homogeneous linear equations relating the same complex numbers are given by the field scattering matrices $\mathcal{T}_l$ at all junctions J_l. In such a manner, we build a linear $4n$ dimensional algebraic system

$$\mathcal{M}(\beta, \kappa; \Omega)\mathcal{S} = 0,$$

determined by a sparse $4n \times 4n$ dimensional matrix $\mathcal{M}$. Nontrivial solutions $\mathcal{S}$ (i.e., nontrivial functions Θ of the problem 31.33) are available only for those Ω which are the complex roots of the complex characteristic equation

$$\det \mathcal{M}(\beta, \kappa; \Omega) = 0. \tag{31.34}$$

The finite number of these roots can be found using Newton iterations and the homotopy method; see Reference [26] for more details.

It is noteworthy that linear configurations of MSLs admit rather simple expressions of the characteristic equations 31.34 involving the response functions $F_l(z, \Omega)$ and $F_r(z, \Omega)$ defined at some longitudinal position z of the MSL:

$$\det \mathcal{M}(\beta, \kappa; \Omega) = 0 \qquad \Leftrightarrow \qquad F_l^{-1}(z, \Omega) = F_r(z, \Omega). \tag{31.35}$$

For example, for the solitary lasers considered in Figure 31.3b and c, $F_l(b_1, \Omega)$ is defined in Equation 31.13, whereas $F_r(b_1, \Omega) = r_2$. In the general case, functions F_l and F_r are defined by a consequent superposition of the sectional transfer matrices $M(\beta, \kappa, \Omega)$ and the left-to-right or right-to-left junction-transfer matrices

$$\mathcal{T}_{j,22}^{-1}\begin{pmatrix} \det\mathcal{T}_j & \mathcal{T}_{j,12} \\ -\mathcal{T}_{j,21} & 1 \end{pmatrix} \qquad \text{or} \qquad \mathcal{T}_{j,11}^{-1}\begin{pmatrix} 1 & -\mathcal{T}_{j,12} \\ \mathcal{T}_{j,21} & \det\mathcal{T}_j \end{pmatrix};$$

see References [23,26,28] for more details.

[†] In the case of nonvanishing $\Delta_\beta = \frac{\beta^+-\beta^-}{2}$, the transfer matrix in each section S_k should be constructed for $\bar{\beta} = \frac{\beta^++\beta^-}{2}$ and later multiplied by the factor $e^{-i\langle\Delta_\beta\rangle_k|S_k|}$ [23].

The calculated optical field function $\Psi(z,t) = (E^+, E^-, P^+, P^-)^T$ can be represented as a superposition of the suitably normalized vector functions $\Theta(\beta, z)$ which are slowly changing with a variation of the propagation factor $\beta(z,t)$:

$$\Psi(z,t) = \sum_{j=1}^{\infty} f_j(t)\Psi_j(\beta(z,t), z). \tag{31.36}$$

Here, $f_j(t)$ is the complex amplitude of the mode, which can denote the mode contribution to the field emission at the laser facet a_k once normalization of mode functions assumes $\Theta_E^-(\beta, a_k) = 1$. According to our notations, index $_1$ denotes the most significant mode having a largest (instant) amplitude $|f|$ or a lowest damping $\Im\Omega$. An increasing index means a decreasing importance of the mode. This numbering does allow us to achieve good approximations of the field function $\Psi(z,t)$ already by low-dimensional truncated mode expansions 31.36.

Calculation of optical modes and expansion of the field function into the modal components can give a broad understanding of different operating regimes in MSLs and explain parameter change-induced transitions between these states observed in simulations and experiments. We have applied our mode analysis for interpretation of experimental observations in different MSLs. Namely, we have explained a stable operation of ring lasers at alternating oscillation or bi- and unidirectional steady state regimes [23]; almost periodically reappearing state transitions and estimation of thermal tuning parameters in master-oscillator power-amplifier device [38,56], DBR laser [14], or ECDL [15]; and strongly asymmetric pulse shapes in QD mode-locked laser [49]. More theoretical examples of our mode analysis can be found in Reference [26].

Steady States:

Any stationary (rotational wave) state of the MSL is determined by an optical mode with a *real* mode frequency

$$(\Psi(z,t), N(z,t)) = \left(\hat{f}\,\Theta(\hat{\beta}, z)e^{i\hat{\omega}t}, \hat{N}(z)\right), \quad \text{where } \Omega(\hat{\beta}) = \hat{\omega} \in \mathbb{R},$$

and $\hat{\beta}(z)$ is a constant in time spatially distributed propagation factor. Let us consider the TW model with sectionally averaged carrier density and neglected nonlinear gain compression given by Equations 31.4, 31.5, 31.14, 31.18, 31.15, and 31.28. In this case, all steady states are fully defined by a set of $n_a + 2$ real numbers $\left(\hat{\omega}, |\hat{f}|^2, \hat{N}_1, \ldots, \hat{N}_{n_a}\right)$, which are a mode frequency, a mode intensity, and sectionally averaged carrier densities within all n_a "active" sections having nonvanishing functions g and $\tilde{n}$. The rotational invariance of the TW model implies freedom in selection of the phase of the complex mode amplitude $\hat{f}$. The set of these real numbers is a root of a nonlinear algebraic system of one complex characteristic equation and n_a real steady-state carrier rate equations:

$$\begin{aligned} &\det \mathcal{M}\left(\beta(\hat{N}), \kappa; \hat{\omega}\right) = 0, \\ &\tfrac{I_r}{q\sigma_r|S_r|} - \mathcal{R}(\hat{N}_r) - |\hat{f}|^2 \tfrac{c_0}{n_g} G(\hat{N}_r, \hat{\omega})\langle\left(\Theta_E, \Theta_E\right)\rangle_r = 0, \quad r = 1, \ldots, n_a. \end{aligned} \tag{31.37}$$

Here, the frequency-dependent gain function G is defined in Equation 31.17, whereas the sectional average $\langle\left(\Theta_E, \Theta_E\right)\rangle_r$ can be expressed as a function of $\hat{\omega}$ and $\hat{N}$ [28].

In the case of the single active section, $n_a = 1$, the steady state frequency $\hat{\omega}$ and threshold carrier density $\hat{N}_1$ can be directly found from the characteristic equation, whereas the remaining equation determines the value of $|\hat{f}|^2$. Assume that the single active section S_1 of linear MSL is located on the left side of the device (see Figure 31.1b), and the optical fields within the adjacent passive section S_2 are governed by the simple relations 31.9. For an illustration of this situation, we have considered a three section passive dispersive reflector laser consisting of the active DFB, passive DBR, and another passive phase tuning section in between. Due to the relation 31.35, we can replace the complex characteristic equation by a couple of real-valued equations,

$$F_l^{-1}(a_2,\hat{\omega}) = F_r(a_2,\hat{\omega}) = e^{-\alpha_2|S_2|}e^{i(\varphi-2\hat{\omega}\tau_2)}F_r(b_2,\hat{\omega}) \qquad \Leftrightarrow$$
$$\begin{cases} \tilde{\mathcal{M}}_\alpha(\hat{N}_1,\hat{\omega}) = e^{\alpha_2|S_2|} \\ 2\hat{\omega}\tau_2 - \tilde{\mathcal{M}}_\varphi(\hat{N}_1,\hat{\omega}) = \varphi \end{cases}, \text{ where } \tilde{\mathcal{M}}(\hat{N}_1,\hat{\omega}) = \tilde{\mathcal{M}}_\alpha e^{i\tilde{\mathcal{M}}_\varphi} = F_l(a_2,\omega)F_r(b_2,\hat{\omega}) . \qquad (31.38)$$

This formulation suggests a simple way for finding the steady states. Namely, each of these equations for fixed parameters α_2 and φ defines one or several curves in frequency ω – carrier threshold N_1 domain, see solid and dashed curves in Figure 31.10. The intersections of these lines determine the steady state pairs $\hat{\omega}, \hat{N}_1$ (hollow bullets in the same figures). It is noteworthy that to any point in the $\omega - N_1$ domain one can attribute a unique triple of loss, phase, and mode power parameters α_2, φ, and $|\hat{f}|^2$. ω and N_1 within the gray shading regions of Figure 31.10 represent the unphysical steady states corresponding to negative damping in the passive section ($\alpha_2 < 0$) and negative mode intensity ($|\hat{f}|^2 < 0$) due to insufficient pumping of the active section.

The fixed level lines of $\tilde{\mathcal{M}}_\alpha$ determined by larger losses $\alpha_2 = 30$ and 40/cm (thin solid-line ellipses located inside of thick solid curves in Figure 31.10) are shrinking toward central points, which are resonances of the solitary DFB laser. Accordingly, the (odd) number of steady states on each ellipse is also reduced. The saddle-node bifurcation that is responsible for creation or annihilation of the steady state pair, occurs at those φ and α_2, where corresponding fixed level lines of $\tilde{\mathcal{M}}_\varphi$ and $\tilde{\mathcal{M}}_\alpha$ become tangent to each other. The last condition formally given by

$$\mathcal{M}_{SN}(\hat{\omega},\hat{N}_1) \overset{def}{=} \partial_\omega\tilde{\mathcal{M}}_\alpha\partial_{N_1}\tilde{\mathcal{M}}_\varphi - \partial_\omega\tilde{\mathcal{M}}_\varphi\partial_{N_1}\tilde{\mathcal{M}}_\alpha = 0$$

is satisfied on the dotted lines of Figure 31.10.

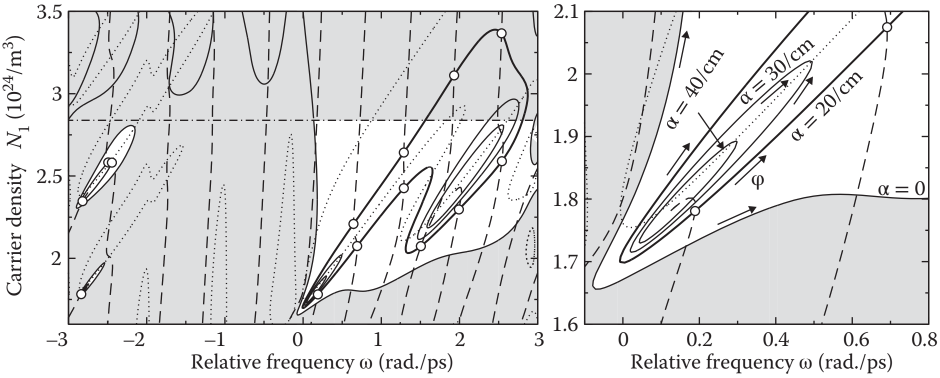

(a) (b)

FIGURE 31.10 Stationary states (frequencies and threshold carrier densities) of a three section DFB laser. Panels (a) and (b) show a global overview and a zoomed-in region close to the minimal threshold mode with $\hat{\omega} \approx 0$. Solid curves represent steady states for an arbitrary φ but only a few fixed α_2. Dashed curves indicate steady states for arbitrary α_2 and fixed $\varphi = 0$. Dotted curve shows positions where saddle-node bifurcations hold. Empty bullets: steady states for $\alpha_2 = 20$/cm and $\varphi = 0$. Dash-dotted line indicates maximal N_1 which can be achieved for considered bias current I. Gray shading corresponds to unphysical states. Small arrows in panel (b) indicate directions of the steady state shift along the fixed loss lines for growing φ. All parameters as in Reference [26].

In general, the interpretation of the steady states for large α_2 (small feedback) is in good agreement with the analysis of the external cavity modes in the Lang–Kobayashi (LK) model of lasers with delayed feedback [18,27]. A decrease of α_2 leads to blowing up and collision of different ellipses. This scenario involves multiple modes of the solitary DFB laser and can be no more explained by the LK model.

Mode Approximation Systems:

For some MSL devices, the TW model (Equations 31.2 through 31.5, and 31.14, 31.15, 31.28) with sectionally averaged carrier densities, linear gain and index change functions, and neglected gain compression terms can be reduced to the finite-dimensional system of ODEs describing an evolution of q complex mode amplitudes f and real sectionally averaged carrier densities N within n_a active sections of MSL:

$$\begin{aligned} \dot{f}_k &= i\Omega_k(N) f_k + \sum_{l=1}^{q}\left(\sum_{r=1}^{n_a} K^r_{k,l}(N)\dot{N}_r\right) f_l, \quad k = 1,\dots,q; \\ \dot{N}_r &= \frac{I_r}{q|S_r|\sigma_r} - \mathcal{R}(N_r) - \Re \sum_{k,l=1}^{q} L^r_{k,l}(N) f_k^* f_l, \quad r = 1,\dots,n_a. \end{aligned} \tag{31.39}$$

This mode approximation (MA) system follows from the substitution of the truncated field expansion (Equation 31.36) into the TW model equations and projection of the resulting field equations onto the linear subspace defined by each of q modes. The nonadjoint nature of the field evolution operator and small but nonvanishing time derivatives of propagation factor $\beta(N)$ imply the appearance of the mode coupling terms $K^r_{k,l}\dot{N}_r$. For the derivation of the MA equations and analytic expressions for carrier and mode frequency Ω-dependent mode-coupling functions, $K^r_{k,l}$ and $L^r_{k,l}$, see Reference [28].

To check the precision of our MA system, we have performed simulations of the TW model and two related MA systems describing the evolution of a mode-locked laser consisting of a saturable absorber and an amplifying section (case of $n_a = 2$). The solid black curve and hollow bullets in Figures 31.11b and c show typical optical spectrum and time trace of the mode-locking pulsations obtained by numerical integrations of the TW model. To determine the most relevant complex mode frequencies $\Omega(N)$

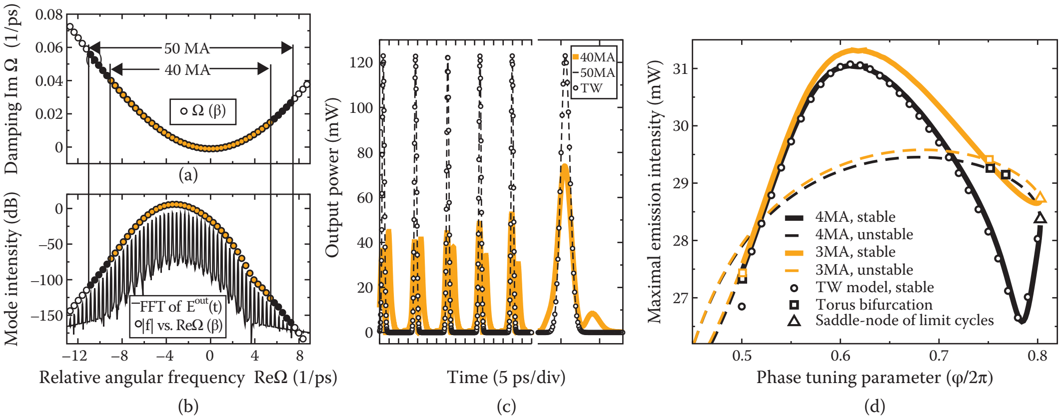

FIGURE 31.11 Calculated (a) complex frequencies Ω, (b) optical spectra as a Fourier-transformed field $E^{-}(a_1, t)$ (black solid curve) and as a discrete set of mode intensities $|f|^2$ versus $\Re\Omega$ (bullets), and (c) a comparison of the calculated transients of the TW model (bullets) and the reduced ODE systems determined by 40 (solid gray) or 50 (dashed black) optical modes in a two-section mode-locked laser. Full black and small gray bullets in panels (a) and (b) indicate the modes used for the construction of 40MA and 50MA systems. (d) Numerical path following of the stable periodic solution of the TW model (bullets) and periodic orbits of 3MA (gray) and 4MA (black) systems in a three-section phase-controlled mode-beating DFB laser [12,28]. Solid and dashed curves indicate stable and unstable orbits. Empty boxes and triangles denote torus and fold bifurcations, respectively.

(Figure 31.11a) and the coefficients f in the field expansion 31.36 (bullets in panel [b]), we have used the carrier densities $N = (N_1, N_2)$, optical fields E, and polarization functions P obtained as a result of the numerical integration of the TW model. For the construction of the 40MA and 50MA systems, we have used the modes indicated by full black and a bit smaller gray bullets in Figures 31.11a and b. Solid gray and black dashed curves in Figure 31.11c represent the numerical integration of these MA systems. One can see that whereas 40MA system fails to reproduce the stable periodic regime, the 50MA system provides a perfect approximation of the TW model. We note that a significant number of excited optical modes in the example considered above does not allow achieving a low dimensional approximation of the TW model. The number of active modes usually is much smaller in MSLs containing one or more DFB sections. In this case, already three or four appropriately selected optical modes are sufficient for a good approximation of the TW model [7,28].

An integration of the MA system (Equation 31.39) remains a nontrivial task, because for each actual set of carrier densities $N = (N_1, \ldots, N_r)$, one should find the corresponding mode frequencies $\Omega_k(N)$, $k = 1, \ldots, q$ by solving the characteristic Equation 31.34 numerically. Since the required computation time of the MA systems grows quadratically with the increasing number of modes, one can integrate the TW model faster than the 50MA system. The usefulness of the MA approach starts to be visible when combining our model reduction technique with the numerical continuation and bifurcation analysis tools [29] suited for investigation of nearly arbitrary systems of ODEs. Figure 31.11d presents an example of numerical bifurcation analysis of 3MA (gray) and 4MA (black) systems describing dynamics of the three-section laser consisting of two active DFB sections and a passive phase tuning section in between ($n = 3$ and $n_a = 2$ in this case). Here, solid and dashed curves represent stable and unstable branches of the periodic orbit implied by beating of two closely located resonances, supported by each DFB section. Empty bullets in the same figure represent the continuation of the stable periodic state by direct integration of the TW model. By comparing the bullets and curves, one can see that both MA systems were able to reproduce the stable branch of the periodic orbit, and identify torus and saddle-node bifurcations where this state have lost its stability. The deviation of the solid gray curve from the bullet positions in Figure 31.11d, however, indicates the insufficiency of the 3MA system to reproduce the orbit shape. More detailed analysis of this laser including a continuation of bifurcations in two parameter domain can be found in Reference [28].

31.11 Conclusions

In this chapter, we introduce a hierarchy of TW models describing nonlinear dynamics in individual semiconductor lasers, various MSLs, and coupled laser systems. To simulate these laser devices, we use our software package LDSL-tool, which treats MSLs as a set of differently interconnected laser sections. At the end of the chapter, we introduce several advanced techniques allowing detailed analysis of the model equations. These methods include computation of optical modes, a study of the mode spectra, expansion of electric fields into modal components, a semianalytic location of all steady states of the MSLs, model reduction, numerical continuation, and bifurcation analysis of the reduced system. Altogether, these advanced possibilities of our software tool allow to achieve a thorough understanding of the processes observed both, in the direct integration of model equations and experiments.

References

1. M.W. Fleming and A. Mooradian. Spectral characteristics of external-cavity controlled semiconductor lasers. *IEEE Journal of Quantum Electronics*, 17:44–59, 1981.
2. A. Argyris, D. Syvridis, L. Larger, V. Annovazzi-Lodi, P. Colet, I. Fischer, J. García-Ojalvo, C.R. Mirasso, L. Pesquera, and K.A. Shore. Chaos-based communications at high bit rates using commercial fibre-optic links. *Nature*, 438:343–346, 2005.

3. A. Uchida, K. Amano, M. Inoue, K. Hirano, S. Naito, H. Someya, I. Oowada, T. Kurashige, M. Shiki, S. Yoshimori, K. Yoshimura, and P. Davis. Fast physical random bit generation with chaotic semiconductor lasers. *Nature Photonics*, 2(12):728–732, 2008.
4. E. Murphy. The semiconductor laser: Enabling optical communication. *Nature Photonics*, 4(5):287, 2010.
5. H.-J. Wünsche, O. Brox, M. Radziunas, and F. Henneberger. Excitability of a semiconductor laser by a two-mode homoclinic bifurcation. *Physical Review Letters*, 88(2):023901, 2002.
6. O. Brox, S. Bauer, M. Radziunas, M. Wolfrum, J. Sieber, J. Kreissl, B. Sartorius, and H.-J. Wünsche. High-frequency pulsations in DFB-lasers with amplified feedback. *IEEE Journal of Quantum Electronics*, 39(11):1381–1387, 2003.
7. M. Radziunas, A. Glitzky, U. Bandelow, M. Wolfrum, U. Troppenz, J. Kreissl, and W. Rehbein. Improving the modulation bandwidth in semiconductor lasers by passive feedback. *IEEE Journal of Selected Topics in Quantum Electronics*, 13(1):136–142, 2007.
8. U. Bandelow, M. Radziunas, A. Vladimirov, B. Hüttl, and R. Kaiser. Harmonic mode-locking in monolithic semiconductor lasers: Theory, simulations and experiment. *Optical and Quantum Electronics*, 38:495–512, 2006.
9. R. Arkhipov, A. Pimenov, M. Radziunas, D. Rachinskii, A.G. Vladimirov, D. Arsenijevic, H. Schmeckebier, and D. Bimberg. Hybrid mode locking in semiconductor lasers: Simulations, analysis and experiments. *IEEE Journal of Selected Topics in Quantum Electronics*, 19(4):1100208, 2013.
10. M. Radziunas, A.G. Vladimirov, E.A. Viktorov, G. Fiol, H. Schmeckebier, and D. Bimberg. Pulse broadening in quantum-dot mode-locked semiconductor lasers: Simulation, analysis and experiments. *IEEE Journal of Quantum Electronics*, 47(7):935–943, 2011.
11. M. Möhrle, B. Sartorius, C. Bornholdt, S. Bauer, O. Brox, A. Sigmund, R. Steingrüber, M. Radziunas, and H.-J. Wünsche. Detuned grating multisection-RW-DFB lasers for high-speed optical signal processing. *IEEE Journal of Selected Topics in Quantum Electronics*, 7(2):217–223, 2001.
12. H.-J. Wünsche, M. Radziunas, S. Bauer, O. Brox, and B. Sartorius. Simulation of phase-controlled mode-beating lasers. *IEEE Journal of Selected Topics in Quantum Electronics*, 9(3):857–864, 2003.
13. S. Bauer, O. Brox, J. Kreissl, B. Sartorius, M. Radziunas, J. Sieber, H.-J. Wünsche, and F. Henneberger. Nonlinear dynamics of semiconductor lasers with active optical feedback. *Physical Review E*, 69:016206, 2004.
14. M. Radziunas, K.-H. Hasler, B. Sumpf, T. Quoc Tien, and H. Wenzel. Mode transitions in DBR semiconductor lasers: Experiments, simulations and analysis. *Journal of Physics B: Atomic, Molecular and Optical Physics*, 44:105401, 2011.
15. M. Radziunas, V.Z. Tronciu, E. Luvsandamdin, Ch. Kürbis, A. Wicht, and H. Wenzel. Study of micro-integrated external-cavity diode lasers: Simulations, analysis and experiments. *IEEE Journal of Quantum Electronics*, 51(2):2000408, 2015.
16. O. Hess and T. Kuhn. Spatio-temporal dynamics of semiconductor lasers: Theory, modelling and analysis. *Progress in Quantum Electronics*, 20(2):85–179, 1996.
17. E. Gehrig, O. Hess, and R. Walenstein. Modeling of the performance of high power diode amplifier systems with an optothermal microscopic spatio-temporal theory. *IEEE Journal of Quantum Electronics*, 35:320–331, 2004.
18. R. Lang and K. Kobayashi. External optical feedback effects on semiconductor injection laser properties. *IEEE Journal of Quantum Electronics*, 16:347–355, 1980.
19. M. Sorel, G. Giuliani, A. Scire, R. Miglierina, J.P.R. Laybourn, and S. Donati. Operating regimes of GaAs-AlGaAs semiconductor ring lasers: Experiment and model. *IEEE Journal of Quantum Electronics*, 39:1187–1195, 2003.
20. A.G. Vladimirov and D. Turaev. Model for passive mode-locking in semiconductor lasers. *Physical Review A*, 72:033808, 2005.

21. U. Bandelow, M. Radziunas, J. Sieber, and M. Wolfrum. Impact of gain dispersion on the spatio-temporal dynamics of multisection lasers. *IEEE Journal of Quantum Electronics*, 37:183–188, 2001.
22. J. Javaloyes and S. Balle. Emission directionality of semiconductor ring lasers: A traveling-wave description. *IEEE Journal of Quantum Electronics*, 45:431–438, 2009.
23. M. Radziunas. Longitudinal modes of multisection edge-emitting and ring semiconductor lasers. *Optical and Quantum Electronics*, 47(6):1319–1325, 2015.
24. U. Bandelow, R. Hünlich, and T. Koprucki. Simulation of static and dynamic proper-ties of edge-emitting multiple-quantum-well lasers. *IEEE Journal of Selected Topics in Quantum Electronics*, 9(3):798–806, 2003.
25. LDSL-tool: A software package for simulation and analysis of longitudinal dynamics of multisection semiconductor lasers. Available at www.wias-berlin.de/software/ldsl.
26. M. Radziunas and H.-J. Wünsche. Multisection lasers: Longitudinal modes and their dynamics. In J. Piprek, editor, *Optoelectronic Devices—Advanced Simulation and Analysis*, chapter 5, pp. 121–150. New York, NY: Springer, 2005.
27. M. Radziunas, H.-J. Wünsche, B. Krauskopf, and M. Wolfrum. External cavity modes in Lang-Kobayashi and traveling wave models. In *SPIE Proceeding Series*, 6184:61840X, 2006.
28. M. Radziunas. Numerical bifurcation analysis of the traveling wave model of multisection semiconductor lasers. *Physica D*, 213:98–112, 2006.
29. E.J. Doedel, A.R. Champneys, T.F. Fairgrieve, Y.A. Kuznetsov, B. Sandstede, and X. Wang. AUTO97: Continuation and bifurcation software for ordinary differential equations (with HomCont). Technical Report TW-330, Department of Computer Science, K.U. Leuven, Leuven, Belgium, 2001.
30. S. Bischoff, J. Mørk, T. Franck, S.D. Brorson, M. Hofmann, K. Frojdh, and L. Prip. Monolithic colliding pulse mode-locked semiconductor lasers. *Quantum and Semiclassical Optics*, 9(5):655–674, 1997.
31. M. Kolesik and J. Moloney. A spatial digital filter method for broad-band simulation of semiconductor lasers. *IEEE Journal of Quantum Electronics*, 37(7):936–944, 2001.
32. A.J. Lowery. New dynamic semiconductor laser model based on the transmission-line modelling method. *IEE Proceedings J – Optoelectronics*, 134(5):281–289, 1987.
33. D.J. Jones, L. Zhang, J. Carroll, and D. Marcenac. Dynamics of monolithic passively mode-locked semiconductor lasers. *IEEE Journal of Quantum Electronics*, 31(6):1051–1058, 1995.
34. E.A. Avrutin, J.H. Marsh, and E.L. Portnoi. Monolitic and multi-gigaHertz mode-locked semiconductor lasers: Constructions, experiments, models and applications. *IEE Proceedings – Optoelectronics*, 147(4):251–278, 2000.
35. C.Z. Ning, R.A. Indik, and J.V. Moloney. Effective Bloch equations for semiconductor lasers and amplifiers. *IEEE Journal of Quantum Electronics*, 33(9):1543–1550, 1997.
36. M. Homar, S. Balle, and M. San Miguel. Mode competition in a Fabry-Perot semi-conductor laser: Travelling wave model with asymmetric dynamical gain. *Optics Communications*, 131:380–390, 1996.
37. A. Perez-Serrano, J. Javaloyes, and S. Balle. Longitudinal mode multistability in ring and Fabry-Perot lasers: The effect of spatial hole burning. *Optics Express*, 19:3284–3289, 2011.
38. M. Spreemann, M. Lichtner, M. Radziunas, U. Bandelow, and H. Wenzel. Measurement and simulation of distributed-feedback tapered master-oscillators power-amplifiers. *IEEE Journal of Quantum Electronics*, 45(6):609–616, 2009.
39. B. Grote, E.K. Heller, R. Scarmozzino, J. Hader, J.V. Moloney, and S.W. Koch. Fabry-Perot lasers: Temperature and many-body effects. In J. Piprek, editor, *Optoelectronic Devices—Advanced Simulation and Analysis*, pp. 27–61. New York, NY: Springer, 2005.
40. H.-J. Wünsche, U. Bandelow, and H. Wenzel. Calculation of combined lateral and longitudinal spatial hole burning in $\lambda/4$ shifted DFB lasers. *IEEE Journal of Quantum Electronics*, 29(6):1751–1760, 1993.

41. U. Bandelow, H. Wenzel, and H.-J. Wünsche. Influence of inhomogeneous injection on side-mode suppression in strongly coupled DFB semiconductor lasers. *Electronics Letters*, 28:1324–1325, 1992.
42. P.G. Eliseev, A.G. Glebov, and M. Osinski. Current self-distribution effect in diode lasers: Analytic criterion and numerical study. *IEEE Journal of Selected Topics in Quantum Electronics*, 3:499–506, 1997.
43. R. Schatz. Longitudinal spatial instability in symmetric semiconductor lasers due to spatial hole burning. *IEEE Journal of Quantum Electronics*, 28(6):1443–1449, 1992.
44. V. Tronciu, S. Schwertfeger, M. Radziunas, A. Klehr, U. Bandelow, and H. Wenzel. Amplifications of picosecond laser pulses in tapered semiconductor amplifiers: Numerical simulations versus experiments. *Optics Communications*, 285:2897–2904, 2012.
45. A. Perez-Serrano, J. Javaloyes, and S. Balle. Bichromatic emission and multimode dynamics in bidirectional ring lasers. *Physical Review A*, 81:043817, 2010.
46. E.J. D'Angelo, E. Izaguirre, G.B. Mindlin, L. Gil, and J.R. Tredicce. Spatiotemporal dynamics of lasers in the presence of an imperfect O(2) symmetry. *Physical Review Letters*, 68:3702–3704, 1992.
47. Y. Barbarin, E.A.J.M. Bente, M.J.R. Heck, Y.S. Oei, R. Nötzel, and M.K. Smit. Characterization of a 15 GHz integrated bulk InGaAsP passively modelocked ring laser at 1.53 μm. *Optics Express*, 14(21):9716–9727, 2006.
48. E.A. Viktorov, T. Erneux, P. Mandel, T. Piwonski, G. Madden, J. Pulka, G. Huyet, and J. Houlihan. Recovery time scales in a reversed-biased quantum dot absorber. *Applied Physics Letters*, 94:263502, 2009.
49. M. Radziunas, A.G. Vladimirov, E.A. Viktorov, G. Fiol, H. Schmeckebier, and D. Bimberg. Strong pulse asymmetry in quantum-dot mode-locked semiconductor lasers. *Applied Physics Letters*, 98:031104, 2011.
50. K. Lüdge and E. Schöll. Quantum-dot lasers—desynchronized nonlinear dynamics of electrons and holes. *IEEE Journal of Quantum Electronics*, 45(11):1396–1403, 2009.
51. A. Markus, M. Rossetti, V. Calligari, D. Chek-Al-Kar, J.X. Chen, A. Fiore, and R. Scollo. Two-state switching and dynamics in quantum dot two-section lasers. *Journal of Applied Physics*, 100:113104, 2006.
52. M. Rossetti, P. Bardella, and I. Montrosset. Time-domain travelling-wave model for quantum dot passively mode-locked lasers. *IEEE Journal of Quantum Electronics*, 47(2):139–150, 2011.
53. V.Z. Tronciu, M. Radziunas, Ch. Kürbis, H. Wenzel, and A. Wicht. Numerical and experimental investigations of micro-integrated external cavity diode lasers. *Optical and Quantum Electronics*, 47(6):1459–1464, 2015.
54. T. Krauss and P.J.R. Laybourn. Very low threshold current operation of semiconductor ring lasers. *IEE Proceedings J – Optoelectronics*, 139(6):383–388, 1992.
55. I.V. Ermakov, S. Beri, M. Ashour, J. Danckaert, B. Docter, J. Bolk, X.J.M. Leijtens, and G. Verschaffelt. Semiconductor ring laser with on-chip filtered optical feedback for discrete wavelength tuning. *IEEE Journal of Quantum Electronics*, 48(2):129–136, 2012.
56. M. Radziunas, V.Z. Tronciu, U. Bandelow, M. Lichtner, M. Spreemann, and H. Wenzel. Mode transitions in distributed-feedback tapered master-oscillator power-amplifier: Theory and experiments. *Optical and Quantum Electronics*, 40:1103–1109, 2008.

32

Mode-Locked Semiconductor Lasers

Eugene Avrutin
and
Julien Javaloyes

32.1 General Principles of Mode Locking, the Important Features of Mode-Locked Semiconductor Lasers, and the Role of Theory and Modeling

In the most general sense, *mode locking* (ML) is a regime of laser operation that involves emitting light in several modes with a time-independent relation between them, i.e., with constant and precisely equidistant frequencies. Usually, the term is used more specifically, referring to what is, rigorously speaking, *amplitude-modulation* (AM) ML, meaning that the phase differences between of adjacent modes are approximately equal. In time domain, this corresponds to the laser's emitting a train of ultrashort optical pulses at a repetition frequency F near the cavity round-trip frequency or its harmonic:

$$F \approx M_\mathrm{h} v_\mathrm{g}/(2L). \tag{32.1}$$

Here, v_g denotes the group velocity of light in the laser resonator and L is the Fabry–Pérot resonator cavity length. In the case of the ring resonator, $2L$ in Equation 32.1 is substituted by the ring cavity length. The harmonic number M_h corresponds to the number of pulses coexisting in the cavity; in the simplest and most usual case, $M_h = 1$. The pulse duration is then of the order of $2L/(N_M v_g)$, with N_M being the number of lasing modes in the spectrum.

In most cases (some important exceptions will be mentioned below), ML does not occur spontaneously and requires a special laser construction and/or operating conditions. Namely, it is usually achieved either by modulation of the laser net gain at a frequency F or its (sub)harmonic (known as *active* ML) or by exploiting nonlinear properties of the medium to shorten the propagating pulse (known as *passive* ML, PML); in both cases, the pulse shortening mechanism needs to be strong enough to counter the broadening effects of gain saturation and dispersion effectively. PML, in turn, is usually achieved by introducing a saturable absorber (SA) into the laser cavity. The SA both facilitates a self-starting mechanism for ML and, most importantly, plays a crucial role in shortening the duration of the circulating pulses. As a variation of this principle, *refractive index nonlinearities* approximately equivalent in their action to saturable absorption have been intensely studied in the last decades; salient examples are *additive pulse ML* and *Kerr lens ML* in solid-state lasers, see, e.g., Haus (2000) for more detail.

A combination of active and passive methods of ML is known as *hybrid* ML; if the external modulation is in the form of short pulses, the corresponding regime is referred to as *synchronous* ML.

Mode-locked solid-state lasers, often diode pumped, have allowed sub-100 femtosecond pulses to be generated (Brown et al., 2004; Ell et al., 2001; Innerhofer et al., 2003), with peak powers in the range of many kilowatts (partly due to the relatively low repetition rates, typically in the megahertz range or below).

In *semiconductor diode lasers*, the most basic physical mechanisms underlying the generation of short pulses are fundamentally similar to those of other types of lasers, but a number of features are very different, as regards both technology and physics.

From the practical and technological point of view, diode lasers have a number of advantages: They represent the most compact and efficient sources of picosecond and subpicosecond pulses. They are directly electrically pumped, and the bias current can be easily adjusted to determine the pulse duration and the optical power, thus offering, to some extent, electrical control of the characteristics of the output pulses. These lasers also offer the best option for the generation of high-repetition rate trains of pulses, owing to their small cavity size L in Equation 32.1 and hence the large values of F, well into multigigahertz range. Being much cheaper to fabricate and operate than most other types of lasers, ultrafast semiconductor lasers also offer the potential for dramatic cost savings in a number of applications that traditionally use solid-state lasers. The deployment of high-performance ultrafast diode lasers could therefore have a significant economic impact by enabling ultrafast applications to become more profitable and even facilitate the emergence of new applications. At the moment, actual and potential applications of mode-locked lasers include time- and wavelength-multiplexed communications, metrology, biomedical applications, etc.; see Avrutin and Rafailov (2012) for an overview.

From the point of view of physics, which underlies the technology, most of the distinct features of semiconductor lasers, including mode-locked ones, lie in the energy spectrum of semiconductors that consists in continuous bands of energy with relatively high density of states, as opposed to discrete levels in solid-state lasers. Most mode-locked semiconductor lasers operate on fundamental interband transitions (though there has been some work on active ML of intersubband quantum cascade lasers; see, e.g., Revin et al., 2016 and references therein). Semiconductors thus have both a higher gain per unit length (which is one of the reasons of the short cavity length being possible) and a higher nonlinear refractive index than other gain media (the relation between carrier density dependences of gain and refractive index in semiconductor lasers is often quantified via Henry's linewidth enhancement factor α_H that, as discussed below, plays an important role in the theory of ML). The interaction of the pulse with the gain and saturable absorption and the resulting large changes in the nonlinear refractive index lead to significant self-phase modulation, imparting a noticeable *chirp* to the ML pulses, usually up-chirp in the case of passively mode-locked lasers and down-chirp in actively mode-locked ones. This increases the *time-bandwidth product* of the pulse and has been one of the important limitations in obtaining pulse durations of the order of 100 fs *directly* from the diode lasers, with picosecond pulses being the norm. Furthermore, a strong saturation of the gain also results in stabilization of the pulse energy, which limits the average and peak power to substantially lower levels than in vibronic/solid-state lasers. Output average power levels for mode-locked laser diodes are usually between 0.1 and 100 mW, while peak power levels remain between 10 mW and 1 W. Only with additional amplification/compression setups, can the peak power reach the kW level (Kim et al., 2005). Another distinction of semiconductor lasers is that the typical scales of carrier recombination times in semiconductor materials are of the order of hundreds of picoseconds, comparable to the ML repetition time, leading to a rich variety of dynamic instabilities in the laser behavior, some of which, as will be discussed later, determine the *lower* limit for stable ML frequency (and therefore the longest possible laser cavity) for given material parameters.

There has been a large variety of semiconductor laser designs used for ML, from external cavity ones operating at sub-GHz rates to monolithic ones reaching terahertz repetition frequencies (Avrutin et al., 2000), with laser design strongly affecting, not just the laser performance, but the relative importance of the underlying physical effects in determining this performance.

This combination of practical promise, versatility, and scientific challenge has made mode-locked semiconductor lasers an important topic of research for more than two decades; they have arguably attracted considerably more attention than all other methods of ultrashort pulse generation taken together. The most recent years have seen considerable progress in both improving the theoretical understanding of ML in semiconductor lasers and using this understanding to improve their performance in terms of power, pulse duration/chirp, stability, repetition rates accessible, and integrability issues.

This progress has been partly summarized in previous reviews on ML in semiconductor lasers, with some of them (Avrutin et al., 2005) explicitly concentrating on modeling and simulation and others (Avrutin et al., 2000; Avrutin and Rafailov, 2012) paying significant attention to it. Here, we shall partly follow the logic and layout of the previous paper (Avrutin and Rafailov, 2012), but will attempt to present a more modern perspective and cover the recent results by ourselves and other researchers.

32.2 ML Techniques in Laser Diodes: The Main Features

The main advantages of ML over other methods of generating ultrafast pulses by laser diodes are the higher repetition rate pulses and shorter pulse durations. To realize these advantages to the fullest, a variety of ML techniques and device structures have been investigated and optimized (Vasil'ev, 1995). All three main forms of ML—active, passive, and hybrid—have been extensively studied for semiconductor lasers.

Purely *active* ML in a semiconductor laser can be achieved by direct modulation of the gain section current with a frequency very close to the pulse repetition frequency in the cavity or to a subharmonic of this frequency. Alternatively, an electroabsorption segment of a multielement device can be modulated to produce the same effect, or a separate modulation section introduced. The main advantages of active ML techniques are the resultant low jitter (essentially determined by the electrical generator imposing the modulation) and the ability to synchronize the laser output with the modulating electrical signal, which is a fundamental attribute for optical transmission and signal processing applications. However, high repetition frequencies are not readily obtained through directly driven modulation of lasers because fast microwave modulation, particularly of current, becomes progressively more difficult with increase in frequency.

PML of semiconductor lasers typically utilizes an SA region in the laser diode. Upon start-up of laser emission, the laser modes initially oscillate with relative phases that are random; in other words, the temporal radiation pattern consists of irregular bursts. If one of these bursts is energetic enough to provide energy, or more accurately fluence (energy per unit area) of the order of the saturation fluence of the absorber, it will partly bleach the absorption. This means that around the peak of the burst where the intensity is higher, the loss will be smaller, while the low-intensity wings become more attenuated. The pulse generation process is thus initiated by this family of intensity spikes that experience lower losses within the absorber carrier lifetime. The dynamics of absorption and gain play a crucial role in pulse shaping. In steady state, the unsaturated losses are higher than the gain. When the leading edge of the pulse reaches the absorber, the loss saturates more quickly than the gain, which results in a net gain window, as depicted in Figure 32.1. The absorber then recovers from this state of saturation to the initial state of high loss, thus attenuating the trailing edge of the pulse. It is thus easy to understand why the saturation fluence and the recovery time of the absorber are of primary importance in the formation of mode-locked pulses.

In practical terms, the SA can be monolithically integrated into a semiconductor laser by electrically isolating one section of the device (Figure 32.2a). By applying a reverse bias to this section, the carriers photogenerated by the pulses can be more efficiently swept out of the absorber, thus enabling the SA to recover more quickly to its initial state of high loss. An increase in the reverse bias serves to decrease the

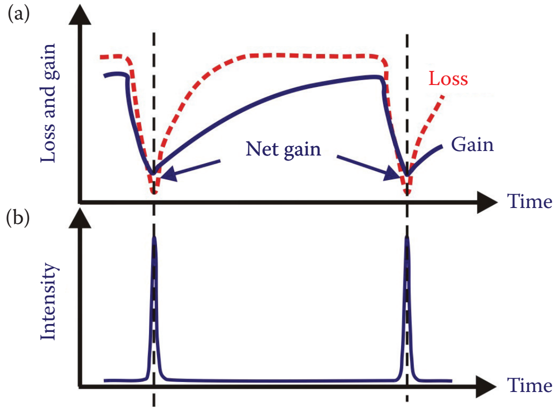

FIGURE 32.1 Schematic illustration of the mechanism of passive mode locking: (a) the loss and gain dynamics that lead to (b) pulse generation.

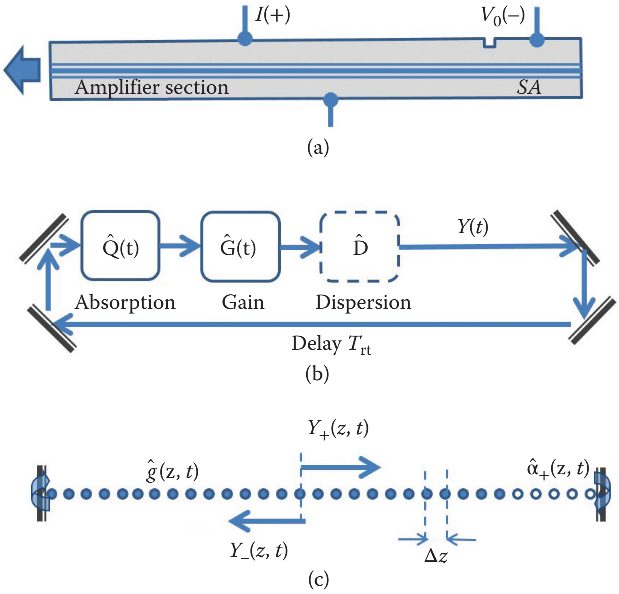

FIGURE 32.2 Schematic of (a) the simplest design of an edge-emitting passively mode locked laser, and its representation in (b) the lumped model of Sections 32.3.1 and 32.3.3, and (c) the traveling-wave model (TWM) of Section 32.3.4.

absorber recovery time, which will have the effect of further shortening the pulses (a faster absorber may act to shorten the trailing as well as the leading edge of the pulse). Alternatively, an SA can also be implemented through ion implantation on one of the facets of the laser, thus increasing the nonradiative recombination (Delpon et al., 1998).

PML provides the shortest pulses achievable by all three techniques, albeit at the expense of somewhat larger pulse jitter and radio frequency (RF) linewidth than in active or hybrid ML. It can be intuitively understood in the following way: Active ML generates a fixed AM of the gain while PML induces a modulation that is proportional to the pulse energy, meaning potentially more efficient mode coupling. Besides, the absence of an RF source simplifies the fabrication and operation considerably. PML also allows for higher pulse repetition rates than those determined solely by the cavity length, by means of harmonic ML ($M_h > 1$ in Equation 32.1; some means of achieving this are considered in more detail below).

Hybrid ML can be achieved by applying RF modulation either to gain or to the SA section. It has been shown, however, that the more efficient method is the latter one, in which case the SA doubles as an electroabsorption modulator. In this case, the pulse generation may be seen as initiated by a modulation provided by the RF signal, while further shaping and shortening are assisted by the SA. This process results in high-quality pulses, synchronized with an external source.

32.3 Theoretical Models of ML in Semiconductor Lasers

Any model of mode-locked laser dynamics should account for pulse shortening by modulation (active/hybrid ML) and/or saturable absorption (passive/hybrid ML) and for pulse broadening by saturable gain and cavity dispersion (including gain/loss dispersion and group velocity/phase dispersion), as discussed above. In addition, if spectral properties are to be accounted for accurately, self-phase modulation needs to be included in the model. In this section, we shall cover general principles of the possible approaches, concentrating on the relatively recent advances in ML theory that have underpinned the significant progress in understanding the details of ML dynamics.

32.3.1 Small-Signal Time-Domain Models and Self-Consistent Pulse Profile

Conceptually the simplest, and historically the oldest, models of mode-locked lasers are *time-domain lumped models* (Figure 32.2b), based on the approximation that the pulsewidth is much smaller than the repetition period, and treating a hypothetic ring laser with unidirectional propagation. The amplification and gain/group velocity dispersion (GVD), which in reality are experienced by the pulse simultaneously, may then be approximately treated in two independent stages. This allows the representation of the distributed amplifier in the model by a lumped *gain element* performing the functions of amplification and self-phase modulation. Mathematically, this element can be described by a nonlinear integral or integro-differential operator acting on the complex pulse shape function (complex slow amplitude) $Y(t)$, t being the *local* time of the pulse. The model was originally designed for solid-state and gas lasers, whose long lengths make for a round-trip time many orders of magnitude longer than the pulse duration, so separate timescales are introduced explicitly for the pulse (the short timescale) and relaxation period between pulses (the long timescale).

The gain operator takes the form

$$\hat{G}Y(t) = \exp\left(\frac{1}{2}(1 - i\alpha_{Hg})G(t)\right) Y(t), \tag{32.2}$$

with α_{Hg} the Henry linewidth enhancement factor in the amplifier and $G(t) = \Gamma \int g(z - v_g t, t)dz$ the total gain integrated over the length of the amplifying region (v_g being the group velocity of light). Further analytical progress can be made by using spatially resolved rate equations for the carrier density N_g in the gain region $\frac{\mathrm{d}N_g(z,t)}{\mathrm{d}t} = -g(N_g)\frac{P(z,t)}{\hbar\omega A_x} - \frac{N_g}{\tau_g}$, where P is the power of light, $\hbar\omega$ the photon energy, A_x the cross section of the optical beam (mode) in the gain section, and τ_g the gain recovery time. A number of approximations are then made. Those involve neglecting dispersion and fast nonlinearities, assuming (which is a safe assumption in semiconductor active media) that $\tau_g \gg \tau_p(\tau_p$ being the pulse duration), so gain relaxation during the pulse can be neglected, and assuming a linear dependence of gain on the carrier density: $g(N_g) \approx \sigma_g(N_g - N_{tr}), \sigma_g = \mathrm{d}g/\mathrm{d}N$ being the gain cross section (the derivative of the gain on the carrier density) and N_{tr} the transparency carrier density. With these assumptions, an approximate explicit expression for $G(t)$ on the short timescale commensurate with the pulse duration can be obtained. In the case of $G \ll 1$, it takes the form

$$G(t) = G_{-} \exp(-U(t)/U_g). \tag{32.3}$$

Here, $U(t) = \int_{-\infty}^{t} P(t')\mathrm{d}t' = v_g \hbar\omega A_X \int_{-\infty}^{t} |Y(t')^2 \mathrm{d}t'$ is the pulse energy up to the time t, $G_{-} = \Gamma \int g(z, t \to -\infty)\mathrm{d}z$ is the total amplification in the gain element at the time before the arrival of the pulse, and

$$U_g = \frac{\hbar\omega A_X}{\sigma_g} \tag{32.4}$$

is the saturation energy of the amplifier.

The SA, if any, is also considered as a lumped element, described, in the simplest case, by an operator similar to Equation 32.3:

$$\hat{Q}_S Y(t) = \exp\left(-\frac{1}{2}(1 - i\alpha_{H\alpha})Q_S(t)\right) Y(t), \tag{32.5}$$

with the absorber linewidth enhancement factor $\alpha_{H\alpha}$, and the dimensionless slow saturable absorption $Q_S = \Gamma \int \alpha(z - v_g t, t)\mathrm{d}z$, in the ideal slow absorber approximation and with $Q \ll 1$, given by

$$Q_S(t) = Q_{-} \exp(-U(t)/U_\alpha). \tag{32.6}$$

Here, again, the total initial absorption $Q_{-} = \Gamma \int \alpha(z, t \to -\infty)\mathrm{d}z$, and the absorber saturation energy is

$$U_\alpha = \frac{\hbar\omega A_{X\alpha}}{\sigma_\alpha}, \tag{32.7}$$

where $\sigma_\alpha = |\mathrm{d}\alpha/\mathrm{d}N|$ is the SA cross section, and, depending on the construction, the cross section of the beam $A_{X\alpha}$ in the SA may be different from that of the amplifying section; as shown below, it is usually advantageous to have $A_{X\alpha} < A_X$.

Equation 32.6 is obtained in the same way as Equation 32.3 by using the spatially resolved rate equation for the carrier density in the absorber region $\frac{\mathrm{d}N_\alpha(z,t)}{\mathrm{d}t} = \alpha(N_\alpha)\frac{P(z,t)}{\hbar\omega A_{X\alpha}} - \frac{N_\alpha}{\tau_\alpha}$, with τ_α the absorber relaxation time and, and making the same assumptions: assuming a linear dependence of the absorption on the SA carrier density $\alpha(N_\alpha) \approx \alpha_0 - \sigma_\alpha N_\alpha$, with α_0 the unsaturated absorption, and neglecting the SA relaxation during the pulse. The latter is known in the theory of ML as *the ideal slow absorber* approximation, meaning that the SA recovery time τ_α, like that of gain τ_g, needs to be much longer than the pulse duration τ_p. However, while the assumption $\tau_g \gg \tau_p$ is readily fulfilled in semiconductor lasers ($\tau_g \sim 1$ ns), the assumption $\tau_\alpha \gg \tau_p$ may be strained ($\tau_\alpha \sim 10$ ps), which may necessitate some modifications to the model, described below, to improve its accuracy.

Absorption in semiconductor SAs tends, in addition, to contain a subpicosecond component that acts as a "fast" SA (recovery time $\ll \tau_p$) even for short pulses ($\tau_p \sim 1$ ps), typically generated by semiconductor lasers. Some lumped time-domain models (Haus and Silberberg, 1985) also include "fast" effects in the SA (SA nonlinearities) as an equivalent fast absorber characterized by an operator $\hat{Q}_F Y(t) = \exp\left(-\frac{1}{2}Q_F(t)\right) Y(t)$ and with an equivalent absorption:

$$Q_F(t) = Q_{iF}(1 - \varepsilon_\alpha \,|Y(t)|^2). \tag{32.8}$$

Then, the total absorption is

$$\hat{Q}Y(t) = \hat{Q}_S\hat{Q}_F Y(t). \tag{32.9}$$

Gain nonlinearities may, in principle, be included in the same way, although a more accurate account of dynamics may be preferable, particularly in the case of quantum dot (QD) materials.

Finally, in the traditional form of a lumped model, the dispersion of material gain and refractive index, together with any artificial dispersive elements present in the cavity, such as a distributed Bragg reflector (DBR), are combined in a lumped *dispersive element*. In the frequency domain, its effect on the pulse may be written as

$$\hat{D}Y^T(\omega) = e^{i\varphi_0}\left[\frac{1}{1 - i(\omega - \omega_p)/\gamma} + D(\omega - \omega_0)^2\right] Y^T, \tag{32.10}$$

where Y^T is the Fourier transform of the complex pulse shape $Y(t)$, ω_p and $\gamma \ll \omega_p$ are the peak frequency and the bandwidth of the dispersive element (defined by the gain curve of the amplifier and the frequency selectivity of a grating element, if it is present in the cavity), and ω_0 is the reference frequency as in the analysis of amplifiers. The value of ω_p may change during the pulse (due to gain curve variation with carrier density, most importantly the gain peak shift); this modifies the dispersive operator (Leegwater, 1996), although in the majority of papers on the subject, the effect is not included. ϕ_0 denotes the phase shift introduced by the element and D is the equivalent dispersion (including the GVD of the passive waveguide and the effective dispersion of the external grating element, if any). To rewrite the operator (Equation 32.10) in the time domain, one may expand the first term around the reference frequency ω_0 noting that $|\omega_p - \omega_0| \ll \omega_0$. Then, after a standard transformation, $(\omega - \omega_0)Y^T \div id/dt\; Y$ (Equation 3.7) becomes a differential operator; if the exponential is expanded keeping the first two terms, the operator is reduced to second order.

The dynamics of ML process are then described by cascading the operators and setting:

$$Y_{i+1}(t) = \left(\sqrt{\kappa}\hat{G}\hat{Q}\hat{D}\right) Y_i(t), \tag{32.11}$$

where i is the number of the pulse round-trip (determining the "slow" evolution of the ML pulse), the time t is on the fast timescale commensurate with the pulse duration, and the dimensionless parameter $\kappa < 1$ introduces the total (integrated) unsaturable intensity losses in the cavity, both distributed and due to outcoupling. The model reflects the balance of the main processes affecting the pulse in a mode-locked laser in that the saturable absorption operator $\hat{Q}$ acts to narrow the pulse down, whereas the gain saturation $\hat{G}$ and the dispersion operator $\hat{D}$ act to broaden it. The *stationary* ML equation is thus obtained by writing out the condition that the broadening and narrowing cancel each other, and the shape of the pulse is conserved from one repetition period to the next. In the operator notation introduced above, this means

$$\left(\sqrt{\kappa}\hat{G}\hat{Q}\hat{D}\right) Y(t) = e^{i\delta\psi}Y(t + \delta T), \tag{32.12}$$

where δT is the shift of the pulse or detuning between the repetition period and the round-trip of the "cold" cavity (or its fraction in case of locking at harmonics of the fundamental frequency), and $\delta\psi$ is the optical phase shift induced by the round-trip. In between the pulses, on the slow timescale commensurate with the round-trip time, gain and SA are allowed to recover with their characteristic relaxation times, according to the rate equation for carrier density with $S = 0$. This allows one to calculate the values of gain and saturable absorption at the onset of the pulse, given the pulse energy and repetition period (the only point at which this latter parameter enters a lumped time-domain model).

In the approximation of no dispersion ($\widehat{\mathrm{D}} = 1$), the broadening of the pulse by gain saturation alone in the lumped model cannot compensate for the shortening by the absorption. The model in this approximation thus predicts the steady output in the form of a series of *infinitely short* (delta function-like) pulses; neither the pulse shape nor the duration can be analyzed in this approximation. However, it is possible to determine the total pulse *energy* and also analyze the stability of the solutions by requiring that net gain both immediately before the pulse and immediately after the pulse is smaller than one that translates into

$$\begin{aligned} G_- - Q_- - \ln\kappa &< 0 \\ G_+ - Q_+ - \ln\kappa &< 0. \end{aligned} \tag{32.13}$$

Here G_-, Q_- are the total (integrated) gain and absorption immediately before the pulse, and G_+, Q_+ are the values immediately after the pulse. This is known as New's theory of ML (strictly speaking, G. New's original 1970s paper (New, 1974) related to nonsemiconductor lasers in which $\ln(1/\kappa) \ll 1$; however, Equation 32.13 is also applicable in the generalized version of the theory proposed by Vladimirov et al. (2004) and Vladimirov and Turaev (2005) and covered in more detail below).

Analytical approximations for the *pulse shape and duration* have been originally obtained in the case of weakly nonlinear analysis, that is to say if the pulse energy is smaller than $U_{\mathrm{G,A}}$ and the gain and loss (saturable and unsaturable) during one round-trip are small ($\ln(1/\kappa), G, Q \ll 1$). Then, the exponentials in the formulas for the gain and loss operators may be expanded in Taylor series keeping terms up to the second order in Equations 32.3 and 32.6 (weak to moderate saturation of gain during the pulse):

$$\exp\left(-\frac{U(t)}{U_{\mathrm{g},\alpha}}\right) \approx 1 - \frac{U(t)}{U_{\mathrm{g},\alpha}} + \frac{1}{2}\left(\frac{U(t)}{U_{\mathrm{g},\alpha}}\right)^2, \tag{32.14}$$

and to the first order in Equations 32.2 and 32.5 (small gain and loss):

$$\exp\left(\frac{1}{2}(1 - i\alpha_{\mathrm{Hg}})G(t)\right) \approx 1 + \frac{1}{2}(1 - i\alpha_{\mathrm{Hg}})G(t); \exp\left(-\frac{1}{2}(1 - i\alpha_{\mathrm{H\alpha}})Q(t)\right) \approx 1 - \frac{1}{2}(1 - i\alpha_{\mathrm{H\alpha}})Q(t) \tag{32.15}$$

(the accuracy of the model can be improved by expanding these equations, too, to the second rather than first order).

Then, following the route pioneered by H. Haus in the first papers on ML in lasers of an arbitrary type (Haus, 1975) and later adapted specifically to diode lasers (Koumans and vanRoijen, 1996; Leegwater, 1996), the ML Equation 32.12 is rewritten as a complex second-order integro-differential equation known as the master equation of ML, which permits an analytical solution of the form

$$Y(t) = Y_0 \exp(i\Delta\omega t)\left(\cosh\frac{t}{\tau_{\mathrm{p}}}\right)^{-1+i\beta}, \tag{32.16}$$

known as the *self-consistent profile* (SCP). The corresponding theoretical approach is known as the SCP, or Haus's ML theory, as applied to semiconductor lasers (in lasers of other kind, for instance, the account for both slow and fast absorbers is typically not necessary). Assembling the terms proportional to the zeroth, first, and second power of $\tanh(t/\tau_{\mathrm{p}})$ in the ML equation, one obtains three complex, or six real, transcendental algebraic equations (Koumans and vanRoijen, 1996; Leegwater, 1996) for six real variables: pulse amplitude $|Y_0|$, duration measure τ_p, chirp parameter β, optical frequency shift $\Delta\omega = \omega - \omega_0$, repetition period detuning δT, and phase shift arg (Y_0) (which is not a measurable parameter, so in reality there are five meaningful equations). These equations, being nonlinear and transcendental, generally speaking, cannot be solved analytically, but still allow for some insight into the interrelation of pulse parameters. For example, it can be deduced (Leegwater, 1996) that the pulse duration may be considerably shortened by the presence of a fast (instantaneous) component in the saturable absorption and the achievable pulse durations are estimated about 10 times the inverse gain bandwidth, decreasing with increased pulse energy.

By requiring the net small-signal gain before and after the pulse to be negative (Equation 32.13) so that noise oscillations are not amplified, the SCP approach also allows the parameter range of the stable ML regime to be estimated.

Some conclusions from the SCP approach are borne out by more precise models (see below). In particular, it highlights the role of *the gain-to-absorber saturation energy ratio*:

$$s = \frac{U_g}{U_\alpha} = \frac{\sigma_\alpha A_{Xg}}{\sigma_g A_{X\alpha}} \tag{32.17}$$

in the ML laser performance. A minimum value of $s > 1$ is needed to achieve ML at any range of parameters at all and the range of stable ML operation broadens with an increased s. Colliding pulse mode-locked configurations, linear or ring, increase the pulse stability and also lead to shorter pulses by increasing the parameter s.

The SCP model also predicts, correctly, that increasing the dispersion parameter D also increases the parameter range for ML, at the expense of broadening the pulses, and that the slight variation of the frequency F around the estimate (Equation 32.1) shows a minimum in its dependence on current or unsaturated gain.

When applied more quantitatively, however, the SCP model is not too accurate and cannot adequately describe details of pulse shape and spectral features. Indeed, the pulse shape given by the expression (Equation 32.16) is always symmetric, which, in general, needs not, and often is not, the case in practice. Nor are the dynamic regimes of ML faithfully reproduced by the classic SCP model. The reason for this is a large number of approximations involved in the SCP approach, which have been progressively removed by various researchers at the expense of making the model more complex and, in some cases, requiring numerical rather than semianalytical analysis of the pulse profile, even if the model is still lumped.

First, achieving the SCP requires that the relaxation of gain and absorber during the pulse is negligible so that the gain and absorber operators can be written in the form of Equations 32.3 and 32.6. As mentioned above, this is a safe assumption in semiconductor lasers as regards gain media, but not necessarily the SA. The obvious upgrading to the model is then to include the dynamics of the saturable absorption Q by a characteristic recovery time τ_α. If at the same time we abandon the approximation $Q \ll 1$, then the necessary equation will take the form

$$\begin{gathered} \frac{\mathrm{d}Q(t)}{\mathrm{d}t} = -X(Q)Q\frac{P(t)}{U_\alpha} - \frac{Q_0 - Q}{\tau_\alpha}; \\ X(Q) = \frac{1 - \exp(-Q)}{Q}. \end{gathered} \tag{32.18}$$

Here, $Q_0 = \alpha_0 - L_\alpha$ (L_α being the absorption region length) is the unsaturated total absorption (at repetition periods $T_{rep} \gg \tau_\alpha$, $Q_- = Q_0$), and X is the geometric factor that stems from averaging the absorption over the length of the absorber area for traveling-wave absorption (in the case of small absorption ($Q_0, Q \ll 1$) treated above, we obtain a constant $X = 1$).

Equation 32.18 is then used with Equation 32.5 instead of Equation 32.6, which it obviously reproduces in the limiting case of $X = 1$, and $\tau_\alpha \gg \tau_p$, or $\tau_\alpha \to \infty$ on the short timescale $t \sim \tau_p$. Unfortunately, even this apparently minor modification to the model means that a closed-form solution in the form of Equation 32.16 is no more possible even with $Q_0, Q \ll 1 (X = 1)$, and the iteration-type procedure (Equation 32.11) has to be repeated numerically until a steady-state profile that satisfies Equation 32.12 is found.

Studies with such a modified SCP model found that even with $X = 1$ in Equation 32.18 (small gain/absorption case) and even with absorber recovery times a few times greater than the pulse duration, the finite τ_α makes some difference to the results, noticeably shortening the pulse, making its shape less symmetric, and affecting boundaries of stable ML regime (Dubbeldam et al., 1997).

32.3.2 Frequency and Time-Frequency Treatment of ML and Dynamic Modal Analysis

An approach conceptually alternative to the time-domain analysis of ML, but to an extent sharing the small-signal nature of the model discussed above, is offered by the technique of modal analysis, static or dynamic (as in Avrutin et al., 2003 and references therein and also in Nomura et al., 2002 and Renaudier et al., 2007). In this approach, instead of analyzing the pulse shape dynamics, a modal decomposition is used and the dynamics of mode amplitudes and phases are analyzed. The advantage of the modal expansion is that the time steps can be much longer than in the spatially distributed models of ML (such as the ones described the following section). Indeed, the stiffness of the dynamics in the modal approach is governed by the temporal evolution of the modal amplitudes, and as PML consists in a steady-state regime for those, one foresees that a modal representation of PML may give rise to smooth solutions—this indeed was shown to be the case (Avrutin et al., 2003). In comparison, spatially distributed models naturally need the time step to be much shorter than the pulsewidth, as discussed in more detail in the following section. Besides, the number of variables can be smaller in the modal analysis, particularly in the case of laser designs with a spectrally selective element where only a few modes are excited, making this approach particularly efficient in analyzing, say, long-scale dynamics of external locking of DBR hybridly mode-locked lasers. It also has the logical advantage of describing steady-state ML as a steady-state solution and, conceptually, allows considering the emergence of stable PML as an order–disorder phase transition in a dissipative system, highlighting the fundamental physical features of PML in addition to its technological implications. Frequency domain analysis can be used as supplementary to time-domain models for some specific problems, as for example the analysis of harmonic operation in a coupled-cavity structure (Yanson et al., 2002), where it actually gives some analytical insight into the modal selectivity of the cavity. Frequency, or time-frequency, modal expansion-based approach to ML is also extremely useful (Kim and Lau, 1993) for analyzing the noise and linewidth properties of the ML signal, as the noise can be seen as exciting higher order *supermodes* (combination of modes) in addition to the fundamental order supermode that is actually realized in ML.

However, the modal expansion approach has a major intrinsic limitation in that it relies on the inherent assumption of weak to modest nonlinearity and modulation, meaning that the results obtained using this method agree reasonably well with time-domain simulations only for the case of high ML frequencies, typically above 100 GHz (short or harmonic cavities) and/or at relatively small currents above threshold. Large-signal instabilities, such as the chaotic leading edge instability, are not predicted accurately, and the accuracy of the frequency-domain models at high amplitudes cannot be guaranteed. In addition, finding the modal structures of complex multisection photonic devices can be cumbersome. Therefore, though the frequency and time-domain analysis of ML originally was introduced approximately simultaneously (reflecting the two major representations of ML, the sequence of periodic pulses and a comb of locked modes), in the context of semiconductor lasers the work on frequency-domain models remains limited. Instead, theoretical progress has been mainly associated with the time-domain models, as they permit a large-signal approach (large modulation of population inversion, or alternatively large nonlinearity) that we cover in the next sections.

32.3.3 Large-Signal Time-Domain Approach and Delay-Differential Equation Model

Both the assumption of weak to moderate pulse saturation during the pulse and, even more so, that of small gain and absorption per pass, as used in small-signal time-domain models discussed in Section 32.3.1, may become even more tenuous in semiconductor lasers than the assumption of an ideally slow absorption—in fact, in edge-emitting lasers, the small-gain assumption is almost always completely inapplicable since at least one of the laser facets is usually uncoated (or even AR-coated to reduce the reflectance to 0.05%–0.1%) to increase the output power, so the outcoupling losses are by necessity significant, making for large gain per pass even with small saturable absorption. Then, it makes sense to abandon the expansions (Equations 32.14 and 32.15) in the fully numerical procedure and use the full exponential form of Equations 32.2 through 32.8, as well as the more accurate full expression for X in Equation 32.18, thus moving from a small-signal SCP model to a *large-signal iterative model* (see, e.g., Khalfin et al., 1995). This also means that the fast nonlinearities of gain and absorption, and possibly part of the dispersion, may be included directly into the gain and absorber operators.

Even in its large-signal form and with the finite absorber (and gain, if necessary) relaxation time taken into account, the iterative procedure (Equation 32.11) is still somewhat artificial in that it requires a trial pulse shape to start with, and explicitly separates the timescale into the short timescale of the pulse and the long timescale of the repetition period. Moreover, if the time window of the pulse is taken as much smaller than the repetition period (which is the standard thing to do if the repetition period is much longer than the pulse), any instabilities related with secondary pulses arising far away from the main pulse may be missed by the model. In semiconductor lasers, neither of these assumptions is well justified, as the pulse may be only about an order of magnitude shorter than the repetition period, so that the separation of scales is not as justified as in lasers of other types, and the chaotic instabilities with several competing pulse trains are a very real threat.

An elegant solution to these modeling limitations is offered in the form of the most sophisticated and the most realistic of the lumped models of mode-locked lasers. In this form of the lumped approach, the two different scales for pulse analysis are, in general, abandoned, and the iteration procedure (Equation 32.11) is substituted by a *delay* one. In a general form, this procedure may be written as

$$Y(t) = \left(\sqrt{\kappa}\hat{\mathrm{G}}\hat{\mathrm{Q}}\hat{\mathrm{D}}\right) Y(t - T_{\mathrm{RT}}), \tag{32.19}$$

where T_{RT} is again the round-trip of the cold cavity, and t is still the local time of the pulse.

A particularly useful form of this model is obtained if the dispersion operator $\hat{D}$ is expanded as a differential one. An efficient form of such an expansion has been derived by Vladimirov et al. (Vladimirov et al., 2004; Vladimirov and Turaev, 2005) who showed that for a bandwidth limiting element with a Lorentzian spectrum similar to Equation 32.10:

$$\hat{\mathrm{D}} \cdot Y^{\mathrm{T}}(\omega) = \left[\frac{1}{1 - i(\omega - \omega_{\mathrm{p}})/\gamma}\right] Y^{\mathrm{T}} \tag{32.20}$$

(i.e., neglecting GVD), assuming without much loss of generality that the peak gain frequency ω_{p} coincides with one of the laser resonator modes, and taking it as the reference optical frequency, we can rewrite Equation 32.19 as

$$Y(t) = -\gamma^{-1}\frac{\partial Y(t)}{\partial t} + \left(\sqrt{\kappa}\hat{\mathrm{G}}\hat{\mathrm{Q}}\right) Y(t - T_{\mathrm{RT}}). \tag{32.21}$$

Equation 32.21 is a delay-differential one, and the model thus becomes the *delay-differential equation*, or DDE, *model* of ML in semiconductor lasers. The development of this model has been arguably the greatest advance in the theoretical analysis of mode-locked lasers since the original papers by Haus and New (of which it is a rigorous generalization and which it reproduces in limiting cases). It allows a full self-contained treatment of mode-locked operation, including a possibility of some (if by necessity limited) analytical progress with a platform for a full large-signal numerical analysis, which gives a complete, and qualitatively correct (if not necessarily completely accurate), picture of all possible regimes of ML laser dynamics and allows a number of important trends to be identified. Therefore, we shall present it here in some detail, following the original papers (Vladimirov et al., 2004; Vladimirov and Turaev, 2005).

The operators $\hat{G}$ and $\hat{Q}$ can be calculated using Equations 32.2 through 32.6 (in this version of the DDE model, no fast absorption is present); the integrated absorption Q is found in Equation 32.18, and for the integrated gain G, a similar equation is written. Assuming that the pulse in the unidirectional cavity treated by the model passes the absorber before the amplifier, the equation takes the form

$$\frac{\mathrm{d}G(t)}{\mathrm{d}t} = -\left[\exp\left(G(t)\right) - 1\right]\exp(-Q(t))\frac{P(t)}{U_{\mathrm{g}}} + \frac{G_0 - G(t)}{\tau_{\mathrm{g}}}. \tag{32.22}$$

Here, G_0 is the unsaturated gain determined by the pumping conditions.

Equations 32.21, 32.18, and 32.22 are a closed system suitable for a detailed numerical simulation of both stationary and dynamic behavior of PML. They can also be fairly easily adapted to allow numerical analysis of *hybrid* ML behavior. As shown in Vladimirov and Turaev (2005), the DDE model also allows for significant *analytical* progress, similar to one achieved with classical New's and Haus's models as described above, but for a more general case of large single-pass gain and absorption, more relevant for most semiconductor laser constructions than the classical SCP. In the analytical procedure, the slow absorption and gain approximation have to be reintroduced, and the slow (relaxation of gain and absorption between pulses) and fast (evolution during the pulse) stages of laser dynamics are, as in the traditional SCP model, treated separately. Considering the slow stage results in equations connecting the gain and absorption before and after the pulse, we get

$$G_- = G_0 - (G_0 - G_+)\exp(-T_{\mathrm{RT}}/\tau_{\mathrm{g}}), \tag{32.23}$$

and

$$Q_- = Q_0 - (Q_0 - Q_+)\exp(-T_{\mathrm{RT}}/\tau_{\alpha}). \tag{32.24}$$

At the fast stage, as usual in the theory of short pulses in lasers and amplifiers, the relaxation terms are omitted, and so Equations 32.18 and 32.22 take the form

$$\frac{\mathrm{d}G(u)}{\mathrm{d}u} = -\left[\exp\left(G(u)\right) - 1\right]\exp(-Q(u)); \ \frac{\mathrm{d}Q(u)}{\mathrm{d}u} = -s\left(1 - \exp\left(-Q(u)\right)\right), \tag{32.25}$$

where u is the dimensionless energy within the pulse, $u(t) = U(t)/U_{\mathrm{g}}$, and $U(t) = \int_{-\infty}^{t} P(t')\mathrm{d}t' = v_{\mathrm{g}}\hbar\omega A_{X\mathrm{g}}\int_{-\infty}^{t}|Y|^2(t')\mathrm{d}t'$. Introducing $u_{\mathrm{p}} = U_{\mathrm{p}}/U_{\mathrm{g}}$, $U_{\mathrm{p}} = U(t \to \infty)$ as the total dimensionless pulse energy (the time of minus infinity on the short timescale meaning the time before the pulse, and plus infinity, covering the entire time of substantial pulse energy, i.e., the entire pulse duration), one can integrate Equation 32.25 to get another set of equations connecting the prepulse and postpulse gain and absorption:

$$Q_+ = Q(u_{\mathrm{p}}) = \ln\left[1 + \exp(-su_{\mathrm{p}})(\exp(Q_-) - 1)\right], \tag{32.26}$$

$$G_+ = G(u_{\mathrm{p}}) = -\ln\left[1 - \frac{1 - \exp(-G_-)}{\left[\exp(-Q_-)\left(\exp(su_{\mathrm{p}}) - 1\right) + 1\right]^{1/s}}\right]. \tag{32.27}$$

The pulse energy itself may be calculated from Equation 32.21 by taking the modulus square of both sides of the equation and integrating over the pulse. The result can be expressed as

$$\gamma^{-2} v_g \sigma_g \int_{-\infty}^{\infty} \left| \frac{\partial Y}{\partial t} \right|^2 dt + u_p = \kappa \ln \frac{\exp(G_-) - 1}{\exp(G_+) - 1}. \tag{32.28}$$

In general, the integral of the left-hand side cannot be calculated analytically. Two particular cases when this is possible have been analyzed in Vladimirov and Turaev (2005).

The first is the case of a model without spectral filtering when the integral can be set to zero. As noted by Vladimirov and Turaev (2005), this is a fairly crude approximation, as in fact the value of the integral does not disappear even in the limit of infinitely wide gain dispersion curve ($\gamma \to \infty$). Indeed, the integral is over the time of the pulse, and as such roughly proportional to the pulse duration. In the theories of ML, this duration scales as γ^{-1} meaning that $\left| \frac{\partial Y}{\partial t} \right|^2 \propto \gamma^2 Y^2$, so that the integral remains finite as $\gamma \to \infty$. In fact, as mentioned above, the theory with $\gamma \to \infty$ cannot predict the pulse shape or duration, leading to pulses collapsing to a delta-function shape. The total pulse *energy*, however, can be estimated *approximately* by neglecting the integral in the left-hand side of Equation 32.28 and thus obtaining an equation for u_p in the form

$$u_p = \kappa \ln \frac{\exp(G_-) - 1}{\exp(G_+) - 1}. \tag{32.29}$$

Equations 32.23, 32.24, and 32.26 through 32.29 form a closed system of five (nonlinear and transcendental) equations for the five unknowns: $G_\pm$, $Q_\pm$, and u_p. Vladimirov and Turaev (2005) identified this system as the *generalized New's model*, as it does not include spectral filtering (as the original New's model) but, unlike this model, does include arbitrarily large gain and absorption per pass, which are both essential features of diode lasers. The (numerical) solution gives the dependence of pulse energy (though neither duration nor peak power) on pulse parameters, represented by the unsaturated gain (which is related to pumping current) and absorption (which is related to the reverse bias applied to the absorber and the bandgap detuning between the gain and absorber sections). The other fundamental absorber parameter also dependent on the reverse bias, the absorber lifetime, only enters the calculations through the relaxation Equation 32.24 and does not influence the results from this model at all if $\tau_\alpha \ll T_{RT}$ (in which case, obviously, $Q_- \approx Q_0$).

The solution to this nonlinear algebraic equation system can then be substituted into the inequalities (32.13) to analyze the stability boundaries of the ML operating range with respect to the leading-edge and trailing-edge instability. The curves, in general, can only be calculated numerically; however, Vladimirov and Turaev (2005) noted that the leading-edge and trailing-edge instability boundaries met at the codimension-2 point lying on the linear threshold line (G_0-Q_0-ln$\kappa = 0$). This point can be calculated explicitly as

$$Q_0 = \ln \frac{\kappa(s-1)}{s\kappa - 1}; \; G_0 = \ln \frac{s-1}{s\kappa - 1}. \tag{32.30}$$

This means that the condition $s > 1$ for any range of successful ML to be present, derived in the traditional SCP approach for the case of small gain and loss per period, needs to be generalized in the case of arbitrary losses in the cavity as

$$s\kappa > 1. \tag{32.31}$$

In a more realistic construction, an extra geometric factor could also be required to take into account the fact that the absorber may be saturated by both the forward and reverse propagating wave simultaneously, which is not taken into account by a unidirectional ring laser model on which the approach above is based.

In the case of G_0,Q_0,ln$\kappa \ll 1$, Equations 32.26 and 32.27 simplify to Equations 32.3 and 32.6, such that the equation for the pulse energy simplifies to $Q_- \frac{\exp(su_{\mathrm{p}})-1}{s} - G_- \left(\exp(u_{\mathrm{p}}) - 1\right) - u_{\mathrm{p}} \ln\kappa = 0$, which is the equation for u_{p} featured in the original New's theory of ML.

The second case when full (semi) analytical solution of the DDE model (with relaxation terms during the pulse neglected) is possible is when the dispersion is taken into account, but the saturation of gain and absorption during the pulse is assumed to be small, as in the Haus model of ML (though the gain and absorption themselves are not necessarily small, unlike the case of the traditional Haus model). Vladimirov and Turaev (2005) called this the generalized Haus model. In this case, a steady-state solution is sought in the form similar to Equation 32.12 in our notations, $Y(t + T_{\mathrm{RT}}) = e^{-i\delta\psi} Y(t - \delta T)$. Then, from Equation 32.21,

$$\gamma^{-1} \frac{\partial Y(t - \delta T)}{\partial t} + Y(t - \delta T) = F(u(t))Y(t), \tag{32.32}$$

where

$$F(u) = \sqrt{\kappa} \exp\left(G(u)(1 - i\alpha_{\mathrm{Hg}}) - Q(u)(1 - i\alpha_{\mathrm{Hq}}) - i\delta\psi\right) \tag{32.33}$$

is the "complex net gain," which can be written out explicitly, substituting the expressions (Equations 32.26 and 32.27) (with u instead of u_{p}) for $G(u)$ and $Q(u)$.

Next, assuming that the single-pass pulse shift is significantly smaller than the pulse duration and that the saturation of both the gain and absorption during the pulse is weak enough ($u(t) < u_{\mathrm{p}} << 1/s$)—the latter being the underlying assumption of Haus's theory—both sides of Equation 32.32 can be expanded in Taylor series up to the second-order terms in their respective arguments:

$$Y(t - \delta T) \approx Y(t) - \frac{\partial Y}{\partial t}\delta T + \frac{1}{2}\frac{\partial^2 Y}{\partial^2 t}\delta T^2,$$

and, generalizing the expansions (Equations 32.14 and 32.15) of the original Haus's theory:

$$F(u) \approx F_0 + F_o' u + \frac{1}{2}F_o'' u^2;\ F_0 = F|_{u=0};\ F_o' = \left.\frac{\partial F}{\partial u}\right|_{u=0};F_o'' = \left.\frac{\partial^2 F}{\partial u^2}\right|_{u=0}. \tag{32.34}$$

Then, the equation governing the pulse evolution is obtained in the form

$$\delta T\left(\frac{\delta T}{2} - \gamma^{-1}\right)\frac{\partial^2 Y}{\partial^2 t} - \left(\gamma^{-1} - \delta T\right)\frac{\partial Y}{\partial t} + \left(F_0 - 1 + F_o' u(t) + \frac{1}{2}F_o'' u^2(t)\right) Y = 0. \tag{32.35}$$

Recalling the definition of $u \propto \int |Y|^2 \mathrm{d}t$, one identifies this second-order nonlinear differential equation as the generalization of the master equation of ML in Haus's theory, which admits solutions of the same form (Equation 32.16) as the original master equation. Six equations are then obtained for six real parameters: peak pulse power, duration, time shift δT, optical frequency shift $\Delta\omega$, phase shift per round-trip $\delta\psi$, and the chirp parameter β.

The stability limits in the generalized Haus's form can be obtained by substituting these solutions into the conditions (Equation 32.13). In general, they depend on the linewidth enhancement factors; however, for direct comparison with other models, the case of $\alpha_{\mathrm{Hg}} = \alpha_{\mathrm{H\alpha}} = 0$ is useful. Results of such analysis, reproduced from Vladimirov and Turaev (2005), are plotted in Figure 32.3. In the plot, the subscript N refers to results from New's model, generalized (solid lines) or standard (dashed lines); and the subscript

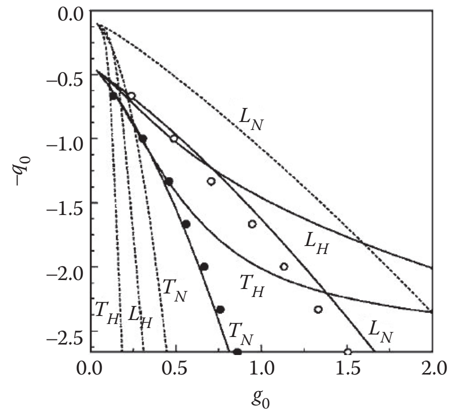

FIGURE 32.3 Stability boundaries of mode locking (ML) with respect to leading (L) and trailing (T) edge instabilities, calculated semianalytically in the DDE approach using traditional and generalized New's (N) and Haus's (H) models. In the calculations, $s = 25$, $T_{RT}/\tau_\alpha = 1.875$, $\tau_\alpha/\tau_g = 0.0133$, $\kappa = 0.1$; $g_0 = (\tau_\alpha/\tau_g)G_0$ as in text; q_0 corresponds to Q_0 in text. (From Vladimirov AG, Turaev D, *Phys Rev A*, 72, 033808, 2005. Reproduced with permission).

H to those from Haus's model (calculated with zero linewidth enhancement factors). The filled/empty dots are the leading/trailing instability boundary calculated by numerical integration of the model. In this numerical integration, the gain and absorber operators are treated on a continuous timescale, without the need to introduce separate timescales for pulse and the free relaxation period as in the iterative procedure. As seen in the figure, standard Haus's and New's models are extremely inaccurate in predicting the instability boundaries of ML in a typical diode laser (with the range predicted by New's model being too wide, and that from Haus's model, too narrow, as noted also in Dubbeldam et al., 1997). The generalized Haus's model gives good agreement within its validity limits at low currents/unsaturated gain values, while the generalized New's model gives very good agreement with numerical simulations at all parameter values (there are some modest deviations that are discussed in more detail below), the reason being that the spectral filtering term neglected in New's approach simply happens to be small in typical diode lasers. Thus, the large-signal nature of the DDE model is proven to be a very important advantage over the classical ML theories.

Apart from allowing some analytical progress in the limiting cases, the DDE model also allows the use of numerical techniques that have been developed for the analysis of DDEs, in particular of numerical packages that allow a full bifurcation analysis of DDEs. Such a study was indeed performed in Vladimirov and Turaev (2005), comprising the full (in)stability analysis of the stationary solution of the DDE. The stationary solution (the steady-state light-current characteristic of the laser) itself is found by seeking the steady-state light output in the form of $Y(t) = Y_{0s}\exp(i\Delta\omega_s t)$. Substituting this into the original Equations 32.21, 32.18, and 32.22 gives the steady-state amplitude and frequency in the parametric form

$$\left.\begin{aligned} &\kappa \exp\left(G_s(Y_0) - Q_s(Y_0)\right) - \Delta\omega_s^2 = 0,\\ &\Delta\omega_s\gamma^{-1} + \tan\left[\Delta\omega_s T_{RT} + \left(\alpha_{Hg}G_s(Y_0) - \alpha_{H\alpha}Q_s(Y_0)\right)/2\right] = 0 \end{aligned}\right. . \tag{32.36}$$

Equation 32.36 is a transcendental trigonometrical equation and thus has an infinite set of formal solutions, corresponding to the cavity modes. The steady-state solution, as usual in the laser theory, is the one with the lowest value of the threshold gain $G_s(Y = 0)$, in other words, the closest to the peak of the gain spectrum. Figure 32.4, after Vladimirov and Turaev (2005), shows the results of a numerical bifurcation analysis of this solution. The line H_1 indicates the *Andronov–Hopf bifurcation* (transition from a steady state to a periodically oscillating solution with an amplitude smoothly increasing from zero as the controlling parameter,

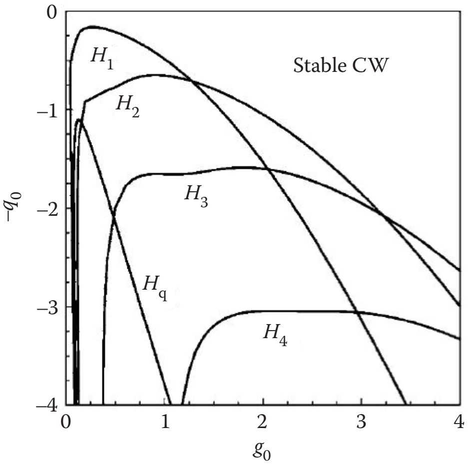

FIGURE 32.4 Bifurcation analysis of the steady-state solutions of the DDE model. Parameters used: $\gamma\tau_\alpha = 33.3$; $\alpha_{Hg,\alpha} = 0$, the rest as in Figure 32.3. The notations H_1, H_2, etc. refer to different harmonic numbers M_h; H_q is the boundary of the Q-switching instability. (From Vladimirov AG, Turaev D, *Phys Rev A*, 72, 033808, 2005. Reproduced with permission).

for example, the unsaturated gain in this case, increases beyond a critical value) corresponding to oscillations at the fundamental ML frequency. ML is predicted for a certain range of conditions regarding the values of the unsaturated gain and absorption, above threshold, whereas at high enough unsaturated gain (or current) and low enough absorption, continuous wave (CW) lasing is expected to be stable. The line H_q indicates the Andronov–Hopf bifurcation corresponding to *passive Q-switching* instability, also known as self-sustained pulsations, which essentially corresponds to the well-known relaxation oscillations in the laser. The positive feedback provided by the SA, which essentially favors pulsed operations, transforms the relaxation oscillations from damped to self-sustained pulsations. The frequency of these oscillations is determined mainly by the unsaturated gain, the gain cross section, the gain relaxation time, and the losses in the cavity, and is typically of the order of 1 GHz, or about an order of magnitude below the ML frequency. Thus, at low frequencies and with high enough amount of saturable absorption in the cavity, the ML pulse train is expected to be modulated by the self-pulsing envelope. The lines H_m, $m > 1$, show the bifurcations corresponding to a solution oscillating at the *m*th *harmonic* of the fundamental ML frequency. At high enough values of unsaturated absorption, there are ranges of G_0 (or current) in which ML at higher harmonics is predicted to be stable, but ML at fundamental harmonic is not.

These predictions are confirmed by a full numerical integration of the DDE model (Figure 32.5), showing the extrema of the laser intensity time dependence calculated for different values of the pumping parameter $g_0 = (\tau_\alpha/\tau_g)G_0$. For each unsaturated gain, the initial transient is omitted before the start of registering signals. At low values of g_0 (and thus current), the laser exhibits a regime when the ML pulse power is modulated by a passive Q-switching envelope, originally with nearly 100% modulation depth (Figure 32.6a). As the pumping parameter increases, the Q-switching modulation gradually decreases in amplitude and eventually the modulation regime undergoes the backward bifurcation, moving to a stable ML regime (this corresponds to the border of the trailing-edge instability in Figure 32.3). Within the area of stable ML, the fundamental round-trip frequency, a train of short pulses, is observed as in Figure 32.7a, whose amplitude increases with G_0. At higher still pumping, the laser dynamics see areas of harmonic ML at the second and third harmonic of the fundamental ML frequency (see Figure 32.7b and c), separated by narrow areas of unstable operation. Finally, the ML breaks up completely with the onset of chaotic modulation of the pulse power, with multiple pulse trains competing in the cavity, as in Figure 32.6b (the regimes separating fundamental frequency ML and harmonic ML areas are similar). Eventually, the system

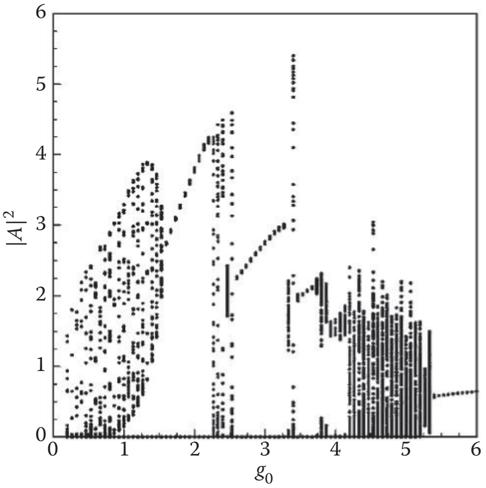

FIGURE 32.5 Bifurcation diagram obtained by direct numerical implementation of a DDE model. $Q_0 = 4$, the other parameters as in Figure 32.3. $|A^2| \propto |Y^2|$ is the normalized output intensity. (From Vladimirov AG, Turaev D, *Phys Rev A*, 72, 033808, 2005. Reproduced with permission).

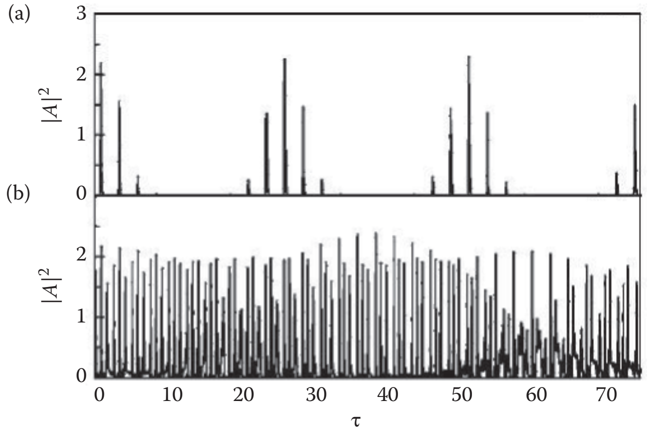

FIGURE 32.6 Illustration of the aperiodic regimes in Figure 32.5: combined mode-locking/Q-switching regime at $G_0 = 50$ (a) and chaotic pulse competition regime at $G_0 = 350$ (b). $|A^2| \propto |Y^2|$ is the normalized output intensity, $\tau = t/\tau_\alpha$ the normalized time. (From Vladimirov AG, Turaev D, *Phys Rev A*, 72, 033808, 2005. Reproduced with permission).

undergoes a transition to CW single-frequency operation in agreement with the bifurcation diagrams of Figure 32.3.

An interesting result obtained in Vladimirov and Turaev (2005) is that, while the conditions (Equation 32.13) of negative net gain before and after the pulse are useful indications of the stability ranges of mode-locked operation, the onset of instabilities in numerical simulations does not coincide with those limits *exactly*. This may be caused in part by the omission of gain dispersion in the analytical study and in part by the neglect of absorber relaxation during the pulse. However, there is also a genuine physical reason for the discrepancy, in that not all small fluctuations in a ML laser were found to grow into full-scale instabilities even if a window of positive gain preceded the ML pulse. Instead, stable ML operation was shown to be possible for a range of parameter (unsaturated gain and absorption) values such that before the pulse,

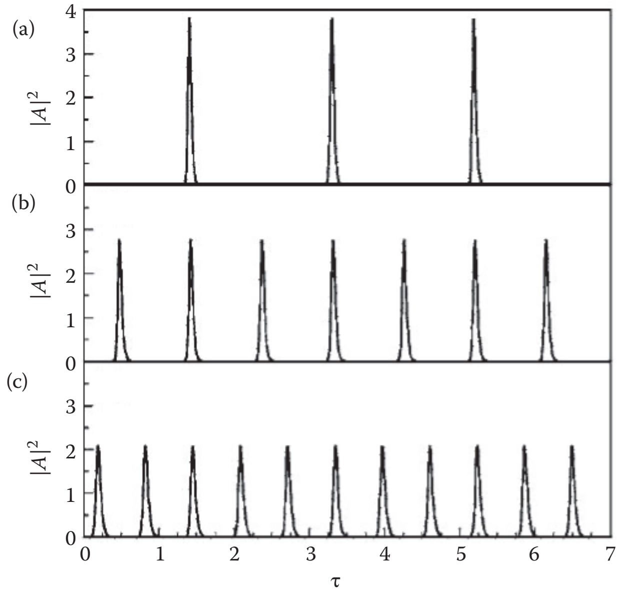

FIGURE 32.7 Illustration of the periodic regimes in Figure 32.5: fundamental frequency ML at $G_0 = 150$ (a) and first and second harmonic ML $G_0 = 225$ (b) and 270 (c). $|A^2| \propto |Y^2|$ is the normalized output intensity, $\tau = t/\tau_\alpha$ the normalized time. (From Vladimirov AG, Turaev D, *Phys Rev A*, 72, 033808, 2005. Reproduced with permission).

the fast absorption had recovered to its unsaturated value, but the slower gain continued recovery, leading to a window of positive net gain preceding the pulse (it may be worth noting that some previous studies, using modifications of Haus's model for semiconductor lasers, indicated the possibility of positive net gain at the *trailing* edge of a stable ML pulse as well; see, e.g., Vladimirov and Turaev, 2005). The possibility of stable ML operation despite a positive net gain window is confirmed by more accurate traveling-wave simulations. One of the consequences of this effect is that the onset of instabilities may be expected to be sensitive to perturbations such as spontaneous noise. The effect of spontaneous emission was indeed studied analytically and numerically in Vladimirov and Turaev (2005), with the noise introduced as a delta-correlated random term in the right-hand side of Equation 32.21. It was concluded that, while the onset of Q-switching oscillations (trailing pulse edge instability) is a dynamic process independent of noise, the onset of the chaotic envelope instability (leading edge instability) is strongly affected by the noise, with an increase in the noise narrowing the window of stable ML. This is fully confirmed by the more complex traveling-wave models (TWMs) described below.

The DDE model, when used as a numerical tool is, not only fully large-signal, but also self-starting: It does not require a trial pulse to start with and can reproduce the emergence of ML pulse train from randomly pulsing light output that is seen as the laser crosses the threshold condition. Thus, the model removes most of the shortcomings traditionally associated with lumped models of mode-locked lasers and presents a relatively simple yet very powerful tool for analyzing the qualitative tendencies of their behavior. As illustrated above, it combines analytical possibilities and numerical methods very naturally within the same framework and, as will be discussed in more detail later, predicts correctly virtually all the dynamic regimes and tendencies observed in a real laser.

An important advantage of the DDE model is that, although strictly speaking derived for the artificial unidirectional ring geometry, it captures enough of the main features of ML to be applicable, with some caution, to predict—at least qualitatively—the phenomena in mode-locked lasers of all types and designs.

An important example is the work presented in Marconi et al. (2014) where the DDE was used to analyze the behavior of mode-locked lasers with *long* delays (cavity round-trip times), comparable to, or even exceeding, the lifetime of carriers in the gain section ($T_{RT} >\sim \tau_g$, unlike the analysis in Vladimirov and Turaev (2005) where the typical situation was $\tau_\alpha < T_{RT} < \tau_g$). Marconi et al. (2014) used a bifurcation analysis similar to that discussed above and presented in Figure 32.3 to analyze the stability of various cavity configurations. The results are shown in Figure 32.8, similar to that presented in Marconi et al. (2014). It was found that the Andronov–Hopf bifurcation mathematically describing the onset of fundamental harmonic ML as discussed above, which is *supercritical* in the case of a short resonator so that ML exists only above its bifurcation point, becomes *subcritical* for a certain value of $T_{RT}/\tau_g > 1$. This means that the (fundamental) ML operation regime can exist below its bifurcation point, coexisting with the CW solution. At longer delays still, the area of stable ML extends below the CW threshold, meaning that ML can coexist with the off solution, thereby implying a bistability between them. Interestingly, during this folding phenomenon, the fundamental ML branch eventually disconnects from the CW solution, meaning that the ML appears for long delays through a saddle-node bifurcation of limit cycles instead of a nascent Andronov–Hopf bifurcation of the CW solution, making this scenario impossible to analyze by any weakly nonlinear analysis such as dynamic modal analysis (Section 32.3.2).

The change in dynamical scenario that occurs in Figure 32.8c has a profound consequence on the mode-locked solutions, as it can be seen in Figure 32.8c and d: The fundamental PML solution becomes stable even in the limit $T_{RT}/\tau_g \gg 1$. Moreover, a very large number of pulsing solutions with different number of pulses per round-trip and different arrangements become stable for the same parameter values. The authors reconstructed analytically some of these solutions, using the generalized New's approximation discussed above, for $T_{RT}/\tau_g = 1$ and restricting the analysis to equally spaced pulses solutions (harmonic PML), as presented in Figure 32.8d. Clearly, all these branches of solutions extend well below the laser threshold, where they stably coexist among them and with the off solution (although the authors noted that New's approximation of neglecting spectral filtering leads to an overestimation of the breadth of the ML region below threshold). This means that the harmonic mode-locked solution of maximal order that exists below threshold becomes fully decomposable, since essentially any pulse of this solution can be set on or off, which the authors confirmed by injecting a digitally modulated sequence of optical pulses into the cavity, which remained stable after a large number of round-trips, meaning that the laser worked as an active version of an optical buffer memory.

The model used in Marconi et al. (2014) was a DDE in its classical form of Vladimirov and Turaev (2005), derived for a hypothetical unidirectional ring laser with large gain and absorption per round-trip (and with the linewidth enhancement factors set to zero as the dynamic effects studied did not significantly depend on them), but the theoretical predictions of the paper were realized experimentally (Marconi et al., 2014)

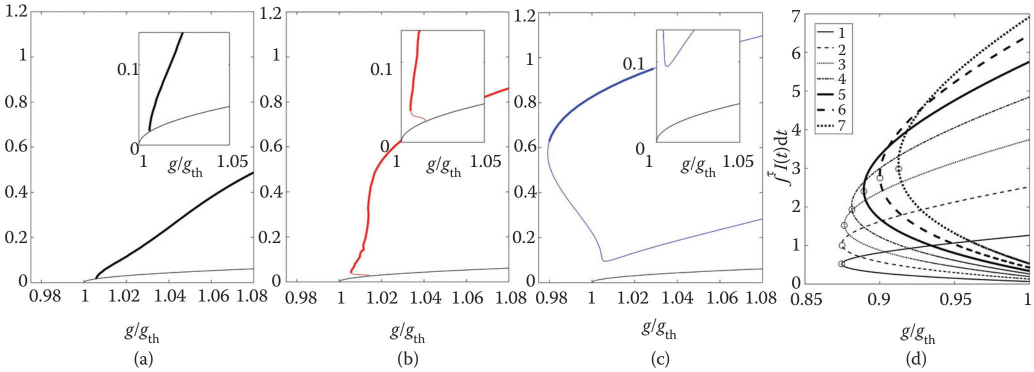

g/g_{th} (a) g/g_{th} (b) g/g_{th} (c) g/g_{th} (d)

FIGURE 32.8 (a) through (c) Bifurcation diagrams similar to that of Figure 32.3 for different cavity round-trip times: $T_{RT}/\tau_g = 1.2$ (a), 2 (b), 4 (c). In the case of a double mode-locked branch, the upper branch is stable and the lower one unstable. Harmonic ML branches are not shown. (d) Folding of harmonic ML branches with a different number for $T_{RT}/\tau_g = 16$. (Reproduced from Marconi M. et al., *Phys Rev Lett*, 112, 223901, 2014).

using a *vertical external cavity surface-emitting* laser (VECSEL). A laser of this type consists of an amplifying (gain) chip and a semiconductor saturable absorber mirror (SESAM) chip, separated by an unguided free-space propagation path (with collimating optics to direct the beam and control the ratio of the spots over the two facets). Various harmonic regimes were realized with this laser, with the number of pulses between 0 and 19 successfully coexisting at high enough currents. The authors then went on (Marconi et al., 2015) to realize the multistability in the long laser to *generate individually addressable* pulses and sequences of pulses, all very well reproduced by the same DDE model.

This work is an important testament to the generality, power, and versatility of the DDE models: The experiments were stimulated by the theoretical predictions which in turn relied on the analytical capabilities (bifurcation analysis using analytical continuation techniques) unique, among semiconductor laser ML theories, to the DDE approach.

It can be pointed out that VECSELs, in fact, are the one class of mode-locked semiconductor lasers for which a delay-differential model, although of a somewhat different form to that used in Vladimirov and Turaev (2005), may be expected to give a fully *quantitative*, as well as qualitative, description of the behavior of a specific and realistic laser construction. As both the gain chip and SESAM are very short asymmetric resonators, with the gain section "length" much shorter than the spatial pulse duration, the lumped-element formalism is a very natural one for their description. The fact that no integration over length is needed for calculating G and Q allows the use of generic nonlinear $g(N)$ and $\alpha(N)$ dependences with no loss of accuracy, as well as introduction of fast gain and absorption saturation omitted in the original DDE of Vladimirov and Turaev (2005). A model based on an approach of this type was successfully used to analyze the dynamics of external-cavity VECSELs in a simple linear cavity (with the laser and SA chips facing each other and the output being from a partially reflecting mirror located between them). The predicted dynamic regimes, pulse durations, and stability ranges matched the ones previously reported in experimental papers, not only qualitatively, but with a reasonable numerical agreement (Mulet and Balle, 2005).

The mathematical distinction of the DDE model usable for quantitative and rigorous description of realistic VECSELs, such as the one used in Mulet and Balle (2005), from the one reported in Vladimirov and Turaev (2005) is, first, that gain and absorption operators, as well as the rate equations for the carriers, need to be modified to take into account the resonator nature of the amplifier and absorber sections and the short length of their active parts. Second, given the Fabry–Pérot rather than ring nature of the resonator, rather than having a single DDE for the light amplitude with the delay time equal to the cavity round-trip, the model for VECSELs in a linear geometry needs separate equations for the dynamics of light amplitudes in the gain and absorber chips, each of them containing a delayed term with a delay equal to *half* of the cavity round-trip.

With further delayed terms introduced, a model of this type can describe different VECSEL geometries, including a folded (rather than linear) cavity one and a colliding pulse operating VECSEL (Avrutin and Panajotov, in preparation).

More advanced constructions known as MIXCELs (standing for mode-locked integrated external cavity surface emitting laser) with the quantum well (QW) gain and QD absorber layers located in one chip, could be described by a similar, possibly even somewhat simpler, model, with the single chip reflectance operator containing the effects of both the gain and the absorption; the model for such a design would therefore be even closer to that of Vladimirov and Turaev (2005).

In the case of *edge-emitting* lasers, the application of a DDE model to a specific, realistic design is somewhat more tenuous. First of all, the DDE model as studied in Vladimirov and Turaev (2005) does not account for fast gain and saturable absorption nonlinearities due to interband processes. Although it could be possible to include them in the QD case, at least in some approximation, the explicit introduction of fast nonlinearities is not necessarily the best strategy. Instead, separate rate equations for dot and reservoir populations can be used. Second, Equations 32.18 and 32.22 for the gain G and absorption Q integrated over the length of the amplifier/absorber element are only accurate if both the gain and absorption have a simple linear dependence on the carrier densities in the corresponding elements, which is in itself an approximation (or if $G, Q \ll 1$). Third, the geometry of the system analyzed in a DDE model in the form presented in Vladimirov and Turaev (2005) is, as in most lumped models, somewhat artificial in that Equations 32.2 and 32.5 are, strictly speaking, valid only in a hypothetical unidirectional ring cavity. In a real laser, the pulse passes through both the amplifier and absorber twice, not once, with the reflected pulse traveling through areas in which gain or absorption has been already partially saturated by the incident pulse, and possibly partially recovered.

An attempt at taking into account a realistic edge-emitting tandem laser geometry in a large-signal *lumped* iterative (not DDE) model, with an end reflector by introducing averaging of gain/absorption over the corresponding sections, with reflections at facets taken into account, was made in a relatively early paper by Khalfin et al. (1995); the model gave good qualitative predictions of the laser performance; however, such an approach has its own inaccuracies as discussed in Avrutin et al. (2000), since it implicitly assumes pulse duration greater than the round-trip time, which by definition is not the case in mode-locked lasers and the results of Khalfin et al. (1995) were never compared to predictions of more accurate models to ascertain their accuracy.

More recently, a study specifically investigating modeling a Fabry–Pérot edge-emitting laser using a DDE model, importantly with a detailed comparison to the more rigorous and accurate model of a travelling wave type (see the next section), has been presented (Rossetti et al., 2011b). The simulations were performed for the special case of QD mode-locked lasers; however, the results appear to be quite generic. Rossetti et al. (2011b) improved the accuracy of the DDE approach by separating the laser into a number F_s of longitudinal sections (e.g., $F_s = 28$ sections were used in the calculations presented in the paper), some of which belong to the gain region and others to the SA, which results in what the authors termed a multisection DDE approach. Essentially, in the notations used here (the formalism of Rossetti et al., 2011b was somewhat more complicated because of account for two-level transitions peculiar to QDs), in a multisection DDE model, Equation 32.21 is rewritten with the single product $\sqrt{\kappa}\hat{G}\hat{Q}$ substituted by a concatenation of gains and losses in individual segments:

$$Y(t) = -\gamma^{-1}\frac{\partial Y(t)}{\partial t} + \left(\prod_{k=1}^{F_s}\sqrt{\kappa_k}\hat{G}_k\right)Y(t - T_{\mathrm{RT}}). \tag{32.37}$$

Here, the loss $\sqrt{\kappa_k}$ includes both the distributed losses inside the segment and any lumped scattering/outcoupling loss between the segments k and $k+1$. The complex gain operator $\hat{G}_k$ for each section is calculated in the way similar to Equation 32.2 if the section is within the gain region and similar to Equation 32.5 if it belongs to an SA, with the length used being the length of the section. The gain (or loss) in each segment is calculated from a local rate equation for population inversion. The use of a number of segments gives the model some longitudinal resolution and allows for a more accurate modeling of the outcoupling losses; although not explicitly done in the model of Rossetti et al. (2011b), it can also include fast gain and absorption saturation in addition to the slow processes described by rate equations. The model, however, still contains a single delay term helping maintain the calculation efficiency that is one of the main advantages of the DDE approach. To account for bidirectional propagation, the Fabry–Pérot resonator had to be represented, somewhat artificially, by an equivalent ring resonator twice the length of the Fabry–Pérot one, with the SA length also doubled, and the distributed losses allocated carefully to represent the loss in the realistic cavity. With these approximations, the laser performance simulated by the multisection DDE approach was in good (though not perfect, e.g., the pulse amplitude was accurate to typically within about 10%) agreement with the traveling wave one as regards the pulse shapes, amplitudes, durations, and stability of the results with respect to a chaotic envelope instability. As in most QD mode-locked lasers, the design simulated did not show Q-switching instability, owing to the large damping of the relaxation oscillations, so it is not certain whether the multisection DDE model would accurately predict its limits in a laser in which Q-switching could occur. It can be said that the multisection DDE approach has some similarity to the decimated traveling wave one considered below, though unlike it still retains the unidirectional ring cavity assumption.

The DDE model also has been used recently to investigate the performance of a number of laser cavity designs and operating regimes more complex than purely PML in a simple tandem cavity, whether monolithic or VECSEL type.

In Arkhipov et al. (2013), the DDE model was used to analyze the performance of *hybridly*, rather than passively, mode-locked lasers. As in the experiments with which the calculations were compared, and as in previous simulations using a TWM (Avrutin et al., 1996), the hybrid ML was implemented by voltage modulation at an approximately resonant frequency applied to the SA. Within the DDE approach, this requires the modification of Equation 32.18 in the form

$$\frac{\mathrm{d}Q(t)}{\mathrm{d}t} = -\frac{Q_0 - Q}{\tau_\alpha}\left(1 + a_{\mathrm{mod}}(1 + \mathrm{F}_{\mathrm{mod}}(t))\right) - \left(1 - \exp(-Q)\right)\frac{P(t)}{U_\alpha}. \qquad (32.38)$$

Here, a_{mod} is the amplitude of absorption modulation, $\mathrm{F}_{\mathrm{mod}}(t)$ is a periodic function of time, and $\mathrm{F}_{\mathrm{mod}}$ is a periodic function of time defined so as to vary within the limits $-1 < F_{\mathrm{mod}}(t) < 1$. The authors investigated various modulation profiles, the most straightforward of which was sinusoidal modulation $\mathrm{F}_{\mathrm{mod}}(t) = \cos(2\pi f_{\mathrm{mod}} t)$. The modulation frequency could be near resonance with the fundamental ML frequency, with $f_{\mathrm{mod}} = f_{\mathrm{P}} + \Delta f_{\mathrm{mod}}, \Delta f_{\mathrm{mod}} \ll 1/T_{\mathrm{rt}}$, with $f_{\mathrm{P}} \approx 0.9723/T_{\mathrm{rt}}$ being the free-running PML frequency, or at its second harmonic $f_{\mathrm{mod}} = 2f_{\mathrm{P}} + \Delta f_{\mathrm{mod}}$, or second subharmonic $f_{\mathrm{mod}} = f_{\mathrm{P}}/2 + \Delta f_{\mathrm{mod}}$.

Note that Equation 32.38 captures an important feature of voltage modulation of an SA: Both the unsaturated absorber and the relaxation time are modulated simultaneously.

The efficient DDE model allowed, first and foremost, for very effective numerical search for the *locking range* of hybrid ML (the range of frequency detunings $\delta f = \Delta f_{\mathrm{mod}} T_{\mathrm{rt}}$ within which stable hybrid ML was observed for a given modulation amplitude). This was done by long-time (3000 periods, with the last 200 periods stored) direct numerical simulation of the system (Equations 32.18, 32.21, and 32.22). For improved accuracy, the authors used dual characterization of the locking range, using, first, a straightforward bifurcation diagram with the field maxima and minima plotted, and, second, a stroboscopic diagram where, for each considered δf_{mod}, field intensities separated from each other in time by the interval $1/f_{\mathrm{mod}}$ were collected. Once locking was achieved and the period of the field intensity time trace became equal to $1/f_{\mathrm{mod}}$, all stroboscopic map points had the same value; otherwise, multiple values of the stroboscopic map at a given δf were observed. Figure 32.9 (reproduced from Arkhipov et al., 2013 with permission) illustrates both procedures, as illustrated in Figure 32.9a and b, as well as the calculated *locking tongue* (locking range borders in the coordinates δf, a_{mod}), shown in Figure 32.9c. The latter was in very good qualitative agreement with the observed values. The figure shows the fundamental harmonic locking range (the second harmonic one was very similar as could be expected); however, the simulations also predicted, for the first time and in agreement with the experiments published in the same paper, that a narrower range of *subharmonic* locking was also present due to internal nonlinearities in the laser.

In addition to numerical analysis, the DDE allowed an *analytical* asymptotic model for the calculation of the locking range to be developed, which was in very good qualitative agreement with the numerical simulations up to the modulation amplitude of $a_{\mathrm{mod}} \sim 0.5$–$0.6$. Most importantly, it was shown, in agreement with numerical results, that the magnitude of the locking range was *directly proportional* to the modulation amplitude, a fact also seen in other numerical simulations but only proven analytically in Arkhipov et al. (2013). Explicit, if rather complex, expressions for the proportionality coefficient between the locking range and a_{mod} were derived using perturbative analysis of the periodic ML solution.

Finally, Arkhipov et al. (2013) addressed the issue of the asymmetry of the locking range (it is easier to speed the laser up than to slow down), long known for hybrid ML and shown by both experiments and previous simulations; the authors attributed it to the variation of the absorber relaxation time and hence the average absorption value with modulation.

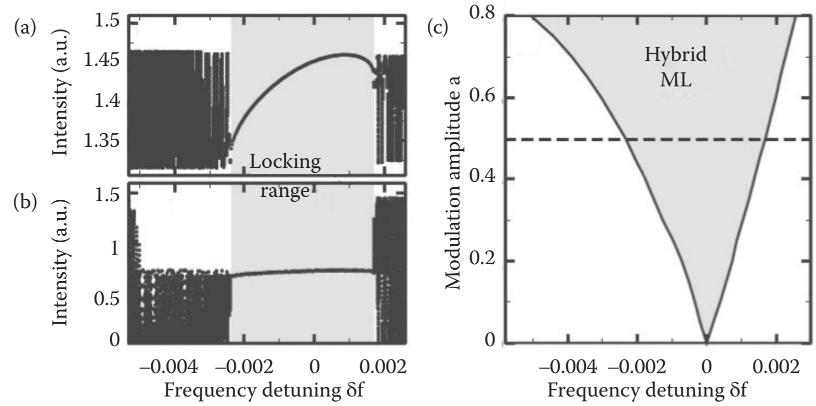

FIGURE 32.9 Numerical DDE estimate of the locking range of a hybrid ML laser. (a) Local maxima of the intensity time trace and (b) 1/fm periodic stroboscopic map points of emitted field intensity time trace at fixed modulation amplitude $a = 0.5$. In the locking range (gray), all ML pulses have the same peak intensity. (c) Locking tongue in the plane of two parameters: frequency detuning δf and modulation amplitude a. (From Arkhipov A. et al., *IEEE J Sel Top Quantum Electron*, 19, 1100208, 2013. Reproduced with permission).

The DDE was also used for modeling the dynamics of mode-locked lasers under the more special conditions of optical injection with a single (Rebrova et al., 2011) or, most recently, dual (Arkhipov et al., 2016c) optical lines, as well as under the condition of external optical feedback (Jaurigue et al., 2015, 2016; Otto et al., 2012). In all of these conditions, the versatility of the DDE allowed analytical insight into operating conditions, as well as direct numerical simulations.

Interestingly, the somewhat abstract nature of the DDE model led to the fact that two very different forms of the model could be used successfully to analyze the situations that in the experiment can be quite similar. In Jaurigue et al. (2015) and Otto et al. (2012), a model with multiple delays (as in the generalized Lang-Kobayashi model of a single-frequency laser with optical feedback from a strong external reflector) was used to analyze ML under external optical feedback, whereas in Arkhipov et al. (2015b), harmonic ML in a compound cavity consisting of an active laser subcavity and a passive one formed by an external reflector (which is very similar to optical feedback) was investigated by modeling both cavities as unidirectional ring ones as in the traditional form of the DDE; mathematically, the compound cavity was represented by two coupled DDEs. Both models showed, and were used to estimate the ranges of, fully or partially rendered harmonic regimes given an integer rational relation between the cavity lengths, and stressed the importance of the subwavelength variations in the cavity length (represented by phase shifts of light amplitude). All of these had been previously independently investigated for Fabry–Pérot laser geometries using frequency-domain and/or traveling wave time-domain models (see the next section), e.g., in Avrutin and Russell (2009). However, the advantage of the DDE model was, first, the possibility of efficient and instructive analysis of the bifurcation diagrams of the laser and, second, the generality as the results apply not just to Fabry–Pérot resonators but to other designs such as ring lasers.

A special version of the DDE model was developed (Viktorov et al., 2006) for analyzing *QD* mode-locked lasers. Detailed description of the properties of QDs as an active medium is beyond the scope of this chapter; the reader is referred to a specialized monograph (Rafailov et al., 2011) or the relevant chapters in the current handbook. In brief, there are two major (interrelated) features that distinguish the QDs from other semiconductor active media, particularly in the context of ML. The first of these is the complex carrier kinetics which in the case of the gain media involves the relatively slow (~5–10 ps) capture of carriers (electrons and holes) into the QDs and subsequent interlevel relaxation, and in the SA sections, the relatively complex nature of carrier escape involving intermediate levels (Viktorov et al., 2009). The second specific feature of QDs as an active medium is the noticeably nonequilibrium distribution of carriers between dots of different sizes and compositions (which therefore have different energy levels resulting in the inhomogeneous broadening of the laser line), and the possibility of dual-wavelength lasing due to the existence of (at least) two electron levels in each dots, the ground and excited state.

The original DDE model of QD mode-locked lasers (Viktorov et al., 2006) ignored inhomogeneous broadening and the excited-level transitions, and thus captured the first of these characteristic features but not the second. The equation for light field in the model was thus essentially the same as in the standard DDE but the equations for gain and absorber dynamics were changed more significantly to reflect the specific features of QDs. Still, even in this simplified form, the model allowed an explanation for a number of features of QD mode-locked lasers, such, first, as the suppressed Q-switching instability (Viktorov et al., 2006) due to the slow carrier capture in the gain section and, second, the enhanced ML at high temperatures due to faster SA relaxation (Cataluna et al., 2006, 2007). Later, more advanced versions of DDE for QD ML lasers have been developed with inhomogeneous broadening and lasing from different levels taken into account, e.g., Cataluna et al. (2010) and also Rossetti et al. (2011b) already mentioned above.

To summarize, DDE models are a very powerful tool capable of predicting, qualitatively describing, and giving unique analytical insight into all the main features and many of the peculiarities of ML in a semiconductor laser. With some caution, models of this type can be used for quantitative description of the performance of a specific laser design, but the reliability and accuracy of such a procedure may be limited in the case of realistic, multisection edge-emitting laser designs, particularly as they often comprise, in addition to the gain and absorber section, elements such as Bragg mirrors, phase-tuning sections, etc.

For these purposes, TWMs are preferable; they will be considered in the next section.

32.3.4 TWMs: The General Considerations

The most accurate and realistic, though usually the most computationally intensive, approach to simulating edge-emitting mode-locked lasers is offered by *distributed time-domain*, or *TWMs* (shown schematically in Figure 32.2c), which treat the propagation of an optical pulse through a waveguide medium with spatial as well as temporal resolution. The model then starts with decomposing the optical field in the laser cavity into components propagating forward (subscript "+") and backward (subscript "–") in the longitudinal direction (say, z):

$$Y(r,t) = \Phi(x,y)\left(Y_+ \exp(i\beta_{ref}z) + Y_- \exp(-i\beta_{ref}z)\right)\exp(-i\omega_{ref}t), \tag{32.39}$$

with Φ being the transverse/lateral waveguide mode profile and ω_{ref} and

$$\beta_{\text{ref}} = n(\omega_{\text{ref}})k_{\text{ref}} = n(\omega_{\text{ref}})\omega_{\text{ref}}/c$$

being the reference optical frequency and the corresponding wave vector, respectively. This results in a reduced equation for slowly varying amplitudes $Y_\pm$, which has the form

$$\pm\frac{\partial Y_\pm}{\partial z} + \frac{1}{v_{\text{g}}}\frac{\partial Y_\pm}{\partial t} = \left(\frac{1}{2}(\hat{g}_{\text{mod}} - \alpha_{int}) + ik_{\text{ref}}\widehat{\Delta\eta}_{\text{mod}}\right)Y_\pm + iK_{\pm,\mp}Y_\mp + F_{\text{spont}}(z,t). \tag{32.40}$$

The equation is directly solved numerically without the partially analytical integration involved in deriving (Equations 32.2 and 32.5).

The gain and saturable absorption coefficients are most often parametrized as functions of the carrier density and, through the gain and absorption compression coefficients ε_{g} and ε_α, on the photon densities, which is most efficiently implemented using simple relations:

$$g = \frac{g_{\text{lin}}(N)}{1 + \varepsilon_g S}; \quad \alpha = \frac{\alpha_{\text{lin}}(N)}{1 + \varepsilon_\alpha S}, \tag{32.41}$$

where $S = |Y_+|^2 + |Y_-|^2$. Note that taking the total intensity in the denominator of Equation 32.41 for both left- and right-traveling waves, although often used, may be an oversimplification for some problems as it assumes identical cross- and self-saturation coefficients between left- and right-traveling waves. A more accurate analysis may be important, in particular, in ring lasers (see Chapter 31 for more details).

The carrier density dependences of the linear gain and absorption $g_{\text{lin}}(N)$ and $\alpha_{\text{lin}}(N)$ are, in the simplest version of the model, taken in the standard linear $g_{\text{lin}}(N) = \sigma_g(N - N_{\text{tr}})$ or logarithmic $g_{\text{lin}}(N) = \sigma_g N_{\text{tr}} \ln \frac{N+N_1}{N_{\text{tr}}+N_1}$ forms typical for semiconductor laser modeling in general (Coldren et al., 2012) (N_{tr} being the transparency carrier density and $\sigma_g$characterizing the gain cross section near transparency as shown in Sections 3.1 and 3.2; for the absorption, the linear approximation $\alpha_{\text{lin}}(N) = \alpha_0 - \sigma_\alpha N$, also as shown in Sections 32.1 and 32.2, is most often used). In more accurate implementations (e.g., Javaloyes and Balle, 2010b), absorption $g_{\text{lin}}(N)$ and $\alpha_{\text{lin}}(N)$ are calculated microscopically with varying degrees of rigor; some of these implementations will be discussed in more detail in Section 32.5. The compression factors $\varepsilon_{g,\alpha}$ also may be either introduced phenomenologically or calculated microscopically for the two main types of optical nonlinearities in bulk and QW lasers: spectral hole burning and dynamic carrier heating. As pulse duration decreases and particularly for multi-GHz ML, the finite (subpicosecond) relaxation times $\tau_{\text{nl}}^{(g,a)}$ of the nonlinearities become important. To take those into account, Equation (32.41) can be substituted by phenomenological relaxation equations: $\frac{d\alpha}{dt} = \frac{1}{\tau_{\text{nl}}^{(a)}}\left(\frac{\alpha_{\text{lin}}}{1+\varepsilon_\alpha S} - \alpha\right); \frac{dg}{dt} = \frac{1}{\tau_{\text{nl}}^{(g)}}\left(\frac{g_{\text{lin}}}{1+\varepsilon_g S} - g\right)$ (Martins et al., 1995). Some authors choose not to introduce $\varepsilon_{g,\alpha}$ due to carrier heating at all, instead including microscopic analysis of carrier temperature dynamics (Bischoff et al., 1997) and gain-carrier temperature dependence into the model. In QD lasers, with their strong spectral hole-burning effects (nonequilibrium carrier distribution in energy, with the energy levels resonant with the photon energy preferentially depleted), and relatively slow intradot relaxation, kinetic processes are often treated explicitly without introducing $\varepsilon_{g,\alpha}$ (see Section 32.5.1).

The dynamic correction $\Delta\beta = \Delta\eta_{\text{mod}} k_{\text{ref}}$ to the propagation constant, in bulk and QW lasers, is often approximated as related to the gain variation by means of a single parameter, the Henry's linewidth enhancement factor α_H (with different values used for the gain and absorber sections), e.g., using a relation $\Delta\beta = \Delta\beta_{\text{SPM}} = -\alpha_H(g - g_{\text{th}})$, the latter parameter being the threshold (or any other reference) value of peak gain. This phenomenological approach, although the simplest and the most traditional, ignores the fact that the spectral dependence of gain and carrier-induced refractive index correction can be different, so the linewidth enhancement factor should be, generally speaking, spectrally and carrier density dependent.

The gain dispersion represented by the operator nature of gain $\hat{g}_{\text{mod}}$ (and to a certain extent GVD, represented by the operator nature of the modal refractive index $\widehat{\Delta\eta}_{\text{mod}}$) is very important in determining the *stability range* of ML (unless there is a dispersive element in the laser construction such as a DBR). As mentioned before, in the lumped model, no stable ML with a finite pulsewidth can be simulated in the absence of dispersion. In the distributed model, most models not including gain dispersion cannot predict stable ML either. Some authors (Bischoff et al., 1997) reported stable ML with finite pulsewidths simulated without the dispersion term, but the model of Bischoff et al. (1997) included finite relaxation times of nonlinearities, which may have had a side effect of introducing *effective* dispersion. As regards the numerical implementation of dispersion, in mode-locked laser constructions realized so far, the spectrum of mode-locked lasers, although quite broad, is still usually significantly narrower than that of gain/absorption, meaning that only the top of the gain curve needs to be represented accurately. Therefore, in most studies reported so far, the dispersion has been approximated in frequency domain, i.e., as function of $\Delta\omega = \omega - \omega_{\text{ref}}$, as a simple, Lorentzian curve in complex numbers (similar to Equation 32.10 with $D = 0$), or Equation 32.20, equivalent to approximating the spectral properties of the material by those of an equivalent two-level medium with homogeneous broadening:

$$P_{\pm}^{\mathrm{T}}(\Delta\omega) = -i\hat{g} \cdot Y_{\pm}^{\mathrm{T}}(\Delta\omega) = -i\frac{g(N,S)}{1 - i\left(\Delta\omega - \Delta\omega_{\mathrm{p}}(N)\right)/\gamma(N)} Y_{\pm}^{\mathrm{T}}(\Delta\omega), \tag{32.42}$$

where the superscript T means Fourier transformed variable in frequency domain; $\gamma(N)$ is the gain spectral width parameter as in Equations 32.10 and 32.20; $\Delta\omega_{\mathrm{p}}(N)$ is the spectral shift of the gain peak from the reference frequency, and $g(N,S)$ can be implemented as in Equation 32.41 (for the absorption, the same method can be used). In time domain, this can be implemented numerically by two alternative but largely equivalent methods. The first one, used in a number of papers (e.g., Bandelow et al., 2001), and traceable to early work on pulse generation in lasers with active media with homogeneously broadened gain spectrum (Fleck, 1968), consists of introducing a separate differential equation for gain polarization, as in the DDE approach. With the gain spectrum centered at the reference frequency ($\Delta\Omega'' = 0$), it takes a particularly simple form, similar to that of Equation 32.21 in the DDE approach:

$$\frac{\partial P_{\pm}(z,t)}{\partial t} = -\gamma\left(P_{\mathrm{f,b}}(z,t) - i\frac{g}{2}(N,S)Y_{\mathrm{f,b}}(z,t)\right). \tag{32.43}$$

The second method of introducing gain dispersion involves using digital filters of varying complexity (Avrutin et al., 2000, 2005; Heck et al., 2006). In the case of a simple Lorentzian gain, the filter is straightforwardly represented as an infinite impulse response (IIR) one of the form of

$$P_{\pm} = -i\hat{g}Y_{\pm} = -i\frac{\gamma}{2}\int_{o}^{\infty} g(z,t-\tau)Y_{\pm}(z,t-\tau)\exp\left(-\tilde{\gamma}_{\mathrm{p}}\tau\right)\mathrm{d}\tau;\ \tilde{\gamma}_{\mathrm{p}} = \gamma - i\Delta\omega_{\mathrm{p}}. \tag{32.44}$$

In practice, the integral requires only storing one iteration in the computer memory: For small integration steps Δt it is easily implemented using a slight generalization of the formula given originally in Schell et al. (1991) as

$$P_{\pm}(t) = \exp\left(-\tilde{\gamma}_{\mathrm{p}}\Delta t\right)P_{\pm}(t-\Delta t) - i\left(\gamma/\tilde{\gamma}_{\mathrm{p}}\right)\left(1 - \exp\left(-\tilde{\gamma}_{\mathrm{p}}\Delta t\right)\right)\frac{g(t)}{2}Y_{\pm}(t).$$

This method of gain dispersion implementation is more tolerant to the simulation time step than the separate differential equation (Equation 32.43), but may be not very accurate if the steps are not small enough (Avrutin et al., 2005; Schell et al., 1991). A more complex, but also somewhat more robust, form of a digital filter implementation of dispersion was described in Carroll et al. (1998) and applied to ML (see, e.g., Jones et al., 1995).

In a recent paper (Javaloyes and Balle, 2010b), a more complex digital filter, representing a more accurate model of the spectra of the complex dielectric permittivity (gain/absorption and refractive index), derived from a microscopic approach and allowing for the realistic fundamental absorption edge spectrum to be modeled, has been implemented; this will be discussed in Section 32.5.

The dispersive nature of the correction $\widehat{\Delta\beta} = k_{\mathrm{ref}}\widehat{\Delta\eta}_{\mathrm{mod}}$ to the (real part of) the propagation constant is usually less important than gain dispersion. In cases when very short (subpicosecond) pulses may be expected in the simulation, the operator $\hat{\Delta\beta}$ may include an additional term describing GVD of the structure (Avrutin et al., 1996)

$$\hat{\Delta\beta} Y = k_{\mathrm{ref}}\widehat{\Delta\eta}_{\mathrm{mod}} Y = \hat{\Delta\beta}_{\mathrm{SPM}} Y - \frac{\beta_2}{2}\frac{\partial^2 Y}{\partial^2 t^2}, \tag{32.45}$$

where the first term describes the self-phase modulation effects, and the second, the GVD, with $\beta_2 = \frac{1}{c}\frac{\mathrm{d}n_{\mathrm{g}}}{\mathrm{d}\omega}$ the first-order GVD coefficient, n_{g} being the group velocity refractive index of the laser waveguide. Numerical simulations (Avrutin et al., 1996) show that GVD affects the parameters of picosecond pulses significantly for the dispersion values of $\mathrm{d}n_{\mathrm{g}}/\mathrm{d}\omega \sim 10^{-14}$ s. Thus, this term is usually negligible in most QW lasers (where the GVD magnitude is estimated as $\mathrm{d}n_{\mathrm{g}}/\mathrm{d}\omega = 10^{-16}$–$10^{-15}$ s) and indeed is omitted in most models of mode-locked laser diodes published to date. In the microscopic or semimicroscopic implementations of TWM (Section 32.5), the dynamic and spectral variation of real, as well as imaginary, part of the dielectric permittivity of the material, and thus the active layer contribution to GVD, is implemented self-consistently. The dispersion (material and waveguide) of the passive waveguide structure is neglected but is believed to be weaker.

The terms containing the forward-back and back-forward propagating coupling constants $K_{\pm,\mp}$ need be included in the model only if a *Bragg grating* is present at the position z (and time t); the constants $K_{\pm}$ and $K_{\mp} = K_{\pm}^{*}$ are, in general, complex due to both refractive index and gain/absorption grating being possible. In the context of a mode-locked laser, accounting for a grating may be needed either if the laser construction contains a DBR section, or to account for *standing wave-induced gratings, or short-scale spatial hole burning* that is important if pulses propagating in opposite directions collide in the active medium (coherent colliding pulse effect). The standing wave-induced grating exists due to the carrier population being increased in the antinodes of the standing wave. Within the SA, where ML pulses are typically engineered to collide, this decreases the local absorption (Martins et al., 1995) and forms an absorption (and possibly refractive index, due to self-phase modulation) grating, to which the fast nonlinearities responding to the standing wave also contribute. The magnitude of the periodic carrier density modulation is then given by the equation (Martins et al., 1995)

$$\frac{\mathrm{d}}{\mathrm{d}t}N_{\mathrm{grat}}(z,t) = -\frac{N_{\mathrm{grat}}(z,t)}{\tau_{\mathrm{grat}}} + \frac{v_{\mathrm{g}}}{2}\left(Y_{+}^{*}\hat{\alpha}Y_{-} + Y_{-}^{*}\hat{\alpha}Y_{+}\right), \tag{32.46}$$

where $\hat{\alpha} = -\hat{g}$ is the saturable absorption operator; the grating relaxation time in QW materials is mainly determined by ambipolar diffusion with the coefficient D_a:

$$\frac{1}{\tau_{\mathrm{grat}}} = \frac{1}{\tau_{\alpha}} + \frac{16\pi^2 D_{\mathrm{a}} n_{\mathrm{g}}^2}{\lambda^2}, \tag{32.47}$$

where λ is the lasing wavelength in vacuum. An estimate gives a value of ~1 ps for the ambipolar diffusion coefficient of 2×10^{-4} m^2/s typical for III–V materials. From the magnitude of carrier density modulation, the coupling in QWs can be estimated as $K_{\mathrm{fb}} \approx i\frac{\partial\alpha}{\partial N}N_{\mathrm{grat}}(z,t)(1 - i\alpha_{\mathrm{H}\alpha})$. Assuming the Henry factor of the absorber is small, as was done in Martins et al. (1995), the grating becomes a purely absorption grating, smoothed down by diffusion. Equation 32.46 is written in terms of SA rather than gain section parameter since in ML lasers designed to utilize the colliding pulse effects, pulses traveling in different directions collide in the SA rather than the gain sections (the former, as will be discussed in the following section, assists ML, the latter impedes it). However, a TWM should contain the grating population in all type of sections; in gain sections, the gain operator $\hat{g} = -\hat{\alpha}$ is used.

The final term in Equation 32.40 is the random noise source that leads to the self-starting of the model and is essential for modeling of noise and pulse jitter. At the laser facets, standard reflection/transmission boundary conditions are imposed on $Y_\pm$; thus, unlike the delay-differential model, the traveling wave one accounts accurately for the laser geometry.

The traveling-wave equations are coupled with coordinate-dependent rate equations for the relevant populations. In the context of QW and bulk lasers:

$$\frac{\mathrm{d}}{\mathrm{d}t}N(z,t)=\frac{J(z,t)}{ed_\mathrm{a}}-N\left(BN+\frac{1}{\tau_\mathrm{nr}}+CN^2\right)-v_\mathrm{g}Re\left(Y_+^*\hat{g}Y_++Y_-^*\hat{g}Y_-\right), \tag{32.48}$$

with J/ed as the pumping term, J being the current density, e the elementary charge, d_a the active layer thickness, τ_nr the nonradiative recombination rate, and B and C are usually identified as the bimolecular recombination constant and the Auger recombination rate, respectively. Carrier capture dynamics is sometimes taken into account by adding an extra equation for carrier densities in the contact layers, but its significance for most mode-locked lasers (with the exception of QD active media and possibly some specially engineered QW constructions) tends to be modest, except where direct current modulation is involved.

TWMs are very powerful and general and their use is not restricted to ML edge-emitting lasers (see Chapter 31).

The main limitations of TW models are, first, the absence of any analytically solvable cases—the approach is by its very essence numerical, though some analytical insight is given by the modal decomposition of the traveling wave solution (see Chapter 31). Second, there is the fact that, in their traditional form, TWMs pose considerably higher requirements on the computing time and memory compared to delay-differential models. This is mainly due to the fact that, in the traditional implementation of the TWMs, time and space steps are usually related as $\Delta z = v_\mathrm{g}\Delta t$, meaning that the computational timescales as $1/\Delta t^2$ and need to be sufficiently short (a typical spatial step being 1–5 μm) to reproduce the pulse characteristics faithfully (the problem is mathematically stiff). However, with the development of computer resources, this limitation has become progressively less important; and the numerical technique of *decimation* has allowed efficient decoupling of time and space steps (see Section 32.5.2). Several commercial or free software simulators of laser diodes include traveling-wave approach of some form as the core of their solver; some of those are directly applicable and have indeed been applied for the analysis of ML lasers; see, e.g., Avrutin and Rafailov (2012), Section 32.5.2 Avrutin and Rafailov (2012), and Chapter 31.

32.4 The Main Predictions of Mode-Locked Laser Theory

In this section, we shall overview some of the main results of ML modeling that can be obtained on a mainly phenomenological level.

32.4.1 Operating Regime Depending on the Operating Point

The most basic result of all the modern ML theories, confirmed by the experiments, is that the dynamics of semiconductor lasers intended for ML can be quite rich and can show, apart from stable ML near the fundamental round-trip frequency, a number of other dynamic regimes. Here, we shall briefly discuss the general trends in their dependence on the laser parameters.

One of the most important features in the dynamic map of operating regimes of a mode-locked laser is the self-sustained pulsations, or passive Q-switching instability at low currents. As shown in Figure 32.5, produced by the DDE model, the range of currents, or unsaturated gain, values in which this regime is observed increases with the amount of saturable absorption in the laser (which, in a given laser construction, either QW or QD, may be varied to some extent with reverse bias, due to electroabsorption). The other model parameter affected by the reverse bias is the *absorber lifetime* τ_α, which is known to decrease approximately exponentially with the reverse bias in QW materials (see Nikolaev and Avrutin, 2003 and references therein) and to some extent in QDs too (Malins et al., 2006). The dependence of the Q-switching range on τ_α is not straightforward; the *Q*-switching range tends to be broadest at a certain absorber recovery time, of the order of the round-trip time though somewhat longer, as can be seen for example in Figure 32.10. At longer τ_α values, the SP range slightly decreases. However, it also decreases as τ_α is *decreased*, and when τ_α reaches a certain value, of the order of a fraction of the round-trip, the Q-switching instability disappears completely, leaving a broad area of stable ML. This is illustrated in Figure 32.10, which is produced using a TWM and shows approximate borders of different dynamic regimes for a representative laser with a short, relatively broadband (length 50 μm, coupling coefficient $\kappa = 120\ \text{cm}^{-1}$) DBR section similar to that realized in Bandelow et al. (2006) and with a cavity length designed for the fundamental ML frequency either near 80 GHz (Figure 32.10a) or near 40 GHz as in the experimental study (Figure 32.10b).

The importance of both τ_α and the unsaturated absorption in determining ML properties means, first, that care needs to be taken when interpreting the bias voltage effects on the performance of either QW or QD mode-locked laser, as the unsaturated absorption, the saturable absorption cross section, and the SA recovery time τ_α are all likely to be affected. The effect on the latter is probably the most significant though, as the dependence of τ_α on voltage is quite strong (exponential), while the effect on the unsaturated absorption appears, from measured threshold currents, to be more modest. Second, it means that for the same absorber parameters, longer lasers with longer repetition periods are less likely to suffer from the Q-switching instability, which needs to be kept in mind when analyzing the dynamics of QD lasers (due to the relatively low gain, these often have to be quite long if stable operation at the ground level wavelength band is desired).

The lower current (or unsaturated gain) limit of the self-pulsing instability may be positioned either below or above the low boundary of ML itself, depending on the gain and absorber saturation energies (*s*-parameter) and the absorber recovery time. If the boundary for ML is below that for self-pulsing (which tends to happen in longer lasers, when τ_α is significantly smaller than T_{RT} but not small enough to completely eliminate self-pulsing), then the stable ML range is split in two by the self-pulsing area, with an area of stable ML seen below the Q-switching limit at currents just above the threshold. The area is narrow, however, and the pulse powers generated in this regime are typically rather low. If, on the other hand, the boundary for ML is above that for self-pulsing (which tends to be the case for shorter lasers or longer absorber relaxation time, when $T_{RT} > \tau_\alpha$), then an area of pure self-pulsing, with noisy/chaotic filling of pulses, is seen at small to modest excess currents above threshold, as in Figure 32.5; as the current is increased, the pulses acquire a regular structure and the combined ML/SP regime develops.

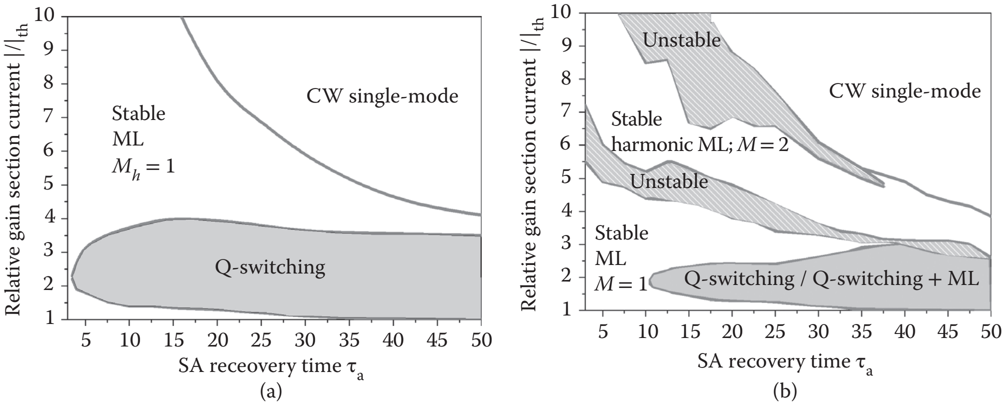

(a)

(b)

FIGURE 32.10 Schematic diagram of regimes in a generic QW mode-locked laser operating at the repetition rate of 80 GHz (a) and 40 GHz (b), calculated using a phenomenological TWM.

Comparing Figure 32.10a and b, we notice that the dynamics of the laser become richer with the increase of the cavity round-trip time, or, equivalently, of the number of modes in the laser spectrum. Indeed, the dynamic behavior of the short-cavity laser in Figure 32.10a displays only regular deterministic regimes (Q-switching, ML, CW) and only the fundamental frequency ML ($M_h = 1$ in Equation 32.1). In contrast, the dynamics of the longer laser in Figure 32.10b contain a range of currents corresponding to stable *harmonic* ML with $M_h = 2$, as in the DDE model. It is separated from fundamental frequency ML by a band of currents in which the laser shows the second (after Q-switching) main type of instability of ML: the leading edge, or chaotic, instability. As was shown by the DDE model, the onset/lower border of this instability is pushed somewhat toward higher currents by the increased amount of absorption in the laser. In addition, as illustrated in Figure 32.10b, shortening absorber relaxation time also somewhat decreases the risk of this instability.

At high currents, the unstable operating regime gradually evolves into some type of (irregular) quasi-CW operation (few modes present), which for some parameter values, with higher currents still, gives way to single-frequency, stable CW operation, as shown in Figure 32.10 (for longer τ_α) and predicted also by DDE. Whether or not this true single-frequency CW operation is achieved at a practically feasible current depends on the length of the laser and the gain bandwidth; longer lasers (with a repetition frequency ~10 GHz and below) with broader gain spectrum tend to not reach true CW under any realistic pumping current, instead operating in a chaotic quasi-CW regime with a narrow spectrum including only a few modes.

In shorter lasers, as in Figure 32.10, a direct transition from stable ML, fundamental (Figure 32.10a) or harmonic (Figure 32.10b), to CW operation is also possible. This takes the form of a Hopf bifurcation, with the ML pulses acquiring a constant background with increased current and then their amplitude gradually reducing to zero resulting in CW operation.

32.4.2 The Main Parameters That Affect Mode-Locked Laser Behavior

In addition to determining the operating *regime* of the laser as discussed in the previous section, the theoretical models allow also the effects of the operating point on the main parameters of the optical pulse to be analyzed. Here, we shall concentrate mainly on the PML regime, in which case the most important parameters whose effect on the laser behavior the modeling can allow us to investigate are as follows:

32.4.2.1 The Pumping Current

The pulse *amplitude* grows with pumping current, as illustrated in Figure 32.11, calculated by a traveling-wave simulation of the laser of Figure 32.10b. Notice that qualitatively the behavior of the pulse amplitude shown in Figure 32.11a is quite close to the bifurcation behavior seen from Figure 32.5, except that in the TWM, and with the inevitably different set of parameters, only the second rather than third harmonic operation is predicted (it was also noted by some authors (Vladimirov et al., 2009) that the dynamics of an ML laser in the TWM can predict stable or unstable trailing pulses at different time detuning from the prevalent pulse stream, whereas the DDE simulation gives only harmonic operation even in unstable regimes).

As regards the pulse *duration* shown in Figure 32.11b, it has been predicted by early frequency-domain theories (Lau and Paslaski, 1991) to reach a minimum near the area of Q-switching instability; this has been later confirmed by both experiments and time-domain simulations and can be also seen in Figure 32.11b. The pulse duration thus tends to grow with current within the stable ML range *above* the upper boundary of Q-switching. On the other hand, if an area of stable ML below the Q-switching range is observed (which, as discussed above, is sometimes the case in longer resonators), then a *decrease* of pulse duration with current can be expected within this area.

32.4.2.2 The Absorber Relaxation Time

The dependence of the pulse duration on τ_α (and this on the absorber bias) within the stability range is shown in Figure 32.12. As seen in the figure, to achieve stable ML, the absorber relaxation time needs to be

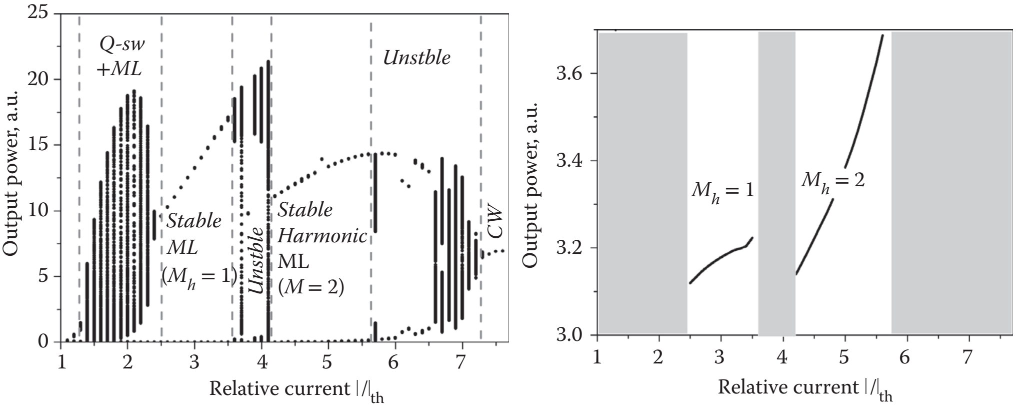

(a)

(b)

FIGURE 32.11 (a) Simulated dependence of the pulse amplitude on the pumping current (bifurcation diagram) for the laser of Figure 32.10b for one value of absorber recovery time, calculated with a phenomenological TWM. (b) Calculated pulse duration for the same laser within the current ranges for stable ML.

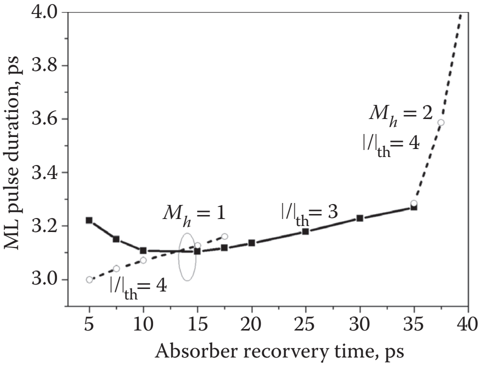

FIGURE 32.12 Typical simulated dependence of pulse duration on the absorber recovery time for two current values: simulations using a phenomenological TMW. Laser design same as in Figure 32.10b.

within a certain range. Values of τ_α above a certain value produce instabilities of either leading or trailing edge type, and may mean switching to harmonic ML. Within the stable ML range, a decrease in τ_α tends to shorten the pulses, due to both the effects of partial absorber relaxation during the pulse and, probably more significantly, to the fact that the slow relaxation of the absorber leads to the absorber being always partially saturated, thus reducing the initial absorption Q_-. This trend can sometimes be reversed for *very* short τ_α, of the order of a few picoseconds, when the absorber may not be saturated efficiently; therefore, there may be an optimum τ_α for shortest pulse generation, though for some laser parameter values this optimum τ_α may be so small as to be technologically unattainable.

The requirement of small τ_α in ML has been recognized from the early days. The methods of reducing τ_α in experiments included, first, ion implantation in early work (Deryagin et al., 1994; Zarrabi et al., 1991), second, choosing QW materials for faster sweepout, e.g., AlGaInAs rather than InGaAsP quaternaries (Green et al., 2011; Hou et al., 2010a,b, 2013) or even QD materials in which SA dynamics is known to be fast (Erneux et al., 2009; Rafailov et al., 2011; Viktorov et al., 2009), third, engineering the QW profile to include steps or oblique rather than vertical walls (Nikolaev and Avrutin, 2004), and fourth, using unitraveling carrier absorbers (Scollo et al., 2005, 2009); see Avrutin and Rafailov (2012) for more detail.

32.4.2.3 The s-Factor, or the Absorber to Gain Saturation Energy Ratio

While it is well known that the increase in s (determined by Equation 32.17) facilitates ML, it is not immediately intuitively clear whether an increased s helps ML stability, as it is known (Kuznetsov, 1985) that the passive Q-switching regime, which is one of the instabilities affecting ML, is also facilitated by an increase in s. However, the results from both DDE and traveling-wave simulations (Bandelow et al., 2006) show that in fact it is the stable ML range that is increased with s at the expense of the Q-switching (or self-pulsing) range.

In VECSELs, the most straightforward way of increasing the s parameter is manipulating the spot ratio of the gain module and the SESAM. For instance, the fast absorption saturation, or the high ratio s, was crucial in achieving the bistability between the off-state and the ML state necessary for low-repetition rate ML and addressable pulse generation studied in Marconi et al. (2014, 2015); this was achieved by placing the SESAM in the Fourier plane of the focusing lens so that the spot area $A_{X\alpha}$ was determined only by the diffraction limit. In *monolithic* diode lasers, a similar strategy can be pursued to some degree by *tapering* the laser waveguide so that the absorber region is narrower than the gain region. Used originally for Q-switching QW lasers in a "bow-tie" construction with the narrow SA in the middle of the cavity and the two amplifier sections tapering outward (Williams et al., 1994), this strategy has later been realized most convincingly in QD mode-locked lasers (Nikitichev et al., 2011a,b; Thompson et al., 2006, 2009); see Avrutin and Rafailov (2012) for an overview of results achieved. More often, monolithic structures use the same waveguide structure in the gain and absorber sections for ease of fabrication and fiber coupling, and so $A_{X\alpha} = A_{Xg}$. The parameter s is then equal to the *absorber-to-gain cross section ratio* $s = \sigma_a/\sigma_g$. QWs, with their sublinear (approximately logarithmic) dependence of gain on carrier density (population inversion) have long been seen as superior to bulk material for ML performance, since the sublinear $g(N)$ helps achieve $\sigma_a/\sigma_g > 1$. Vladimirov et al. (2004) and Vladimirov and Turaev (2005) used their DDE analysis to conclude further that when designing a QW laser for ML purposes, a structure with a *smaller number* of QWs was preferable to one with a larger number—indeed, the smaller number of QWs means a smaller confinement factor, hence a higher threshold carrier density and therefore a smaller $\mathrm{d}g/\mathrm{d}N$ at threshold due to the sublinear $g(N)$, which in turns gives a higher value of the ratio s. These considerations influenced the choice of structures with just two to three QWs for realizing DBR ML lasers capable of generating very stable pulses about 2-ps long at 40 Gb/s (Bandelow et al., 2006). It may be argued that the same logic also, in part, accounts for the success of QD mode-locked lasers, in which the dependence of gain on the (total) carrier density in the active layer is even more sublinear than in QWs; however, it has to be borne in mind that the concept of total carrier density is somewhat misleading in QDs; a more accurate picture is given by more complex analysis, considering separately the population of the dots themselves and of the reservoir that supplies them with carriers.

32.4.2.4 Gain and Group Velocity Dispersion Parameters

Most models of mode-locked laser operation predict that without *gain* dispersion, stable ML with a finite pulse duration is impossible, and so the gain dispersion, or width of gain curve, represented by the parameter γ in the DDE or ω_L in the TWM, should play an important role in determining the pulsewidth and stability. Within the range of gain dispersion typical in mode-locked semiconductor lasers, which usually corresponds to $\hbar\omega_L$ of the order of tens of meV (or the wavelength range of tens of nm) and does not change too much with operating conditions or construction, gain dispersion is not the most drastic factor limiting the pulsewidth. However, achieving a broad gain spectrum is still desirable. This may be one of the advantages of QD active media, as discussed below.

GVD, like gain dispersion, acts to broaden the pulses in the case of normal dispersion, which is the usual situation in semiconductor lasers. As discussed above, the effect of this parameter is modest in most semiconductor lasers since the pulse durations at which it would become important (~100 fs) are never achieved; however, with stronger GVD possible in QD lasers, some account for this effect may be necessary.

32.4.2.5 The Gain and Absorber Compression Coefficients

Pulses generated by ML lasers tend to be of picosecond duration. This is below the critical pulsewidth at which the fast gain saturation, rather than the average carrier density dynamics, begins to dominate the pulse amplification and shaping, at least in the gain section; this critical pulse duration has been estimated (Mecozzi and Mork, 1997; Mork and Mecozzi, 1997) to be of the order of $\frac{\varepsilon_g}{v_g \frac{dg}{dN}}$. With typical semiconductor parameters, this estimate gives values of the order of 10 ps. Thus, the gain compression (and, similarly, absorber compression) effects and the coefficients that describe them (if introduced) may be expected to play a significant part in ML properties.

In practice, the effect of nonlinearities is twofold. First, gain compression tends to broaden ML pulses, with absorption compression having the opposite effect. Second, and in some regards more important, an increase in gain compression *stabilizes ML operation*, suppressing the *Q*-switching instability (the latter can be easily shown by rate equation analysis of Q-switched lasers (Avrutin et al., 1991). Again, fast absorber saturation has the opposite effect.

32.4.2.6 The Self-Phase Modulation in the Gain and Absorber Sections

Within the simplest phenomenological approach, the linewidth enhancement factors have a relatively modest effect on pulse *energy* for a given current and absorption, but a more noticeable one on amplitude and duration. They do not significantly affect the onset of the *Q*-switching instability (the lower current or unsaturated gain limit of ML stability), but have a stronger effect on the upper limit of ML stability associated with the irregular envelope and pulse competition. Mode-locked behavior is the most stable when the gain and absorber linewidth enhancement factors are not too different from each other. According to the DDE model predictions, the most stable operating point (which also corresponds to the highest pulse amplitude and lowest duration) is for $\alpha_{\mathrm{Hg}} = \alpha_{\mathrm{H}\alpha}$. Traveling-wave and modal analysis predicts that the best-quality ML is achieved with $\alpha_{\mathrm{Hg}} > \alpha_{\mathrm{H}\alpha}$, see, e.g., Salvatore et al. (1996); the discrepancy is likely to be caused by the different geometry of the long amplifier and the shorter absorber. The main parameter determined by the linewidth enhancement factors is the *chirp* (dynamic shift of the instantaneous frequency) of the pulse. Passively mode-locked pulses tend to be up-chirped (with the instantaneous optical frequency increasing toward the end of the pulse) when the absorber saturation factor $\alpha_{\mathrm{H}\alpha}$ is small and the chirp is mainly caused by α_{Hg}. With a certain combination of α_{Hg} and $\alpha_{\mathrm{H}\alpha}$ (typically $\alpha_{\mathrm{Hg}} > \alpha_{\mathrm{H}\alpha}$), an almost complete compensation of chirp is possible; with $\alpha_{\mathrm{H}\alpha} > \alpha_{\mathrm{Hg}}$, the pulse is typically down-chirped (Salvatore et al., 1996). As up-chirp is observed more frequently than down-chirp in experiments, one may conclude that typical values of $\alpha_{\mathrm{H}\alpha}$ are smaller than α_{Hg}. In active ML, *down-chirp* is typically observed, while hybrid ML allows the chirp to be tuned to some extent, and there is typically a combination of bias and current or voltage modulation amplitude for which the chirp is minimized and close to zero, if only in a very narrow range of operating parameters. In a more detailed semimicroscopic model discussed in Section 32.5, the linewidth enhancement factor is not introduced *explicitly*, with gain and refractive index correction being implemented as imaginary and real part of the same complex dielectric permittivity, respectively, but the tendencies would appear to be general enough to merit being taken into account.

32.4.2.7 The Laser Geometry and Saturable Absorber Location

All the results discussed above could be obtained using either DDE or TWMs, though the latter usually give slightly more realistic predictions (e.g., both types of models predict harmonic operation at high currents, but in the case of multi-GHz PML ($T_{\mathrm{rt}} \ll \tau_{\mathrm{g}}$), operation at harmonics above the second one, predicted by the DDE model, is usually not observed experimentally; TWMs tend to predict only fundamental and second harmonic operation, which agrees with the experiment (Bandelow et al., 2006). The effects of a realistic laser cavity geometry (Fabry–Pérot versus ring cavity, absorber position and length, facet reflectances, etc.) on the ML characteristics are one area where the TWMs have an obvious advantage. They are, for example, highly suitable for analyzing the effects of specialized *harmonic* ML designs for high-frequency generation. These fall into two categories.

The first is colliding pulse mode-locking (CPM), including *multiple (MCPM)* (Martins et al., 1995; McDougall et al., 1997) and *asymmetric (ACPM)* (Shimizu et al., 1995, 1997) colliding-pulse ML constructions. These achieve ML at the M_h-th harmonic by positioning one SA (in CPM or ACPM) or several SAs (in MCPM) at fraction(s) $M'_\mathrm{h}/M_\mathrm{h}$ of the laser cavity length, where $M'_\mathrm{h} < M_\mathrm{h}$ is an integer, and M' (or at least some of the values of M'_h in case of MCPM) and M are mutually prime. The standard CPM corresponds to $M_\mathrm{h} = 2$ (and obviously $M'_\mathrm{h} = 1$) with the SA in the center of the cavity. Constructions of this type have produced ML operation at rates of up to 860 GHz (Shimizu et al., 1997) (in that particular case, $\lambda = 1.55$ μm ACPM construction used $M'_\mathrm{h} = 5, M_\mathrm{h} = 12$). A more detailed review is given in Avrutin et al. (2000). The alternative harmonic ML technique is the use of a *spectrally selective laser cavity*. This may be in the form of a *compound cavity*, which has one or several *intracavity reflectors* (ICRs) positioned at fractions $M'_\mathrm{h}/M_\mathrm{h}$ of the laser cavity length, rather like the SAs in the MCPM or ACPM technique. The highest ML repetition rates reported to date have been achieved by GaAs/AlGaAs ($\lambda \approx 0.89$ μm) lasers with the ICRs in the shape of deeply etched slots, either single or multiple in a 1-D photonic-bandgap (PBG) mirror arrangement (Yanson et al., 2002). A 608-μm long cavity used ICRs at 1/33 of the cavity lengths, giving $F = 2.1$ THz (similar structures with lower M_h values produced ML at bit rates of the order of hundreds of GHz depending on M_h and L).

TWMs have been long since been used for detailed analysis of the CPM (highlighting the importance of *incoherent* colliding pulse effect, the fact that the SA is saturated simultaneously by pulses propagating in both directions, as described by Equation 32.48, as opposed to coherent CPM effect, the self-induced grating described by Equation 32.46, which in semiconductors is less important than in other active media due to diffusion smoothing of the grating). All studies also predict higher stability and shorter pulses with CPM than with ordinary PML, in good agreement with experiment. A version of TWM was also used to explain and analyze the first realization of MCPM (Martins et al., 1995).

In terms of compound-cavity harmonic ML, TWM can help analyze the effects of the slot reflectances and positions (Yanson et al., 2002; Hou et al., 2010b, 2013) and bias current (Hou et al., 2013), with very good qualitative, and good quantitative, agreement with experiments. A TWM study was also used to propose and analyze the use of an alternative method of harmonic selectivity in a mode-locked laser resonator, a sampled grating reflector (Kim et al., 1999), later successfully realized experimentally, see, e.g., Hou et al. (2014) and references therein.

In principle, qualitative analysis can also be possible with DDE models (in fact, CPM can be analyzed, and ACPM predicted, in VECSEL structures using a DDE model (Avrutin and Panajotov, in preparation)), but this requires a customized model for each design whereas TWMs adapt to new design through a simple change of parameters. Harmonic ML is also one area where the time-frequency domain approaches (Section 32.3.2), despite their limitations, can give some insight into the cavity geometry required for successful harmonic operation (Martins et al., 1995; Yanson et al., 2002); however, TWM is still preferable for full quantitative description of the regime.

In addition to CPM, TWM modeling was also used to highlight another possibility allowing for a better saturation of the SA, which consists in placing the absorber close to antireflection-coated laser facet. This design is termed anticolliding mode-locking (ACML) and is inverse to that used for solid-state lasers where the absorber is usually placed close to a high reflection mirror, leading to self-colliding pulse mode-locking (SCML). In this latter situation, the pulse is allowed to interfere constructively with its own reflection onto the mirror leading to an improved absorber bleaching. For semiconductor laser diodes, however, such interferometric effects are rather weak due to the large value of the carrier diffusion coefficient which, in turn, reduces the coherent population grating created by the pulse self-interference as illustrated by Equation 32.47. The analysis of the ACML (Javaloyes and Balle, 2011) showed that this design leads to a substantial increase in output power, a reduction in amplitude and timing jitter, and an enlargement of the range of currents where stable PML can be obtained. The reason is a consequence of the strong increase of the laser field along the cavity axis and as it propagates toward the anti-reflection facet, yielding a more intense saturation of the absorber, and comparatively a weaker saturation of the gain. These regimes where the field is widely nonuniform along the cavity is one of the cases where a proper analysis demands using a TWM approach.

TWM was also used for analysis and optimization of the geometry of a number of other ML laser designs. Simulations of long-cavity ($F_{\mathrm{rep}} \sim 10$ GHz) actively, passively, and hybridly mode-locked DBR lasers predicted that the optimal hybrid and PML performance could be achieved by placing the SA near the facet rather than at the DBR (Hasler et al., 2005), probably largely due to the more efficient absorber saturation as discussed above (Javaloyes and Balle, 2011). TWM studies were also used to predict, in agreement with experiment, that extended cavity laser designs containing a passive section were preferable to all-active ones in terms of pulse duration and chirp (Camacho et al., 1997).

32.5 Microscopic and Semimicroscopic Approaches in Mode-Locked Laser Modeling

32.5.1 The Basics of Microscopic Input in Mode-Locked Laser Simulations

As discussed above, phenomenological models of ML, either of delay-differential or traveling wave types, can be successfully used to predict a number of qualitative tendencies and, to a degree, qualitative parameters of the ML process. However, for detailed comparison with experiments, some microscopic input regarding the gain and SA section material is highly desirable. Some attempts at adding elements of microscopic analysis to models of the type described in the previous section has been undertaken for some time, see, e.g., Bischoff et al. (1997) for a relatively early example. The main challenge, and the main need for microscopic input, arguably, is the accurate modeling of interplay of the *spectral and temporal properties* of the material and laser dynamics. Most importantly, in most QW and, in some cases, QD lasers, the operating wavelength is at the sharp edge of the SA absorption spectrum. As the absorber is saturated, the absorption edge shifts, which lead to a change in the operating point, variation in the absorber saturation parameters affects self-phase modulation, etc. Likewise, due to the absorber selectivity, the operating point can be detuned from the gain peak in the amplifier section. In particular, this makes it difficult to construct a simulated map of regimes in the plane of "gain section bias current/absorber bias voltage," since the voltage affects simultaneously the absorber recovery time (relatively easy to model semimicroscopically as discussed below) and, more importantly, the spectral position of the absorption edge hence the unsaturated absorption and the cross section. This complex interplay of effects is difficult to capture with Equation 32.42 or any of its time-domain implementations, for the SA in particular, and to a degree for the gain section too. A more accurate (and thus ideally microscopically informed) model of gain and, particularly, saturable absorption spectrum as function of population (carrier density), and ideally temperature, is thus required.

The difficulty with this problem is that a realistic microscopic evaluation of gain/absorption in semiconductors is a formidable problem. To do so rigorously requires a many-body quantum mechanical approach (Chow and Koch, 1999), which is a task so complex from the point of view of the various physical effects at work, and so computationally resource-intensive that, at the time of writing, only a handful of research teams worldwide have both the expertise and the computer capacity to attempt it, and to our knowledge only one (the partnership between the Philipps-Universität Marburg and the University of Arizona) is performing this task routinely. The approach has been applied to some mode-locked laser problems, notably single-pass pulse modifications (Bottge et al., 2014) and steady-state ML pulse formation (Kilen et al., 2016) in ultrashort-pulse mode-locked VECSELs, and has informed some work on edge-emitting ML lasers, but to the best of our knowledge not yet been integrated into full analysis of high-bit-rate ML dynamics.

Even in the simpler single-particle approximation ignoring many-body effects, microscopic evaluation of the gain/absorption spectrum in a semiconductor material is, in general, rather nontrivial. For the case of a QW, or, with some reservations, QD active medium, the gain in the single-particle approach is calculated as

$$g(\hbar\omega) = A\sum_{\mu,\nu}\int\left|M^2_{\mu\nu}\right|(E_{\mathrm{e-h}})\rho_{\mu\nu}(E_{\mathrm{e-h}})\left(f_{\mathrm{e}}(E_{\mathrm{e}}^{(\mu)})+f_h(E_{\mathrm{h}}^{(\nu)})-1\right)L'\left(\hbar\omega-E_{\mathrm{e-h}}\right)\mathrm{d}E_{\mathrm{e-h}}. \tag{32.49}$$

Here, A is a proportionality coefficient, $E_{\mathrm{e-h}}$ is the electron–hole energy separation, $E_{\mathrm{e}}^{(\mu)}$ and $E_{\mathrm{h}}^{(\nu)}$ are the energies of the electron in the conduction subband (in the case of a QW material) or level (in the case of QD material) μ and the hole in the valence subband/level ν, which are fully defined by the subband/level numbers and energy separation. Furthermore, $M^2_{\mu\nu}$ and $\rho_{\mu\nu}$ are the squared matrix element of the transition and the reduced density of states, respectively (each of which, in general, varies with energy and is, in general, calculated from a transcendental equation in the case of nonparabolic QW subbands), f_{e} and f_{h} are the electron and hole distribution functions (which in the case of QW materials are very close to Fermi distributions given by the carrier density N and temperature T, and for QDs, in general, need to be calculated from separate kinetic equations), and L'' is the bell-shaped linewidth broadening function.

For a bulk semiconductor material (rarely used in mode-locked diode lasers), the summation over μ and ν is not necessary as there are no multiple subbands in the valence and conduction bands, and the reduced density of states and the matrix element are simple analytical functions of energy.

Still, the expression for the gain/absorption spectrum, in general, can only be evaluated numerically in all cases. The refractive index modulation, needed to consider self-phase modulation in mode-locked lasers, is then reconstructed using Kramers–Kronig relations.

The results are rather difficult to parametrize and to implement in a time-domain model. Simple linear or logarithmic approximations of the microscopic results, often used in the phenomenological models described in the previous section, capture the carrier density dependence of the gain peak and the saturated absorption, but not the spectrum.

The first step toward simplifying the problem is to approximate the linewidth broadening function L'' (which in the general case of a non-Markoffian phase relaxation characteristic of a highly populated semiconductor has quite a complex shape) by a simple Lorentzian form, which follows from a density matrix analysis with a Markoffian phase relaxation with a constant decay rate γ_T and is thus essentially identical to the function describing homogeneous broadening in a two-level system (Equation 32.42):

$$L'(\Delta\omega) = \mathrm{Re}L(\Delta\omega) = \frac{1}{\pi}\frac{\gamma_T}{\gamma_T^2+\Delta\omega^2};\, L(\Delta\omega) = \frac{1}{\pi}\frac{1}{\gamma_T - i\Delta\omega}. \tag{32.50}$$

This form of L' is advantageous because the dynamic correction to the refractive index or the real part of the dielectric permittivity ("imaginary gain") is then calculated using the same equation as Equation 32.49 but using the complementary linewidth broadening function $L''(\Delta\omega) = ImL(\Delta\omega) = \frac{1}{\pi}\frac{\Delta\omega}{\gamma_T^2+\Delta\omega^2}$, eliminating the need for Kramers–Kronig transformation and allowing both gain and refractive index variation to be implemented in time domain as discussed below.

Two main routes can then be successfully followed for using the results of Equation 32.49 in time-domain analysis required for ML simulations.

The first one consists in using a number of approximations in order to simplify the expression (Equation 32.49) (and its imaginary counterpart for the refractive index variation) to a level that permits the integration in energy to be performed analytically, and thus can be realistically parametrized as a (analytical) function of carrier density N and photon energy $\hbar\omega$. This has been achieved (Balle, 1998; Javaloyes and Balle, 2010a) by considering a QW material with a single, parabolic subband for both electrons and holes (hence constant reduced density of states), ignoring the energy dependence of M^2 (and γ_T) and considering (at least in the original version of the model) a very low (mathematically, zero) temperature. In the *frequency* domain (Balle, 1998), this results in a complex dielectric permittivity correction (with the refractive index correction as the real part and the gain as the imaginary part) in the form

$$\chi(\omega, N) = -\chi_0 \left[2 \ln\left(1 - \frac{D}{u-i}\right) - \ln\left(1 - \frac{b}{u-i}\right)\right]. \tag{32.51}$$

Here, χ_0 is a constant proportional to the matrix element M^2 (Balle, 1998) (which in practice can be used as a fitting parameter in the model), $D = \frac{\pi d_{\mathrm{QW}} \hbar}{m \gamma_T} N$ is the reduced carrier density, d_{QW} and $m = \left(m_{\mathrm{e}}^{-1} + m_{\mathrm{h}}^{-1}\right)^{-1} \approx m_{\mathrm{e}}$ being the QW thickness and the reduced mass of the electron–hole pair; $b = \frac{\hbar k_m^2}{2 m \gamma_T}$, k_m being the maximum wave vector in the first Brillouin zone of the semiconductor crystal; and the frequency of the optical transition is parameterized as $u = \frac{\hbar\omega - E_{\mathrm{g}}}{\hbar \gamma_T}$, where the bandgap E_{g} includes N- and T-dependent renormalization.

This result was used, among other applications, in the work in DDE modeling of mode-locked VECSELs (Mulet and Balle, 2005) discussed in Section 32.3.3. In such lasers, the operating frequency and the spectral selectivity of the laser cavity are mainly determined by the resonator properties of the gain chip. A full time-domain implementation of the gain spectrum was thus not required; instead, the complex dielectric permittivity was linearized around the spectral point of operation which, as mentioned in Section 32.3.3, was sufficient to achieve very good qualitative, and good quantitative, agreement with previously reported experiments.

In time domain, the general form of polarization has the same form as Equation 32.44

$$P_{\pm} = \int_{o}^{\infty} \chi(\tau) Y_{\pm}(t - \tau) \mathrm{d}\tau. \tag{32.52}$$

The time-domain version of Equation 32.51 results (Javaloyes and Balle, 2010a) in an integration kernel more complex than the simple exponential of Equation 32.44, specifically of the form

$$\chi_{\mathrm{g}}(\tau, N) = \chi_0 e^{-\left(\gamma_T + i\left(\omega_{\mathrm{g}} - \omega_{ref}\right)\right)\tau} \frac{2 e^{-i\gamma_T D \tau} - 1 - e^{-i\gamma_T b \tau}}{\tau}. \tag{32.53}$$

Here, $\omega_{\mathrm{g}} = E_{\mathrm{g}}/\hbar$; the rest of parameters are the same as in Equation 32.51 and the normalized carrier density D is, strictly speaking, evaluated at the time $t - \tau$; however, since the carrier density even in the faster recovering SA, let alone the gain section, does not change noticeably on the timescale of $1/\gamma_{\mathrm{T}}$, using the value at time t is usually accurate enough (Javaloyes and Balle, 2010a). Despite being, strictly speaking, only applicable for very low temperatures such that $\kappa_{\mathrm{B}} T \ll \hbar \gamma_T$, the kernel (Equation 32.53) is a reasonable approximation for the highly degenerate gain medium. Its accuracy can be further improved to include the finite temperature, though this results in a more complex expression including special functions.

For the case of SAs, an alternative kernel expression was derived (Stolarz et al., 2011) with a finite temperature taken into account from the start, but with the Fermi distribution functions substituted by Boltzmann exponentials, which is usually a safe approximation for the weakly degenerate SA material; in this case,

$$\chi_{\alpha}(\tau, N) = \chi_0 e^{-\left(\gamma_T + i\left(\omega_{\mathrm{g}} - \omega_{\mathrm{ref}}\right)\right)\tau} \left\{ D \left[\frac{a_c}{a_c + i\gamma_T \tau} + \frac{a_v}{a_v + i\gamma_T \tau}\right] - \frac{1 - e^{-i\gamma_T b \tau}}{i\gamma_T \tau} \right\}, \tag{32.54}$$

where $a_{c,v} = \frac{m}{m_{c,v}} \frac{\hbar \gamma_T}{\kappa_B T}$ and the rest of the parameters are as in Equation 32.53. Unlike the simple purely Lorentzian kernel of Equation 32.44, neither of the functions (Equations 32.53 and 32.54) allow for a simple iterative solution using only the previous point in time; instead, the integral must in practice go to an integration limit in τ of about $\tau_{\mathrm{lim}} \sim (3\text{–}6)/\gamma_{\mathrm{T}}$, making the number of previous points necessary for the integration $\tau_{\mathrm{lim}}/\Delta t$.

Despite being managed/mitigated in part by the efficient numerical implementation (Javaloyes and Balle, 2010a), this approach is still quite taxing on the computer resources if implemented straightforwardly in a TWM, since the need for numerical integration in the dispersion operator adds to the general limitations of the TWM approach (the stiffness of the problem requiring a small time step, and computational timescaling as $1/\Delta t^2$ due to the $\Delta z = v_{\mathrm{g}}\Delta t$ condition). Its efficiency can, however, be improved drastically with the *decimation* technique discussed in Section 32.5.2.

The semimicroscopical approach in this form was successfully used to model a number of mode-locked laser designs, including a "straightforward" two-section laser with an SA at a facet (Javaloyes and Balle, 2010b), a colliding-pulse mode-locked laser (Tandoi et al., 2013), and a specialist ring laser with an intracavity filter for spectral flattening and pulse duration reduction (Moskalenko et al., 2013); we shall consider the results of Tandoi et al. (2013) here in somewhat more detail as an illustration of the possibilities and certain limitations of the model.

While the quantitative agreement with experimental results is still not entirely accurate, microscopic models of this type have allowed a number of new possibilities compared to purely phenomenological approaches. The first of these is a much more meaningful, and directly comparable with experiments, prediction of the map of regimes in the "gain section current/absorber bias" plane. Indeed, in QW materials, the voltage applied to the SA has a double effect. First, it decreases the absorber recombination time. To a good accuracy, this is described with an exponential dependence, e.g., in Tandoi et al. (2013), an expression

$$\tau_{\mathrm{SA}} \approx \tau_0 \exp[-F/(f F_0)] \tag{32.55}$$

was used, with $F_0 = (\kappa_{\mathrm{B}} T)/(e d_{\mathrm{QW}})$ being the activation field predicted by the simple thermionic excitation theory (Cavailles et al., 1992), and a correction factor f is introduced heuristically to take into account the interplay between tunneling and thermionic processes (and possibly any well profile distortion). The values $f = 0.5$ and $\tau_0 = 50$ ps were given by fitting the measured $\tau(V_0)$ but agreed well with estimates from more sophisticated theory (Nikolaev and Avrutin, 2003). Second, in materials where the quantum-confined Stark effect (QCSE, absorption shift with voltage) is significant, a voltage variation changes the bandgap, thus affecting the operating point of the laser (unsaturated absorption and saturation cross section), which the microscopic model successfully captures. This tends to be more pronounced in InGaAsP than in aluminum-containing quaternaries. Strictly speaking, QCSE affects also the shape of the absorption spectrum, but this is as yet to be included in the model, since to the best of our knowledge there is as yet no accurate calculation of absorption in a QW with both carriers and electric field present.

Finally, analysis of CW ML behavior requires, in addition to models of absorption spectrum and the recovery time, also a model of the current heating in the absorber. Indeed, the material bandgap that features in the kernels (Equations 32.53 and 32.54) is the renormalized temperature- (and carrier density-) dependent one, and the absorber can get significantly (up to about 10°) heated by the photocurrent flowing through it. This can be modeled (Tandoi et al., 2013) using a separate equation for the absorber bandgap:

$$\frac{\mathrm{d}E_{\mathrm{g}}^{(\mathrm{SA})}}{\mathrm{d}t} = -\gamma_{\mathrm{therm}}\left(E_{\mathrm{g}}^{(\mathrm{SA})} - E_{\mathrm{g0}}^{(\mathrm{SA})} + 2\pi R_{\mathrm{th}} j_{\mathrm{SA}}\left(\left|V_{\mathrm{SA}}\right| + V_{\mathrm{bi}}\right)\right). \tag{32.56}$$

Here, R_{th} is the thermal resistance of the SA, the photocurrent density can be estimated as $j_{\mathrm{SA}} = \mathrm{e}N_{\mathrm{SA}}d_{\mathrm{QW}}/\tau_{\mathrm{SA}}$, and the voltage seen by the active region in the SA is a sum of the built-in potential drop $V_{\mathrm{bi}} = E_{\mathrm{g0}}^{(\mathrm{SA})}/e$ and the applied reverse bias $\left|V_{\mathrm{SA}}\right|$. The parameters of the model were fitted in Tandoi et al. (2013) with the experimental measurements, and then the thermal relaxation rate γ_{therm}, which in reality is of the order of inverse microseconds, sped up to $10^8\ \mathrm{s}^{-1}$, still slower than all characteristic times of laser dynamics but within the possibilities of the model.

Several features observed from the experimental results were well reproduced by the model, e.g., the optimal pulses around 600 fs long were found in the case of a SA occupying 4% of the cavity; some deviation from the best experimental results (430 fs) can be attributed to the approximate nature of the fitting of the gain curve with the two-band model (Equation 32.53).

With the microscopically informed gain and SA models as well as the voltage dependence on the SA recovery time, we constructed in Tandoi et al. (2013) maps of major characteristics of laser behavior in the "amplifier section current—absorber voltage" plane (Figure 32.13). The evolution of the ML quality as a function of the current followed the predictions of the DDE and TWM theories, with a minimal bias current to obtain the ML. The inspection of the time traces indicates that the degradation at high currents is due to the leading-edge instability and to the competition with other harmonics ML solutions, where three or four pulses propagate within the cavity. The evolution of the dynamical regimes as a function of the reverse bias was more subtle. In the AlGaAs materials studied in Tandoi et al. (2013), QCSE was weak and only the SA recovery time varied. This was, however, sufficient to capture the essential physical effects at work and to reproduce the output power decrease and the photocurrent density increase with V_{SA}. A faster SA has enough time to recover its full absorption between pulses and, therefore, presents the full amount of its unsaturated absorption to the pulse, which allows increased losses and photocurrent. Additionally, the photocurrent generated in the SA induces a detuning of the SA bandgap, which eventually hinders ML and decreases the output power. This is due to the fact that the SA can efficiently be modulated only within a limited spectral region around the bandgap and that the absorption increases on the blue side of the spectrum.

The alternative approach to including microscopically informed gain and absorption spectra into a mode-locked laser model has been so far implemented mainly in the context of QD lasers. In QD media, carriers are localized in individual dots and so the global carrier–carrier collisions that establish a common quasi Fermi level in a bulk or QW material are not present. QD lasers still show inhomogeneous

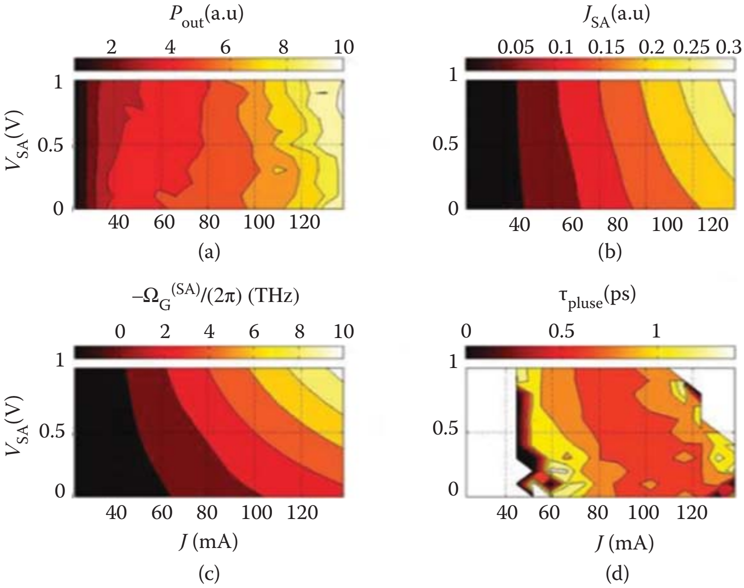

FIGURE 32.13 Parameter maps as a function of the SA reverse bias and of the gain section currently calculated using a TMW with decimation and analytical gain dispersion spectrum, for (a) output power P_{out}, (b) photocurrent density j_{SA} flowing out of the SA section, (c) bandgap of the SA section $-E_g^{(SA)}/h$, and (d) pulsewidth τ_{pulse}. The SA was 4% of the cavity length (optimal case, in agreement with measurements). (From Tandoi G. et al., *IEEE J Sel Top Quantum Electron*, 19, 1100608, 2013. Reproduced with permission).

broadening described mathematically by an equivalent of the reduced density of states in Equation 32.49, but the nature of this broadening is different from the case of bulk or QW materials and stems, not from a continuous energy spectrum of electrons and holes at each point in the material, but from the presence of a large number of dots, with fluctuating dot size and composition, and thus energy levels, in any microscopically large material sample, as already mentioned in Section 32.3.3. The Fermi energy distribution among the carriers occupying the multiple energy levels is established, not by the fast carrier–carrier collisions as in bulk and QW, but by slower processes of capture and escape and is thus only approximate at room temperatures and nonexistent at cryogenic temperatures. The gain thus cannot always be parameterized as a function of the total carrier density N. Instead, the populations of multiple individual levels need to be determined dynamically by solving rate equations including the kinetic processes of capture, interlevel relaxation, and escape, as well as spontaneous and stimulated recombination (see Rafailov et al., 2011 and the corresponding chapter in this handbook for a detailed description). In this case, trying to obtain an integral in Equation 32.49 analytically is problematic (some approximate methods have been discussed in Rafailov et al. (2011) for the room temperature case, but their accuracy has not been tested). Instead, a number of dynamic variables representing population of levels, or slices of the energy spectrum of the carriers in the material (different values of $E_{\text{e-h}}$ in Equation 32.49), at each point in time and space are introduced; the problem thus becomes not two, but (at least) three-dimensional: time, space, and transition energy. To reproduce a spectrum faithfully, the width of the slice should be smaller than, or at least comparable to, the homogeneous broadening γ_T. This approach to QD ML laser modeling is much more complex than the simpler one ignoring the inhomogeneous broadening as presented in Viktorov et al. (2006), but is also much more accurate. Its computational efficiency is comparable to that of using the analytical dielectric permittivity (Equations 32.52 through 32.54). Indeed, on the one hand, the number of variables characterizing carrier polarization (gain and refractive index modulation) at each point is not just the carrier density but the populations of the individual levels, but on the other hand, polarization relaxation of each individual level is Lorentzian (Equation 32.50), so an easy and efficient integration kernel of the type of Equation 32.44 can be implemented.

The resulting model has been used for mapping stability limits in a mode-locked laser and analysis of pulse shape and chirp (Rossetti et al., 2011a,b), as well as the analysis of the effects of laser cavity geometry (absorber location, cavity reflectivities) (Simos et al., 2013; Xu and Montrosset, 2013), in particular finding the optimum SA length (Xu and Montrosset, 2013).

The microscopic approach of this type can be implemented both in the traveling-wave formalism as in the papers above (particularly with decimation to improve the otherwise problematic numerical efficiency) and in a DDE model, particularly the multisection version (MS-DDE) as discussed in Section 32.3.3 (Rossetti et al., 2011b). With inhomogeneous broadening included, an MS-DDE model was used for the analysis of problems including the peculiarities of ML operation involving both ground- and excited-level transitions (Xu et al., 2012), as well as for modeling-tapered laser structures (Nikitichev et al., 2012), the latter in agreement with both a TWM simulation by the same authors and with experiments.

In Pimenov and Vladimirov (2014), a multilevel approach was presented for a TWM of a "generic" inhomogeneously broadened medium, not necessarily QD. It can be foreseen that potentially, it can be used for lasers with QW and bulk active layers, for example for a short-cavity QW laser where transitions from both first and second electron levels (disregarded in Equations 32.52 through 32.54) can become important. In principle, it could allow an arbitrary set of carrier density-dependent spectra, possibly calculated using a many-body approach and/or using realistic QW parameters such as multiple-level transitions, strain, etc., by necessity omitted in Equations 32.52 through 32.54, to be approximated and reproduced in the time-domain model. To a degree, the analytical spectrum approach (Equations 32.52 through 32.54) offers such an approximation possibility as well by treating the effective masses of carriers and matrix elements as fitting parameters, which has the advantages of involving much fewer parameters, but may be somewhat less flexible.

32.5.2 Improving the Numerical Efficiency of TWMs: Decimation/Space–Time Folding

So far, we have considered, on the one hand, the DDE models (Section 32.3.3) which are simple, efficient, instructive, and allow automated bifurcation analysis by numerical continuation and in the simplest cases also analytical insight, but are not always accurate in reproducing the behavior or realistic edge-emitting laser constructions, and, on the other hand, full TWM models (Section 32.3.4) which are potentially very accurate in representing a realistic laser, but rather computationally intensive and incompatible with automated bifurcation analysis.

The numerical technique of decimation presented below, which builds on an earlier model for laser designs where gain and SA dispersion are negligible compared to the effect of a lumped dispersive element (reflector) such as a DBR (Vladimirov et al., 2009) to apply to the general case of significant gain and SA dispersion (Javaloyes and Balle, 2012b), allows the advantages of both models to be combined to a large degree.

The starting point for the technique is a TWM in the general form of Equation 32.40, which can be compactly rewritten (keeping only the deterministic part so far) as

$$\pm\frac{\partial Y_\pm}{\partial z} + \frac{1}{v_\mathrm{g}}\frac{\partial Y_\pm}{\partial t} = Z_\pm = P^t_\pm - \alpha_\mathrm{f} Y_\pm, \tag{32.57}$$

where $\alpha_\mathrm{f} = \alpha_{int}/2$ is the "field" internal loss, and the "total" polarization $P^t_\pm$ includes the dynamic coupling terms:

$$P^t_\pm = \left(\frac{1}{2}\hat{g}_\mathrm{mod} + ik_\mathrm{ref}\widehat{\Delta\eta}_\mathrm{mod}\right)Y_\pm + i\hat{K}_{\pm,\mp}Y_\mp. \tag{32.58}$$

(Note that the dynamic coupling terms can include dispersion in the same way as the "copropagating" polarization terms, as is indeed the case in the semimicroscopic model used in Javaloyes and Balle (2010a,b), though this is not likely to have a major effect as the dynamic coupling is usually weak anyway.) The formal solution of Equation 32.51 is obtained in the form

$$Y_\pm(z,t) = Y_\pm(z \mp v_\mathrm{g}\tau, t-\tau) + \Xi_\pm(z,t); \quad \Xi_\pm(z,t) = \int\limits_0^\tau Z_\pm(z \mp v_\mathrm{g}(\tau-\vartheta), t-\tau+\vartheta)\mathrm{d}\vartheta. \tag{32.59}$$

Then, assuming that the time interval is sufficiently short for the variation of the field along the traveling coordinate $\xi_\mp = z \mp v_\mathrm{g}t$ to be modest (crucially, no such requirement is made to the variations in z and t *separately*—in short-pulse ML, these can be quite strong due to the steep pulse fronts, but the evolution in the pulse shape as it propagates is relatively gentle meaning that variation along $\xi_\mp$ remains gentle), it is possible to approximate $\Xi_\pm(z,t) = \frac{v_\mathrm{g}\tau}{2}(Z_\pm(z \mp v_\mathrm{g}\tau, t-\tau) + Z_\pm(z,t))$. Then, using a (1,1) Padé approximation $\exp(x) \approx (1+x/2)/(1-x/2)$, one obtains a final formula relating the fields and polarizations at the previous and current points:

$$\left(1+\frac{\alpha_\mathrm{f}\tau}{2}\right)Y_\pm(z,t) = \left(1-\frac{\alpha_\mathrm{f}\tau}{2}\right)Y_\pm(z \mp v_\mathrm{g}\tau, t-\tau) + \frac{v_\mathrm{g}\tau}{2}(P^t_\pm(z \mp v_\mathrm{g}\tau, t-\tau) + P^t_\pm(z,t)). \tag{32.60}$$

This formula can be, and is, implemented directly in a numerical solver, in which a laser is separated into a number of segments n_sect with a length $v_\mathrm{g}\tau_j, j = 1, \ldots, n_\mathrm{sect}$.

Accurate calculation of the polarization with the spectrum taken into account still requires a small *temporal* integration step Δt (commensurate with $1/\gamma_T$); however, crucially, when using Equation 32.59 as a basis of the numerical procedure, the *spatial* step $v_g\tau_j$ is limited only by the degree of uniformity with the field (roughly speaking, the requirement that $v_g\tau_j \left|g_{\text{mod}\,j}\right| << 1$, $g_{\text{mod}j}$ being the characteristic value of the modal gain (or absorption) in the section of the laser with the length $v_g\tau_j$). This is a much less stringent requirement, meaning that the space and time steps are essentially decoupled and the computational time therefore scales, not as $1/\Delta t^2$ as in the straightforward TWM, but only approximately as $1/\Delta t$.

From the numerical point of view, it is important to have an integer relation between the time and space steps:

$$\tau_j = n_{dj}\Delta t, \tag{32.61}$$

where the integer number n_{dj} is the *decimation factor* of the spatial section *j*. It is not necessary (nor advisable) for all the sections to have the same decimation factor; e.g., typically, in the SA part of a passively or hybridly mode-locked laser (where the field is less uniform), it is advisable to set the decimation factor smaller than in the more uniform gain sections. For numerical simplicity, identical decimation factors are typically used in all gain sections and in all SA sections, e.g., $n_{d(\text{gain})} = 71$ and $n_{d\text{SA}} = 8$ were used in Tandoi et al. (2013). This implies that the computation time required in a model with decimation is only a few percent of the time needed for the same calculation with a straightforward TWM model, which is indeed the case.

Mathematically speaking, a model with decimation is a set of n_{sect} delayed algebraic equations (DAEs) with the delay of $\tau_j = n_{dj}\Delta t$ in each section *j*. This section replaces having to deal with n_{dj} spatial steps which would be the case in a straightforward TWM analysis, which is why the alternative (original) term for the decimation technique is *folding space into time delay*. As the number of the DAEs in a typical simulation is not large ($<\sim 10$), the decimated model, unlike a straightforward TWM, is compatible with the numerical tools for bifurcation analysis.

The decimation/space-time folding technique of Tandoi et al. (2013) was not the first attempt at improving the efficiency of the traveling-wave solver. For example, this was attempted, with some degree of success, in the semianalytical TWM technique by Carroll et al. (Jones et al., 1995; Carroll et al., 1998), in which, however, the (homogeneous broadening type) digital filter was explicitly incorporated into the solver and the condition $\Delta z = v_g\Delta t$, eliminated in the decimated TWM, still stood. The decimation technique is thus both much more powerful and more versatile in that it can be used with *any arbitrary method* of calculating the polarization $P^t_\pm$, including either of the two microscopic approaches discussed in Section 32.5.1, or indeed a phenomenological two-level type dispersion representation of Equation 32.44.

However, the decimation technique is both particularly useful and particularly instructive with the analytical kernel technique of Equations 32.54 and 32.57, for which it was originally derived and used (which is the reason we have chosen to place the description of the model within the section on microscopic input). Figure 32.14 illustrates the "stencils" showing the time and space points required for propagating the fields in three major cases: (1) the TWM with a homogeneously broadened line (Figure 32.14a), (2) a straightforwardly implemented TWM with the analytical kernel (Figure 32.14b), and (3) the decimated model with the same analytical kernel and $n_{d(\text{gain})} = 8$, $n_{d\text{SA}} = 2$ (Figure 32.14c). The sparsity of the stencil clearly shows how the decimation allows the sophistication of the microscopic model to be retained while drastically improving the efficiency of the calculation.

We note, following Javaloyes and Balle (2012b), that the decimated TWM contains as particular cases the two other major model types discussed in previous sections. Indeed, with $n_{d(\text{gain})} = n_{d\text{SA}} = 1$, it reduces to a straightforward TWM of Section 32.3.4. For a unidirectional ring cavity (and particularly for a homogeneously broadened line), it reproduces the DDE approach of Section 32.3.3 (Javaloyes and Balle (2012b) noted also that for a single-frequency laser, their model can, in principle, reduce to a generalized complex rate equations formalism, but that is by definition not relevant for ML). A decimated TWM with an analytical kernel technique for gain/refractive index dispersion has been implemented to include a number of laser geometries including but not restricted to mode-locked lasers, and is available online as free software (MATLAB® toolkit) under GPL license (Javaloyes and Balle, 2012a).

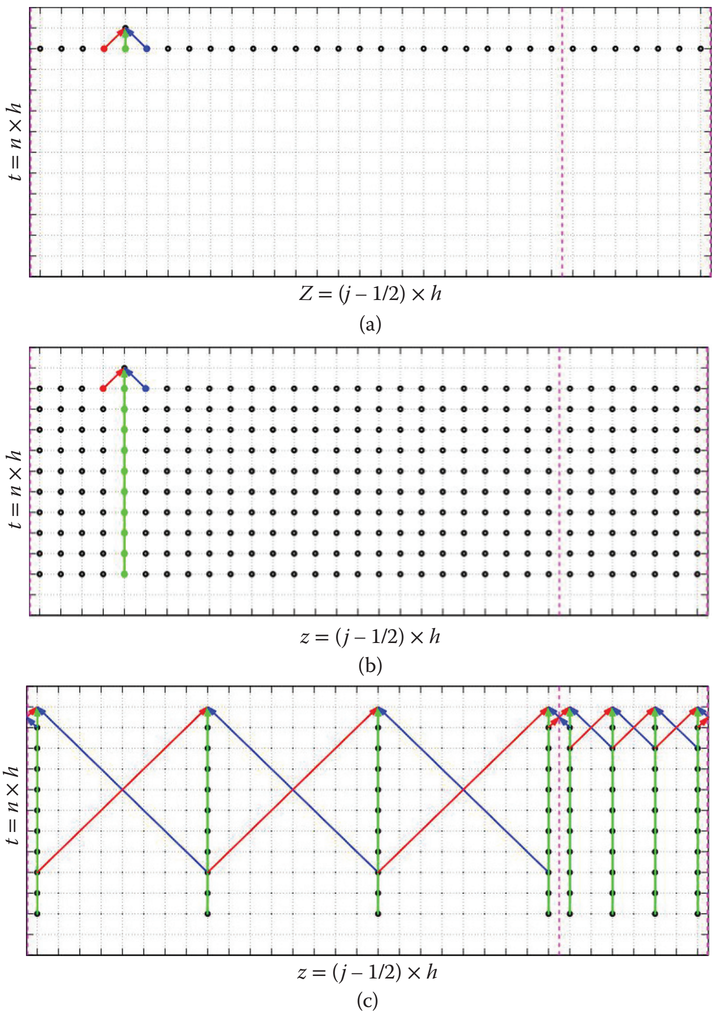

FIGURE 32.14 Calculation "stencils" illustrating field propagation in traveling wave modeling. (a) TWM with homogeneous broadening (Lorentzian gain spectrum), (b) analytical gain spectrum in a straightforward TWM, and (c) analytical gain spectrum in a TWM with decimation.

32.6 Some Novel Problems and Challenges in Mode-Locked Laser Modeling

32.6.1 Coherent Population Effects as a Possible Saturable Absorption Mechanism

One of the most important developments in mode-locked semiconductor laser technology in the recent years has been the direct generation of ultrashort (tens to a couple of hundreds of femtoseconds) pulses that until recently have been the domain of solid-state lasers only. Only one type of semiconductor lasers has been reported to produce such pulses so far, namely an optically pumped VECSEL, with the gain and SESAM chips in a folded (V-shaped) external cavity arrangement (Klopp et al., 2009, 2011; Quarterman et al., 2009; Wilcox et al., 2008). One of the teams that produced the femtosecond ML pulses attributed their results to coherent effects in the SESAM elements, namely the optical (ac) Stark effect. This effect, related to self-induced transparency, has the relaxation rate equal to the inverse of the dephasing (coherence decay) time. In semiconductors, this time is determined by carrier–carrier (and carrier–phonon) collisions and is of the order of 50–100 fs. This belongs to the *fast*, rather than slow, absorber regime, when the SA recovery time is shorter than the pulse duration. Indeed, theoretical analysis (Mihoubi et al., 2008; Wilcox et al., 2008), based on iterative small-signal time domain approach not dissimilar to that covered in Section 32.3.1 for a standard SA, showed that the pulse duration possible with this mechanism is about twice the dephasing time, which agrees well with the experiments. Further developments of this work are ongoing and are likely to rely not only on the experimental progress but also achieving better understanding of the limits and the requirements on the laser model through improved modeling.

There has also been work recently on the theoretical analysis of (so far, hypothetical) coherent ML through self-induced transparency effects in an *edge-emitting* class B (possibly semiconductor) laser geometry (see, e.g., Arkhipov et al., 2015a, 2016a,b), which promises femtosecond pulses but relies on *extending* the phase relaxation time, possibly by working under cryogenic conditions.

32.6.2 Spontaneous ML in Single-Section Lasers

Most of the discussions above concerned passive or hybrid ML constructions including an SA. However, in recent years, a very interesting development in ML laser technology occurred, when several teams have observed—and utilized—ML in single-section lasers without SA sections and without any external modulation either. The ML in this case was not of a pure AM ML type and the laser output only acquired short-pulse characteristics after external chirp compensation.

This effect has been observed in *quantum dash* (see, e.g., Duan et al., 2009; Gosset et al., 2006; Rosales et al., 2011), *QD* (Lu et al., 2011; Renaudier et al., 2005), QW (Sato, 2003; Yang, 2011), and even bulk materials (Yang, 2011), as well as in intersubband, far-infrared quantum cascade lasers (Faist et al., 2016 and references therein) showing that the effect is fairly generic. Further optimization of these lasers may partly depend on the establishment of full understanding of their behavior, yet at the time of writing, a full, universally agreed, theoretical explanation for ML in single-section lasers is still pending, and it is not impossible that different effects can play the main part in different constructions. In the past, some authors (Shore and Yee, 1991; Yee and Shore, 1993) used frequency-domain models with postulated, and differing, self- and cross- nonlinearity coefficients to show that nonlinearities in single-section semiconductor lasers could lead to a steady-state regime with fixed phases; this was predicted to produce, not the AM ML that corresponds to short-pulse emission, but the so-called frequency modulation ML, in which the phases of adjacent modes differ approximately by π, and the outcome is a CW-like regime with periodic carrier frequency oscillation. More recent works (Nomura et al., 2002; Renaudier et al., 2007), also using frequency-domain analysis with microscopically calculated (Nomura et al., 2002) or phenomenological (Renaudier et al., 2007) description of linear and nonlinear gain, predicted a possibility of ML-type signal generation, including AM ML for certain cavity lengths and active layer parameters, in a single-section laser with three modes involved in lasing, due to mode coupling by population pulsations/four-wave mixing effects. This appears to agree with traveling-wave modeling (Section 32.3.4) analysis for the case of a DBR laser without an SA (Bardella and Montrosset, 2005); Bardella and Montrosset (2005) also identified the role of four-wave mixing in their construction. Recently, a microscopic TWM analysis of a *QD* single-section laser has been presented (Gioannini et al., 2015), relying on both the nonequilibrium occupation of multiple levels due to inhomogeneous broadening and an additional phenomenological gain compression coefficient. The authors concluded that the suppressed carrier diffusion and the fast ground state (GS) gain recovery, typical of quantum dashes and QDs, were the mechanisms behind the phase-locking among the laser modes. Time-domain modeling on single-section ML (comb generation) in quantum cascade lasers has also been reported (Tzenov et al., 2016), though it has to be noted that the short upper state lifetime in those lasers makes their dynamics very different to that of other semiconductor lasers.

Further work extending the understanding achieved this far to other active media is desirable and hopefully forthcoming.

32.7 Concluding Remarks

We have attempted to review the most important developments in semiconductor mode-locked laser modeling. The topic is very dynamic and fast developing, so the choice of emphasis in this review was by necessity subjective; we apologize to those authors whose work may not have been given due prominence.

Acknowledgment

J.J. acknowledges financial support project COMBINA (TEC2015-65212-C3-3-P MINECO/FEDER UE)

References

Arkhipov R, Pimenov A, Radziunas M, Rachinskii D, Vladimirov AG, Arsenijevic D, Schmeckebier H, Bimberg D (2013) Hybrid mode locking in semiconductor lasers: Simulations, analysis, and experiments. *IEEE J Sel Top Quantum Electron* 19:1100208.

Arkhipov RM, Amann A, Vladimirov AG (2015b) Pulse repetition-frequency multiplication in a coupled cavity passively mode-locked semiconductor lasers. *Appl Phys B-Lasers Opt* 118:539–548.

Arkhipov RM, Arkhipov MV, Babushkin IV (2015a) On coherent mode-locking in a two-section laser. *Jetp Lett* 101:149–153.

Arkhipov RM, Arkhipov MV, Babushkin I (2016a) Self-starting stable coherent mode-locking in a two-section laser. *Opt Commun* 361:73–78.

Arkhipov RM, Arkhipov MV, Babushkin I, Rosanov NN (2016b) Self-induced transparency mode locking, and area theorem. *Opt Lett* 41:737–740.

Arkhipov RM, Habruseva T, Pimenov A, Radziunas M, Hegarty SP, Huyet G, Vladimirov AG (2016c) Semiconductor mode-locked lasers with coherent dual-mode optical injection: Simulations, analysis, and experiment. *J Opt Soc Am B-Opt Phys* 33:351–359.

Avrutin EA, Arnold JM, Marsh JH (1996) Analysis of dynamics of monolithic passively mode-locked laser diodes under external periodic excitation. *IEE Proc-Optoelectron* 143:81–88.

Avrutin EA, Arnold JM, Marsh JH (2003) Dynamic modal analysis of monolithic mode-locked semiconductor lasers. *IEEE J Sel Top Quantum Electron* 9:844–856.

Avrutin EA, Marsh JH, Portnoi EL (2000) Monolithic and multi-gigahertz mode-locked semiconductor lasers: Constructions, experiments, models and applications. *IEE Proc-Optoelectron* 147:251–278.

Avrutin EA, Nikolaev VV, Gallagher D (2005) Monolithic mode-locked semiconductor lasers. In: *Optoelectronic Devices—Advanced Simulation and Analysis* (Piprek J, ed.), pp. 185–215. New York, NY: Springer.

Avrutin and Panajotov, in preparation.

Avrutin EA, Portnoi EL, Chelnokov AV (1991) Effect of nonlinear amplification on characteristics of quality modulation regime in semiconducting laser with fast saturated absorbers. *Pisma V Zhurnal Tekhnicheskoi Fiziki* 17:49–54.

Avrutin EA, Rafailov EU (2012) Advances in mode-locked semiconductor lasers. In: *Advances in Semiconductor Lasers* (Coleman JJ, Bryce AC, Jagadish C, eds.), San Diego: Academic Press, pp. 93–147.

Avrutin EA, Russell BM (2009) Dynamics and spectra of monolithic mode-locked laser diodes under external optical feedback. *IEEE J Quantum Electron* 45:1456–1464.

Balle S (1998) Simple analytical approximations for the gain and refractive index spectra in quantum-well lasers. *Phys Rev A* 57:1304–1312.

Bandelow U, Radziunas M, Sieber J, Wolfrum M (2001) Impact of gain dispersion on the spatio-temporal dynamics of multisection lasers. *IEEE J Quantum Electron* 37:183–188.

Bandelow U, Radziunas M, Vladimirov A, Huttl B, Kaiser R (2006) 40 GHz mode-locked semiconductor lasers: Theory, simulations and experiment. *Opt Quantum Electron* 38:495–512.

Bardella P, Montrosset I (2005) Analysis of self-pulsating three-section DBR lasers. *IEEE J Sel Top Quantum Electron* 11:361–366.

Bischoff S, Mork J, Franck T, Brorson SD, Hofmann M, Frojdh K, Prip L, Sorensen MP (1997) Monolithic colliding pulse mode-locked semiconductor lasers. *Quantum Semiclass Opt* 9:655–674.

Bottge CN, Hader J, Kilen I, Moloney JV, Koch SW (2014) Ultrafast pulse amplification in mode-locked vertical external-cavity surface-emitting lasers. *Appl Phys Lett* 105:261105.

Brown CTA, Cataluna MA, Lagatsky AA, Rafailov EU, Agate MB, Leburn CG, Sibbett W (2004) Compact laser-diode-based femtosecond sources. *New J Phys* 6:175.

Camacho F, Avrutin EA, Cusumano P, Helmy AS, Bryce AC, Marsh JH (1997) Improvements in mode-locked semiconductor diode lasers using monolithically integrated passive waveguides made by quantum-well intermixing. *IEEE Photonics Technol Lett* 9:1208–1210.

Carroll JE, Whiteaway J, Plumb D (1998) *Distributed Feedback Semiconductor Lasers*, 2nd Edition. Stevenage: IET.

Cataluna MA, Nikitichev DI, Mikroulis S, Simos H, Simos C, Mesaritakis C, Syvridis D, Krestnikov I, Livshits D, Rafailov EU (2010) Dual-wavelength mode-locked quantum-dot laser, via ground and excited state transitions: Experimental and theoretical investigation. *Opt Express* 18:12832–12838.

Cataluna MA, Viktorov EA, Mandel P, Sibbett W, Livshits DA, Kovsh AR, Rafailov EU (2006) Temperature dependence of pulse duration in a mode-locked quantum-dot laser: Experiment and theory. In: *The 19th Annual Meeting of the IEEE Lasers and Electro-Optics Society* (IEEE, ed), pp. 798–799. Montreal, Canada.

Cataluna MA, Viktorov EA, Mandel P, Sibbett W, Livshits DA, Weimert J, Kovsh AR, Rafailov EU (2007) Temperature dependence of pulse duration in a mode-locked quantum-dot laser. *Appl Phys Lett* 90:101102–101103.

Cavailles JA, Miller DAB, Cunningham JE, Wa PLK, Miller A (1992) Simultaneous measurements of electron and hole sweep-out from quantum-wells and modeling of photoinduced field screening dynamics. *IEEE J Quantum Electron* 28:2486–2497.

Chow WW, Koch SW (1999) *Semiconductor Laser Fundamentals. Physics of the Gain Materials*. Berlin, Heidelberg: Springer.

Coldren LA, Corzine SW, Mashanovitch ML (2012) *Diode Lasers and Photonic Integrated Circuits*, 2nd Edition. New York, NY: Wiley.

Delpon EL, Oudar JL, Bouche N, Raj R, Shen A, Stelmakh N, Lourtioz JM (1998) Ultrafast excitonic saturable absorption in ion-implanted InGaAs/InAlAs multiple quantum wells. *Appl Phys Lett* 72:759–761.

Deryagin AG, Kuksenkov DV, Kuchinskii VI, Portnoi EL, Khrushchev IY, Frahm J (1994) Generation of high repetition frequency subpicosecond pulses at 1.535 mu-m by passive mode-locking of InGaAsP/InP laser diode with saturable absorber regions created by ion implantation. In: *14th IEEE International Semiconductor Laser Conference*, pp 107–108. New York, NY: IEEE.

Duan GH, Shen A, Akrout A, Van Dijk F, Lelarge F, Pommereau F, LeGouezigou O, Provost JG, Gariah H, Blache F, Mallecot F, Merghem K, Martinez A, Ramdane A (2009) High performance InP-based quantum dash semiconductor mode-locked lasers for optical communications. *Bell Labs Tech J* 14:63–84.

Dubbeldam JLA, Leegwater JA, Lenstra D (1997) Theory of mode-locked semiconductor lasers with finite absorber relaxation times. *Appl Phys Lett* 70:1938–1940.

Ell R, Morgner U, Kartner FX, Fujimoto JG, Ippen EP, Scheuer V, Angelow G, Tschudi T, Lederer MJ, Boiko A, Luther-Davies B (2001) Generation of 5-fs pulses and octave-spanning spectra directly from a Ti: Sapphire laser. *Opt Lett* 26:373–375.

Erneux T, Viktorov EA, Mandel P, Piwonski T, Huyet G, Houlihan J (2009) The fast recovery dynamics of a quantum dot semiconductor optical amplifier. *Appl Phys Lett* 94:113501.

Faist J, Villares G, Scalari G, Rosch M, Bonzon C, Hugi A, Beck M (2016) Quantum cascade laser frequency combs. *Nanophotonics* 5:272–291.

Fleck JA (1968) Emission of pulse trains by Q-switched lasers. *Phys Rev Lett* 21:131–133.

Gioannini M, Bardella P, Montrosset I (2015) Time-domain traveling-wave analysis of the multimode dynamics of quantum dot Fabry-Perot lasers. *IEEE J Sel Top Quantum Electron* 21:1–11.

Gosset C, Merghem K, Martinez A, Moreau G, Patriarche G, Aubin G, Landreau J, Lelarge E, Ramdane A (2006) Subpicosecond pulse generation at 134 GHz and low radiofrequency spectral linewidth in quantum dash-based Fabry-Perot lasers emitting at 1.5 µm. *Electron Lett* 42:91–92.

Green RP, Haji M, Hou LP, Mezosi G, Dylewicz R, Kelly AE (2011) Fast saturable absorption and 10 GHz wavelength conversion in Al-quaternary multiple quantum wells. *Opt Express* 19:9737–9743.

Hasler KH, Klehr A, Wenzel H, Erbert G (2005) Simulation of high-power pulse generation due to modelocking in long multisection lasers. *IEE Proc-Optoelectron* 152:77–85.

Haus HA (1975) Theory of mode-locking with a slow saturable absorber. *IEEE J Quantum Electron* 11:736–746.

Haus HA (2000) Mode-locking of lasers. *IEEE J Sel Top Quantum Electron* 6:1173–1185.

Haus HA, Silberberg Y (1985) Theory of mode-locking of a laser diode with a multiple-quantum-well structure. *J Opt Soc Am B-Opt Phys* 2:1237–1243.

Heck MJR, Bente E, Barbarin Y, Lenstra D, Smit MK (2006) Simulation and design of integrated femtosecond passively mode-locked semiconductor ring lasers including integrated passive pulse shaping components. *IEEE J Sel Top Quantum Electron* 12:265–276.

Hou LP, Avrutin EA, Haji M, Dylewicz R, Bryce AC, Marsh JH (2013) 160 GHz passively mode-locked AlGaInAs 1.55 mu m strained quantum-well lasers with deeply etched intracavity mirrors. *IEEE J Sel Top Quantum Electron* 19:1100409.

Hou LP, Haji M, Dylewicz R, Stolarz P, Qiu BC, Avrutin EA, Bryce AC (2010b) 160 GHz harmonic mode-locked AlGaInAs 1.55 mu m strained quantum-well compound-cavity laser. *Opt Lett* 35:3991–3993.

Hou LP, Haji M, Marsh JH (2014) Mode-locking and frequency mixing at THz pulse repetition rates in a sampled-grating DBR mode-locked laser. *Opt Express* 22:21690–21700.

Hou LP, Stolarz P, Dylewicz R, Haji M, Javaloyes J, Qiu BC, Bryce C (2010a) 160-GHz passively mode-locked AlGaInAs 1.55-mu m strained quantum-well compound cavity laser. *IEEE Photonics Technol Lett* 22:727–729.

Innerhofer E, Sudmeyer T, Brunner F, Haring R, Aschwanden A, Paschotta R, Honninger C, Kumkar M, Keller U (2003) 60-W average power in 810-fs pulses from a thin-disk Yb: YAG laser. *Opt Lett* 28:367–369.

Jaurigue L, Nikiforov O, Scholl E, Breuer S, Ludge K (2016) Dynamics of a passively mode-locked semiconductor laser subject to dual-cavity optical feedback. *Phys Rev E* 93:022205.

Jaurigue L, Pimenov A, Rachinskii D, Scholl E, Ludge K, Vladimirov AG (2015) Timing jitter of passively-mode-locked semiconductor lasers subject to optical feedback: A semi-analytic approach. *Phys Rev A* 92:053807.

Javaloyes J, Balle S (2010a) Quasiequilibrium time-domain susceptibility of semiconductor quantum wells. *Phys Rev A* 81:062505.

Javaloyes J, Balle S (2010b) Mode-locking in semiconductor Fabry-Perot lasers. *IEEE J Quantum Electron* 46:1023–1030.

Javaloyes J, Balle S (2011) Anticolliding design for monolithic passively mode-locked semiconductor lasers. *Opt Lett* 36:4407–4409.

Javaloyes J, Balle S (2012a) Freetwm: A simulation tool for semiconductor lasers. In: Freetwm: A simulation tool for semiconductor lasers.

Javaloyes J, Balle S (2012b) Multimode dynamics in bidirectional laser cavities by folding space into time delay. *Opt Express* 20:8496–8502.

Jones DJ, Zhang LM, Carroll JE, Marcenac DD (1995) Dynamics of monolithic passively mode-locked semiconductor lasers. *IEEE J Quantum Electron* 31:1051–1058.

Khalfin VB, Arnold JM, Marsh JH (1995) A theoretical-model of synchronization of a mode-locked semiconductor-laser with an external pulse stream. *IEEE J Sel Top Quantum Electron* 1:523–527.

Kilen I, Koch SW, Hader J, Moloney JV (2016) Fully microscopic modeling of mode locking in microcavity lasers. *J Opt Soc Am B-Opt Phys* 33:75–80.

Kim BS, Chung Y, Kim SH (1999) Dynamic analysis of mode-locked sampled-grating distributed Bragg reflector laser diodes. *IEEE J Quantum Electron* 35:1623–1629.

Kim I, Lau KY (1993) Frequency and timing stability of mode-locked semiconductor lasers-passive and active mode locking up to millimeter wave frequencies. *IEEE J Quantum Electron* 29:1081–1090.

Kim K, Lee S, Delfyett PJ (2005) 1.4kW high peak power generation from an all semiconductor mode-locked master oscillator power amplifier system based on eXtreme Chirped Pulse Amplification (X-CPA). *Opt Express* 13:4600–4606.

Klopp P, Griebner U, Zorn M, Klehr A, Liero A, Weyers M, Erbert G (2009) Mode-locked InGaAs-AlGaAs disk laser generating sub-200-fs pulses, pulse picking and amplification by a tapered diode amplifier. *Opt Express* 17:10820–10834.

Klopp P, Griebner U, Zorn M, Weyers M (2011) Pulse repetition rate up to 92 GHz or pulse duration shorter than 110 fs from a mode-locked semiconductor disk laser. *Appl Phys Lett* 98:071103.

Koumans R, vanRoijen R (1996) Theory for passive mode-locking in semiconductor laser structures including the effects of self-phase modulation, dispersion, and pulse collisions. *IEEE J Quantum Electron* 32:478–492.

Kuznetsov M (1985) Pulsations of semiconductor lasers with a proton bombarded segment: Well-developed pulsations. *IEEE J Quantum Electron* 21:587–592.

Lau KY, Paslaski J (1991) Condition for short pulse generation in ultrahigh frequency mode-locking of semiconductor lasers. *IEEE Photonics Technol Lett* 3:974–976.

Leegwater JA (1996) Theory of mode-locked semiconductor lasers. *IEEE J Quantum Electron* 32:1782–1790.

Lu ZG, Liu JR, Poole PJ, Jiao ZJ, Barrios PJ, Poitras D, Caballero J, Zhang XP (2011) Ultra-high repetition rate InAs/InP quantum dot mode-locked lasers. *Opt Commun* 284:2323–2326.

Malins DB, Gomez-Iglesias A, White SJ, Sibbett W, Miller A, Rafailov EU (2006) Ultrafast electroabsorption dynamics in an InAs quantum dot saturable absorber at 1.3 μm. *Appl Phys Lett* 89:171111–171113.

Marconi M, Javaloyes J, Balle S, Giudici M (2014) How lasing localized structures evolve out of passive mode locking. *Phys Rev Lett* 112:223901.

Marconi M, Javaloyes J, Camelin P, Gonzalez DC, Balle S, Giudici M (2015) Control and generation of localized pulses in passively mode-locked semiconductor lasers. *IEEE J Sel Top Quantum Electron* 21:1101210.

Martins JF, Avrutin EA, Ironside CN, Roberts JS (1995) Monolithic multiple colliding pulse mode-locked quantum-well lasers: Experiment and theory. *IEEE J Sel Top Quantum Electron* 1:539–551.

McDougall SD, Vogele B, Stanley CR, Ironside CN (1997) The crucial role of doping for high repetition rate monolithic mode locking of multiple quantum well GaAs/AlGaAs lasers. *Appl Phys Lett* 71:2910–2912.

Mecozzi A, Mork J (1997) Saturation effects in nondegenerate four-wave mixing between short optical pulses in semiconductor laser amplifiers. *IEEE J Sel Top Quantum Electron* 3:1190–1207.

Mihoubi Z, Daniell GJ, Wilcox KG, Tropper AC (2008) *Numerical Model of a Vertical-External-Cavity Surface-Emitting Semiconductor Lasers Mode-Locked by the Optical Stark Effect*. New York, NY: IEEE.

Mork J, Mecozzi A (1997) Theory of nondegenerate four-wave mixing between pulses in a semiconductor waveguide. *IEEE J Quantum Electron* 33:545–555.

Moskalenko V, Javaloyes J, Balle S, Smit M, Bente E (2013) Dynamics of colliding pulse passively semiconductor mode-locked ring lasers with an intra-cavity Mach-Zehnder modulator. In: *2013 Conference on and International Quantum Electronics Conference Lasers and Electro-Optics Europe*. Cleo Europe/Iqec.

Mulet J, Balle S (2005) Mode-locking dynamics in electrically driven vertical-external-cavity surface-emitting lasers. *IEEE J Quantum Electron* 41:1148–1156.

New GHC (1974) Pulse evolution in mode-locked quasicontinuous lasers. *IEEE J Quantum Electron* 10:115–124.

Nikitichev DI, Ding Y, Cataluna MA, Rafailov EU, Drzewietzki L, Breuer S, Elsaesser W, Rossetti M, Bardella P, Xu T, Montrosset I, Krestnikov I, Livshits D, Ruiz M, Tran M, Robert Y, Krakowski M (2012) High peak power and sub-picosecond Fourier-limited pulse generation from passively mode-locked monolithic two-section gain-guided tapered InGaAs quantum-dot lasers. *Laser Phys* 22:715–724.

Nikitichev DI, Ding Y, Ruiz M, Calligaro M, Michel N, Krakowski M, Krestnikov I, Livshits D, Cataluna MA, Rafailov EU (2011a) High-power passively mode-locked tapered InAs/GaAs quantum-dot lasers. *Appl Phys B-Lasers Opt* 103:609–613.

Nikitichev DI, Ruiz M, Ding Y, Tran M, Robert Y, Krakowski M, Rossetti M, Bardella P, Montrosset I, Krestnikov I, Lifshits D, Kataluna MA, Rafailov EU (2011b) Passively mode-locked monolithic two-section gain-guided tapered quantum-dot lasers: II. Record 15 Watt peak power generation. In: *CLEO Europe*, p CB3.4. Munich.

Nikolaev VV, Avrutin EA (2003) Photocarrier escape time in quantum-well light-absorbing devices: Effects of electric field and well parameters. *IEEE J Quantum Electron* 39:1653–1660.

Nikolaev VV, Avrutin EA (2004) Quantum-well design for monolithic optical devices with gain and saturable absorber sections. *IEEE Photonics Technol Lett* 16:24–26.

Nomura Y, Ochi S, Tomita N, Akiyama K, Isu T, Takiguchi T, Higuchi H (2002) Mode locking in Fabry-Perot semiconductor lasers. *Phys Rev A* 65:043807.

Otto C, Ludge K, Vladimirov AG, Wolfrum M, Scholl E (2012) Delay-induced dynamics and jitter reduction of passively mode-locked semiconductor lasers subject to optical feedback. *New J Phys* 14:113033.

Pimenov A, Vladimirov AG (2014) Theoretical analysis of passively mode-locked inhomogeneously broadened lasers. In: *14th International Conference on Numerical Simulation of Optoelectronic Devices* (Piprek J, Javaloyes J, eds.), pp. 151–152. 1–4 September 2014, Palma de Mallorca, Spain.

Quarterman AH, Wilcox KG, Apostolopoulos V, Mihoubi Z, Elsmere SP, Farrer I, Ritchie DA, Tropper A (2009) A passively mode-locked external-cavity semiconductor laser emitting 60-fs pulses. *Nat Photonics* 3:729–731.

Rafailov EU, Cataluna MA, Avrutin EA (2011) *Ultrafast Lasers Based on Quantum Dot Structures*. New York, NY/Berlin: Wiley.

Rebrova N, Huyet G, Rachinskii D, Vladimirov AG (2011) Optically injected mode-locked laser. *Phys Rev E* 83:8.

Renaudier J, Brenot R, Dagens B, Lelarge F, Rousseau B, Poingt F, Legouezigou O, Pommereau F, Accard A, Gallion P, Duan GH (2005) 45 GHz self-pulsation with narrow linewidth in quantum dot Fabry-Perot semiconductor lasers at 1.5 μm. *Electron Lett* 41:1007–1008.

Renaudier J, Duan GH, Landais P, Gallion P (2007) Phase correlation and linewidth reduction of 40 GHz self-pulsation in distributed Bragg reflector semiconductor lasers. *IEEE J Quantum Electron* 43:147–156.

Revin DG, Hemingway M, Wang Y, Cockburn JW, Belyanin A (2016) Active mode locking of quantum cascade lasers in an external ring cavity. *Nat Commun* 7:11440.

Rosales R, Merghem K, Martinez A, Akrout A, Tourrenc JP, Accard A, Lelarge F, Ramdane A (2011) InAs/InP quantum-dot passively mode-locked lasers for 1.55-mu m applications. *IEEE J Sel Top Quantum Electron* 17:1292–1301.

Rossetti M, Bardella P, Montrosset I (2011a) Time-domain travelling-wave model for quantum dot passively mode-locked lasers. *IEEE J Quantum Electron* 47:139–150.

Rossetti M, Bardella P, Montrosset I (2011b) Modeling passive mode-locking in quantum dot lasers: A comparison between a finite-difference traveling-wave model and a delayed differential equation approach. *IEEE J Quantum Electron* 47:569–576.

Salvatore RA, Sanders S, Schrans T, Yariv A (1996) Supermodes of high-repetition-rate passively mode-locked semiconductor lasers. *IEEE J Quantum Electron* 32:941–952.

Sato K (2003) Optical pulse generation using Fabry-Perot lasers under continuous-wave operation. *IEEE J Sel Top Quantum Electron* 9:1288–1293.

Schell M, Weber AG, Scholl E, Bimberg D (1991) Fundamental limits of sub-ps pulse generation by active mode-locking of semiconductor lasers: The spectral gain width and the facet reflectivities. *IEEE J Quantum Electron* 27:1661–1668.

Scollo R, Lobe HJ, Holzman JE, Robin E, Jackel H, Erni D, Vogt W, Gini E (2005) Mode-locked laser diode with an ultrafast integrated uni-traveling carrier saturable absorber. *Opt Lett* 30:2808–2810.

Scollo R, Lohe HJ, Robin F, Erni D, Gini E, Jackel H (2009) Mode-locked InP-based laser diode with a monolithic integrated UTC absorber for subpicosecond pulse generation. *IEEE J Quantum Electron* 45:322–335.

Shimizu T, Ogura I, Yokoyama H (1997) 860 GHz rate asymmetric colliding pulse modelocked diode lasers. *Electron Lett* 33:1868–1869.

Shimizu T, Wang XL, Yokoyama H (1995) Asymmetric colliding-pulse mode-locking in InGaAsP semiconductor lasers. *Opt Rev* 2:401–403.

Shore KA, Yee WM (1991) Theory of self-locking FM operation in semiconductor lasers. *IEE Proc J Optoelectron* 138:91–96.

Simos H, Rossetti M, Simos C, Mesaritakis C, Xu TH, Bardella P, Montrosset I, Syvridis D (2013) Numerical analysis of passively mode-locked quantum-dot lasers with absorber section at the low-reflectivity output facet. *IEEE J Quantum Electron* 49:3–10.

Stolarz PM, Javaloyes J, Mezosi G, Hou L, Ironside CN, Sorel M, Bryce AC, Balle S (2011) Spectral dynamical behavior in passively mode-locked semiconductor lasers. *IEEE Photonics J* 3:1067–1082.

Tandoi G, Javaloyes J, Avrutin E, Ironside CN, Marsh JH (2013) Subpicosecond colliding pulse mode locking at 126 GHz in monolithic GaAs/AlGaAs quantum well lasers: Experiments and theory. *IEEE J Sel Top Quantum Electron* 19:1100608.

Thompson MG, Rae A, Sellin RL, Marinelli C, Penty RV, White IH, Kovsh AR, Mikhrin SS, Livshits DA, Krestnikov IL (2006) Subpicosecond high-power mode locking using flared waveguide monolithic quantum-dot lasers. *Appl Phys Lett* 88:133119–133113.

Thompson MG, Rae AR, Xia M, Penty RV, White IH (2009) InGaAs quantum-dot mode-locked laser diodes. *IEEE Journal Sel Top Quantum Electron* 15:661–672.

Tzenov P, Burghoff D, Hu Q, Jirauschek C (2016) Time domain modeling of terahertz quantum cascade lasers for frequency comb generation. *Opt Express* 24:23232–23247.

Vasil'ev P (1995) *Ultrafast Diode Lasers: Fundamentals and Applications*. Boston: Artech House.

Viktorov EA, Erneux T, Mandel P, Piwonski T, Madden G, Pulka J, Huyet G, Houlihan J (2009) Recovery time scales in a reversed-biased quantum dot absorber. *Appl Phys Lett* 94:263502.

Viktorov EA, Mandel P, Vladimirov AG, Bandelow U (2006) Model for mode locking in quantum dot lasers. *Appl Phys Lett* 88:201102–201103.

Vladimirov AG, Pimenov AS, Rachinskii D (2009) Numerical study of dynamical regimes in a monolithic passively mode-locked semiconductor laser. *IEEE J Quantum Electron* 45:462–468.

Vladimirov AG, Turaev D (2005) Model for passive mode locking in semiconductor lasers. *Phys Rev A* 72:033808.

Vladimirov AG, Turaev D, Kozyreff G (2004) Delay differential equations for mode-locked semiconductor lasers. *Opt Lett* 29:1221–1223.

Wilcox KG, Mihoubi Z, Daniell GJ, Elsmere S, Quarterman A, Farrer I, Ritchie DA, Tropper A (2008) Ultrafast optical Stark mode-locked semiconductor laser. *Opt Lett* 33:2797–2799.

Williams KA, Sarma J, White IH, Penty RV, Middlemast I, Ryan T, Laughton FR, Roberts JS (1994) Q-switched bow-tie lasers for high-energy picosecond pulse generation. *Electron Lett* 30:320–321.

Xu TH, Montrosset I (2013) Quantum dot passively mode-locked lasers: Relation between intracavity pulse evolution and mode locking performances. *IEEE J Quantum Electron* 49:65–71.

Xu TH, Rossetti M, Bardella P, Montrosset I (2012) Simulation and analysis of dynamic regimes involving ground and excited state transitions in quantum dot passively mode-locked lasers. *IEEE J Quantum Electron* 48:1193–1202.

Yang WG (2011) Single-section Fabry-Perot mode-locked semiconductor lasers. *Adv Optoelectron* 2011:780373.

Yanson DA, Street MW, McDougall SD, Thayne IG, Marsh JH, Avrutin EA (2002) Ultrafast harmonic mode-locking of monolithic compound-cavity laser diodes incorporating photonic-bandgap reflectors. *IEEE J Quantum Electron* 38:1–11.

Yee WM, Shore KA (1993) Multimode analysis of self-locked FM operation in laser diodes. *IEE Proc J Optoelectron* 140:21–25.

Zarrabi JH, Portnoi EL, Chelnokov AV (1991) Passive-mode locking of a multistripe single quantum-well GaAs-laser diode with an intracavity saturable absorber. *Appl Phys Lett* 59:1526–1528.